

This microfiche was produced according to ANSI / AIIM Standards and meets the quality specifications contained therein. A poor blowback image is the result of the characteristics of the original document.

DOE/NASA/5776-2
NASA CR-195432

Collected Papers on Wind Turbine Technology

May 1995

(NASA-CR-195432) COLLECTED PAPERS
ON WIND TURBINE TECHNOLOGY (DASCOM
Engineering) 236 p

N95-27970
--THRU--
N95-27992
Unclas

G3/44 0049890

Prepared for
NATIONAL AERONAUTICS AND SPACE ADMINISTRATION
Lewis Research Center
Under Contract NAS3--25776

for
U.S. DEPARTMENT OF ENERGY
Conservation and Renewable Energy Technologies
Office of Management and Administration

DOE/NASA/5776-2
NASA CR-195432

Collected Papers on Wind Turbine Technology

David A. Spera, editor
DASCON Engineering
Bay Village, OH 44140

May 1995

Prepared for
National Aeronautics and Space Administration
Lewis Research Center
Cleveland, Ohio 44135
Under Contract NAS3-25776

for
U.S. DEPARTMENT OF ENERGY
Conservation and Renewable Energy Technology
Office of Management and Administration
Washington, D.C. 20545
Under Interagency Agreement DE-AI01-76ET20320

Preface

A major program of research and development projects on wind turbines for generating electricity was conducted at the NASA Lewis Research Center from 1973 to 1988. Most of these projects were sponsored by the U.S. Department of Energy (DOE), as a major element of its Federal Wind Energy Program. One other large-scale wind turbine project was sponsored by the Bureau of Reclamation of the U.S. Department of Interior (DOI). From 1988 to 1995, NASA wind energy activities have been directed toward the transfer of technology to commercial and academic organizations.

As part of these technology transfer activities, a total of 22 previously unpublished manuscripts have been assembled and are presented here in order to share the results of valuable research on wind turbines with the wind energy community. A wide variety of wind turbine technology topics are discussed, including the following:

-- Wind and wake models	3 papers
-- Airfoil properties	5 papers
-- Structural analysis and testing . .	5 papers
-- Control systems	3 papers
-- Variable-speed generators	3 papers
-- Acoustic noise	3 papers

Both experimental and theoretical investigations are described, with results which are relevant to the design, analysis, and testing of modern wind turbines.

Wind energy activities sponsored under or related to the NASA/DOE wind turbine development program are documented in approximately 620 publications by over 520 authors and co-authors. These include technical reports by NASA-Lewis personnel, reports by NASA contractors and grantees, papers presented at NASA-sponsored workshops and conferences by researchers from many different organizations, and outside publications by authors who conducted research on and around NASA/DOE experimental wind turbines. A complete listing of citations to these publications, many with abstracts, can be obtained from the following reference:

Spera, D. A., 1995, *Bibliography of NASA-Related Publications on Wind Turbine Technology, 1973 - 1995*, NASA CR-195462, DOE/NASA/5776-3, Cleveland, Ohio: NASA Lewis Research Center.

David A. Spera
Editor

Author Index

Barton, R. S.	157, 199
Blissel, W. A.	175
Connell, J. R.	1
Gluck, R.	79
Gregorak, G. M.	53
Grosveld, F. W.	211
Hinrichsen, E. N.	153, 185
Harris, W. L.	229
Hoffman, J. A.	79
Hosp, T. J.	157
Hubbard, H. H.	211
Hudson, T. L.	185
Jacobs, E. W.	207
Kelley, N. D.	221
Lipo, T. A.	185, 191
Lobitz, I. W.	89
Loyd, B.	229
McKenna, H. E.	221
Miller, A. H.	27
Miller, G. E.	67
Miller, R. D.	139
Mirandy, L.	99, 115
Ostowari, C.	35
Reddoch, T. W.	185
Schanzenbach, G. P.	157
Shepherd, K. P.	211
Shiple, S. A.	139
Snyder, M. H.	47
Spera, D. A.	17
Sridhar, S.	79
Strain, J. C.	99, 115
Tangler, J. L.	35
Thomas, R. J.	185
Wentz, W. H.	47
Wilson, R. E.	41
Zimmerman, D. K.	139

Contents

	Page
Preface	i
Author Index	ii

Part I: Wind and Wake Models

Basic Principles and Recent Observations of Rotationally-Sampled Wind	1
<i>J. R. Connell</i>	
Model of Rotationally-Sampled Turbulence for Predicting Fatigue Loads in Wind Turbines	17
<i>D. A. Spera</i>	
Large HAWT Wake Measurement and Analysis	27
<i>A. H. Miller, H. L. Wegley, and J. W. Buck</i>	

Part II: Airfoil Properties

Synthesization of Post-Stall Airfoil Characteristics for Aerodynamic Analysis of Horizontal-Axis Wind Turbines	35
<i>J. L. Tangler and C. Ostowari</i>	
Preliminary Analysis of Dynamic Stall Effects on a 91-meter Wind Turbine Rotor	41
<i>R. E. Wilson</i>	
Comparative Wind Tunnel Tests of NACA 23024 Airfoils With Several Aileron and Spoiler Configurations	47
<i>W. H. Wentz and M. H. Snyder</i>	
Comparative Wind Tunnel Tests at High Reynolds Numbers of NACA 64-621 Airfoils With Two Aileron Configurations	53
<i>G. M. Gregorek</i>	
Comparative Performance Tests on the Mod-2 2.5-MW Wind Turbine With and Without Vortex Generators	67
<i>G. E. Miller</i>	

Part III: Structural Analysis and Testing

Design of a Real-Time Wind Turbine Simulator Using a Custom Parallel Architecture ..	79
<i>J. A. Hoffman, R. Gluck, and S. Sridhar</i>	
A NASTRAN-Based Computer Program for Structural Dynamic Analysis of Horizontal-Axis Wind Turbines	89
<i>D. W. Lobitz</i>	

	Page
Aeroelastic Stability of Wind Turbine Blade/Aileron Systems	99
<i>J. C. Strain and L. Mirandy</i>	
Calculation of Design Loads for the Mod-5A 7.3-MW Wind Turbine System	115
<i>L. Mirandy and J. C. Strain</i>	
Comparison of Measured and Calculated Dynamic Loads for the Mod-2 2.5-MW Wind Turbine System	139
<i>D. K. Zimmerman, S. A. Shipley, and R. D. Miller</i>	

Part IV: Control Systems

Analysis Methods for Wind Turbine Control and Electrical System Dynamics	153
<i>E. N. Hinrichsen</i>	
Control System Design for the Mod-5A 7.3-MW Wind Turbine Generator	157
<i>R. S. Barton, T. J. Hosp, and G. P. Schanzenbach</i>	
Use of Blade Pitch Control to Provide Power Train Damping for the Mod-2 2.5-MW Wind Turbine	175
<i>W. A. Blissel</i>	

Part V: Variable-Speed Generators

A Conceptual Framework for Evaluating Variable Speed Generator Options for Wind Applications	185
<i>T. W. Reddoch, T. A. Lipo, T. L. Hudson, E. N. Hinrichsen, and R. J. Thomas</i>	
Variable Speed Generator Technology Options for Wind Turbine Generators	191
<i>T. A. Lipo</i>	
Variable Speed Generator Application on the Mod-5A 7.3-MW Wind Turbine	199
<i>R. S. Barton</i>	

Part VI: Acoustic Noise

Measurement and Prediction of Broadband Noise from Large Horizontal-Axis Wind Turbine Generators	211
<i>F.W. Grosveld, K. P. Shepherd, and H. H. Hubbard</i>	
Observed Acoustic and Aeroelastic Spectral Responses of a Mod-2 Turbine Blade to Turbulence Excitation	221
<i>N. D. Kelley, H.E. McKenna, and E. W. Jacobs</i>	
Anechoic Wind Tunnel Study of Turbulence Effects on Wind Turbine Broadband Noise	229
<i>B. Loyd and W. L. Harris</i>	

BASIC PRINCIPLES AND RECENT OBSERVATIONS OF ROTATIONALLY SAMPLED WIND

James R. Connell

N95-27971

Pacific Northwest Laboratory
Richland, Washington 99352

ABSTRACT

The concept of rotationally sampled wind speed is described. The unusual wind characteristics that result from rotationally sampling the wind are shown first for early measurements made using an 8-point ring of anemometers on a vertical plane array of meteorological towers. Quantitative characterization of the rotationally sampled wind is made in terms of the power spectral density function of the wind speed. Verification of the importance of the new concept is demonstrated with spectral analyses of the response of the MOD-OA blade flapwise root bending moment and the corresponding rotational analysis of the wind measured immediately upwind of the MOD-OA using a 12-point ring of anemometers on a 7-tower vertical plane array.

The Pacific Northwest Laboratory (PNL) theory of the rotationally sampled wind speed power spectral density function is tested successfully against the wind spectrum measured at the MOD-OA vertical plane array. A single-tower empirical model of the rotationally sampled wind speed is also successfully tested against the measurements from the full vertical plane array.

Rotational measurements of the wind velocity with hotfilm anemometers attached to rotating blades are shown to be accurate and practical for research on winds at the blades of wind turbines. Some measurements at the rotor blade of a MOD-2 turbine using the hotfilm technique in a pilot research program are shown. They are compared and contrasted to the expectations based upon application of the PNL theory of rotationally sampled wind to the MOD-2 size and rotation rate but without teeter, blade bending, or rotor induction accounted for.

Finally, the importance of temperature layering and of wind modifications due to flow over complex terrain is demonstrated by the use of hotfilm anemometer data, and meteorological tower and acoustic doppler sounder data from the MOD-2 site at Goodnoe Hills, Washington.

INTRODUCTION

Rotational sampling is a method of determining the character of the wind encountered by a segment of a rotating wind turbine blade. The concept of rotational sampling has undergone extensions in theory and observations and has been applied to wind turbine test and design. The basic principles of rotational sampling and some of our recent rotational measurements of the wind are presented in this paper.

Early in the development of the rotational sampling concept, wind measurements using vertical plane arrays of propeller anemometers in circles were analyzed to simulate the wind velocity experienced just ahead of a chordwise slice of a rotating rotor blade. Figure 1 is a sketch of the larger of those

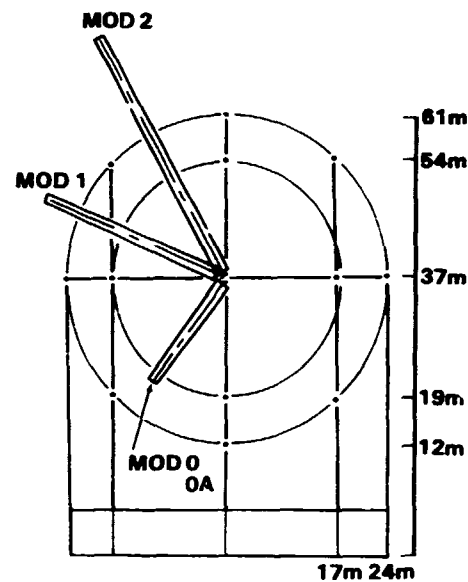


Figure 1--Sketch of the 37-m diameter vertical plane array at Hanford, Washington site

isolated vertical plane arrays, with circles of rotation, wind turbine blades and a height scale superimposed upon it.

Figure 2 shows graphs of the cross-disk (axial) wind speed as a function of time at each anemometer location on the vertical plane array (VPA) for an 8-minute period. The wind speed time series were smoothed slightly to remove the high-frequency fluctuations. Distinct similarities and differences between winds at different locations but at identical times can be seen at each of the eight locations around the circle. The wind speed fluctuations experienced by a point rotating around the circle of anemometers at the speed of a point on a rotor blade are obtained by sampling wind speed values from graph to graph around the circle and incrementing time with each change of graph (or location around the circle). This construction of a new time series of the wind speed fluctuations is called rotational sampling.

A time series of rotationally sampled axial wind speed is shown along with a time series of the axial wind speed measured at a single nonmoving point in the top graph in Figure 3. The substantial differences in character of these two time series are discussed in the next section.

CHARACTERISTICS OF ROTATIONALLY SAMPLED WIND VELOCITY

The time series of the wind speed in Figure 3 indicate qualitatively how differently the wind is seen by a stationary point and by a point revolving around a circle in a vertical plane set at right angles to the

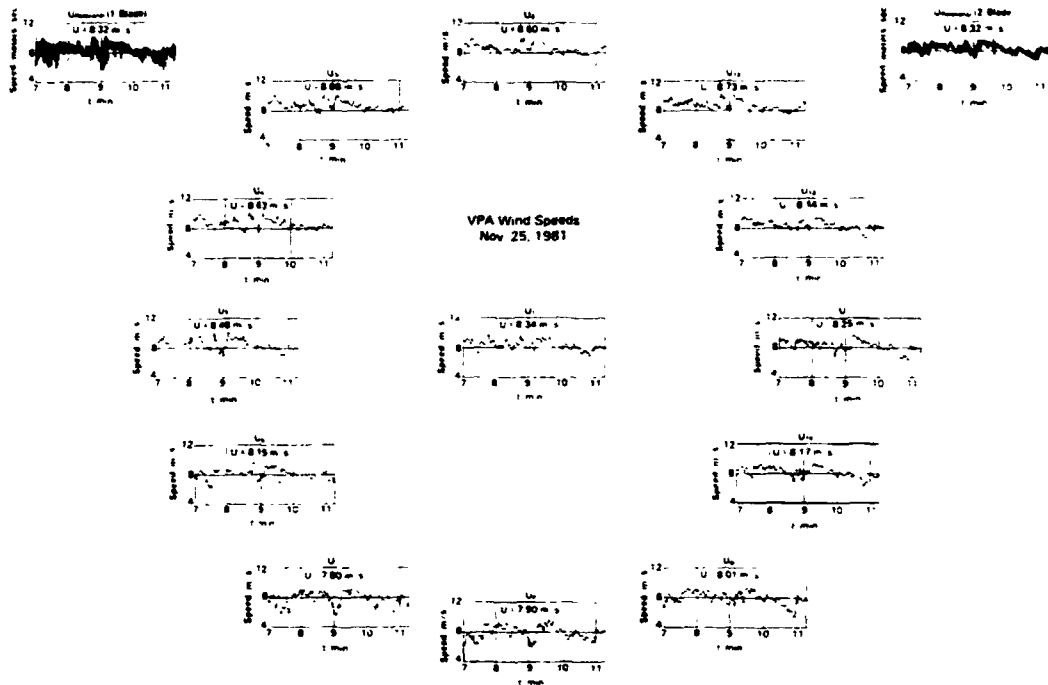


Figure 2--Graphs of axial wind speed as a function of time at each anemometer on the 37-m diameter vertical plane array

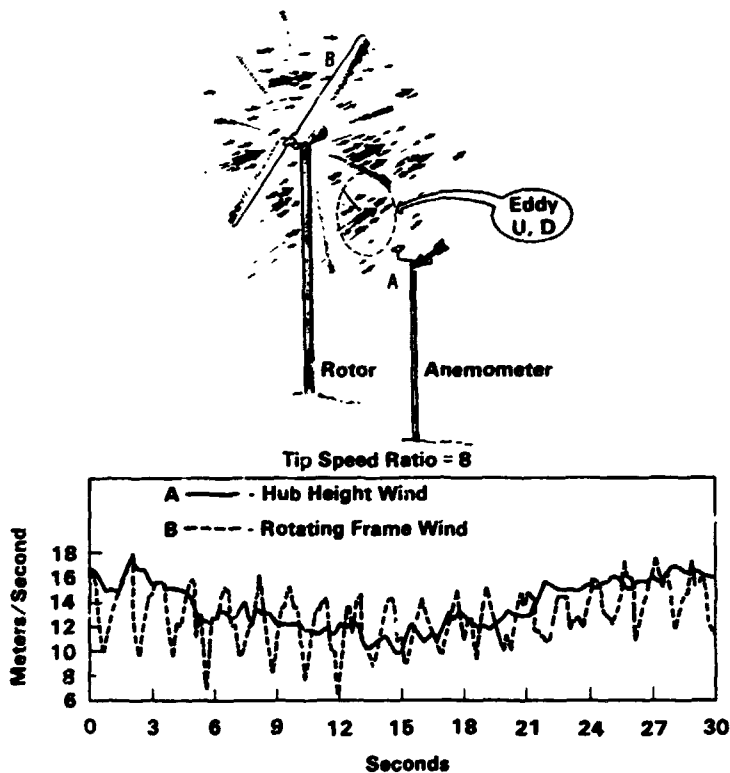


Figure 3--Schematic of wind at a wind turbine along with sample time series of real rotationally sampled wind speed

mean direction of the wind in the atmospheric boundary layer. To characterize a complicated time series of rotationally sampled wind speed fluctuations quantitatively, it is possible to

separate the time series into a large set of long time series of simple sine waves, each with a distinct single frequency of fluctuation and each with a specific constant amplitude of fluctuation.

If the values of all of these sine waves are added together at each instant the resulting single time series is exactly the original complicated time series.

It is relatively easy to see the contribution of the sine wave components to the total turbulence because the frequency and amplitude of oscillation of each time series are easily and unambiguously quantified. The amplitude associated with each frequency is often given as the amount of fluctuating wind energy per unit mass of air per unit span of frequency-of-fluctuation. This is called the power spectral density of the wind speed. A single curve of the power spectral density of the wind, covering all frequencies of sinusoidal components, characterizes the original wind time series in a distinct and quantitative manner. Schematic examples of the power spectral density plots for wind at a single point at the hub height of a wind turbine and for the rotationally sampled wind at a point moving in a vertical circle around the hub are shown by the solid curve in Figure 4.

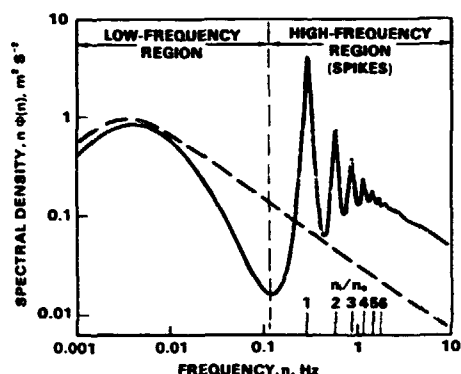


Figure 4--Schematic example of power spectral density graphs of single point wind speed (dashed curve) and rotationally sampled wind speed (solid curve)

The high-frequency region of the spectrum extends from half the frequency of rotation, $0.5 n(0)$, to the highest frequencies. In a more detailed classification, a midfrequency region surrounding the dip at the boundary between the low and high frequency regions of the spectrum is included. The regular set of spikes in the high frequency region is often labeled according to their center frequency, non-dimensionalized by the frequency of the rotation rate of the rotor. These frequencies are called the 1-P, 2-P, ... $[n(i)/n(0)]$ -P frequencies corresponding to the nondimensionalized frequencies marked and labeled in the lower right portion of the graph in Figure 4.

The main difference between the spectra for nonmoving and rotational sampling points is that the rotational spectrum has much more energy throughout the high frequency region. For rotational sampling, additional energy is concentrated in narrow bands, producing spikes at characteristic frequencies in the spectrum. Since rotational sampling does not produce turbulence, the total energy represented by the spectrum must not be different than the average of the energy of turbulence at the nonmoving points on the circle. This means that the fluctuations that are experienced at lower frequencies by nonmoving points are "shifted" to higher frequencies in specific ways by the rota-

tional sampling. Of course the rotational sampling does incorporate energy of fluctuation relative to the blade due to movement through the mean wind shear, but, as we shall see, even the rotational spectrum for turbulence and no wind shear looks like that shown in Figure 4.

The drawing of the wind turbine rotor in Figure 3 indicates the complex wind distribution the rotor experiences. The demonstrated character of the rotationally sampled wind led us to assert that measured response of a wind turbine was quite different than previously supposed and would correlate well with rotationally sampled wind, whereas it would not correlate well with wind measured at nonmoving points. An experiment set up at the MOD-OA turbine site in Clayton, New Mexico, confirmed the expectation and placed the concept of rotationally sampled wind on a firm foundation of observation and theory.

CORRELATION OF ROTATIONALLY SAMPLED WIND TO MEASURED MOD-OA RESPONSE

A vertical plane array of propeller anemometers on seven towers was installed two rotor diameters upwind of the MOD-OA wind turbine as shown in Figure 5. The circle of anemometers was centered on hub height with a radius equal to the rotor radius. Electrical signals representing time series of a few rotor response variables and generator power output were provided by NASA to be recorded digitally at fast sampling rates by PNL. The wind velocity data from the VPA were also recorded digitally at suitable rates on the same magnetic tape.

The flatwise root bending was expected to reflect most directly the fluctuations of the axial wind. (In fact we suggested the idea that the wind turbine should be its own best anemometer through flatwise root bending of the blades, torque of the rotor, and power out of the generator.) The spectra of the flatwise root bending moment for three different wind conditions are shown in the top row of Figure 6. The corresponding spectra for the power out of the generator are shown in the bottom row of Figure 6. The detailed similarity of the bending moment spectra to the rotationally sampled wind speed spectra previously discussed is strong. Figure 7 contains the spectra for the rotationally sampled wind corresponding to the three cases of Figure 6. The upper row of graphs is for the wind as measured; the lower row of spectra have the effect of mean wind shear removed. If one were to overlay the upper row of wind spectra on the flatwise root bending moment spectra of Figure 6, the two would appear to be nearly identical out to at least four times the rotation frequency of the rotor, and to be similar at higher frequencies. In the lower set of wind graphs, the mean wind shear appears to have the greatest effect for the case with a stably stratified atmosphere. In the neutral and unstable cases, the mean wind shear apparently has a much more moderate role in wind fluctuation effects on the turbine rotor.

This direct correlation between turbine and wind, without benefit of a transformation of the wind into turbine rotor response through an aerodynamic model and a mechanical model of the MOD-OA, is quite instructive, but less complete than desired. Efforts initiated by PNL to compute a suitable transformation from the wind have not yet been brought to a satisfactory completion. However, we have brought



Figure 5--Photograph of PNL seven-tower vertical plane array near the 200 kW MOD-0A at Clayton, New Mexico

wind theory far enough that a test of the theory against the wind measurements using the Clayton VPA has been fruitful. The theory of the rotationally sampled wind spectrum is discussed in the next section.

THEORY OF THE SPECTRUM OF ROTATIONALLY SAMPLED WIND SPEED FLUCTUATIONS

A theoretical description of the rotationally sampled wind speed is useful for verifying the rotational analysis of measurements from the VPA or direct

rotational measurements of the wind. The theory is especially helpful if there is concern that the effect of measurement or analysis errors on the character of the measurement-derived wind time series is significant. A tested wind theory is also a potentially convenient and low-cost tool for use in design and analysis of wind turbine response. Three approaches were initiated to develop a theory of the rotationally sampled wind speed spectral density function. Two of them represent the relation between the wind simultaneously at several radial locations but with, as yet, inadequate accuracy.

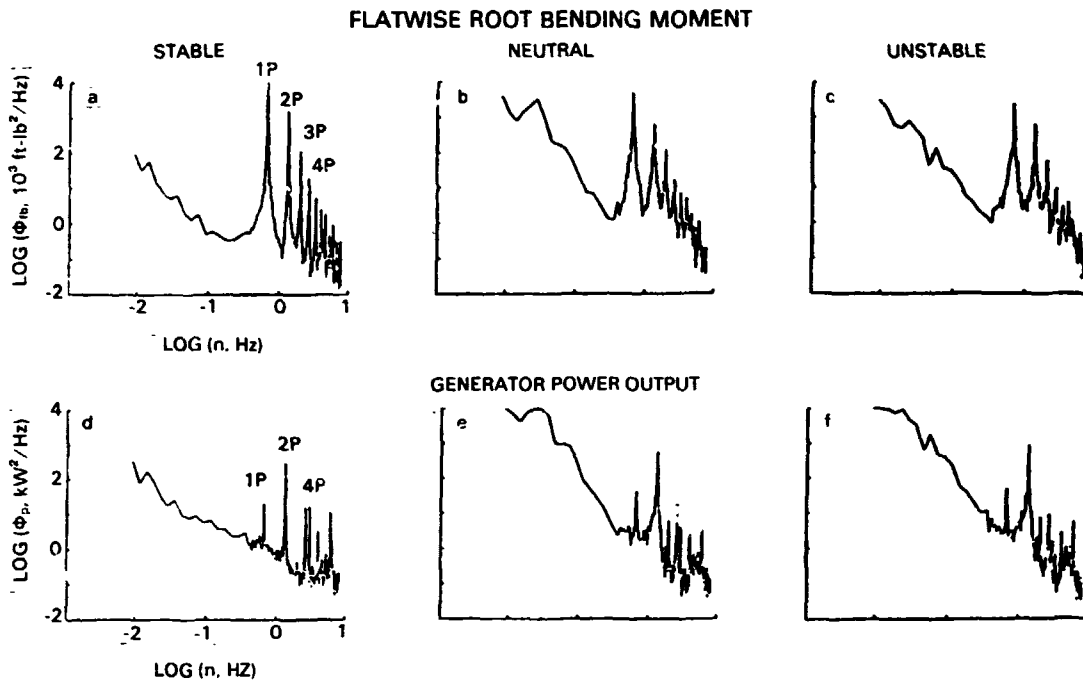


Figure 6--Power spectral density graphs of MOD-0A response to wind for three wind conditions. Top row: flapwise root bending moment. Bottom row: generator power output.

1 - BLADE SIMULATION

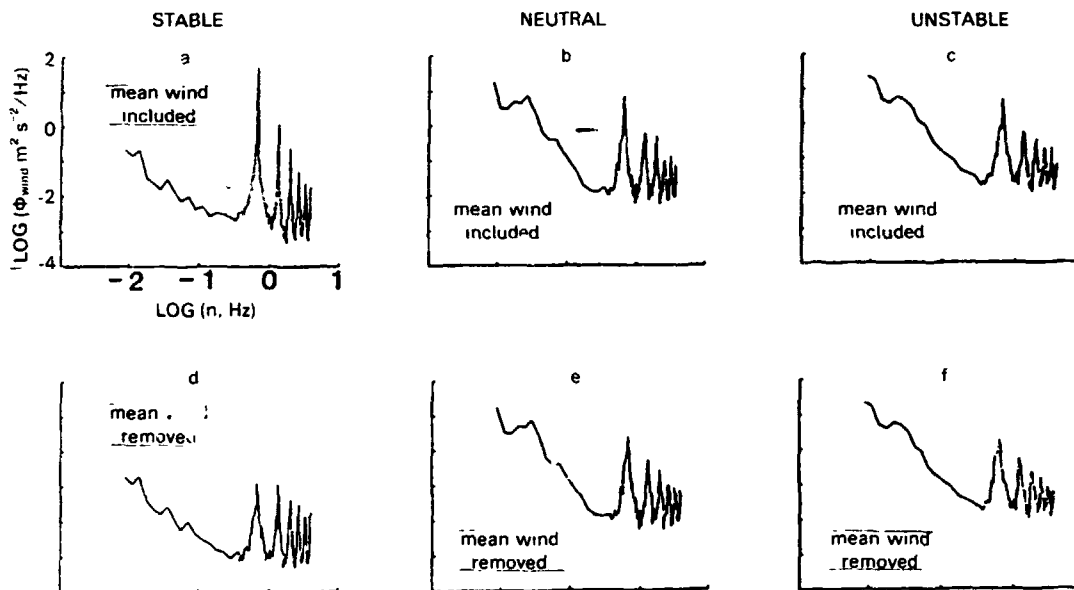


Figure 7--Power spectral density graphs of rotationally sampled axial wind speed corresponding to the MOD-0A response graphs in Figure 6. Top row: complete wind. Bottom row: mean wind shear effect removed.

Of the three theoretical constructs, at this time the simplest one results in the most accurate and complete spectrum. It is also the least costly to calculate using a digital computer. It was formulated in cylindrical coordinates with economy and accuracy for rotor problems in mind. It has the present restriction

that it does not give the phase relation between the wind at several radial locations.

An example of the theoretical spectral density of the axial wind speed compared to the spectrum calculated from measurements of axial wind using the VPA at

Clayton is shown in Figure 8. The goodness of this comparison is taken to confirm the concept of the rotationally sampled wind and to indicate the accuracy of the theory for normal wind conditions. A quantitative comparison between measurement and theory is conveniently made using integrals of the spectra over small bands of frequency surrounding individual spikes of the spectra. The magnitudes of energy of fluctuation that result, called partial variances, are plotted as a function of center frequencies in Figure 9. Comparisons for the three different atmospheric stability cases are shown in the three graphs. Theory deviates the most from measurement for the case of stable stratification, for which the basic assumptions of the theory are least suited.

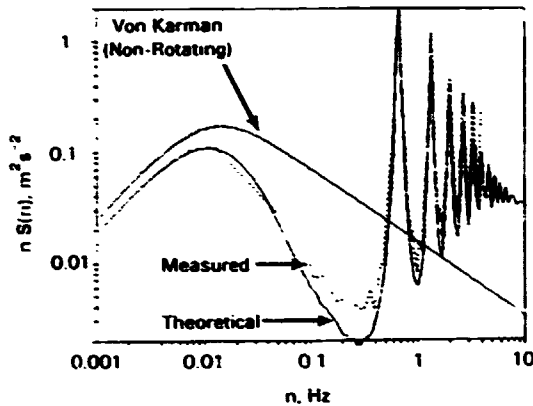


Figure 8--Comparison of theoretical power spectral density function of rotationally sampled wind speed for a MOD-OA wind turbine with rotationally sampled wind speed measured at the MOD-OA vertical plane array. Nearly neutral case.

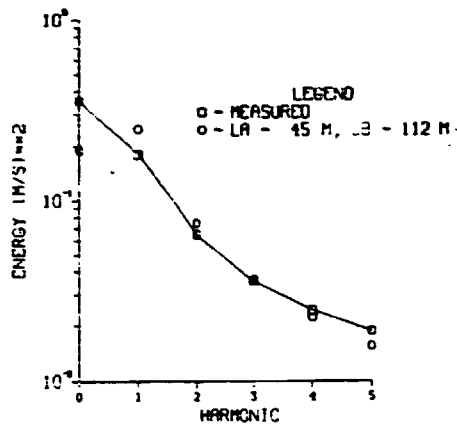


Figure 9--Theoretical variance of rotationally sampled wind speed for each spectral spike compared with the corresponding variance of wind speed measured at the MOD-OA vertical plane array. Nearly neutral case.

A SINGLE TOWER MODEL OF ROTATIONALLY MEASURED WIND SPEED

For conditions of terrain or atmospheric stability in which the present theory is unsuitable a full rotational measurement of the wind is not possible,

it would be helpful if turbulence data from several heights on a single tower could be analyzed to give a useful approximation. A model, STRS-2, was developed using wind measurements from the center tower of the VPA at Clayton.

The wind speeds at the VPA center tower were composited into the STRS-2 model of a rotationally measured time series using a special type of rotational sampling of the data from anemometers, with appropriate lead times and lag times at different heights. The result, compared to the spectra derived using the full VPA, is shown for three stability conditions in the spectra in Figure 10. The model is suitable for some purposes without correction; correction factors were also developed for the MOD-OA rotor diameter and hub height and the wind conditions at Clayton. However, the applicability of the model and correction factors to other sizes of turbines and other wind conditions is unknown.

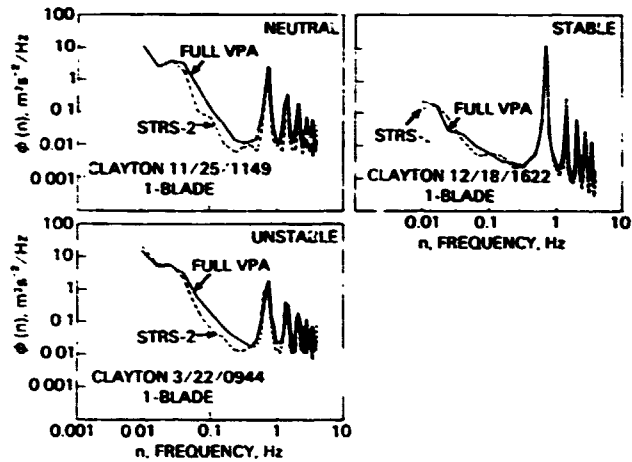


Figure 10--STRS-2 model rotationally sampled wind spectra derived from anemometers on a single meteorological tower compared to full vertical plane array rotational spectra

The need to test existing models of rotationally sampled wind characteristics scaled up for turbines larger than the MOD-OA led to additional measurement programs using wind velocity sensors whose use for the larger turbine geometries is more economical than use of propeller anemometers on arrays of towers. The remainder of this paper discusses results from the use of fast-responding hotfilm anemometers placed on rotating booms and on a MOD-2 rotor, 300 feet in diameter.

HOTFILM ANEMOMETER ROTATIONAL MEASUREMENTS OF THE WIND

To make rotational measurements of the wind at a location very near a rotating blade with acceptable economy and accuracy, the hotfilm anemometer was specialized and tested using a rotating boom apparatus similar to the one shown in Figure 11. The tiny wind velocity sensor is placed on a probe extending ahead of the leading edge of the boom, which is rotated at known speed using an electric motor. The three components of the wind relative to the moving sensor, which were measured under light wind conditions, are characterized by the three spectra shown in Figure 12. These spectra are for the horizontal axis

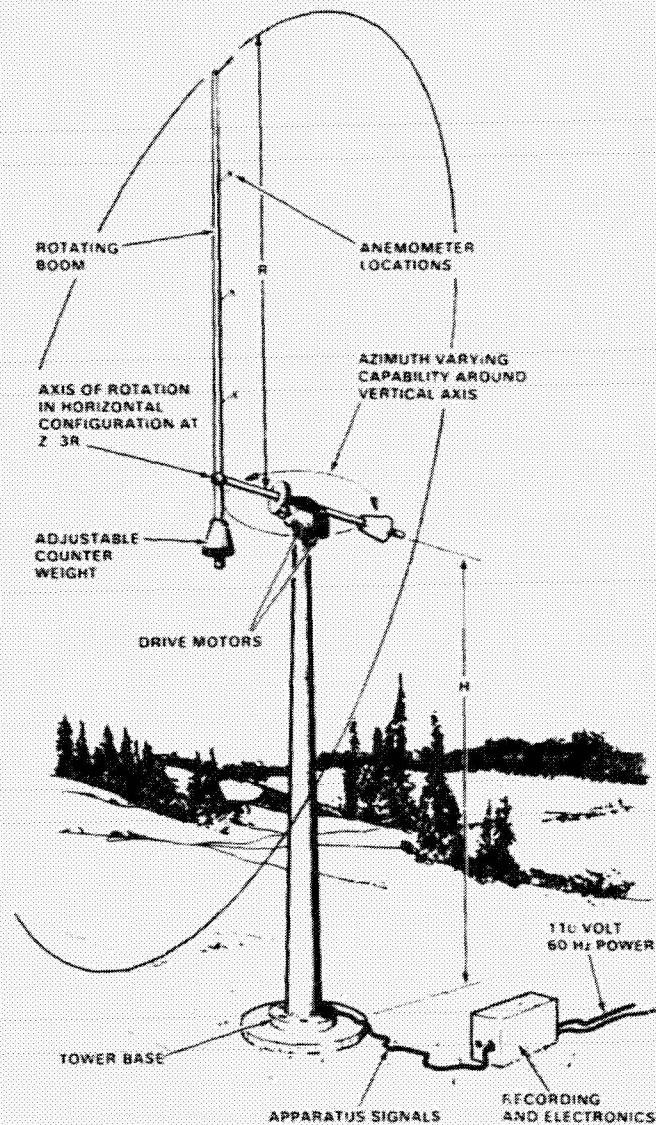


Figure 11--Picture of a rotating boom apparatus for rotational measurement of wind velocity and testing of turbulent wind velocity sensors

of rotation configuration. The results verify the earlier rotational sampling results from the VPAs. The hotfilm measurements require precise calibration and data reduction to achieve the required accuracy of measurement. One useful demonstration of the accuracy that may be achieved is the comparison of wind measurements made using two hotfilm anemometers placed 6 inches apart at the tip of the rotor on the rotating boom apparatus. The results for one example are shown in Figure 13. The axis of the rotating boom was vertical for this example. Thus the sensors traveled in a horizontal circle, moving with and against the wind at opposite sides of the circle. The mean wind speeds relative to the sensors for a 6-minute period are identical for the two sensors with an error of less than 0.5%. They also agree with the relative wind speed calculated as the product of boom radius and rotation angular velocity.

The time series of speed of the tangential wind speed for the two anemometers shown in the top graph of Figure 13 indicate that the measurements are nearly

identical at each instant. The cross-disk or transverse velocity time series are also nearly identical. The main difference is due to slight differences in angle of attack of the two anemometers as indicated by the nonzero magnitudes of the mean transverse velocities. These geometrical problems may be resolved in the computational data reduction phase of the wind data analysis.

With the knowledge that highly accurate rotational measurements of the wind velocity could be made with the hotfilm anemometers, we initiated measurements of the wind at the blades of a MOD-2 wind turbine, 300 feet in diameter. Some results from a pilot study at Goodnoe Hills, Washington, are discussed in the next section.

ROTATIONAL MEASUREMENTS OF THE AXIAL WIND SPEED OF A MOD-2 WIND TURBINE ROTOR

Pilot measurements at the MOD-2, unit number 2, at Goodnoe Hills were made in August 1983. The location

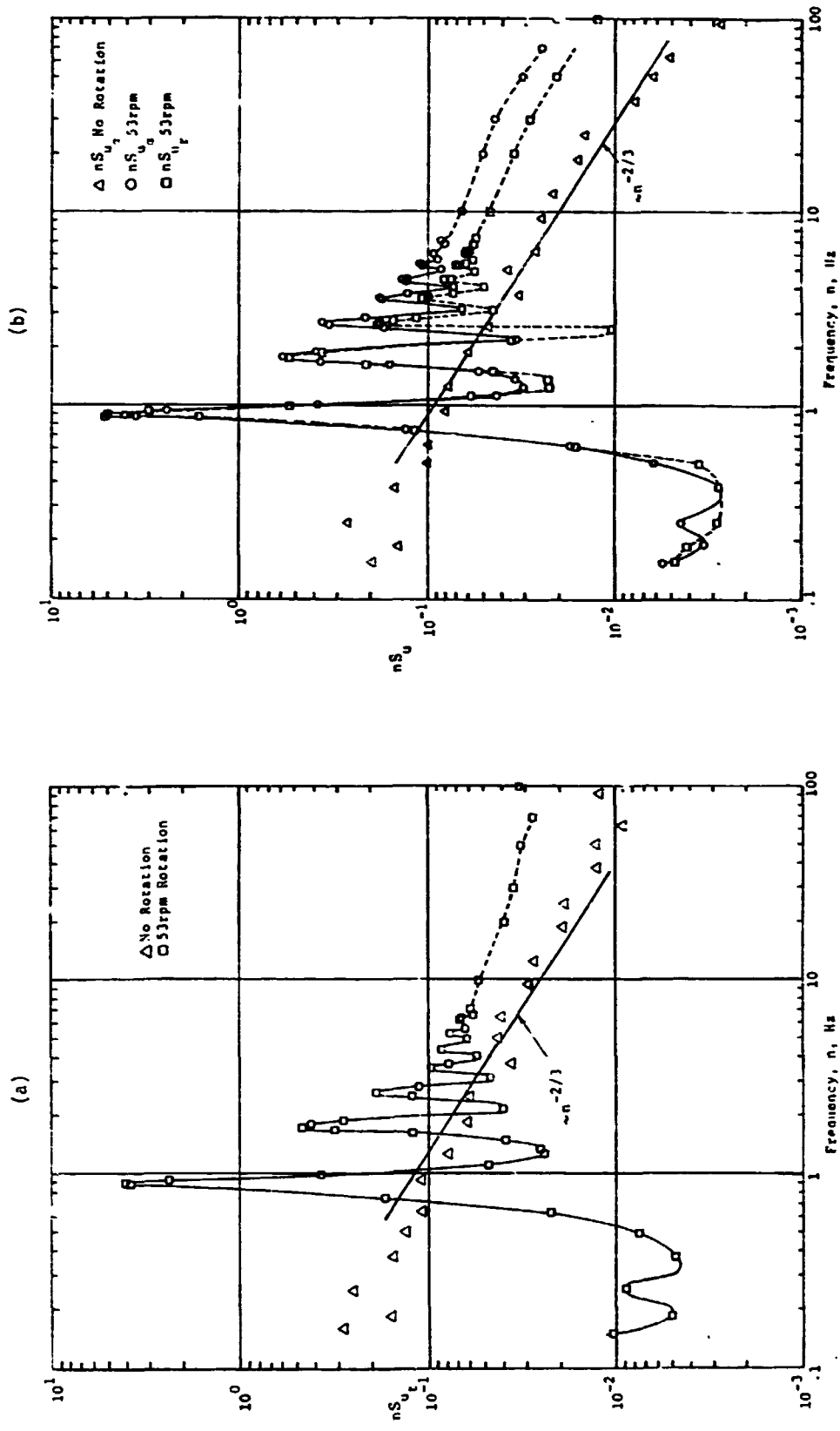


Figure 12--Power spectral density curves of three orthogonal components of the wind velocity rotationally measured with hotfilm anemometers on the PNL rotating boom in horizontal axis configuration
 a) wind tangential to sensor rotation path b) wind radial and wind axial to rotation circle

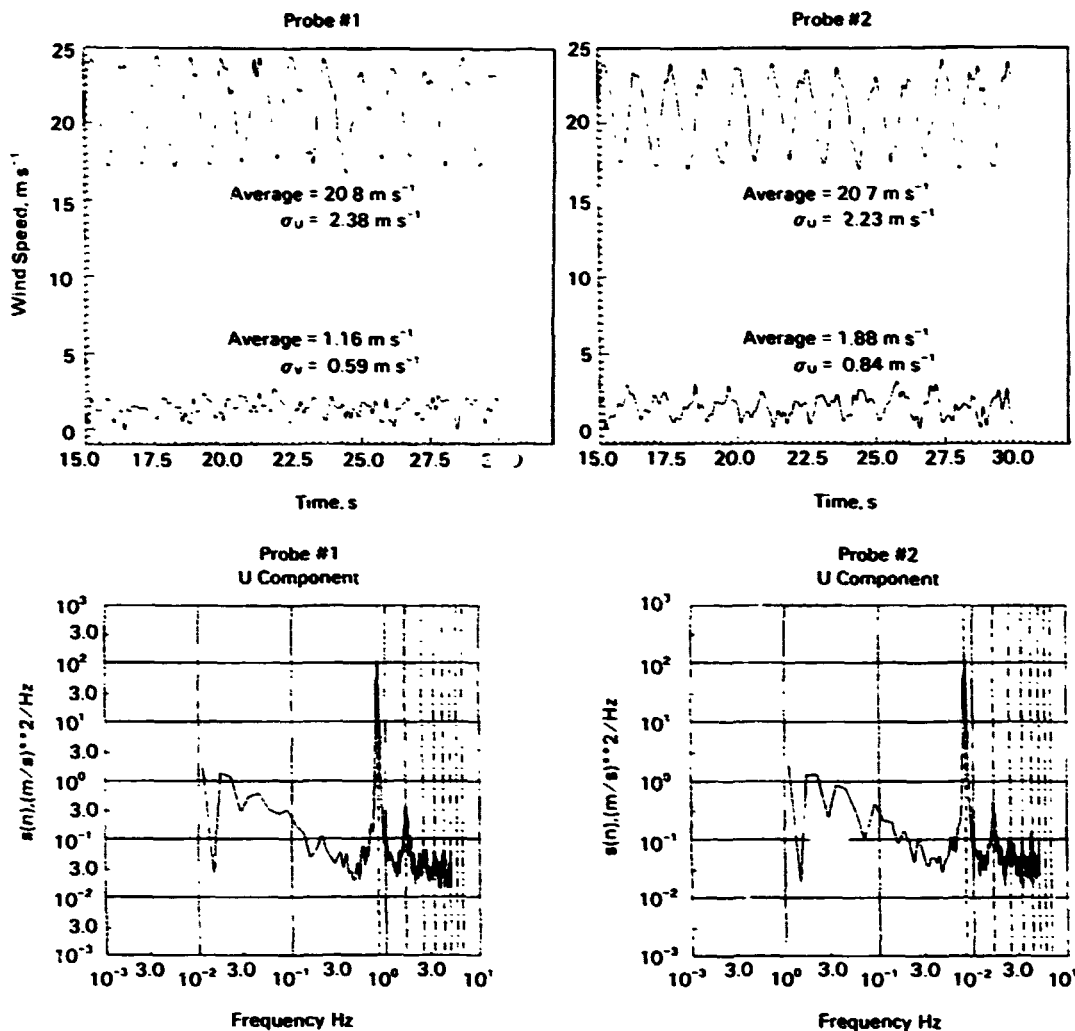


Figure 13--Comparison of time series and spectra of wind velocity components rotationally measured by two side-by-side hotfilm anemometers on a vertical axis rotating boom. Top two graphs: tangential wind speed. Bottom two graphs, axial (cross disk) wind speed.

of hotfilm anemometer booms on the rotor is shown in Figure 14. One probe was placed at the 0.7 radius position on each blade. Another pair of probes was placed at the 0.2 radius positions on the rotor. (These locations were dictated by the availability of attachment structures for use in the pilot program.) The wind velocity was thus measured relative to the motion of the rotor. That motion included rotation, teeter and blade bending.

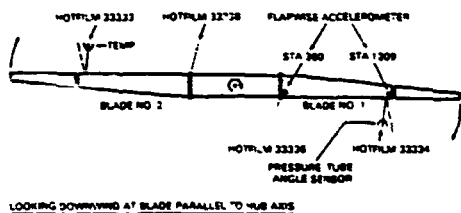


Figure 14--Location of hotfilm anemometers on the rotor blade for the 1984 pilot study at the MOD-2 #2 wind turbine at Goodnoe Hills

As we expected, we observed rotationally measured wind spectra that look somewhat like the spectra for rigid rotors discussed previously, but with some deviations in spectral energy distribution due to the teeter and flap motions. Also, we expected from theory to observe spectral shapes at an 0.7 R location distinctly different from those at an 0.2 R location. This latter expectation is demonstrated in Figure 15, which contains plots of the theoretical rotationally sampled wind speed spectrum. They were calculated for 10 radial locations along a blade of a MOD-2 for typical turbulent wind conditions in simple terrain. The rotational sampling effect is diminished at the 0.1 R and 0.2 R locations especially because the linear speed of rotation of the sensor at these small radii is small.

One example of the actual spectral density functions of the axial or cross-disk wind measured rotationally from each of the four locations on the rotor is shown in Figure 16. The expectation that the inner radial location would experience diminished rotational effect at frequencies higher than the rotation

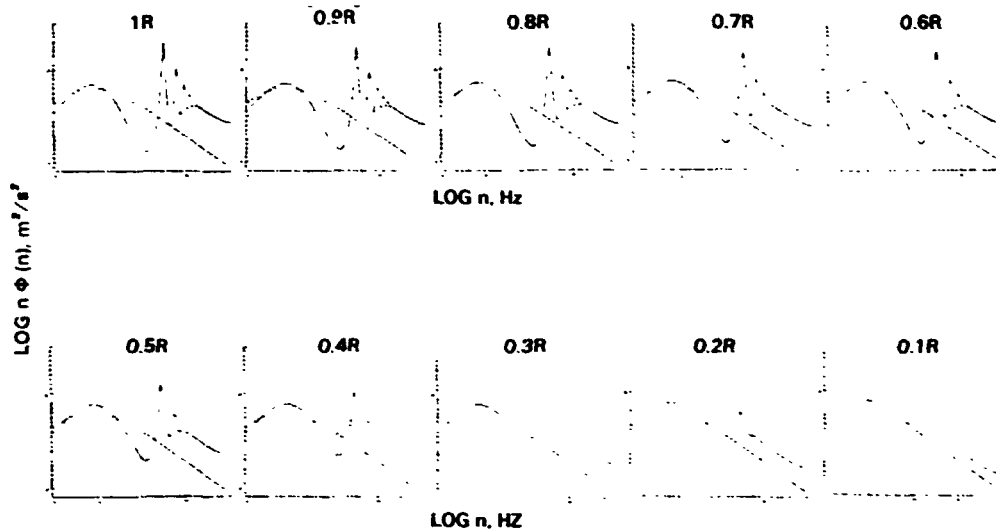


Figure 15--Expected radial distribution of power spectral density functions of the rotationally sampled axial wind speed derived from PNL theory. Neutral case.

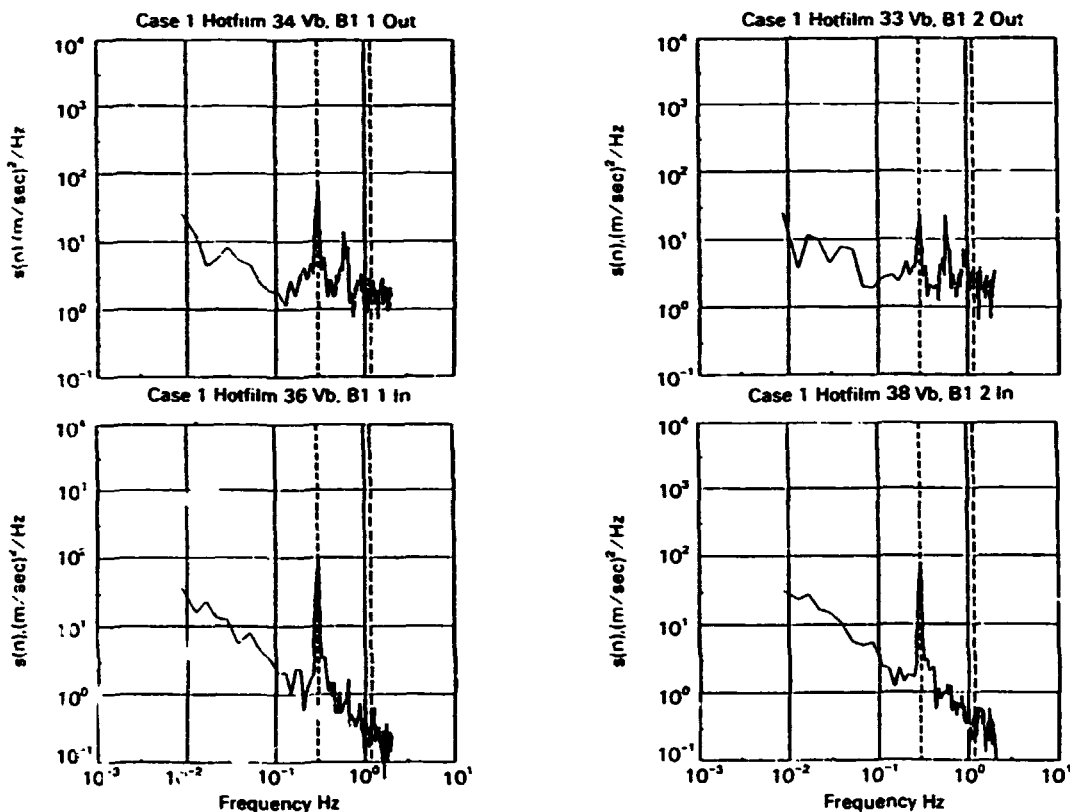


Figure 16--Power spectral density functions of rotationally measured axial wind speed at four diametral locations, for MOD-2 #2 wind turbine. Neutral case.

frequency of the rotor is clearly verified. The large spikes in the spectra at 0.2 R at the frequency of rotation of the rotor were not predicted by the theory. However, the theory did not include modified mean wind shear caused by flow induced by the nacelle, tower and the inner sections of the blades of the turbine.

The spectra for the wind at the 0.7 R locations on each blade are nearly identical to each other. The

differences may be due to differences in motion and orientation of the two blades. Compared to the spectra obtained from the VPA, rotating boom, and theory, the MOD-2 wind spectra at 0.7 R have substantial differences in the high frequency spikes. One reason for the differences is that the VPA and rotating boom winds were measured and analyzed relative to coordinate systems that were rigidly fixed in a single plane. Similarly, the theoretical model was applied to the rigid rotor case. However,

the sensors of wind for the MOD-2 were attached to a teetering and bending rotor blade. This may be the reason why the spectra for the MOD-2 have relatively smaller spikes at 1P (teeter), 3P and 4P (flapwise or axial blade bending). Nevertheless, the sensors measure the wind experienced immediately ahead of the rotor blades, which is the correct location to describe the wind used in a time-domain aerodynamic model of the rotor.

A brief look at the MOD-2 flapwise blade bending moment spectra in Figure 17, corresponding to the wind spectra in Figure 15, is instructive. The root bending moments for the two blades are shown in the bottom two graphs. They are identical, perhaps due to the effect of rotor teetering in forcing a sharing of the effect of the bending forces on each whole blade. The moments for the tip sections are not quite identical to each other; but they are not directly coupled to each other through the teetering mechanism. The spikes of the spectra around 1P and 2P are approximately of the same relative magnitude as they are in the wind spectra at the 0.7 R locations. The 3P response is light, reflecting the smallness of the wind spectrum spike and the lack of resonance at that frequency. The 4P blade spike is substantially larger than the corresponding wind spike, reflecting the first flapwise symmetric bending mode near that frequency.

These preliminary efforts at describing the relation of the blade bending spectra to the rotationally

measured wind spectra need to be replaced by accurate dynamic modeling of the response of the turbine using a model that has been tested for a simpler wind turbine and simpler conditions for rotationally sampled wind measurements. The wind and turbine data that seem to be required for this first phase are available from the VPA experiments at the Clayton MOD-0A site. Some modeling of the MOD-2 case has begun at other laboratories.

EFFECTS OF ATMOSPHERIC TEMPERATURE LAYERING

The impact of atmospheric temperature stratification and of the attendant mean wind and turbulence stratification on the character of rotationally measured wind velocity is substantial. We would be negligent in not including at least an example of the effect in this paper. Figure 18 shows time series of the voltage signals from a hotfilm anemometer on the blade of the MOD-2 for four different examples of temperature layering in the atmosphere. In each case the voltage from film 2 is closely proportional to the wind velocity crossing the disk of the rotor.

In the strong inversion case at the top of Figure 18, the wind speed fluctuates with a dominant period equal to that of the rotation of the rotor. The amplitude is rather constant from cycle-to-cycle. Sometimes the variation is so smoothly sinusoidal that there appears to be no turbulence. At other times the turbulence and nonlinearity of wind shear are so great that the waveform is ragged or even

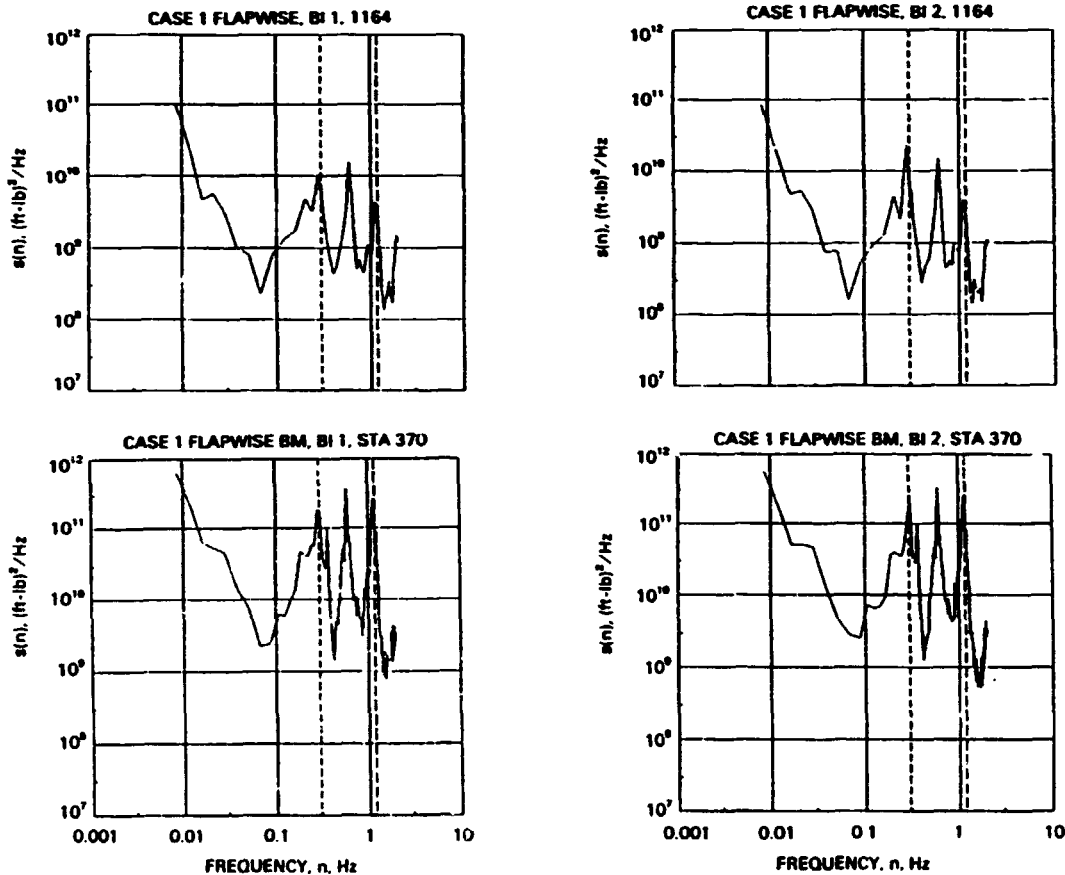


Figure 17--Power spectral density functions of blade flapwise root bending moment corresponding to the wind spectra in Figure 16.

SPLITFILM VOLTAGE VS TIME FOR BLADE 2, $\alpha = 0.28$

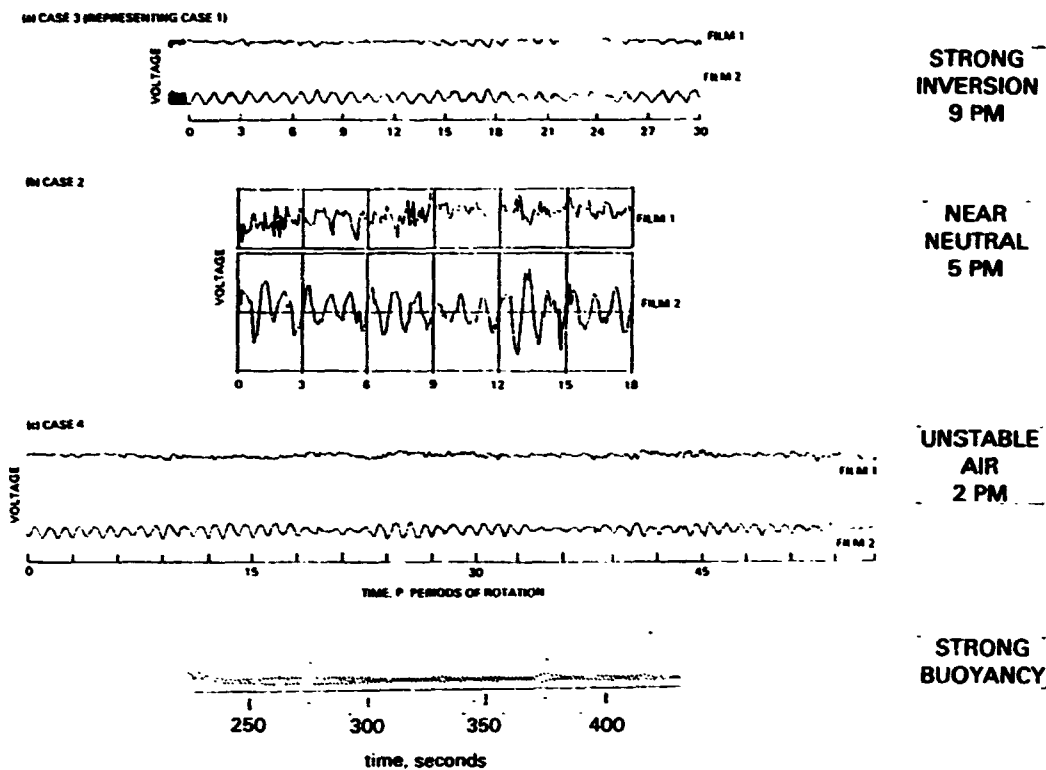


Figure 18--Hotfilm anemometer signals representing the different character of time series of rotationally measured axial wind speed for four different conditions of atmospheric static stability (temperature layering) at the MOD-2 #2 wind turbine

triangular. A more nearly neutral stability of the atmosphere results in turbulence that causes substantial random variations in the shape and amplitude of the cyclic wind time series. This is shown in the second graph, case 2. As the air becomes filled with buoyant motions during the heat of the day, the air is unstable. The character of the rotationally sampled wind then indicates the strong influence of the passage of large turbulent structures that modulate the wind fluctuations at the blade in a regular way. The last two graphs show that in unstable conditions the amplitude of the cyclic variations of the wind may occur in either of two modes. One simply appears to turn on and off the large constant amplitude fluctuations. The other produces a smoothly varying modulation of the cyclic amplitude.

Another factor that may strongly influence the character of the rotationally sampled wind is airflow over complex terrain. This is discussed briefly in the next section.

COMPLEX TERRAIN

Where airflow conditions are not simple (see topographic map of Goodnoe Hills in Figure 19), there is little information from theory or empirical models by which to estimate the character of the turbulent wind. It is not yet known how the changes in character of the wind modify the rotationally sampled wind. What can be shown are the differences in profiles of the mean wind speed and wind speed

variance about the mean at different locations in the complex terrain at Goodnoe Hills, Washington. From the differences one can conclude that there is a need for further research on both complex terrain wind characteristics and rotationally sampled wind at turbine rotors in complex terrain.

In support of this conclusion, consider the vertical profiles of wind at Goodnoe Hills shown in Figure 20. The measurements were made at the three sites identified as PNL, BPA and Acoustic Sounder in the map in Figure 19. Substantial differences are indicated to be due to the separation of the measurement locations by horizontal distances of a few rotor diameters and by vertical distances of a few tens of feet. The meaning of these spatial differences for the character of the rotationally sampled wind is indicated by the theoretical spectra plotted in Figure 21.

The plotted rotational spectra are for a single turbine rotor at the same mean wind speed and same vertical profiles of mean wind and variance. The difference in wind for each spectrum is the length scale characterizing the turbulence elements comprised in the flow. Clearly, substantial effects occur that might not have been expected. Complex terrain can modify length scales of turbulence to create such deviations in character.

CONCLUDING REMARKS

The objective of this paper has been to provide some insight into the basic principles of describing the

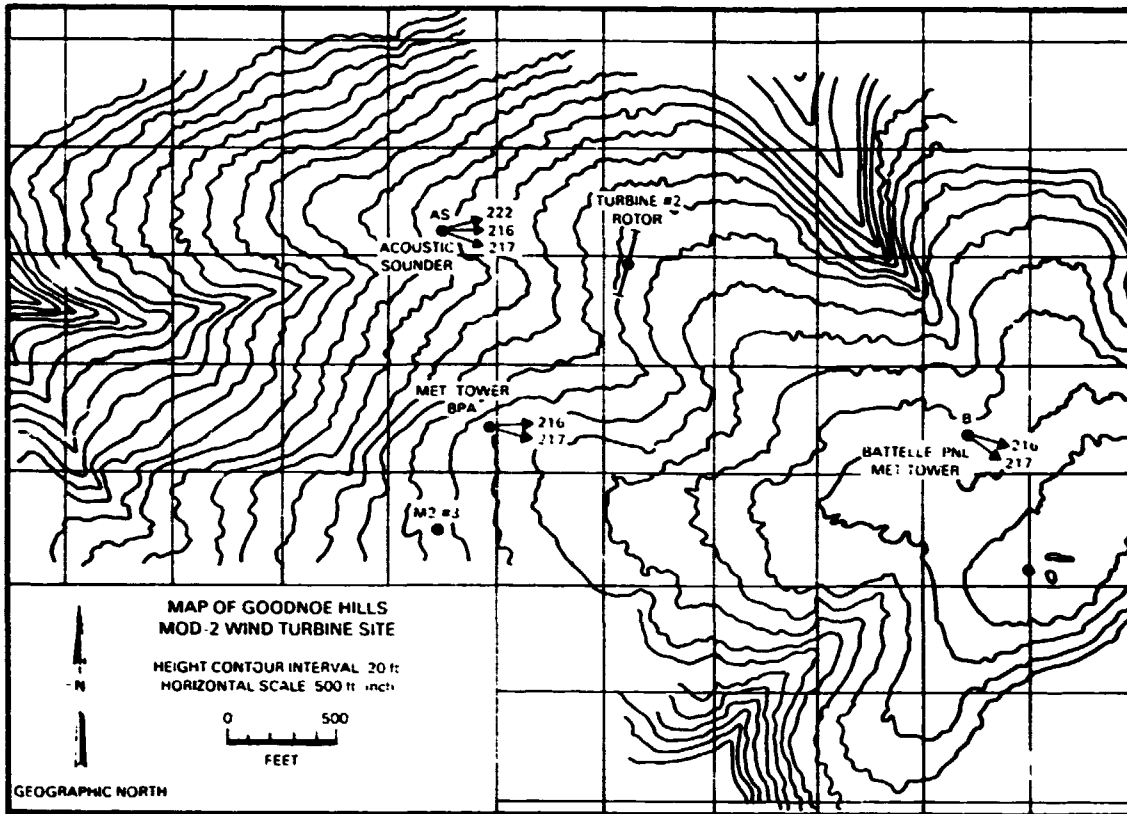


Figure 19--Topographic map of the MOD-2 site at Goodnoe Hills, Washington, showing the location of PNL and BPA meteorological towers and of the acoustic doppler wind velocity profiler relative to MOD-2 #2 location

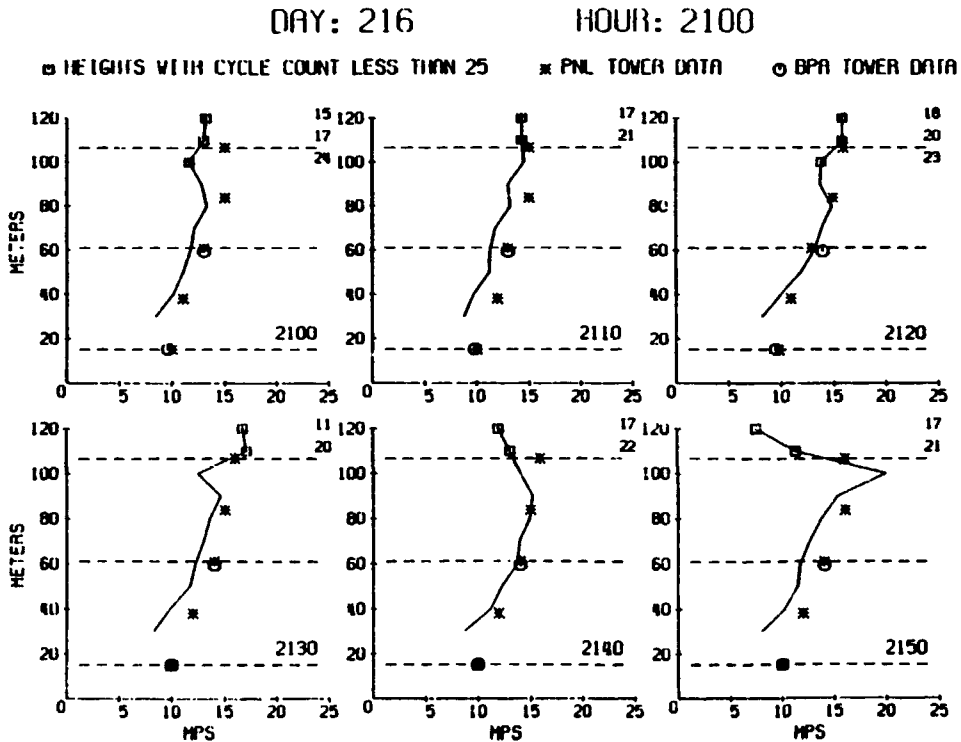


Figure 20--Examples of 10-minute average vertical profiles of wind speed measured at three different locations (PNL, BPA and Acoustic) in the topography of Goodnoe Hills, Washington

Solid Line - Rotational
Dashed Line - von Karman

U = 8.21M/S, Z = 30.5M, R=19.05M, N₀=0.667HZ SIGU=0.90M/S, Z₀=0.005M

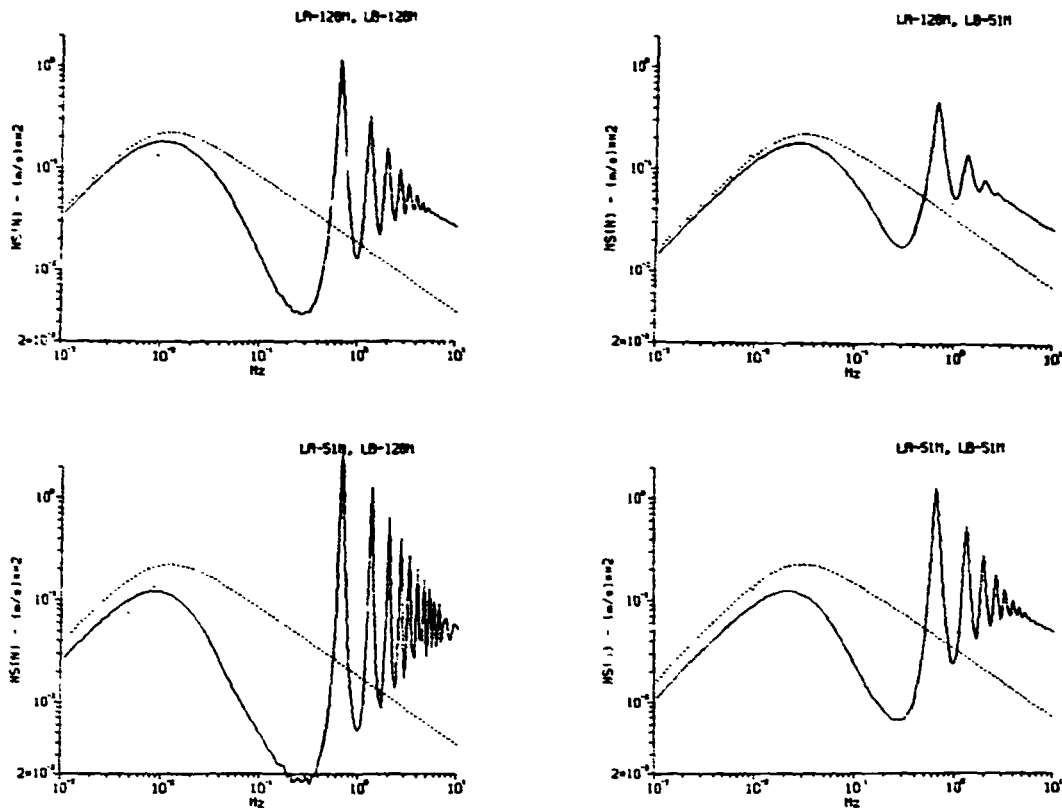


Figure 21--Effect on the theoretical spectrum of rotationally sampled wind speed at a MOD-0A wind turbine due solely to changes in length scales of turbulent wind, simulating one effect of topography

wind fluctuations as they are experienced by a point on a rotating wind turbine blade. The method used in the previous sections was to outline the historical development of an understanding of the rotationally sampled wind and its relation to wind turbine response. Over the years, we have taken a rather wide-ranging, though limited because of programmatic constraints, approach to research into rotationally sampled wind and corresponding response of wind turbines (1,2). Those efforts are briefly recapitulated here.

The research at the MOD-0A in Clayton, New Mexico using a vertical plane array conclusively demonstrates the importance of rotationally sampled wind velocity in explaining the response of a wind turbine to the wind. The pilot research at the MOD-2 in Goodnoe Hills, Washington, using hotfilm anemometers attached to the rotor blades shows that a relatively economical set of rotational measurements of the wind velocity at the rotor of a large wind turbine can be made. The tests of the hotfilm anemometers at the PNL rotating boom apparatus demonstrate that the accuracy of the hotfilm measurements of wind velocity required for design and testing of wind turbines can be achieved and maintained.

We conclude that the PNL theory is sufficiently accurate at all frequencies of wind fluctuation of importance that its extension into the time domain from the frequency domain is warranted. That effort is in progress.

A final conclusion is that the effects of vertical variation of temperature and of complex terrain airflow on the character of rotationally sampled wind velocity are substantial, but are not well known qualitatively and are nearly unknown at the quantitative level. Our understanding of the character of the wind in simple terrain is substantial, requiring significant improvement primarily in understanding of radial variation of the wind velocity along the blade at each instant. Thus, practical use of theory and empirical models of rotationally sampled wind can be made at the present time. On the other hand, radial distributions of wind along the blade, including phase relationships or complex airflow cases, can be handled at the present time only by direct measurements of rotationally sampled wind velocity using the method described in this paper.

REFERENCES

1. Connell, J. R. "Turbulence Spectrum Observed by a Fast-Rotating Wind Turbine Blade", PNL-3426, Pacific Northwest Laboratory, Richland, Washington, 1980.
2. Connell, J. R. "The Spectrum of Wind Speed Fluctuations Encountered by a Rotating Blade of a Wind Energy Conversion System: Observations and Theory", PNL-4083, Pacific Northwest Laboratory, Richland, Washington, 1981.
3. Rosenbrock, H. H. "Vibration and Stability Problems in Large Turbines Having Hinged Blades", C/T 113, ERA Technology, Ltd., Surrey, England, 1955.

ACKNOWLEDGEMENTS

A pioneering bit of theory has lain buried in a small section of a Doctoral Thesis and a report by H. H. Rosenbrock that were published in 1955 in England (3). Rosenbrock's work was brought to light after the first PNL measurement results were published and interpreted in terms of physical processes in the wind.

This project was sponsored by the U.S. Department of Energy. Pacific Northwest Laboratory is operated for the U.S. Department of Energy, under Contract DE-AC06-76RLO 1830, by Battelle Memorial Institute.

A MODEL OF ROTATIONALLY-SAMPLED WIND TURBULENCE
FOR PREDICTING FATIGUE LOADS IN WIND TURBINES

N95-27972

David A. Spera

DASCON Engineering
Bay Village, Ohio 44140

ABSTRACT

Empirical equations are presented with which to model rotationally-sampled (R-S) turbulence for input to structural-dynamic computer codes and the calculation of wind turbine fatigue loads. These equations are derived from R-S turbulence data which were measured at the vertical-plane array in Clayton, New Mexico. For validation, the equations are applied to the calculation of cyclic flapwise blade loads for the NASA/DOE Mod-2 2.5-MW experimental HAWTs, and the results compared to measured cyclic loads. Good correlation is achieved, indicating that the R-S turbulence model developed in this study contains the characteristics of the wind which produce many of the fatigue loads sustained by wind turbines. Empirical factors are included which permit the prediction of load levels at specified percentiles of occurrence, which is required for the generation of fatigue load spectra and the prediction of the fatigue lifetime of structures.

INTRODUCTION

The objective of this study is to draw together two phenomena relating to the structural-dynamic response of horizontal-axis wind turbines (HAWTs). The first is the under-prediction of one category of blade loads on the three NASA/DOE Mod-2 experimental HAWTs located near Goldendale, Washington. One of these 3.2-MW 91.4-m diameter turbines is shown in Figure 1. Measured cyclic flapwise bending moments (in and out of the plane of revolution) have been found to be significantly higher than design predictions based on winds measured from a fixed frame of reference [Beeing 1982].

The second phenomenon considered here is that termed "rotationally-sampled turbulence," which is calculated from measurements of instantaneous wind speed from a rotating frame of reference [Verholek 1978, Connell 1981, Kristensen and Frandsen 1982, Connell and George 1983a and 1983b, and George 1984]. These measurements provide data for simulating the wind speed variations actually experienced by a section of a rotating HAWT blade. The spectra of rotationally-sampled wind speeds has been found to be very different from that of atmospheric turbulence measured with a stationary anemometer.

Figure 2 illustrates the basic method of measuring rotationally-sampled (R-S) turbulence [Verholek 1978]. Mounted on a line of instrument towers perpendicular to the prevailing wind, a set of anemometers is arranged in a circular pattern in a vertical plane, with center elevation H and radius R (in this case, 24.4 m and 12.2 m, respectively). This set of towers and anemometers is called a "vertical plane array" or VPA, and represents the path followed by a blade section of an imaginary HAWT rotor. The wind speed at each anemometer is continuously recorded. Samples from each record are then taken sequentially from consecutive anemometers around the circle, with the sampling interval time determined by the rotational speed and the number of anemometers. Interpolations are made between consecutive samples in order to synthesize a continuous record which represents the wind speeds that a blade section would experience in the rotating frame of reference.

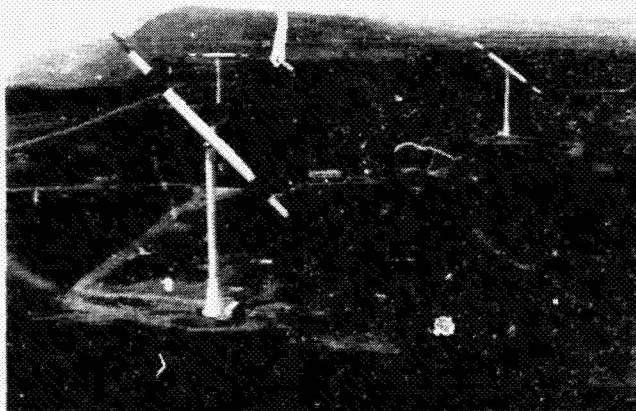


Figure 1. Cluster of three 2.5-MW Mod-2 HAWTs near Goldendale, Washington. (Courtesy of Boeing Aerospace Corporation)

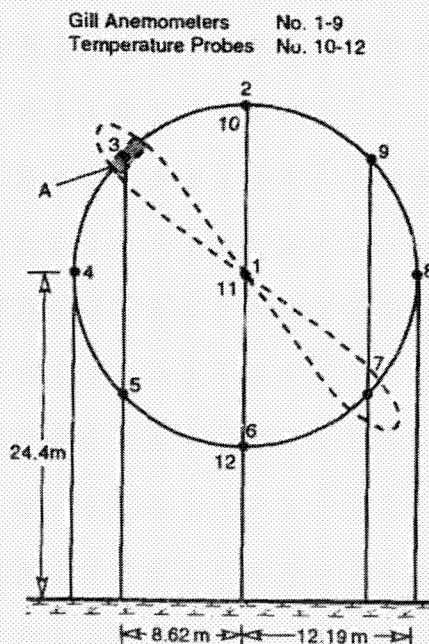


Figure 2. Schematic diagram of a vertical plane array (VPA) of anemometers for measuring wind turbulence experienced by a rotating HAWT blade. Sampling of signals from anemometers 2 to 9 is synchronized with the passage of the hypothetical blade section A. [Verholek 1978]

As illustrated in Figure 3 [Verholek 1978], the power spectrum of rotationally-sampled (R-S) turbulence, line (a), is higher at higher frequencies than that from a stationary anemometer, line (b). Moreover, R-S power is concentrated in "spikes" at frequencies which are integer multiples of the rotational speed. Thus, unsteady wind loading on a rotating HAWT blade may be harmonic in nature, with frequencies equal to multiples of the rotor speed. If so, these wind harmonics could produce a forced harmonic flapwise response in a HAWT blade and increased bending loads.

Drawing together these two phenomena brings us to the purposes of this study, which are (1) to determine if the harmonic content of R-S turbulence is of sufficient size to account for the under-prediction of Mod-2 HAWT cyclic loads, and (2) to develop a practical mathematical model of R-S turbulence that can be used for wind input to structural-dynamic computer codes, resulting in greater accuracy of load predictions.

ROTATIONALLY-SAMPLED TURBULENCE DATA

The R-S turbulence data used in this study were measured by researchers from Battelle's Pacific Northwest Laboratory (PNL) using the VPA located near Clayton, New Mexico [Connell and George 1983a and 1983b, and George and Connell 1984]. The dimensions of this array were $H = 30.5$ m and $R = 19.0$ m, and the rotational frequency was 0.667 Hz. Power spectral densities (PSDs) of 8.5-min segments of the synthesized wind speed were created using a Fast Fourier Transform (FFT) technique. Integration of a PSD over a selected frequency band then gave the variance of speed within this band. R-S turbulence in the frequency band is the square-root of this variance. Dividing the turbulence by the steady wind speed at elevation H then gives the R-S turbulence intensity for the selected frequency band.

Table 1 presents typical data reported by PNL researchers for one data segment. A total of 17 data segments form the basis of the R-S turbulence model developed in this study, taken from the following references: 3 from Connell and George [1983a and 1983b], 12 from George and Connell [1984], and 2 from Powell, Connell, and George [1985]. Of these, 10 were for atmospheric stability conditions ranging from neutral to unstable, while 7 were for stable conditions. Stable atmospheres typically result in larger vertical gradients in wind speed and smaller mixing between winds

TABLE 1. TYPICAL CLAYTON VPA WIND DATA [George and Connell, 1984]

Frequency Band (Hz)	Mid-band Frequency fP	Variance μ (m/s) ²	Turbulence σ (m/s)	Turbulence Intensity σ/U_0
< 0.33		0.498	0.706	0.066
0.33 - 1.00	1	0.431	0.656	0.061
1.00 - 1.67	2	0.146	0.382	0.036
1.67 - 2.33	3	0.070	0.264	0.025
2.33 - 3.00	4	0.037	0.192	0.018
3.00 - 3.67	5	0.032	0.179	0.017

at different elevations. For a discussion of the influence of atmospheric stability on wind shear, see Fromm [1994, pp. 392-396].

MODEL OF ROTATIONALLY-SAMPLED TURBULENCE

Modeling the Clayton VPA Data

To develop a general model of the Clayton VPA results, turbulence intensities for each harmonic number (*i.e.* mid-band frequency/rotational speed) were plotted vs the normalized wind shear measured vertically across the disk, $\Delta U/U_0$, as shown in Figure 4. It can be seen from the trend lines in these plots that (1) only the first harmonic turbulence intensities vary significantly with wind shear across the disk, and its variation is linear, (2) turbulence intensities for each harmonic above the first are roughly equal for all data segments, and (3) atmospheric stability has little, if any, effect on harmonic turbulence intensities.

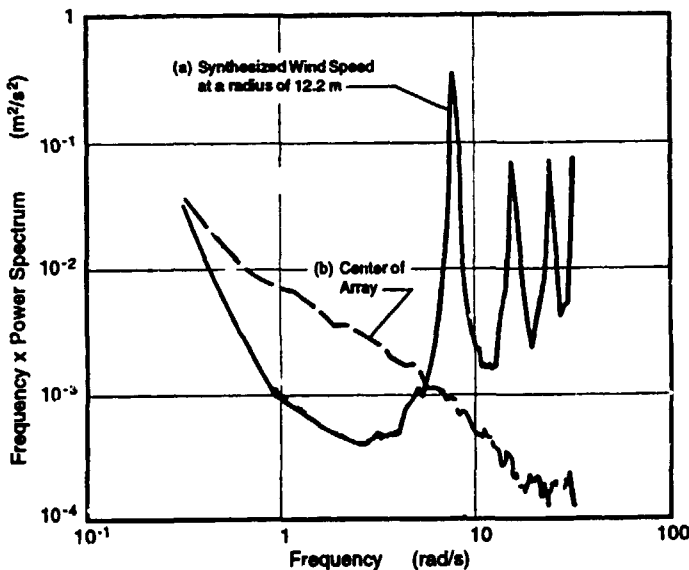


Figure 3. Sample power spectra measured at a VPA, illustrating typical characteristics of both rotationally-sampled and stationary time series of wind speed. (a) Rotationally-sampled wind speeds synthesized into a continuous time series, showing characteristic spikes at multiples of the 7.8 rad/s rotation rate. (b) Stationary time series from the center anemometer in the VPA. [Verholek 1978]

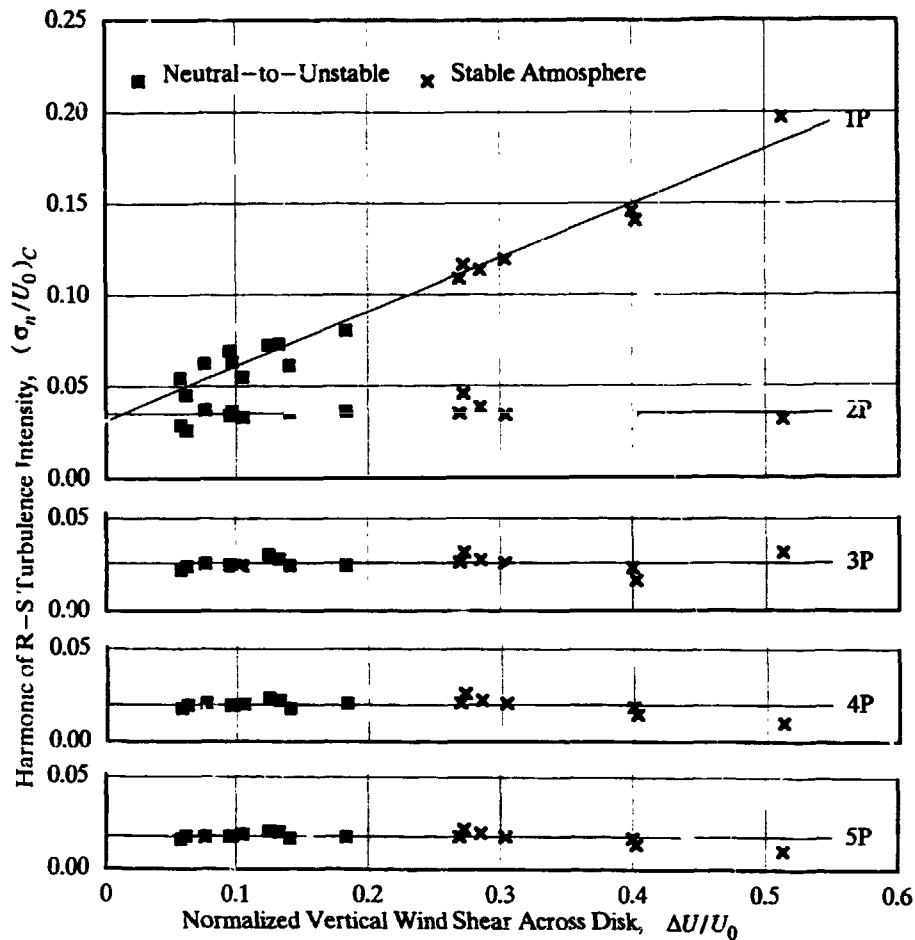


Figure 4. Rotationally-sampled turbulence intensities measured at the Clayton VPA at harmonic frequencies equal to integer multiples of the rotational speed, under neutral-to-stable and unstable atmospheric conditions. Only the first harmonic is influenced by the vertical wind shear across the sampled disk area. [data from PNL]

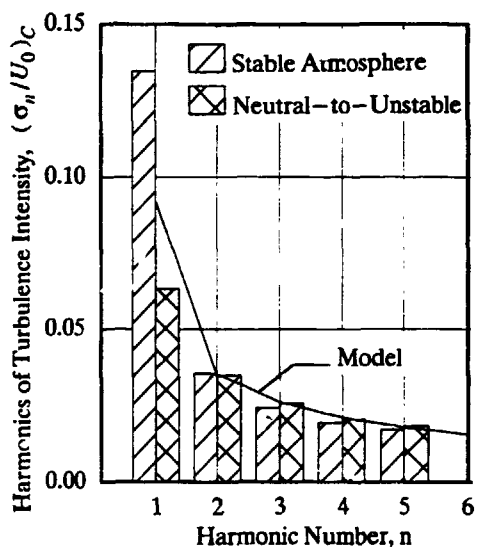


Figure 5. Measured and model harmonic turbulence intensities from the Clayton VPA data. [data from PNL]

Figure 5 presents these same data in another format. Each bar in this figure represents the average turbulence intensity for a given harmonic and atmospheric condition. Again we see that for harmonics above the first, atmospheric stability has little effect. For the first harmonic, the difference between the neutral-to-stable and stable intensities is a result of the larger wind shear across the disk for the stable condition.

The trend line in Figure 5 illustrates the model created here to represent the relationship between R-S turbulence intensity and harmonic number, as defined by the Clayton VPA data. This model is as follows:

$$(\sigma_1/U_0)_C = 0.0311 + 0.297 \Delta U/U_0 \quad (1a)$$

$$(\sigma_n/U_0)_C = 0.059 n^{-0.75} \quad n > 1 \quad (1b)$$

where

σ_n = rotationally-sampled turbulence in the frequency range from $(n - 1/2)P$ to $(n + 1/2)P$ (m/s)

P = rotational sampling frequency (rad/s)

C = subscript denoting Clayton VPA parameters

U_0 = steady free-stream wind speed at hub elevation (m/s)

ΔU = total steady wind shear from top to bottom of rotor swept area (m/s)

We can calculate the steady wind shear across the disk, ΔU , from the well-known logarithmic/linear model of the vertical gradient in the steady wind speed, which is as follows [Frost and Aspliden 1994, pp. 392-395]:

$$U = U_0 \frac{\ln(z/z_0) + \Psi_S(z/L_S)}{\ln(H/z_0) + \Psi_S(H/L_S)} \quad (2)$$

where

- z = elevation above ground level (m)
- z_0 = surface roughness length (m)
- H = elevation of hub above ground (m)
- R = tip radius of rotor (m)
- Ψ_S = atmospheric stability function dependent on z/L_S
- Ψ_S = function of Ψ
- L_S = Monin-Obukhov stability length (m)

For the purposes of this study, we will assume neutral atmospheric stability, for which the function Ψ_S is equal to zero. As shown in Figure 5, this results in a model prediction of the first harmonic turbulence that is intermediate between measurements made under stable and neutral-to-unstable atmospheric conditions. The first harmonic is not a critical wind loading on a teetered-hub rotor like that of the Mod-2 HAWT. For a fixed-hub rotor, however, the first harmonic can be important and the assumption of a stable atmosphere may be reasonable. With the assumption of neutral atmospheric stability, Equation (2) leads to the following expression for the wind shear vertically across a circle of radius R with its center at elevation H :

$$\Delta U/U_0 = \frac{\ln[(H+R)/(H-R)]}{\ln(H/z_0)} \quad (3)$$

Scaling Clayton VPA Data to Other Radii and Elevations

To generalize Equations 1, we must now make additional assumptions about the effects of R and H on R-S turbulence intensity. First, we will assume that the R-S sampling path length and the period for one revolution both increase linearly with sampling radius, which is compatible with general practice of operating HAWT blades at approximately the same tip speed independently of rotor diameter. The longer sampling paths and sampling periods of larger rotors are assumed to result in larger wind speed variations around the perimeter of the sampled circle. For simplicity, this relationship between increasing sampling radius and increasing R-S turbulence intensity is assumed to be linear.

The effect of center elevation on R-S turbulence is assumed to be approximately the same as the elevation effect on turbulence measured at a fixed point. According to Frost and Aspliden [1994, p. 407], an acceptable model for the effect of elevation on longitudinal turbulence at a fixed point is

$$\frac{\sigma_{0,x}}{U_0} = \frac{0.52}{\ln(H/z_0)(0.177 + 0.00139H)^{0.4}} \quad (4)$$

where $\sigma_{0,x}$ = longitudinal turbulence at a fixed point (m/s)

Combining a linear effect of sampling radius with the effect of center elevation given in Equation 4, we obtain

$$\frac{\sigma_n/U_0}{(\sigma_n/U_0)_C} = \frac{R}{R_C} \frac{[\ln(H/z_0)(0.177 + 0.00139H)^{0.4}]_C}{\ln(H/z_0)(0.177 + 0.00139H)^{0.4}} \quad (5a)$$

Once again, the subscript C denotes parameters of the Clayton VPA, which are $R_C = 19.0$ m, $H_C = 30.5$ m, and $z_{0,C} = 0.024$ m. After substituting these Clayton parameters into Equation (5a), the following scaling equation is derived for the R-S turbulence intensities along the tip path of a general HAWT rotor:

$$\frac{\sigma_n}{U_0} = \frac{0.204 R}{\ln(H/z_0)(0.177 + 0.00139H)^{0.4}} \left(\frac{\sigma_n}{U_0} \right)_C \quad (5b)$$

where the Clayton intensities $(\sigma/U_0)_C$ are given by Equations (1).

Spatial Distribution Around the Sampling Circle

The next step in the development of this R-S turbulence model is defining a time-history of wind speed around the sampling circle, in a format that can be used as input to structural-dynamic computer codes. The R-S turbulence is assumed to be quasi-static, which means that a HAWT rotor makes several revolutions before any significant changes occur in the spatial distribution of the wind within the rotor's swept area. Dynamic responses of the rotor blades are assumed to approach a steady state before the wind turbulence changes. With this quasi-static assumption, the time-varying unsteady wind can be converted to a spatially-varying steady wind, for which we shall use the following harmonic format:

$$U_{RS} = U_0 + \sum (A_n \cos n\psi) \quad n = 1, 2, \dots \quad (6)$$

where

- U_{RS} = rotationally-sampled free-stream horizontal wind speed, quasi-steady in time (m/s)
- A_n = amplitude of n th harmonic of wind speed (m/s)
- ψ = azimuthal position in rotor disk area; 0 = down (deg)

Wind turbulence is equal to the standard deviation of the wind speed from its steady value. For each cosine wave in Equation (6), standard deviation and amplitude are related as follows:

$$|A_n| = \sqrt{2} \sigma_n \quad (7)$$

While the absolute values of the harmonic amplitudes can be determined from R-S turbulence data, the signs of these amplitudes cannot. Various patterns of positive and negative signs (equivalent to in-phase and out-of-phase harmonics in Eq. (6)) have been used. For example, Zimmerman *et al.* [1995] assumed negative amplitudes for odd-numbered harmonics and positive amplitudes for even-numbered harmonics. Here we shall obtain a pattern of amplitude signs by examining the resulting vertical wind profile for reasonableness.

Figure 6 [Frost and Aspliden 1994, pg. 391] illustrates the general shapes of typical vertical profiles of the wind speed. To be reasonable, the fluctuations in the quasi-steady profile of our R-S turbulence model should be intermediate between those of the "instantaneous" and "steady" profiles in this figure. Of the many possible combinations of positive and negative harmonic amplitudes, the most reasonable vertical profile is obtained with negative harmonics except for the third and fourth, as shown in Figure 7. The vertical profile obtained with this combination is shown in Figure 8 for the Clayton VPA. Figure 9 illustrates the same spatial distribution of quasi-steady wind speed, but this time as seen by a blade section moving around the sampling circle of the Clayton VPA.

Spatial Distribution Along a HAWT Blade

The final step in the development of an R-S turbulence model of the quasi-steady wind speed within the swept area of a HAWT rotor is defining the wind speed distribution from hub to tip. Earlier the assumption was made that size of R-S turbulence harmonics varied linearly with the sampling radius. However, this assumption alone is not sufficient to define the simultaneous wind

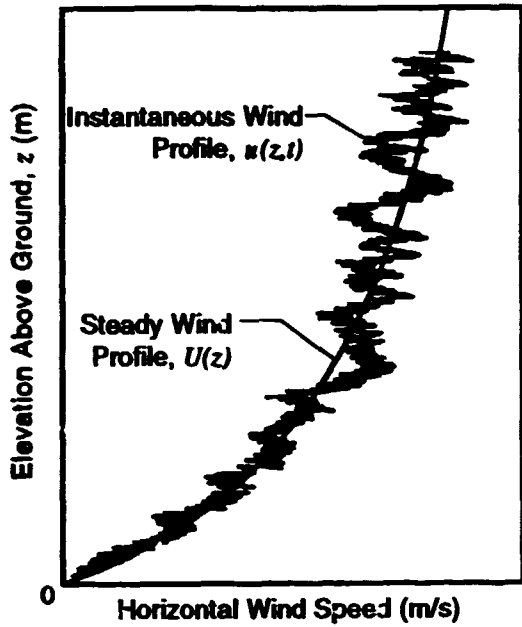


Figure 6. Typical vertical profiles of the wind speed, both instantaneous and steady. [Frost and Aspliden 1994]

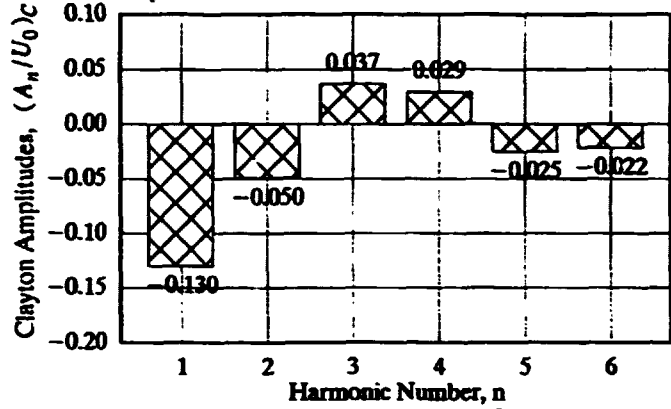


Figure 7. Proposed model amplitudes of rotationally-sampled wind speed for the parameters of the Clayton VPA: $R = 19.0$ m, $H = 30.5$ m, and $z_0 = 0.024$ m. Positive and negative signs are selected to obtain vertical profiles similar to those in Figure 6.

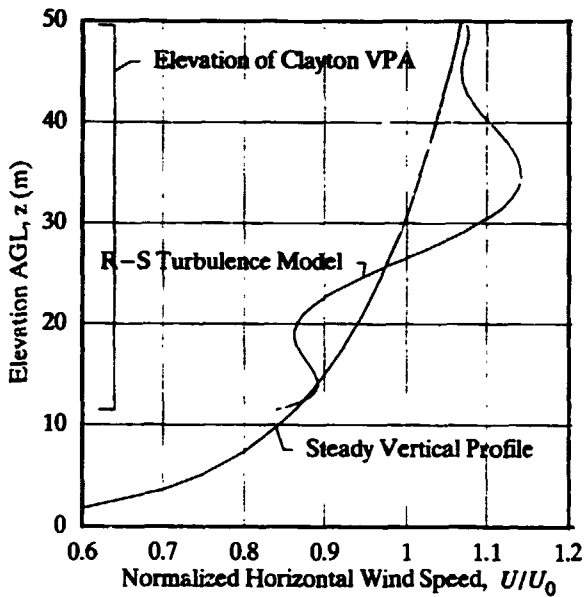


Figure 8. Vertical profile of the wind speed around the Clayton VPA sampling circle, as given by the proposed R-S turbulence model.

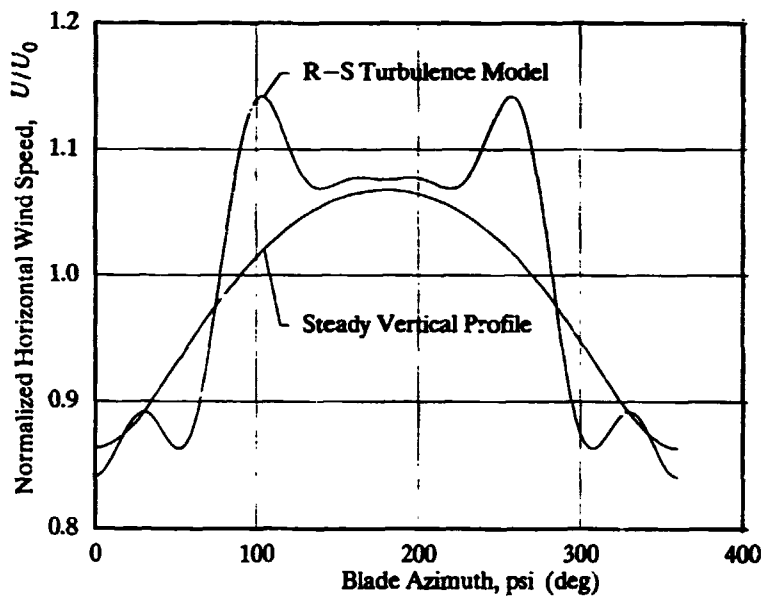


Figure 9. Spatial distribution of the wind speed around the Clayton VPA sampling circle, as given by the proposed R-S turbulence model.

speeds at radii smaller than the sampling radius, because the spanwise distribution of turbulence also depends strongly on the transverse coherence of the wind [Frost and Aspliden, 1994, pg. 410-411, 418]. Coherence is a dimensionless quantity between zero and unity that represents the degree to which two unsteady events, separated in space, are alike in their time histories. If the two time histories are identical their coherence is unity, and if they are completely unrelated their coherence is zero.

Coherences of individual harmonics of R-S turbulence were measured by Zimmerman *et al.* [1995] using wind speed sensors mounted at two locations 69.2 ft apart on a 150-ft Mod-2 HAWT blade. These data are shown in Figure 10, in which the outboard location ($r = 100$ ft) is taken as the reference and therefore has, by definition, a coherence of 1.00. The coherence between the first harmonic at the inboard location ($r = 30.8$ ft) and the first harmonic at the outboard station was found to be high, but equivalent coherences of the higher harmonics were all low for this separation distance.

To generalize these observations, trend curves are first drawn to bound the data, following the form

$$coh = \exp\left[-(\zeta/Z)^2\right] \quad (8)$$

where

- coh = coherence relative to same harmonic at r_o
- r_o = radial distance to reference station (ft)
- ζ = separation distance from reference station, $r_o - r$ (ft)
- Z = empirical length scale (ft)

These data trends are now idealized for purposes of incorporating coherence into the R-S turbulence model. First, the coherence for

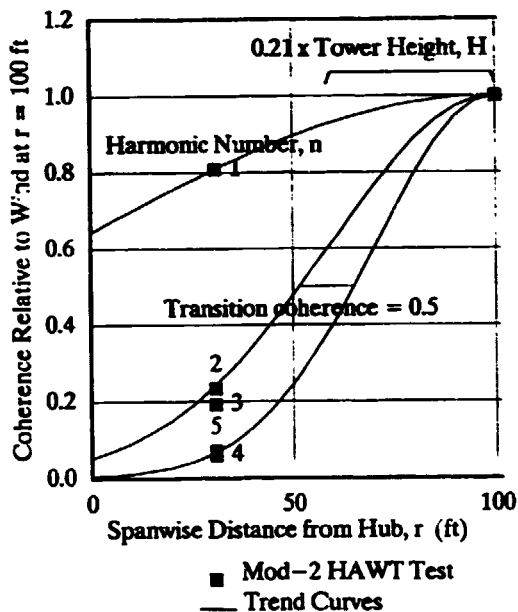


Figure 10. Coherence of individual harmonics of wind speeds rotationally-sampled at two spanwise locations along Mod-2 HAWT blades. [data from Zimmerman *et al.* 1995]

the first harmonic is assumed to be 1.00 for all separation distances, because it closely follows the steady vertical profile illustrated in Figure 9.

For the higher harmonics, where coherence decreases with increasing separation distance, a coherence of 0.5 is selected as identifying a transition between unrelated and related time histories. From the trend lines in Figure 10, this transition coherence occurs at an average separation distance of about 42 ft (*i.e.*, $r = 38$ ft). Following Counihan's empirical model for the integral length scales of crosswind turbulence [Frost and Aspliden 1994, pg. 418], we will assume that the empirical length scale, Z , and the transition separation are both proportional to elevation above ground. Using the Mod-2 tower height of 200 ft as an average elevation, the transition separation distance of 42 ft, obtained from the test data, is generalized to be equal to $0.21 H$.

With the idealized model of coherence shown in Figure 10, the spatial distribution of wind harmonic amplitudes along a HAWT blade are given by the following equations in this R-S turbulence model:

$$A_1(r) = \frac{r}{R} A_1(R) \quad (9a)$$

$$\text{For } n > 1: \quad (9b)$$

$$A_n(r) = \frac{r}{R} A_n(R) \quad \text{if } (R - r) \leq 0.21 H \quad (9c)$$

$$= 0 \quad \text{if } (R - r) > 0.21 H$$

where $() =$ function of $()$

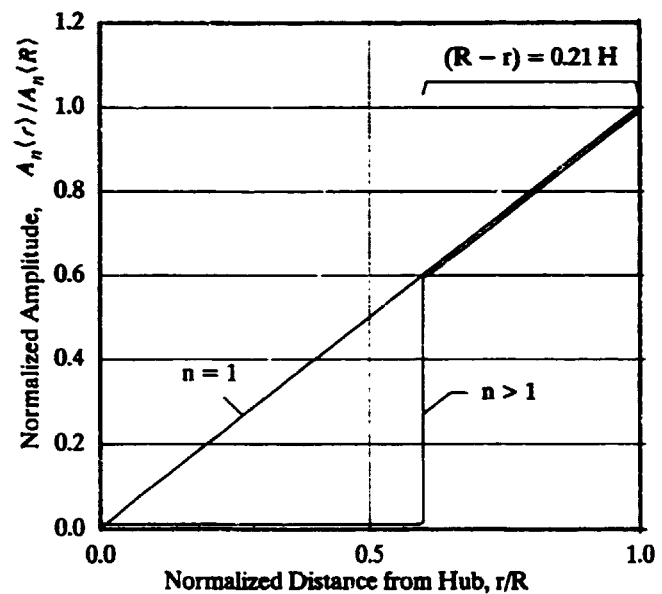


Figure 11. Proposed model of spanwise distribution of harmonic amplitudes of rotationally-sampled turbulence, accounting for reduced coherence of higher harmonics with distance inboard from blade tip.

SUMMARY OF EQUATIONS DEFINING PROPOSED MODEL OF A ROTATIONALLY-SAMPLED TURBULENT WIND FIELD

$$U_{RS}(r, R, H, z_0, \psi) = U_0(H, z_0) + \frac{r}{R} \sum A_{R,n}(R, H, z_0) \cos n\psi \quad n = 1, 2, \dots \quad (10a)$$

$$U_0 = U_r \left[\ln(H/z_0) / \ln(z_r/z_0) \right] \quad (10b)$$

$$A_{R,1} = -U_0 \left\{ 0.04398 S(R, H, z_0) + 0.4120 \ln \left[(H+R)/(H-R) \right] / \ln(H/z_0) \right\} \quad (10c)$$

$$S = \frac{0.204 R}{\ln(H/z_0) (0.177 + 0.00138 H)^{0.4}} \quad (10d)$$

If $(R - r) \leq 0.21 H$:

$$A_{R,2} = -0.0496 S U_0 \quad (10e)$$

$$A_{R,3} = +0.0366 S U_0 \quad (10f)$$

$$A_{R,4} = +0.0295 S U_0 \quad (10g)$$

$$A_{R,5} = -0.0250 S U_0 \quad (10h)$$

$$A_{R,6} = -0.0218 S U_0 \quad (10i)$$

If $(R - r) > 0.21 H$:

$$A_{R,n} = 0 \quad n > 1 \quad (10j)$$

where

U_{RS} = rotationally-sampled free-stream horizontal wind speed, quasi-steady in time (m/s)

$\langle \rangle$ = function of $\langle \rangle$

r = radial distance from rotor axis (m)

R = tip radius of rotor (m)

H = elevation of hub above ground (m)
 z_0 = surface roughness length (m)
 ψ = azimuthal position in rotor disk area; 0 = down (deg)
 U_0 = steady free-stream wind speed at hub elevation (m/s)
 $A_{R,n}$ = amplitude of n th harmonic of wind speed distribution around circle of radius R (m/s)
 U_r = steady free-stream wind speed at reference elevation (m/s)
 z_r = reference elevation = 10 m
 S = scale factor

APPLICATION TO MOD-2 HAWT FATIGUE LOADS

Discrepancies Between Measured and Design Loads

Figure 12 illustrates the discrepancies that were observed during testing of the Mod-2 HAWTs between measured and design cyclic flatwise blade loads. In this figure, bending loads are plotted as a function of steady free-stream wind speed. The areas marked C are envelopes of 50th-percentile loads (i.e., median loads) measured at 21 and 65 percent of span.

The lines marked A are load calculations made with the MOSTAB-HFW computer model with a power-law wind shear providing the non-uniform wind field. MOSTAB-HFW is representative of several available codes which contain teetering, flatwise, and chordwise degrees of freedom. Scale model tests in a wind tunnel indicated that cyclic flatwise blade loads were approximately 65% larger than those predicted by this computer model [Boeing 1979]. Therefore, a factor of 1.65 was applied to the computer predictions to produce the design bending loads marked B in the figure.

A comparison of the design load lines in Figure 12 with the envelopes of the measured loads clearly shows a significant underprediction of cyclic flatwise bending at both outboard and inboard sections of the blades. Our purpose now will be to apply the rotationally-sampled turbulent wind model just developed in place of the power-law wind shear model used in the Mod-2 design, and eliminate discrepancies between measured and predicted cyclic flatwise bending loads.

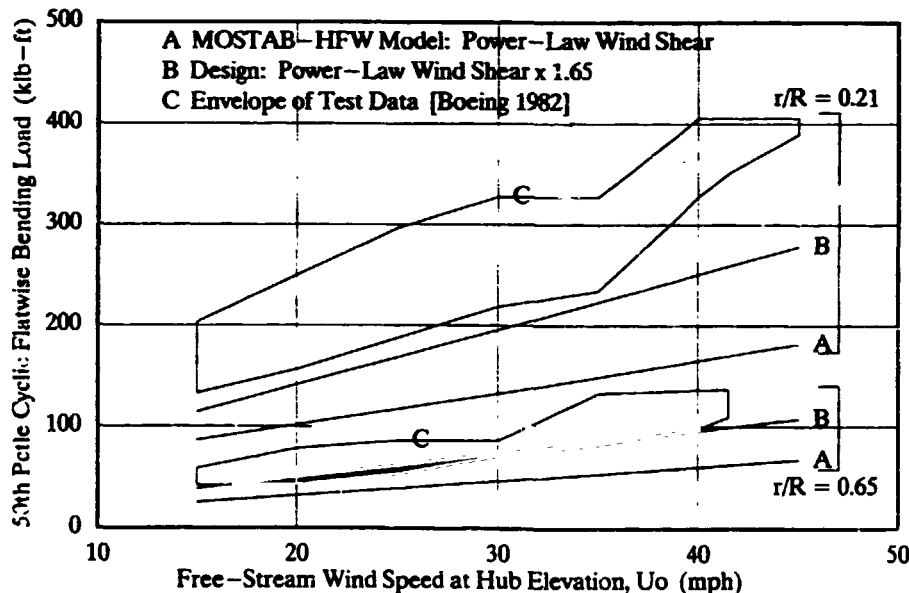


Figure 12. Comparison of calculated and measured cyclic flatwise bending loads at two span wise locations on a Mod-2 HAWT blade, showing underprediction of design loads at the 50th percentile level. [data from Boeing 1982]

Spectrum Load Factor

The spectrum of fatigue loads experienced by an operating wind turbine is quite wide, even at a given steady wind speed [Spera 1994]. Since the rotationally-sampled turbulence model defined by Equations 10 specifies a single spatial distribution for a specified steady wind speed, we will introduce an empirical load factor to be evaluated later from measured spectra of Mod-2 loads, as follows:

$$\delta L(U_0, p) = \delta L_b(U_0) \times \beta(p) \quad (11)$$

where

- δL = cyclic load = $(L_{max} - L_{min})/2$ during one rotor revolution
- p = percentile of load spectrum
- δL_b = baseline cyclic load calculated for free-stream wind speed U_0 and non-uniform wind field defined by Equations (10)
- β = empirical load factor; function of percentile p

Amplitudes of R-S Wind Model Harmonics

Equations (10) will now be used to define a non-uniform wind field which will be used as an input to a structural-dynamic model of the Mod-2 HAWT rotor, in order to calculate cyclic flatwise bending loads on the rotor blades. Parameters defining the Mod-2 rotor and the roughness of the Goldendale, Washington, site are $R = 45.7$ m, $H = 61.0$ m, and $z_0 = 0.024$ m. With Equations (10) and these dimensions, we can calculate the amplitudes of the various wind harmonics flowing into the structural-dynamic model of the Mod-2 rotor, with the results listed in Table 2.

TABLE 2.
AMPLITUDES OF R-S TURBULENCE HARMONICS
FOR A MOD-2 HAWT AT GOLDENDALE, WASHINGTON

Harmonic Number n	Amplitude Intensity $A_{R,n}/U_0$
1	-0.2653
2	-0.1012
3	+0.0746
4	+0.0602
5	-0.0509
6	-0.0444

RESULTS AND DISCUSSION

Cyclic flatwise bending loads on a Mod-2 rotor blade were calculated using the MOSTAB-HFW code with the proposed R-S turbulence wind model, for two blade stations ($r/R = 0.21$ and 0.65) and two percentiles (50th and 99.9th). The results are shown by lines D and E in Figures 13 and 14. Load outputs of the MOSTAB-HFW code have been multiplied by values of the factor β selected to produce correlation with average measured loads.

As noted on Figure 13, load factors of 1.00 produce good agreement between 50th percentile calculated and measured loads at both inboard and outboard blade stations. This indicates that the R-S turbulence measured at Clayton, scaled up to the Mod-2 rotor size in Table 2, is sufficient to account for the discrepancies observed between design and measured cyclic loads at the 50th percentile level, without resorting to any other load factors.

In Figure 14, values of β equal to 2.95 and 3.05 were required to scale the MOSTAB-HFW output (again, with the amplitudes in Table 2 as wind input) to the 99.9th percentile levels at the two blade stations.

In Figure 15, the values of the load factor β which produce agreement between calculated and measured cyclic flatwise bending loads are plotted vs the percentile of load, p , on a scale which defines a normal probability distribution. The selection of power-law for the trend curve is based on the log-normal distribution observed for a large quantity of field test data [Spera *et al.* 1984], and is given by the following equation:

$$\beta = 1.00 (m \sigma)^{0.155} \quad (12)$$

where

- σ = standard deviation of load from mean (50th percentile)
- m = number of standard deviations for load percentile desired; for example
 - $m = 0$ for 50th percentile
 - $m = 1.28$ for 90th percentile
 - $m = 2.33$ for 99th percentile
 - $m = 3.08$ for 99.9th percentile

Thus, once the 50th percentile cyclic flatwise bending loads have been calculated using a structural-dynamics code like MOSTAB-HFW and a wind input defined by Equations (10), a complete spectrum of cyclic loads and resulting fatigue stresses can be calculated by applying Equations (11) and (12). With a cumulative fatigue damage algorithm blade fatigue life can then be estimated [Spera 1994].

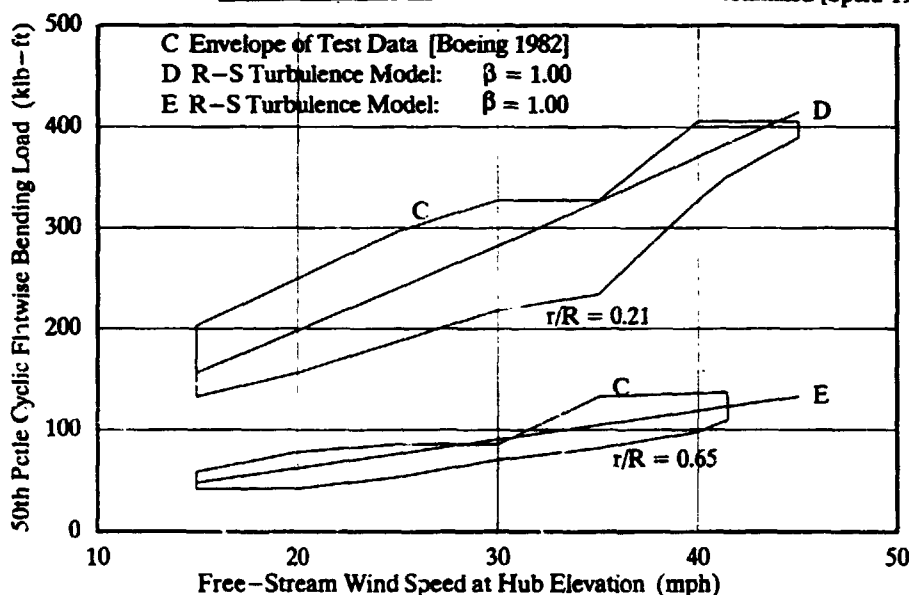


Figure 13. Comparison of 50th percentile cyclic flatwise bending loads calculated using the proposed R-S turbulence model with measured loads. A load factor of 1.00 applied to the output of the MOSTAB-HFW structural-dynamics code is sufficient to obtain correlation both inboard and outboard along the blade. [data from Boeing 1982]

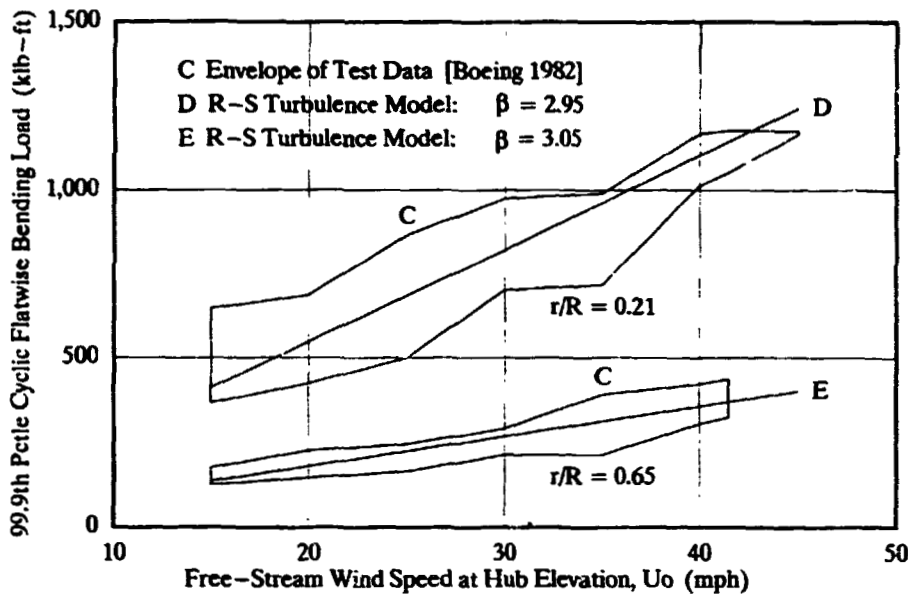


Figure 14. Comparison of 99.9th percentile cyclic flatwise bending loads calculated using the proposed R-S turbulence model with measured loads. Load factors of approximately 3.0 produce correlation both inboard and outboard along the blade. [data from Boeing 1982]

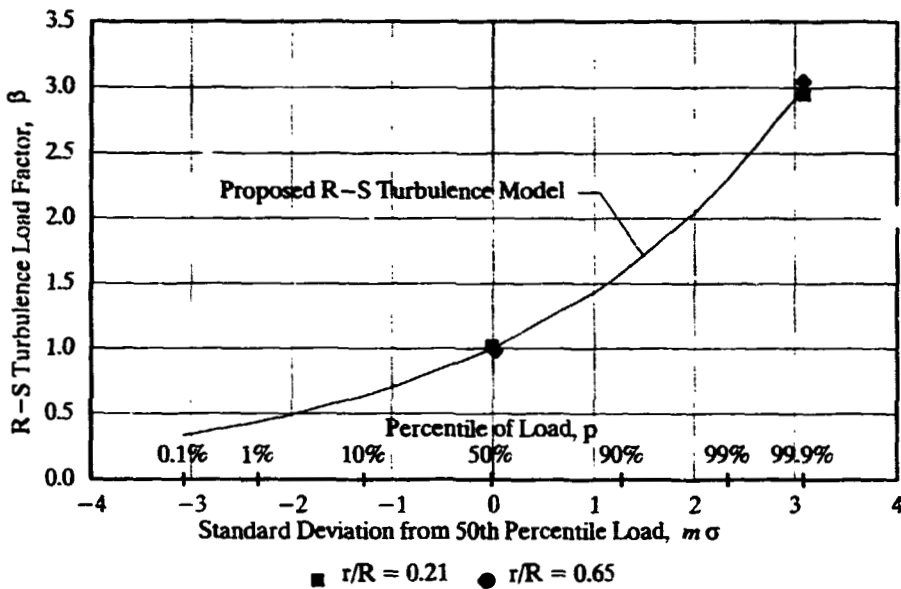


Figure 15. Proposed model of the R-S turbulence load factor with which the spectrum of cyclic flatwise bending loads on a HAWT blade can be calculated from the 50th percentile level of load. The model is based on a log-normal probability distribution.

CONCLUSIONS

1. Rotational sampling of the wind field entering the swept area of a HAWT rotor has shown that turbulence acts as a series of quasi-static harmonic forcing functions on the rotor blades, and that these forcing functions act at frequencies which are integer multiples of the rotor speed.
2. Structural-dynamic computer models of HAWT systems should include R-S turbulence in their wind input modules to adequately evaluate the dynamic response of rotor blades to these harmonic forcing functions and the significance of resulting fatigue damage.
3. Equations are derived herein which define a practical model of a wind field containing R-S turbulence for HAWT structural-dynamic analysis. These equations, based on rotationally-sampled turbulence measured by PNL personnel at the Clayton vertical-plane-array, are in a general form which permits scaling to different rotor diameters, tower elevations, and surface roughnesses.
4. The R-S turbulence measured at the Clayton VPA, scaled up to the Mod-2 HAWT rotor size, is sufficient to account for the discrepancies observed previously between Mod-2 design and measured cyclic loads at the 50th percentile level, without resorting to any other load factors.
5. An empirical load factor model is derived with which the spectrum of cyclic flatwise bending loads on a HAWT rotor blade can be calculated from the 50th percentile load level, based on a log-normal probability distribution typical of many HAWT load spectra.
6. The first harmonic of R-S turbulence intensity is proportional to the steady vertical wind shear across the rotor disk area, but all other harmonics are insensitive to vertical wind shear.
7. Harmonics of R-S turbulence intensity above the first are roughly constant for all wind test conditions.

8. Atmospheric stability has little, if any, effect on harmonic turbulence intensities other than tending to increase the steady vertical wind shear across the rotor disk area and thereby the first harmonic of R-S turbulence.

ACKNOWLEDGMENT

David C. Janetzke of the NASA Lewis Research Center performed the MOSTAB-HFW structural-dynamic analysis of the Mod-2 HAWT, adapting the code's wind input module to accommodate the R-S turbulence model. This work was critical to the study, and the author expresses his appreciation.

REFERENCES

- Boeing Engineering and Construction, 1982a, "Mod-2 Wind Turbine System Concept and Preliminary Design Report, Volume II: Detailed Report, NASA CR-159609, DOE/NASA 0002-80/2, Cleveland, Ohio: NASA Lewis Research Center, p. 5-2.
- Boeing Engineering and Construction, 1982b, "Mod-2 Wind Turbine System Development Final Report, Volume II: Detailed Report, NASA CR-168007, DOE/NASA/0002-2, Cleveland, Ohio: NASA Lewis Research Center, pp. 5-9 to 5-11.
- Connell, J. R., 1981, "The Spectrum of Wind Speed Fluctuations Encountered by a Rotating Blade of a Wind Energy Conversion System: Observations and Theory," PNL-4083, Richland, Washington: Battelle Pacific Northwest Laboratory.
- Connell, J. R., and George, R. L., 1983a, "A New Look at Turbulence Experienced by a Rotating Wind Turbine," Proceedings, Second ASME Wind Energy Symposium, PNL SA-10653, Richland, Washington: Battelle Pacific Northwest Laboratory.
- Connell, J. R., and George, R. L., 1983b, "Scaling Wind Characteristics for Designing Small and Large Wind Turbines," Proceedings, Sixth Biennial Wind Energy Conference and Workshop, B. H. Glenn, ed., Boulder, Colorado: American Solar Energy Society, pp. 513-524.
- Frost, W., and Aspliden, C., 1994, "Characteristics of the Wind," in *Wind Turbine Technology*, D. A. Spera, ed., ASME Press, New York: American Society of Mechanical Engineers, pp. 371-446.
- George, R. L., 1984, "Simulation of Winds As Seen by a Rotating Vertical Axis Wind Turbine Blade," PNL-4914, Richland, Washington: Battelle Pacific Northwest Laboratory.
- George, R. L., and Connell, J. R., 1984, "Rotationally Sampled Wind Characteristics and Correlations with Mod-0A Wind Turbine Response," PNL-5238, Richland, Washington: Battelle Pacific Northwest Laboratory.
- Kristensen, L., and Frandsen, S., 1982, "Model for Power Spectra of the Blade of a Wind turbine Measured from the Moving Frame of Reference," *Journal of Wind Engineering and Industrial Aerodynamics*, Vol. 10, Amsterdam: Elsevier Scientific Publishing Company, pp. 249-262.
- Powell, D. C., Connell, J. R., and George, R. L., 1985, "Verification of Theoretically Computed Spectra for a Point Rotating in a Vertical Plane," PNL-5440, Richland, Washington: Battelle Pacific Northwest Laboratory.
- Spera, D. A., Ensworth, C. B. III, and Janetzke, D. C., 1984, "Dynamic Loads in Horizontal-Axis Wind Turbines, Part I: Field Test Data," Proceedings, Wind Power '85 Conference, SERI/CP-217-2902, Golden, Colorado: National Renewable Energy Laboratory, pp. 457-462.
- Spera, D. A., 1994, "Fatigue Design of Wind Turbines," in *Wind Turbine Technology*, D. A. Spera, ed., ASME Press, New York: American Society of Mechanical Engineers, pp. 547-588.
- Verholec, M. G., 1978, "Preliminary Results of a Field Experiment to Characterize Wind Flow Through A Vertical Plane," PNL 2518, Richland, Washington: Battelle Pacific Northwest Laboratory.
- Zimmerman, D. K., Shipley, S. A., and Miller, R. D., 1995, "Comparison of Measured and Calculated Dynamic Loads for the Mod-2 2.5 MW Wind Turbine System, in *Collected Papers on Wind Turbine Technology*, D. A. Spera, Ed., NASA CR-195432, DOE/NASA/5776-1, Cleveland, Ohio: NASA Lewis Research Center.

LARGE HAWT WAKE MEASUREMENT AND ANALYSIS

A. H. Miller
H. L. Wegley
J. W. Buck

Pacific Northwest Laboratory
Richland, Washington 99352

ABSTRACT

From the theoretical fluid dynamics point of view, the wake region of a large horizontal-axis wind turbine has been defined and described, and numerical models of wake behavior have been developed. Wind tunnel studies of single turbine wakes and turbine array wakes have been used to verify the theory and further refine the numerical models. However, the effects of scaling, rotor solidity, and topography on wake behavior are questions that remain unanswered.

In the wind tunnel studies, turbines were represented by anything from scaled models to tea strainers or wire mesh disks whose solidity was equivalent to that of a typical wind turbine. The scale factor compensation for the difference in Reynolds number between the scale model and an actual turbine is complex, and not typically accounted for. Though it is wise to study the simpler case of wakes in flat topography, which can be easily duplicated in the wind tunnel, current indications are that wind turbine farm development is actually occurring in somewhat more complex terrain.

Empirical wake studies using large horizontal-axis wind turbines have not been thoroughly composited, and, therefore, the results have not been applied to the well-developed theory of wake structure. The measurement programs have made use of both in situ sensor systems, such as instrumented towers, and remote sensors, such as kites and tethered, balloon-borne anemometers.

We present a concise overview of the work that has been performed, including our own, which is based on the philosophy that the MOD-2 turbines are probably their own best detector of both the momentum deficit and the induced turbulence effect downwind. Only the momentum deficit aspects of the wake/machine interactions have been addressed. Both turbine power output deficits and wind energy deficits as measured by the onsite meteorological towers have been analyzed from a composite data set. The analysis has also evidenced certain topographic influences on the operation of spatially diverse wind turbines.

INTRODUCTION

For wind turbines to make up a significant part of the world's energy generation capability, large clusters of turbines will have to be installed. Since the land area available for such installation is limited, not necessarily by the availability of wind but rather by physical, social, economic and operational constraints, future wind turbine clusters will have to be sited so that maximum utilization of the available land is achieved. The distances between turbines will be governed by factors that include the complexity and geomorphology of the local terrain and the relationship of this to the prevailing energy-producing wind. In a steep-sided valley through which the wind blows practically unidirectionally, rows of turbines normal

to the prevailing wind may be erected with lateral separations of only a few diameters. Longitudinally, however, there will be many more rigorous constraints. The second echelon of turbines must be placed sufficiently downstream so that wake effects are minimized. Wakes have two effects on turbine operation. First, the wake created by an upwind turbine manifests itself as a momentum deficit to downwind turbines, thereby affecting the apparent energy capture of the downwind turbines. Second, the induced turbulence created by the upwind turbine may have a significant effect on the long-term structural and aerodynamic loads at downwind turbines and hence increase maintenance or reduce turbine life.

Previous wind turbine wake studies have concentrated on case studies where the field program is specifically set up to make measurements during relatively short periods of time. These measurements actually provide only a quick snapshot of the wake. A technique of data analysis referred to as "binning" was applied to the Goodnoe Hills test site data. In the meteorological community, the process is called compositing where all the appropriate cases are binned according to a (or several) dependent parameters.

CURRENT STUDIES

Data collection at the Goodnoe Hills Candidate Site began long before the actual installation of the MOD-2 turbines. Since then, the PNL Distributed Data System (DDS), a minicomputer-based data acquisition system, was developed and has evolved and routinely collects meteorological data and turbine operating data. Table 1 presents a list of the parameters for which data have been collected. In the current configuration, the system is limited to collecting a maximum of eight turbine parameters from each turbine. (This capability is soon to be expanded to 64 parameters.) These data and their standard deviations are collected at a rate of once every 2 minutes. The standard deviation is based on 120 one-second samples. The DDS is capable of sampling data from all these channels at a rate of several samples per second if needed.

The Goodnoe Hills test site is located adjacent to the Columbia River gorge on the south-central border of Washington State. The site elevation is about 2600 ft MSL. In general terms the site appears to be on a broad, gently rolling plane. Figure 1 is a computer-generated, three-dimensional, isometric plot of the site topography looking from aloft to the northeast. As can be seen, the site terrain is actually far from simple. Figure 2 shows the site in plan view and on a much smaller scale. The site was laid out with the turbines placed in an array with separation distances of 5, 7 and 10 diameters. The axis between any pair of turbine, was determined to be a climatologically high wind azimuth so that there would intentionally be some possibility of the wake

from one of the turbines impacting one of the others. Historically, significant periods of strong winds occur on azimuths of about 200°, 255° and 280°.

TABLE 1. Data Parameters Collected at the Goodnoe Hills Test Site

PNL Tower:

- 1) wind direction at 33 ft
- 2) wind direction at 50 ft
- 3) wind direction at 200 ft
- 4) wind direction at 350 ft
- 5) wind speed at 33 ft
- 6) wind speed at 50 ft
- 7) wind speed at 200 ft
- 8) wind speed at 350 ft
- 9) temperature at 33 ft
- 10) temperature difference between 350 ft and 33 ft
- 11) air flow at 33 ft
- 12) air flow at 350 ft
- 13) pressure at 200 ft
- 14) u-component at 200 ft
- 15) v-component at 200 ft
- 16) w-component at 200 ft

BPA Tower:

- 1) wind speed at 50 ft
- 2) wind direction at 50 ft
- 3) wind speed at 195 ft
- 4) wind direction at 195 ft
- 5) temperature at 50 ft
- 6) pressure at ground
- 7) ice detector
- 8) u-component at 200 ft
- 9) v-component at 200 ft
- 10) w-component at 200 ft

Turbine #1, #2, #3:

- 1) field current
- 2) generator power
- 3) utility power
- 4) generator voltage
- 5) rotor speed
- 6) blade #1 pitch
- 7) yaw error
- 8) nacelle position

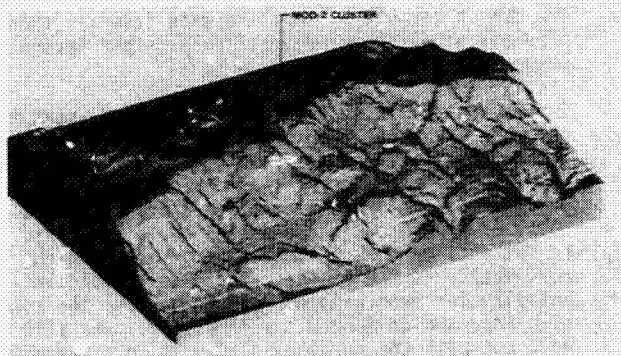


Figure 1--Computer-generated view of the topography at the Goodnoe Hills test site showing the locations of the three turbines. Base dimensions of the map are 4 by 5.5 miles.

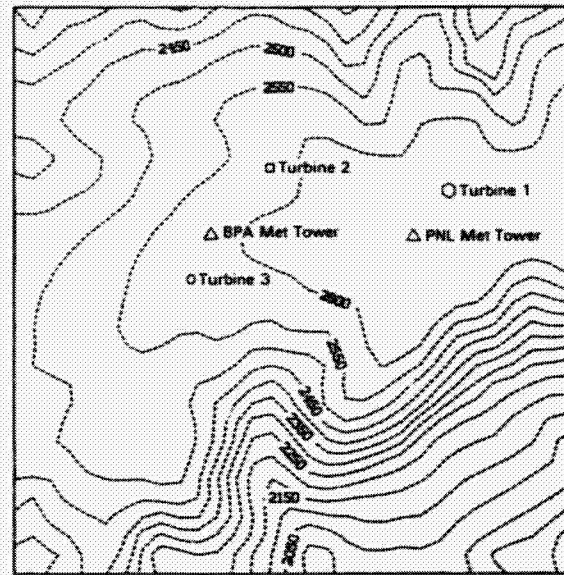


Figure 2--Large-scale map of the Goodnoe Hills test site with 50-ft contours shown

Turbulence at the site has been qualitatively characterized as moderate to strong when the wind is from any one of the prevailing wind directions. As a more quantitative measure, a quantity known as the turbulence intensity was calculated using an entire year's site data. Plots of the resulting analyses are given in Figures 3 and 4. For this analysis the data were not stratified by atmospheric stability. The authors recognize that such a stratification would provide useful information. However, since the analysis was based on the equivalent of 1-s data, the results should evidence worst-case conditions. All the data in each of 72 5°-bins were averaged individually. The turbulence intensity, I , is equal to the RMS of the eddy velocities divided by the mean wind speed:

$$I = \frac{\sqrt{u'^2}}{U} \quad (1)$$

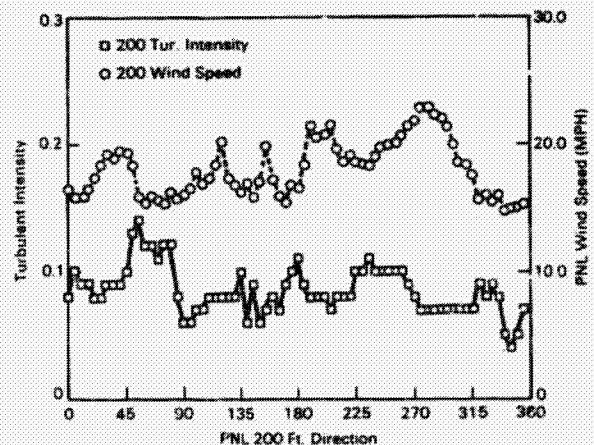


Figure 3--Long-term turbulence intensity versus wind direction measured at the 200-ft level on the PNL meteorological tower

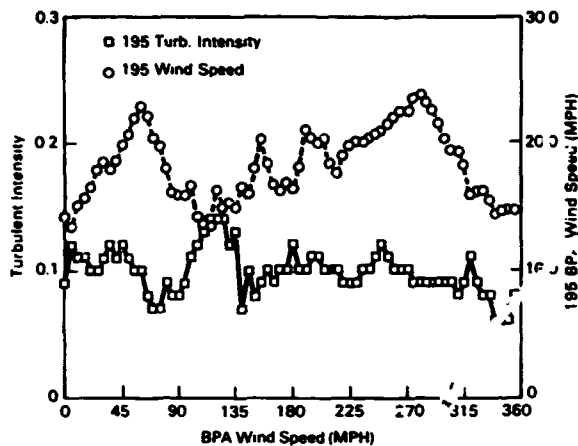


Figure 4--Same as Figure 3 but from the 195-ft level at the BPA tower

Interpretation of Figures 3 and 4 should be approached with caution. The increased turbulence intensity at the PNL tower between 45° and 90° and the marked reduction in wind speed are artifacts associated with the wind shadow cast by the tower. Similarly, in Figure 4, the increased turbulence intensity and reduced wind speed at about 110° show the same effect at the BPA tower, which was installed with a different rotation than the PNL tower. Figure 5 illustrates the effect of tower shadow on the measurement of wind speed. In the quadrant between approximately 45° and 135°, any comparison of the winds at the two towers should be viewed with caution. The first major dip in the data is the effect of the PNL tower shadow on its anemometer while the large peak following represents the effect of the BPA tower shadow on its anemometer. Regardless of these discrepancies, the reader can easily see that for either tower, the average turbulence intensity at hub height is on the order of 0.1. The climatological mean wind speed at the site is 15.3 mph. The Z_0 is roughly 0.05 m, which is expected in open, rolling, brushy or crop land. The turbulence intensity is an indication of a physical phenomenon that plays an important role in the lateral reentrainment of momentum as well as the spread of a turbine wake.

Data collected by the DDS in the period from August through mid-November 1982 were used in this study. The period was restricted because multiple turbine data as well as meteorological data were not available until then. Turbine #2 parameters were not connected until mid-October. The data were cleaned up and screened and a special data set was created specifically for this wake study. In screening the data three criteria were used to qualify the data for inclusion. First, at least one turbine had to be running. This was determined by discriminating on the basis of rotor rpm, nacelle direction and power out. Second, the wind, as measured at the PNL tower, had to be from a direction that would cause the turbine wake to fall on either another turbine or one of the meteorological towers. Data from each azimuth angle from one turbine to each of the others or the towers $\pm 30^\circ$ were incorporated. Third, single values that were judged to be noise rather than data and periods that escaped earlier detection but were actually times when the turbine parameter sensors were being calibrated were eliminated.

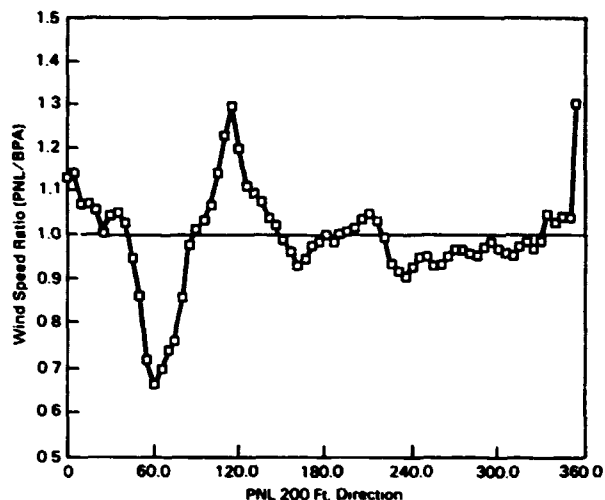


Figure 5--Time-consistent plot of the wind speed ratios measured at the two towers clearly showing the effects of tower shadow on wind speed

Since the MOD-2 turbines are actually huge anemometers in themselves, our concept was to use the turbines as the primary sensors. To check that the transfer functions of wind speed to power were the same for both turbines, all turbine power-out data from both turbines #1 and #3 were binned into 50 power classes for comparison to the wind speeds measured simultaneously at each tower. Figures 6 and 7 show the results of that exercise. In both cases, turbine #1 appears to out-produce turbine #3 at up to about design speed. Then, the reverse occurs. Whether this phenomenon is real or whether it is a calibration error has yet to be determined. In analyzing the composite data, power ratios were the calculated indicator of the sought-after wake effects. The turbine power transfer function cross-over at about design speed may consequently be the cause of some of

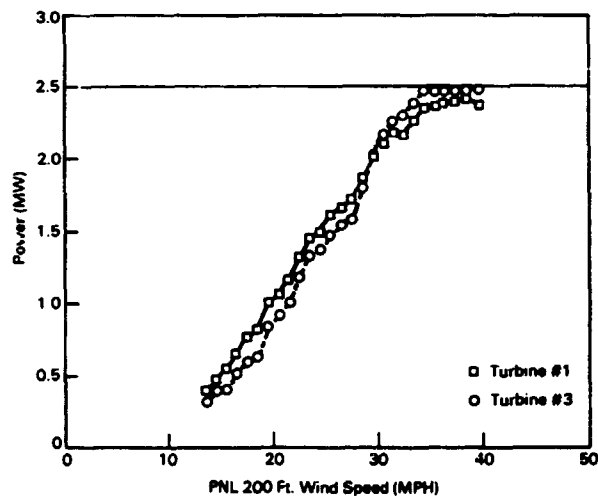


Figure 6--MOD-2 #1 and #3 wind speed to power transfer function using the wind speed measured at the PNL tower

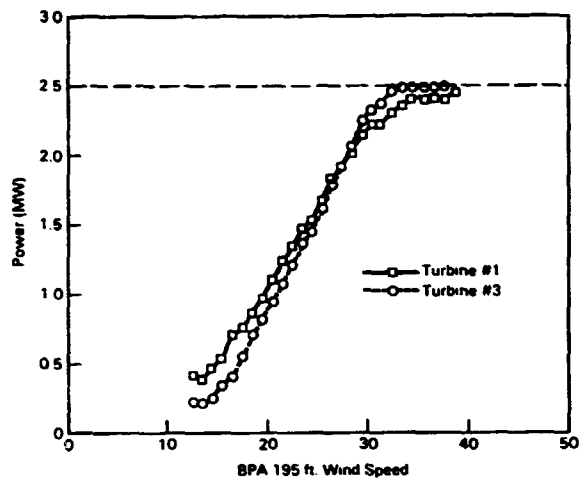


Figure 7--Same as Figure 6 except using the wind speeds measured at the BPA tower

the variance noticed in the various cases. Further analyses based on stability, wind direction, etc. is currently being pursued and the results will soon be available.

RESULTS

When the first graphs of the screened data were plotted, the result we had anticipated was not realized. Figure 8 shows the individual data points for the power ratio of upwind turbine power to downwind turbine power versus azimuth angle. Although there is a moderate hint of an effect, no firm conclusion could be drawn. These data were then subjected to further averaging, or binning, by azimuth angle. That is, they were averaged by 1° azimuth bins with the result shown in Figure 9. The individual data points in this plot are now the average of the data shown in Figure 8. The curved-fit line is a cubic spline fit to the data. It will be noticed that the minimum in the power is both above the power ratio = 1 line and offset to the left. The vertical offset simply implies that for an

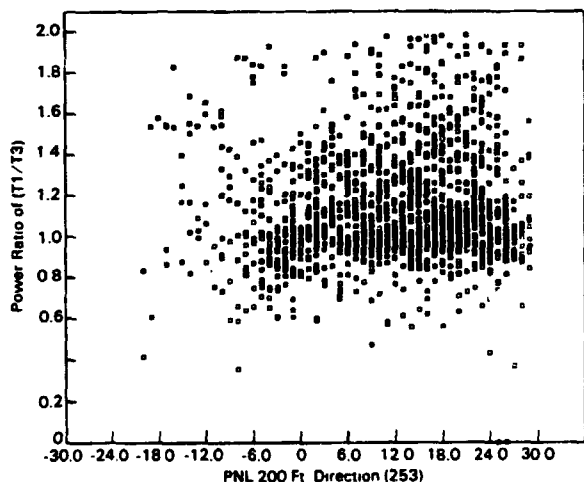


Figure 8--Turbine #1 and turbine #3 power ratio for all cases when the axis of the wake of turbine #3 was in line with turbine #1

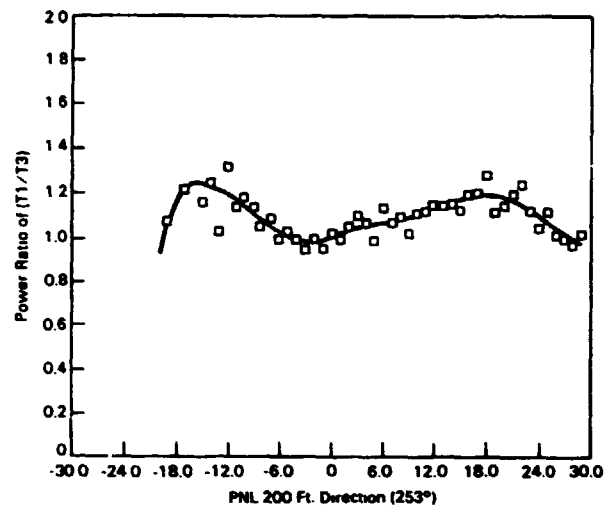


Figure 9--Same as Figure 8 but with all data in each 1° bin averaged. The solid line is a cubic spline fit to the data.

assumed uniform wind field over the entire test site, turbine #1 was out-producing turbine #3. The 200-ft or hub-height wind at the Fin tower was the reference wind in these studies. Since there is no stratification based on power classes, the offset implies that the baseline should be near the turbine power ratio of 1.2 rather than 1. The horizontal offset to the left might be taken lightly as the actual true angle between turbines #1 and #3 was not accurately measured before the analysis. We will discuss this further later. Thinking that the scatter of the data about the cubic spline fit might be explained if the data were stratified by power class, we subdivided the data into as many 500-kW bins as was practical and performed further analyses. Figures 10 through 13 show the results of that stratification. It should be pointed out that the data were screened further for these analyses and the minimum acceptable power was 500 kW.

Figure 10 is the same as Figure 9 but with the 500-kW cutoff and some other identified spurious data removed. Left of the -10° point on the graph, the data represent the average of less than 10 data points and might thereby be discounted. On the right-hand side of the graph, the data are all averages of more than ten values and frequently the average of 40 to 50 2-min average data. The result reinforces the point that at 10 diameters an average 15% power deficit can be expected.

Figure 11 is the composite or average data for all cases in the wake data set when the power out of turbine #3 was between 500 kW and 1 MW. Significantly more scatter is evident in the data but is attributable primarily to fewer primary data points. In only one 1° data bin were there more than 10 data points to be averaged. This suggests that the prominent dip of the spline fit line out at -8° to -10° is, in fact, artificial and that the real wake deficit may be exemplified by the adjacent plateau to the right of the null. Based on the number of data points averaged, the baseline power ratio for this power class might best be assigned to about 1.27, or turbine #1 producing about 20% more power than turbine #3.

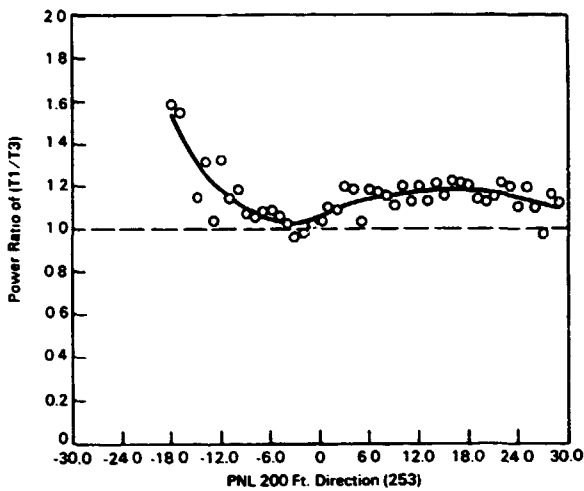


Figure 10--Same as Figure 9 with the minimum power set to 0.5 MW

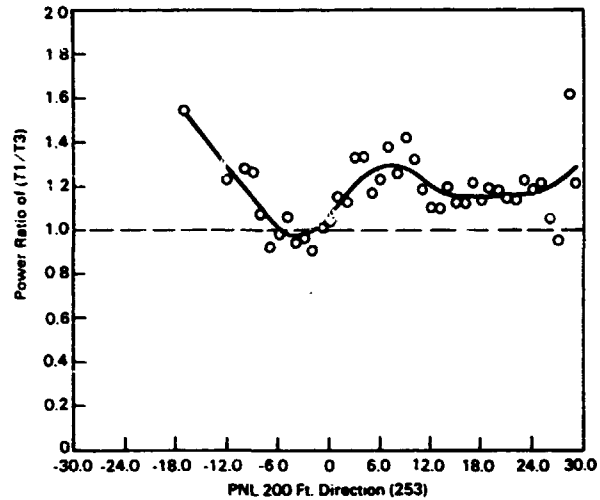


Figure 12--Same as Figure 9 but for those cases when the power out of turbine #3 was between 1.0 and 1.5 MW

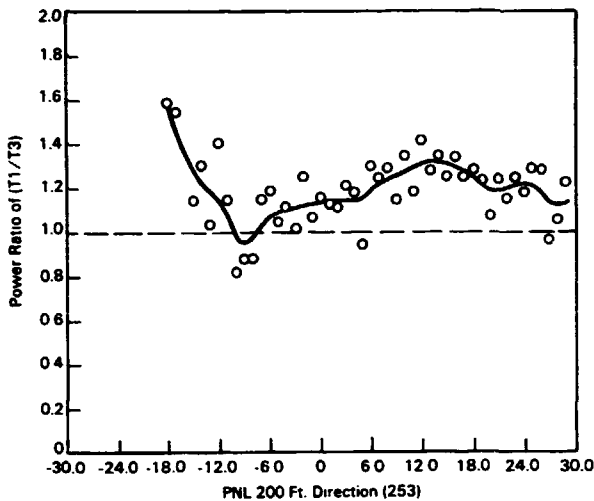


Figure 11--Same as Figure 9 but only for time when the power out of turbine #3 was between 0.5 and 1.0 MW

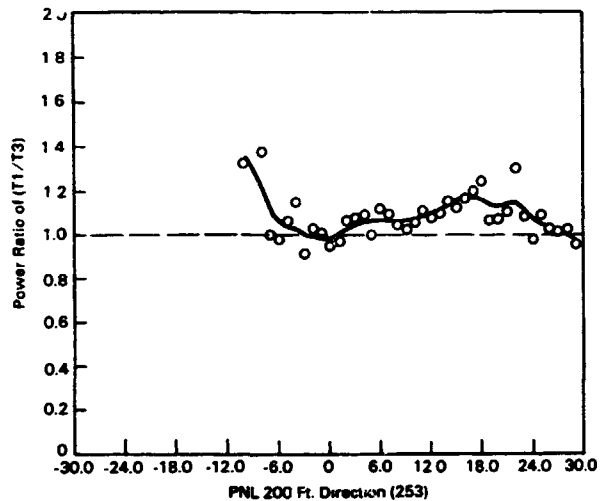


Figure 15--Same as Figure 9 except the power out of turbine #3 was anything greater than 1.5 MW

Figure 12 is the result for the data in the power class 1.0 to 1.5 MW. In this case there were about 25% more data for the entire set and for the most part there were more data in the bins of most importance. The nearly straight line in the 15° to 24° area on the right side of the graph is probably a reasonable approximation of the baseline for comparison. If this is so, then the deficit at the center is close to 20%. The large increase in the power ratio immediately to the right of the wake centerline is not felt to be the result of lateral reentrainment of momentum but rather a decrease in the number of data points averaged (higher variance).

The final power class had to include data from 1.5 to 2.5 MW to provide sufficient data for meaningful analysis. Figure 13 shows this data. In this power class we estimate the power ratio baseline to be about 1.1 and, therefore, the wake deficit for this high power class has been reduced to 11 or 12%. If Figures 10 through 13 were superimposed, one would observe an

interesting, and at this point unexplained, shift or migration of the region of maximum wake deficit to the right or northward, nearer the assumed centerline azimuth. Similarly, with increased power out the effect of the wake is apparently reduced. The lateral migration may be caused by the flow separating from the surface boundary layer at the higher wind speeds, and thereby reducing the ground effect or surface stress.

Although the evidence for a power reduction of the order of 15 to 25% at turbine separation distances of 10 diameters is shown by Figures 9 through 13, one must keep in mind Figure 8, which showed that the standard deviation about that average was very high indeed and that such a deficit is not constant by any means.

To illustrate any effect that can be discerned at closer separations, a small amount of data was

obtained with turbine #2 running and, ostensibly, producing a wake that was impacting turbine #1. These data were included in the wake data set and were analyzed similar to the previously discussed data. Because there were not enough data points, no power class stratification could be accomplished. The resulting analysis is depicted in Figure 14. In this graph, unlike the others, the centerline was fixed at an arbitrary azimuth that roughly splits the angle between turbine #2 and #3 with the vertex at turbine #1. From this, the baseline power ratio appears to be just below 1.0. In this case a power ratio of less than 1 infers that turbine #2 is producing more power at the reference wind speed than is turbine #1. The data at the right end of the graph (where the 276 is marked on the abscissa) represent the wake deficit of turbine #2 as seen by turbine #3. The magnitude of the deficit is about 11 or 12%, and the distance between the two turbines is 7 diameters.

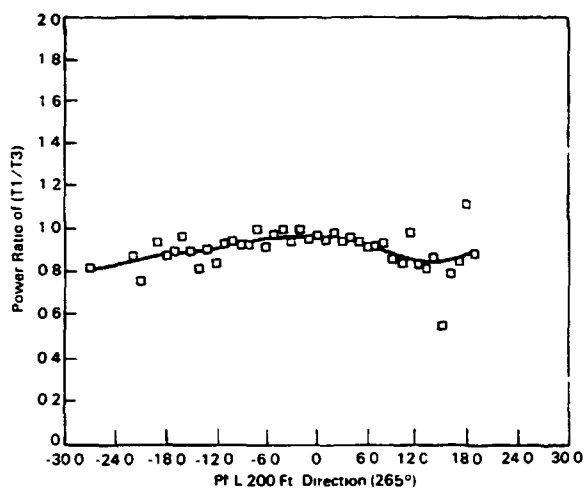


Figure 14--The power ratio of turbines #2 and #1 with the wake of turbine #2 depicted at about 12° to 14°. Some of the data used occurred with all three turbines running and some slight effect of turbine #3's operation can be inferred from the lefthand part of the plot.

In performing these analyses we have attempted to utilize as much data as possible from the Goodnoe Hills test site. As mentioned earlier, the decision to use the MOD-2 wind turbines as the primary sensors for the wakes analysis does not preclude us from looking at other data. There are periods of time when the turbines were running and producing wakes that impacted the meteorological towers. When the wind blows from the WSW to WNW the wake of turbine #3 should be monitored by the instrumented PNL tower. By screening our data in the appropriate manner, we were able to pick out the wake. Figure 15 is a cubic-spline fit to the bin-averaged wind speed data for periods when turbine #3 was running and the wind was from 260° ±30°. On this graph we have plotted the ratio of the measured wind speeds on the ordinate as opposed to the power ratio. The wind speed deficit at the distance of 8.3 diameters (turbine #3 to the PNL tower) is about 20%.

Figure 16 is another example of a turbine wake interacting with the PNL tower. In this instance, the wake-

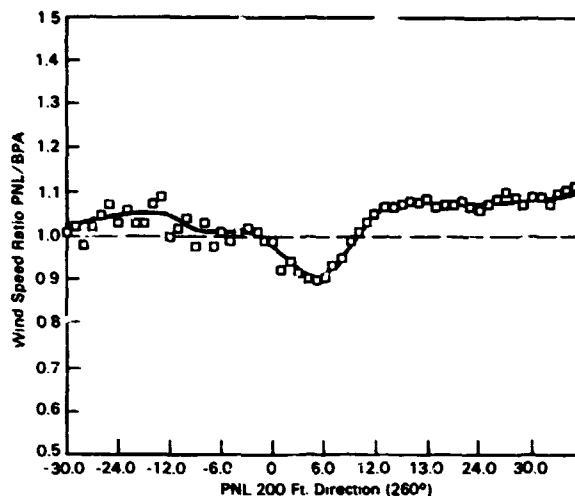


Figure 15--The ratio of measured wind speeds at the PNL and BPA towers with the PNL tower in the wake of turbine #3

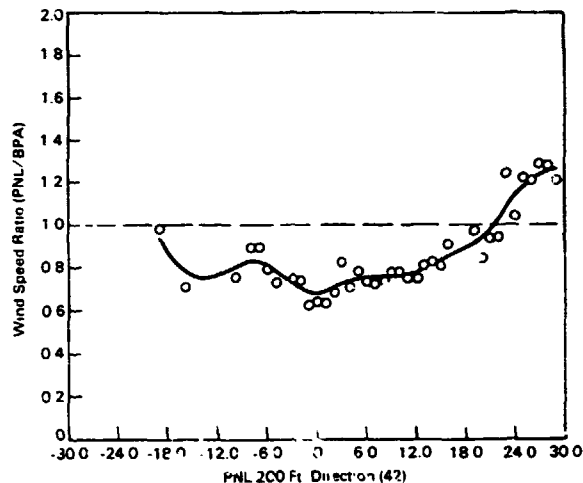


Figure 16--Wind speed ratio of the PNL and BPA measured wind speeds during the occurrence of a wake from turbine #1 at the PNL tower

producing turbine is #1 and the separation distance is only 2.2 diameters. The wind speed deficit, again taking into account the difference in measured wind at the two towers, appears to be approximately 45 to 50%.

How well do these observations compare with other measured wake data? Several researchers have made wake measurements at the MOD-OA at Clayton, New Mexico. Wind speeds in the wake of the turbine were monitored at a vertical plane array two diameters downwind (1). The array consisted of seven 200-ft towers with 12 fast-response anemometers arranged in a circle whose diameter equalled the turbine rotor diameter. Inside this circle was a horizontal line of 5 additional anemometers at hub height. The maximum deficit measured in the case analyzed was 25%. Later, the researchers added a pair of towers to the Clayton site approxi-

mately two diameters away from the MOD-0A on the same azimuth but on the other side of the turbine relative to the seven-tower array (2). Although the authors do not summarize their data, it appears that in the transition region of the wake outside the potential core, the typical deficits that were measured ranged from 25 to 50%, with the greater deficits occurring at the lower mean wind speeds. In identifiable far-wake instances, the deficit measured ranged from 20 to 30%. In these cases also, the larger deficits occurred at the high wind speeds.

SUMMARY AND CONCLUSIONS

Comparison of these study results to current numerical wake models (3,4,5,6) have not been completed. Results are of such a preliminary nature that reporting them here might serve only to do a disservice to both the data analyses and the models. The authors are resolved to complete this work and believe that the data base created will prove to be ultimately useful.

To the best of our knowledge, this is the first opportunity anyone has had to gather, process and analyze wind turbine wake data in this manner. One of this study's major shortcomings is the fact that we currently suffer from a paucity of data when we should have an abundance. This should not be construed as an excuse. The lack of data from a program depending on prototypical equipment (both the data system as well as the turbines) is normal. Since the data would be collected normally, the project becomes time-dependent and in some ways time-intensive but not labor-intensive.

Since the wind is stochastic in nature, attempting to define the structure of a turbine wake with spatially and temporally small samples required by labor-intensive methods is not only tedious but potentially quite inaccurate. The utility of the more labor-intensive methods is potentially in verifying measurements such as we have made at the site. Verification of the possible boundary layer effects on the curvature of the wake as a function of wind speed and/or power extraction would be most difficult and expensive as well as frustrating were it to be attempted with a labor-intensive method.

As mentioned above, the nature of the wind is stochastic in both speed and direction. Many observers or researchers have commented that the wakes and hence the flow at the Goodnoe Hills Test Site do not necessarily go in a straight line. In analyzing the wake data set, indications of this anastomosing phenomenon do not leap out but conversely there are indications of flow veering or backing under some, as yet undefined, circumstances. The wake research program at PNL is part of a larger program involved with atmospheric and topographic influences on wind flow. It is our intention to proceed with both of these research tasks as quickly as possible.

Finally, it would appear from the nature of the data collected at the test site that statistical studies of the power-producing wind speeds and their directions are in order. The three MOD-2s at the test site were laid out such that there was some probability of wake interaction between any pair of the turbines or even all three. If the number of occurrences of wakes impacting downwind turbines as screened by our analysis is any indication, then the impact of wakes may not be significant with proper array design. The per-

cent of time that wakes appeared to impact other turbines was a small percentage of the total time. After making such a statement, we hasten to add that the site is a test site after all. Under those conditions, as opposed to the more typical utility conditions, the opportunity for wake interactions may have been significantly reduced due to human intervention and testing.

This is a preliminary report of ongoing work; considerably more analysis is left to be done. Besides the multivariate analysis that we have outlined here, there is also considerable verification to be done. Some of this can be done relatively soon, some will have to wait for the return to service of the remaining two turbines at Goodnoe Hills. We anticipate that this work will continue for several more years. Although it is tempting to propose that the question of wake momentum deficits could in fact practically be put to rest at this moment, there is some question in our minds if that is so. At the current state-of-the-art of turbine design and construction where large margins are built in for self-protection, the statement that we can calculate wake deficits now may be true if a worst-case condition is all that is desired. Conversely, in the future when designs become more finely tuned and the margins designed and built into turbines are reduced to a bare minimum, we are not comfortable with our current capabilities.

The current state of the wake turbulence-induced stress loads is an unknown. It appears that there is potential for considerable work in this area in the future. Variations of the analyses performed to look at wake deficits using the DDS data may be appropos for turbulence studies; however, the instrumentation and data rate would both have to be supplemented and/or changed.

ACKNOWLEDGEMENTS

The authors are grateful for the assistance of Michael Kosorok whose considerable talents with a computer have proven to be technically most rewarding; to L. L. Wendell whose encouragement and inquiring mind kept us on our toes; to Betsy Owczarski who has the ungrateful job of attempting to teach us the proper use of the English language; to D. S. Renne and D. L. Hadley who started this project and have provided considerable help along the way; and Jack Cadogan of the U.S. Department of Energy (DOE) who supported us in our efforts. A special thanks goes to our able and willing typist who, even when given the manuscript at the eleventh hour, managed to complete the job.

This project was funded by DOE under Contract DE-AC06-76RLO 1830. Pacific Northwest Laboratory is operated for DOE by Battelle Memorial Institute.

REFERENCES

1. Connell, J. R., and R. L. George. "The Wake of the MOD-0A Wind Turbine at Two Rotor Diameters Downwind on December 3, 1981." PNL-4210, Pacific Northwest Laboratory, Richland, Washington, 1982.
2. Doran, J. C., and K. R. Packard. "Comparison of Model and Observations of the Wake of a MOD-0A Wind Turbine." PNL-4433, Pacific Northwest Laboratory, Richland, Washington, 1982.

3. Eberle, W. R. "Wind Flow Characteristics in the Wakes of Large Wind Turbines, Volume 2 - Analytical Model Development." DOE/NASA/0029-1, NASA CR-165380, National Aeronautics and Space Administration, 1981.
4. Lissaman, P. B. S., et al. "Numeric Modeling Sensitivity Analyses of the Performance of Wind Turbine Arrays." PNL-4183, Pacific Northwest Laboratory, Richland, Washington, 1982.
5. Crafoord, C. "Interaction in Limited Arrays of Windmills." Report DM-86, Department of Meteorology, University of Stockholm, 1979.
6. Bossanyi, E. A. "Windmill Wake Decay: A Preliminary Theoretical Model." SERI/TR-635-1:80, Solar Energy Research Institute, Golden, Colorado, 1983.

HORIZONTAL AXIS WIND TURBINE POST STALL
AIRFOIL CHARACTERISTICS SYNTHESIZATION

N95-27974

James L. Tangler
Rockwell International
Wind Energy Research Center
Golden, Colorado 80402-0464

Cyrus Ostowari
Texas A&M University
College Station, Texas 77843-3141

ABSTRACT

Blade-element/momentum performance prediction codes are routinely used for wind turbine design and analysis. A weakness of these codes is their inability to consistently predict peak power upon which the machine structural design and cost are strongly dependent. The purpose of this study was to compare post-stall airfoil characteristics synthesization theory to a systematically acquired wind tunnel data set in which the effects of aspect ratio, airfoil thickness, and Reynolds number were investigated. The results of this comparison identified discrepancies between current theory and the wind tunnel data which could not be resolved. Other factors not previously investigated may account for these discrepancies and have a significant effect on peak power prediction.

1. INTRODUCTION

The cost of a wind turbine is influenced by the designer's ability to predict peak power. Uncertainty in the performance prediction codes for predicting peak power forces the designer to be conservative and oversize the generator and other mechanical components. This practice leads to higher machine cost which in turn increases the resulting energy cost. The ability to predict peak power is dependent on an accurate description of the airfoil lift and drag characteristics immediately after stall. As a rotor approaches peak power, aerodynamic stall progressively envelopes the blade from root to tip. At peak power the root end of the blade is deeply stalled and the tip region, where most of the power is being developed, is passing through the angle of attack range of 15 to 25 degrees. Peak power is most sensitive to the airfoil characteristics over this angle of attack range.

Blade-element/momentum performance prediction codes provide the principle means for rotor design and analysis. With the use of reasonable airfoil data, these codes have been able to provide good estimates of rotor performance provided a substantial portion of the blade is not stalled. Past experience has shown that, for a fixed pitch rotor, when a large portion of the blade is stalled the use of two-dimensional (2-D) airfoil data under-predicts peak power and shows a rapid drop off thereafter relative to measured power. A detailed discussion of this problem is contained in References 1 and 2. The under-prediction of peak power has motivated the development of 3-D post stall airfoil data synthesization routines (References 3 and 4). Of these two routines, that of Reference 3 is more widely used because of its user friendly nature. Without any user interaction the routine automatically provides a smooth curve fit from where the 2-D airfoil data

leaves off up through the highest angle of attack experienced by the blade during stall. The approach of Reference 4 is more subjective and requires the user to provide discrete airfoil data in the light stall region. Both of these routines are based on past studies which show that after stall the airfoil characteristics of lift and drag are strongly governed by blade aspect ratio and are relatively independent of the airfoil geometry and Reynolds number. After stall, lower aspect ratios result in lower values of lift and drag coefficients due to greater flow leakage around the tip that relieves the pressure differential across the blade.

Although the 3-D post-stall airfoil data synthesization routines provided the needed direction to help solve the peak and post-stall power prediction problem an adequate post-stall airfoil data base was not available at the time of their development. Consequently, these methods were tailored to predict peak power based on comparisons for a few machines. Applied to other machines these methods were suspect when predicted and measured peak power were not in agreement. For this reason, it was widely held that the 3-D post-stall synthesization routines needed further verification against a comprehensive post-stall airfoil data base. In an effort to satisfy this need, post-stall airfoil data were acquired in the Texas A&M University wind tunnel.

2. POST STALL WIND TUNNEL TEST

To establish the data base to better verify the post stall synthesization theory, nonrotating wing sections were tested in the Texas A&M 7 x 10 ft wind tunnel. Post stall performance characteristics were established as a function of aspect ratio, airfoil thickness, and Reynolds number. For this purpose the test models had a one foot chord and were of the NACA 44XX family of airfoils. Blade aspect ratios of 6, 9, and 12 and α were tested for airfoil thicknesses of 9, 12, 15, and 18 percent at Reynolds numbers of 250,000, 500,000, 750,000 and 1,000,000. The results from this study showed that the post stall airfoil characteristics of C_L and C_D are a strong function of aspect ratio as expected and a weak function of airfoil thickness. In the post stall region the influence of Reynolds number was negligible for the range tested. A report (Reference 5) containing the results from this study and can be obtained from Rocky Flats Wind Energy Research Center (WERC).

Two plots extracted from this report which illustrate the influence of aspect ratio on C_L and C_D are shown in Figures 1 and 2. Figure 1 shows C_D versus angle of attack for the four aspect ratios. For discussion purposes the figure can be broken down into three distinct angle of attack regions. In the

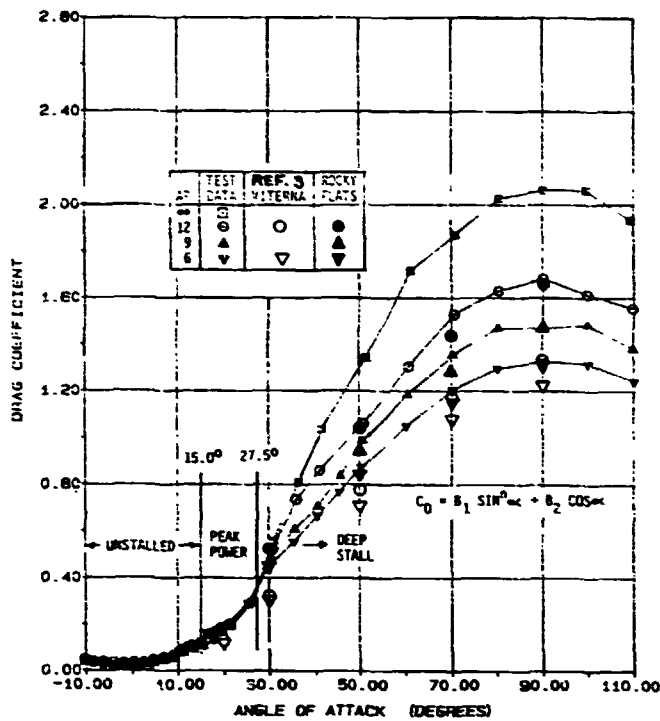


Fig. 1. Effect of Aspect Ratio on Drag Coefficients of the NACA 4418 Airfoil at $RN = 0.25 \times 10^6$.

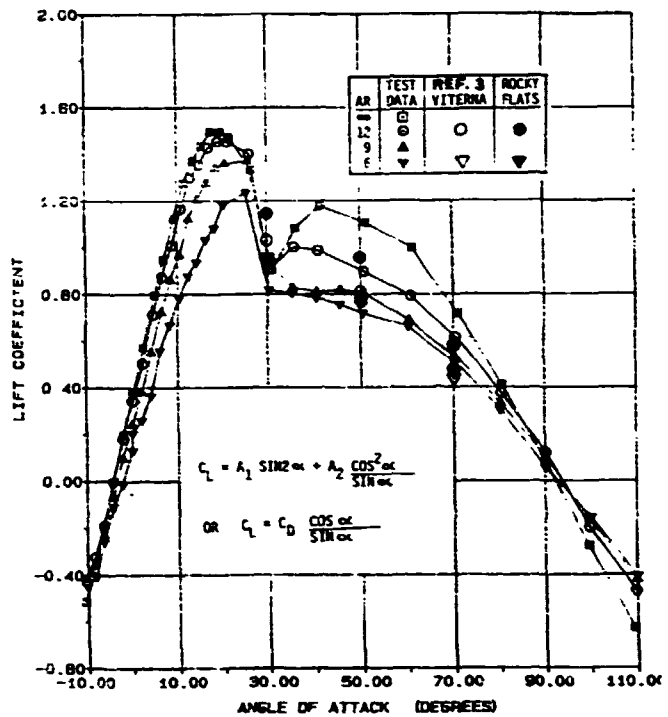


Fig. 2. Effect of Aspect Ratio on Lift Coefficients of the NACA 4418 Airfoil at $RN = 0.25 \times 10^6$.

TABLE 1. POST STALL C_L , C_D EQUATIONS

Equations of Reference 3	
$C_{D_{max}} = 1.11 + 0.018 AR$	$\theta (\alpha=90^\circ)$ (1)
$C_D = B_1 \sin^2 \alpha + B_2 \cos \alpha$	$(\alpha=15^\circ \text{ to } 90^\circ)$ (3)
where:	
$B_1 = C_{D_{max}}$	
$B_2 = \frac{C_{D_S} - C_{D_{max}} \sin^2 \alpha_S}{\cos \alpha_S}$	
$C_L = A_1 \sin 2\alpha + A_2 \frac{\cos^2 \alpha}{\sin \alpha}$	$(\alpha=15^\circ \text{ to } 90^\circ)$ (5)
where:	
$A_1 = B_1/2$	
$A_2 = (C_{L_S} - C_{D_{max}} \sin \alpha_S \cos \alpha_S) \frac{\sin \alpha_S}{\cos^2 \alpha_S}$	

Equations Derived from Texas A&M Data											
$C_{D_{max}} = \frac{1.00 + 0.065 AR}{(0.9 + t/c)}$	$\theta (\alpha=90^\circ)$ (2)										
$C_D = B_1 \sin \alpha + B_2 \cos \alpha$	$(\alpha=27.5^\circ \text{ to } 90^\circ)$ (4)										
where:											
$B_1 = C_{D_{max}}$											
$B_2 = \frac{C_{D_S} - C_{D_{max}} \sin \alpha_S}{\cos \alpha_S}$											
	<table border="1"> <thead> <tr> <th>α</th> <th>C_D</th> </tr> </thead> <tbody> <tr> <td>16°</td> <td>0.100</td> </tr> <tr> <td>20°</td> <td>0.175</td> </tr> <tr> <td>25°</td> <td>0.275</td> </tr> <tr> <td>27.5°</td> <td>0.363</td> </tr> </tbody> </table>	α	C_D	16°	0.100	20°	0.175	25°	0.275	27.5°	0.363
α	C_D										
16°	0.100										
20°	0.175										
25°	0.275										
27.5°	0.363										
Same as equation 5, however the use of the new $C_{D_{max}}$ for evaluating A_1 and A_2 results in a stronger AR influence.											
alternate: $C_L = \frac{C_D \cos \alpha}{\sin \alpha}$	$(\alpha=30^\circ \text{ to } 90^\circ)$ (6)										
with: $C_L = 0.9$	$\theta \alpha = 30^\circ$										

AR - aspect ratio
 C_D - drag coefficient
 C_L - lift coefficient
 t/c - non-dimensional airfoil thickness
 α - angle of attack
 α_S - angle of attack at stall, usually 15°

first region up to 15 degrees, the wings are unstalled and for performance prediction purposes similar 2-D airfoil data for this region is normally acquired from one of many airfoil data catalogs for a desired Reynolds number. However, for this 3-D testing induced drag effects steadily increase with angle of attack with the magnitude being greater for lower aspect ratios. This subtle trend is masked by the accuracy of the data over this angle of attack range. The second angle of attack region from 15 to 27.5 degrees is worthy of special attention since it has the dominant effect on peak power prediction. An important characteristic of this region is that aspect ratio effects cannot be discerned. In this region the higher induced drag associated with lower aspect ratio is neutralized by the lower pressure drag associated with lower aspect ratio. Aspect ratio effects are not seen to have a net influence on drag coefficient until the angle of attack exceeds 27.5 degrees. Above this angle the pressure force across the wing increases as the tip relief diminishes with aspect ratio.

For comparative purposes the post stall synthesis equations of Reference 3 were used to generate corresponding values of C_L and C_D . The calculated values are compared to the test data over the angle of attack range of 20 to 90 degrees as shown by the large open symbols for aspect ratios of 6 and 12. For both aspect ratios the calculated values fall well below measured values. In addition, the equations lack the strong sensitivity to aspect ratio as shown by the data above a 30 degree angle of attack. To better reflect the measured first order aspect ratio and second order airfoil thickness effects, equations 2 and 4 are presented for $C_{D_{max}}$ and C_D , respectively. These equations were used to generate the shaded symbols and show good agreement with test results over the angle of attack range of 27.5 to 90 degrees. The new maximum drag coefficient equation has three times greater sensitivity to aspect ratio. In addition further aspect ratio sensitivity was acquired by using a first order (Sin) term in the drag coefficient equation. The new approximation (Equation 4) only applies over the angle of attack range of 27.5 to 90 degrees versus 15 to 90 degrees used in the original approximation (Equation 3). The discrete values of drag shown in Table 1 for the angle of attack range of 16 to 27.5 degrees are for airfoils having thickness of 12 percent or greater. The wind tunnel test results show that for thinner airfoils a more rapid increase in drag can be anticipated over this local angle of attack range. A step jump in drag is needed to transition from 2-D data to discrete 3-D data. An increase to a value of 0.10 appears reasonable in going from 15 to 16 degrees.

A comparison of the calculated measured lift coefficient versus angle of attack is shown in Figure 2 for the various aspect ratios. Prior to stall a reduction in aspect ratio reduces the slope of the C_L curve. In blade-element/momentum type analyses this trend is approximated through the use of the tip loss factor. In the post stall region the measured lift coefficient undergoes a rapid initial drop off followed by a moderate reduction in C_L up until the angle of attack region of 60 degrees. An approximation of this post stall behavior is obtained using

Equation 5 from Reference 3. The equation provides a continuous drop off from peak C_L to zero at 90 degrees in a manner characteristic of the test data. The equation makes no attempt to approximate the initial drop and recovery the C_L experiences for the higher aspect ratio blades. However, this simplification does not appear to result in significant error. Calculated values of C_L are shown by the large open symbols using this equation with the values of A_1 and A_2 based on the old $C_{D_{max}}$ (Equation 1) as given in Reference 3. Calculated values of C_L using the new $C_{D_{max}}$ (Equation 2) to determine A_1 and A_2 are shown by the solid symbols. Stronger aspect ratio dependency and somewhat better agreement is achieved using the new approximation for $C_{D_{max}}$. This equation provides good results from peak C_L throughout most of the post stall region which typically begins around 15 degrees for most airfoils.

Two interesting characteristics of these data in Figures 1 and 2 is that although the magnitude of C_L and C_D are a function of aspect ratio, the ratio of C_L/C_D for a given angle of attack is found to be independent of aspect ratio throughout the deep stall angle of attack range over 30 degrees. In addition, C_L/C_D or more appropriately L/D , passes exactly through a value of 1.0 at an angle of attack of 45 degrees as would a flat plate. These characteristics are shown by the square symbols in Figure 3. For comparison flat plate theory is represented by the solid line as calculated by the equation $L/D = \cos\alpha/\sin\alpha$. The data points of L/D are seen to approximate the ratio of $\cos\alpha/\sin\alpha$ over the angle of attack range of 30 through 60 degrees. Beyond this point the data points fall above flat plate theory due to the suction developed by the leading edge curvature. Based on this trend equation 5 can be replaced by the flat plate theory alternate of equation 6. Using equation 5, the ratio of L/D will be somewhat on the high side throughout the angle of attack range and will not quite satisfy the observation that $L/D = 1$ at an angle of attack of 45 degrees as does equation 6.

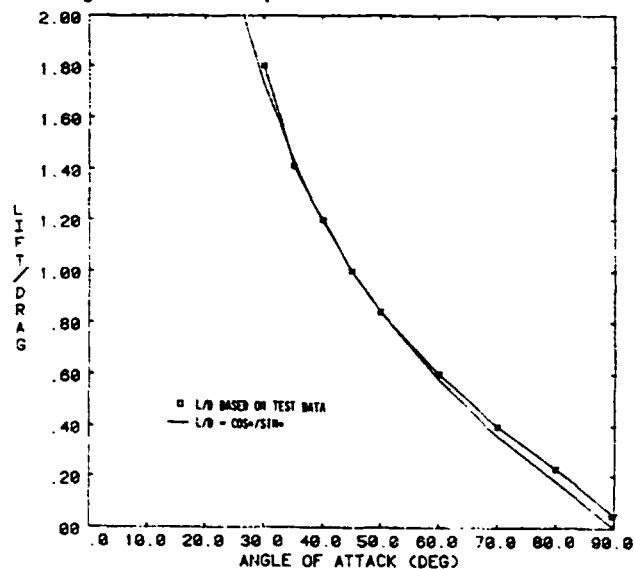


Fig. 3 Effect of Aspect Ratio on Lift/Drag Ratio in Deep Stall

3. PEAK POWER PREDICTIONS

Predicted performance was calculated for three fixed pitch wind turbines using Rocky Flats blade-element/momentum analysis (PROPSH) which is described in Reference 2. Using both the post stall airfoil data synthesization method of Reference 3 and the modified equations based on the Texas A&M wind tunnel data predicted peak power was compared to measured peak power. The machines analyzed were the Jay Carter 25, ESI-54, and the MOD-0. In each case predicted peak power was calculated on the low side of measurements by 3 to 15 percent using the modified equations based on the Texas A&M wind tunnel data. Better agreement was achieved using the synthesization method of Reference 3. Calculated peak power relative to measured power varied from being 2 percent on the low side to 6 percent on the high side. Overall the modified equations based on the wind tunnel data predicted peak power 3 to 12 percent lower than the equations of Reference 3 which were developed by tailoring the equations to correlate with actual peak power measurements.

The better agreement achieved using the equations of Reference 3 is attributed mainly to the higher L/D resulting in the angle of attack range of 15 to 30 degrees. As previously indicated this portion of the post stall region has the greatest impact on peak power prediction. Another factor not to be overlooked is the accuracy of C_{Lmax} associated with the 2-D data tables used in the calculations. Any error in the C_{Lmax} utilized translates into a similar error in the value of peak power.

Speculation as to the difference in L/D resulting from the lift and drag equations of Reference 3 versus the lower L/D resulting from the modified equations based on the Texas A&M wind tunnel data yields some potential explanations. The Texas A&M wind tunnel tests were nonrotational. Aerodynamicists over the years have speculated that for rotating wings centrifugal force effects are present in the boundary layer that result in spanwise flow toward the blade tip. Spanwise flow is thought to enhance performance by delaying separation of the boundary layer. Another source of spanwise flow is the spanwise suction gradient that results from the rotating blades local oncoming velocity being proportional to the blade radius. For both of these causes, the spanwise flow is from blade root to blade tip.

A second scenario that warrants serious consideration when trying to account for low peak power predictions deals with elastic twist of the blade. Prior to stall many airfoils have little or no nose down (negative) pitching moment. When stall occurs in the angle of attack range of 15 to 30 degrees, the moment coefficient rapidly diverges. The resulting large increase in nose down pitching moment can result in elastic twist toward feather which would enhance the power output and delay stall. The twist effect would become greater with windspeed as the stall enveloped the blade while propagated outward toward the tip. The occurrence of just a couple of degrees of elastic twist with increasing windspeed would substantially enhance peak power and post peak power. Elastic twist is a real consideration the manufacturer should be aware of because of its strong influence on

measured post stall power. The degree of elastic twist can be expected to vary from one machine to another depending on the amount of blade torsional stiffness.

4. CONCLUDING REMARKS

The Texas A&M post stall wind tunnel test of the NACA 44XX series airfoils as influenced by airfoil thickness, Reynolds number, and aspect ratio yielded the following findings.

- Reynolds number was found to have an insignificant influence on the airfoil characteristics over the range of 250,000 to 1,000,000.
- Airfoil thickness was found to have little effect on post stall C_L although it does influence C_{Lmax} which is normally acquired from a 2-D airfoil data catalog. Increased thickness did provide some reduction in drag throughout the post stall region.
- Aspect ratio was the dominant influence on the post stall airfoil characteristics. However, this influence was not readily discerned over the angle of attack range of 15 to 30 degrees where the lower induced drag associated with high aspect ratios is being neutralized by a corresponding increase in pressure drag. Above 30 degrees both drag coefficient and lift coefficient increased with aspect ratio such that the resulting ratio of L/D was independent of aspect ratio.

Applying these test results the post stall synthesization equations of Reference 3 were modified. Peak power predictions using the newly modified equations and those of Reference 3 showed that:

- the modified equations underpredicted peak power by 3 to 15 percent
- the equations of Reference 3, because of their more optimistic post stall L/D ratio, provided a better approximation of peak power.

Potential causes of the differences between measured peak power and that predicted using the modified equations based on the Texas A&M data are:

- the inability of nonrotating wind tunnel test to represent the influence of radial flow effects
- elastic twists effects resulting from the divergence of the post stall moment coefficient.

REFERENCES

1. "First Meeting of Specialists on the Aerodynamics of Horizontal-Axis Wind Turbines," Sponsored by Rocky Flats Wind Energy Research Center and NASA Wind Energy Project Office, Wichita, Kansas, April 20-21, 1983.
2. Tangler, J. L., "Assessment of Blade-Element/Momentum Analysis for Horizontal-Axis Wind Turbines," Sixth Biennial Wind Workshop, Minneapolis, Minnesota, June 1983.

3. Viterna, L. A. and Corrigan, R. D., "Fixed Pitch Rotor Performance of Large Horizontal Axis Wind Turbines," paper presented at the DOE/NASA Workshop on Large Horizontal Axis Wind Turbines, (Cleveland, Ohio), July 28-30, 1981.
4. Hibbs, B, and Radkey, R. L., "Calculating Rotor Performance with the Revised 'PROP' Computer Code," RFP-3508 UC-60, February 1983.
5. Ostowari, C., and Naik, D., "Post Stall Wind Turbine Studies of Varying Aspect Ratio Wind Tunnel Blades with NACA 44XX Series Airfoil Sections," RFP-_____, June 1984.

NOTICE

The work reported in this paper was performed under contract No. DE-AC04-76DP03533 for the U.S. Department of Energy.

PRELIMINARY ANALYSIS OF DYNAMIC STALL EFFECTS
ON A 91-METER WIND TURBINE ROTOR

N95-27975

Robert E. Wilson

Oregon State University
Corvallis, Oregon 97331

ABSTRACT

Analytical investigation of dynamic stall on HAWT rotor loads was conducted. Dynamic stall was modeled using the Gormont approach on the MDD-2 rotor, treating the blade as a rigid body teetering about a fixed axis. Blade flapwise bending moments at station 370 were determined with and without dynamic stall for spatial variations in local wind speed due to wind shear and yaw. The predicted mean flapwise bending moments were found to be in good agreement with test results. Results obtained with and without dynamic stall showed no significant difference for the mean flapwise bending moment. The cyclic bending moments calculated with and without dynamic stall effects were substantially the same. None of the calculated cyclic loads reached the level of the cyclic loads measured on the MDD-2 using the Boeing five-minute-average technique.

loads on the time rate of change of the angle of attack as well as the angle of attack, and hysteresis in the lift, drag, and pitching moment. These characteristics would be expected to increase both mean and cyclic loadings. Noll and Ham [2] in their investigation of the effects of dynamic stall on small wind systems concluded that dynamic stall could increase fixed pitch horizontal axis wind turbine normal loads and moments by "about 10 percent." Accordingly, this study was undertaken to examine the possible effects of dynamic stall on the MDD-2 wind turbine. Extensive data on mean and cyclic flapwise loads have been obtained for the MDD-2 [3].

ANALYSIS

Geometry

The analytical model used to investigate the effect of dynamic stall on the mean and cyclic flapwise bending moments consisted of a rigid two-bladed rotor teetering about a fixed point. An existing program [4] was modified to treat a teetering rotor. Figure 1 shows a blade element, the wind, V_W , and the coordinate system. Looking upwind, the rotation of the rotor is counterclockwise with the rotor teeter angle designated as ψ . The axis of rotation, x , is fixed in space so that rotor yaw, represented by the angle δ , is due to shifting of the wind rather than motion of the yaw axis. Each blade of the two-bladed rotor lies in the same plane so that there is no precone to the rotor.

The blade positions differ by an angle of 180° and the teeter angles of the two blades differ in algebraic sign. One blade is designated as the master blade and the position angle, θ , and the teeter angle, ψ , are given for the master blade.

Blade Bending Moment

The blade element illustrated in Figure 1 is shown in Figure 2 as part of a blade section which extends from r , to the blade tip. Loadings due to the aerodynamic forces and the centrifugal accelerations are illustrated in Figure 2. For a blade element of mass per unit span, μ , rotating at a constant angular velocity, Ω , the contribution of the above loadings on the element to the flapwise bending moment at position s , is

$$dM_1 = (s-s_1)(w-\mu\ddot{v})dr - \mu s\Omega^2(v-v_1)dr \quad (1)$$

Here w is the aerodynamic load per unit span. Rigid body motion of the rotor blade due to teeter motion yields $v = r\sin\psi = r\psi$ so that the contribution to the flapwise bending moment becomes

$$dM_1 = (r-r_1)[w - \mu r(\ddot{\psi} + \Omega^2\psi)]dr \quad (2)$$

The motion of the rotor, about the teeter axis when ψ is small and the teeter axis is perpendicular to the blade span ($\delta_3 = 0$) is described by

$$I(\ddot{\psi} + \Omega^2\psi) = M_{net} \quad (3)$$

NOMENCLATURE

- a Speed of sound
- C_L Lift coefficient
- c Blade chord
- I Teeter moment of inertia
- M Flapwise bending moment
- M Mach number
- r Distance along blade
- R Blade radius
- s Distance measured normal to axis of rotation
- v Blade of deflection
- V Wind speed
- w Aerodynamic load per unit span
- W Local relative velocity
- α Time rate of change of angle of attack
- α Angle of attack
- γ_L Dynamic stall parameter
- δ Yaw angle
- δ_3 Teeter axis tilt
- ψ Teeter angle
- μ Blade mass per unit span
- θ Master blade position angle
- Ω Rotor angular velocity

INTRODUCTION

Large horizontal axis wind turbine rotors experience on the order of 10^9 stress cycles during a projected 30-year lifetime. Cyclic loads due to gravity, tower shadow, wind shear, and yaw contribute to stress cycling as well as wind turbulence which can be viewed as a cyclic disturbance in the reference system of the blade. With the exception of gravity, the loads mentioned above are aerodynamic in nature and, since dynamic stall has been identified as playing a significant role in influencing the performance and fatigue life of the vertical axis wind turbine [1], it has been conjectured that dynamic stall plays a similar role in influencing cyclic loads of horizontal axis wind turbines.

The primary characteristics of dynamic stall are the occurrence of stall beyond the angle of attack associated with the static stall, the dependence of the

where

$$I = 2 \int_0^R r^2 \rho dr \quad (4)$$

and the net teeter moment is

$$M_{net} = \int_{Blade 1} r \omega dr - \int_{Blade 2} r \omega dr$$

Substitution of Eq. (3) into Eq. (2) yields an expression for the differential flapwise contributions of the aerodynamic forces and the accelerations (both centrifugal and teetering) to the flapwise bending moment.

$$dM_1 = (r-r_1) \omega dr - \frac{M_{net}}{I} (r-r_1) r \rho dr \quad (5)$$

Measurements of the flapwise bending moment of the MOD-2 wind turbine were made at station 370. At this station, the contributions given in Eq. (6) can be written as

$$M_1 \Big|_{aero} = -0.352 M_{net}$$

Gravitational contributions must also be included. Including the blade twist at station 370 (twist = $\beta = 2.5^\circ$) the bending moments due to gravity are

$$g \int_{r_1}^R (r-r_1) \rho dr [\sin\psi \cos\beta \sin\theta + \sin\beta \cos\theta] \quad (6)$$

For the MOD-2 with small ψ the above contribution is

$$3,219,000 \psi \sin\theta + 142,900 \cos\theta \text{ N-m}$$

The total of the gravitational, aerodynamic, and acceleration contributions to the flapwise bending moment at station 370 is

$$M_1 \Big|_{Total} = M_1 \Big|_{aero} - 0.352 M_{net} + 3.219 \cdot 10^6 \psi \sin\theta + 1.43 \cdot 10^5 \cos\theta \quad (7)$$

The gravity terms play a large role in determining the cyclic bending moments.

Wind Input

The wind input used to model the effects of dynamic stall consisted of a steady wind with a yaw angle of 15° and with wind shear. The surface roughness used was 0.32 m which yields a peak wind speed of $1.107 V_{hub}$ when the blade tip is at its highest position and a minimum wind speed of $0.736 V_{hub}$ when the blade tip is at its lowest position. Examination of Goldendale test site wind measurement records indicated that the mean shear corresponds to a surface roughness of 0.32 m. This surface roughness yields a wind profile that is close to a power law profile exponent of 0.2.

The yaw angle of 15° was selected after examination of the PG&E MOD-2 wind turbine data. It was observed that yaw angles of 15° were sustained for periods in excess of 30 seconds, which is the length of time

necessary for the MOD-2 rotor to fully respond to a step change in wind conditions. Both the wind shear and the yaw produce cyclic changes in the angle of attack. Wind shear changes the velocity component normal to the blades, while the yaw produces cyclic changes in the component of the relative velocity parallel to the blade. Thus, shear-induced changes in angle of attack are greatest at the blade tips while yaw cyclic angles of attack are greatest near the blade roots.

Aerodynamics

The aerodynamic forces on the blades were obtained from integration of the local forces obtained from strip theory. Equating the blade forces on a blade element to the momentum change in differential element, the induced axial velocity was calculated at each angular position at stations along the blade radius. The net aerodynamic moment causing the rotor to teeter was calculated and used to determine the teeter angular velocity. Integration of the teeter angular velocity, $\dot{\psi}$, yielded the teeter angle. The blade forces were determined using the velocity of the air relative to the blades so that the local teeter velocity, $r \cos\psi \dot{\psi}$, (the MOD-2 has no δ_2) played a significant role in determining the induced axial velocity of the air. The tangential induced velocity was neglected.

Strip theory uses the concept of a fully developed wake in the calculation of the induced axial velocity so that there is an implicit assumption that an equilibrium-wake exists. That is, the wake is always in equilibrium with conditions on the blade.

Static aerodynamic data for the NACA 23000 series airfoil used on the MOD-2 were obtained from reference [5]. No correction was included in the calculations for the gap between the movable tips and the fixed portion of the blade and the Prandtl tip loss factor was used to account for decay of the circulation at the blade tips.

Dynamic Stall Model

The Gormont approach [6] was selected to model the effects of dynamic stall based on the simplicity of the method and success in treating dynamic stall in vertical axis wind turbine applications [7]. In the Gormont method

$$C_L = \frac{C_L(\alpha_R)}{\alpha_R - \alpha_{L0}} \alpha_{static} \quad (8)$$

where

$$\alpha_R = \alpha_{static} - \gamma_L \sqrt{\left| \frac{c \dot{\alpha}}{2W} \right|} \left[.25 + .75 \frac{\dot{\alpha}}{|\dot{\alpha}|} \right] \quad (9)$$

and γ_L is a dynamic stall parameter that depends upon the airfoil shape and Mach number. Since the MOD-2 blade varies considerably in thickness ratio along the span, varying from 12% thickness ratio at the tips to 27.2% thickness ratio at $r = 0.3R$, there was little data available on the parameter γ_L . Using extrapolation of the data given in Gormont's report [6], the following form of γ_L was obtained and used for this study:

$$\gamma_L = (2.66 - 6.98 t/c) \left[1 - \frac{M}{1.035 - 2.5 t/c} \right] \quad (10)$$

Table 1 below gives the variation of γ_L over the MOD-2 blade using a local Mach number, $M = r\Omega/a$.

Table 1. Variation of γ_L with Radial Station

r/R	t/c	γ_L
1.00	.12	1.21
.85	.17	.98
.70	.22	.74
.50	.24	.68
.30	.27	.60

The extrapolation used to characterize the dynamic stall parameter does not warrant the display of two-digit accuracy shown in Table 1; the values are shown to indicate the magnitudes used in this study.

Cases Examined

The effect of dynamic stall on the mean flapwise and cyclic bending moments was examined at three wind speeds, 9, 11.5, and 14 m/s. Cases were run with and without dynamic stall. The calculations were started with the rotor in horizontal position with zero teeter angle and the history was determined for six revolutions. Calculations at 14 m/s were made for eight revolutions. The largest cyclic loads were obtained at the final revolution with no appreciable differences being observed between the sixth and eighth revolution. Integration increments of 0.05 R and 0.10 R were used and it was found that the smaller integration increment resulted in an 8.7% increase in mean flapwise bending moment and an increase of 0.8% in the cyclic bending moment.

The results reported are for the 0.10 R integration increment, the larger integration increment having a significant effect on the computation costs, approximately cutting the costs in half.

All the reported runs were made with fixed pitch of 2° on the partial span control surfaces. Interaction between the wind conditions and the control system was not included in this study.

RESULTS

The results obtained for the MOD-2 wind turbine are shown in Figures 3 and 4. Figure 3 shows the mean flapwise bending moment measured at the Goldendale, WA test site as a function of the mean wind speed measured at the BPA tower. Also shown in Figure 3 is the mean flapwise bending moment calculated in this study. There is good agreement between the calculated mean flapwise bending moment and the measured value. The mean flapwise bending moment is almost exclusively due to aerodynamic contributions since the net contribution from gravity and teeter is zero.

Figure 4 shows the cyclic flapwise bending moment data for Goldendale Unit #3. The data shown for 50% occurrence are based on measurements, and the 99.9% case is based on calculations using the 50% data.

The cyclic moments shown as the 50% occurrence were obtained by statistical analysis of the amplitudes of bending moment variations from the mean taken over many cycles. Another method of representing the

cyclic variations is to take the cyclic amplitude as $1/2 (M_{max} - M_{min})$ where M_{max} is the maximum value in a cyclic and M_{min} is the minimum value of the cycle. Table 2, shown below, gives the results in tabular form. Cyclic flapwise bendings calculated using the $1/2 (M_{max} - M_{min})$ method are given along with $(M_{max} - \bar{M})$ and the test results. Using either approach, the calculated cyclic bending moment is below the measured value.

Dynamic stall for the cases considered is observed to have a small effect. At the lowest wind speed considered, 9 m/s, there was virtually no effect of dynamic stall, due to the fact that angles of attack were below static stall over most of the blade. As the wind velocity was increased, dynamic stall effects on the bending moment increase, but the magnitudes of these increases were modest. The results at 14 m/s show that dynamic stall increased the mean bending moment by 2.5% and the cyclic bending moment increased by 3.3% to 9.0% depending upon the method used to calculate the cyclic bending moment. Regardless of the method used to calculate the cyclic bending moment, the calculated values were less than the measured values at the cyclic bending moment obtained from reference [3].

Table 2. Calculated Mean and Cyclic Flapwise Bending Moments at Station 370

Wind Speed m/s	Dynamic Stall	\bar{M} N·m	$\frac{1}{2}(M_{max} - M_{min})^*$ N·m	$M_{max} - \bar{M}$ N·m	ΔM_{cyclic}^{**} (Data) N·m
9.0	No	1929·10 ³	172317	202730	241000
9.0	Yes	1932·10 ³	173656	205033	
11.5	No	2455·10 ³	193661	232386	299000
11.5	Yes	2481·10 ³	198066	248431	
14.0	No	2848·10 ³	229245	274480	357000
14.0	Yes	2918·10 ³	236758	299075	

* Plotted in Figure 3

**Cyclic flapwise bending moment data, 50% occurrence from Figure 4

CONCLUSIONS

The results obtained for cyclic and mean flapwise bending moment for cases with and without dynamic stall show no substantial change due to the inclusion of dynamic stall. Further comparisons of calculated and measured bending moments show good agreement for the mean bending moments and poor agreement for the cyclic bending moments. The cyclic bending moments calculated were for a 15° yaw angle which is a frequent, but not the usual, case for the MOD-2. It is concluded that spatial variations in wind speed due to wind shear and yaw are not the primary drivers of cyclic loading. Further, the effect of dynamic stall on the mean and cyclic bending moments is small. Wind turbulence and rotor flexibility were omitted in this preliminary study of the effects of dynamic stall and, of these omissions, wind turbulence is felt to play a significant role in determining the magnitude of the cyclic loads. The role of dynamic stall in interacting with wind turbulence remains unknown with the major barrier to understanding being the inclusion of wind turbulence in the loading analysis.

REFERENCES

1. Klimas, P.C., "Vertical Axis Wind Turbine Aerodynamic Performance Prediction Methods," Presented at Vertical Axis Wind Turbine (VAWT) Design Technology Seminar for Industry, sponsored by DOE and Sandia Laboratories, Albuquerque, NM, April 1-3, 1980.
2. Noll, R.B. and Ham, N.D., "Dynamic Stall of Small Wind Systems," Rockwell International Corporation, Energy Systems Group, Rocky Flats Plant, Report RFP-3523, UC-60, Golden, CO, Feb. 1983.
3. "MDD-2 Wind Turbine System Development Final Report," Volume I - Executive Summary, Prepared by Boeing Engineering and Construction for NASA Lewis Research Center DOE/NASA/002-1, NASA CR-168006, Sep. 1982.
4. Wilson, F.E. and Patton, E.M., "Design Analysis of Performance and Aerodynamic Loading of Rigid Rotor HAWT," RIO/2227-78/2, UC-60, OSU, Corvallis, OR, Aug. 1978.
5. Wilson, R.E. and Walker, S.N., "Performance Analysis of Horizontal Axis Wind Turbines," Draft Final Report, OSU, Corvallis, OR, Mar. 1984.
6. Gormont, R.E., "A Mathematical Model of Unsteady Aerodynamics and Radial Flow for Application to Helicopter Rotors," USAAMRDL, TR 72-67, May 1973.
7. Oler, J.W., Strickland, J.H., Im, B.J., and Graham, G.H., "Dynamic Stall Regulation of the Darrieus Turbine," Sandia National Laboratories Contractor Report SAND83-7029, Aug. 1983.

The following Appendices involve subjects of general interest to HAWT developers.

APPENDIX A

WAKE EXPANSION MODEL

A simple analytical model for the wake and flow field of a horizontal axis wind turbine can be developed from actuator disk theory. Let the mean axial velocity at the rotor by $u = V(1-\bar{a})$ and the mean axial velocity in the far wake by $u_{FW} = V(1-\lambda\bar{a})$. The axial velocity along the axis of a rotor is approximated by

$$v_x = V \left[1 - \bar{a} - \bar{a} \sqrt{\frac{(\lambda-1)q}{1+q^2}} \right] \quad (A-1)$$

where $q = x/R$, R is the rotor radius and the rotor is at the origin with x measured downstream. The above relation is exact for the velocity along the axis of a rotor with a cylindrical vortex sheet wake when $\lambda = 2$. Using the above equation for v_x throughout the flow field one obtains from the continuity equation

$$v_r = \frac{V\bar{a}(\lambda-1)\eta}{2(1+q^2)^{3/2}}, \quad \eta \equiv \frac{r}{R} \quad (A-2)$$

which yields a linear variation with r for the radial velocity, v_r . The linear variation in radial velocity is in qualitative agreement with the results of a free wake analysis.

Streamlines in the flow may be obtained from the relation:

$$\left(\frac{dr}{dx}\right)_{S.L.} = \left(\frac{dn}{dq}\right)_{S.L.} = \frac{v_r}{v_x} \quad (A-3)$$

Integration of this equation yields

$$\frac{R_{wake}}{R} = \left(1 - \sqrt{\frac{Eq}{1+q^2}}\right)^{-1/2} \quad (A-4)$$

where $E \equiv \bar{a}(\lambda-1)/(1-\bar{a})$. Equation (A-4) may also be used for any streamline that starts at the rotor.

In order to use the above approximation relation, values of \bar{a} and λ are required. The value of \bar{a} is a mean value of the induction at the rotor and can be approximated from the thrust coefficient.

For $C_T < 0.64$, $\lambda = 2$ and

$$C_T = 4\bar{a}(1-\bar{a}) \quad (A-5)$$

which is a quadratic equation.

For $C_T > 0.64$

$$C_T = 0.16 + 2.4\bar{a} \quad (A-6)$$

while λ can be obtained from

$$\lambda = \frac{C_T}{2\bar{a}(1-\bar{a})} \quad (A-7)$$

The equation for the wake boundary is an approximation and although it satisfies continuity, Eq. (A-4) has positive curvature for the streamlines at the rotor. The point of zero curvature for the streamlines is defined by

$$E(q^2 + 5/6) = q \sqrt{1+q^2}$$

The point of zero streamline curvature varies from the rotor at $E=0$ (no wake expansion) to $q \approx 1.47$ for $E=1$ (infinite wake diameter).

APPENDIX B

FREE YAW OF RIGID HUB ROTORS

The stability of rigid hub rotors in free yaw may be described by examination of the change in yaw moment with the yaw angle, δ .

$$k \equiv - \frac{\partial M_{yaw}}{\partial \delta} \quad (B-1)$$

Other yaw moments can cause yaw tracking errors but the yaw stability is determined by magnitude and the algebraic sign of k . While yaw tracking errors are mostly due to the imbalance of in-plane aerodynamic forces due to wind shear and tower shadow, the spring constant, k , is due to the normal aerodynamic forces. Figure B-1 illustrates the role of the coning angle ψ in the stability of rigid hub rotors in free yaw.

A rotor with blade horizontal is shown schematically when viewed from above. The velocity normal to the blades is shown for blade elements on the right hand side and the left hand side of the rotor. The velocity normal to the blade determines the angle of attack; that is

$$\alpha \sim V_{\perp} \quad (B-2)$$

The induction may be different on opposite sides of the rotor; however, the primary dependence is due to the local velocity. It may be observed that

$$V_{\perp R} > V_{\perp L}$$

hence the angles of attack for the illustrated blade will obey

$$\alpha_R > \alpha_L \quad (B-3)$$

for the illustrated figure.

The normal forces on the right hand and left hand sides are proportional to $\alpha C_{L\alpha}$, hence the moment about point O tending to yaw the rotor in the δ -direction is proportional to

$$-C_{L\alpha} (\alpha_R - \alpha_L) \quad (B-4)$$

The spring constant, k , is the result of integration of the differential yaw moment due to yaw over the rotor. If $C_{L\alpha} > 0$ the illustrated rotor will be stable in yaw since the coning angle ψ produces a greater normal force on the blade occupying the right hand side of the rotor than on the left. However, beyond stall for many airfoil sections, $C_{L\alpha} < 0$, and the rotor yaw moment will increase with increasing yaw. In such a case the rotor will operate in stable mode at an upwind position where the coning angle is negative. Thus the stability of rigid rotors horizontal axis wind turbines in yaw can be characterized by the integrated contribution of $C_{L\alpha} \psi$ over the rotor. For a rotor with three or more blades ($B =$ number of blades) the dominant term in the yaw "spring constant" is

$$\frac{B}{2\pi} \int_0^1 \left(\frac{c}{R}\right) \eta^2 X C_{L\alpha} \psi \cos \phi d\eta$$

where

$$\eta = r/R$$

$$X = \frac{R\Omega}{V}$$

ϕ is the local flow angle with respect to the rotor disk.

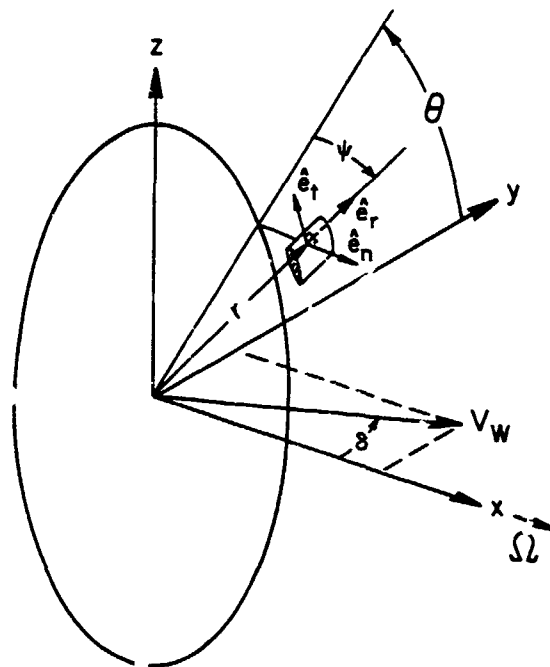


Figure 1. Rotor Geometry and Coordinates

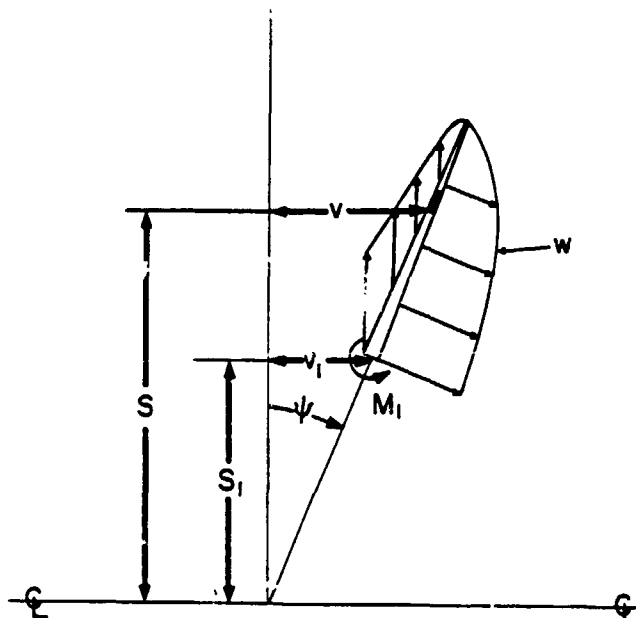


Figure 2. Blade Section with Aerodynamic and Centrifugal Loading

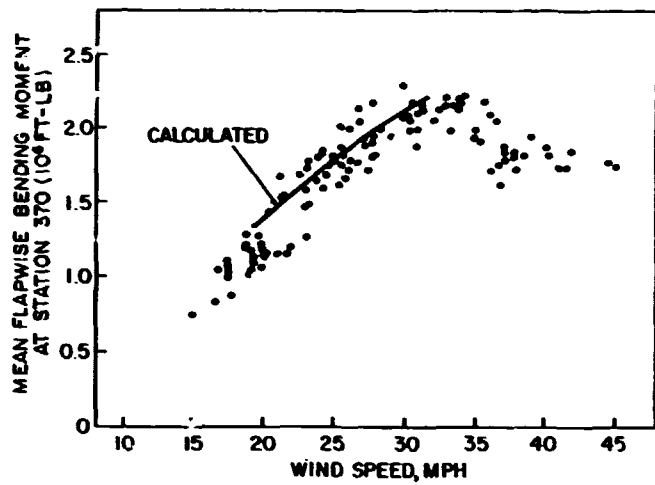


Figure 3. Mean Flapwise Bending Moment at Station 370. Data from Reference [3].

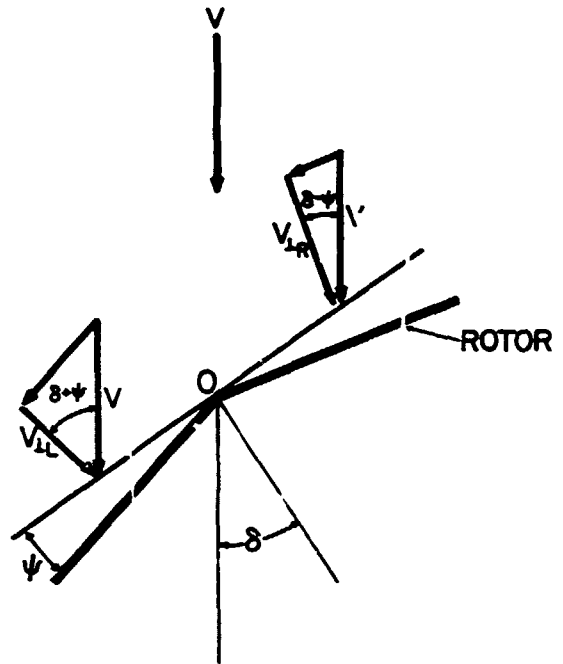


Figure B-1. Wind Turbine in Yaw.

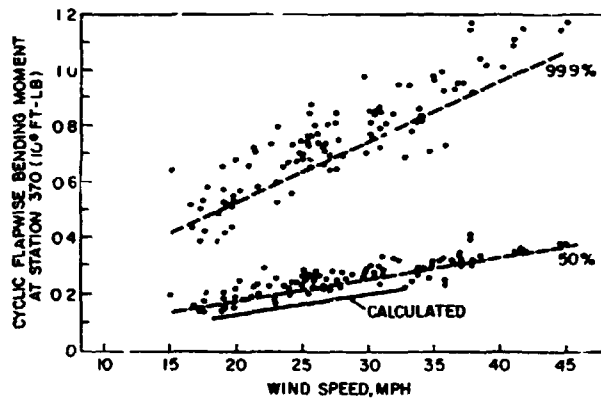


Figure 4. Cyclic Flapwise Bending Moment at Station 370. Data from Reference [3]. Calculated Cyclic Bending Moment is $\frac{1}{2}(M_{\max} - M_{\min})$.

SEVERAL AILERON AND SPOILER CONFIGURATIONS*

W.H. Wentz, Jr., and M.H. Snyder
Wichita State University
Wichita, Kansas 67208

ABSTRACT

This paper reviews research efforts at Wichita State University sponsored by NASA Lewis Research Center to design and evaluate aerodynamic braking devices which will be smaller and lighter than full-chord blade pitch control.

Devices evaluated include a variety of aileron configurations, and spoilers located at both trailing edge and near the leading edge. The paper discusses analytical modeling, wind tunnel tests, and for some configurations, full-scale rotor tests. Current designs have not provided adequate control power at high angles of attack (low tip-speed-ratios). The reasons for these limitations are discussed. Analysis and wind tunnel test data indicate that several options are available to the designer to provide aerodynamic slowdown without full-chord pitch control. Three options are suggested; adding venting in front of the control surface hingeline, using spoilers located near the leading edge, and using a two-piece control combining downward deflection inboard with upward deflection outboard.

NOMENCLATURE

c section chord
 c_d section drag coefficient (drag/qc)
 c_l section lift coefficient (lift/qc)
 c_n section normal force coefficient (normal force/qc)
 c_s section suction force coefficient (suction/qc)
 q local dynamic pressure ($1/2 \rho v^2$)
r local blade radius
R blade maximum radius
 Re blade chord Reynolds number, $V \cdot c / \nu$
TSR tip speed ratio, ($\omega R / V_{wind}$)
V relative wind speed
 V_{wind} wind speed
 α angle of attack
 ϕ relative wind angle
 ν kinematic viscosity
 ω angular velocity

INTRODUCTION

One of the critical design requirements for wind turbines is to provide reliable methods for limiting rpm overspeed in the event of loss of load, or during high wind speeds. Mechanical brakes for this purpose become unacceptably large and heavy for large-scale horizontal-axis machines. Aerodynamic control of rotor overspeed may be accomplished by pitching the entire blade, in the manner commonly used for airpropellers. The mechanism and structure required to accomplish this control become prohibitive on large rotors, however. As an alternative, a portion of the outboard span may be pitched to effect the desired control. This results in considerable weight saving, even though it requires locating actuators rather far from the axis

*Presented at DOE/NASA Horizontal Axis Wind Turbine Technology Workshop, Cleveland, Ohio, May 8-10, 1984.

of rotation. Since rotor torque varies approximately with the cube of the span, the outer portions of the blade produce most of the torque, and are therefore the portions along which control will be most effective. Virtually all current large scale machines utilize part-span pitch control, with the outer 30% being typical. These designs have been demonstrated to be quite effective. With this method of control, the movable section operates at moderate angles of attack, so that typical airfoil control data are adequate for design. Even though outboard panel pitch control has proven effective, it is desirable to further reduce the size, weight and cost of the control system.

Airplanes have long used movable part-chord devices as effective means of controlling aerodynamic forces. Trailing edge "flaps" for producing added lift, or "ailerons" for modulating lift either positively or negatively for roll control, or "spoilers" for reducing lift to effect descent or roll control have all been used in this way.

This paper reports analyses and results of tests of a variety of control devices for wind turbines. Tests were conducted in the WSU 7' x 10' Walter Beech Memorial Wind Tunnel. Model for these tests was the NACA 23024 airfoil. A 9" chord was used so that large angles of attack (0° to 360°) could be tested without adverse wall interference. Reynolds number for most runs was 0.6×10^6 .

AERODYNAMIC ANALYSIS

Strip Theory

The aerodynamics of the wind turbine rotor blade are analyzed by using strip theory, which considers the relative wind at each spanwise station on the blade, and resolves the aerodynamic forces produced on each airfoil-section strip of the blade. This technique follows the same line of analysis as traditional wing lifting-line theory, and is reasonably valid so long as substantial spanwise flow is not present. This approach permits the use of an extensive data base of airfoil design theory and data from 2-dimensional wind tunnel tests to design rotors, much as two-dimensional wind tunnel tests and strip theory were used by Orville and Wilbur Wright for their first propeller design. Figure 1 illustrates the strip method applied to a rotor, with pertinent velocities, force components and angles. This figure, which has been simplified by neglecting induced velocity effects, illustrates the relationship between relative wind angle, wind speed and rotor angular velocity. Figure 2 shows the variation of flow angle with spanwise position and TSR for an untwisted rotor. As shown, at high tip-speed-ratio (TSR), the flow angle will be relatively small, and conversely for low TSR the angles will be large. Therefore, during the initial phases of rotor slowdown, the angles will be small,

but as the rotor rpm is decreased, the local flow angles will become large.

Airfoil Section Properties

Typical airplane wings operate over an angle of attack range from near zero to a few degrees beyond stall, which is usually below 20 degrees. Wind turbine rotors, by contrast, operate at angles of attack ranging from 90° during start-up to near zero degrees at normal operating rpm and wind speed. This means that an airfoil data base which may be quite adequate for airplane design, is often inadequate for wind turbine aerodynamic braking analysis. For this reason, high angle of attack wind tunnel tests have been conducted at Wichita State University for a number of airfoils, with and without control surfaces (Refs. 1 and 2).

As noted earlier, during normal operation, efficient wind turbine rotors are at relatively high TSR, with correspondingly small blade angles over the important outer portions of the blade. Many large-scale wind turbine rotors are designed with zero twist and zero blade angle out of the plane of rotation (beta) for ease of manufacture and structural simplicity. For these reasons, the present study is restricted to rotors with zero twist and zero beta. The velocity and force vectors in Figure 1 show that the pertinent aerodynamic force component which produces torque is the forward chordwise component, or "leading-edge suction" force. This force component and its companion component (normal force), are derived from lift and drag components by the coordinate transformation equations below:

$$c_s = c_l \sin(\alpha) - c_d \cos(\alpha) \quad (1)$$

$$c_n = c_l \cos(\alpha) + c_d \sin(\alpha) \quad (2)$$

For symmetric airfoils, c_l and c_d are approximately represented by the familiar relationships below:

$$c_l = 2 * \pi * \sin(\alpha) \quad (3)$$

$$c_d = c_{d0} \quad (4)$$

Substituting (3) and (4) into (1), the following relationship results:

$$c_s = 2 * \pi * \sin^2(\alpha) - c_{d0} * \cos(\alpha) \quad (5)$$

While c_s is less familiar than c_l and c_d , it is the single parameter which governs blade torque. Since the function of aerodynamic braking devices is to produce zero or negative torque, these devices must provide zero or negative c_s over the required angle of attack range.

Typical Airfoil c_s Data

A typical c_s versus alpha plot is shown in Figure 3. This plot shows that there two regions of positive

c_s , and therefore four angles of attack for which c_s is zero. This means that there are several equilibrium states for which the rotor torque is zero. In fact, consideration of the excess torque required to accelerate the rotor will illustrate that only the two states for which c_s is increasing as alpha increases are in stable equilibrium, and these are the possible operational "run-a-way" states. These characteristics were identified and discussed in reference 1. The first region of positive c_s is in the low-to-moderate angle of attack range, before separation and c_{lmax} . The second regime of positive c_s occurs at angles of attack above about 60°. This second regime is primarily a result of the nose radius of the airfoil, and will be present irrespective of trailing edge control device, since the flow over the aft portion of the airfoil is separated for these angles. Fortunately, the equilibrium angle of attack for this state is so high that the rpm will be acceptably low, even for hurricane wind speed. Thus the design requirement for a control device is that the c_s remain negative for all angles of attack below about 60°. The remainder of this study focusses on methods for achieving this goal.

Figure 4 shows c_s versus alpha curves for an airfoil without control and the same airfoil with 20% chord aileron and 20% chord trailing edge spoiler. Both aileron and spoiler produce adequate negative c_s at low angles of attack. An interesting characteristic of these curves is that as angle of attack is increased, the c_s shows a parabolic increase, as indicated by equation (6). This trend has been observed for virtually all configurations. The increase in c_s with alpha is nearly irrespective of airfoil and trailing edge control device, and continues until stalling occurs, as evidenced by simultaneous attainment of maximum values for c_l and c_d . While many configurations were tested which produced negative c_s for all angles below stall, all configurations of ailerons or aft mounted spoilers exhibited the steep c_s versus alpha relationship, with c_s approaching zero or becoming positive before section stalling occurred.

Reynolds Number Effects

While a number of control devices tested provided negative c_s for all angles of attack below 60°, many of them exhibit a sharp peak in the c_s curve at the stalling angle of attack (typically 20° to 30°). It is well known that increase in Reynolds number will increase the stalling angle and c_{lmax} of most airfoils. Since large scale rotors will typically operate at Reynolds numbers higher than the wind tunnel tests, full scale hardware can be expected to have higher stalling angles, and consequently have positive c_s for some angles below the 60° requirement. The non-linear character and high slope of the c_s curve makes the performance particularly sensitive to Reynolds number. Figure 5 shows data which illustrate how increasing Reynolds number results in positive c_s for a limited alpha range below 60°. Rotors with this type control device will exhibit slowdown only to the zero c_s angle of attack, which may be at an unacceptably high rpm. Alternative methods for improving control effectiveness at high angles of attack are given in the sections which follow.

Effects of Venting

The problem identified with respect to the performance of trailing edge devices for aerodynamic control is that at angles of attack in the range of 20 to 30 degrees, the suction force tends toward zero, and may become positive for a limited angle of attack range before again becoming negative. Thus, what is needed is a mechanism to limit the $c_{l, \max}$ of the airfoil with upward deflected aileron. One possible means to limit $c_{l, \max}$ is to allow air to "leak" from the lower surface to the upper surface at high angles. This is accomplished rather easily by providing a slot or gap near the deflector hingeline. A configuration can be designed with such a gap, which would be closed when the control surface is at zero deflection, and open for large deflection angles. Figure 6 shows wind tunnel tests of the effects of hingeline gaps, and illustrates that the gap is effective in the critical angle of attack range, without penalty to control effectiveness at low angles. While some performance penalty is noted at very high angles of attack, venting does provide improved performance at angles of attack near stall. Tunnel flow studies reveal that the flow through the slot is from upper to lower surface at low angles. At about 20 degrees, the flow direction changes, and flow is from lower to upper surface for angles of attack greater than 20 degrees. This leak flow evidently reduces $c_{l, \max}$ and therefore limits peak c_l . Limited higher Reynolds number tests indicate that the gap flow will reduce the sensitivity of the peak c_l to Reynolds number.

Wind tunnel tests by Templin and Rangi (Ref. 4 and Fig. 7) show similar trends, and indicate that venting is effective in reducing the suction peak in the 20° to 30° alpha range. Their data were obtained using an NACA airfoil, and are presented using a coefficient based on aerobrake chord rather than airfoil chord. Even though these results do not show positive suction in this regime, it is possible that increase in Reynolds number above the 1.7×10^6 test value or change of airfoil section could result in positive suction. Data from WSU tests for a similar double spoiler arrangement are shown on this plot for reference. The trend of the WSU data is strikingly similar to the NRC data, and illustrates that while the NRC data do not show positive c_l in this alpha range, higher Reynolds number might result in positive c_l . The comparison serves to point out the tendency for positive suction force for unvented control devices, and the advantage of venting.

Effects of Hingeline Location

As an alternative to large chord trailing edge control, spoilers with forward hingeline locations have been studied. Analytical studies have been conducted using a computational procedure developed by Dr. Alan Elcrat, professor of mathematics at Wichita State University, to analyze the effects of locating spoilers at various positions along the airfoil chord. A computer code has been developed for this purpose. This analysis uses a conformal mapping technique from potential flow aerodynamic theory to establish the inviscid flow pattern. Then theoretical aerodynamic forces associated with an airfoil plus spoiler are calculated. While the method currently treats the airfoil and spoiler as thin flat plates, the results are expected to reasonably predict trends for thick, cambered

airfoils with spoilers, just as classical thin airfoil theory is known to properly predict trends of lift versus angle of attack for airfoils with thickness for angles below stall. The analysis results show interesting trends for spoiler effectiveness. The lift increments for given spoiler chord and deflection are relatively insensitive to hingeline location for zero angle of attack. On the other hand, as spoiler hingeline is moved forward, the c_l versus alpha slope is reduced as a result of the loss of suction pressures aft of the spoiler trailing edge. This should have the important consequence of reducing the sharp rise of c_l versus alpha, which should reduce the tendency for c_l to become positive for angles of attack below 60°. This latter consideration is especially important for the case of large-scale wind turbine rotor design. Based upon these theoretical considerations, wind tunnel tests were conducted to evaluate spoilers at forward hingeline positions, at high angles of attack. The results of those tests are shown in Figure 8.

These test data show that the trends predicted by the theoretical analysis have been demonstrated. In particular, the negative c_l for a given spoiler chord and deflection at zero angle of attack is essentially independent of hingeline for zero angle of attack. However, the forward hingeline configurations are shown much more effective at higher angles of attack. It remains to demonstrate that this performance can be achieved at the larger Reynolds numbers of full scale operation, and in the real environment of a rotating blade. It must be noted that locating spoilers near the leading edge of an airfoil poses special problems to insure that the power generating performance of the airfoil is not compromised due to gaps, hinges, poor fit, etc. Further, structural designers do not favor this location because of intrusions into the torsion carrying skin.

Combined Up and Down Controls

The undesirable characteristic of the upward deflected spoiler or aileron is that the suction becomes nearly zero or positive at high angles of attack. These high angles of attack occur over the portion of the span somewhat removed from the tip, that is, over the region from 30% to 60% span (see Figure 2.) Just as upward control surface deflection delays stalling angle, downward deflection results in early stalling and consequently in negative suction at high angles of attack. Thus, a downward deflected aileron on the inboard span will be fully stalled at the low tip-speed-ratios necessary for shutdown. Therefore, upward control deflection over the outer span could be combined with downward control deflection over the 30% to 60% span region. The outboard control would provide adequate control at high TSR values. As TSR is reduced for shutdown, the inboard control would be deflected downward to provide positive aerodynamic braking over this portion of the blade. This concept, while more complex than a single control surface, is promising enough to merit further consideration.

ROTOR TESTS

Large-scale tests of aileron-type control devices have been conducted by NASA Lewis researchers at the Plum Brook site, using the 125 ft. diameter MOD-0A machine. These results are reported in more detail in a separate paper, but selected results are shown

here. Figure 9 shows equilibrium rpm versus wind speed from full-scale tests of the NASA MOD-0A turbine with 20% chord aileron with 60° deflection, a simulated 30% chord aileron with 90° deflection, and approximate results for a 38% chord aileron with 90° deflection. Increasing the chord and deflection of the aileron results in additional slowdown, but the equilibrium TSR is still not as low as desired. The chord dimension of the control device might be further increased, but the disadvantage of this approach is that the cost of the control device, both in terms of size and weight, is increased. At some point, the control device may become as expensive as the full-chord pitch control it is designed to replace!

RESEARCH IN PROGRESS

WSU has a small (20-inch diameter) rotor test rig fitted with dynamometer for torque and thrust measurement. This rig has been used for rotor wake and flow visualization studies, and is currently being used for evaluation of spoiler hingeline location effects. While the small scale provides only very low Reynolds number data, the rig is useful in that rotational effects are present.

Reflection-plane wind tunnel tests are planned at WSU to evaluate the section characteristics of a 30% control device with large (5-10% chord) venting. It is believed that this design will provide adequate control throughout the angle of attack range, with aerodynamic balance to reduce control actuator requirements. Twenty-inch rotor tests are planned for this device to further evaluate it in a rotating environment.

CONCLUSIONS

1. Wind tunnel tests, full-scale tests, and analysis have revealed problems associated with the design of part-chord control devices at high angle of attack.
2. Three concepts for improving control effectiveness have emerged from the present studies:
 - (a) Hingeline venting added to an upward deflecting 30% chord control device.
 - (b) Spoilers with forward hingeline locations.
 - (c) A two-control system with outboard aileron deflected upward and inboard aileron deflected downward.
3. Evaluation is continuing for all three concepts above.

REFERENCES

1. Wentz, W.H.Jr., Snyder, M.H. and Calhoun, J.T.: "Feasibility Studies of Spoiler and Aileron Control Systems for Large Horizontal-Axis Wind Turbines," AIAA Jour. of Energy, Vol.5, No.5, Sept-Oct. 1981.
2. Snyder, M.H. and Wentz, W.H.Jr.: "Wind Tunnel Tests of Four Airfoils for Use on Wind Turbines," WER-16, Wichita State University (in preparation).
3. Snyder, M.H., Wentz, W.H.Jr., and Ahmed, A.: "Reflection Plane Test of Control Devices on a Thick Airfoil at High Angles of Attack," WER-23, Wichita State University, Sept. 1983

4. Templin, R.J., and Rangi, R.S.: "Some Recent VAWT Aerodynamics at NRC Canada," Paper presented at 4th Annual VAWT Aerodynamic Seminar, Sandia Laboratories, Jan. 1984.

This research was sponsored by NASA Lewis Research Center under Grant NSG-3277.

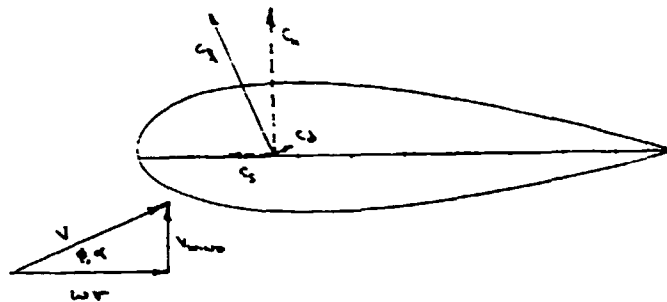


FIGURE 1 - ROTOR VELOCITY AND FORCE COMPONENTS

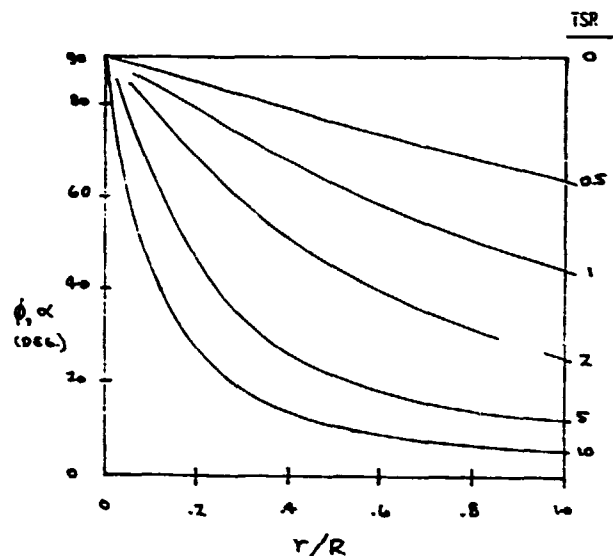
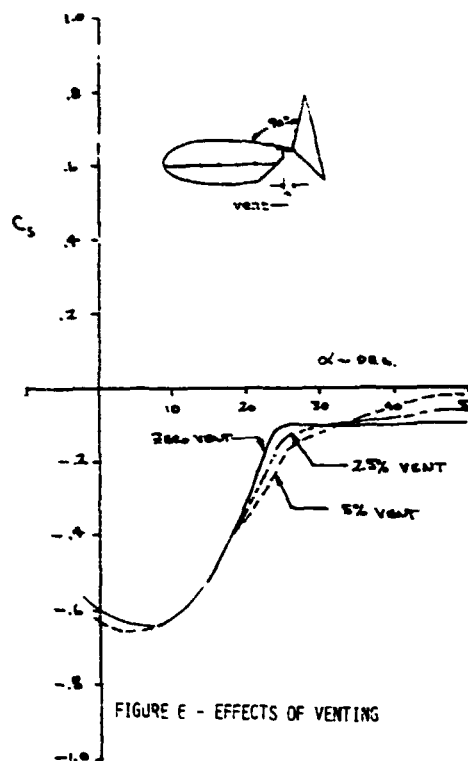
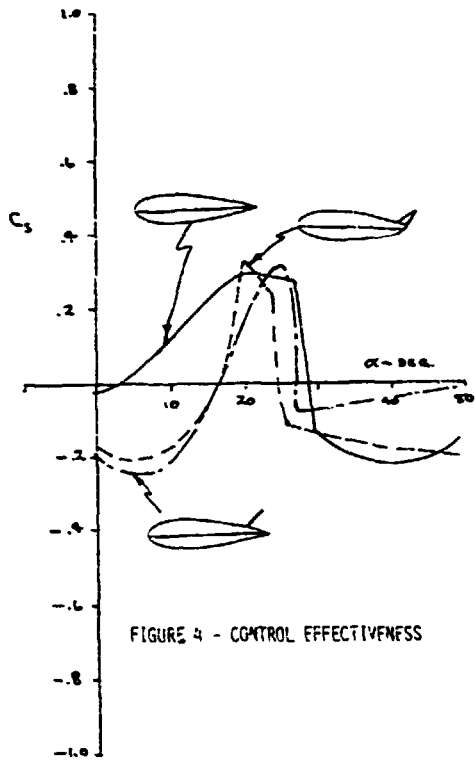
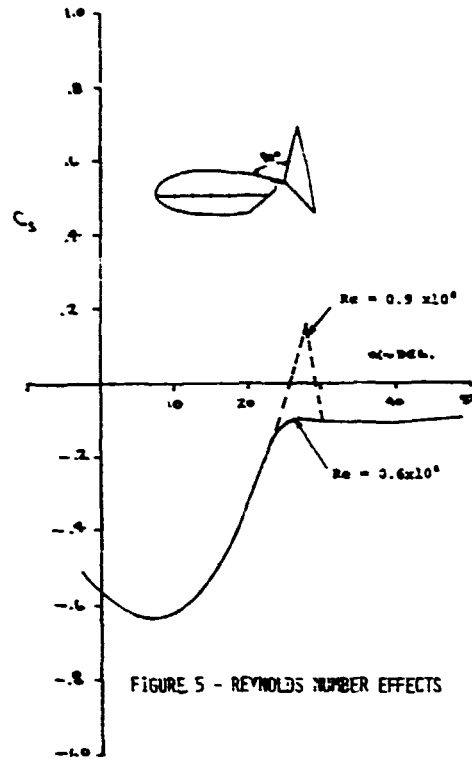
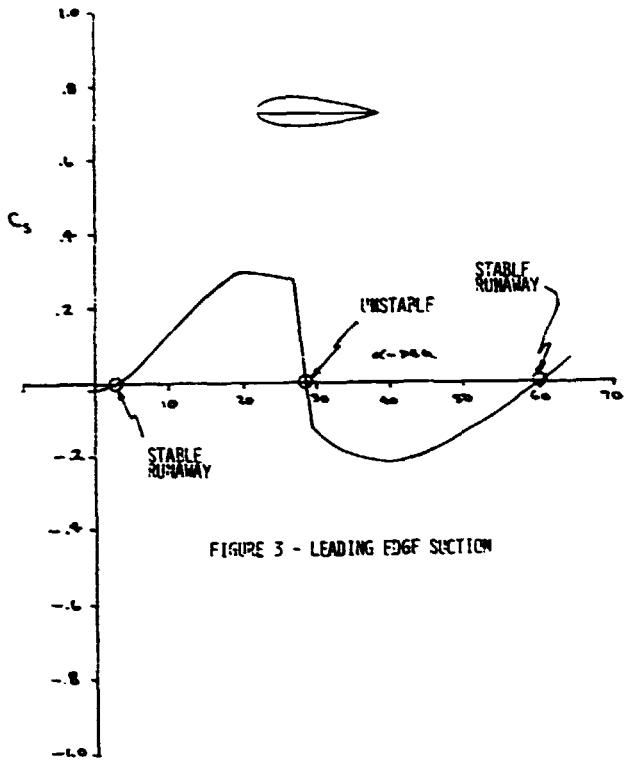


FIGURE 2 - ROTOR FLOW ANGLES



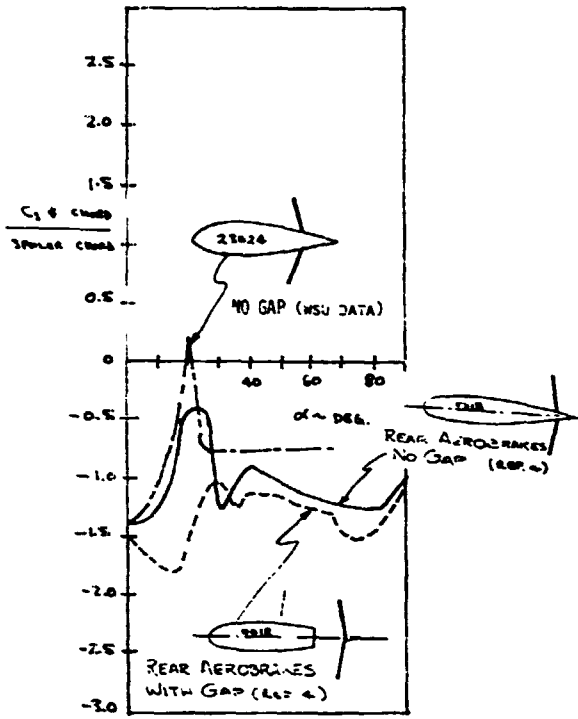


FIGURE 7 - NRC TESTS WITH VENTING

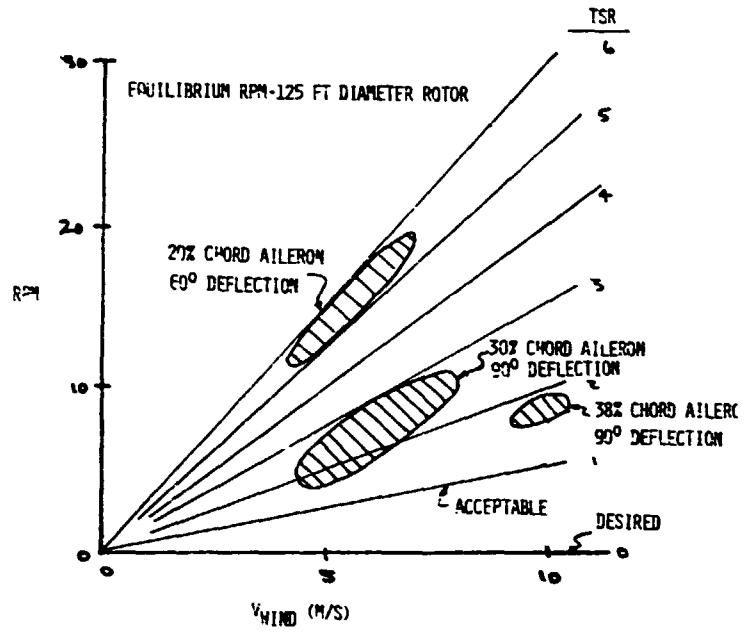


FIGURE 9 - LARGE-SCALE ROTOR CONTROL

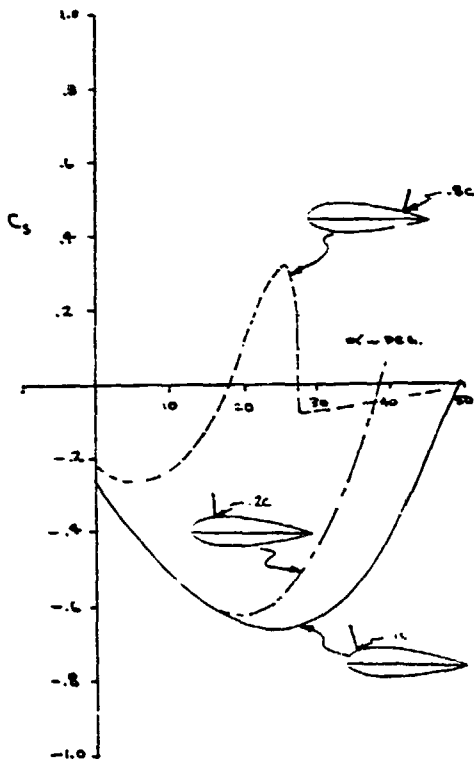


FIGURE 8 - EFFECTS OF HINGELINE LOCATION

COMPARATIVE WIND TUNNEL TESTS AT HIGH REYNOLDS NUMBERS OF NACA 64 621 AIRFOILS WITH TWO AILERON CONFIGURATIONS*

G. M. Gregorek

The Ohio State University
Columbus, Ohio 43220

ABSTRACT

An experimental program to measure the aerodynamic characteristics of the NACA 64-621 airfoil when equipped with plain ailerons of 0.38 chord and 0.30 chord and with 0.38 chord balanced aileron has been conducted in the pressurized O.S.U. 6" x 12" High Reynolds Number Wind Tunnel. Surface pressures were measured and integrated to yield lift and pressure drag coefficients for angles of attack from -3° to $+42^\circ$ and for selected aileron deflections from 0° to -90° at nominal Mach and Reynolds numbers of 0.25 and 5×10^6 . When resolved into thrust coefficient for wind turbine aerodynamic control applications, the data indicated the anticipated decrease in thrust coefficient with negative aileron deflection at low angles of attack; however, as angle of attack increased, thrust coefficients eventually became positive. All aileron configurations, even at -90° deflections showed this trend. Hinge moments for each configuration complete the data set.

NOMENCLATURE

C_D	Drag coefficient, $D/qc(l)$
C_H	Hinge moment coefficient, $H/qc_A^2(l)$
C_L	Lift coefficient, $L/qc(l)$
C_P	Pressure coefficient, $P - P_\infty/q$
C_T	Thrust coefficient, $C_T = C_L \sin \alpha - C_D \cos \alpha$
c	Airfoil chord
c_A	Aileron chord
M	Mach number
P	Surface pressure
P_∞	Free stream pressure
q	Dynamic pressure, $q = \frac{1}{2} \rho V^2$
Re	Reynolds number, $Re = \rho V c / \mu$
α	Angle of attack
δ	Aileron deflection
ρ	Air density
x/c	Nondimensional chordwise coordinate
y/c	Nondimensional normal coordinate

INTRODUCTION

Aerodynamic controls have been used on wind turbine machines, both to modulate power and to brake the rotor during high wind conditions. As wind turbines increase in size, an aileron type of control becomes attractive. Although ailerons have been effectively used on aircraft for many years, the technical literature applicable to the wind turbine and upon which to base an

aileron control system is sparse. The specialized wind turbine needs for data on thick airfoils operating at angles of attack above stall and with large negative aileron deflections are not available. This paper presents the results of an experimental program to expand the data base for aileron control of wind turbines.

A thick airfoil that is a candidate for wind turbine application is the NACA 64-621 section. The present program used this airfoil and fabricated, for testing, two dimensional models with plain ailerons of 0.38 chord and 0.30 chord and an aerodynamically balanced aileron of 0.38 chord. The models were evaluated in The Ohio State University 6" x 12" pressurized wind tunnel at nominal Mach number of 0.25 and Reynolds number, based on the 4" model chord, of 5×10^6 . Surface pressures were measured, which when integrated, produced lift, pressure drag and moment coefficients. The angle of attack ranged from -3° to $+42^\circ$ and the aileron deflections were 0° , -10° , -15° , -30° , -45° and -90° for the 0.38c plain aileron and 0° , -15° , -30° and -90° for the other two ailerons. The surface pressures of each aileron configuration were integrated to yield the hinge moment as a function of angle of attack and deflection.

EXPERIMENTAL FACILITIES

The O.S.U. 6" x 12" High Reynolds Number Wind Tunnel shown in Figure 1 is a two-dimensional facility designed specifically to test airfoils near full scale Reynolds numbers. It is a pressurized, blow down, wind tunnel equipped with an advanced data processing system, and capable of operating at stagnation pressures near 500 psia and at Mach numbers from 0.2 to 1.1.

In a typical test run of 15 seconds duration, surface pressures are obtained at one angle of attack, one Reynolds number and one Mach number. An on-line computer controls the test sequence once the air supply valve is opened, actuating pressure cut-off valves at the desired test condition, initiating a pitot probe traverse of the wake one chord downstream of the model, and closing the air supply valve on completion of the wake traverse. The 48 port scannivalve/cut-off valves shown in Figure 2 trap the surface pressures for sampling after tunnel shut down. A Harris Slash 6 computer processes the electrical signal from the trapped pressures to engineering format, and the test results in the form of C_p vs x/c , integrated lift, drag, and pitching moment coefficients are displayed on the data operator's CRT. The raw data is stored on magnetic tape for a permanent record and the processed information made into hard copy plots and printouts. The next test cycle can be set up; depending upon the required air supply, 40 or more such test runs can be made per day.

*Presented at the Horizontal-Axis Wind Turbine Technology Workshop, May 8-10, 1984 in Cleveland, Ohio. Supported by NASA Lewis Resch Cntr, Grant NAG 3-330.

The models are mounted to circular plates that fit flush into the wind tunnel side walls as illustrated in Figure 3. With multi-element models, the main element mounts to a rectangular cut-out in this disc; model angle of attack is changed by rotating this disc. The aileron is fitted into a small disc that sets into the main circular plate. The small disc has its center at the hinge location so that the aileron can be rotated about the hinge line independent of the main element angle of attack. With these two separate mounting discs, model main element angle of attack can be varied from 0° to 360° and aileron deflection can be varied similarly. For the present model tests, with the hinge located on the upper surface of the airfoil, aileron deflections of 0° to -100° are possible.

The model airfoils are presented in Figure 4. They have a 4 inch chord and 6 inch span and are cast from precision molds of aluminum-epoxy material. To sustain the high airloads when deflected -90° , the ailerons had graphite roving distributed internally. The pressure taps were formed into the main element and flap during the molding process.

The airfoil and the three aileron contours are presented in Figure 5. The location of the hinge lines are given in terms of non-dimensional coordinates as $x/c = 0.635$, $y/c = 0.0825$ for both 0.38 chord models and as $x/c = 0.712$ and $y/c = 0.0677$ for the 0.30 chord aileron.

RESULTS AND DISCUSSION

The wind tunnel test program consisted of more than 100 runs at nominal Mach number of 0.25 and Reynolds number of 5×10^5 , with the major part of the program focussed upon the 0.38c plain aileron. Angles of attack from -9° to $+45^\circ$ were examined for this configuration at five aileron deflections ranging from 0° to -90° . Limited tests of the other two aileron configurations - the 0.38c balanced aileron and the 0.30c plain aileron - were made at selected test conditions; the purpose of these tests were to evaluate the effects of aerodynamic balance and changing chord length by comparing the results with the 0.38c plain aileron baseline. All models had two dimensional trip strips of 0.002 inch (.0005c) located at .05c on the upper and lower surfaces to assure a turbulent model boundary layer.

Pressure Distributions

Three pressure distributions typical of those measured on the 0.38c plain aileron are presented in Figure 6 to illustrate the change in pressure distribution with angle of attack when aileron deflection is fixed at zero degrees. The square symbols represent the pressure coefficients on the upper surface, the diamond symbols, the lower surface pressure coefficients. The main element pressures are plotted from $x/c = 0$ to 0.60 while the aileron pressure are displayed from $x/c = 1.00$ to 1.40; this displacement of the aileron pressure distribution has been performed to distinguish between the pressures on the aft face of the main element and on the forward face of the aileron.

The distributions of Figure 6 show that as angle of attack increases from 0° to 18° lift coefficient increases from $C_L = 0.38$ to $C_L = 1.18$. The plateau in

the aileron pressures in Figure 6b indicates the flow has separated entirely on the upper aileron surface and the lift coefficient has reached $C_L = 1.0$ at 9° angle of attack. When the angle of attack is doubled to 18° , the lift has increased only to $C_L = 1.18$ while the separated zone has moved forward to the main element and has reached $x/c = 0.40$

Figure 7 indicates the pressure distributions obtained on the 0.38c plain aileron at a fixed angle of attack when the aileron is deflected trailing edge up. As the aileron is deflected from 0° to -15° and then to -30° , lift coefficient at fixed angle of attack of 9° decreases from $C_L = 1.00$ to 0.35 and finally to $C = -0.02$. Of interest is the complete change of pressure distribution on the aileron as it is deflected. The low negative pressure coefficients of the separated upper aileron surface increase to positive values as the aileron deflects, while the lower surface pressure coefficients, initially positive become negative. The pressure plateau of Figure 7c shows that the lower surface of the aileron has now separated. These pressure changes, of course, result in the loss of lift measured, but also an increase in drag and a change in the aileron hinge moment. In fact, the hinge moment changes from a negative value - an aerodynamic moment that tends to move the aileron trailing edge up - to a positive hinge moment at the -30° deflection.

The pressure distributions obtained from the 0.38c balanced and 0.30c plain aileron are compared with the baseline 0.38c plain aileron at 18° angle of attack and -30° aileron deflection. At 18° , the baseline aileron lift has increased to $C_L = 0.89$ from the -0.02 shown at angle of attack 9° in Figure 7c. The 0.38c balanced aileron has a higher lift, $C_L = 1.03$, than the baseline, mainly due to the ability of the balanced aileron to influence the main element surface pressures, spreading the upper and lower pressures to increase lift. In the same manner, the smaller chord 0.30c plain aileron has the lowest lift, $C_L = 0.71$, due to the inability of the aileron to alter the main element pressures.

These pressure distributions and the integrated lift coefficients follow trends established by earlier airfoil tests at modest angles of attack. Even when the aileron is deflected at extreme angles, -90° , for example, the distributions, though irregular in appearance, are rational. Figure 9 illustrates the pressure distribution for the 0.38 plain and balanced ailerons at 18° angle of attack and -90° aileron deflection. The large negative deflection has accelerated the flow on the lower surface so that it has low pressure surface (the square symbols are the upper surface C_p). Further, the aileron is carrying a high positive hinge moment with high pressure on the forward (upper) surface and a low pressure on the aft (lower) surface. These extreme conditions at angle of attack lead to large negative lift coefficients for both aileron configurations, $C_L = -0.89$ and $C_L = -0.57$ for the plain and balanced configurations, respectively.

When the angle of attack is increased from 18° to 36° for this extreme negative aileron deflection of -90° , the pressure distributions proceed through a drastic change. Figure 10 compares the distributions measured at these two angles of attack for the baseline 0.38c plain aileron.

As shown in Figure 10b for 36° angle of attack, the upper surface of the main element is now the low pressure surface; it is essentially flat, indicating it lies in a separated zone. The lower surface, at 18° angle of attack the low pressure region, now is the high pressure surface. Similarly, the upper aileron surface has low pressure coefficients and of the same order as the main element pressure coefficients, while the lower aileron surface has a higher (though still negative) pressure coefficient. The net result of this pressure distribution is that the lift coefficient has increased from $C_L = -0.89$ to $C_L = +0.70$ as angle of attack changed from 18° to 36°.

This somewhat surprising behavior of the NACA 64-621 airfoil with ailerons deflected to large negative deflections producing substantial positive lift when at angles of attack above stall was duplicated by all three aileron configurations tested. The impact of this post-stall behavior on the other aerodynamic characteristics of the aileron configurations is treated next.

Aerodynamic Characteristics

Each of the surface pressure distributions obtained in the test program were integrated to determine a normal and an axial coefficient for the main element and aileron. These component coefficients were then resolved into a total two dimensional lift and drag coefficient based on airfoil chord. An axial thrust coefficient, C_T defined as

$$C_T = C_L \sin \alpha - C_D \cos \alpha \quad (1)$$

was formulated from the resulting lift and drag coefficients.

These three aerodynamic characteristics are displayed as a function of angle of attack for the 0.38c plain aileron in Figure 11. The maximum lift coefficient is observed to decrease from $C_L = 1.22$ when $\delta_A = 0^\circ$ to $C_L = 1.0$ and $C_L = 0.83$ as aileron deflection increases to -10° and -15° . At $\delta_A = -45^\circ$, the maximum lift has recovered to $C_L = 1.0$ when angle of attack has increased to 27° while an aileron deflection of -90° leads to a maximum $C_L = 0.7$ at 36° angle of attack. The lift curve slopes for aileron deflections less than 30° are noted to be linear below $C_L = 0.8$.

At aileron deflections below -30° , the drag coefficients show a generally parabolic form, increasing from $C_D = 0.01$ near zero angle of attack to $C_D = 0.40$ at angles near 24° . When the aileron is deflected to -45° and above, the drag decreases initially with angle of attack before starting to follow the parabolic upward trend. At -90° , for example, drag coefficient falls from $C_D = 0.60$ at zero to 0.22 at 33° angle of attack before starting to rise. This behavior is caused by the distribution of pressure noted earlier at high angles of attack and flap deflections; high pressures on the upper surface of the deflected aileron drop due to massive flow separation at high attack angles and the axial force on the aileron is reduced.

When these lift and drag characteristics are combined according to Equation (1), Figure 11c results. The positive values of C_T at low angles of attack and deflection are desirable and necessary to drive the rotor to produce power, however, for the rotor to

decelerate in high wind conditions, the aileron deflections must generate negative thrust coefficients. For modest angles of attack, the large aileron deflections do, indeed, create substantial negative values as shown in Figure 11c. Thrust coefficients increase from $C_T = -0.30$ and $C_T = -0.8$ for the -45° and -90° deflections to zero at angles of attack of 19° and 33° , respectively. Above these angles, a region of positive thrust coefficients exist. The -45° deflection shows a peak $C_T = 0.24$ at 24° before decreasing to zero at 34° angle of attack; the -90° deflection has a maximum $C_T = 0.14$ at 36° angle of attack that decreases to zero beyond 45° angle of attack. These positive zones of thrust coefficient may reflect adversely upon the ability of this aileron configuration to brake the rotor.

The aerodynamic characteristics of the 0.38c balanced aileron are presented in Figure 12. The symbols are the experimental data; the broken lines represent the results at corresponding aileron deflections of the 0.38c plain aileron. The most striking point of Figure 12a is the large lift coefficient measured at the -90° aileron deflection, above $C_L = 1.2$ at 32° angle of attack. In contrast, the peak lift coefficient for the plain aileron was $C_L = 0.7$ at 36° . Further, the balanced aileron appears to decrease the angle of zero lift about 4° . The thrust coefficients displayed in Figure 12b indicate that the low aileron deflections produce low values of C_T than the corresponding C_T of the plain aileron, but the high lift of the -90° deflection decreases the effectiveness of the balanced aileron. Thrust coefficient becomes positive at 28° and peaks at $C_T = 0.21$ at 33° angle of attack.

Performance of the 0.30c plain aileron is shown in Figure 13. For the -90° aileron deflection, lift becomes positive at 24° angle of attack, reaching a maximum of $C_L = 0.9$ at 33° angle of attack. The smaller chord plain aileron exhibits positive thrust coefficients at the -90° deflection as do the other two aileron configurations, crossing $C_T = 0$ at 27° angle of attack and peaking near $C_T = 0.20$ at 33° angle. The 0.30 plain aileron has less ability to generate negative thrust coefficients, $C_T = -0.4$ compared to $C_T = -0.75$ of the 0.38 plain aileron, and can shift the angle of attack for zero thrust to 27° in contrast to the 33° angle for zero thrust of the larger chord plain aileron.

Hinge Moments

The pressures distributed on the aileron surfaces produce an aerodynamic moment about the hinge line, and knowledge of this moment is important when designing an aileron control system. By integrating the pressures measured on the aileron with respect to the hinge line, this aerodynamic hinge moment can be obtained. This moment is shown in coefficient form in Figure 14 for the 0.38c plain aileron where the hinge moment coefficient is defined by equation (2) below,

$$C_H = \frac{H}{q C_A^2} \quad (2)$$

with a positive hinge moment defined as a moment tending to rotate the aileron trailing edge down. At low angles of attack and aileron deflection the hinge moment variations with increasing angle of attack and deflection. At high deflection angles the positive

hinge moment is almost independent of angle of attack until angles of attack above 20° ; hinge moment then decreases rapidly, changing sign at 24° and 32° angle of attack for the -45° and -90° aileron deflections, respectively.

Figure 15 indicates the hinge moments obtained on the balanced aileron and in the 0.30c plain aileron. As anticipated, the balanced aileron reduces the hinge moment for all cases when compared to the 0.38c plain aileron. Similarly, the hinge moment of the 0.30c plain aileron at -90° aileron deflection is lower than the baseline. All three configurations demonstrate the change in hinge moment sign at post stall angles of attack.

By cross plotting the hinge moment information, the angle to which the aileron will deflect to make the hinge moment zero may be obtained. The float angle is shown in Figure 16 as a function of angle of attack for the three aileron configurations.

SUMMARY

Three aileron configurations of the NACA 64-621 airfoil have been examined in the OSU 6" x 12" high Reynolds number wind tunnel at Mach number 0.25 and Reynolds number of 5×10^6 based on the 4 inch model chord. The purpose of the test was to contribute to the existing aerodynamic data base of candidate wind turbine airfoils and to measure the performance of the three aileron configurations at high angles of attack and aileron deflection to evaluate their suitability for wind turbine power modulation and braking.

Pressure distributions obtained on the 0.38c plain aileron; 0.38c balanced aileron and 0.30c plain aileron

were integrated to obtain lift, drag and thrust coefficients at angles of attack to 45° and angles of aileron deflection to -90° . Reduction of the data leads to the following observations:

i) At modest angles of attack all aileron configurations behaved normally, with both lift coefficient and thrust coefficient decreasing with increasing negative aileron deflection. Maximum lift coefficient decreased as well.

ii) At angles of attack above 20° and aileron deflections above -30° the pressure distributions indicated massive separation on the upper surface accompanied by low upper surface pressures, resulting in increasing positive lift.

iii) As a result of this lowered upper surface pressure at -90° aileron deflection, for example, positive thrust coefficients were measured at angles of attack above 33° , 28° , and 27° for the 0.38c plain, 0.38c balanced and 0.30c plain aileron, respectively. These regions of substantial positive thrust coefficients existed for more than 10° for all configurations.

iv) Use of aileron deflection as a power modulation method is feasible, and as an aerodynamic braking system is possible when angles of attack can be limited to those producing negative thrust coefficients. The 0.38c plain aileron was most successful as a brake, followed by the 0.38c balanced aileron and the 0.30c plain aileron.

v) Hinge moments measured on the three configurations were maximum for the 0.38c plain aileron, with the balanced 0.38c aileron airfoil less.

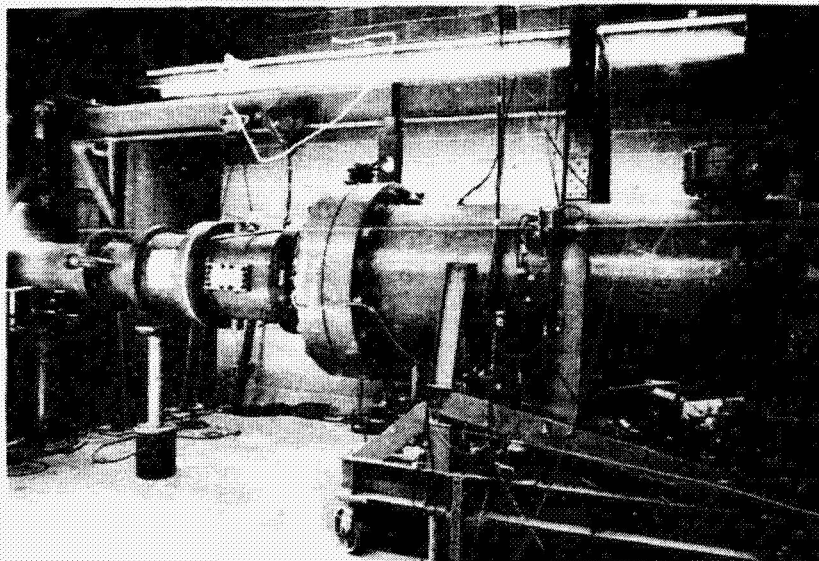


FIGURE 1. The OSU Pressurized 6" x 12" Airfoil Wind Tunnel.

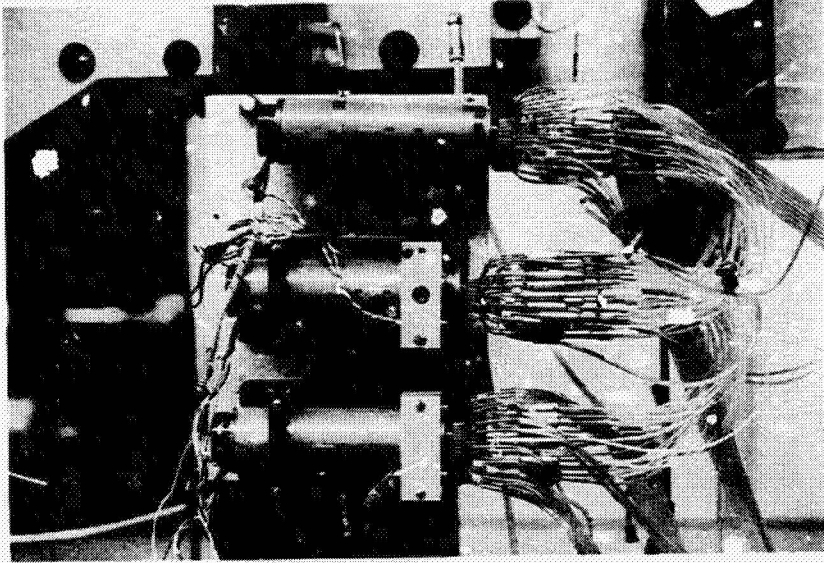


FIGURE 2. Scanning Valve, Check Valves For Pressure Sensing.

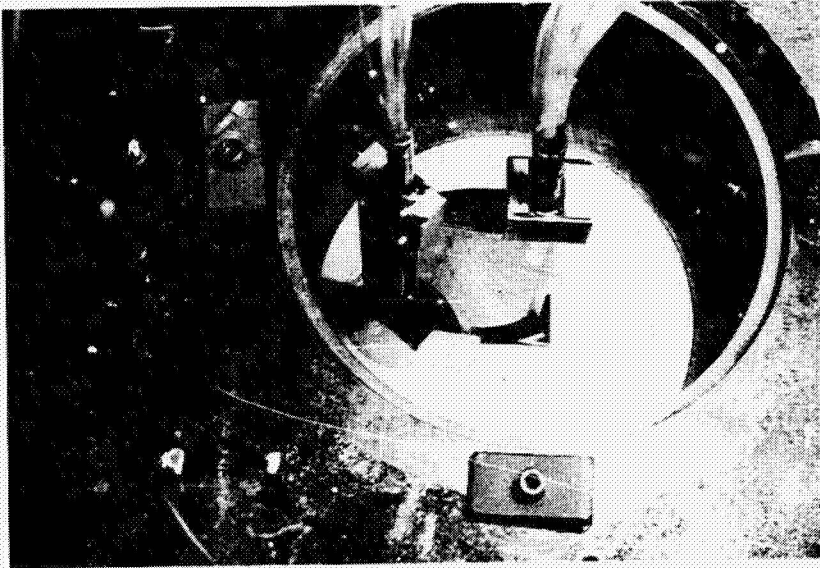


FIGURE 3. Model Installed in Wind Tunnel.

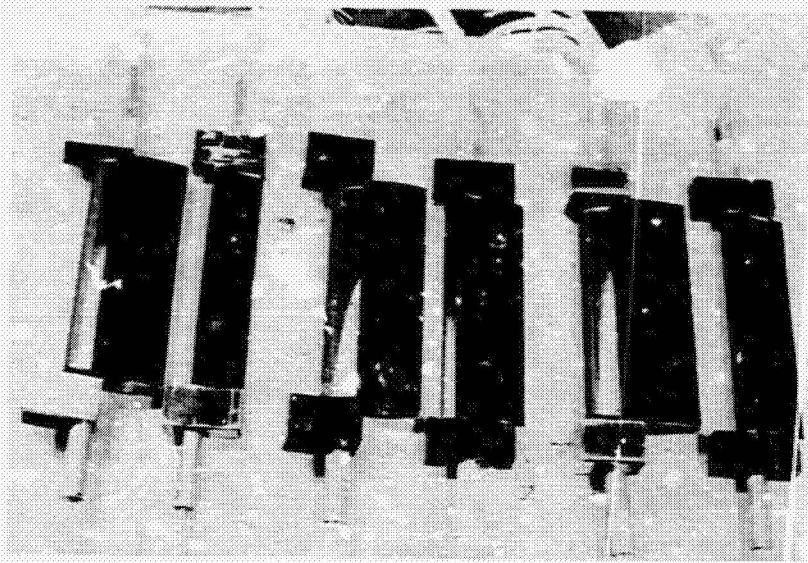
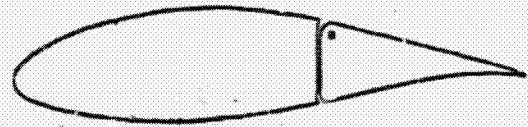
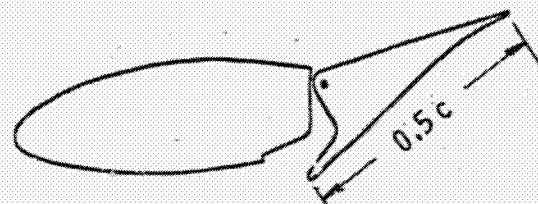


FIGURE 4. The 0.30c Plain, 0.38c Balanced and 0.38c Plain Aileron Models.



0.38c PLAIN AILERON

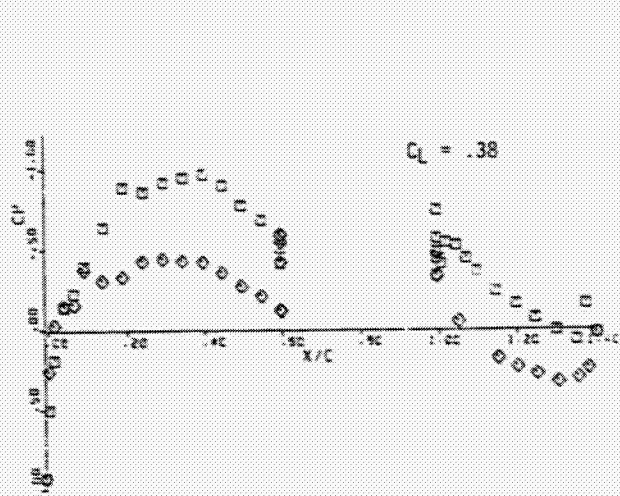


0.38c BALANCED AILERON

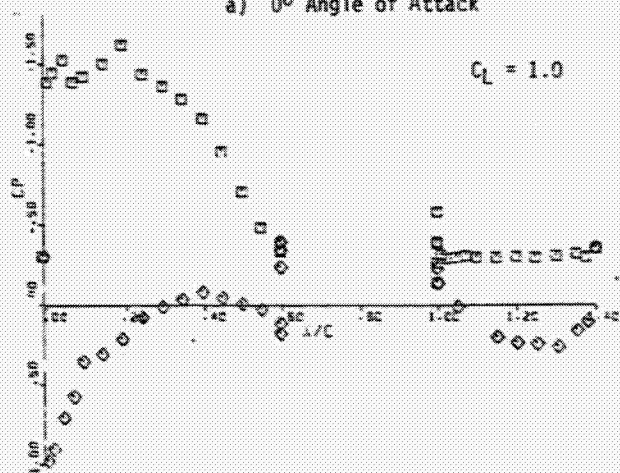


0.30c PLAIN AILERON

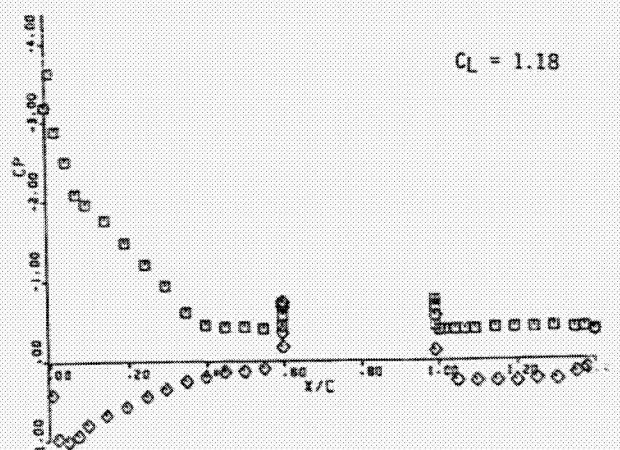
FIGURE 5. NACA 64 621 Airfoils With The Aileron Configurations Tested.



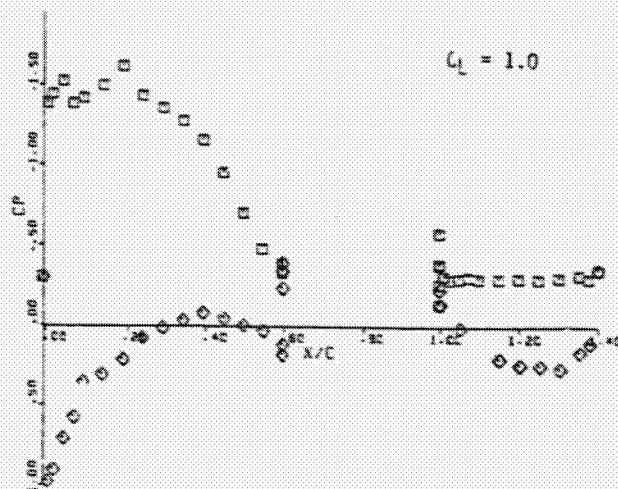
a) 0° Angle of Attack



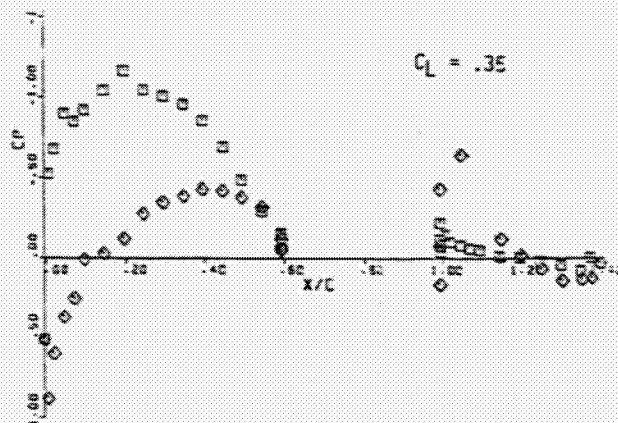
a) 9° Angle of Attack



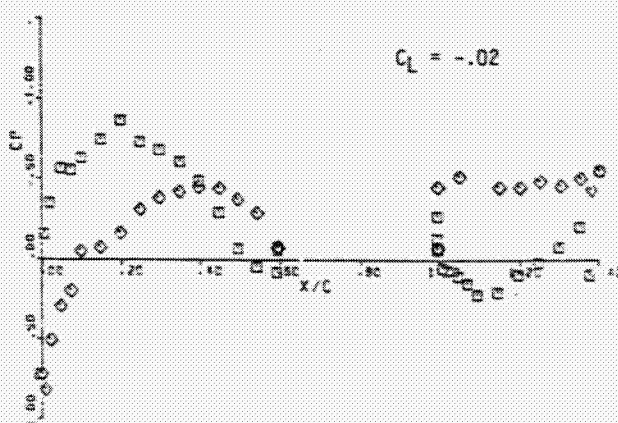
c) 18° Angle of Attack



a) 0° Aileron Deflection



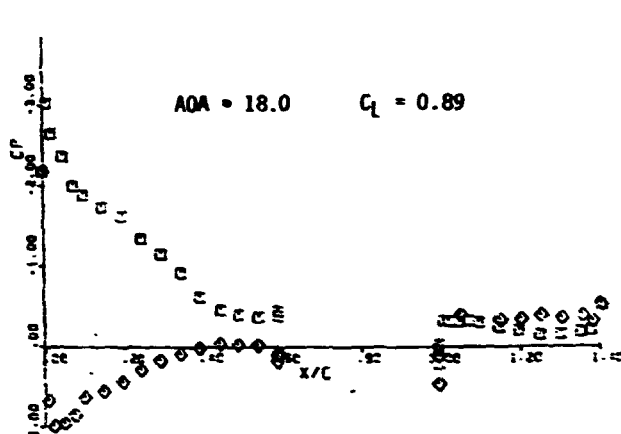
b) -15° Aileron Deflection



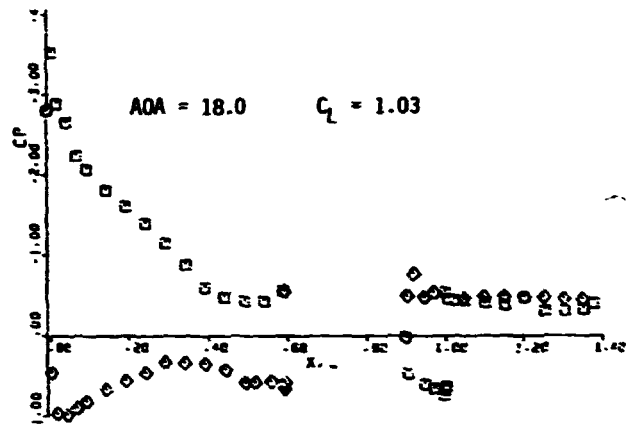
b) -30° Aileron Deflection

FIGURE 6. Pressure Distribution on 0.38c Plain Aileron With Aileron Deflection 0° and Angle of Attack 0°, 9°, and 18°.

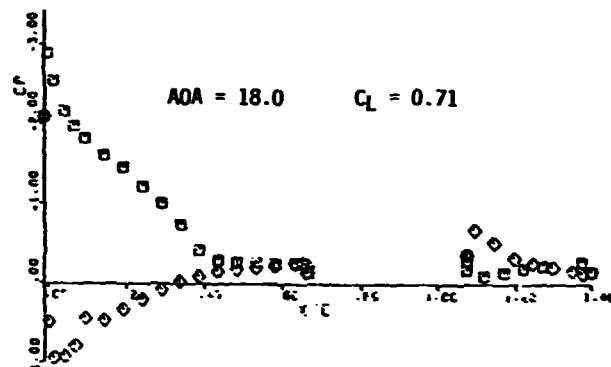
FIGURE 7. Pressure Distribution on 0.38c Plain Aileron at 9° Angle of Attack and Aileron Deflections 0°, -15° and -30°.



a) 0.38c Plain Aileron



b) Balanced Aileron



c) 0.30 Plain Aileron

FIGURE 8. Pressure Distribution on the Three Configurations at 18° angle of Attack and Aileron Deflection -30° .

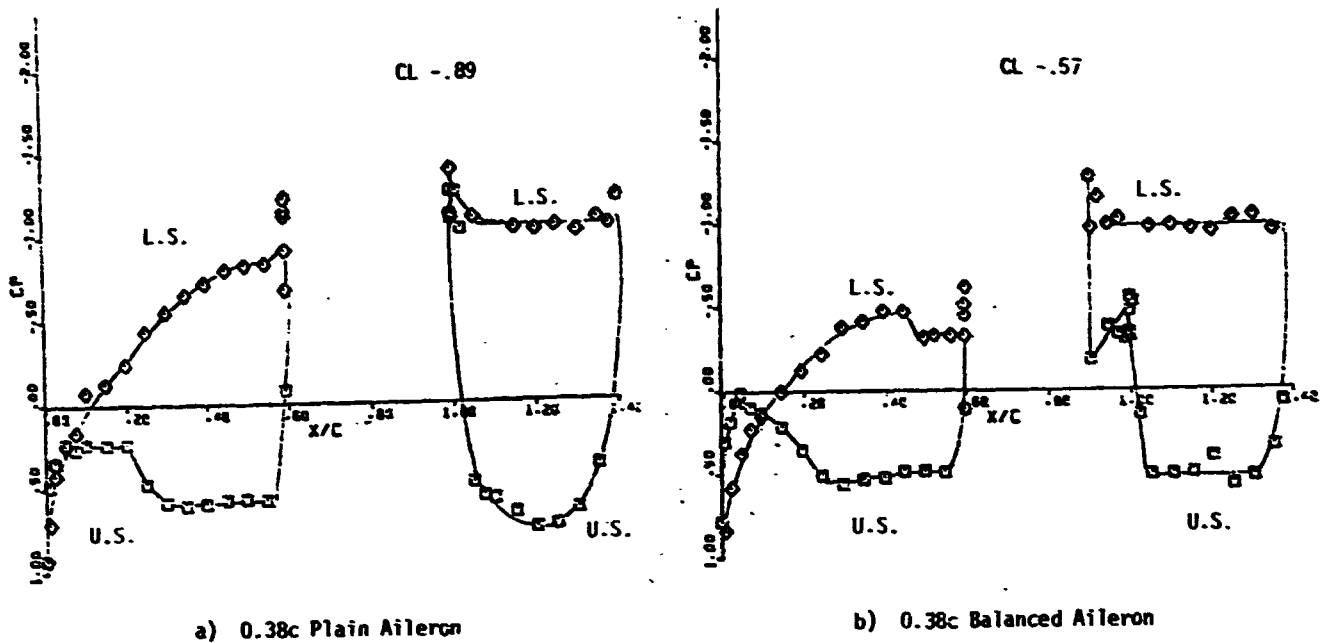


FIGURE 9. Pressure Distribution on Plain and Balanced 0.38c Aileron at 18° Angle of Attack and -90° Aileron Deflection.

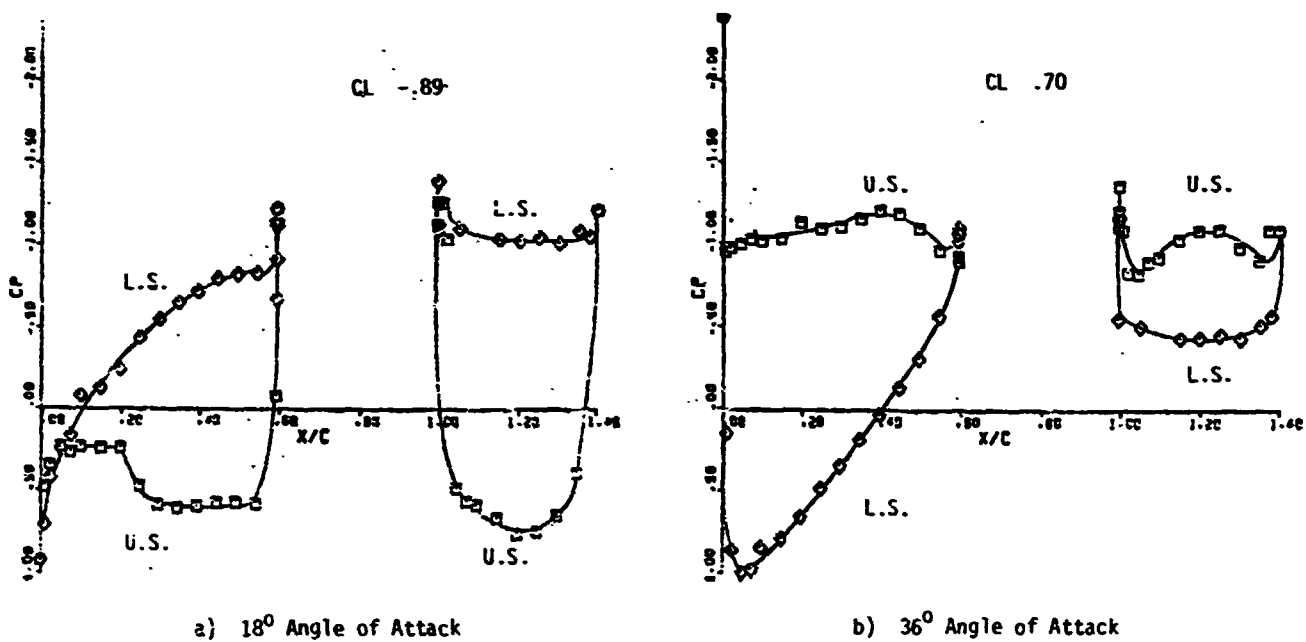
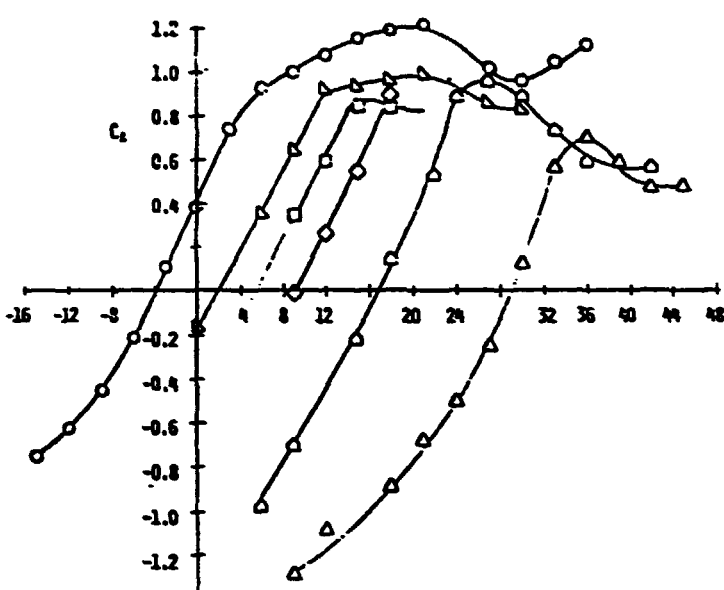
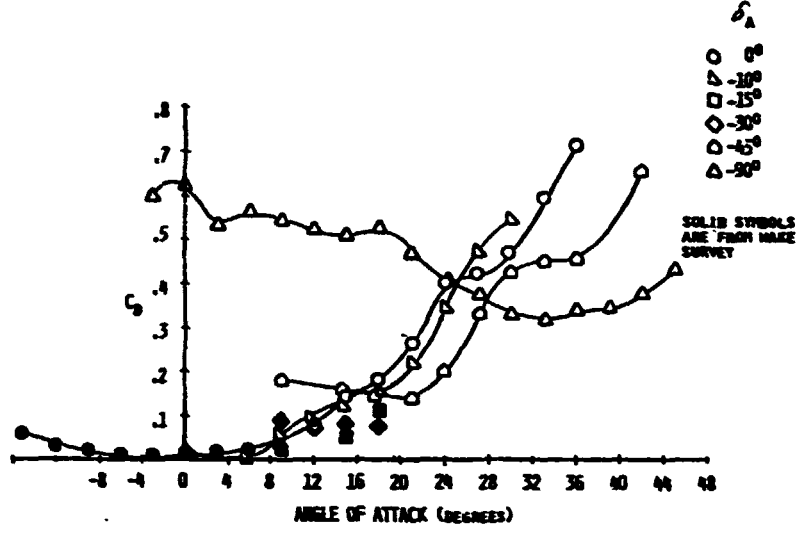


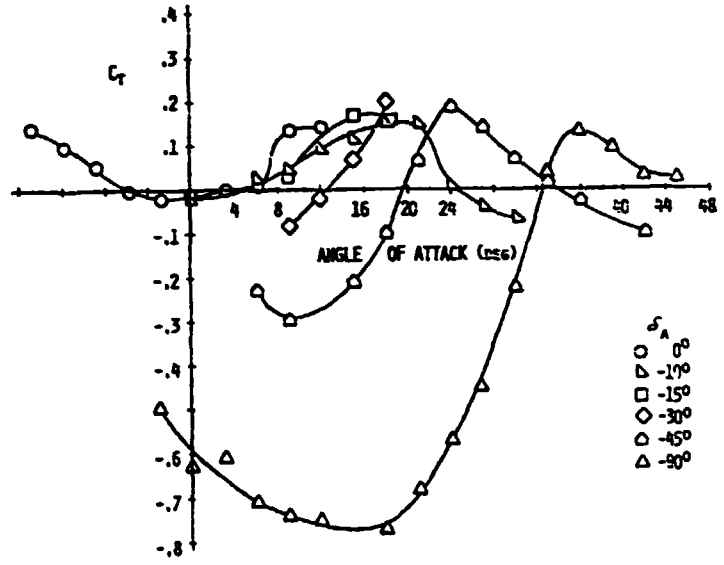
FIGURE 10. Pressure Distribution of 0.38c Plain Aileron at 18° and 36° Angle of Attack and -90° Aileron Deflection.



a) Lift Coefficient
vs
Angle of Attack

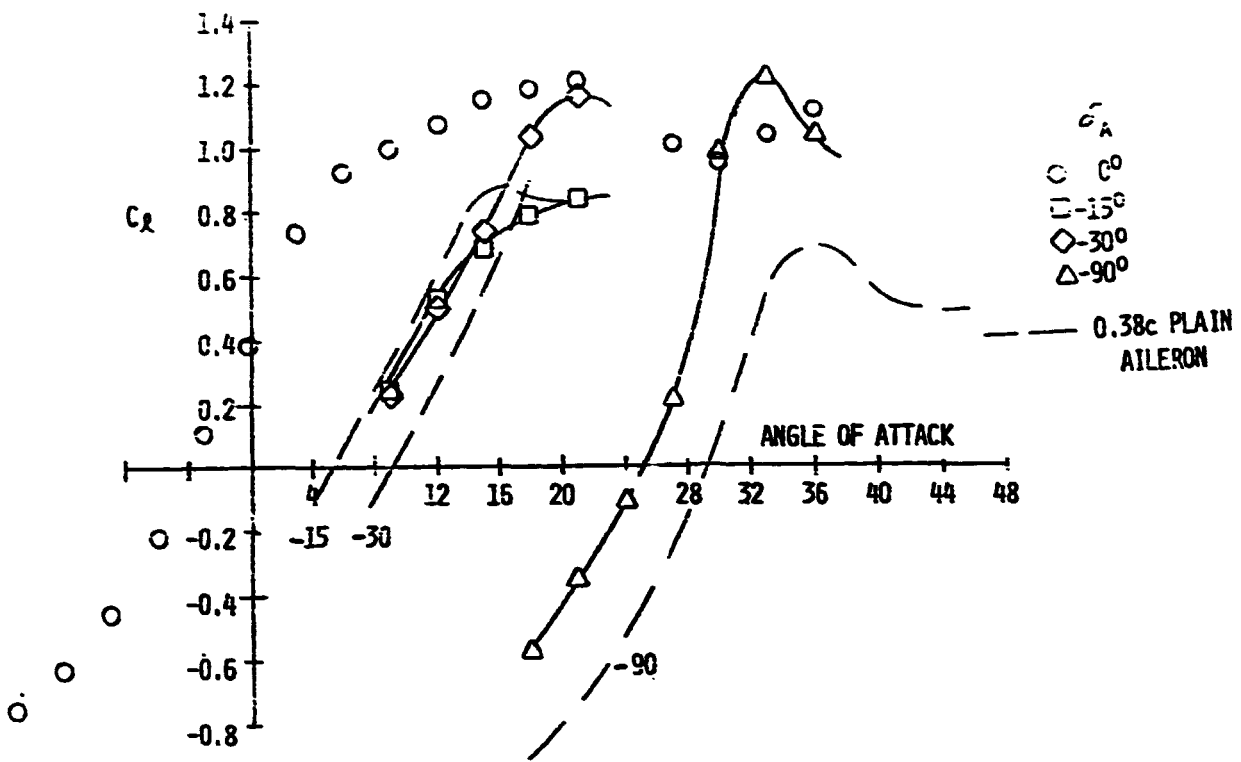


b) Drag Coefficient
vs
Angle of Attack

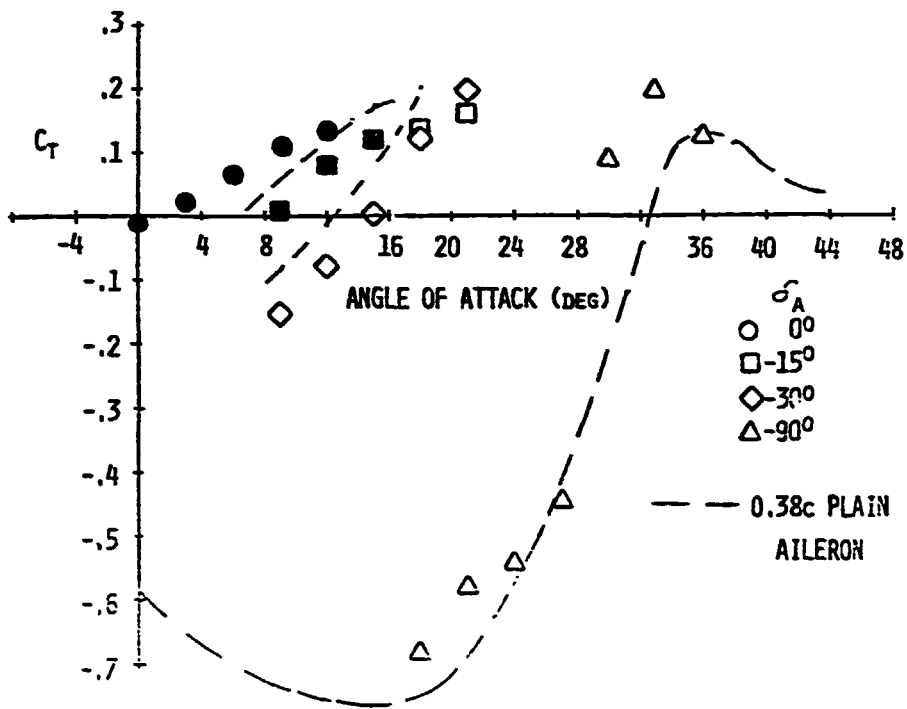


c) Thrust Coefficient
vs
Angle of Attack

FIGURE 11. Aerodynamic Characteristics of the 0.38c Plain Aileron at $M = 0.2$ and $Re = 5 \times 10^6$.

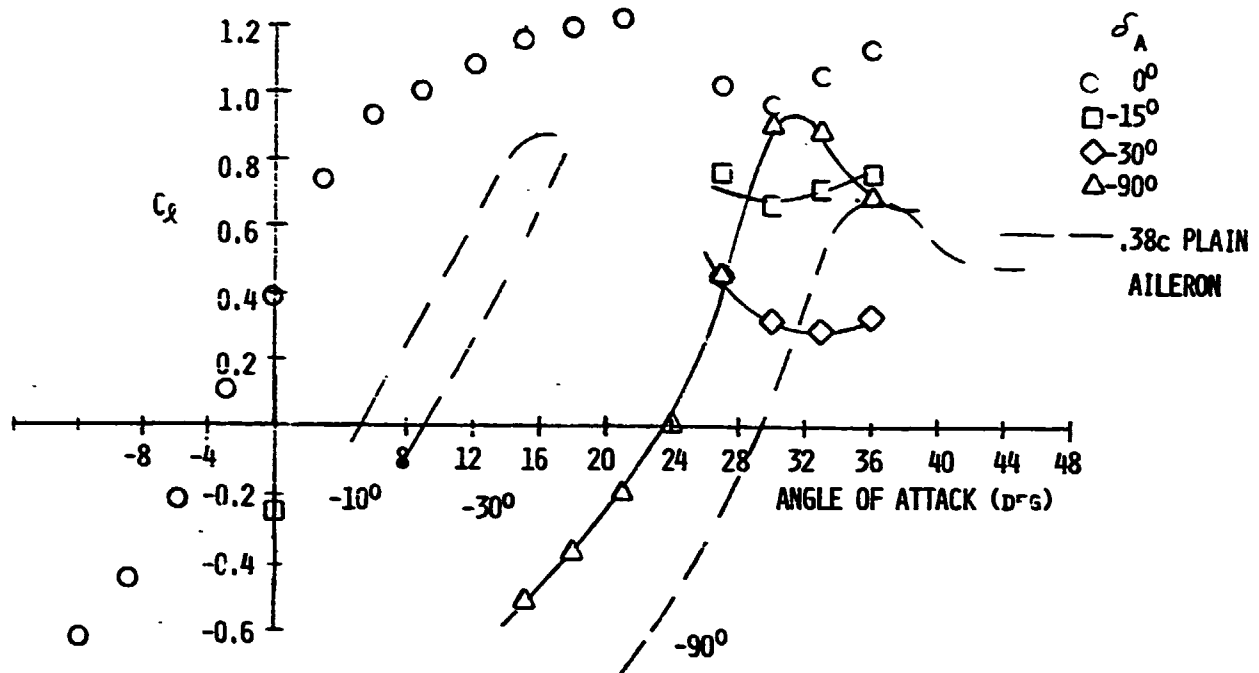


a) Lift Coefficient vs Angle of Attack

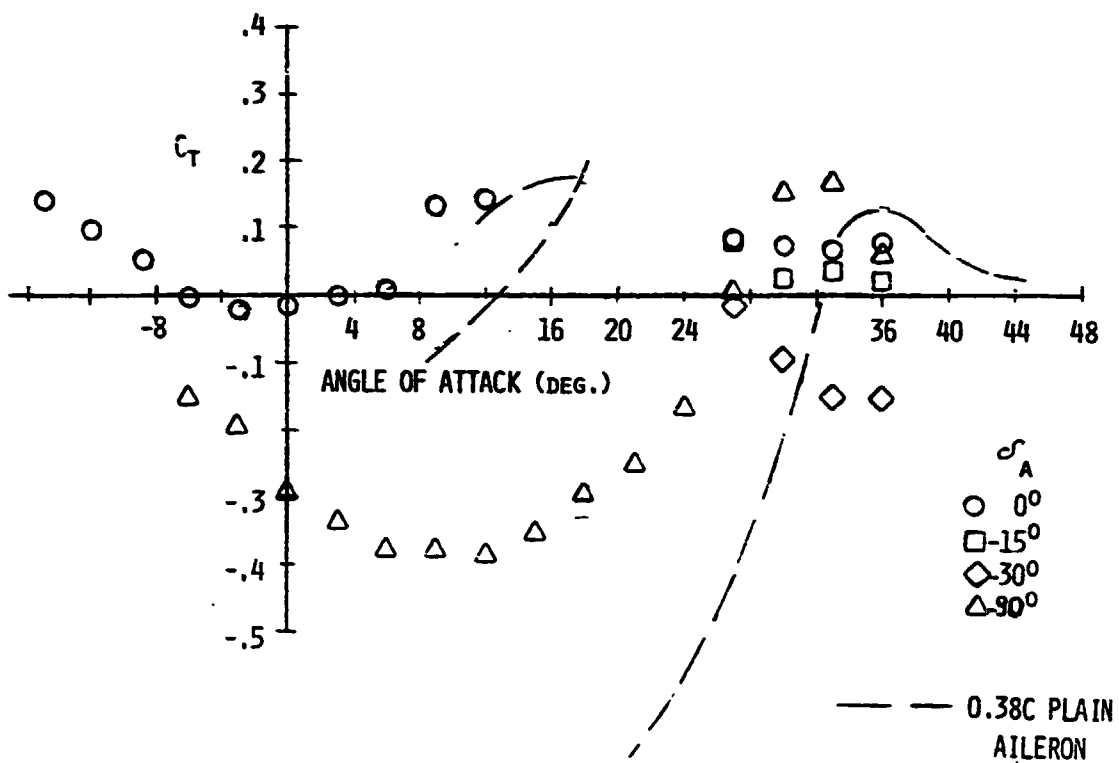


b) Thrust Coefficient vs Angle of Attack

FIGURE 12. Lift and Thrust Coefficients of the 0.38c Balanced Aileron.



a) Lift Coefficient vs Angle of Attack



b) Thrust Coefficient vs Angle of Attack

FIGURE 13. Lift and Thrust Coefficients of the 0.30c Plain Aileron.

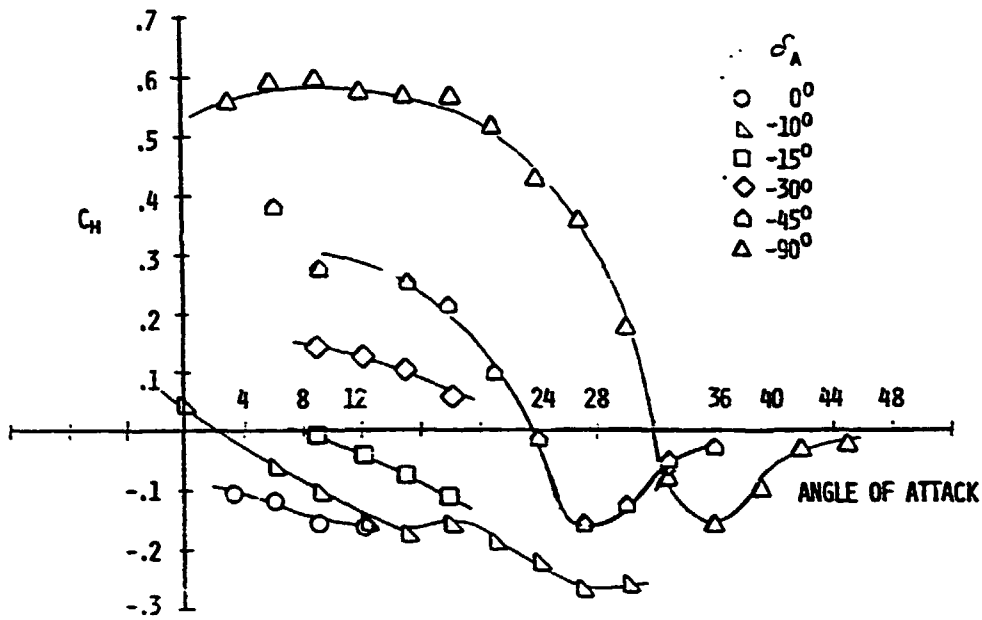


FIGURE 14. Hinge Moment Coefficient vs. Angle of Attack for the 0.38c Plain Aileron.

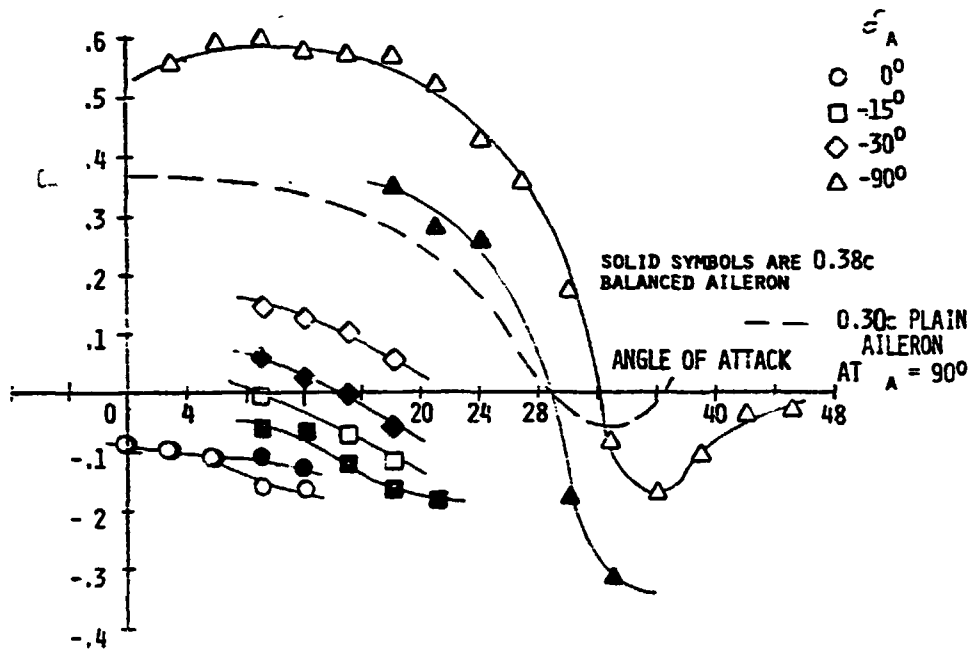


FIGURE 15. Hinge Moment Comparisons for the 0.30c Plain and 0.38c Balanced Aileron.

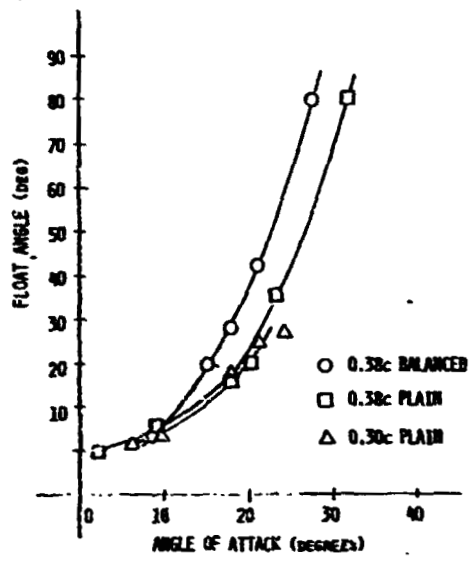


FIGURE 16. Angle for Zero Hinge Moment vs Angle of Attack

COMPARATIVE PERFORMANCE TESTS ON THE MOD-2,
2.5-MW WIND TURBINE WITH AND WITHOUT VORTEX GENERATORS*

G. E. Miller

N95-27978

Boeing Aerospace Company
Seattle, Washington 98124

ABSTRACT

A test program was conducted on the third Mod-2 unit at Goldendale, Washington, to systematically study the effect of vortex generators (VG's) on power performance. The subject unit was first tested without VG's to obtain baseline data. Vortex generators were then installed on the mid-blade assemblies, and the resulting 70% VG configuration was tested. Finally, vortex generators were mounted on the tip assemblies, and data was recorded for the 100% VG configuration. This test program and its results are discussed in this paper. The development of vortex generators is also presented.

NOMENCLATURE

AEP	Annual Energy Production
BPA	Bonneville Power Administration
Met	Meteorological
NACA	National Advisory Committee for Aeronautics
PGandE	Pacific Gas and Electric Company
PNL	Pacific Northwest Laboratories (Battelle)
Sta	Radial Station (Inches)
VG	Vortex Generator
WTS	Wind Turbine System

INTRODUCTION

Analytical studies using wind tunnel data as input indicated that vortex generators could be used to increase Mod-2 power performance in below-rated operation. Subsequent tests conducted on the PGandE Mod-2 unit located in Solano County, California, demonstrated that power performance was improved substantially by installing VG's on the mid-blade assemblies. The Solano test results will be published by PGandE through the Electric Power Research Institute.

Later, in support of the Mod-5B program, it became necessary to confirm that a larger improvement in power performance could be obtained if VG's were mounted on both the mid-blade and tip assemblies. Therefore, a test program was planned and conducted to systematically study the effect of VG spanwise extent on Mod-2 power performance. This test program and its results are presented in this paper. First, however, the development of vortex generators will be discussed.

VORTEX GENERATOR DEVELOPMENT

A variety of vortex generating devices have been developed for boundary layer control over the past 35 years or so. In Reference 1, Pearcey describes several types of vortex generators and discusses their application to the prevention of shock-induced boundary layer separation. When this phenomenon

*Presented at the DOE/NASA Workshop on Horizontal Axis Wind Turbine Technology, May 8-10, 1984 in Cleveland, Ohio.

occurs on the wings of high speed aircraft, additional drag is produced and the aircraft's stability and control may be adversely affected. Vortex generators are often mounted on the wings of jet transports to delay flow separation and prevent the occurrence of control problems.

The majority of wind turbine rotors do not encounter shock-induced boundary layer separation because they operate in the incompressible flow regime. The Mod-2 rotors, however, experience another type of boundary layer separation that begins at the trailing edge and progressively moves forward along the suction surface as the angle of attack increases. This type of separation occurs when the boundary layer can no longer follow the blade surface as it traverses a region on which an adverse pressure gradient is imposed by the external flow. With increasing angle of attack below stall, this separation process results in gradual loss of lift and an additional, undesirable drag increment. This separation process also results in the gentle trailing edge stall that is characteristic of most thick airfoils.

The fixed pitch Mod-2 mid-blade assemblies utilize thick airfoils that are required to function at large angles of attack throughout much of the operational wind speed range. Therefore, the power production of the mid-blade assemblies is limited primarily by this separation process. The power production capability of the mid-blade assemblies could be improved if the stall angle and maximum lift of these airfoils could be increased by delaying the boundary layer separation process.

To achieve this goal, Boeing conducted a series of wind tunnel tests to explore the use of vane-type vortex generators as high lift devices on thick airfoils operating in flow conditions appropriate to large horizontal axis wind turbines. Initially, corotational and counterrotational VG patterns were studied. These two patterns are illustrated in Figure 1. For the same vane size and spacing, counterrotational VG's were slightly more effective in generating maximum lift than corotational VG's. Therefore, most of the testing was directed toward optimizing the counterrotational configuration.

The VG pattern found to be most effective in producing maximum lift is illustrated in Figure 2. This high lift VG pattern uses the larger of the two vane sizes shown and was used to design the mid-blade VG's. The effect of this high lift VG pattern on the lift and drag characteristics of a 24 % thick airfoil is presented in Figure 3. Note that the vortex generators increased the lift over the entire angle of attack range shown. Also note that the stall angle is increased by 6 degrees and the maximum lift is increased by 90%. The minimum drag penalty for this VG installation is only 20 counts. For lift coefficients greater than 0.7, however, the drag is lower with the VG's installed.

The second, smaller vane shown in Figure 2 was also developed in the wind tunnel. Relative to the results obtained with the larger VG's, the smaller VG's produced 5% less maximum lift; but the minimum drag penalty is reduced by 70%. The smaller VG's were developed for application to the blade tips which always operate below stall. Consequently, maximum lift is of secondary importance; however, any additional drag resulting from premature boundary layer separation is undesirable. Premature boundary layer separation could be triggered by distributed roughness or manufacturing contour imperfections, especially when located near the leading edge. For a given operating pitch schedule, the smaller VG's would produce a net drag reduction and some additional lift so that the power contribution from the tip assemblies is increased.

Before proceeding into the discussion of the Mod-2 test, a brief discussion of vortex generator physics will be presented. In the literature, the interaction of the VG's with the boundary layer on the mounting surface is described as a mixing process between the high energy external flow and the low energy boundary layer fluid. This mixing process reenergizes the boundary layer allowing it to follow the airfoil surface for a greater distance into a region with an adverse pressure gradient before separation occurs.

Flow visualization studies were included in the ongoing wind tunnel tests to examine this interaction process. The observed flow field for a well designed counterrotational VG pattern is illustrated in Figure 4. The observed flow field is very similar to that presented in Reference 1. As indicated in Figure 4, each vane produces a discrete vortex just outside the local boundary layer. As these vortices trail downstream, the vortices from toed-out vane pairs (looking toward the leading edge) gradually approach one another. The resulting vortex pairs generate a secondary flow which evacuates low energy fluid from the adjacent portions of the boundary layer. This low energy fluid is entrained by the viscous vortex cores. Simultaneously, the vortex pairs impress the high energy external flow against the adjacent portions of the boundary layer. Some high energy fluid is also entrained by the vortex cores. The effect of this secondary flow is to confine separation effects to the aft portion of the suction surface beneath the vortex pairs. As a result, lift capability is increased and form, or pressure, drag is reduced. At the higher angles of attack, wake surveys show a dramatic reduction in low energy wake fluid corresponding to a net drag reduction.

TEST DESCRIPTION

The subject test was conducted on the third Mod-2 unit, which is located on a site approximately 17 miles east of Goldendale, Washington. The first and second Mod-2 units are also located at this site. A general arrangement of the Goldendale site is illustrated in Figure 5. The test unit is situated near the southwest corner of the site. The two meteorological towers at the Goldendale site are also indicated in this figure.

A brief description of the test unit is presented in Figure 6. A detailed description of the Mod-2 WTS

is contained in Reference 2. Except for the vortex generator installations described below, the configuration of Unit #3 was not altered during the test.

The subject test was conducted during July and August, 1983. This test was conducted in parallel with another test which studied the effect of vortex generators on loads. The results of that test are presented in Reference 3.

At the beginning of the test, Unit 3 did not have vortex generators. This initial configuration was operated from July 8 through July 13, 1983, to obtain baseline data. Vortex generators were then installed on the mid-blade assemblies as illustrated in Figure 7. The resulting 70% VG configuration was operated from July 19 through July 28, 1983. Vortex generators were then installed on the tip assemblies as illustrated in Figure 8. The resulting 100% VG configuration was then operated from August 1 to September 1, 1983. However, most of the operational hours for the third configuration occurred during the first eight days of August.

DATA PROCESSING

During the test period, data from Unit #3 and the meteorological towers was recorded on magnetic tape for posttest processing. The various stages of the data processing sequence are discussed in this section.

The data tapes were first used to generate analog traces showing the beginning and end of each data run. These traces were used to determine start and stop times for power production. These traces also included the air pressure and temperature recorded from the BPA met tower. An average air density ratio for each data run was determined from the atmospheric parameters. The air density ratio was used to refer the measured generator power to standard sea level ambient conditions.

The power production interval of each run was then divided into convenient 10 minute intervals for digital processing. Smooth wind conditions were not considered in selecting the time intervals. At the beginning and end of each run, one minute intervals were also identified to provide a zero power check.

The appropriate data channels were then digitized during the 1 minute and 10 minute intervals. The digitizing rate was 10 samples per second. Next the mean value of each channel was calculated for each time interval. A zero power correction derived from the 1 minute intervals was then applied to the 10 minute average power levels. Finally, the 10 minute power levels were referred to standard sea level conditions using the following formula:

Referred Power = Measured Power / Air Density Ratio .

During the test period, the air density ratio at the site was approximately 0.90. Therefore, the referred power is approximately 11% greater than the measured power. For measured power levels greater than approximately 2250 kW, this procedure will generate referred power levels greater than rated power. If the test unit were operating at a site with standard sea level ambient conditions, however, the control system would have trimmed the power

output for these data points to the rated level. Therefore, since the purpose of the power referral step is to derive the power-velocity curve for a sea level standard site, the referred power cannot be greater than rated power.

TEST RESULTS

The measured variations of power output with wind speed for the three configurations are first discussed separately. Then a comparison between the three power-velocity curves is presented. Standard sea level ambient conditions are assumed in this discussion. The power output was measured in the nacelle at the generator terminals. The wind speed was measured at the 195 ft. level on the BPA met tower.

A total of 72 power-velocity data points were obtained for the baseline configuration without VG's. These data points presented in Figure 9. Most of these data points occur in the wind speed interval from 20 to 34 mph. Only a few data points were obtained at wind speeds less than 20 mph. The highest wind speed at which data was obtained is 34.8 mph. The distribution of data points with wind speed is shown in Figure 10.

Because of the noticeable data scatter, a least-squares polynomial curve fit was used to obtain the power variation with wind speed. A third order polynomial was selected as the best fit based upon minimization of the standard error. This curve fit and its formula are also shown in Figure 9.

The rated wind speed for the zero VG configuration is approximately 32 mph for standard sea level conditions. Note that the average generator power measured during rated power operation is only 2460 kW. The observed deviation of the measured rated power level from the 2500 kW power setpoint can be attributed to data system calibration error and pitch control dynamics.

A total of 78 power-velocity data points were obtained for the 70% VG configuration. These data points are plotted in Figure 11. Most of the data points occur within two wind speed intervals. The first interval is from 16 to 23 mph, and the second interval is from 29 to 36 mph. The data point distribution with wind speed is shown in Figure 12. The highest wind speed at which data was obtained is 37.3 mph.

The below-rated power data for the 70% VG configuration was approximated by applying a least-squares linear curve fit. A higher order curve fit could not be justified because of the small number of data points for wind speeds from 23 to 29 mph. The resulting curve fit and its formula are shown in Figure 11. From this curve fit, a rated wind speed of approximately 28.5 mph can be inferred for standard sea level conditions.

Several hours of rated power operation were recorded while testing the 70% VG configuration. The data points obtained from this data clearly show that the mean power output during rated power operation is 2460 kW.

A total of 49 power-velocity data points were obtained for the 100% VG configuration. These data points are presented in Figure 13. All of these data points occur in the wind speed interval from 16 to 30 mph. The data point distribution in Figure 14 shows that these data points are distributed fairly uniformly across this wind speed interval.

The below-rated power data for the 100% VG configuration was approximated by applying a least-squares polynomial curve fit. A linear curve fit was selected based upon minimization of the standard error. This curve fit and its formula are also shown in Figure 13.

The rated wind speed for the 100% VG configuration is approximately 27 mph. As noted for the other two configurations, the average power level for rated power operation is 2460 kW.

The curve fits to the power-velocity data for the three configurations are compared in Figure 15. When operating below-rated power, the 100% VG configuration produces the most power, while the no VG configuration produces the least power. The power output of the 70% VG configuration is approximately halfway between that of the other two configurations. The installation of the 70% VG's reduced the rated wind speed from approximately 32 mph to 28.5 mph. With the addition of the tip VG's, the rated wind speed was reduced further to approximately 27 mph. The minimum operating wind speed of approximately 13.8 mph is not affected by the VG installation.

The annual energy production (AEP) was also calculated for the three measured power-velocity curves. These AEP results are shown on Figure 15 relative to the baseline configuration without VG's. Note that the 100% VG configuration increased the AEP by 15.2%, while the 70% VG configuration resulted in an 8.6% AEP increase. The Mod-5B Weibull wind speed distribution shown in Figure 16 was used in these calculations.

Analytical studies using wind tunnel data as input support the AEP increment obtained for the 100% VG configuration. However, these studies indicate that the AEP increment for the 70% VG configuration should be approximately 2% greater. The discrepancy is believed to result from the lack of data for the 70% VG configuration for wind speeds from 23 to 29 mph. The few data points obtained in this wind speed interval agree quite well with predictions. Furthermore, excellent agreement between analysis and data was obtained for the 70% VG configuration tested at Solano.

SUMMARY

The results of this test program can be summarized as follows:

- 1) The Mod-2 power production in below-rated operation is maximized by installing vortex generators on both the mid-blade and tip assemblies.

- 2) For the Mod-5B Weibull wind speed distribution, the 100% VG configuration increased the annual energy production by 15.2%, while the 70% VG configuration resulted in an 8.6% AEP increase. Because of insufficient data, the AEP increment for the 70% VG configuration may be too low. Analytical studies indicate that the AEP increase for the 70% VG configuration is approximately 10.5%. This analytical prediction is consistent with the Solano data.

The results of this test program confirmed the design decision to install vortex generators on both the mid-blade and tip assemblies of the Mod-5B rotor.

REFERENCES

1. Pearcey, H. H., "Shock-Induced Separation and Its Prevention by Design and Boundary Layer Control," Boundary Layer and Flow Control, Vol. 2, ed. by Lachmann, G. V., Pergamon Press, New York, 1961.
2. Boeing Engineering and Construction Company, Mod-2 Wind Turbine System Development Final Report, Volume 2 - Detailed Report, NASA CR-168007, September 1982.
3. Zimmerman, D. K., Shipley, S. A. and Miller, R. D., "Comparison of Measured and Calculated Dynamic Loads for the Mod-2, 2.5-MW Wind Turbine System," presented at DOE/NASA Workshop on Horizontal Axis Wind Turbine Technology, May 8-10, 1984 in Cleveland, Ohio.

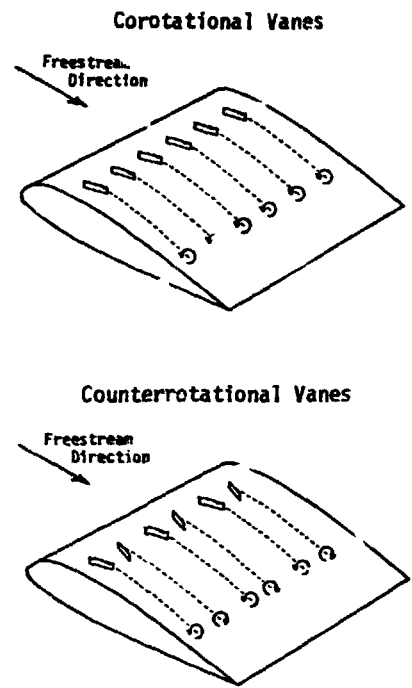


Figure 1. Comparison Of Corotational And Counterrotational Vane-type Vortex Generators.

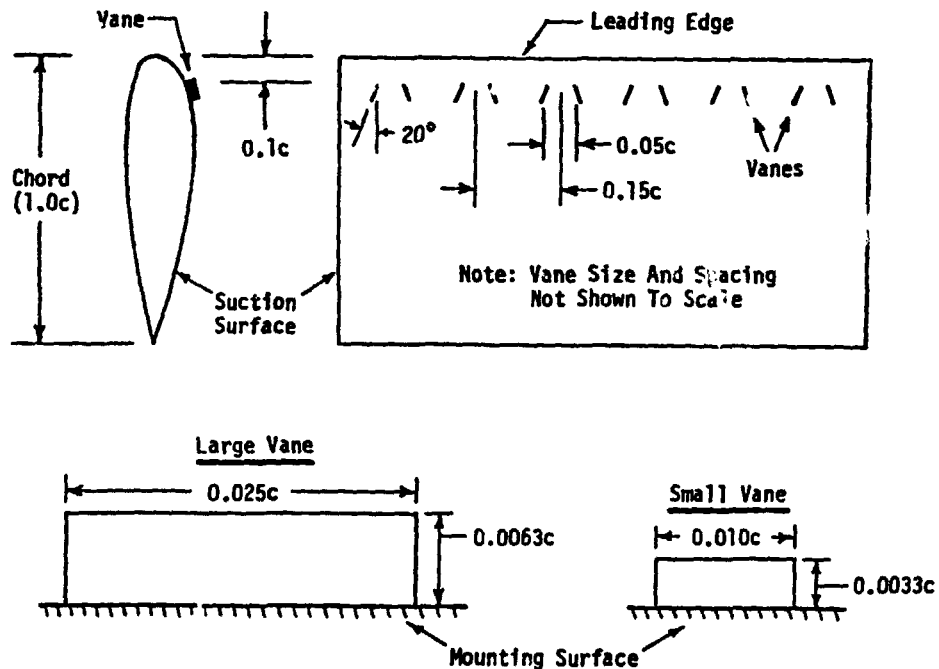


Figure 2. Counterrotational Vortex Generator configurations.

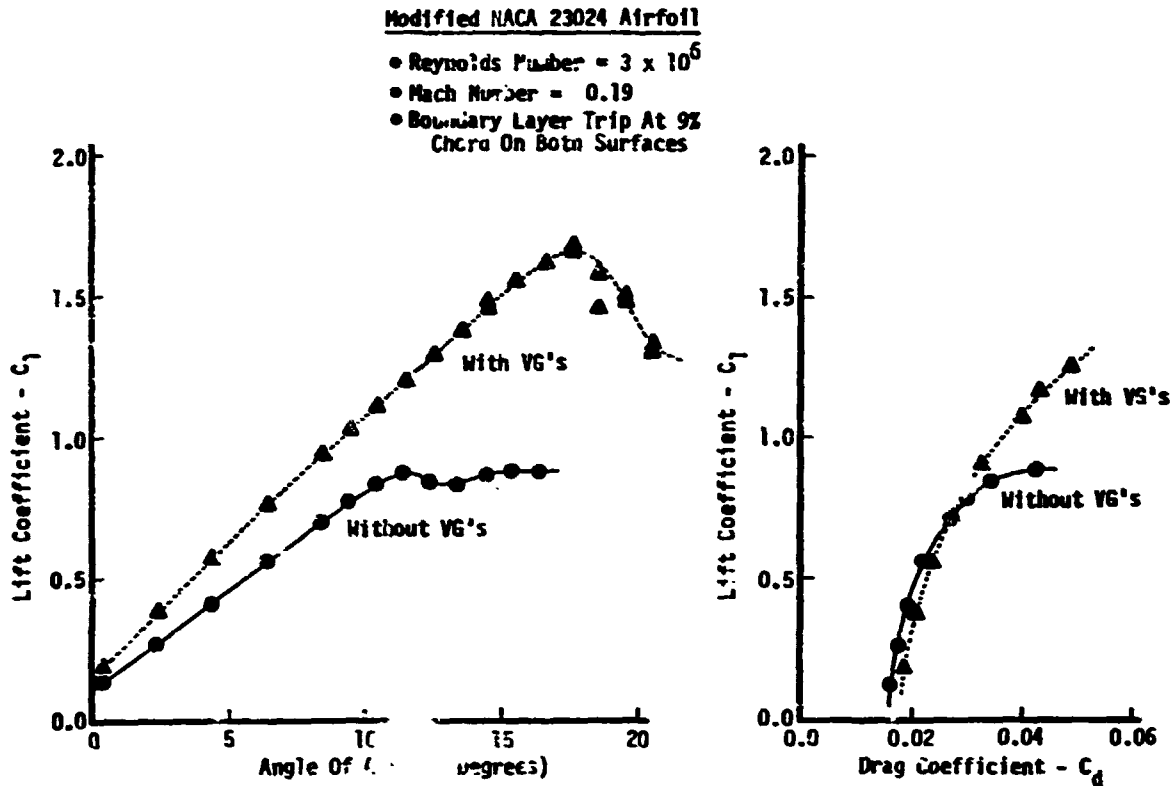


Figure 3. Effect Of Vortex Generators On Two-Dimensional Airfoil Lift And Drag Characteristics.

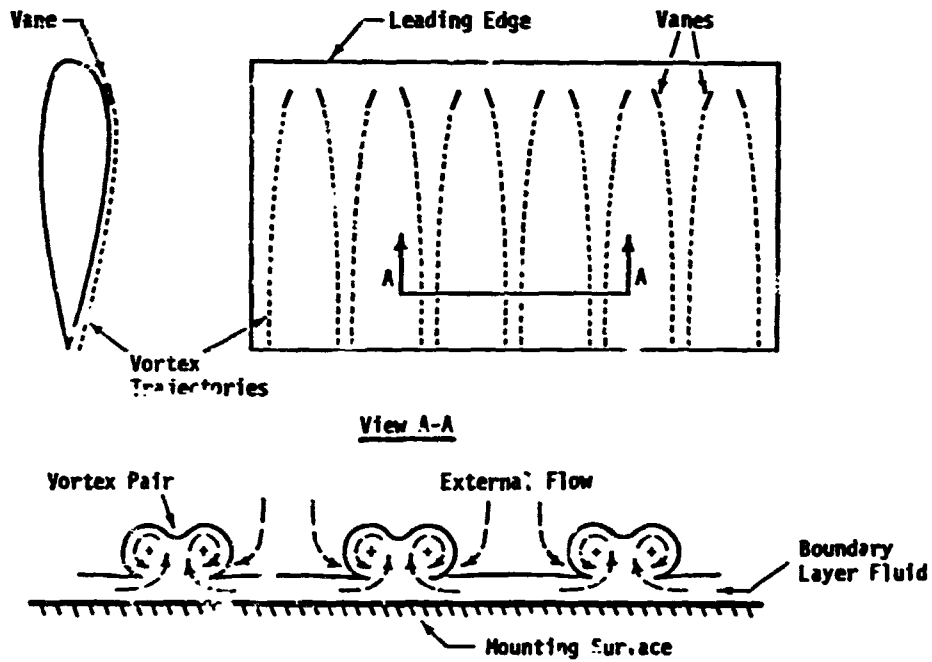


Figure 4. Observed Flow Structure For Counterrotational Vortex Generators.

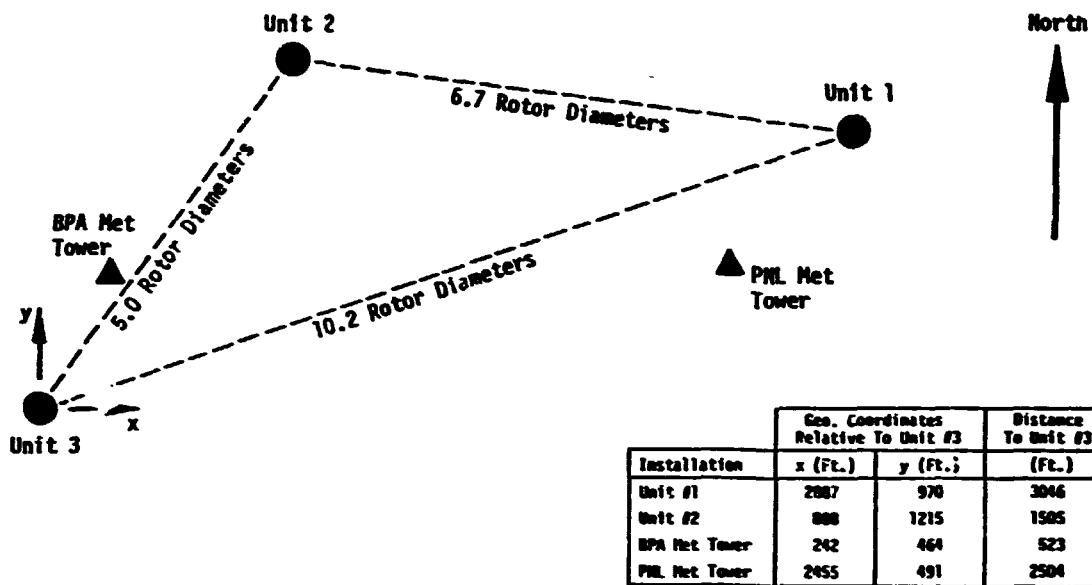


Figure 5. General Arrangement Of Goldendale Site.

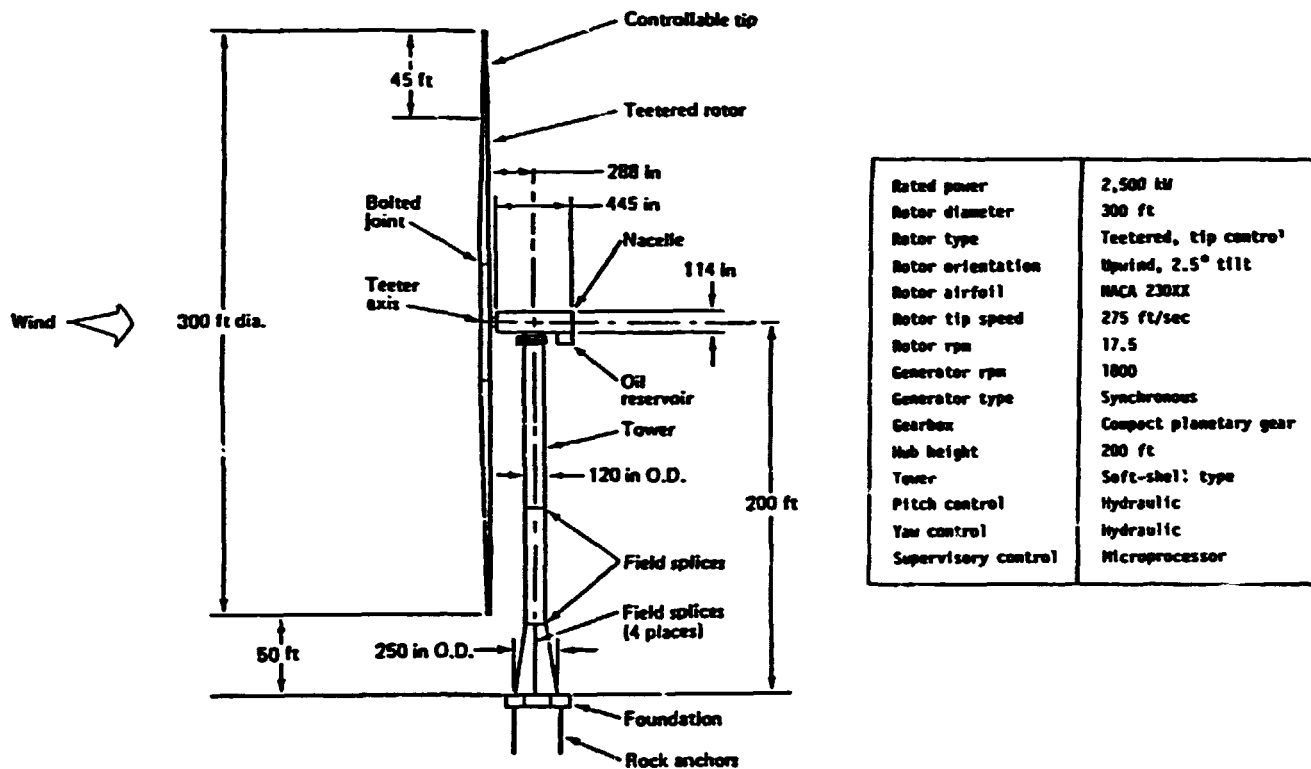


Figure 6. Description Of Mod-2 WTS.

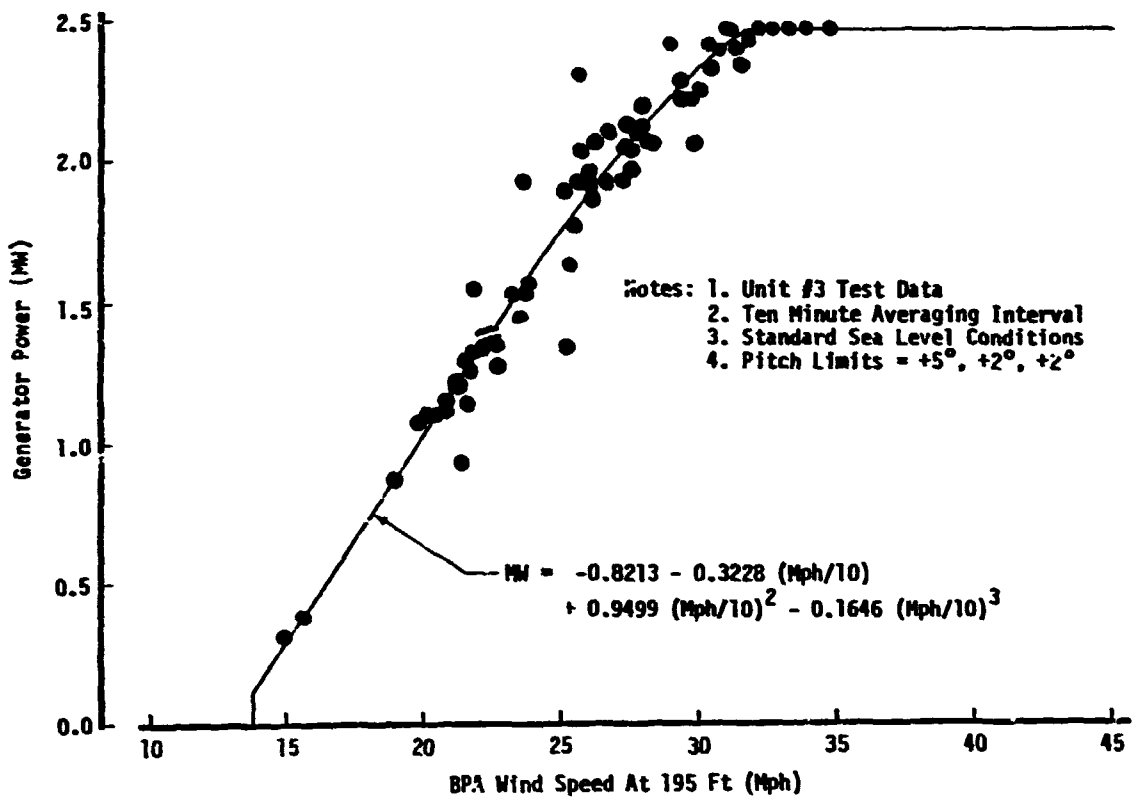


Figure 9 Mod-2 Power Performance Without Vortex Generators.

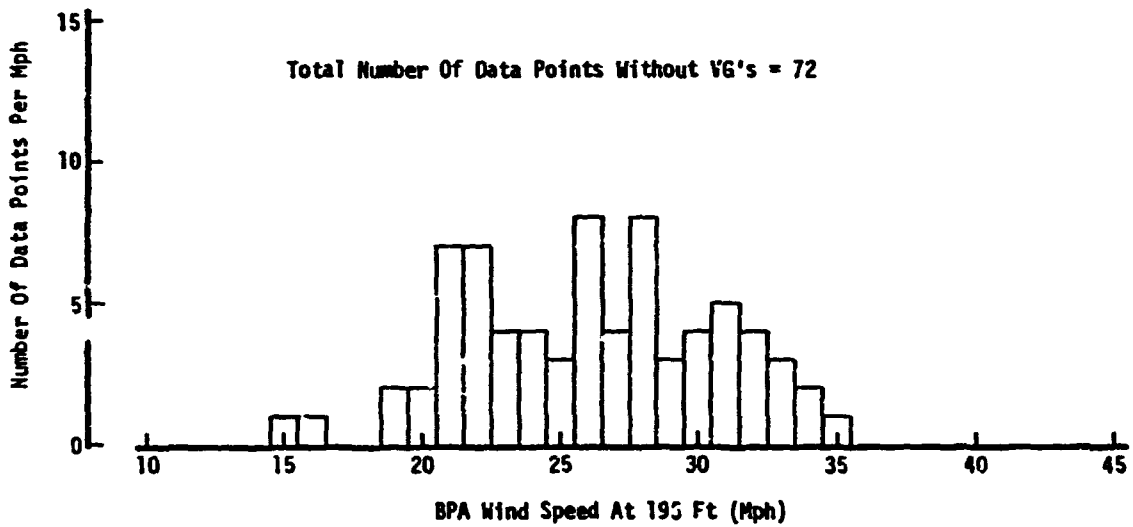


Figure 10. Data Point Distribution Without Vortex Generators.

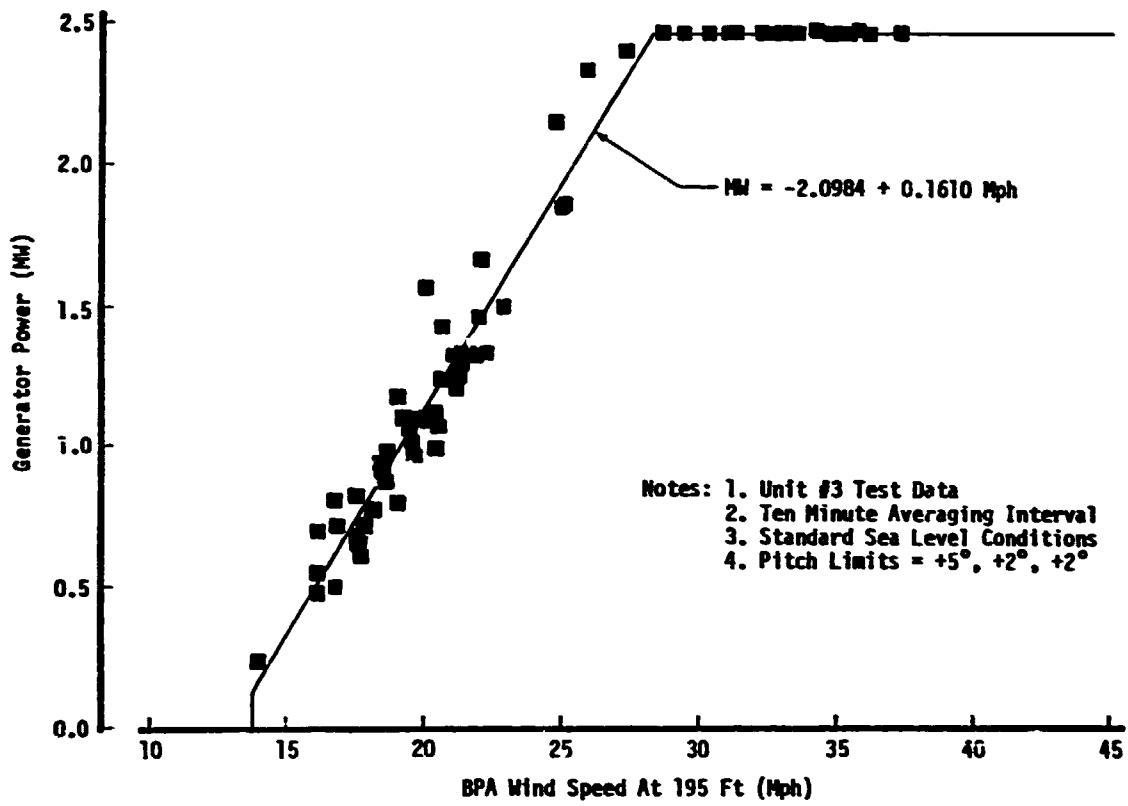


Figure 11. Mod-2 Power Performance With 70% Vortex Generators.

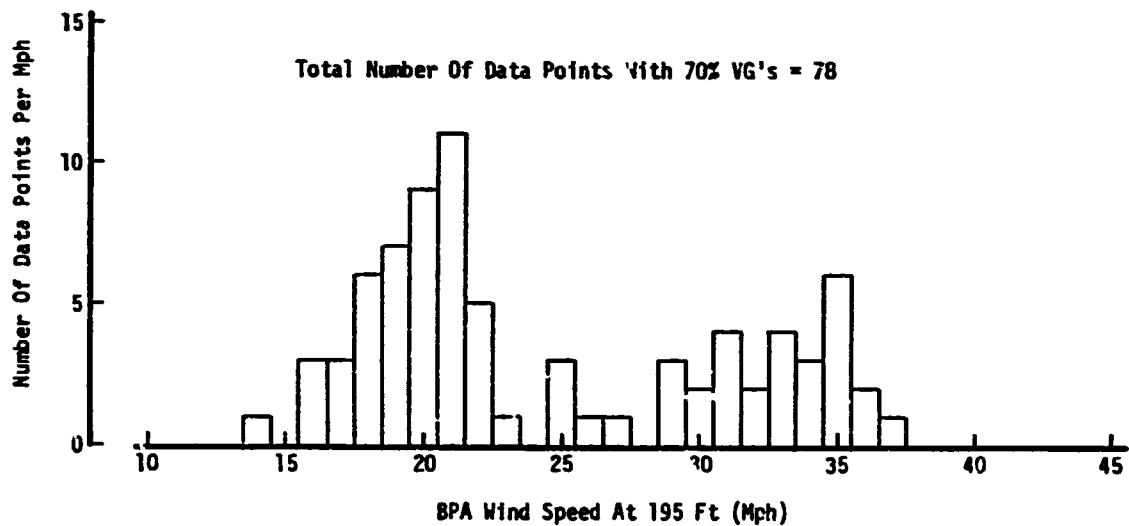


Figure 12. Data Point Distribution With 70% Vortex Generators.

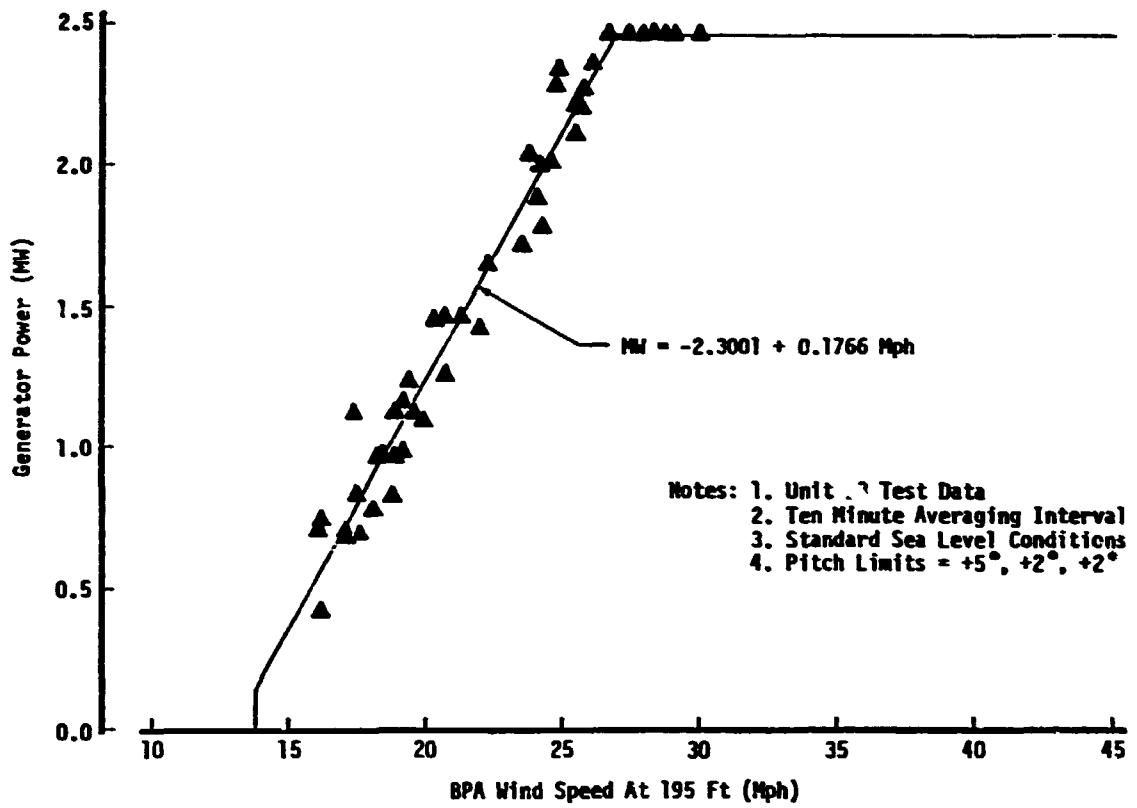


Figure 13. Mod-2 Power Performance With 100% Vortex Generators.

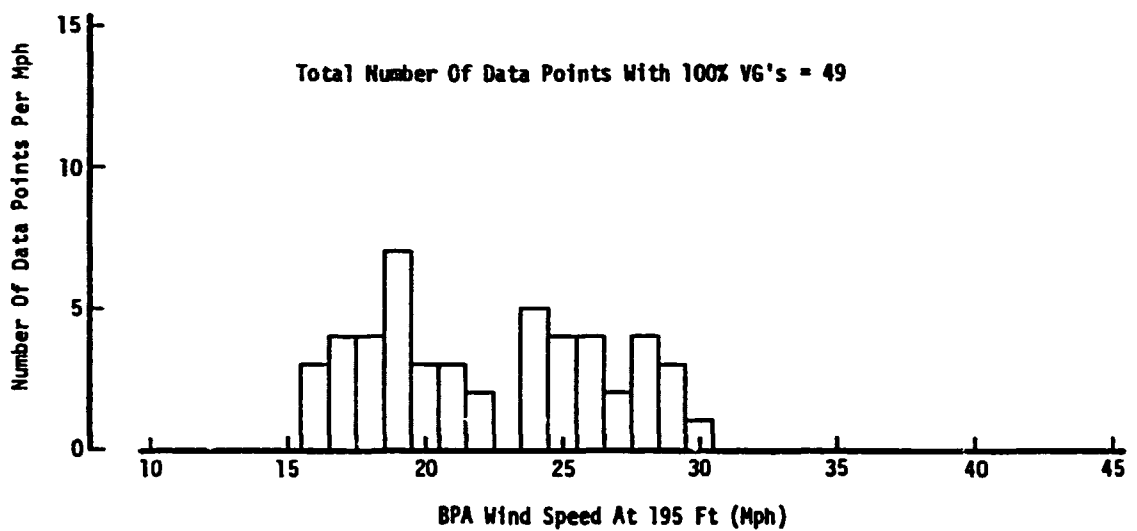


Figure 14. Data Point Distribution With 100% Vortex Generators.

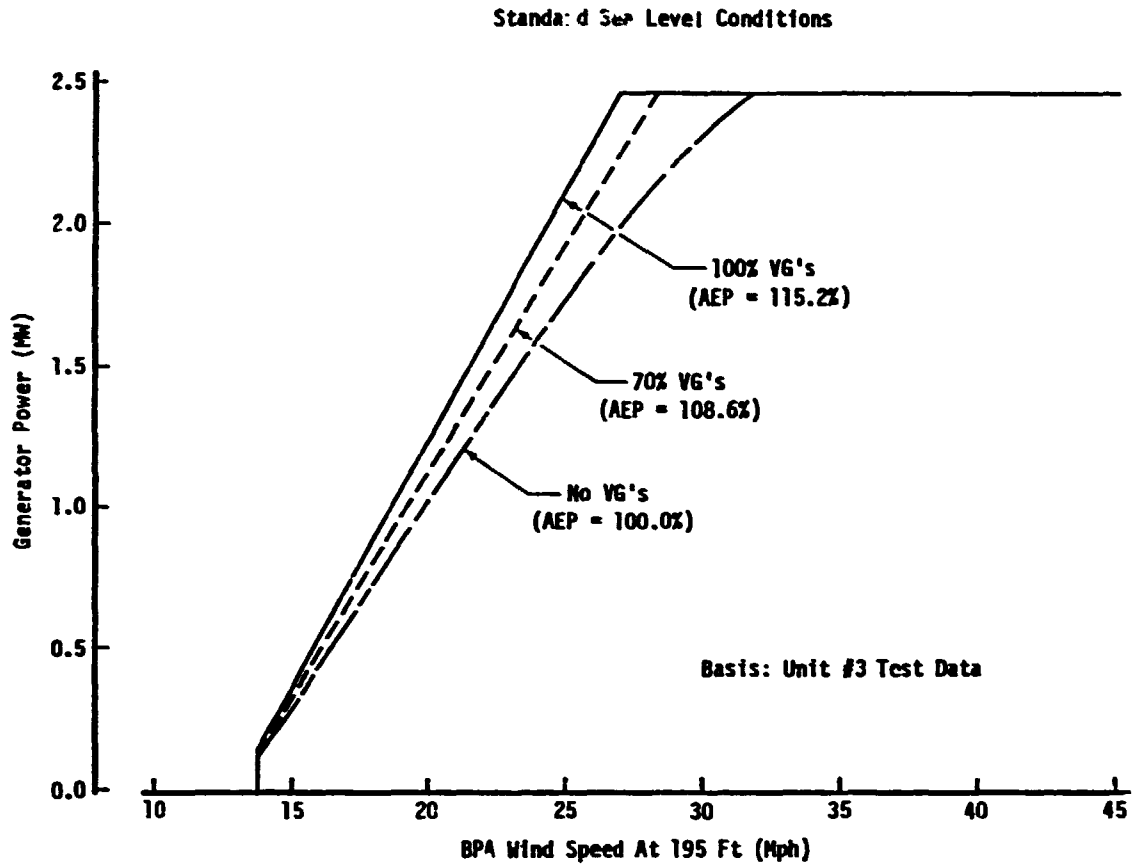


Figure 15. Mod-2 Power Performance Summary.

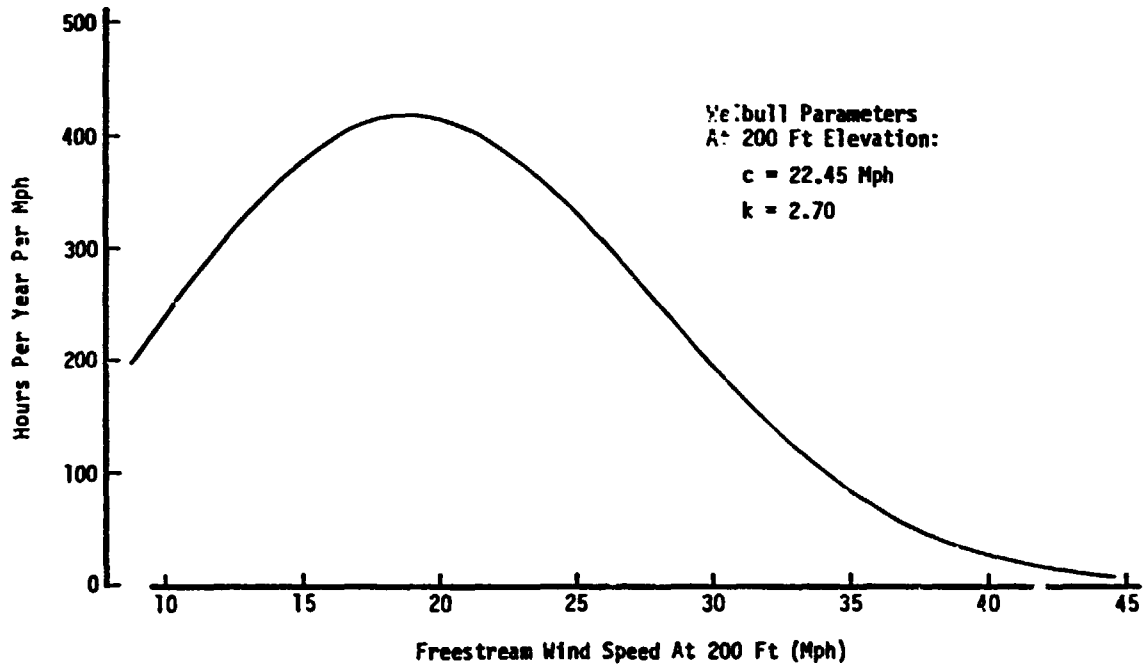


Figure 16. Mod-5B Weibull Wind Speed Distribution At 200 Ft Elevation.

DESIGN OF A REAL-TIME WIND TURBINE SIMULATOR USING A
CUSTOM PARALLEL ARCHITECTURE

N95-27979

John A. Hoffman, Paragon Pacific, Inc.,
El Segundo, California

and

R. Gluck and S. Sridhar, TRW Space and Technology Group,
Redondo Beach, California

ABSTRACT

The design of a new parallel-processing digital simulator is described. The new simulator has been developed specifically for analysis of wind energy systems in real time. The new processor has been named: the Wind Energy System Time-domain simulator, version 3 (WEST-3).

Like previous WEST versions, WEST 3 performs many computations in parallel. The modules in WEST 3 are pure digital processors, however. These digital processors can be programmed individually and operated in concert to achieve real-time simulation of wind turbine systems. Because of this programmability, WEST 3 is very much more flexible and general than its two predecessors.

The design features of WEST-3 are described to show how the system produces high-speed solutions of nonlinear time-domain equations. WEST 3 has two very fast Computational Units (CUs) that use minicomputer technology plus special architectural features that make them many times faster than a microcomputer. These CU units are needed to perform the complex computations associated with the wind turbine rotor system in real time. The parallel architecture of the CU causes several tasks to be done in each cycle, including an IO operation and the combination of a multiply, add, and store.

The WEST 3 simulator can be expanded at any time for additional computational power. This is possible because the computational units are interfaced to each other and to other portions of the simulation using special serial buses. These buses can be "patched" together in essentially any configuration (in a manner very similar to the programming methods used in analog computation) to balance the input/output requirements. CUs can be added in any number to share a given computational load. This flexible bus feature is very different from many other parallel processors which usually have a throughput limit because of rigid bus architecture.

INTRODUCTION

The need for real-time simulation arises during many phases of the development and operation of systems with complex dynamical characteristics. The wind energy system represents such a complex system with many components whose dynamical characteristics couple and interact.

Simulation tools are indicated for such systems, to-

-support the initial design effort: for new systems,

-analyze the performance of system designs under the many variations in environment they will experience during their life cycles,

-evaluate failure modes and effects.

The mathematical models for a high-fidelity wind turbine simulation are very complex, especially if the significant aerodynamic nonlinearities are included. This complexity requires a powerful digital processor if real-time solution speeds are to be attained. Recent experiences with the control of wind energy systems, for example, has again underscored the need for good simulation tools to support the design and evaluations of control systems before these are placed in the actual operational environment.

Most past simulations have been nonreal-time, due largely to the inadequate computational throughputs of available computers in solving the complicated dynamical math models associated with wind energy systems. These slower simulations have provided valuable design support, but have been very limited in their use because of their cost and complexity.

The real time facility is very desirable if the simulation is to produce significant output within reasonable periods of time and at modest cost. Such fast simulations can provide invaluable support for the design process. The real-time capability is essential if the simulator is to be used in a mixed mode, where actual field hardware is validated in a simulation environment before being integrated into the final wind energy system. This validation process can reduce the risk of operating with new control systems, for example, by proving the systems in a simulation environment before risking operation with a real system.

The Wind Energy System Time-domain (WEST) series of simulation systems has been developed over the past few years to meet the needs for powerful real-time simulation tools to support future development of wind systems. The next section of this paper presents a background description of the WEST system developments that have preceded the current development of the WEST-3 article.

A description of the WEST-3 hardware system concept follows the background presentation. The software tools available to support development of programs to run on WEST-3 are then described. Finally, some of the plans for future refinement of WEST-3 are presented.

BACKGROUND

The original WEST unit was derived from a rotorcraft simulation system. The equations were modified for the wind turbine, and additional mathematical models were added for components not found in rotorcraft: the wind, tower, wind turbine controls, power generating equipment and the power train connecting the rotor to the generation system. The WEST-1 article is a hybrid system incorporating both digital and analog hardware. Because of the fast throughput needs, the hardware performing the mathematical calculations is substantially analog, with digital systems in place to act as executive controllers over the analog processes.

The WEST-2 system is also hybrid. It received expanded and refined mathematical models that were added to the baseline models of WEST-1. New features in WEST-2 included statistical math models for the wind and a programmable general-purpose hybrid subsystem for use in designing and evaluating new systems such as wind turbine controls.

The initial effort toward development of WEST-3 was directed toward the addition of specific additional computational facilities. Needed were math models for the rotor gimbal (teetering) system, higher-frequency blade aeroelastic degrees of freedom, expanded numbers of modes for the tower and supports and more refined models for the wind environment. The initial plans called for the refinement of WEST-2 to add these and some other needed improvements.

Before work in updating WEST-2 began, a new technology was emerging from a project supported by TRW Incorporated. This effort was directed toward simulation of large spacecraft structures, and produced an all-digital parallel processing concept promising orders-of-magnitude increases in digital system computational throughput. In the face of this new and promising technology, the decision was made to redirect the WEST-2 refinement effort toward a totally new system, WEST-3.

The generic technology incorporated in WEST-3 has been given the name: "Custom-Architected Parallel Processing System", CAPPS. The CAPPS concept removes many of the objections raised in the past regarding architectures such as the WEST-1 and -2 systems. The primary limitation in these systems is seen in their analog implementations which are "hardwired" and which possess the limitations in significant figure accuracy associated with analog embodiments. The primary advantage of the analog architecture is, of course, its parallelism; this feature gives analog systems significant speed advantages over digital processors.

The CAPPS concept essentially borrows from the analog technology its best feature: its parallelism and therefore its speed. CAPPS also retains the primary advantages of the digital technology: programmability and accuracy. A special

interconnecting concept was developed for CAPPS allowing the computational units (individual digital processors) to be configured into any overall system arrangement tailored to the specific application.

The next section of this paper describes the specific hardware architecture of the CAPPS in detail.

WEST-3 represents the most advanced simulation technology available in the WEST series of systems. The earlier units still have considerable utility; these can provide many of the functions needed in supporting future wind energy system simulation programs. The WEST-3 is a much more general system, however, and therefore has many application areas other than wind system simulation. CAPPS units with hundreds of computational units are envisaged, which promise simulation speeds orders of magnitudes faster than those currently available even with the fastest computers ever constructed.

THE CAPPS ARCHITECTURE

Figure 1 is a logical block diagram of the CAPPS concept. A series of "Computational Units" (CUs) are interfaced with a patch panel system via a series of serial "Input/Output (IO)" data ports. These ports can be configured in any random manner connecting the CUs together in optimum configurations depending on the problem being solved. Each port is represented physically in the system by a single wire.

Each CU is in itself a very high speed digital computer. The current CU design has a 270 nanosecond (about 1/4 microsecond) instruction execution time. A complete series of operations is performed in a single

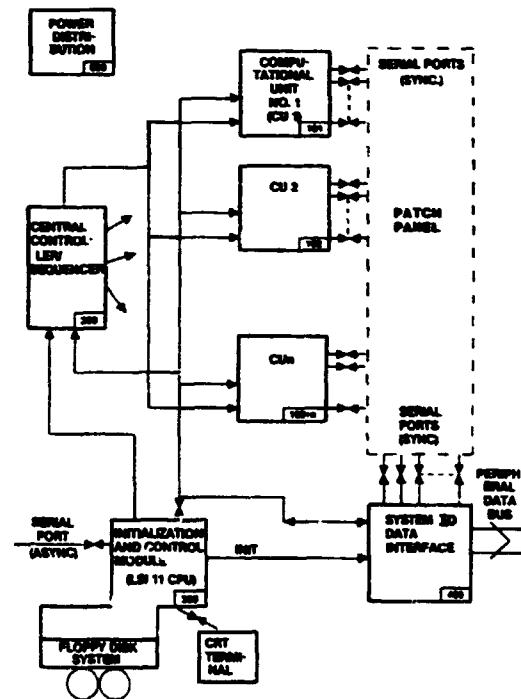


FIGURE 1 CAPPS SYSTEM LOGIC DIAGRAM

instruction, including:

- instruction fetch
- instruction decode
- two operand fetches
- a result store
- a full word multiply of two arbitrary operands
- an arithmetic logic operation on two operands, including add, subtract, shift or boolean operation (OR, AND, Exclusive OR, etc.)
- a full word IO operation (either input or output under software control)

The performance of all of these operations in one instruction cycle makes the design of a CU a very fast processor, even in singular operation.

The IO operation performed during each instruction cycle is automatic and enables as many CUs as desired to be connected together in any random configuration for parallel processing operations. This feature makes the overall CAPPS design truly unique; there are no longer any real limits placed on the time frame or speed associated with the solution of any technical problem. The number of CUs can be increased without bound until adequate computational resources are available to perform the problem at hand.

Figure 2 presents a more detailed definition of the CU architecture. Note that separate instruction and processing memories (RAMs) are incorporated so that a new instruction (and all associated operand addresses) can be fetched and decoded while the last instruction is being executed. Additionally, the CU incorporates a parallel multiplier which is a dedicated arithmetic subsystem that multiplies two operands together in about 100ns. The rest of the Arithmetic Logic Unit (ALU) is also depicted by Figure 2, along with the accumulator and loop back to processing RAM for storing the resulting calculation.

The architecture presented by Figure 2 is often referred to as a "pipelined" system, in that multiple computational stages are connected in a string and perform "added value" computations on a data flow as it moves down the imaginary computational pipeline.

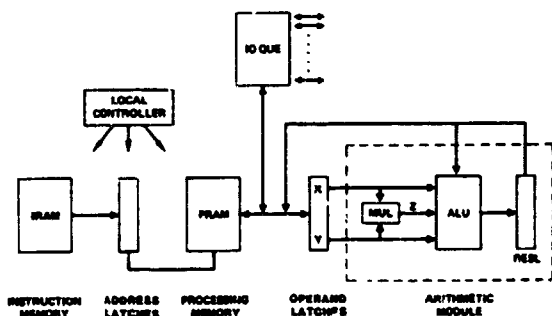


FIGURE 2 COMPUTATIONAL UNIT OF THE CAPPS

Figure 2 also shows the IO Que; this is the subsystem that enables the interfacing of the CUs in any random configuration, a capability that is unique to the CAPPS architecture. The IO Que in the present design incorporates 16 IO ports, although this number could easily be increased or decreased for future specialized designs. The Que has 32 registers, each with a 16-bit capacity. The Que is separated into two "banks" (say bank A and bank B), each with 16 registers. Figure 3 shows the register arrangement in the IO Que design.

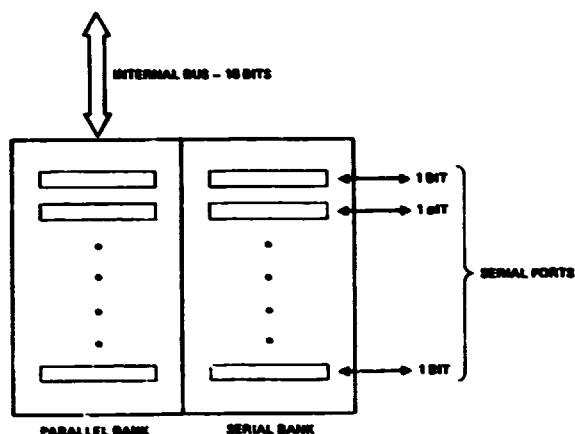


FIGURE 3 IO QUE SYSTEM OF A COMPUTATIONAL UNIT

During operations, one bank is in parallel mode while the other is in serial mode. The parallel bank experiences parallel data operations between its registers and the CU processing memory. A full word is moved into or out from a register in the parallel bank during each instruction execution.

No parallel accesses occur in the serial bank, because this bank performs as a series of 16 shift registers during operations. During each CU instruction cycle, each of the 16 registers shifts in or shifts out one bit from or to the serial port (single wire) connected to it.

The IO Que "toggles" every 16 instructions. At the end of each group of 16 instructions, all 16 registers in the parallel bank have been interfaced to processing RAM (via a procedure often called DMA for Direct Memory Access) and all bits have been shifted into or out from all of the registers in the serial bank. After the set of 16 cycles, the serial bank is switched to parallel mode and the parallel bank is toggled to serial mode. The process continues indefinitely, as long as the CUs are in operation.

Figure 1 shows the "Central Controller/Sequencer" (CCS) subsystem which synchronizes the operations of all the CUs. The entire CAPPS unit has only one clock (in the CCS) which clocks all of the CUs in phase. In this way, all CUs receive or transmit data bits over their serial ports synchronized together. Each unit has an internal strobe that advises when to send or receive bits.

Figure 4 shows an example of how a series of CUs might be connected together to solve a particular problem. Note that there are no constraints on the arrangements of the buses or ports among the CUs; also, of course, there is no limit on the number of CUs that can be connected to share in the execution of a problem.

Because the CAPPS has been designed specifically for the simulation of large numbers of time-domain equations possessing significant nonlinearities, the instructions in the CU have been heavily biased to perform operations consistent with these types of equations. For example, the CU instruction has a three operand format. Two operands are fetched, processed (including multiplied), added or subtracted from an accumulating sum (if desired) and then stored. Most processors have two operand instructions, so more instructions are required to do operations such as sums of products.

In simulations of structural dynamics, controls and many other applications, the equations appear substantially as sums of products. This is the primary form of processing associated with math models in matrix or tensor form. For these types of equations, the three-operand instruction is significantly more powerful than the two-operand systems. Hence, the computational throughput is enhanced accordingly, for these types of problems.

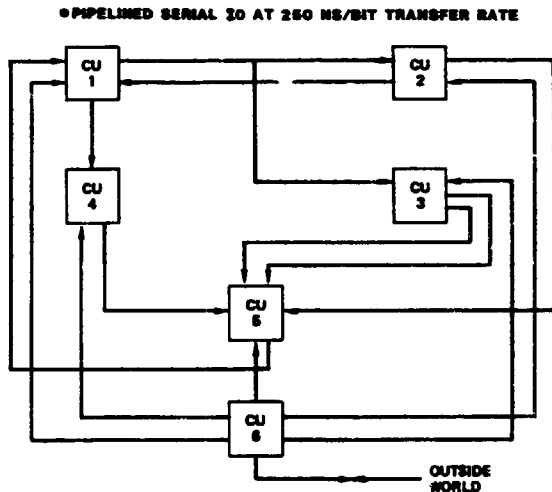


FIGURE 4 TYPICAL SIMULATION CONFIGURATION

In this and other ways, the CAPPS architecture has been biased specifically for the application; the system therefore achieves much faster speeds than processors that are designed for more general applications.

Because the CU architecture is accessible (i.e., it is not built into a chip where it cannot be changed to match special needs), it can always be enhanced in special ways for special problems. For example, additional memory banks may be added for parallel fetches if large tables of data are to be processed. The CUs can be altered at any time to match the needs of the application.

Figure 1 also shows the Initialization and Control Module (ICM). The ICM is responsible for loading data into the CUs at initialization time, usually from the disks also depicted by Figure 1. The ICM loads code, data tables, flags, etc. into the processors. It then clears the program counters in all CUs at once, and then instigates parallel execution.

The WEST-3 ICM incorporates a 16-bit microcomputer system, the Digital Equipment Corporation (DEC) LSI 11. This processor was chosen because of the very large body of proven software that exists for this system, including a reliable Fortran compiler.

Although the ICM performs many sophisticated tasks associated with CU management, it is itself too slow to contribute significantly to the actual calculations made by the system.

The CUs incorporate built-in logic analyzers which allow the ICM to "single step" through programs and read the data on the many internal CU buses. The data is displayed on a terminal or printed to aid programmers in developing codes for CU execution.

At initialization time, the ICM loads IO tables into all of the CUs. These tables tell each CU which parameters are to be communicated over which IO ports. Whether the operations are to be input or output is also specified for each port. Data can be communicated in blocks, so each port can transmit blocks of parametric data of any size. A single port can connect to many CUs and transmit the same blocks to all of them. Additionally, ports can be connected together so that a number of CUs transmit data over them in time-multiplexed fashion. The ports can be shorted without damage, and can drive lines at least 10 feet long.

The port data rate is 4 megabits per port. All ports on a CU communicate with the outside world at 64 megabit rates.

Figure 1 also shows a "System IO Data Interface (SIDI)". The interface will change from unit to unit depending on the needs to connect the CAPPS to other computer devices. Large mainframe computers, disk drives and graphics terminals are candidates for the SIDI peripheral data bus. The SIDI will enable the communications of massive amounts of data in various formats. The SIDI can also incorporate analog interfaces, digital-to-synchro converters or other special devices depending on the application. The SIDI incorporated in WEST-3 is a pure analog interface at this time. It converts internal digital signals to

analog for up to 64 independent channels for display on standard devices such as strip-chart recorders and memory oscilloscopes. The WEST-3 SIDI also has provision for 64 channels of analog input information, so that the simulator can be connected to real wind turbine control hardware, wind measurement signals, etc., to act as a component within an overall simulation environment.

THE WEST-3 DEVELOPMENT PROCESS

WEST-3 was actually fabricated twice during the full development process. The first unit performed its calculations correctly but unreliably. Also, it was unable to attain full-speed operation.

There were a number of problems with this first CAPPS prototype, including:

-Logic Errors in the design, particularly in the controllers (e.g., the CCS and ICM interfaces). There were also some major items needed, however, (such as a special IO counter) that were not included in the first design.

-The system wiring computer program was not directed to place specific modules in specific places in the system when the first prototype was fabricated. Although this program attempts to optimize wire lengths, its built-in algorithms were simply inadequate. The result was excessively long buses which developed "cross-talk" problems (spurious communications between proximate lines in a bus due to electromagnetic and/or capacitive coupling at high frequencies).

-The grounding system which has worked acceptably in the past was inadequate for the high speed CU. It developed large transients which were able to falsely clock and clear registers in the system.

-Excessive delays appeared in the system due to the choice of (relatively slow) "LS" digital logic for implementation of the CUs.

-Unbalanced timing appeared, especially in a number of the control functions, due to excessive logic stages in certain critical signal paths, and due to unequal numbers of logic stages in areas requiring balance.

-Excessive noise on the bus between the ICM and the CUs caused errors in data loaded in the CUs at initialization time and data measured using the built-in logic analyzers.

Because of these many problems, the original WEST-3 was completely reconstructed. Major design changes were made to eliminate the problems observed with the first system. The changes made are summarized below:

• Special logic functions, especially the controllers, were isolated to single boards enabling convenient changing of the logic to correct errors, and more importantly, enabling "fine tuning" of the system timing to get maximum performance.

• Modules in the system were carefully located (the wire list program automatic-placement mode was preempted by designer location choices) to minimize bus lengths. Compromises were made favoring buses with critical timing over those with less stringent requirements.

• A new grounding system was developed and installed incorporating large gold-plated strips and mil spec connectors on the strips and boards to engage the grounds.

• The "LS" logic technology was discarded and new integrated circuits were purchased of the "F" TTL line (for "fast"). The F TTL technology is brand new. It features the low power consumption of LS, and is faster than "S" TTL. Indeed, F logic rivals the very fast ECL technology while enjoying significantly lower energy requirements and involving the much simpler TTL design rules.

• The control logic was carefully tailored and balanced using digital delay networks on critical timing modules. The networks enabled the adjusting of pulse timing in increments of 5 ns, to fine tune the system for maximum speed.

• A special ICM Interface using the latest (low noise) CMOS technology was incorporated to eliminate data communication errors between the ICM and CUs.

• Because of the very high speeds associated with the F logic, control lines in the CUs begin to behave as transmission lines. To avoid large pulses caused by reflected waves on these lines, they were terminated with resistors chosen to match their characteristic impedances. These terminators reduced the noise signatures on the control lines to acceptable levels.

• Much of the CCS pulse-shaping logic was moved from the CCS to local controller modules, thus reducing line lengths for critical timing signals. Now only two twisted-pair lines communicate the clock and a synchronizing signal between the CCS and the CUs.

As mentioned previously, the new system performed reliably and accurately at maximum speed.

THE ICM DEVELOPMENT

A number of difficulties were encountered with the ICM in reducing it to practice. A poorly taped printed circuit board packaging the LSI 11 processor developed crosstalk problems and had to be refabricated. Additionally, problems with the standard software available for the FDP1103 (particularly associated with the disk and system port handlers) required development of new handler programs and a special interrupt controller not originally planned for the ICM system.

These problems have now been solved so that the compatible ICM modules are now available for integration into the WEST 3 article. At the present

time, the ICM resides in an enclosure separate from the WEST-3 computational units.

THE HARDWARE VALIDATION

The WEST-3 design was proven at the maximum anticipated speed of 270ns per instruction cycle. Two programs were developed and executed. The first was loaded with the internal logic analyzer to exercise each instruction in the full CU set and print the results. The results were examined to prove proper static operation of all elements of the system.

A looping function generation program which exercised most instructions in the set was then developed and executed. The generated traces, linear and parabolic sawtooth functions, were output through the analog SIDI system and displayed on a memory oscilloscope. These exercises proved correct dynamic operation of the CU at full speed.

THE TRW DEMONSTRATION

TRW Inc. has developed a demonstration code for the CAPPs unit using a benchmark math model which bears considerable similarity to the types of spacecraft dynamics problems they wish to solve at high speed. The benchmark problem is for a flexible whirling beam undergoing a despinn maneuver in space.

The whirling beam benchmark was run on a single CU first, and then on both CUs in WEST-3, demonstrating full parallel operation. Figure 5 compares the theoretical response of the beam derived by a separate simulation to that achieved with WEST-3. Clearly the WEST-3 solution duplicates the baseline, proving the accuracy of WEST-3 and its ability to solve complicated dynamics problems using CUs wired in parallel.

The next section discusses the performance comparisons made for the CAPPs technology and other commercially available processors.

PERFORMANCE

In the course of searching for an advanced processor or concept to use for future simulations of spacecraft systems, TRW Inc. ran the whirling beam benchmark problem on a number of commercially available advanced processors. Figure 6 presents the results for the whirling beam problem. The performance of WEST-3 is seen to exceed the best of all the available processors with only two CUs. Note that the AD-10 performed the best of the commercially available processors,

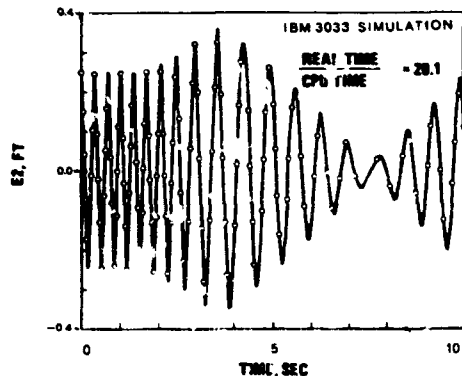


Figure 5 Demonstrator's Simulation of the Whirling Flexible Beam Problem

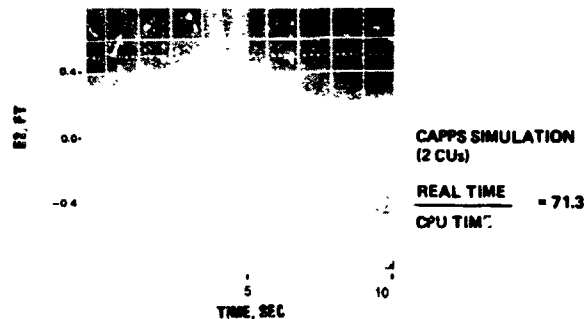
COMPUTER	VENDOR	HOST COMPUTER	REALTIME/ CPU TIME
AD-10	APPLIED DYNAMICS INTL	POP 11/34	58.4
CRAY 1	BOEING COMPUTER SERVICE	-	44.72
IBM 3081	IBM	-	27.78
IBM 3033	IBM	-	20.10
FPS 164	FLOATING POINT SYSTEMS, INC.	VAX 11/780	8.33
HEP H1000	DENELCOR, INC	-	4.08
CAPPs (2 PROCESSORS)			71.30

Figure 6 Simulation Results for the Whirling Flexible Beam Benchmark Problem.

better than the Cray super computer. Figure 7 presents another performance comparison among the latest available computer, a projected CAPPs configuration. Note especially the cost for running a typical spacecraft problem: \$49,000 for a single case (100 seconds of real time in the simulation of a complex orbiter spacecraft) using the TRW IBM computer. The CAPPs cost is projected at only \$23 for the same case, including reasonable acquisition, maintenance and operational costs.

Of course, Figure 7 does compare "service" processors with a CAPPs unit operating as a dedicated processor. An attempt was made to make a valid comparison in this case, however, by assessing all costs needed to run CAPPs in dedicated mode over its estimated life cycle. The weekly useable production time of CAPPs was conservatively estimated at only 18 hours to make the comparison.

Figures 6 and 7 reveal the very powerful promise of the CAPPs technology in general for future simulation needs. Applications other than simulation are, of course, indicated for this concept. Included among these are signal processing, control and automation tasks.



COMPUTER	VENDOR	CPU TIME/ REAL TIME	LENGTH OF RUN (CPU MINS)	COST OF RUN (\$)	MEASURED RESULTS
CRAY 15	BOEING COMPUTER SERVICE	103.2	5.00	5,400	
CYBER 205	CDC	410.0	11.20	22,000	
IBM 3081	IBM	702.3	22.01	20,320	
IBM 3083 (TRM)	IBM	1070.0	45.20	45,000	
CAPPS	ESTIMATED RESULTS FOR 20 CYCLES	10.0	0.30	25	

FIGURE 7 SIMULATION RESULTS FOR THE ORBITER-RMS-PEP
SPACECRAFT BENCH MARK PROBLEM

SOFTWARE SUPPORT

Figure 8 depicts the software modules currently available for supporting the development of code for CAPPS CU. Two general capabilities are available: the system that produces code for actual CU residency, and the simulator.

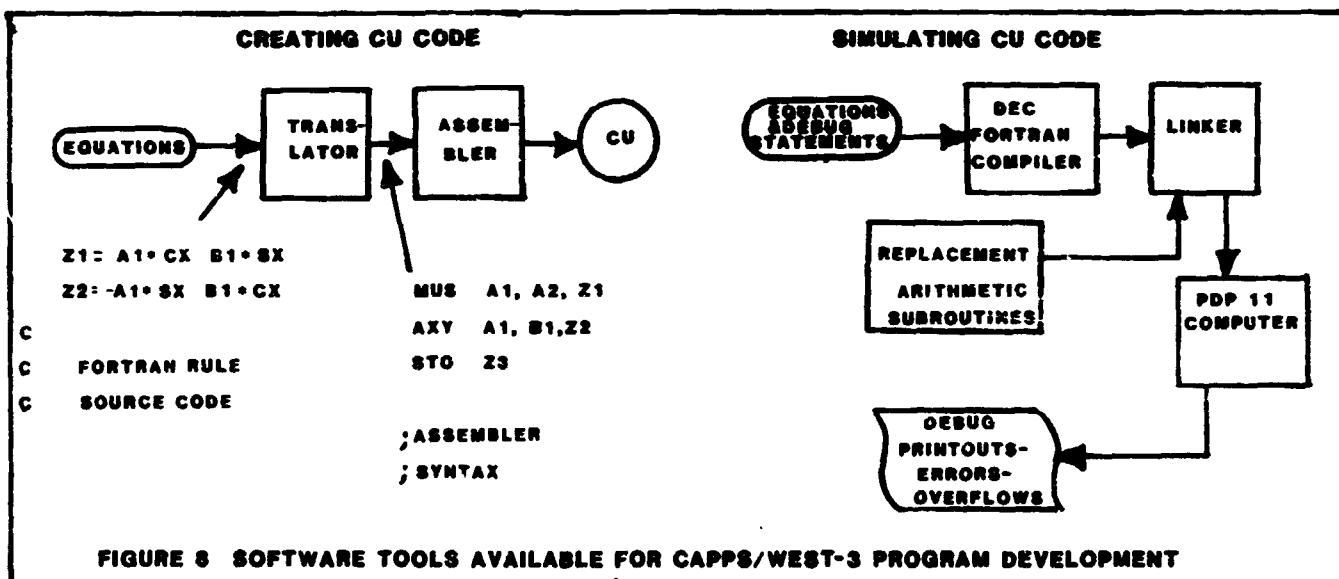
We have developed a translator and assembler for the CU. The translator receives equations prepared in accordance with Fortran rules, and decomposes them into assembler form. Figure 8 shows examples of equations input to the translator, and the assembler syntax that emerges. The assembler then converts the results produced by the translator, and other assembly-language code supplied by the programmer (if any) into machine code. The machine code files are ready for direct loading into the CU for execution.

In addition to these development tools, considerable software has been developed for ICM residency which supports the operation of the WEST-3 and aids in validating programs prepared for the unit. ICM-resident codes load the CUs, provide for "single stepping" the CU through code for debugging purposes, and allow other convenient facilities such as "peeking" and "poking" CU memory to view intermediate computational results and to set up test scenarios used during program validation.

A special simulator program has also been developed, which will execute programs prepared for the CU on a PDP 11 microcomputer. The ICM can execute the simulator. The user can embed debug code (such as debug printouts, breakpoint logic, etc.) into the programs read by the simulator. The simulator will duplicate the actions of the CU and produce intermediate results to aid the programmer in debugging programs developed for the CU.

The tools currently available for CU program development and debugging are not as sophisticated as a system incorporating a macro assembler, linker and Fortran compiler, but they do provide very significant services which approach the convenience of a full system. It is much simpler to develop CU code with the currently available tools than it is to develop programs in pure assembly language.

The next section discusses current limitations and future plans now being implemented for the CAPPS technology; continuing development of software tools is slated to be a major element in these future endeavors.



C-2

LIMITATIONS AND FUTURE PLANS

The current CAPPS CU architecture incorporates a 16 bit data bus and integer arithmetic. Equations prepared for the CU must therefore be scaled and cast as integer expressions. Additionally, the system does not currently have standard software modules available for it, the most pressingly needed being a Fortran compiler, linker and full macro assembler.

These limitations are not precluding the development of a complete mathematical model for the wind energy system application of CAPPS in the WEST-3 embodiment, but they do make the programming task more specialized and time consuming. Accordingly, a number of major developments are currently underway which will eliminate many of the limitations in the present WEST-3 system. More specifically, the following are now under development:

- A 32-bit hardware floating point processor that will operate at the same speed as the current CAPPS instruction cycle (270 ns per instruction).

- A hardware translator that will receive and execute code prepared initially in Fortran, macro assembly, or many other forms (Pascal, Basic, etc.). A translator will reside in each CU and act as an executive host processor. It will load directives for the CU so that the CU will perform the heavy processing tasks using library routines written for efficient CU operations. The resident translator will make the CU "transparent" to the user. The operating system planned for this new concept is the familiar RT-11 system offered by Digital Equipment Corporation, which has been available for years as a reliable and mature system for use in the PDP 11 line of minicomputers.

- More refined ICM resident software modules for use particularly in debugging programs.

- A winchester disk drive to augment the floppy disks now used with the ICM.

These and other refinements should be available for the CAPPS technology within the next year.

OPTIONAL ARCHITECTURES

Architectures other than the pure CAPPS arrangement of Figure 1 have been designed for the WEST-3 application. Figure 9 is the original configuration proposed for WEST-3. This system incorporates CAPPS subsystems, including the two devices called "Fast Processors" in Figure 1. These are essentially computational units that have been interfaced to an array of microcomputers to share the entire WEST-3 computational load.

The microcomputers are very slow compared to the CAPPS computational units, but they do have mature software support. In the original WEST-3 concept, the microcomputers were to execute math models associated with relatively slow elements of the system such as

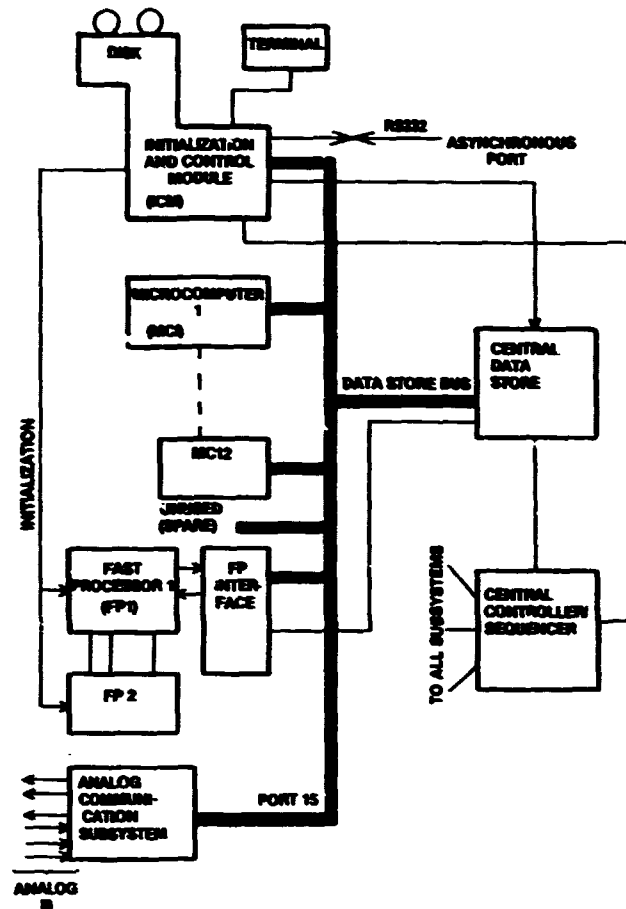


Figure 9 Optional WEST-3 Design

the tower, control system and wind models. The fast processors were to solve the complex equations associated with the rotor system. A "central data store" or shared memory is incorporated in the design to facilitate communication among the microcomputers, the ICM and the fast processors.

Since the inception of the original WEST-3 architecture of Figure 9, considerable effort has been expended toward developing software tools for programming the computational units. The availability of the translator and assembler modules discussed above have made programming of the computational units much more convenient and efficient than if pure assembly language programming were to be used. The desirability of the array of microcomputers has therefore diminished.

Figures 1 and 9 represent blends of processors that can be defined for an application depending on the specific characteristics of the equations being solved. The present thinking prefers larger numbers of computational units and fewer of the slower microcomputers for the WEST-3 application.

CLOSURE

The WEST-3 system has demonstrated the technical feasibility of the overall CAPPS concept. It affords the utilization of processors in massively parallel configurations, with a flexible bus architecture that can be tailored for the application. Since communication problems among individual processors has been a major limitation on parallel processors of the past, the CAPPS promises to offer significant increases in computational throughput largely because of its flexible configurational means.

A detailed mathematical model for the total wind energy system has been developed for WEST-3, and is currently being validated on the system. The models derive from those of WEST-1 and -2, but have been reformulated for digital solution. Additionally, significant additional modelling fidelity has been added, including a rotor gimbal, two more blade aeroelastic modes (for a total of three modes) and more generality in the control system, electrical power system and supporting structure models.

ACKNOWLEDGMENT

Many individuals have contributed to the development of the advanced simulation technology incorporated in WEST-3. The authors wish to express their appreciation to these people, and particularly, to Mr. Dan Weisz and Mr. Milton D. Campbell for their dedicated efforts in supporting this project.

WEST-3 has been developed under funding from the NASA Lewis Research Center, Cleveland Ohio, and the United States Department of Energy, Washington, D.C. The authors also wish to thank Mr. David Janetzke and Mr. Harold Neustadter of NASA Lewis for their considerable support and encouragement throughout the WEST-3 development program.

A NASTRAN-BASED COMPUTER PROGRAM FOR STRUCTURAL
DYNAMIC ANALYSIS OF HORIZONTAL AXIS WIND TURBINES*

N95-27980

Don W. Lobitz

Sandia National Laboratories
Albuquerque, New Mexico 87185

ABSTRACT

This paper describes a computer program developed for structural dynamic analysis of horizontal axis wind turbines (HAWTs). It is based on the finite element method through its reliance on NASTRAN for the development of mass, stiffness, and damping matrices of the tower and rotor, which are treated in NASTRAN as separate structures. The tower is modeled in a stationary frame and the rotor in one rotating at a constant angular velocity. The two structures are subsequently joined together (external to NASTRAN) using a time-dependent transformation consistent with the hub configuration. Aerodynamic loads are computed with an established flow model based on strip theory. Aeroelastic effects are included by incorporating the local velocity and twisting deformation of the blade in the load computation. The turbulent nature of the wind, both in space and time, is modeled by adding in stochastic wind increments. The resulting equations of motion are solved in the time domain using the implicit Newmark-Beta integrator. Preliminary comparisons with data from the Boeing/NASA MOD2 HAWT indicate that the code is capable of accurately and efficiently predicting the response of HAWTs driven by turbulent winds.

INTRODUCTION

Throughout the history of the DOE-sponsored horizontal axis wind turbine (HAWT) program efforts have been undertaken to develop tools for the structural dynamic analysis of HAWTs. A number of capabilities have emerged, including natural mode and frequency calculations with NASTRAN, rigid-rotor aerodynamic load codes, dynamic flexible-rotor codes fixed in space at the hub, and full dynamic models of the rotor turning on the tower.

The NASTRAN mode and frequency analysis is capable of tracking some of the frequencies as they increase with increasing rotor speed due to centrifugal stiffening but is not adequate for those which are sensitive to other rotating coordinate system effects.

The rigid-rotor codes require the rigid body motion of the rotor as input and then compute the aerodynamic loads along a blade as it moves through one revolution for steady atmospheric conditions. The calculated loads are integrated to obtain static section loads and moments at any station. Even with this simple model, if a reasonable rigid body motion is prescribed, mean loads are predicted with good accuracy. However, the vibratory flapwise loads are generally, substantially underpredicted. An example of a rigid-rotor aerodynamic load code is the PROP software [Ref. 1], developed at Oregon State University.

The flexible-rotor codes use aerodynamic load models which are similar to those used in the rigid-rotor case, but motion of the rotor relative to the hub is permitted. Thus the motion of the rotor as well as the applied loads are computed. Through the interdependence of rotor motions and the aerodynamic loads, this software accounts for aeroelastic effects. With these codes, as before, the mean response of the rotor is accurately predicted, but the vibratory response is underpredicted. Probably the most widely used of these codes is MOSTAB [Ref. 2], which is a derivative of a code developed by Paragon Pacific for the dynamic analysis of helicopters.

The full dynamic models add the interactions between the tower and the rotor to the flexible-rotor software described above. Within the confines of small displacement theory, the rotor is modeled in a rotating frame, the tower in a fixed one, and the two structures are connected using time-dependent constraints or forces. Generally a transient integration technique is used to solve the resulting equations of motion. Even with the increased level of sophistication, these codes still underpredict the vibratory response. Two examples are the MOSTAS code [Ref. 3], which is from the same family as MOSTAB, and DYLOSAT [Ref. 4], a proprietary code developed by the Boeing Aerospace Company.

The software described here, named HAWTDYN, is of the full dynamic model class. Two features which set it apart from other codes in this class are its use of NASTRAN for mass, stiffness and damping matrices, and output processing, and the inclusion of stochastic wind increments in the aerodynamic load computation. Time-dependent constraints, which produces time-varying coefficients in the equations of motion, are used to connect the rotor to the tower. Aerodynamic loads are computed using interference factors predicted by the PROP code [Ref. 1] for a pre-established rotor orientation. Aeroelastic effects are included by incorporating the local velocity and twisting deformation of the blade in the load computation. The stochastic wind increments are computed by the method outlined in Ref. 5. The resulting equations of motion are solved in the time domain using the implicit Newmark-Beta integrator.

Results are presented for a model of the MOD2 wind turbine which was designed and fabricated by the Boeing Aerospace Company (BAC). In addition to a fan-plot, which shows how the natural frequencies of the turbine vary with operating speed, structural load time series have been obtained for two stochastic winds, one with a mean of 20 mph, and the other 27 mph. These time series are reduced and compared with field measurements. In order to determine the effect of the tower on the structural response, the model was modified to fix the rotor hub. With this alteration, HAWTDYN is consistent with the codes of the flexible-rotor class except for its inclusion of stochastic

*This work performed at Sandia National Laboratories supported by the U. S. Department of Energy under Contract Number DE-AC04-76D00789.

wind effects. Results are also presented for this model.

The following sections contain a description of the mathematical model upon which HAWTDYN is based, the details of the MOD2 finite element model, presentation and discussion of results, and concluding remarks.

HAWTDYN MATHEMATICAL MODEL

Due to its power and versatility in modeling structures, the finite element method has been chosen as a framework for the derivation of the equations of motion for the HAWT. For this derivation, two coordinate systems are employed in order to represent motions throughout the structure as small relative to the appropriate frame. Thus the tower is modeled in a fixed frame and the rotor in one which rotates at the operational speed of the turbine about an axis which is fixed in space. The origins of both coordinate systems are fixed at the initial hub location. For the latter case, rotating frame effects, such as Coriolis and centrifugal forces, must be included. Considering the tower and rotor as separate structures, the equations of motion for each are represented below:

$$\begin{aligned} M_T \ddot{U}_T + C_T \dot{U}_T + K_T U_T &= F_T, \quad (1) \\ M_R \ddot{U}_R + (C_R + C_\Omega) \dot{U}_R + (K_R - S_\Omega) U_R &= F_c + F_g + F_a. \end{aligned}$$

Here the subscripts T and R refer to the tower and rotor respectively. The quantities, C_Ω and S_Ω , which derive from rotating coordinate system effects, are the Coriolis and softening matrices. The softening matrix accounts for changes in the centrifugal force that result from the structural deformations. These matrices are developed in detail in Ref. 6. On the right hand sides of the equations are the applied forces, with the subscripts c, g and a referring to the centrifugal, gravitational and aerodynamic forces, respectively.

These equations can be combined into one matrix equation as follows:

$$\begin{bmatrix} M_T & 0 \\ 0 & M_R \end{bmatrix} \begin{bmatrix} \dot{U}_T \\ \dot{U}_R \end{bmatrix} + \begin{bmatrix} C_T & 0 \\ 0 & C_R + C_\Omega \end{bmatrix} \begin{bmatrix} \dot{U}_T \\ \dot{U}_R \end{bmatrix} + \begin{bmatrix} K_T & 0 \\ 0 & K_R - S_\Omega \end{bmatrix} \begin{bmatrix} U_T \\ U_R \end{bmatrix} = \begin{bmatrix} F_T \\ F_c + F_g + F_a \end{bmatrix} \quad (2)$$

Denoting the time-dependent constraint relation which connects the rotor to the tower, consistent with the hub configuration, as Λ , the final set of displacements, velocities and accelerations, U , \dot{U} and \ddot{U} , can be derived from,

$$\begin{aligned} \begin{bmatrix} U_T \\ U_R \end{bmatrix} &= \Lambda U, \quad \begin{bmatrix} \dot{U}_T \\ \dot{U}_R \end{bmatrix} = \dot{\Lambda} U + \Lambda \dot{U}, \\ \begin{bmatrix} \ddot{U}_T \\ \ddot{U}_R \end{bmatrix} &= \ddot{\Lambda} U + 2\dot{\Lambda} \dot{U} + \Lambda \ddot{U}. \end{aligned} \quad (3)$$

If the matrices of Eqn. (2) are renamed \bar{M} , \bar{C} and \bar{K} , and the force vector, \bar{F} , the following equation is obtained from the combination of Eqns. (2) and (3), and premultiplication by Λ^T :

$$\begin{aligned} (\Lambda^T \bar{M} \Lambda) \ddot{U} + (\Lambda^T \bar{C} \Lambda + 2\Lambda^T \dot{\bar{M}} \Lambda) \dot{U} \\ + (\Lambda^T \bar{K} \Lambda + \Lambda^T \dot{\bar{M}} \dot{\Lambda} + \Lambda^T \dot{\bar{C}} \Lambda) U = \Lambda^T \bar{F}. \end{aligned} \quad (4)$$

The transformation matrix, Λ , only modifies terms in the matrices associated with tower or rotor connection nodes, and, by judicious selection of the physical modeling at these points, certain terms in Eqn. (4) can be simplified. For example, if the tower connection node possesses only lumped translational mass, the terms, $\Lambda^T \bar{M} \Lambda$, $\Lambda^T \dot{\bar{M}} \Lambda$, and $\Lambda^T \dot{\bar{C}} \Lambda$, are rendered independent of time and need only be computed once. Moreover, if the tower connection node is not directly involved in any damping, the term $\Lambda^T \dot{\bar{C}} \Lambda$ also becomes time-independent and $\Lambda^T \dot{\bar{C}} \Lambda$ vanishes. The remaining quantity, $\Lambda^T \bar{K} \Lambda$, will normally be a function of time and must be recomputed at each time step.

Replacing the coefficient matrices of Eqn. (4) by M , C and K , the system equations of motion are obtained and presented below:

$$M \ddot{U} + C \dot{U} + K U = F. \quad (5)$$

Eqn (5) is complicated by the fact that centrifugal stiffening, which arises due to the spanwise stretching of the blade under the action of the centrifugal loads, must be taken into account. This stretching causes the stiffness to be a function of the deformation [Ref. 6], necessitating more complex solution procedures. To avoid this complexity, the stiffness matrix, K_c , in Eqn. (1) is modified to be commensurate with the quasi-static displacement field associated with the centrifugal loads. This is accomplished through iterative solution of the following equation:

$$\left[K_R(U_R) \right] \begin{bmatrix} U_R \end{bmatrix} = \begin{bmatrix} S_\Omega \end{bmatrix} \begin{bmatrix} U_R \end{bmatrix} + \begin{bmatrix} F_c \end{bmatrix}. \quad (6)$$

The resulting approximate or mean stiffness matrix represents the rotor stiffness for the operating speed corresponding to the centrifugal loads in Eqn. (6). Thus solutions of Eqn. (5) must be interpreted as motions about a prestressed state.

The aerodynamic forces of Eqn. (1) are computed, taking into account blade velocities and deformations relative to the rotating coordinate system. This provides for the representation of aerodynamic stiffness and damping in the equations of motion. In order to compute these forces, a local blade coordinate system is defined using instantaneous unit chord and span vectors, e_c and e_s , which account for initial blade position and prewist, and the local blade deformations. The positive senses are from leading to trailing edge for chord, and from hub to tip for the span. The third instantaneous unit direction is identified as the flap vector, e_f , and defined by the cross product of the chord and span vectors. The

relative wind velocity vector, W_r , is given by the following expression.

$$W_r = (1-\epsilon) W_m + W_{si} - \left[\dot{U}_R + \Omega \times (X_R + U_R) \right]. \quad (7)$$

Here, W_m is the mean axial wind, which can include variations due to wind shear and tower shadow; ϵ is the velocity reduction factor corresponding to a trim solution for the mean wind; W_{si} is the axial stochastic wind increment computed using the methods described in Ref. 5; Ω is the operating speed of the turbine; and, X_R is the initial local position vector. The direction of lift, e_L , is obtained by taking the cross product of W_r and e_c , and then adjusting the sign of the resulting vector so that its dot product with e_c is negative. The direction of drag, e_D , is subsequently computed to be perpendicular to the direction of lift and e_c , this time adjusting the sign so that the dot product of the resulting vector with e_c is positive. With these directions defined, the angle of attack, and the lift and drag forces per unit length are given by.

$$\begin{aligned} \tan \alpha &= - \frac{e_D \cdot e_f}{e_D \cdot e_c} \\ L &= \frac{1}{2} \rho a W_n^2 C_L(\alpha) e_L \\ D &= \frac{1}{2} \rho a W_n^2 C_D(\alpha) e_D \end{aligned} \quad (8)$$

In Eqn. (8), ρ is the air density, a is the length of the chord and C_L and C_D are the coefficients of lift and drag respectively. The quantity, W_n , is the magnitude of the component of the relative wind vector normal to the span vector, computed as follows:

$$W_n = |W_r \times e_s|. \quad (9)$$

The lift and drag forces are combined with the gravity forces to obtain the total force vector per unit length. This vector is numerically integrated along the length of each blade element, using a Galerkin formulation to obtain concentrated nodal forces.

Time-domain solutions to Eqn (5) are obtained numerically using an implicit integration technique. For equations with constant coefficients implicit methods are unconditionally stable, which means that the size of the time step is only limited by the desired frequency resolution. The option for larger time steps provides a means to analyze structural response to stochastic loading, which requires long-time solutions. The equations of motion for the HAWT contain time-dependent coefficients, and therefore, unconditional stability is not guaranteed. However, certain "ad hoc" procedures can be implemented which improve the stability and permit reasonably large time steps.

The first implicit scheme implemented, the Hilber-Hughes algorithm [Ref 7], exhibited unstable growth in the high-frequency response, even though it is

advertised to numerically dampen these modes. This may have been caused by the fact that the algorithm is not entirely consistent with the Newton method of equation solution. Experience has indicated that efforts to make the solution procedure conform to this method usually produce a stabilizing effect. For example, the stability of the response was significantly improved by changing the evaluation of the damping term in Eqn (5) from the beginning to the end of the time step. Because of its conformity to the Newton method, the Newmark-Beta implicit integration scheme [Ref. 8] was the final choice for the solution procedure.

Eqn. (5), discretized in time according to this algorithm, is presented below:

$$\begin{aligned} M \ddot{U}_{t+\Delta t} + C \dot{U}_{t+\Delta t} + K_{t+\Delta t} U_{t+\Delta t} &= F_{t+\Delta t}, \\ U_{t+\Delta t} &= U_t + \Delta t \dot{U}_t + \Delta t^2 \left[\left(\frac{1-\beta}{2} \right) \ddot{U}_t + \beta \ddot{U}_{t+\Delta t} \right], \\ \dot{U}_{t+\Delta t} &= \dot{U}_t + \Delta t \left[(1-\gamma) \ddot{U}_t + \gamma \ddot{U}_{t+\Delta t} \right], \\ \beta &= .3025, \quad \gamma = .6. \end{aligned} \quad (10)$$

The final form of the equation is obtained by making the substitutions indicated in Eqn. (10) and rearranging so that only terms associated with $\ddot{U}_{t+\Delta t}$ appear on the left hand side, as follows.

$$\begin{aligned} \left[M + \Delta t \gamma C + \Delta t^2 \beta K_{t+\Delta t} \right] \ddot{U}_{t+\Delta t} \\ = \left[-\Delta t (1-\gamma) C - \Delta t^2 \left(\frac{1-\beta}{2} \right) K_{t+\Delta t} \right] \ddot{U}_t \\ + \left[-C - \Delta t K_{t+\Delta t} \right] \dot{U}_t \\ + \left[K_{t+\Delta t} \right] U_t + F_{t+\Delta t}. \end{aligned} \quad (11)$$

Even with the provisions described above to stabilize the solution procedures, a small amount of growth still occurs for some of the HAWT models that have been created. Although the origin of this growth, be it physical or numerical, has not yet been determined, it can be eliminated by the incorporation of structural damping (of the order of 5% of critical).

In order to avoid duplication of such things as development of finite element matrices, solution procedures, and input and output processing, the MacNeal-Swendler version of NASTRAN was selected as the basis for this development. This particular code was chosen for several reasons. First, NASTRAN is a general purpose finite element code which contains the necessary input options required for producing reasonably accurate models of HAWTs. Solution procedures are available which provide for inclusion of centrifugal stiffening effects in the rotor. The DMAP programming feature of NASTRAN, which allows the user to modify the code without dealing with the FORTRAN coding, proved to be very helpful even though it was not heavily used. The direct matrix input (DMI) option, by which matrices can be modified through the input data deck was also invaluable. And finally, because of NASTRAN's widespread use, familiarity with its BULK DATA input lends a degree of user-friendliness to the present software.

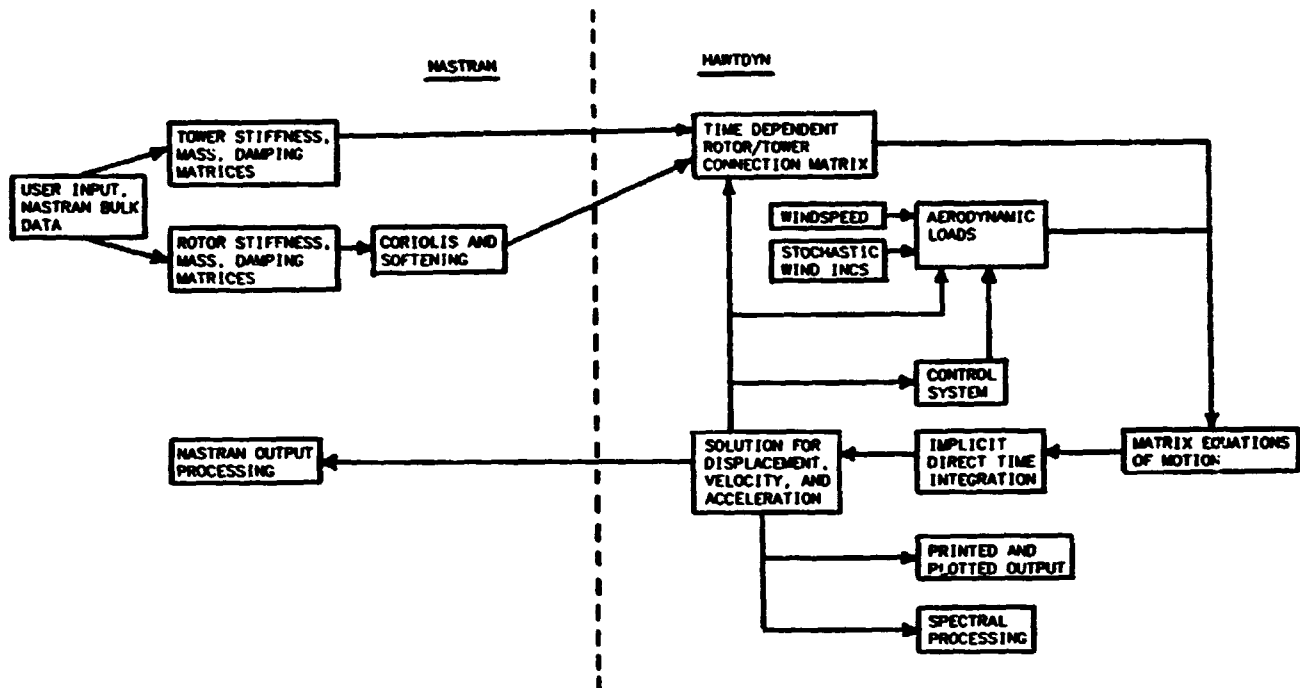


Figure 1. HAWTDYN dynamic analysis method.

The relationships between NASTRAN and HAWTDYN are displayed in the block diagram of Fig. 1. The tower mass, stiffness and damping matrices are developed in NASTRAN relative to a fixed coordinate system. The rotor is modeled in a rotating frame with the stiffness matrix reflecting the effects of centrifugal stiffening. The Coriolis and softening matrices are computed external to NASTRAN and included through the DMI input option. These two sets of matrices are then supplied to HAWTDYN where they are tied together with a rotor/tower connection matrix, which models the particular hub configuration. Aerodynamic loads are obtained using the mean windspeed, the stochastic wind increments, and the local blade motion. Although an active control system has not yet been incorporated into the HAWTDYN software, it would also provide an input to the aerodynamic load computation. The resulting equations of motion are solved using implicit direct time integration. Computed displacement time histories can be printed, plotted, and, in some cases, spectrally analyzed. The NASTRAN code is reentered for computation of structural loads and stresses.

The PROP code [Ref. 1] has been incorporated into the HAWTDYN software to supply the local free stream wind, interference factors associated with a prescribed orientation of the rotor, and lift and drag coefficients. This relationship is shown in Fig. 2, along with details of the load computation. After the relative wind is obtained using the free stream wind modified by the interference factor, the stochastic wind increments, and the local blade motion, the angle of attack is computed and transmitted to PROP for the determination of the coefficients of lift and drag.

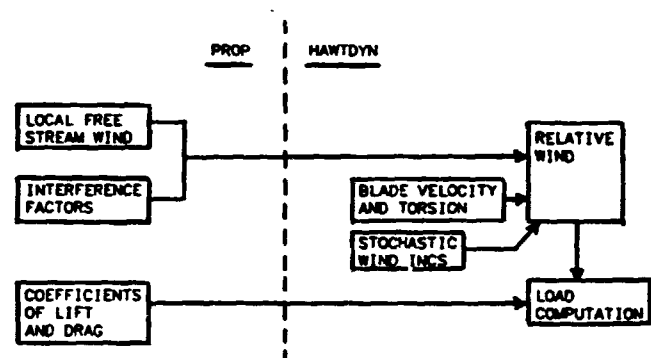


Figure 2. Aerodynamic load computation in HAWTDYN.

DESCRIPTION OF THE MOD2 FINITE ELEMENT MODEL

For an initial test of the performance of HAWTDYN a finite element model of the MOD2 was created. The MOD2 was chosen because of the general interest in that turbine and the availability of experimental data. The model was actually developed using a NASTRAN BULK DATA deck assembled at the Boeing Aerospace Company (BAC) in June of 1981. The BAC model consists of 15 nodes per blade and 14 tower nodes. For HAWTDYN this model was reduced using the NASTRAN ASET option to 5 tower nodes and 5 nodes per blade. This reduced model is shown in Fig. 3. Blade stations 370 and 1164 are indicated in this figure for future reference.

Table 1. Comparison of Predicted and Measured Frequencies for the Parked MOD2 Rotor

Mode	Freq (/rev) Meas.	Freq (/rev) BAC Model	Freq (/rev) HAWTDYN	% Error
Drive Train	.45	.42	.42	8.6
Tower Fore/Aft	1.23	1.23	1.24	.8
Tower Lateral	1.28	1.25	1.25	2.3
Symmetric Flap	3.30	3.77	3.76	13.9
Symmetric Chord	6.17	6.79	6.69	8.4
Antisym Flap	6.55	7.03	7.03	7.3
Nacelle Pitch	8.23	8.71	8.74	6.2
2nd sym Flap	9.60	10.01	10.01	4.3

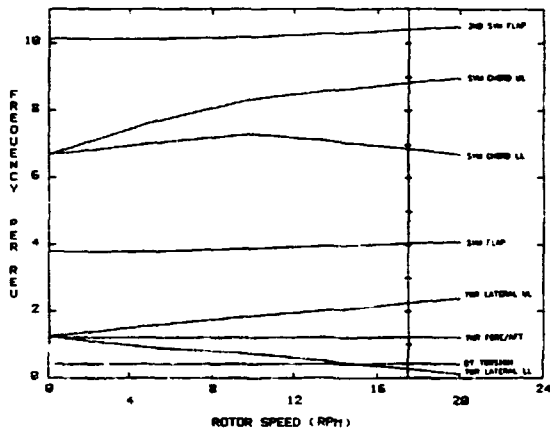


Figure 4 Predicted fanplot for the MOD2

PRESENTATION AND DISCUSSION OF RESULTS

In this section to some qualitative observations are discussed, and the predicted response of the MOD2 is presented for windspeeds of 20 and 27 mph. In both cases a turbulent wind increment history is included. For purposes of comparison, results are shown for steady winds at the same windspeeds. Computations are also presented for a configuration of the MOD2 where the hub is fixed in space.

Two qualitative aspects of the results are mentioned here to promote confidence in the HAWTDYN software. First, the aerodynamic damping in the fore-aft direction is definitely present in the solutions and seems to be on the order of 5% of critical. And second,

HAWTDYN seems to be correctly predicting the response of the rotor to wind shear in that computed displacements indicate a slight turning of the rotor out of the wind about a vertical axis. This motion produces a more uniform relative velocity vector with respect to the angular position of the rotor, and tends to neutralize the effect of wind shear. These results are qualitatively consistent with observed behavior.

For the forced response of the turbine, gravity and wind loading are applied. The wind loads correspond to a wind shear resulting from a surface roughness factor of .25, a value consistent with the MOD2 site at Goodnoe Hills. In addition, the turbulence intensity is set at 20%, also representative of the site. Tower shadow for a width of 15 feet is included through an option in the PROP code. The steady component of the relative wind velocity vector is computed at each Gaussian integration point along the blade (two integration points per element). The stochastic increments are calculated at three stations per blade (stations 874, 1329, and 1855) and linearly interpolated or extrapolated to the Gauss points. Fig. 5 shows the stochastic wind increments for all six stations on the rotor, corresponding to the mean windspeed of 27 mph. At any particular time the width of this band of curves is an indication of the variability of the wind across the rotor.

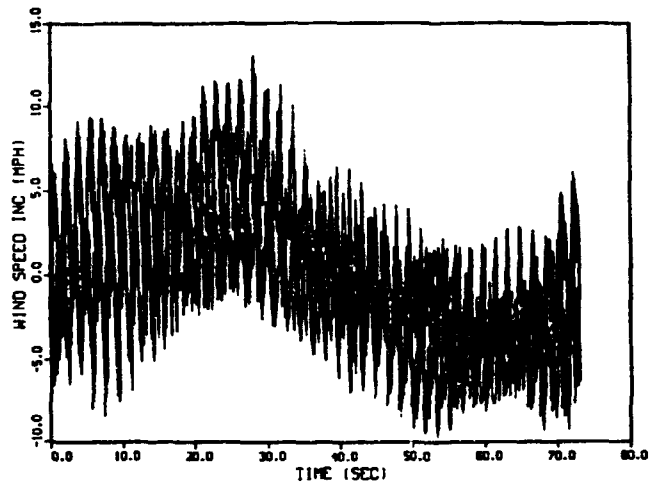


Figure 5. Stochastic wind increments for a 27 mph mean wind at the six MOD2 rotor stations, three per blade

The predicted edgewise response to this wind at station 370 is presented in Fig. 6. For the first three revolutions on the curve, only gravity and steady wind loads are acting. Thus these three cycles represent the steady response of the turbine. Over the fourth cycle the stochastic wind increments are gradually included. The total response of the rotor to all loadings is shown from revolution 5 through 23. For all sections of the curve the response is predominately 1/rev with only slight variations in amplitude. This indicates that the edgewise moments are dominated by the gravity loading, and are not significantly affected by the turbulence in the wind.

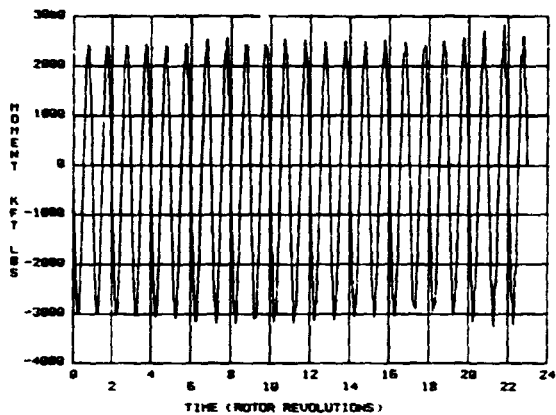


Figure 6. Predicted chordwise bending moment for a turbulent wind with a 27 mph mean at station 370 of the MOD2 blade.

The flapwise response at station 370 is shown in Fig. 7. Again the first three cycles represent the steady response and cycles 5 through 23 display the total response. In this case the differences between the steady and total responses are quite dramatic. In addition to a roughly four-fold increase in the cyclic amplitude, the frequency content changes from 2/rev to predominately 4/rev. Thus, for the flapwise moments, the stochastic wind loading dominates the response, in contrast to the edgewise case.

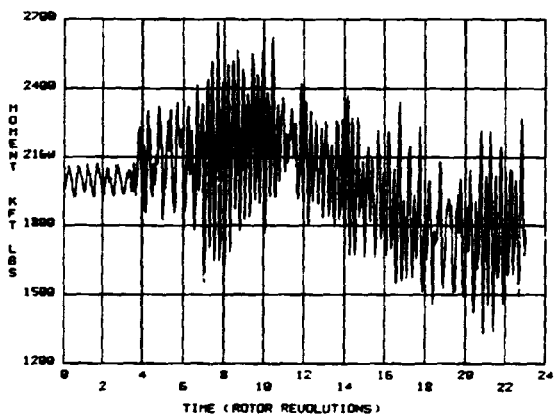


Figure 7 Predicted flapwise bending moment for a turbulent wind with a 27 mph mean at station 370 of the MOD2 blade.

In order to compare with experimental data, the same types of data reduction that are done on the field measurements must be done on the predicted results. To this end, the curve of Fig. 7 is first truncated to delete the first four cycles, filtered with highpass filter to eliminate frequencies below .25/rev and finally truncated again to delete spurious results near the end of the record caused by end-effect problems associated with the filtering. The end product is presented in Fig. 8

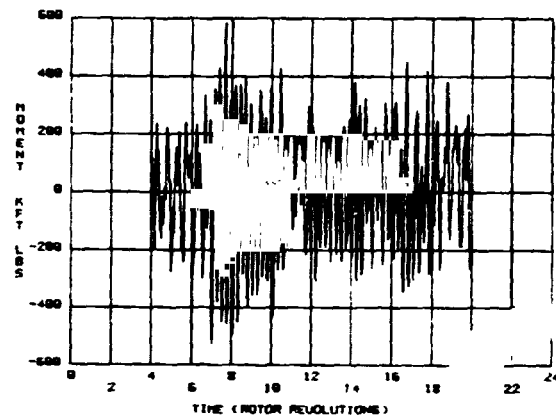


Figure 8. Predicted flapwise bending moment filtered using a highpass filter with a cut-off frequency of .25/rev.

Two additional forms of data reduction are done on the curve of Fig. 8. First it is transformed to determine its frequency content using the fast Fourier transform. The transformed curve, which is shown in Fig. 9, clearly indicates the dominance of the 4/rev component of the response. This dominance is the result of the nearness of the frequency of the symmetric flapwise bending mode to 4/rev at the operating speed. Consistent with the steady wind response, a significant 2/rev component is also present in the total response.

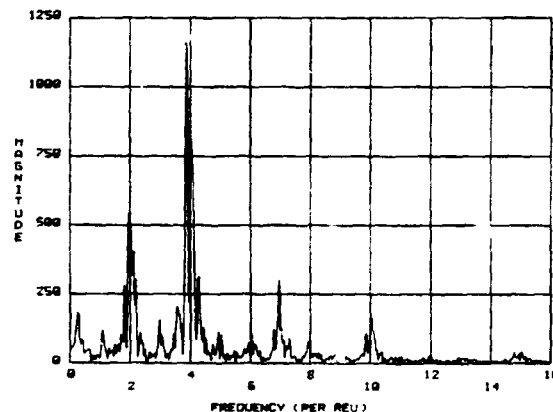
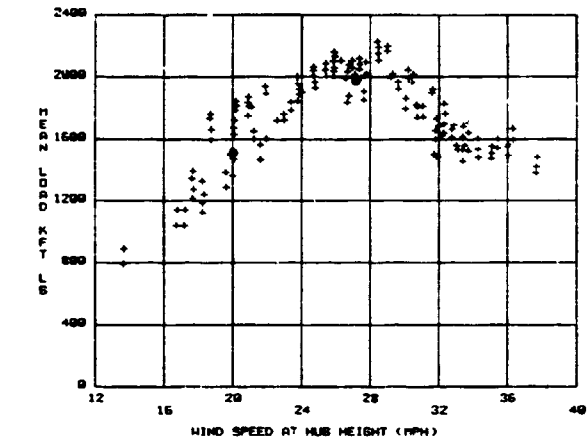


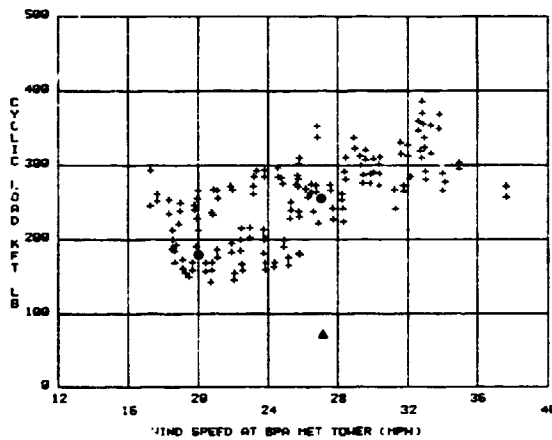
Figure 9 Fast Fourier transform of the filtered flapwise bending moment predictions

The second form of data reduction consists of cycle counting to obtain a 50 percentile cyclic value. The first step of this procedure involves tabulating all the maximum and minimum values between the zero crossings of Fig. 8. The 50 percentile cyclic value is then obtained by averaging the absolute values of each of the tabulated results

In Fig. 10(b) the 50 percentile cyclic flapwise moment at station 370 is displayed as a function of wind-speed. The experimental data denoted in this figure by the "plus" signs was collected from the MOD2 cluster at Goodnoe Hills in July of 1983. Predictions for two mean windspeeds, 20 and 27 mph, are indicated on the plot by the solid circles. In both cases the predictions fall within the scatter band of the data. The solid triangle corresponds to the predicted value



(a)



(b)

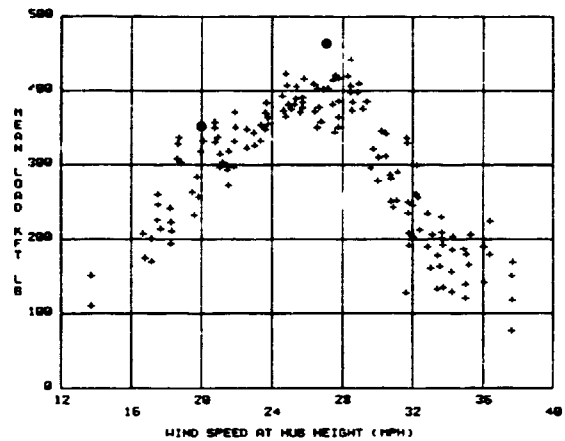
Figure 10. Comparison of predictions, denoted by the solid circles and triangle, to data, denoted by the plus signs, at station 370 of the MOD2 blade, (a) mean flapwise bending moment, (b) cyclic flapwise bending moment.

for a steady 27 mph wind. The importance of including turbulent wind effects in the structural dynamic analysis of HAWTs is clearly demonstrated by this figure

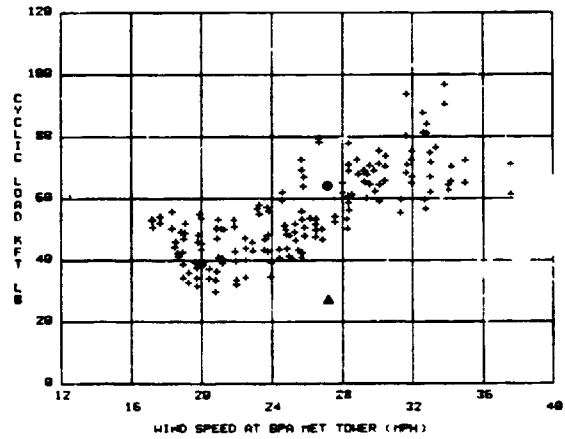
Fig. 10(a) shows the corresponding mean value of the flapwise moment at station 370. As in the cyclic case, the predictions fall within the scatter band of the data. Although not displayed on the plot, the steady wind prediction at 27 mph coincides with the value shown for the total response. This indicates

that the inclusion of stochastic wind effects does not seem to be critical for accurately computing mean flapwise moments.

For station 1164, results similar to those of Fig. 10 are shown in Fig. 11. Again the predictions are generally within the data scatter band, with the mean flapwise moment at the high rim of the band. This slight overprediction is probably caused by the fact that the continuous blade loads are integrated to form concentrated nodal forces. In the static case for a uniform load, this discretization of the load produces moments which are correct at the node points, but overpredicted everywhere in between.



(a)



(b)

Figure 11. Comparison of predictions, denoted by the solid circles and triangle, to data, denoted by the plus signs, at station 1164 of the MOD2 blade, (a) mean flapwise bending moment, (b) cyclic flapwise bending moment.

To examine the role that the tower plays in the response of the MOD2, the hub of the rotor was constrained so that it could not translate. This did not compromise its ability to teeter however. For the same turbulent wind with the 27 mph mean, results show a reduction in the 50 percentile cyclic flapwise moment of approximately 10 percent. Thus, for the

MOD2, it may be possible to eliminate the tower from the analysis without significantly degrading the accuracy of the results. This elimination considerably simplifies the analysis procedures. However, this observation for the MOD2 cannot be generalized to all HAWTs. The critical issue in excluding the tower is the degree to which its presence modifies the natural frequencies of the rotor.

The computer resources required by HAWTDYN are modest. The MOD2 model, which contains 67 degrees of freedom, requires 240 cp seconds on the CRAY computer to obtain solutions out to 80 seconds. The relatively large time step of .008 seconds, made possible by the use of an implicit integration method, was used for these calculations. Although tests were conducted to establish the accuracy of this time step, no attempts were made to find the largest possible time step consistent with accuracy and stability restrictions. Thus, it may be possible to reduce the cp time below the value reported here.

CONCLUSIONS

In the design and analysis of dynamic systems three areas of concern are routinely addressed: the natural frequencies of the system, the excitation frequencies, and the ability of the distributed forces to excite the natural modes. For HAWTs, the task of addressing these areas of concern is not routine. The identification of the natural frequencies of the system is complicated by the fact that the frequencies must be obtained for the turbine in its operational configuration. From the analysis point of view, this entails connecting the rotor, which moves relative to a rotating frame, to the tower which moves relative to a stationary one. This precludes the use of standard solution techniques for obtaining the natural frequencies and modes of the structure. The determination of the excitation frequencies and the spatial distribution of the forces is more involved because of the turbulent nature of the wind. Not only is the turbulence difficult to model, but sophisticated methods for predicting the resultant loads have not been developed. However, with proper attention to creating structural and aerodynamic load models that contain the major physical aspects of the problem, reasonably accurate results can be obtained.

In the present case, the HAWTDYN software has produced accurate predictions for the MOD2 turbine, for two windspeeds. These results are of a preliminary nature and should be viewed as such until more of the validation process has been completed. This process includes making predictions for several existing turbines at a number of wind conditions, and comparing the results with available experimental data. In order to generate more confidence in the present MOD2 finite element model, it should be upgraded so that the computed natural frequencies are in better agreement with measured ones and some development effort should be expended in HAWTDYN to properly model the tip control mechanism.

Even though some aspects of the modeling are crude, HAWTDYN has produced some promising results. The inclusion of turbulent wind effects has dramatically influenced the MOD2 response predictions, bringing them into agreement with measured data. The use of implicit integration methods has posed no insurmountable problems and has made it possible to obtain the long-time solutions required to analyze HAWTs driven by turbulent winds. After the validation pro-

cess has been completed, it is expected that HAWTDYN will be suitable for accurately evaluating the structural response of alternate HAWT designs.

ACKNOWLEDGEMENTS

The work reported here was made possible through the contributions of a number of individuals. R. H. Praasch of Sandia National Laboratories provided the impetus for the project through his early inquiries to NASA-Lewis and DOE. Valuable assistance was received from D. C. Janetzke and T. L. Sullivan of NASA-Lewis through general consultation and the provision of MOD2 information. Valuable consultation was also forthcoming from S. A. Shipley of the Boeing Aerospace Company on observed behavior of the MOD2. R. E. Wilson of Oregon State University provided the software for the PROP code which he developed. And finally, P. S. Veers of Sandia National Laboratories modified software he generated to compute turbulent wind fields for VAWTs, for calculation of the stochastic wind increments. The inclusion of these increments proved to be crucial to the good agreement that was obtained between the predictions and measured data.

REFERENCES

1. Patton, E. M., and Wilson, R. E., "Design Analysis of Performance and Aerodynamic Loading of Non-Flexible Horizontal Axis Wind Turbines," Oregon State University, RLO/2227-78-2, UC-60, August 1978.
2. Dugundji, J., and Wendell, J. H., "General Review of the MOSTAS Computer Code for Wind Turbines," NASA CR-185385, June 1981.
3. Hoffman, J. A., Dreier, M. E., Williamson, D. R., and Henninger, W. C., "Mathematical Methods Incorporated in the Wind Energy System Coupled Dynamics Analysis," Paragon Pacific Inc., Report PPI-1014-7, January 1977.
4. DYLOSAT-Proprietary Software Developed by R. D. Miller of the Boeing Aerospace Company, 1983.
5. Veers, P. S., "Modeling Stochastic Wind Loads on Vertical Axis Wind Turbine Blades," Proceedings of the 25th SDM Conference, Palm Springs, May 1978.
6. Weingarten, L. I., and Nickell, R. E., "Non-Linear Stress Analysis of Vertical Axis Wind Turbine Blades," Sandia National Laboratories, SAND74-0378, April 1975.
7. Hilber, H. M., Hughes, T. J. R., and Taylor, R. L., "Improved Numerical Dissipation for Time Integration Algorithms in Structural Dynamics," Earthquake Engineering and Structural Dynamics, Vol. 5, pp. 283-292, 1977.
8. Newmark, N. M., "A Method of Computation for Structural Dynamics," Journal of the Engineering Mechanics Division, ASCE, Vol. 85, EM3, pp. 67-94, 1959.
9. Andrews, J. S., and Baskin, J. M., "Development Tests for the 2.5 Megawatt MOD-2 Wind Turbine Generator," Proceedings of the Large Horizontal-Axis Wind Turbines Workshop, NASA Conference Publication 2270, Cleveland, July 1981.

BLADE/AILERON SYSTEMS

J. C. Strain, General Electric Co.

L. Mirandy, General Electric Co.

ABSTRACT

Aeroelastic stability analyses have been performed for the MOD-5A blade/aileron system. Various configurations having different aileron torsional stiffness, mass unbalance, and control system damping have been investigated. The analysis was conducted using a code recently developed by the General Electric Company - AILSTAB. The code extracts eigenvalues for a three degree of freedom system, consisting of: (1) a blade flapwise mode, (2) a blade torsional mode, and (3) an aileron torsional mode. Mode shapes are supplied as input and the aileron can be specified over an arbitrary length of the blade span. Quasi-steady aerodynamic strip theory is used to compute aerodynamic derivatives of the wing-aileron combination as a function of spanwise position. Equations of motion are summarized herein. The program provides rotating blade stability boundaries for torsional divergence, classical flutter (bending/torsion) and wing/aileron flutter. It has been checked out against fixed-wing results published by Theodorsen and Garrick.

The MOD-5A system is stable with respect to divergence and classical flutter for all practical rotor speeds. Aileron torsional stiffness must exceed a minimum critical value to prevent aileron flutter. The nominal control system stiffness greatly exceeds this minimum during normal operation. The basic system, however, is unstable for the case of a free (or floating) aileron. The instability can be removed either by the addition of torsional damping or mass-balancing the ailerons.

The MOD-5A design was performed by the General Electric Company, Advanced Energy Program Department under Contract DEN3-153 with NASA Lewis Research Center and sponsored by the Department of Energy.

INTRODUCTION

Although aileron systems have widespread use on fixed-wing aircraft very few rotors have been designed with aileron controls. Large wind turbines, in particular, have used pitchable blade sections for power regulation and to start-up and shut-down. General Electric's 400 ft. diameter, 7.3MW MOD-5A was originally designed with a pitchable tip spanning the outer 25% of blade radius. As the design progressed, further studies determined that substantial weight and cost savings could be obtained by switching to an aileron control system. This provided the impetus for the work described in this work.

In this paper we first describe the development of AILSTAB, a three degree of freedom stability analysis program. The results of the MOD-5A rotor blade stability analysis are then presented. Also included are the results of investigations, which are parametric in nature and show trends which should be similar for other WTG's.

NOMENCLATURE

- a - distance, midchord to elastic axis, as percent of chord
- \bar{a} - lift curve slope; lift coefficient per radian
- b - semichord
- c - distance, midchord to aileron hinge, as percent of chord
- c(k) - Theodorsen's coefficient
- C_A - elemental aerodynamic damping matrix
- \bar{C}_A - integrated aerodynamic damping matrix
- C_S - elemental structural damping matrix

\bar{C}_S - integrated structural damping matrix
 e - distance, midchord to leading edge of aileron, as percent of chord
 h - blade flap bending degree of freedom
 I_α - torsional moment of inertia of blade, less aileron, about elastic axis; per unit length
 I_B - torsional moment of inertia of aileron, about hinge; per unit length
 K_A - elemental aerodynamic stiffness matrix
 \bar{K}_A - integrated aerodynamic stiffness matrix
 K_{CF} - elemental centrifugal stiffness matrix
 \bar{K}_{CF} - integrated centrifugal stiffness matrix
 K_S - elemental structural stiffness matrix
 \bar{K}_S - integrated structural stiffness matrix
 M_α - blade mass, less aileron; per unit length
 M_B - aileron mass; per unit length
 M_A - elemental aerodynamic mass matrix
 \bar{M}_A - integrated aerodynamic mass matrix
 M_S - elemental structural mass matrix
 \bar{M}_S - integrated structural mass matrix
 r - blade radial station, dimensional
 S_h - Southwell coefficient, blade bending
 V - local velocity
 α - blade torsion degree of freedom
 β - aileron torsion degree of freedom
 ζ_h - critical damping ratio, blade bending
 ζ_α - critical damping ratio, blade torsion
 ζ_β - critical damping ratio, aileron torsion
 ρ - air mass density; per unit length
 σ_α - static moment of blade, less aileron, about elastic axis; per unit length
 σ_β - static moment of aileron, about hinge; per unit length
 ϑ_h - flapwise deflection mode shape
 ϑ_α - blade torsion mode shape
 ϑ_β - aileron torsion mode shape
 $\vartheta_{\theta h}$ - flapwise rotation mode shape

Ω - rotor speed, radians/second
 ω_f - flutter frequency, radians/second
 ω_h - blade bending frequency, radians/second
 ω_α - blade torsional frequency, radians/second
 ω_β - aileron torsional frequency, radians/second

METHODS OF ANALYSIS

The AILSTAB rotor blade stability analysis program was developed in a manner very similar to that which would be used for a fixed wing. The differences between rotor and fixed wing analyses are the variation of local velocity with span on a rotor blade, and the variation of stiffness with rotor rpm due to the centrifugal forces. The AILSTAB computer code can be used to predict divergence and classical blade bending/torsion flutter, as well as aileron torsion/blade bending flutter.

SYSTEM DESCRIPTION

The three degrees of freedom (DOF) in the analysis are blade flapwise bending (h), blade torsion (α), and aileron torsion (β). Figure 1 depicts these DOF and their sign conventions. The conventions are such that h is negative for a bending deflection toward the suction side of the airfoil. α is positive for a "nose up" rotation, and β is positive for an "aileron down" rotation and is measured relative to α .

Three other parameters required for the analysis are depicted in this figure. All three are measured from the airfoil's midchord, are positive toward the trailing edge, and are expressed as a percentage of the semichord. The distance to the elastic axis is denoted "a", the distance to the aileron leading edge is "e", and the distance to the aileron hinge is denoted "c".

Figure 2 shows the three DOF (mode shapes) depicted in three dimensions.

ASSUMPTIONS

The following set of assumptions, all of which are believed to be reasonable, were made in developing the computer code.

1. The equations of motion were linearized.
2. Three degrees of freedom at a time, one flapwise, plus the blade and aileron torsion modes, are sufficient to determine the stability.
3. Aerodynamic strip theory with no stall was used, i.e. the aerodynamic derivatives are independent of α .
4. The local velocity is equal to Ωr , the rotational velocity times the radial distance, i.e. the free wind velocity is neglected.
5. The Theodorsen coefficient, $c(k)$, is equal to 1.0, i.e. Quasi-steady aerodynamics are used. This should give conservative results for both blade-bending/torsion flutter and blade-bending/aileron torsion flutter.
6. Aerodynamic derivatives for an unsealed gap (ref. 1) are used if c.p.e.

EQUATIONS OF MOTION

The equations of motion were developed for a representative airfoil element of length "dr" and integrated along the span of blade with weighting as determined by the mode shapes. The aerodynamic equations incorporated in this analysis were those of Smilg and Wasserman (ref. 1). Inertial equations of motion were derived with centrifugal stiffening terms added. The final form of the equations is:

$$[\bar{M}_S - \bar{M}_A] \begin{Bmatrix} \ddot{h} \\ \ddot{\alpha} \\ \ddot{\beta} \end{Bmatrix} + [\bar{C}_S - \bar{C}_A] \begin{Bmatrix} \dot{h} \\ \dot{\alpha} \\ \dot{\beta} \end{Bmatrix} + [\bar{K}_S + \bar{K}_{CF} - \bar{K}_A] \begin{Bmatrix} h \\ \alpha \\ \beta \end{Bmatrix} = 0$$

where the matrices subscripted S (structural) and A (aerodynamic) are composed of elemental mass, damping, and stiffness terms integrated along the blade span with modal weighting.

$$\text{i.e. } [\bar{M}_S] = \int_{\text{span}} L \begin{bmatrix} \rho h \\ \rho \alpha \\ \rho \beta \end{bmatrix} [M_S] \begin{Bmatrix} \rho h \\ \rho \alpha \\ \rho \beta \end{Bmatrix} dr$$

The stiffness contribution due to centrifugal stiffening, K_{CF} , is formed similarly with a mode shape of flapwise rotations substituted for the flapwise deflection mode shape.

$$\text{i.e. } [\bar{K}_{CF}] = \int_{\text{span}} L \begin{bmatrix} \rho h \\ \rho \alpha \\ \rho \beta \end{bmatrix} [K_{CF}] \begin{Bmatrix} \rho h \\ \rho \alpha \\ \rho \beta \end{Bmatrix} dr$$

A detailed description of the terms in the elemental matrices is presented in the appendix.

SYSTEM STABILITY

In order to determine the blade's flutter stability, the integrated mass, stiffness and damping matrices are formed into a six by six dynamical matrix from which complex eigenvalues and eigenvectors are determined. The form of the dynamical matrix is:

$$\begin{bmatrix} -M^{-1}C & -M^{-1}K \\ I & 0 \end{bmatrix}$$

where

$$M = -\bar{M}_A + \bar{M}_S$$

$$C = -\bar{C}_A + \bar{C}_S$$

$$K = -\bar{K}_A + \bar{K}_S + \bar{K}_{CF}$$

$$I = 3 \times 3 \text{ unit matrix}$$

The critical damping ratios (ζ), and the frequencies in hz (f_f), are determined from the eigenvalue (R) as follows.

$$\zeta = -\frac{\text{REAL}(R)}{\text{ABS}(R)}, \quad f_f = \frac{\text{ABS}(R)}{2\pi}$$

The output of the AILSTAB stability analysis program is eigenvalues, and eigenvectors if desired. The program is organized so that a series of cases may be run for a particular configuration, with rpm varied. The critical damping ratio and coupled frequencies are determined from the complex eigenvalues, and the damping in each mode can be plotted vs. rpm to illustrate system stability. In the case of blade bending/aileron torsion flutter there is a range of rpm between which the instability exists. By plotting the range of unstable rpm vs. a design parameter such as aileron control system stiffness, aileron damper, or mass balance, a stability boundary may be constructed.

DESCRIPTION OF ANALYZED SYSTEM

The MOD-5A is a 7.2MW wind turbine with a teetered rotor. Ailerons on the outer 40% of the 200 ft. radius blades are used to regulate power and to shut down. The ailerons are hinged at their leading edge and are 40% of the chord width.

Three blade flapwise mode shapes were used in the

analysis. They were 1) the teeter mode with a frequency of 1 per rev, 2) the 1st collective with a frequency of 7 radians/second, and 3) the 1st cyclic with a frequency of 13.8 radians/second. These mode shapes were calculated for an isolated blade (i.e., not attached to the wind turbine). The collective mode of the isolated blade is found by providing a cantilevered root condition in the flapwise direction. The cyclic mode is determined by providing a pinned root condition in the flapwise direction. A plot of these three flapwise modes is presented in Figure 3. Southwell coefficients may be input to the program so that both the collective and cyclic frequencies may be varied with rpm to account for the varying centrifugal stiffening. For the MOD-5A analysis the important instability occurred at a low enough rpm so that the centrifugal stiffening was not important to the results.

The three aforementioned flapwise modes were each in turn analyzed in combination with the blade torsion mode shape and an aileron torsion mode. Higher modes than these were also analyzed, but were not found to be critical. The blade torsion mode had a frequency of 51 radians/second. By comparison, the ailerons are essentially rigid in torsion with cantilevered frequencies above 400 radians/second. For all practical purposes, the aileron natural frequencies are dominated by the control system stiffness and oscillate as a rigid body. Rather than attempting to model the actual aileron torsional natural mode, the frequency, or equivalently the actuator stiffness was varied, to determine the minimum requirements. In this way failure modes, such as loss of actuator hydraulic stiffness, are fall-outs of the analysis. In addition to aileron frequency sweeps, variations in aileron torsional damping, mass-balancing, and aileron spanwise length were considered. The ailerons center of gravity is aft of the 6% chord hinge line. The aft center of gravity has a de-stabilizing effect.

ANALYSIS RESULTS

The most critical condition will be discussed first. It occurs when the root torsional stiffness provided by the actuators is lost and the aileron is free to rotate about its hinges. This cannot happen under

normal circumstances, so it represents a system failure. Stability boundaries are presented in terms of control system stiffness, control system damping, and the degree of mass-balance. A final case considers the stability of an aileron spanning only the outer 27.5% of the blade.

FREE AILERON

Figures 4a-c show damping vs. rotor speed for the baseline blade with a free, unbalanced aileron (the aileron torsion frequency of 1 per rev or 1P, is due to centrifugal stiffening). Below each damping curve, the natural frequencies are plotted vs. rpm. Both coupled (dashed lines) and uncoupled (solid lines) frequencies are shown. At rpm's where uncoupled frequencies coincide, a decrease in stability is noted in the corresponding damping curve. The Figures 4a, b, and c, illustrate the stability with the teeter, flap collective, and flap cyclic modes, respectively. Aileron torsion coupling is seen to cause an instability only with the flap collective mode. The ailerons are unstable in the region of low rotor speed, 3-12 rpm, which is typical of wing and aileron systems with an unbalanced mass. In particular, there is the possibility of instability when the aileron torsional frequency is less than the flapwise frequency. The system in Figure 4 becomes stable again at 12 rpm, because the torsional aerodynamic spring increases the aileron frequency beyond that of the first flapwise mode. The instabilities, which are seen in all plots between 55 and 60 rpm, are classical bending-torsion flutter of the blade.

STABILITY BOUNDARIES

A flutter boundary for the MOD-5A blade with unbalanced aileron is given in Figure 5. To generate the boundary, the aileron root torsion spring was increased in increments to find the stiffness at which the torsion mode became stable. At any value of stiffness where an instability occurred, the values of rpm between which the mode was unstable were found and plotted. This figure shows that an aileron torsional frequency of 7.5 radians/second is needed to provide neutral stability. This same procedure was followed for the addition of aileron torsional damping rather than a spring. The resulting flutter boundary is presented in Figure 6.

The comparison of stiffness and damping requirements is an interesting sidelight to the stability problem. If the damping rate is multiplied by the flutter frequency, the effective impedance, in stiffness units of the damper is found. Figure 7 contains plots of impedance vs. flutter damping ratio at 6 rpm for both spring and damper systems. The system's stability is largely a function of the aileron torsional impedance whether it be derived from a spring or a damper. This conclusion is further strengthened by Figure 8 which shows the stability boundaries in terms of impedances. The approximate equivalence of spring and damper impedance effects is an important consideration during dynamic conditions, such as pitch change in which the hydraulic actuator impedance has both spring and damper characteristics.

To prevent flutter without need for a minimum aileron torsional stiffness or damper, balance weights would have to be added to the ailerons. With the ailerons unbalanced, the minimum damping ratio calculated in the AILSTAB rpm sweep was approximately -12%, as can be discerned from Figure 4b. The variation of modal damping with RPM is shown for a fully (100%) mass-balanced aileron in Figure 9. The system is stable. The variation of minimum damping in the aileron mode is shown for varying degrees of mass-balance in Figure 10. Neutral stability can be obtained with an 85% mass-balanced system.

EFFECT OF AILERON LENGTH

Similar analyses to those discussed above were performed with the free aileron section extending from .725 radius to the tip, rather than from .60 radius. In this configuration the different modal weighting caused an instability of the aileron coupling with the blade cyclic bending mode. Aileron torsion coupling with the blade collective bending mode also produced an instability, as it had with the longer aileron.

Since the shorter aileron was unstable in coupling with the higher frequency cyclic flapwise mode with a flutter frequency of approximately 14 radians/second, a higher dimensional damping coefficient was required to stabilize it. The longer aileron had unstable coupling only with the collective mode,

which had a flutter frequency of approximately 7 radians/second.

The damping vs. rpm plots for the 27.5% span, free, unbalanced aileron analysis are presented in Figure 11.

Stability boundaries of rpm vs. aileron frequency are plotted in Figure 12 to show the effect of added root torsional stiffness. Boundaries for the addition of torsional damping are shown in Figure 13. To again demonstrate the similarity of results from adding impedance, whether from stiffness or damping, rpm vs. impedance stability boundaries are shown in Figure 14.

CONCLUDING REMARKS

The free unbalanced aileron caused the system to become unstable either with a length of 40% or of 27.5% of blade radius.

These instabilities can be removed with the addition of impedance to the aileron torsion degree of freedom. The actuator stiffness normally supplies an impedance well in excess of that required, but on the MOD-5A torsional dampers have been added to protect the system in the event of an actuator system failure. These dampers are passive elements which will always be operative. The damper forces far enough below those which are present due to the aerodynamic forces in normal operation so that their presence will not penalize control system design.

An alternate method of stabilizing the system would be through the addition of balance weights to the aileron. This method was deemed unwieldy and torsional dampers chosen instead.

REFERENCES

1. Scanlan, R.H. and Rosenbaum, R., "Aircraft Vibration and Flutter", MacMillan Co., 1951.

ACKNOWLEDGEMENTS

This work was performed by the General Electric Company under contract DEN 3-153 with NASA-Lewis Research Center. The authors would like to extend their thanks to David A. Spera and Timothy L. Sullivan of the NASA Wind Energy Project Office for their support throughout the program.

APPENDIX

Equations of Motion

STRUCTURAL (Left Hand Side)

$$[M_S] \begin{Bmatrix} \ddot{h} \\ \ddot{\alpha} \\ \ddot{\beta} \end{Bmatrix} + [C_S] \begin{Bmatrix} \dot{h} \\ \dot{\alpha} \\ \dot{\beta} \end{Bmatrix} + [K_S] \begin{Bmatrix} h \\ \alpha \\ \beta \end{Bmatrix} + [K_{CF}] \begin{Bmatrix} h \\ \alpha \\ \beta \end{Bmatrix}$$

$$\begin{aligned} M_S(1,1) &= M_\alpha + M_\beta \\ M_S(1,2) &= \sigma_\alpha + \sigma_\beta + b(c-a)M_\beta \\ M_S(1,3) &= \sigma_\beta \\ M_S(2,2) &= I_\alpha + I_\beta + 2b(c-a)\sigma_\beta + b^2(c-a)^2 M_\beta \\ M_S(2,3) &= I_\alpha + I_\beta + b(c-a)\sigma_\beta \\ M_S(3,3) &= I_\beta \end{aligned}$$

Other structural mass terms are symmetric.

$$\begin{aligned} C_S(1,1) &= 2\omega_h M_\alpha \zeta_h \\ C_S(2,2) &= 2\omega_\alpha I_\alpha \zeta_\alpha \\ C_S(3,3) &= 2\omega_\beta I_\beta \zeta_\beta \end{aligned}$$

Other damping terms are zero.

$$\begin{aligned} K_S(1,1) &= \omega_h^2 M_\alpha + S_h \Omega^2 M_S(1,1) \\ K_S(2,2) &= \omega_\alpha^2 I_\alpha + \Omega^2 M_S(2,2) \\ K_S(3,3) &= \omega_\beta^2 I_\beta + \Omega^2 M_S(3,3) \end{aligned}$$

Other stiffness terms are zero.

The above structural mass, stiffness, and damping matrices are all multiplied by mode shapes at each radial station and integrated.

i.e.

$$\bar{M}_S = \int_0^N [\theta_h \theta_\alpha \theta_\beta]^T [M_S] [\theta_h \theta_\alpha \theta_\beta] \Delta r$$

S_h in the above stiffness equation, is the

southwell coefficient for the flapwise mode. It is an approximation used to relate the rotating and non-rotating blade natural frequencies.

$$\omega_{ROT}^2 = \omega_{NON-ROT}^2 + S_h \Omega^2$$

$$\begin{aligned} K_{CF}(1,2) &= r \Omega^2 M_S(1,2) \\ K_{CF}(1,3) &= r \Omega^2 M_S(1,3) \\ K_{CF}(2,3) &= \Omega^2 M_S(2,3) \\ K_{CF}(2,1) &= K_{CF}(1,2) \\ K_{CF}(3,1) &= K_{CF}(1,3) \\ K_{CF}(3,2) &= K_{CF}(2,3) \end{aligned}$$

Diagonal terms are zero.

This centrifugal stiffness matrix is multiplied by mode shapes at each radial station and integrated. Unlike the structural stiffness matrix, the first row and column are multiplied by the modal rotation rather than deflection.

i.e.

$$\bar{K}_{CF} = \int_0^N [\theta_h \theta_\alpha \theta_\beta]^T [K_{CF}] [\theta_h \theta_\alpha \theta_\beta] \Delta r$$

$$\text{where, } \theta_{\theta h} = \frac{d\theta_h}{dr}$$

AERODYNAMIC (Right Hand Side)

$$[M_A] \begin{Bmatrix} \ddot{h} \\ \ddot{\alpha} \\ \ddot{\beta} \end{Bmatrix} + [C_A] \begin{Bmatrix} \dot{h} \\ \dot{\alpha} \\ \dot{\beta} \end{Bmatrix} + [K_A] \begin{Bmatrix} h \\ \alpha \\ \beta \end{Bmatrix}$$

$$\begin{aligned} M_A(1,1) &= -\pi \rho b^2 \\ M_A(1,2) &= \pi \rho ab^2 \\ M_A(1,3) &= \rho (T_1 + (c-e)\theta_2) b^2 \\ M_A(2,2) &= -\pi \rho (a^2 + 1/8) b^4 \\ M_A(2,3) &= \rho [T_2 + (e-a)T_1 + 1/4(c-e)\theta_6 \\ &\quad - (a + 1/2)(c-e)\theta_3] b^4 \\ M_A(3,3) &= \frac{\rho}{\pi} [T_3 + (c-e)\theta_7 - (c-e)^2 \theta_4] b^4 \end{aligned}$$

Other mass terms are symmetric.

$$C_A(1,1) = -\rho \bar{a} \Omega r b c(k)$$

$$C_A (1,2) = -1/2 \rho \bar{a} \Omega r b^2 + \rho \bar{a} (a - 1/2) \Omega r b^2 c (k)$$

$$C_A (1,3) = 1/2 \frac{\rho}{\pi} \bar{a} T_0 \Omega r b^2 + \frac{\rho}{\pi} \bar{a} [(c-e) \theta_1 - 1/2 T_{11}] \Omega r b^2 c (k)$$

$$C_A (2,1) = \rho \bar{a} (a + 1/2) \Omega r b^2 c (k)$$

$$C_A (2,2) = 1/2 \rho \bar{a} (a - 1/2) \Omega r b^3 + \rho \bar{a} (1/4 - a^2) \Omega r b^3 c (k)$$

$$C_A (2,3) = \frac{\rho}{\pi} \bar{a} [P - 1/2 (a - 1/2) T_0 + 1/2 (c-e) \theta_3] \Omega r b^3$$

$$+ \frac{\rho}{\pi} \bar{a} [(a + 1/2) T_{11} - (a + 1/2) (c-e) \theta_1] \Omega r b^3 c (k)$$

$$C_A (3,1) = \frac{\rho}{\pi} \bar{a} [(c-e) \theta_{31} - 1/2 T_{12}] \Omega r b^2 c (k)$$

$$C_A (3,2) = 1/2 \frac{\rho}{\pi} \bar{a} [(c-e) \theta_{32} - (P - T_1 - 1/2 T_0)] \Omega r b^3$$

$$+ \frac{\rho}{\pi} \bar{a} [1/2 (a - 1/2) T_{12} + (1/2 - a) (c-e) \theta_{31}] \Omega r b^3 c (k)$$

$$C_A (3,3) = 1/2 \frac{\rho}{\pi^2} \bar{a} [1/2 T_0 T_{11} + (c-e) (\theta_{30} + \theta_{10}) - (c-e)^2 \theta_{30}] \Omega r b^3$$

$$+ 1/2 \frac{\rho}{\pi^2} \bar{a} [-1/2 T_{11} T_{12} + (c-e) (\theta_{21} \theta_{31} + \theta_{11} \theta_{30})$$

$$- 2 (c-e)^2 \theta_{11} \theta_{31}] \Omega r b^3 c (k)$$

$$K_A (1,1) = 0$$

$$K_A (1,2) = -\rho \bar{a} (\Omega r)^2 b c (k)$$

$$K_A (1,3) = -\frac{\rho}{\pi} \bar{a} T_{10} (\Omega r)^2 b c (k)$$

$$K_A (2,1) = 0$$

$$K_A (2,2) = \rho \bar{a} (a + 1/2) (\Omega r)^2 b^2 c (k)$$

$$K_A (2,3) = -1/2 \frac{\rho}{\pi} \bar{a} [T_0 + T_{10}] (\Omega r)^2 b^2 + \frac{\rho}{\pi} \bar{a} (a + 1/2) T_{10} (\Omega r)^2 b^2 c (k)$$

$$K_A (3,1) = 0$$

$$K_A (3,2) = + \frac{\rho}{\pi} \bar{a} [(c-e) \theta_{31} - 1/2 T_{12}] (\Omega r)^2 b^2 c (k)$$

$$K_A (3,3) = 1/2 \frac{\rho}{\pi^2} \bar{a} [(c-e) \theta_{30} - (T_0 - T_0 T_{10})] (\Omega r)^2 b^2$$

$$+ 1/2 \frac{\rho}{\pi^2} \bar{a} [2 (c-e) \theta_{11} \theta_{31} - T_{10} T_{12}] (\Omega r)^2 b^2 c (k)$$

$$\begin{aligned}
T_1 &= -1/3 \sin(\cos^{-1}C) (2+C^2) + C \cos^{-1}C \\
T_3 &= -(1/8+C^2) (\cos^{-1}C)^2 + 1/4 C \sin(\cos^{-1}C) \cos^{-1}C (7+2C^2) \\
T_6 &= -\cos^{-1}C + C \sin(\cos^{-1}C) \\
T_5 &= -1 + C^2 -(\cos^{-1}C)^2 + 2C \sin(\cos^{-1}C) \cos^{-1}C \\
T_7 &= -(1/8+C^2) \cos^{-1}C + 1/8 C \sin(\cos^{-1}C) (7+2C^2) \\
T_{10} &= \sin(\cos^{-1}C) + \cos^{-1}C \\
T_{11} &= (\cos^{-1}C) C (1-2C) + \sin(\cos^{-1}C) (2-C) \\
T_{12} &= \sin(\cos^{-1}C) (2+C) - \cos^{-1}C (2C+1) \\
P &= -(\sin(\cos^{-1}C))^2 / 3 \\
\theta_1 &= \pi - \cos^{-1}(-e) + \sin(\cos^{-1}(-e)) \\
\theta_2 &= (\pi - \cos^{-1}(-e)) (1-2e) + \sin(\cos^{-1}(-e)) (2-e) \\
\theta_3 &= \pi - \cos^{-1}(-e) - \sin(\cos^{-1}(-e)) e \\
\theta_5 &= \sin(\cos^{-1}(-e)) (1+e) \\
\theta_6 &= 2(\pi - \cos^{-1}(-e)) + \sin(\cos^{-1}(-e)) / 3 (2+e) (1-2e) \\
\theta_8 &= (\pi - \cos^{-1}(-e)) (-1-2e) + \sin(\cos^{-1}(-e)) (2+e) \\
\theta_{31} &= \pi - \cos^{-1}(-e) - \sin(\cos^{-1}(-e)) \\
\theta_{10} &= \theta_{31} \theta_5 \\
\theta_{17} &= \theta_3^2 + [\sin(\cos^{-1}(-e))]^2 \\
\theta_{32} &= \pi - \cos^{-1}(-e) + \sin(\cos^{-1}(-e)) (1+2e) \\
\theta_{35} &= 2 [\sin(\cos^{-1}(-e))]^2 \\
\theta_{36} &= \theta_{32} \theta_3 + 2 [\sin(\cos^{-1}(-e))]^2 \\
\theta_{37} &= \theta_3 (\theta_2 - \theta_3)
\end{aligned}$$

The aerodynamic mass, damping, and stiffness matrices are all multiplied by their mode shapes at each radial station and integrated.

i.e.

$$\bar{M}_A = \sum_0^N [\theta_h \theta_\alpha \theta_\beta]^T [M_A] [\theta_h \theta_\alpha \theta_\beta] \Delta r$$

DIVERGENCE

Torsional divergence, if present, will show up in the roots of the stability equations. The following has been added so that the divergence speed, which often lies beyond the RPM range of interest, may be computed directly.

To determine the blade's divergence speed the square of the rotational rotor velocity, Ω^2 , must be factored out of the lower-right-hand 2 x 2 partition of the integrated aerodynamic stiffness matrix,

\bar{K}_A . The same partition is factored out of the structural stiffness matrix \bar{K}_S (the Southwell coefficient terms were ignored here). The two resulting partitions are then set equal to each other and the characteristic equation solved as shown below.

$$K_A' = \begin{bmatrix} \bar{K}_A(2,2) & \bar{K}_A(2,3) \\ \bar{K}_A(3,2) & \bar{K}_A(3,3) \end{bmatrix} \cdot \frac{1}{\Omega^2}$$

$$K_S' = \begin{bmatrix} \bar{K}_S(2,2) & \bar{K}_S(2,3) \\ \bar{K}_S(3,2) & \bar{K}_S(3,3) \end{bmatrix}$$

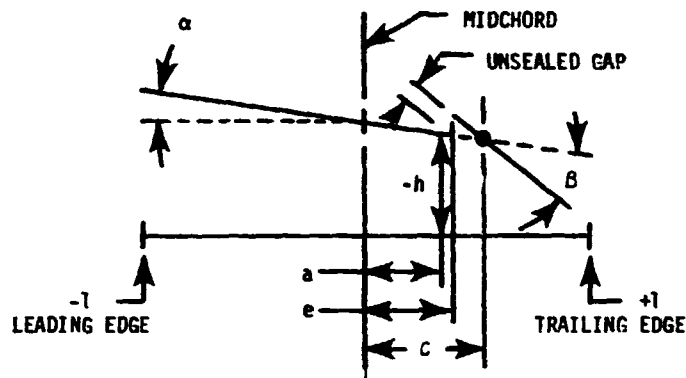
$$\begin{vmatrix} K_S'(1,1) - K_A'(1,1) \Omega^2 & K_S'(1,2) - K_A'(1,2) \Omega^2 \\ K_S'(2,1) - K_A'(2,1) \Omega^2 & K_S'(2,2) - K_A'(2,2) \Omega^2 \end{vmatrix} = 0$$

$$K_S'(2,1) = K_S'(1,2) = 0.$$

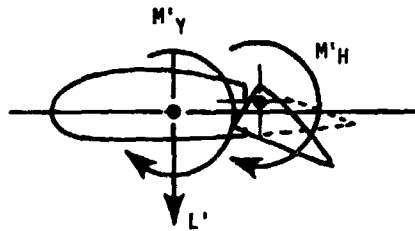
Expanded, the resulting equation is:

$$\Omega^4 (k_A'(1,1) k_A'(2,2) - k_A'(1,2) k_A'(2,1)) - \Omega^2 (k_S'(2,2) k_A'(1,1) + k_S'(1,1) k_A'(2,2)) + k_S'(1,1) k_S'(2,2) = 0.$$

which is easily solved for Ω , the flutter speed in radians/second.



- | | | |
|----------|---|--------------------------------------|
| a | = | DISTANCE - MIDCHORD TO ELASTIC AXIS |
| e | = | DISTANCE - MIDCHORD TO AILERON L/E |
| c | = | DISTANCE - MIDCHORD TO AILERON HINGE |
| h | = | BLADE FLAPWISE DEFLECTION |
| α | = | BLADE TORSION ANGLE |
| B | = | AILERON TORSION ANGLE w.r.t. |



- | | | |
|-----|---|--|
| L' | = | RUNNING LIFT FORCE |
| | - | POSITIVE POINTING FROM SUCTION SIDE TOWARD PRESSURE SIDE AS DEFINED IN REFERENCE 1 |
| M'Y | = | RUNNING MOMENT ABOUT ELASTIC AXIS |
| M'H | = | RUNNING AILERON HINGE MOMENT |

Figure 1. Sign Conventions and Terminology

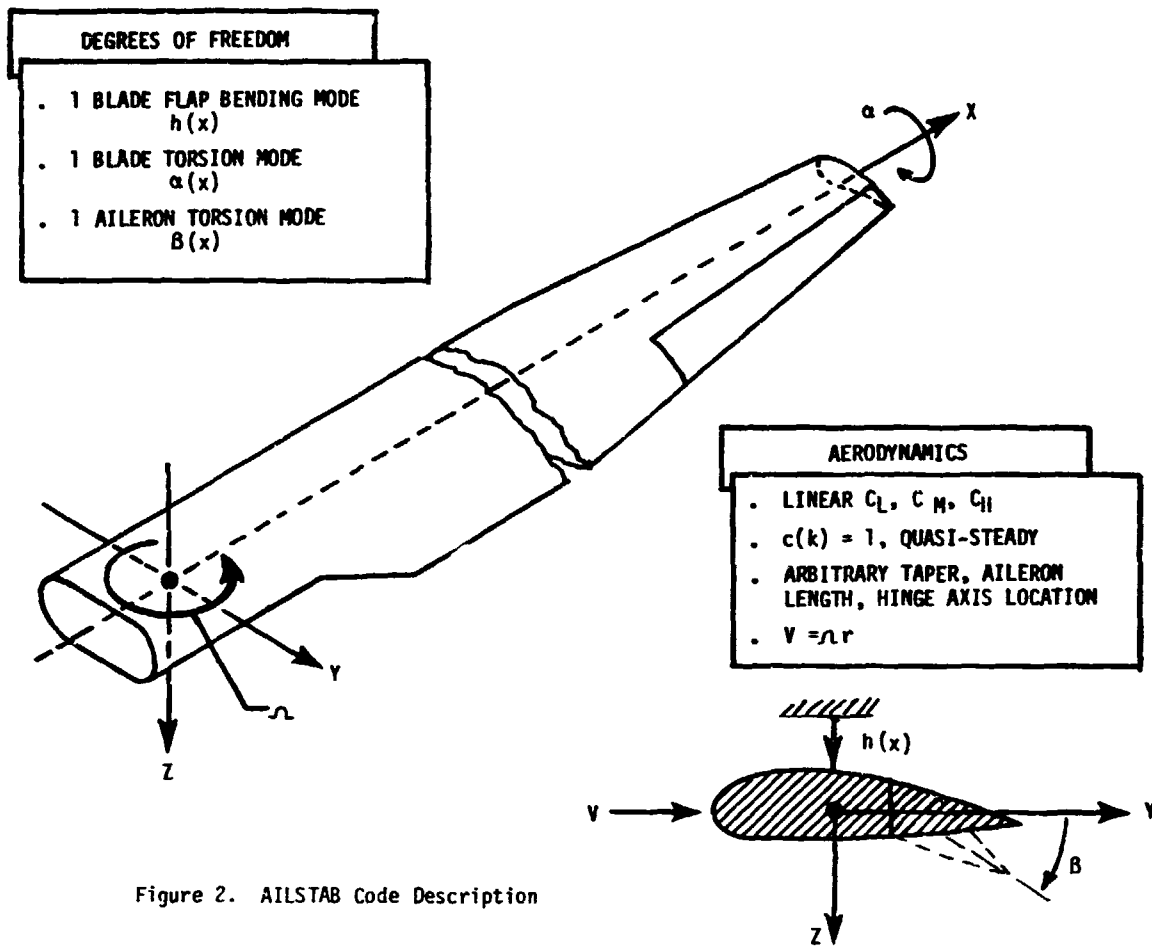


Figure 2. AILSTAB Code Description

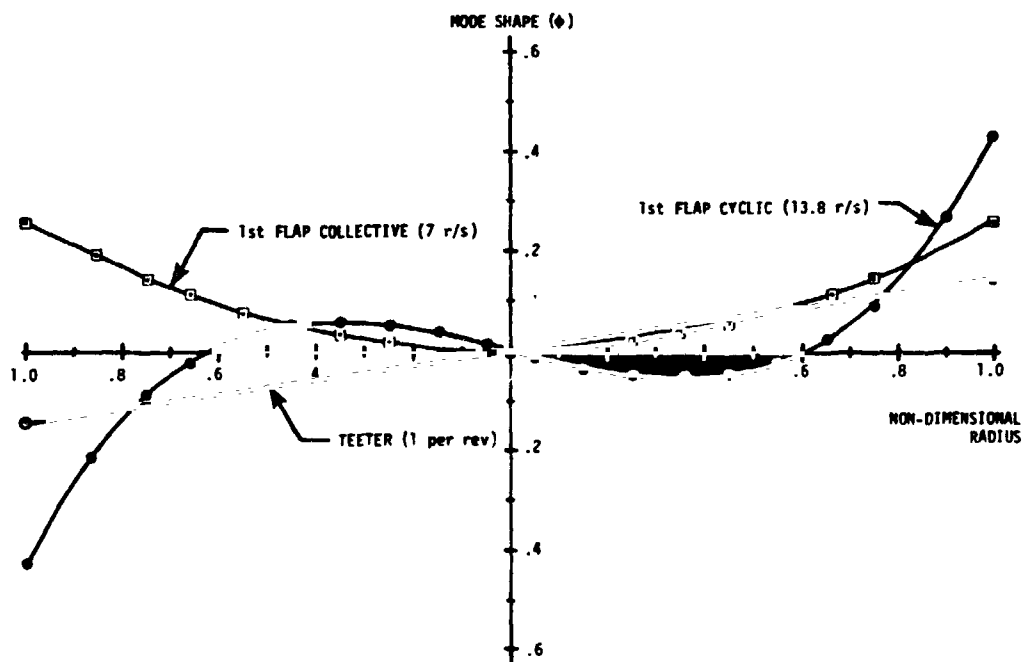


Figure 3. MOD-5A Blade Flapwise Modes

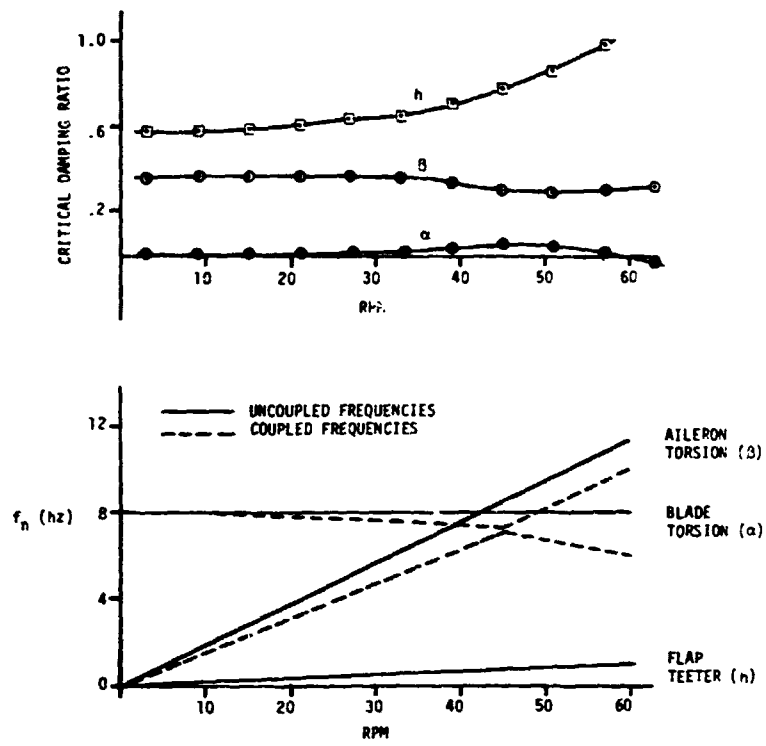


Figure 4a. Flap Teeter Mode Stability
Free Unbalanced Aileron

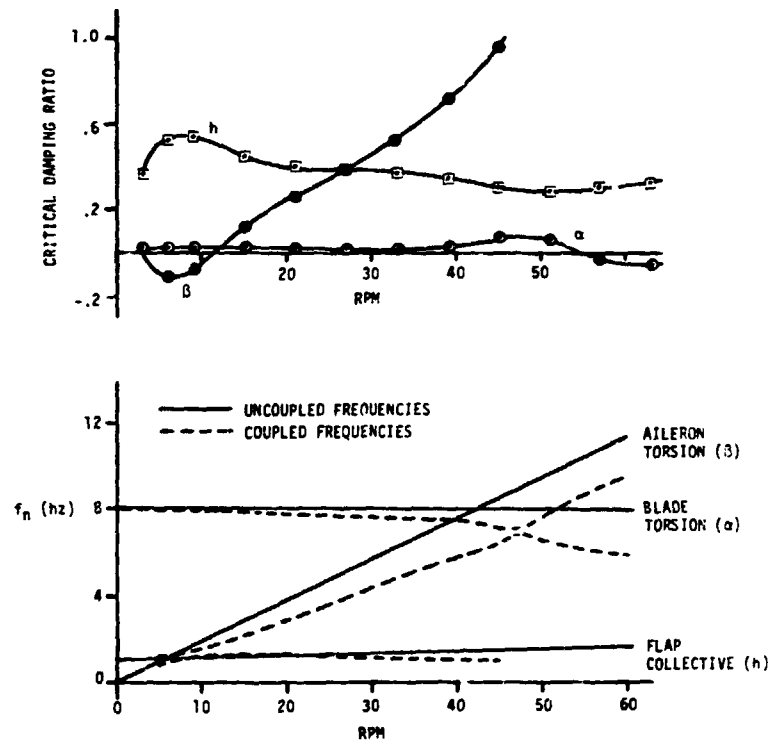


Figure 4b. 1st Flap Collective Mode Stability
Free Unbalanced Aileron

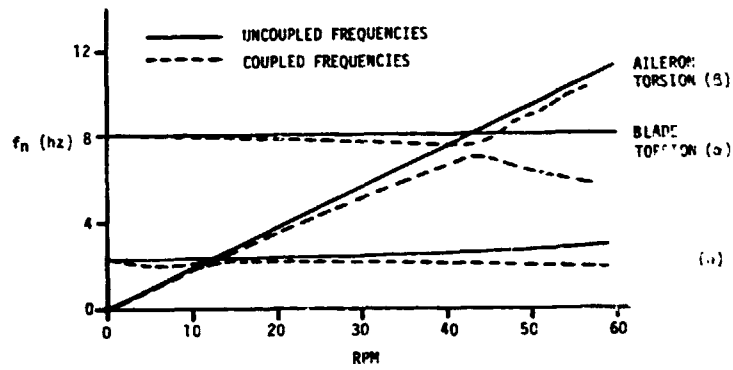
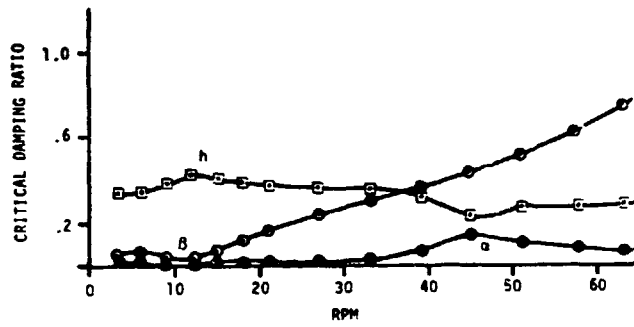


Figure 4c. Flap Cyclic Mode Stability Free Unbalanced Aileron

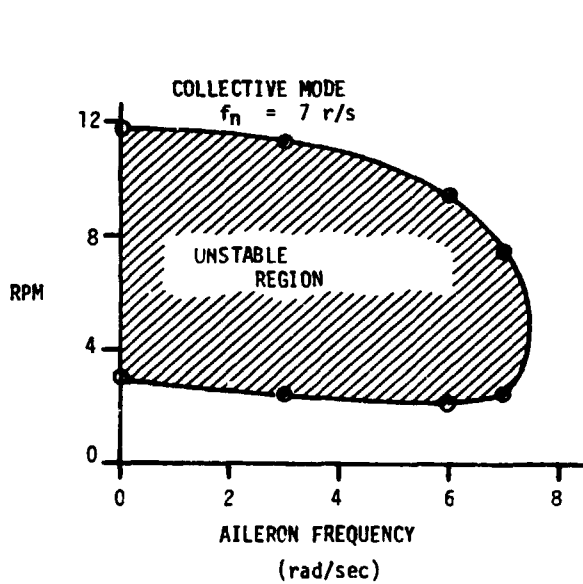


Figure 5. MOD-5A Flutter Boundary - Shown in Terms of Aileron Torsional Frequency

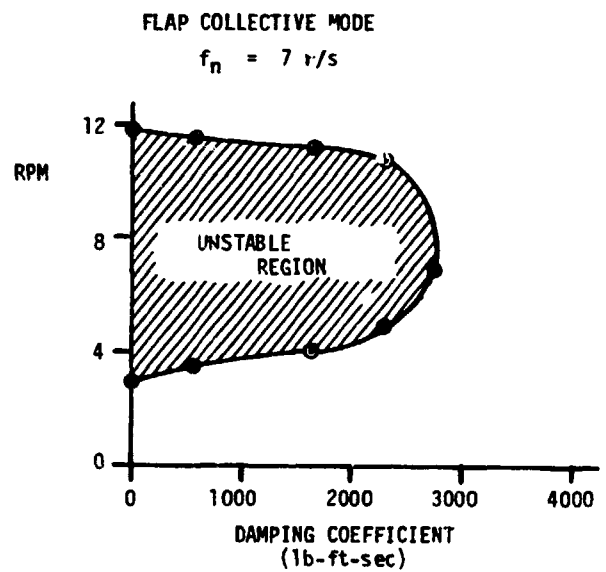


Figure 6. MOD-5A Flutter Boundary - Shown in Terms of Aileron Hinge Damping

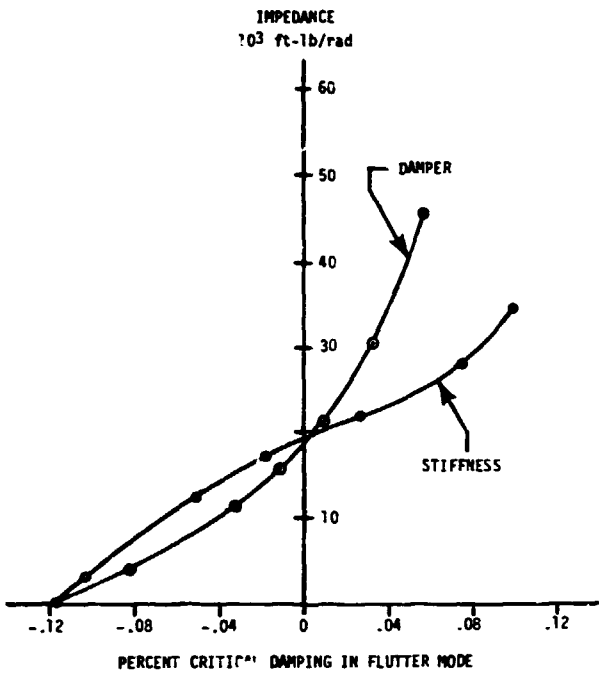


Figure 7. Variation in Modal Damping with Aileron Torsional Impedance, Shown for 6 RPM.

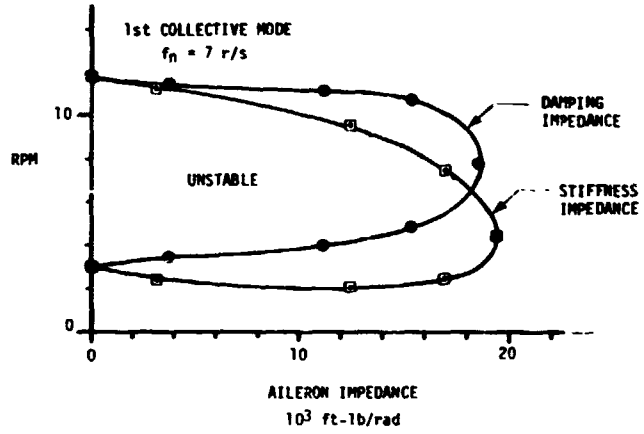


Figure 8. MOD-5A Flutter Boundary Unbalanced Aileron .60R - 1.0R

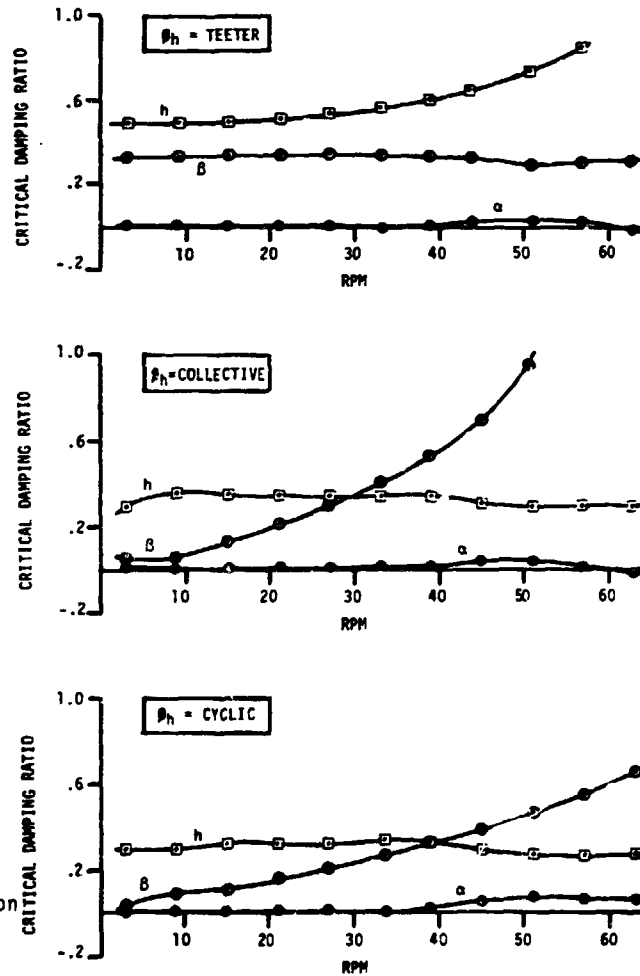


Figure 9. Stability of Free 100% Balanced Aileron .60 - 1.0R

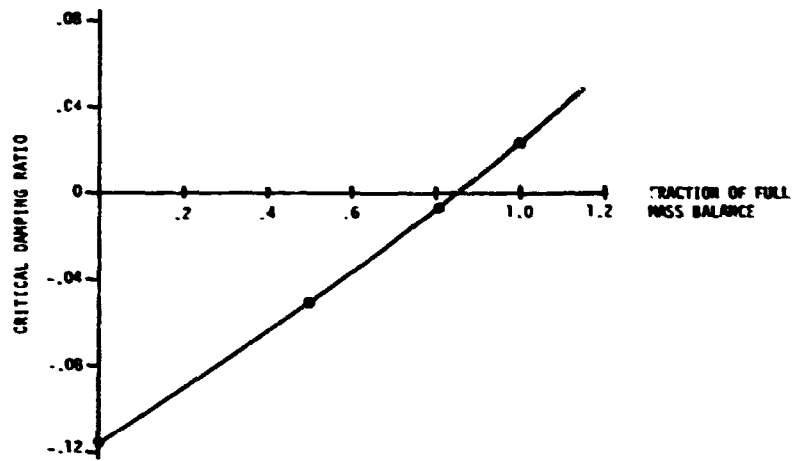


Figure 10. Flutter Damping Coefficient vs. Mass Balance

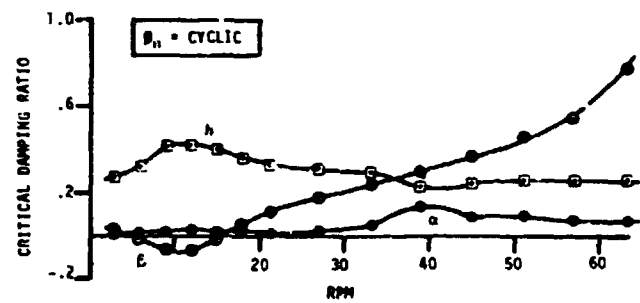
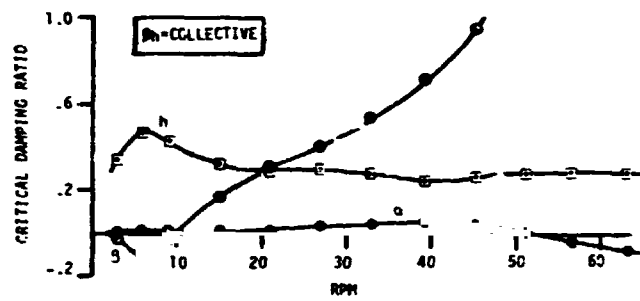
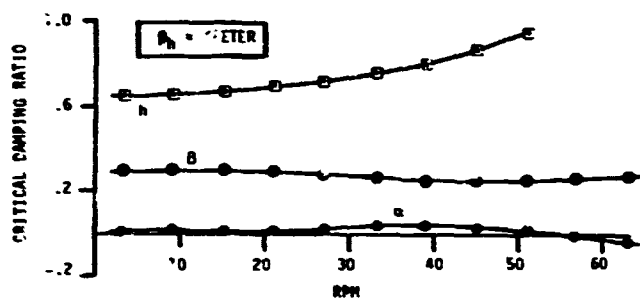


Figure 11. Stability of Free Unbalanced Aileron
Extending from .725R - 1.0P

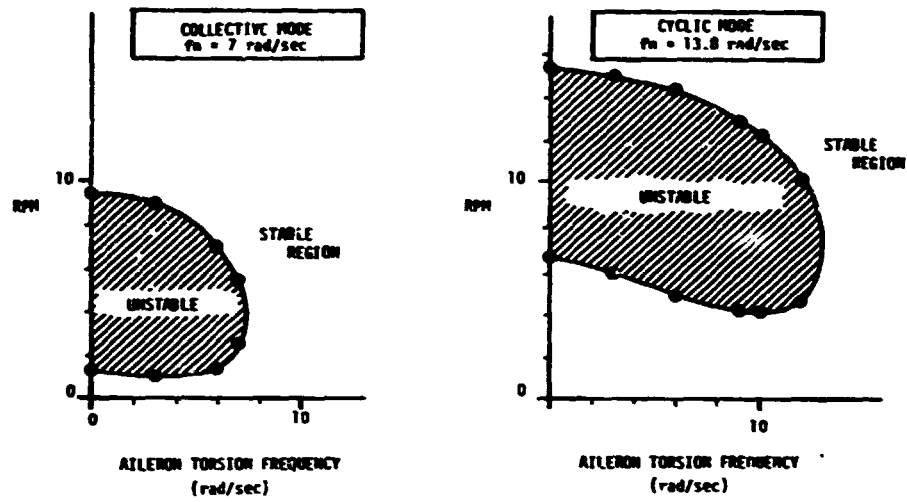


Figure 12. MOD-5A Flutter Boundaries
Unbalanced Aileron .725P - 1.0P
Shown as a Function of Aileron
Torsional Frequency

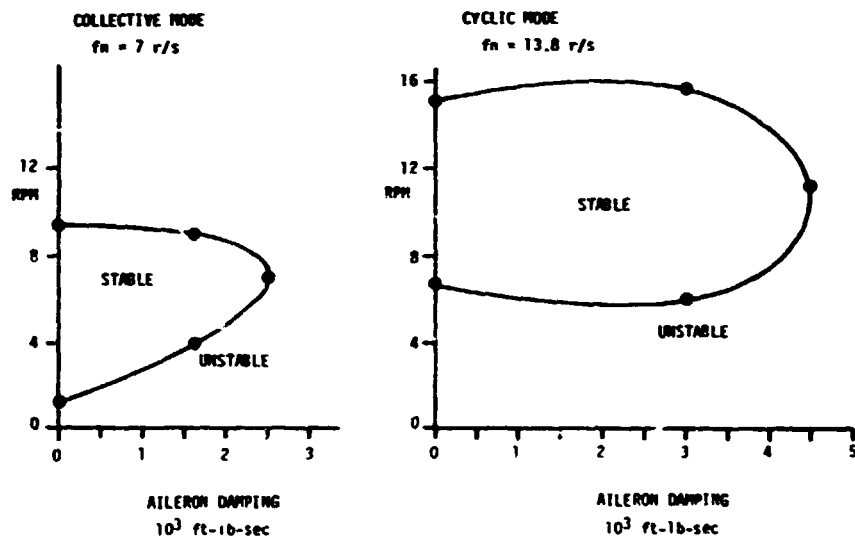


Figure 13. MOD-5A Flutter Boundaries
Unbalanced Aileron .725P - 1.0P
Shown as a Function of Aileron
Damping

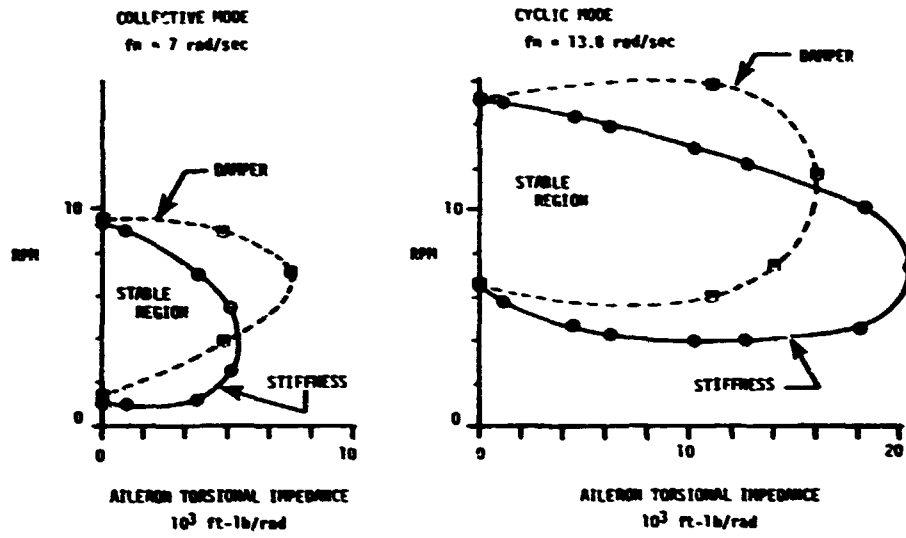


Figure 14. MOP-5A Flutter Boundaries
 Unbalanced Ailerons .725P - 1.0P
 Shown as a Function of Aileron
 Torsional Impedance

CALCULATION OF DESIGN LOADS FOR THE MOD-5A
7.3 MW WIND TURBINE SYSTEM

L. Mirandy, General Electric Co.
J. C. Strain, General Electric Co.

ABSTRACT

Design loads are presented for the General Electric MOD-5A wind turbine. The MOD-5A system consists of a 400 ft. diameter, upwind, two-bladed, teetered rotor connected to a 7.3 MW variable-speed generator. Fatigue loads are specified in the form of histograms for the 30 year life of the machine, while limit (or maximum) loads have been derived from transient dynamic analysis at critical operating conditions. Loads prediction was accomplished using state of the art aeroelastic analyses developed at General Electric. Features of the primary predictive tool - the Transient Rotor Analysis Code (TRAC) are described in the paper. Key to the load predictions are the following wind models: (1) yearly mean wind distribution, (2) mean wind variations during operation, (3) number of start/shutdown cycles, (4) spatially large gusts, and (5) spatially small gusts (local turbulence). The methods used to develop statistical distributions from load calculations represent an extension of procedures used in past wind programs and is believed to be a significant contribution to Wind Turbine Generator analysis. Test/theory correlations are presented to demonstrate code load predictive capability and to support the wind models used in the analysis. In addition, MOD-5A loads are compared with those of existing machines.

The MOD-5A design was performed by the General Electric Company, Advanced Energy Program Department under Contract DEN3-153 with NASA Lewis Research Center and sponsored by the Department of Energy.

INTRODUCTION

The MOD-5A was designed by the General Electric Company as part of the Department of Energy sponsored program to develop multi-megawatt, utility-class, wind turbine generators. It is a two-bladed, horizontal-axis, 400 foot diameter,

upwind design. The MOD-5A features a teetering rotor and laminated wood blades with ailerons over the outboard 40% of the blades to regulate power and to shut down. It incorporates a 7.3 megawatt variable-speed generator. However, due to resonances, there are only two nominal rotor speeds - 13.8 and 16.8 RPM. Additional aspects and further discussion of the MOD-5A are contained in Reference 1.

This paper summarizes the loads analysis conducted for the MOD-5A. The analytical techniques are described, followed by comparison of theoretical predictions with test data to support the methods and models used. Test data were taken from the General Electric 2MW, 200 ft. diameter MOD-1, the Boeing 2.5MW, 300 ft. diameter MOD-2, and the Hamilton Standard 4MW, 256 ft. diameter SVU-WTS 4. The MOD-5A design loads presented herein, are 15% to 25% higher than the theoretical predictions to allow for uncertainties. The machine has been designed to these loads.

METHODS OF ANALYSIS

The WTG loads analysis began with the construction of a dynamic model to determine the natural modes and frequencies of the system. State-of-the art finite element and modal-synthesis techniques were applied. Since these methods are accepted standards in the aerospace industry, they will not be addressed here. Rather, we will focus on the aeroelastic and wind models used for the wind turbine loads analysis.

The experience gained, and methods developed during the MOD-1 program served as a cornerstone for the MOD-5A analysis. Extensive correlation studies and code verification exercises were conducted before the MOD-5A program. Our loads prediction

capabilities were enhanced during the MOD-5A program, particularly in the areas of transient analysis, wind modelling and load statistics. These topics are discussed in the following paragraphs.

Aeroelastic Codes

Two aeroelastic codes were used to predict design loads for the MOD-5A: GETSS, General Electric Turbine System Synthesis and TRAC, Transient Rotor Analysis Code.

GETSS - GETSS was developed during the MOD-1 program and was used to predict the MOD-5A's fatigue loads during the preliminary design phase. The code was verified by NASA during the MOD-1 program, by correlating its predictions with MOD-0 test data. It provided excellent load estimates for MOD-1 and was verified for soft tower and teetering rotor configurations during the MOD-5A contract.

The GETSS analysis flow is shown in Figure 1. The system's structural dynamics are approximated by piecewise linear models of the entire system; wherein natural modes are input for discrete rotor positions. As the blades rotate, the dynamical equations switch from one model to the next. A time history solution is determined over as many revolutions as are required to produce a steady-state response; the last rotor cycle is then used to compute steady-state fatigue loads. Aerodynamic and gravitational forces are computed as a function of the rotor position by the computer code, WINDLD, before the time history calculations, and are applied to the right side of the modal equations. Aeroelastic coupling comes from aerodynamic modal damping coefficient calculations computed by the computer code, QAERO, before the time history calculations. Finally, interface design loads are computed from the modal response. The code can handle a large number of system modes at relatively low computational cost, because the modal equations are decoupled linear, second-order equations, for which there are very efficient numerical integration algorithms. More detailed code descriptions may be found in the MOD-1 final design report (Ref. 4).

TRAC - TRAC was developed during the MOD-5A program to predict transient loads. The program was checked, using steady-state loads calculated by the GETSS code as a benchmark. The verification provided confidence in the calculations made by both programs. In this paper, we show correlation between TRAC fatigue and limit load predictions with MOD-1 data. TRAC also agreed qualitatively with MOD-2 on the subject of interactions between the structure and the control system. TRAC was used to compute all the MOD-5A's final design loads.

The self-explanatory features of the code are illustrated in Figure 2. It does not use piecewise-linear modal inputs, as GETSS does. Rather, separate inputs are provided for rotating and fixed system modes. Complete inertial and aerodynamic coupling between the degrees of freedom has been retained in the development. Furthermore, non-linear inertia terms, caused by finite elastic deflections of the blade, are included. As such, the equations are highly coupled. A Runge-Kutta numerical integration has been used to obtain solutions. Loads are calculated after each time step using the "modal acceleration" technique, which is superior to basing loads on elastic deflections (modal deflection technique). When the rotor speed varies during a transient solution, the blade stiffness terms are adjusted using Southwell coefficients, which are computed within the program. The NASA interim turbulence model was incorporated into the code for fatigue load computation, however, the capability of analyzing only wind shear or tower shadow, or both, was retained.

Wind Models

The wind models used to compute design loads are classified in Table 1. Wind models used for limit and fatigue load calculations appear separately. The same large gust model is used in each case (I.2 and II.3). Models II.2, II.3 and II.4 will be described in this section. The other models appearing in the table are self-explanatory.

MEAN WIND VARIATIONS - These variations produce shifts in mean load levels which must be considered as fatigue cycles. For example, if the machine is

operating in a 20 mph wind and during 10 minutes the wind shifts to 30 mph and returns to 20 mph, a fatigue cycle results from the difference in load levels at 20 and 30 mph. The load shift, which can be viewed as a "DC" phenomenon, was dubbed a Type IIA load. In order to quantify the variation in mean wind speed, 4 months of data taken at Amarillo, TX by PNL-Battelle was statistically analyzed. Figure 3 outlines the analysis and the results. In addition to mean wind shift statistics, the data was used to compute the number of start-stop cycles that would be experienced by a MOD-5A. It might be added that the yearly wind speed distribution at Amarillo is quite similar to the specification in the MOD-5A Statement of Work.

LARGE GUSTS - Figure 4 summarizes the large gust model used for the MOD-5A design. The MOD-5A Statement of Work wind PSD specification was integrated to determine the root mean square gust value. The cut-off frequency of .02 Hz, used in the integration, was based on a spatial coherence model developed during MOD-2, and used in conjunction with the MOD-5A rotor diameter. The relevant formula appears below:

$$COH = \exp(-fxdKy)$$

where:

- f = cut-off frequency (Hz)
- x = fraction of rotor disc for which the coherence is sought. A value of 1.0 (or the whole disc) was used.
- d = rotor diameter (meters)
- Ky = .37 - .005V, V = wind speed (m/s)

Gusts having a coherence equal to or greater than 0.50 were conservatively treated as rotor encompassing gusts. This formula leads to a cut-off frequency of .018 Hz at 25 mph and .022 Hz at 50 mph. An average of .02 Hz was used for all wind speeds. This cut-off frequency implies an average gust period of 50 seconds, which is supported by MOD-2 test measurements discussed in the verification section of this paper. A Rayleigh distribution was selected for the gust amplitudes on the basis of PNL-Battelle's "Gust-0" measurements reported in PNL 3138. The gust model in Figure 4 is used to compute both fatigue loads and limit loads. It will be shown that MOD-2 loads data supports the gust amplitudes we have used.

LOCAL TURBULENCE - Gusts smaller than the rotor diameter produce variations in the apparent wind speed experienced by the rotating blades at harmonics of the rotor speed. The situation is illustrated in Figure 5. This harmonic forcing produces fatigue loads which occur every rotor cycle. Measurements and data analysis conducted by PNL-Battelle identified and began to quantify the magnitudes of these turbulent inputs. NASA developed an "Interim Turbulence Model" from this data, which conveniently expresses the root mean square values of the harmonic forcing for rotors of different sizes. GE adopted NASA's model and extended it to include gust probabilities. The formulas are summarized in Table 2. GE assumed the probability distribution of the random harmonic coefficients was Rayleigh, as would be the case for a narrow-band process. The Rayleigh assumption also seems to be supported by the ratios of 99.9th percentile to 50th percentile loads generally found in flap bending moment test data. Correlation of this turbulence model with MOD-1 loads appears in the verification section of this paper.

Load Statistics

Fatigue loads for the MOD-5A were expressed as probability distributions (or histograms) to be applied for the 30-year life of the machine. This section describes the methodology used in deriving the fatigue load statistics. Fatigue loads were segregated into three categories, shown in Figure 6; the same categories used in previous wind turbine generator programs. The Type I loads represent the alternating loads, which occur at 1 or 2P (where P stands for "per revolution"). For design purposes, all load components were conservatively assigned a 2P occurrence rate. The local turbulence model was used to derive Type I loads. The Type II loads stem from gusts, that cause a shift in mean load during the gust. This mean shift, and the normally occurring alternating loads were used to compute a cycle of fatigue loading for each gust occurrence. The large gust model was used to compute Type II loads. Similar Type IIA loads, which stem from longer mean wind speed variations, are not shown in the figure. The Type III loads represent the "ground to air to ground" cycle and have a frequency

of occurrence equal to the number of start-stop cycles. Type III loads were computed from the delta loads between normal operation, through shutdown, to the parked state. Note that shutdown transients can produce wider deltas in some load components than simply considering the normal operating and parked conditions. The number of Type I, II, IIA, and III cycles expected over 30 years are 3.5×10^8 , 1.4×10^7 , 1.5×10^6 and 35,000, respectively.

The first step in determining the life cycle fatigue loads was to obtain the mean wind statistics of the site. The wind specification in the Statement of Work was used for MOD-5A. The operation of the wind turbine was separated into discrete wind bins, as illustrated in Figure 7. The total number of Type I cycles, which was based on the number of rotor cycles, and Type II cycles, which was based on the number of gusts, were computed for each bin.

In the second step, mean and alternating steady-state loads were computed from cut-in to cut-out speeds, using TRAC. The wind speeds analyzed did not necessarily correspond to the bin mean wind speeds; instead a sufficient number of wind speeds was chosen to construct smooth curves of load versus wind velocity. In this way, the data could be applied to wind sites other than the one selected. The steady-state loads were computed using the root mean square wind speed harmonic variations given by the NASA Interim Turbulence Model. The third step determined the distribution of Type I loads for each bin. First the steady-state loads data were converted to 50th percentile values on the basis of a Rayleigh distribution. Data measurements from existing wind turbines indicated that Type I loads were well fitted by a log-normal distribution and so this distribution was used to compute loads at other percentiles. The slope of the distribution was based on existing teetered rotor test data. It is believed that the log-normal distribution stems from the sum of a constant (or deterministic) load level and stochastic loads with a Rayleigh distribution. This premise was supported by the MOD-1 fatigue load correlation study reported in the subsequent section, wherein loads were computed for various turbulence amplitude percentiles and were compared to measured values. Both the measurements and

predictions appeared to be log-normal.

In the fourth step, of Figure 7, the procedures used to obtain Type II and Type IIA loads are summarized. A probability distribution of gust amplitude was constructed on the basis of the wind turbulence model. Mean and alternating loads were used to determine the Type I' loads corresponding to a sufficient number of discrete gust amplitudes. The load probabilities were equal to the gust probabilities from which they were derived. The zeroth percentile load (no gust) was equal to the steady-state, 50th percentile load. Note that the Type II load distribution was not assumed to follow any prescribed probability law; instead it was constructed directly from the wind turbulence model and associated response load. Type II calculations were further refined to account for load amplification during a gust, which is caused by the dynamics of the control system.

Type III loads were determined from the differential load encountered in the transition between normal operation and the parked state.

Finally, in the sixth step, composite fatigue histograms were constructed from all the data. These histograms define the total fatigue loading that is projected to occur over 30 years. The cyclic loads are presented in the form of a histogram as shown, or equivalently as a cumulative probability. These loads, along with statistics of the corresponding mean loads, were supplied to the designers. The procedure was computerized, for rapid turnaround and to allow life cycle loading for various wind sites to be generated with little effort.

VERIFICATION OF CODES AND MODELS

The GETSS code was correlated with MOD-0 data supplied by NASA during the MOD-1 program and during the conceptual design of the MOD-5A. These validation results will not be repeated here. Rather, this section focuses on substantiating the wind models that have been adopted and the loads predicted by the TRAC code. Specifically, it will cover shutdown transients, Type I load probability

distributions and Type II loads in the subsequent paragraphs.

Shutdown testing performed during the MOD-1 check-out was simulated using the TRAC code. Figure 8 shows a typical simulation, in which rotor speed, pitch angle, and blade flap bending moment at .35R are plotted versus time. Following about 3 seconds of steady-state operation at 25 rpm, the blades were feathered at 8°/sec for 1.5 seconds followed by a 2°/sec pitch rate for the remainder of the shutdown. (The dual feather rate was used on MOD-1 to guard against high loads). The time histories show that the rotor speed decreased continuously after feather, while the flap bending moment reached a peak at about 5 seconds. Similar analyses were conducted for shutdowns from other initial rotor speeds and the peak flap bending loads were recorded. Figure 9 compares theoretically predicted loads with test measurements made at two blade stations. Here, peak moments were plotted against the rotor speed at which the shutdown was initiated. There was excellent agreement between the test and the theory.

Probability distributions of MOD-1 flap-bending moments measured at three blade radial stations are compared with theoretical predictions in Figure 10. These represent Type I cyclic (1/2 peak-peak) loads. A band of measured data is shown along with discrete test points taken on a typical day of operation. The theoretical loads were computed using NASA's Interim Turbulence Model with the TRAC code. Points at three percentiles were generated by ascribing turbulence disturbance amplitudes according to a Rayleigh distribution. Tower shadow was also included in the model. The results indicated excellent agreement between test and theory at mid-span, while predictions were at the top and bottom of test scatter for outboard and inboard locations, respectively. In view of the contingency factors of 15-25%, which were applied to all MOD-5A load predictions, the turbulence model was considered to be satisfactory for design purposes.

Type II loads were extracted from MOD-2 data tapes supplied by NASA. Occurrences were counted according to positive slope crossings of the mean

load versus time. Figure 3 shows the similar procedure, used for wind data. Figure 11 contains a table of the frequency of Type II load occurrences along with the number of wind speed shifts. Note that there are more cycles of the wind speed point measurement (81.9/hr.) than of the loads (55-61/hr.), which makes sense because all the shifts in wind speed may not be spatially large enough to cause a change in mean rotor loads. Below the table, a scattergram of Type II load magnitude is plotted against load period. Higher loads correspond to higher periods, as would be expected because the large rotor enveloping gusts have longer periods. About a 50 second period, or more, was needed to produce peak load levels. The average frequency of MOD-2 loads (55-61/hr.) agreed well with what was modelled for the MOD-5A (65/hr.). If anything, the MOD-5A would be expected to have a lower frequency because of its increased size, so this analysis was slightly conservative.

Type II load probability distributions are plotted in Figure 12. MOD-5A predictions for similar wind conditions are also shown. The MOD-5A predictions were in line with the scaled test data, if not somewhat conservative. This analysis provided confidence in the modelling of Type II loads on the MOD-5A.

MOD-5A DESIGN LOADS

System Dynamic Model

The natural modes and frequencies were calculated from a model of the MOD-5A system. The dynamic mathematical model was made up of models of each substructure, which were unified by the stiffness coupling method of modal synthesis. The MOD-5A wind turbine substructures and their coupling interfaces are shown in Figure 13. The substructures were the rotor, the yoke and rotor support, the bedplate and nacelle and their associated hardware, and the tower.

The natural modes and frequencies of each substructure, except the blade, were calculated using NASTRAN or a similar finite element program. The blade modes and frequencies were determined using a proprietary GE program called STRAP (Static Row Analysis Program). STRAP is a finite element

beam modelling program that includes the stiffening effects of centrifugal forces.

The stiffness links used to unify the substructures were derived as follows:

- o Rotor to Yoke - The links were derived from stiffness data obtained from the manufacturer of the teeter bearing. The teeter bearing is elastomeric and has stiffness in all 6 degrees of freedom.
- o Low Speed Shaft to Bedplate - The links were calculated by inverting a bedplate flexibility matrix obtained from detailed NASTRAN load cases.
- o Bedplate to Tower - The link was derived from manufacturer's data on the yaw bearing and yaw hydraulics, and from the structural design of the upper yaw housing (the lower yaw housing was included in the tower finite element model). A scalar spring element was created from yaw bearing stiffnesses in 5 degrees of freedom and yaw brake stiffness (or yaw hydraulic stiffness depending on the case investigated) in the yaw degree of freedom. This scalar spring was then added in series with a beam model of the upper yaw housing.

SCAMP (Stiffness Coupling Approach Modal-synthesis Program), a proprietary GE computer program, unified the substructures. This modal synthesis method has been used extensively at the General Electric Space Division for spacecraft analysis and was also successfully used in the MOD-1 program. The method uses the free substructure vibration modes and frequencies to determine the modes of the entire system. These substructures, as defined by the stiffness coupling method, have no common degrees of freedom and are coupled together by the stiffness links that relate the free attachment coordinates of the substructures. Details of the method are documented in Reference 3.

The system modes and frequencies were calculated with the blades in both the vertical and horizontal positions. Typical mode shapes with the rotor in a vertical position are shown in Figure 14. The drive train and teetering modes are simply rigid body rotations of the rotor about the drive shaft and teeter pin, with little or no motion of the remaining system elements. The fundamental tower bending mode, shown for the direction normal to the axis of rotation, exhibits a small amount of yaw rotation caused by the offset center of gravity of

the nacelle. The tower bending mode in the direction of the drive shaft axis is not shown, but it has nearly the same natural frequency, and considerably more blade elastic deflection in the softer flapwise direction. The final elastic mode shape displays collective flapwise bending of the blades. The mode shape plots are used to provide insight into the response of the system.

Table 3 contains a summary of the system natural frequencies for the baseline design. The calculations were made with the blades in vertical and horizontal positions at 13.8 and 16.8 rpm. Frequencies are shown in Hz and P. The numbers in parentheses denote P values at the 13.8 rpm. The last column earmarks the harmonics that should be avoided in each mode. E stands for even, and O, for odd. For example, fixed system modes of the tower must avoid even integers of rotor speed with a two bladed rotor, while rotor cyclic modes must avoid odd integers. Figure 15 depicts frequency placement of the MOD-5A graphically. The hatched areas indicate frequency ranges that should be avoided, to preclude resonant excitation. Symbols connected by horizontal lines indicate that the frequency changes in going from a vertical to horizontal blade position.

All system frequencies are well placed with the possible exception of the first flap collective which is at 4.2P. The blade design, however, is compatible with the loads predicted for this blade. Furthermore, dominant blade fatigue stresses were due to chord bending loads which are not effected by this frequency. There is still reason for concern, though, because of the uncertainty in some variables used in the load calculations. The variable most in question is the amount of 4P turbulence in the wind at the chosen site. The loads would be sensitive to this turbulence, since the blade resonance is near the excitation frequency. To eliminate this risk, methods to raise or lower the flapwise frequency were investigated near the end of final design. Three feasible avenues were identified:

1. Structural modification - (blade thickness and/or chord).
2. Addition of ballast weight to the outboard blade (the earlier, heavier,

partial-span-control configuration had a desirable 3P frequency, which increased to the present 4.2P when lighter weight ailerons were substituted in their place).

3. Change of operating RPM (this could be done in the field on the MOD-5A because of the variable-speed-generator).

Were the MOD-5A to be built, it is likely that one of the above modifications would be implemented to minimize risk.

Design Operating Conditions

The MOD-5A loads were based on cut-in and cut-out wind speeds of 14 mph and 60 mph, respectively, at the hub height. Fatigue cycles for 30 years of operation were computed for the MOD-5A Statement of Work Wind Duration Curve. The wind bins used to generate the fatigue data are summarized in Table 4, along with the numbers of Type I, II, and IIA cycles for each bin. Gust and mean wind shift amplitudes at the bin mean wind speeds are contained in Table 5. Gust amplitudes up to and including the 99.9th percentile were used to predict the fatigue loads. The 99.99th percentile gust was used to compute limit loads.

Critical operating conditions used to compute limit loads are summarized in Table 6. The system was designed to withstand the first four conditions without damage. The last case represented an extreme condition, which the MOD-5A could withstand without catastrophic failure such as losing a blade. Table 7 summarizes additional events which were analyzed, but were not critically important for the MOD-5A.

Interfaces Loads

The design loads were calculated at the locations listed in Table 8. A full set of shear and moment loads (V_x , V_y , V_z , M_x , M_y , M_z) were supplied at these points. The sign conventions for the main blade and the fixed system are shown in Figure 16. The coordinate directions lie on principal axes and twist with the cross-sections of the blade airfoil. The dimensions of the system and the locations of the non-blade interfaces are shown in Figure 17.

The interface design loads were specified in 3 sets of tables:

- (1) histograms combining Type I, Type II, and Type IIA fatigue loads (359×10^5 cycles in 30 years)
- (2) Type III fatigue loads (35,000 cycles in 30 years)
- (3) limit loads for each critical operating condition

Because of the volume of this data, only highlights are presented herein.

A sample histogram is displayed in Table 9. Each row corresponds to a bar of the histogram. Columns 1 and 2 provide the number of cycles in and the cumulative probability associated with each bar. The range of cyclic loads for each bar, the bar width, is defined in columns 3 and 4. Columns 5 and 6 are these same dimensional loads divided by the maximum cyclic value, while columns 7 and 8 are similarly non-dimensionalized by the 50th percentile cyclic load at the rated wind speed. The remaining columns provide statistics of the mean, or mid-range, load for each bar of the histogram. Included below the table are the root-mean-cubed value of all cyclic load occurrences and the average mean load for 30 years of operation.

Probability distributions of alternating blade flap bending moments are shown in Figure 18 for three radial stations. The load magnitudes have been divided by the mean flap-bending moment at the rated wind speed, 32 mph, to allow comparison with data from other wind turbines. The curves display a slight increase in slope above the 99.9th percentile that is caused by Type II load occurrences. Type III fatigue levels, indicated by horizontal lines, are slightly greater than the maximum Type I and II values. To lend credence to the predictions, scaled test data from the Boeing MOD-2 and Hamilton Standard SVU2 wind turbines are included on the plot. This data suggests that MOD-5A predictions are appropriate, and even somewhat conservative. Figure 19 contains probability distributions of the alternating blade chord bending moment, normalized by the one-g moments. Here the loads are dominated by gravity, so there is only a slight increase between the 50th and 99.99th percentile. This trend was also true for MOD-2 test results, which are not shown.

Tower fatigue bending moment distributions are plotted in Figure 20. In this case the alternating moments at the base of the tower have been normalized by the mean bending moment created by the rotor aerodynamic thrust at rated wind speed. The alternating thrust moment (M_y) is far more sensitive to gusts than M_z , which accounts for the differences in the probability distributions. The MOD-5A predictions appear to be consistent with MOD-2 data, which is also included in the figure. The earlier MOD-2 data, in the upper curve, was taken before improvements were made to the control system, so it exhibits higher loads.

Vibratory rotor torques are plotted in Figure 21. Alternating torque levels, and likewise power levels, are below 10% of rated torque for over 90% of the operating time. The pronounced increase in load above the 98th percentile is due to Type II gusts and shifts in mean wind speed. Curves of yaw bearing moments and drive torque are included in Figure 22.

Normalized blade limit loads are summarized in Figure 23. The flap bending moments are from 2.25-3 times the mean moment at rated wind speed. Chord bending moments are about 2 g's at the root, where gravitational effects are greatest. They increase to about 9 g's at the tip, where the aileron drag forces far exceed the one g loads. Normalized fixed system limit loads are reported at selected interfaces in Table 10.

Selected Component Loads

Ailerons

The coordinate system used to define loads on the aileron is illustrated in Figure 24. Again, the axes are fixed to the structure and rotate with the aileron. Unlike other load components, local aileron loads are defined by running shears (V_x , V_y , V_z in lb/ft) and a running hinge moment (M_h in ft-lb/ft) as a function of the blade span, from the start of the aileron at .60R to the outmost section at .99R. Load/unit span rather than stress resultants were used, because this allowed the hinge locations and their end conditions to be varied during the design without changing the external loads. Furthermore, aerodynamic and inertial loads

are specified separately, so that the inertia loads could be made consistent with the actual final design weight by using appropriate g factors.

Operational limit loads appear in Figures 25 and 26. The airloads were based on an aileron deflection of -45° , which is greater than would be needed to stop the machine. Thus, these loads are somewhat greater than would be experienced with the MOD-5A, which has force-limited actuators to prevent excessive aileron angles during critical conditions. In addition to the overspeed-shutdown, the ailerons were also designed to withstand a 130 mph hurricane wind while parked. With the exception of inboard pitching moments, the hurricane condition is less critical.

Fatigue loads have been defined by mean and alternating load components. The aerodynamic mean loads are shown in Figure 27. These loads were applied for all fatigue cycles, while the alternating loads noted in the figure caption were assigned probability distributions similar to the main blade. Alternating inertia loads (not shown) are on the order of one g, while the dominant steady load is due to centrifugal force.

Because the design for the ailerons was not as mature as other system components, these structural loads were developed conservatively. This approach was adopted to ensure a safe configuration on the first design iteration.

Blades

Stress resultants acting on the main blade structure were defined at the interfaces quoted in Table 8. These loads, which were discussed earlier, were used to size the primary structure of the blade. In this section, blade internal and external pressure distributions are addressed. These produce membrane and plate bending stresses.

The pressure loads on the blade are closely related to blade venting, because venting influences the internal pressure. A blade sealed against the atmosphere would experience excessive pressure loads. Therefore, a vented design was adopted. Inboard and outboard vents were incorporated, because they minimize pressure loads and promote a

sanitary environment inside the blade. The trailing edge section, which extends from the blade root to the ailerons at .60R, is vented at .10R and .60R. The two forward cells of the blade cross-section are vented at .10R and the tip (1.0R).

The internal pressure in the cavities of the blade at the non-dimensional spanwise station, x , is given by:

$$p_g = p_i - p_o = q_t \left(x^2 - \frac{1}{2} (x_1^2 + x_2^2) \right)$$

where,

$$q_t = \frac{1}{2} \rho V_t^2$$

ρ = air density

V_t = tip speed

x_1 and x_2 are the non-dimensional spanwise locations of the vents

p_i = absolute pressure in the cavity at station x

p_o = vent pressure (taken to be atmospheric)

p_g = gage pressure within the cavity

The external pressures on the blade surface are obtained from the airfoil pressure distribution. Figure 28 contains plots of airfoil pressure coefficient (C_p) vs the chordwise location for critical operating conditions. This data is furnished at three spanwise locations, $x = .25, .55,$ and $.95$. Dimensional gage pressures on the exterior surfaces are given by

$$p_g = p_e - p_o = q_t x^2 C_p$$

The external pressures were used with the previously defined internal pressures in the blade structural analysis. The following pressures for the parked blade in hurricane conditions were also analyzed:

internal gage pressure = 0

external gage pressure = $1/2 \rho V^2 C_{ph}$

where:

ρ = air density

V = wind speed (130 mph)

C_{ph} = 1.0 windward side (constant across surface)

= .40 leeward side (constant across surface)

These values of C_{ph} correspond to a drag coefficient of 1.4. In all the analyses, the pressures defined in this section were multiplied by a contingency factor of 1.15.

Teeter Brakes

Some form of teeter restraint is necessary to prevent impact into hard stops during abnormal operating conditions. Conditions are particularly severe during high wind shutdowns, with a yaw error. Comprehensive parametric studies led to the selection of a two-stage, friction brake system as protection for the rotor, because it introduced the minimum load into the system. The brake schedule is illustrated in Figure 29. During most of the operation, the teeter angle will be less than 2.5° , and the brakes will be totally disengaged. If for any reason the teeter angle exceeds $\pm 2.5^\circ$ the first set of brakes will engage. This brake level can handle all but the most severe conditions. In the very few instances in which the teeter angle exceeds 5° , the full brake force will be applied and maintained and the system will be shut down. Transient dynamic analyses have shown that this brake system will keep operational teeter angles below 6° . When parked, the brakes are set at their highest level, to protect the system from dissymmetries in the oncoming wind. During startup, the high brake level is maintained until the rotor speed exceeds 6 rpm, then the schedule illustrated in Figure 29 is adopted for the remaining operation.

The supporting structure for the brake system is designed to 1.15 times the maximum brake level, or 2.76×10^6 ft.-lb.

Gearbox/Drivetrain

Special considerations were necessary in developing the fatigue spectrum for the gearbox design. Because the gear teeth are continually cycling between full load and no load, the absolute value of the torque governs the fatigue design. Therefore, a probability distribution of the sum of mean plus alternating rotor torques was developed. This distribution is referred to as the gearbox torque duty cycle.

The gearbox torque duty cycle is illustrated in Figure 30. Torque levels were normalized by the

rated value. The curves depict the load level probability of a sample taken at random during the 30 years of operation. Because certain of the fatigue loads, such as that caused by wind shear, reach a peak magnitude at a preferred rotor azimuth, the gears that are always in contact at a given rotor position (upper curve) must be distinguished from those that are not. In the first case the design is driven by the most highly loaded tooth, while in the second case the design takes advantage of the fact that load peaks are distributed among the many teeth.

The operation of the cycloconverter limits the maximum torque during normal operation to less than 1.3 times the rated value. Hence, the probability distributions may be truncated at this level for the purposes of gearbox fatigue design. The gearbox can withstand two times the rated torque as an extreme overload. This torque is much greater than the maximum anticipated torque for the system.

Other drive train components, such as shafting, used the interface torque loads which were presented in Figure 21 and Table 10.

STATISTICAL ANALYSIS OF MEASURED LOADS

In past NASA/DOE wind turbine programs, fatigue load test data has been reduced using a Type I statistical analysis. Specifically, digitized waveforms are scanned and a maximum and minimum value are found during each rotor cycle. The maximum/minimum pairs are then used to compute mean and alternating loads for each rotor cycle. The alternating loads, in turn, are ordered from lowest to highest, and a probability distribution is thereby established. Since each rotor cycle is analyzed independently, the distributions found are consistent with the definition of Type I loads given earlier.

It is generally agreed that a Type I analysis alone is insufficient to predict fatigue damage for complex stress-strain time histories. Dowling (Reference 4) accesses various methods for counting fatigue cycles from irregular waveforms. He concluded that the "rainflow" or closely related "range-pair" method provides the best estimate of

fatigue damage. In the rainflow technique, the maximum from one rotor cycle may combine with the minimum of another to yield a fatigue occurrence. The rainflow method, detailed in Reference 4, has been coded at General Electric for application to WTG data tapes.

Figure 31 compares MOD-2 blade flap bending data which has been processed by both the rainflow and standard Type I analysis techniques. Also shown are the shifts in mean loads assigned to Type II gust response. It is interesting to note that at the high probabilities, the rainflow loads are approximately equal to the Type I plus Type II amplitudes. In any event, it is clear that loads evaluation from Type I data alone can lead to unconservative conclusions. While existing wind statistics are insufficient to enable rainflow counting of theoretically predicted loads, the problem has been addressed at least in part on the MOD-5A by including Type II, Type IIA, and Type III cycles in the fatigue design load histograms. Reference to the combined Type I, II, and IIA distributions, in Figure 18, indicates a trend similar to the rainflow data.

CONCLUDING REMARKS

The following conclusions are drawn from this work:

1. Methods for the accurate prediction of transient limit loads are in place.
2. Test data supports the methods used for fatigue load prediction on the MOD-5A. It is important combine fatigue cycles due to local turbulence with those due to global changes in mean wind speed. Statistical techniques to accomplish this have been presented and demonstrated in this paper. Additional research on local turbulence would be beneficial to increase confidence in and further quantify the model used. In particular, site-to-site differences, the spatial distribution of turbulence, and the phasing of turbulence harmonics could be profitably explored.
3. The rainflow method should be used to analyze wind turbine fatigue loads test data, in favor of current techniques.

REFERENCES

1. Pijawka, W.C., "Status of DOE/NASA MOD-5A Wind Turbine Project", to be published in the proceedings of the DOE/NASA Workshop on Horizontal Axis Wind Turbine Technology, held May 1984.
2. MOD-1 WIND TURBINE GENERATOR ANALYSIS AND DESIGN REPORT, Vol. 1, DOE/NASA/0058-79/2, NASA CR-159495, May 1979.
3. Kubar, E.J., "Selected System Modes Using the Dynamic Transformation with Modal Synthesis", Shock and Vibration Bulletin, August 1974, pp. 91-102.
4. Dowling, N.E., "Fatigue Failure Predictions for Complicated Stress-Strain Time Histories", Journal of Materials, JMLSA, Vol. 7, No. 1, March 1972, pp. 71-87.

ACKNOWLEDGEMENTS

This work was performed under contract DEN 3-153 with NASA-Lewis Research Center. The authors would like to express their particular thanks to David A. Spera and Timothy L. Sullivan of the NASA Wind Energy Project Office for their support throughout the program.

Table 1 Classification of Wind Models

I WIND MODELS FOR LIMIT LOADS	
1.	Hurricane z - per MOD-5A SOW
2.	Large Rotor Enveloping Gusts (99.99%ile)
3.	Yaw Misalignments
4.	Wind Shear - per MOD-5A SOW
II WIND MODELS FOR FATIGUE LOADS	
1.	Yearly Mean Wind Distribution - Weibull per MOD-5A SOW
2.	Mean Wind Variations
3.	Large Rotor Enveloping Gusts (Up to 99.9%ile)
	Note: Same as Model I.2.
4.	Local Turbulence - per NASA Interim Turbulence Model
5.	Tower Shadow - per Potential Flow Theory for Upwind Rotor
6.	Wind Shear - per MOD-5A SOW

Table 2 Formulas for the Wind Turbulence Model

$$V_{TURB}(x, \phi, P) = \sum_{i=1}^6 V_{TMS_i} \cos i(\phi + \theta_i) \sqrt{2 \ln(1-P)}$$

where

- V_{TURB} = Wind speed variation due to turbulence
- x = Non-dimensional blade spanwise station
- P = Probability that turbulence input is less than or equal to V_{TURB}
- V_{TMS_i} = RMS of turbulence velocity at the i^{th} rotor harmonic per NASA Interim Turbulence Model
- i = Rotor harmonic
- ϕ = Rotor blade angular position
- θ_i = Phase of i^{th} harmonic (set = constant for MOD-5A analysis - theoretically random)

$$V_{TMS_i} = \frac{\Delta V_s}{2 \sqrt{2}} \frac{1}{i + .75}$$

ΔV_s = Difference in wind speed between the highest and lowest points in the rotor disc as predicted by the wind shear model in the MOD-5A SOW.

Table 3 MOD-5A System Natural Frequencies

	VERTICAL		HORIZONTAL		HARMONICS TO AVOID
	Hz	P	Hz	P	
1) DRIVE TRAIN	0.		0.		E
2) TOWER	.28 (.23)	1. (1.)	.28 (.23)	1. (1.)	-
3) TOWER Z	.340	1.21 (1.48)	.340	1.21 (1.48)	E
4) TOWER Y	.341	1.22 (1.48)	.344	1.23 (1.50)	E
5) FLAP COLLECTIVE	1.17	4.18 (5.00)	1.17	4.18 (5.00)	E
6) DRIVE TRAIN	1.33	4.75 (5.78)	1.33	4.75 (5.78)	E
7) CHORD CYCLIC	1.40	5.71 (6.96)	1.84	6.57 (8.00)	O
8) FLAP CYCLIC	2.37	8.46 (10.3)	2.3	8.25 (9.96)	O
9) TOWER C-L TORSION	2.24	8.00 (9.74)	1.80	6.43 (7.83)	E
10) TOWER Z (2nd)	3.03	10.8 (13.2)	3.23	11.7 (14.0)	E
11) FLAP COLLECTIVE (2nd)	3.14	11.2 (13.6)	3.11	11.1 (13.4)	E
12) CHORD COLLECTIVE	4.08	14.6 (17.7)	4.08	14.6 (17.7)	E
13) TOWER Y (2nd)	4.18	14.9 (18.2)	4.18	14.9 (18.2)	E
14) FLAP CYCLIC (2nd)	4.56	16.3 (19.7)	4.56	16.3 (19.7)	O

* Per rev nos. in parenthesis are for 13.8 rpm
 E = even
 O = odd

Table 4 MOD-5A Wind Bin and Fatigue Cycle Summary

BIN	MID-POINT (MPH @ HUB)	RANGE (MPH)	NORMIN. RPH	NO. OF FATIGUE CYCLES PER 30 YEARS			
				TYPE I	TYPE II	TYPE IIA	TYPE III
1	16.5	14 - 19	13.8	92.7E6	4.05E6	.365E6	---
2	21.5	19 - 24	13.8	93.5E6	4.08E6	.368E6	---
3	26.0	24 - 28	16.8	71.3E6	2.55E6	.230E6	---
4	31.5	28 - 35	16.8	66.5E6	2.37E6	.214E6	---
5	40.0	35 - 45	16.8	19.2E6	.68E6	.062E6	---
6	52.5	45 - 60	16.8	.86E6	.03E6	2800.	---
TOTAL				344.E6	13.8E6	1.24E6	35000.

NOTES: FATIGUE CYCLES BASED ON .96 AVAILABILITY
TYPE I CYCLES BASED ON 2P OCCURRENCE RATE

Table 5a Amplitude of Large Rotor Enveloping Gusts Used for Type II and Limit Loads

BIN	V _{MEAN} (MPH)	ΔV = TOTAL GUST MAGNITUDE (MPH) FOR S ¹ ILE				
		40%	65%	99%	99.9%	99.99%
1	16.5	1.83	3.60	5.51	6.75	7.79
2	21.5	2.39	4.89	7.18	7.79	10.2
3	26.0	2.89	5.87	8.68	10.6	12.1
4	31.5	3.50	6.87	10.5	12.9	14.9
5	40.0	4.45	8.73	13.4	16.4	18.9
6	52.5	5.84	11.45	17.5	21.5	24.8

$\Delta V = 11 V_{MEAN} \sqrt{-2 \ln(1-P)}$, P = S/100
V RANGE = V_{MIN} TO (V_{MEAN} + ΔV) FOR UPGUSTS
V RANGE = (V_{MEAN} - ΔV) TO V_{MEAN} FOR DOWNGUSTS

Table 5b Amplitudes of Mean Wind Shifts Used for Type IIA Loads

BIN	V _{MEAN} (MPH)	ΔV = S ¹ IFT MAGNITUDE (MPH) FOR S ¹ ILE				
		40%	65%	99%	99.9%	99.99%
1	16.5	1.33	2.6	4.01	4.91	5.69
2	21.5	1.74	3.41	5.22	6.39	7.33
3	26.0	2.10	4.12	6.31	7.73	8.89
4	31.5	2.55	5.00	7.65	9.37	10.8
5	40.0	3.23	6.35	9.71	11.9	13.7
6	52.5	4.25	8.33	12.8	15.6	18.1

$\Delta V = .08 V_{MEAN} \sqrt{-2 \ln(1-P)}$
V RANGE = (V_{MEAN} - ΔV) TO (V_{MEAN} + ΔV) FOR ALL SHIFTS

Table 6 Critical Limit Load Conditions

CONDITION	COMMENTS
1. HURRICANE (130 MPH @ HUB)	TOWER BENDING AND FOUNDATION CRITICAL
2. CONTROL HARDWARE FAILURE (60 MPH, 0° AILERON ANGLE)	INBOARD BLADE/ROTOR CRITICAL
3. 99.99%ILE GUST AT RATED WIND SPEED, 25% OVERSPEED, DESYNCRONIZATION AND SHUTDOWN	OUTBOARD BLADE CRITICAL
4. SHUTDOWN @ CUT-OUT WIND SPEED WITH YAW ERROR	SETS DESIGN REQUIREMENTS FOR YEETER BRAKES
5. 50% OVERSPEED, HIGH WIND ADVERSE AILERON SETTING	SURVIVAL CONDITION, SYSTEM DESIGNED TO PREVENT CATASTROPHIC FAILURE

Table 7 ADDITIONAL TRANSIENT EVENTS ANALYZED

CONDITION	COMMENTS
1. GUSTS/SHUTDOWNS @ WIND SPEEDS OTHER THAN RATED	GUST @ RATED WIND SPEED PRODUCED LARGEST LOADS
2. ONE SET OF ALLIGONS STUCK (I.e. MISMATCH BETWEEN THE 2 BLADES)	<ul style="list-style-type: none"> LOADS NOT CRITICAL DUE TO TEETERING RELIEF SUFFICIENT MOTOR/TOWER CLEARANCES SUFFICIENT BRAKING TORQUE ON ONE BLADE FOR SHUTDOWN
3. 180° SHIFT IN WIND DIRECTION WITHIN 10 SECONDS	LOADS/SHUTDOWNS NOT CRITICAL
4. START UP/SHUTDOWN THROUGH TOWER RESONANCE	MOD-SA CONTROL SYSTEM AVOIDS BUILT UP AT RESONANCE. LOADS NOT CRITICAL.

TABLE 8 SYSTEM INTERFACES

Interface	Location	Comment
1	.GR	
2	.BR	
3	.7BR	
4	.6BR	Main Blade Station
5	.5BR	
6	.4BR	
7	.3BR	
8	.25R	
9	.2BR	
10	.1BR	
11	.OR	
12	Tower Bearing	Rotating System
13	Rotor - CL	Center of Tower Bearing Non-rotating
14	Rotor/Hubcell	
15	Yaw Bearing	
16	Tower 124	(Foot Above ground!)
17	Tower 117	
18	Tower 51	(Tower bruckle)
19	Tower base	
20	Alligons	Load/span from .GR to .9BR

Table 9 Typical Load Histogram Presentation

CUMULATIVE FATIGUE HISTOGRAM OUTPUT											
TOWER BASE NZ											
HALF-RANGE FATIGUE LOADS						CORRESPONDING MID-RANGE LOAD DISTRIBUTION					
NO. CYCLES IN 30 YEARS (TYPES 1+2)	CUM PROB	LOAD LEVFLS	NORMALIZED LOAD LEVELS	LOAD/50% AT RATED	MEAN	STANDARD DEVIATION	MAXIMUM	MINIMUM			
0.	0.	0.	0.	0.	0.	0.	0.	0.	0.	0.	0.
0.	0.	0.178E 06	-0.357E 06	0.03 - 0.07	0.08 - 0.15	0.	0.	0.	0.	0.	0.
0.	0.	0.357E 06	-0.535E 06	0.07 - 0.10	0.15 - 0.23	0.	0.	0.	0.	0.	0.
0.	0.	0.535E 06	-0.713E 06	0.10 - 0.14	0.23 - 0.31	0.	0.	0.	0.	0.	0.
0.	0.	0.713E 06	-0.891E 06	0.14 - 0.17	0.31 - 0.38	0.	0.	0.	0.	0.	0.
0.	0.	0.891E 06	-0.107E 07	0.17 - 0.20	0.38 - 0.46	0.	0.	0.	0.	0.	0.
0.	0.	0.107E 07	-0.125E 07	0.20 - 0.24	0.46 - 0.54	0.	0.	0.	0.	0.	0.
0.	0.	0.125E 07	-0.143E 07	0.24 - 0.27	0.54 - 0.62	0.	0.	0.	0.	0.	0.
0.	0.	0.143E 07	-0.160E 07	0.27 - 0.30	0.62 - 0.69	0.	0.	0.	0.	0.	0.
0.784E 06	0.00213	0.160E 07	-0.178E 07	0.30 - 0.34	0.69 - 0.77	-0.317E 07	0.480E 06	-0.192E 07	-0.335E 07		
0.616E 07	0.01680	0.178E 07	-0.196E 07	0.34 - 0.37	0.77 - 0.85	-0.307E 07	0.574E 06	-0.192E 07	-0.347E 07		
0.171E 08	0.06416	0.196E 07	-0.214E 07	0.37 - 0.41	0.85 - 0.92	-0.295E 07	0.649E 06	-0.192E 07	-0.347E 07		
0.320E 08	0.15338	0.214E 07	-0.232E 07	0.41 - 0.44	0.92 - 1.00	-0.282E 07	0.698E 06	-0.192E 07	-0.347E 07		
0.482E 08	0.28771	0.232E 07	-0.254E 07	0.44 - 0.48	1.00 - 1.10	-0.269E 07	0.733E 06	-0.131E 07	-0.347E 07		
0.390E 08	0.39679	0.254E 07	-0.277E 07	0.48 - 0.53	1.10 - 1.20	-0.248E 07	0.798E 06	-0.457E 06	-0.347E 07		
0.278E 08	0.47380	0.277E 07	-0.300E 07	0.53 - 0.57	1.20 - 1.29	-0.196E 07	0.905E 06	-0.457E 06	-0.347E 07		
0.302E 08	0.55802	0.300E 07	-0.322E 07	0.57 - 0.61	1.29 - 1.39	-0.134E 07	0.743E 06	-0.457E 06	-0.347E 07		
0.377E 08	0.66306	0.322E 07	-0.345E 07	0.61 - 0.66	1.39 - 1.49	-0.105E 07	0.560E 06	-0.457E 06	-0.347E 07		
0.414E 08	0.77622	0.345E 07	-0.368E 07	0.66 - 0.70	1.49 - 1.59	-0.937E 06	0.486E 06	-0.337E 06	-0.347E 07		
0.364E 08	0.87972	0.368E 07	-0.391E 07	0.70 - 0.74	1.59 - 1.69	-0.793E 06	0.441E 06	-0.135E 06	-0.347E 07		
0.228E 08	0.94334	0.391E 07	-0.412E 07	0.74 - 0.78	1.69 - 1.78	-0.703E 06	0.419E 06	-0.158E 06	-0.347E 07		
0.117E 08	0.97882	0.412E 07	-0.436E 07	0.78 - 0.83	1.78 - 1.88	-0.658E 06	0.384E 06	0.364E 06	-0.347E 07		
0.837E 07	0.99074	0.436E 07	-0.459E 07	0.83 - 0.87	1.88 - 1.98	-0.613E 06	0.347E 06	-0.284E 06	-0.347E 07		
0.217E 07	0.99879	0.459E 07	-0.481E 07	0.87 - 0.91	1.98 - 2.08	-0.575E 06	0.308E 06	-0.457E 06	-0.347E 07		
0.787E 06	0.99901	0.481E 07	-0.504E 07	0.91 - 0.96	2.08 - 2.17	-0.569E 06	0.203E 06	-0.457E 06	-0.347E 07		
0.322E 06	0.99990	0.504E 07	-0.527E 07	0.96 - 1.00	2.17 - 2.27	-0.487E 06	0.453E 02	-0.457E 06	-0.457E 06		

TOTAL CYCLES = 0.366E 09

ROOT MEAN CUBED IS 0.322E 07 AVERAGE MEAN IS -0.172E 07

Table 10 Normalized Fixed System Limit Load Summary

CONDITION	ROTOR TORQUE	RESULTANT BENDING / TG	RESULTANT BENDING /	
	RATED TORQUE	ROTOR/HACE-LE	YAW BEARING	
HURRICANE	---	1.0	1.00	2.35
CONTROLS FAILURE ≥ 60 MPH	1.39	1.57	.60	1.91
99.99% GUST @ RATED	1.26	1.44	.60	1.93
SHUTDOWN @ CUT-OUT WITH YAW ERROR	NOT CRITICAL	1.15	1.22	NOT CRITICAL
CYCLOCONVERTER MISAP	1.73	---	---	---

* Normalized by bearing moment due to rotor aerodynamic thrust at rated wind speed.

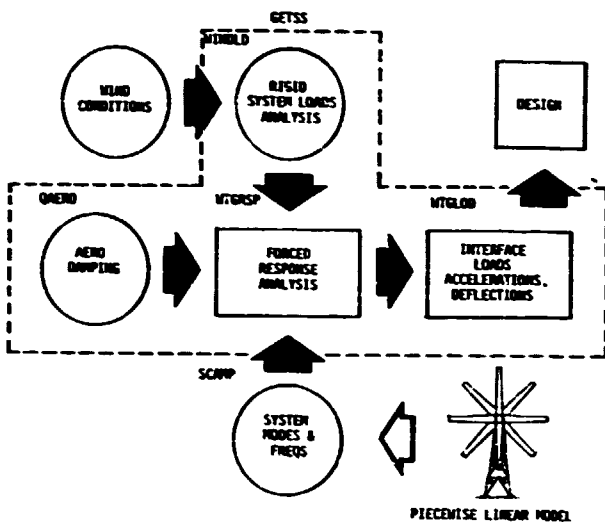


Figure 1. GETSS Analysis Flow

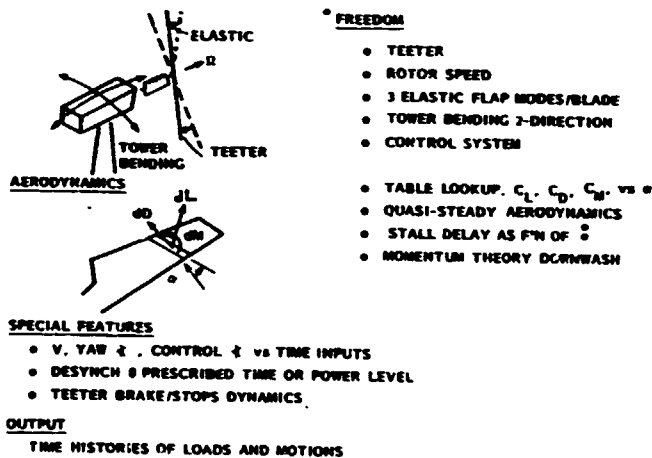


Figure 2. Features of the TRAC Code

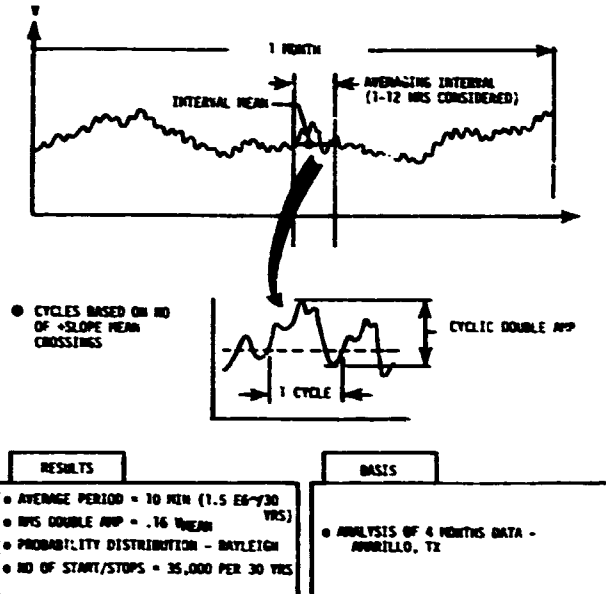


Figure 3. Development of Mean Wind Variation Model

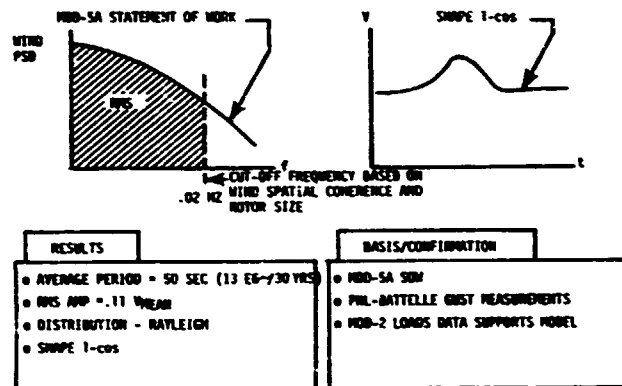


Figure 4. Development of Large Rotor-Enveloping Gust Model

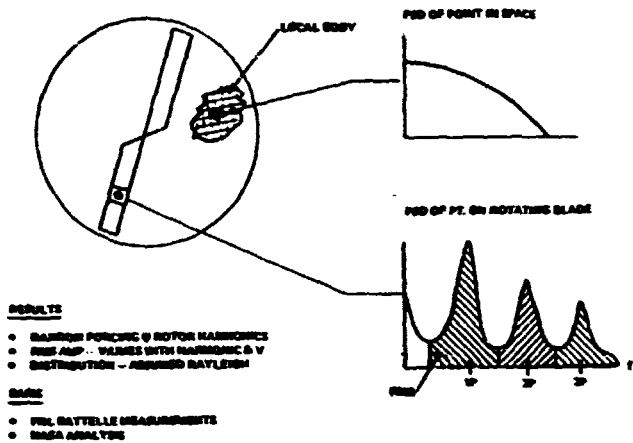
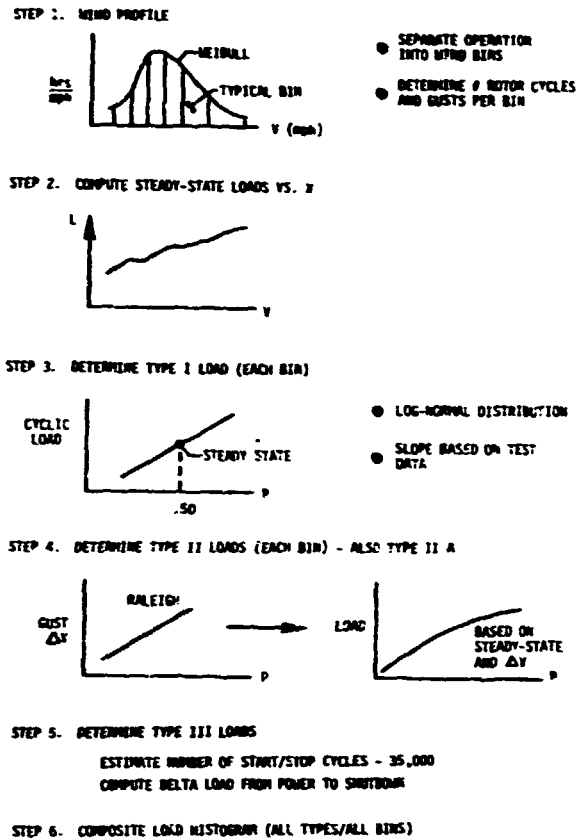


Figure 5. Development of Loca's Turbulence Bin Model



• STATISTICS OF CORRESPONDING MEAN LOADS
 ↓
 TO DESIGNERS

Figure 7. Procedure for Determining Life Cycle Fatigue Loads

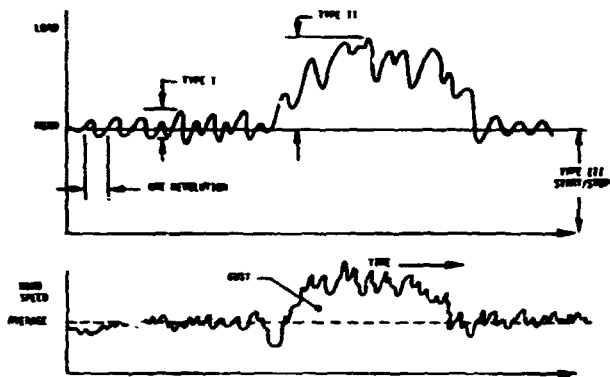


Figure 6. Fatigue Load Types

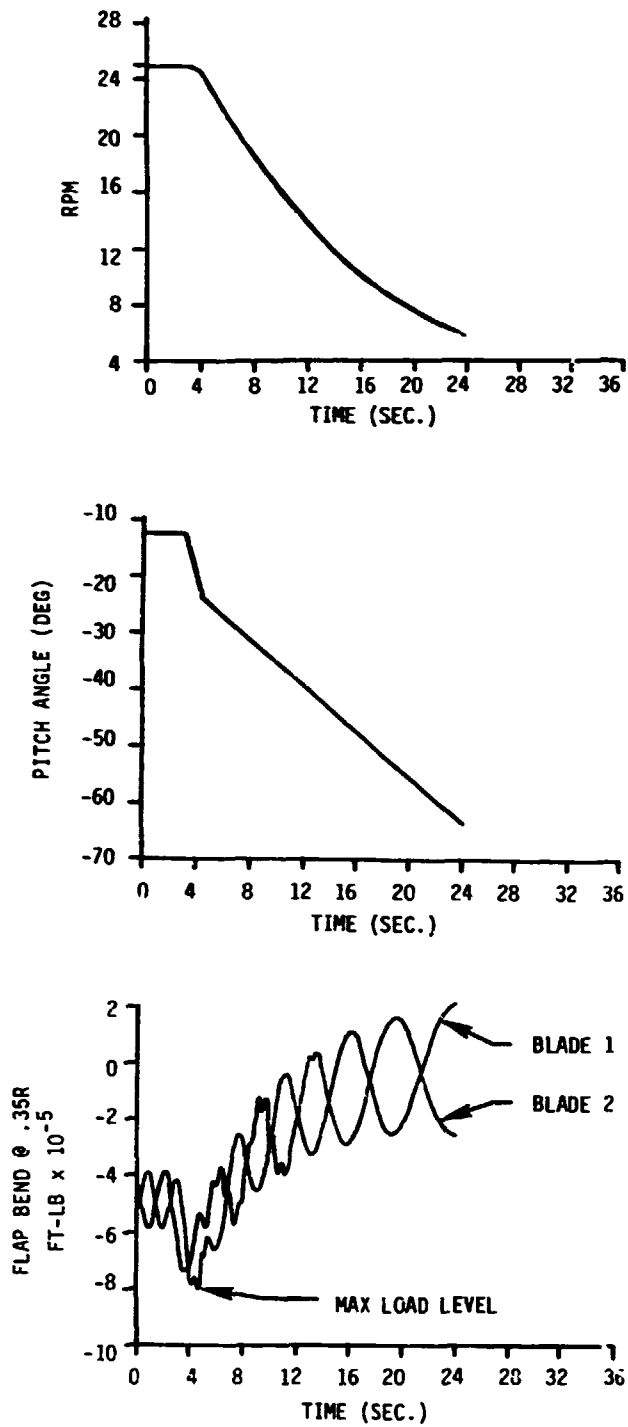


Figure 8. Simulation of MOD-1 Shutdown Using the TRAC Code

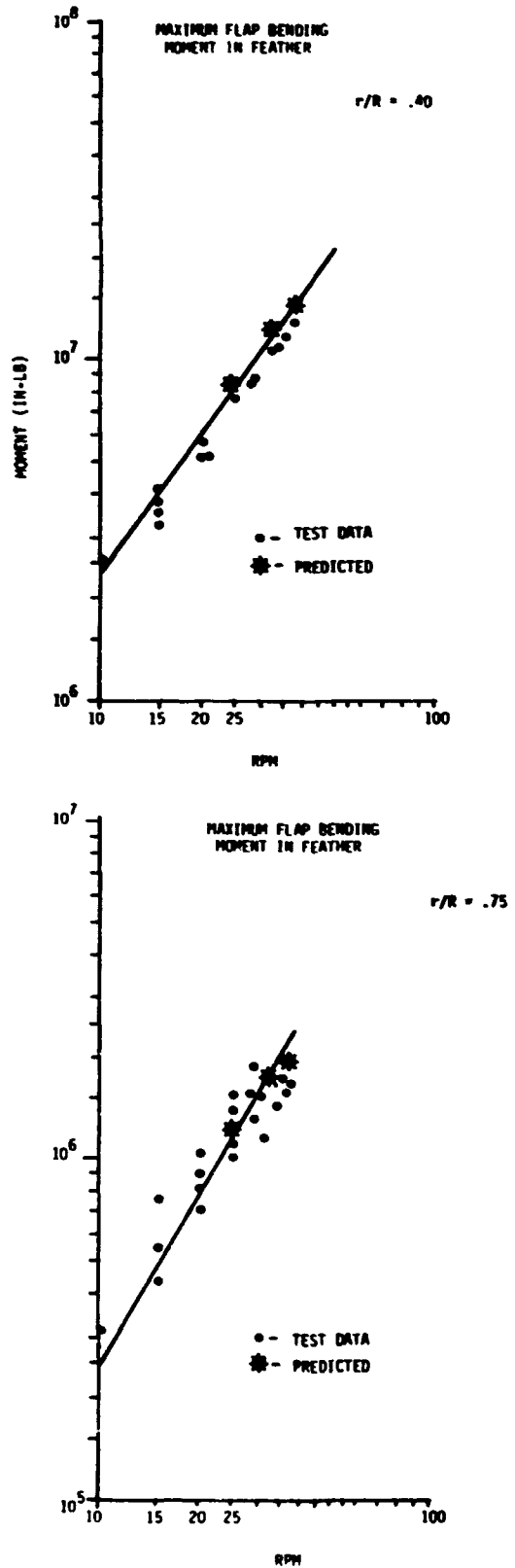


Figure 9. Comparison of MOD-1 Shutdown Test Blade Loads with Theoretical Predictions

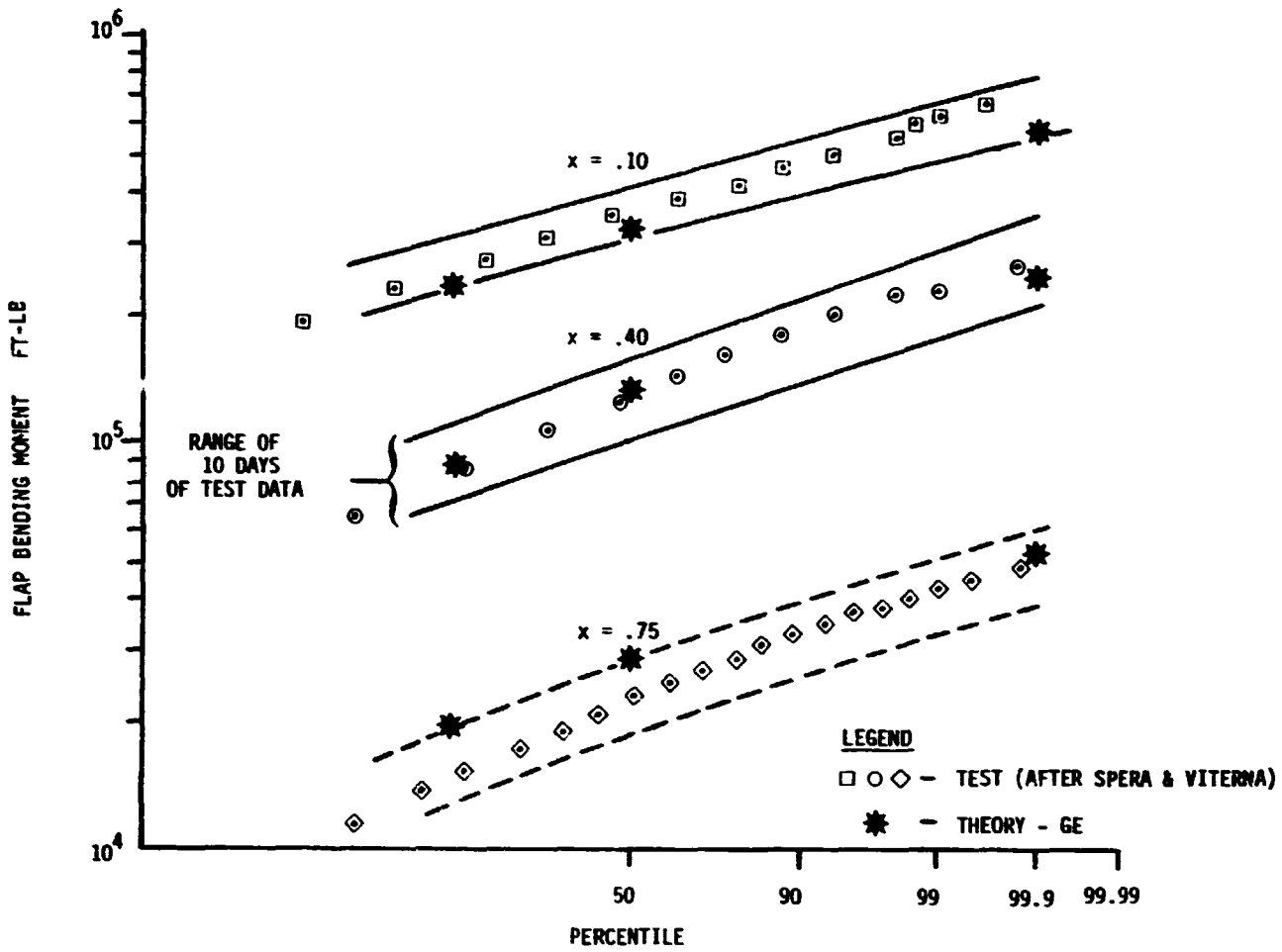


Figure 10. Test/Theory Correlation of MOD-1 Type I Fatigue Loads

HOUR	V @ 195	# CYCLES/HOUR	
		.20R	.65R
1	76	40	63.8
2	81.5	86.5	64.5
3	78.1	46.5	53.1
4	78.1	59.4	87.7
5	95.6	42.1	36.6
AVG	81.9	54.9	61.1

MOD-5A
Prediction
65 Cycles/Hr

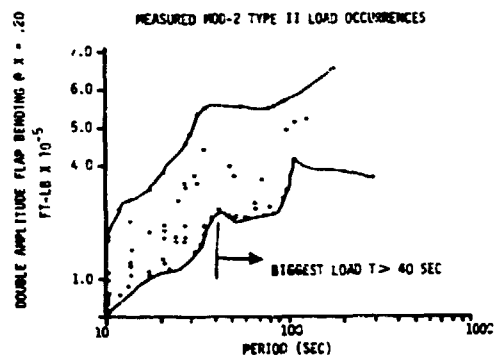


Figure 11. Frequency of Occurrence of MOD-2 Type II Load Measurements

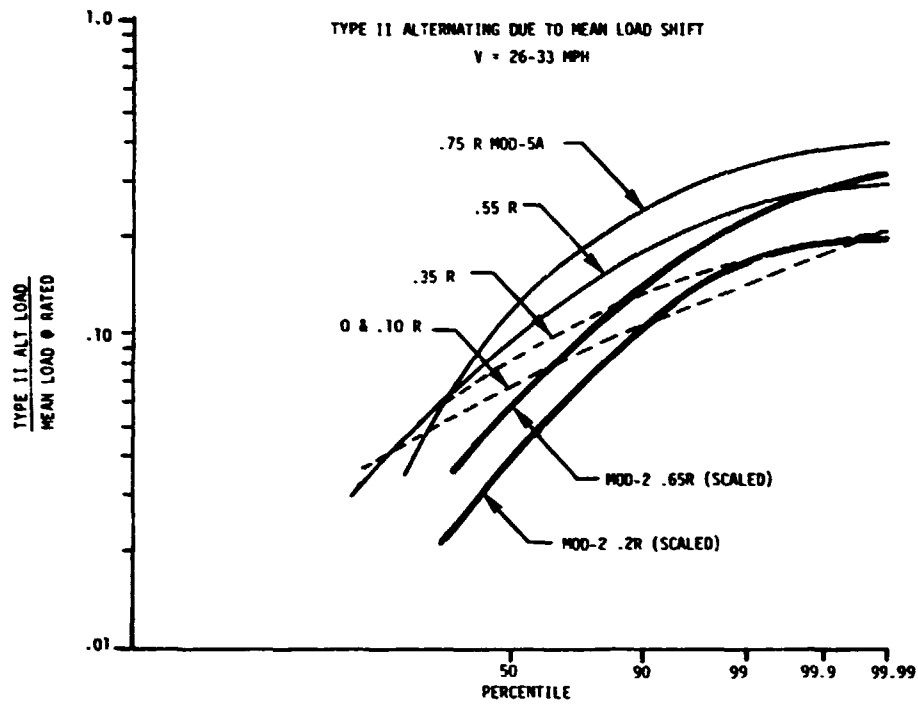


Figure 12. Comparison of MOD-5A Type II Load Predictions with Scaled MOD-2 Measurements

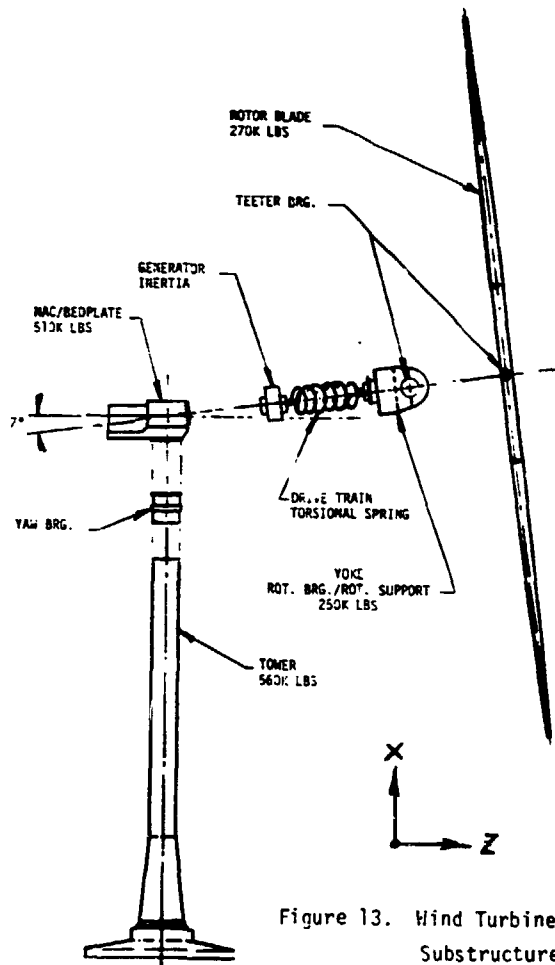


Figure 13. Wind Turbine Model Substructures

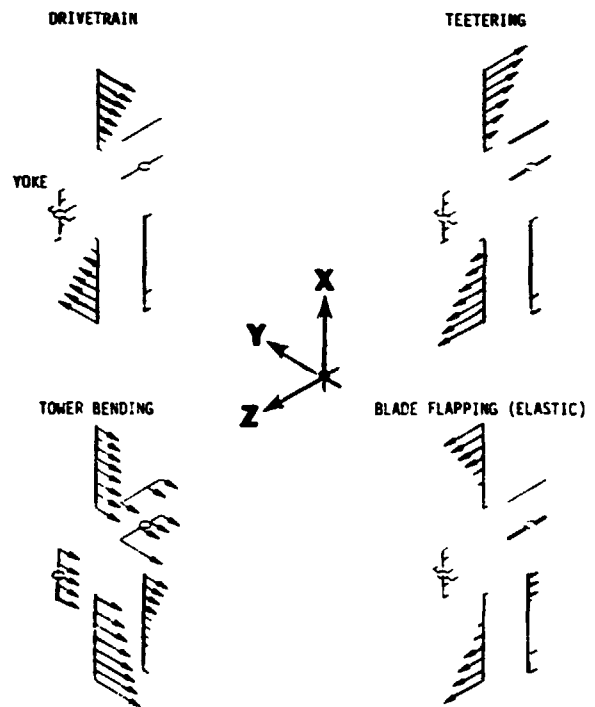


Figure 14. Coupled Mode Shapes

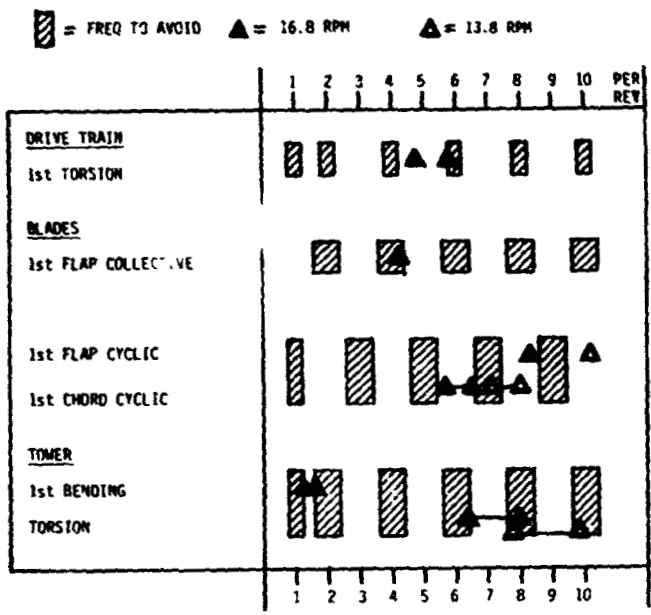


Figure 15. MOD-5A Natural Frequency Placement

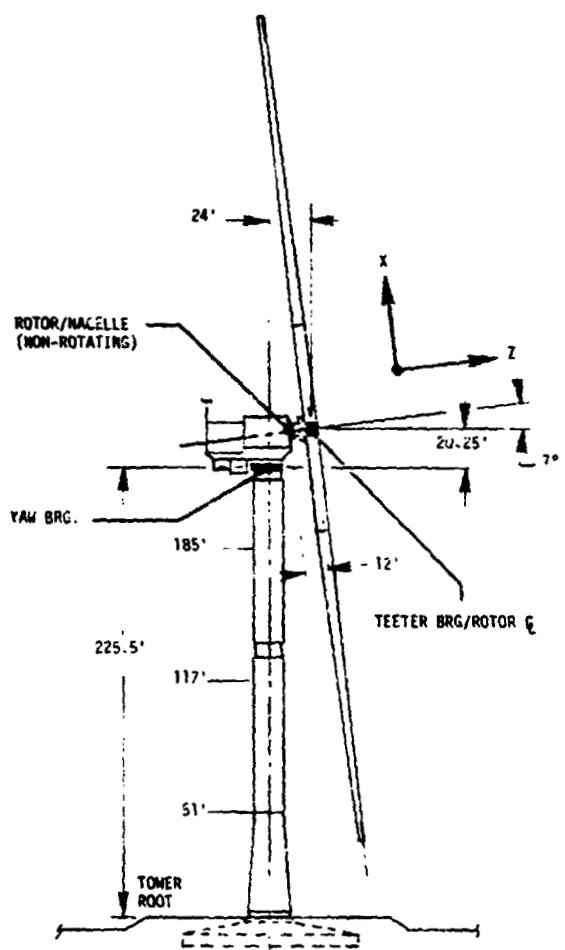
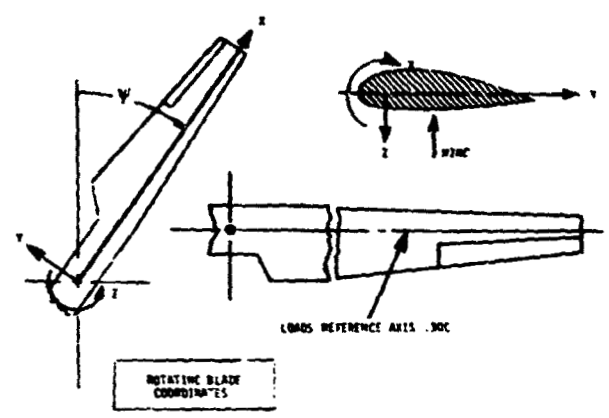


Figure 17. System Dimensions and Interfaces

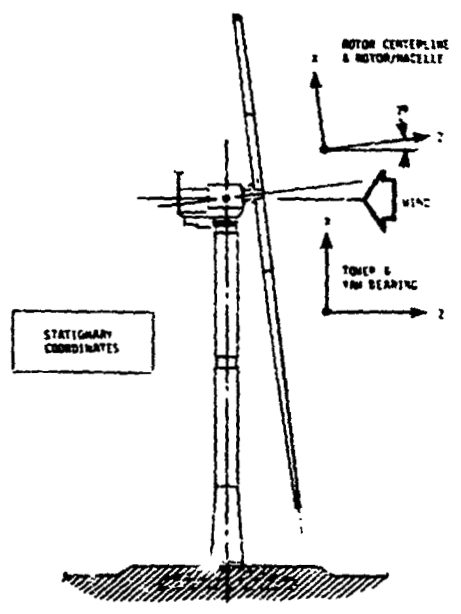


Figure 16. Sign Conventions

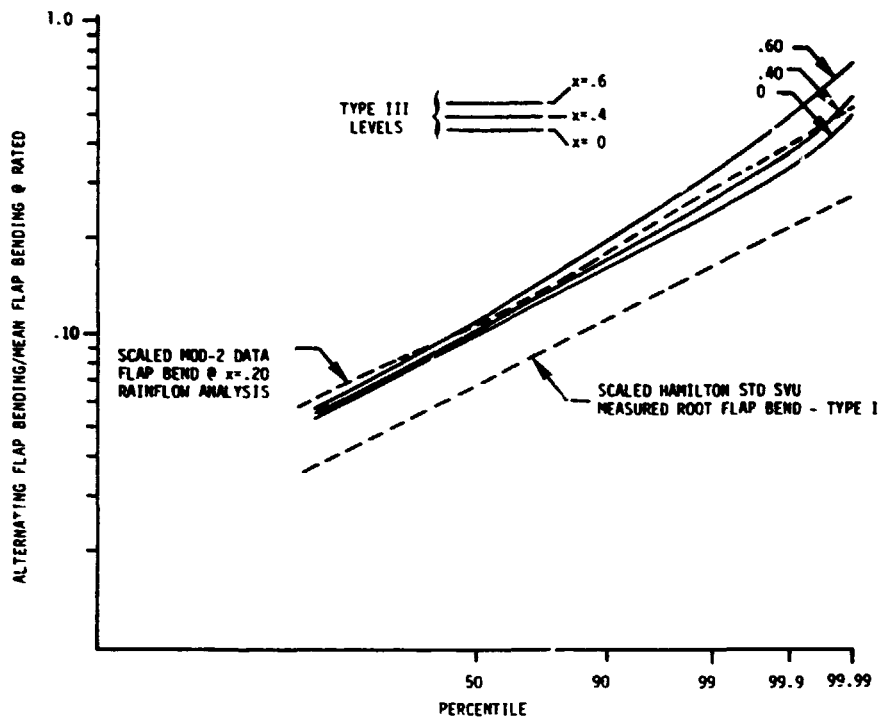


Figure 18. Blade Flapwise Bending Moment Probability Distributions

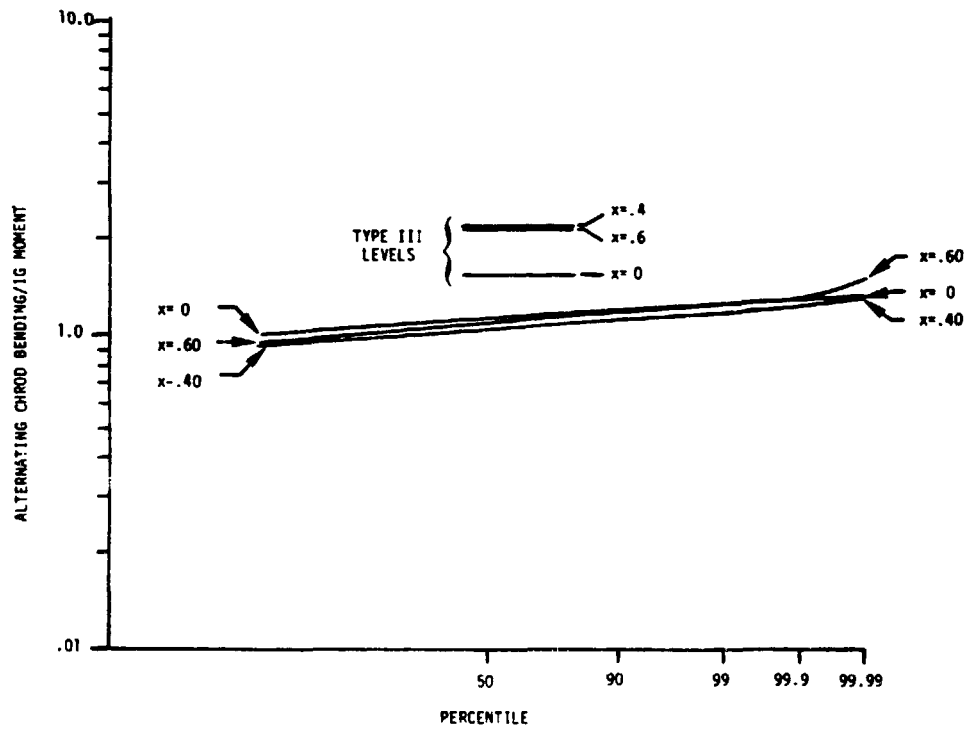


Figure 19. Blade Chordwise Bending Moment Probability Distributions

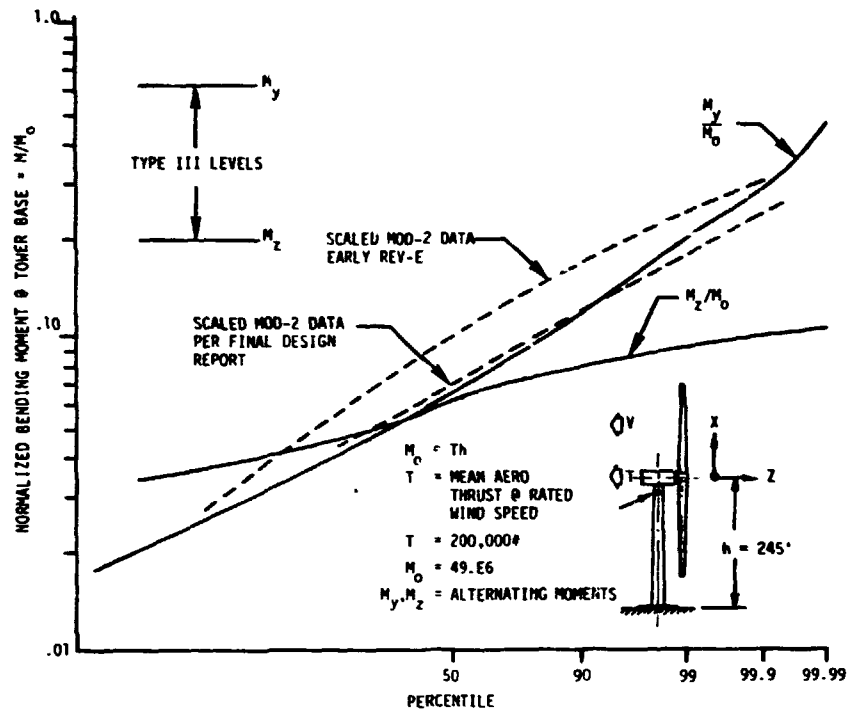


Figure 20. Tower Root Bending Moment Probability Distributions

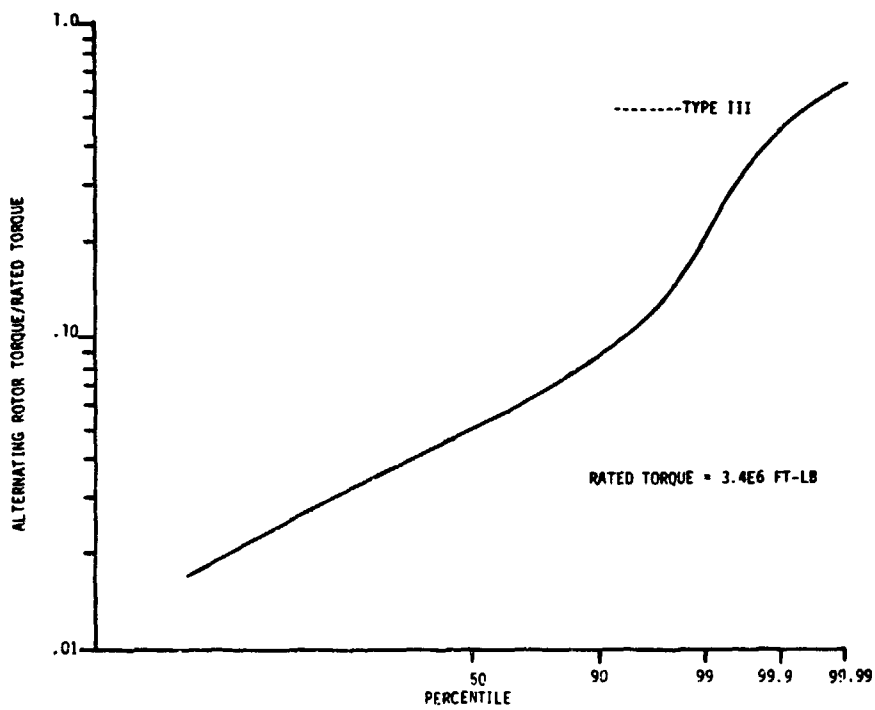


Figure 21. Rotor Torque Probability Distribution

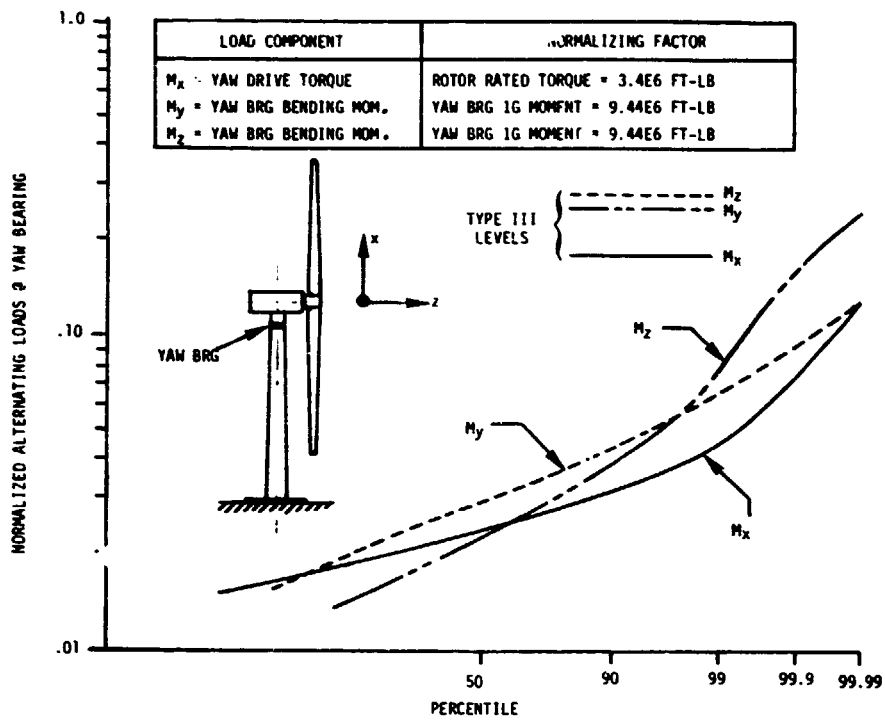


Figure 22. Yaw Bearing Bending Moment and Drive Torque Probability Distributions

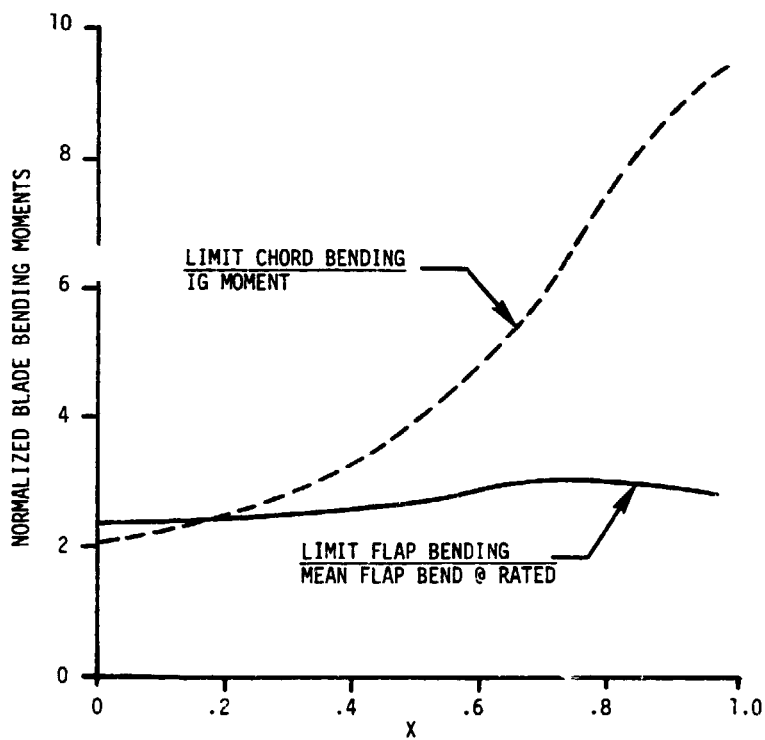


Figure 23. Blade Limit Loads

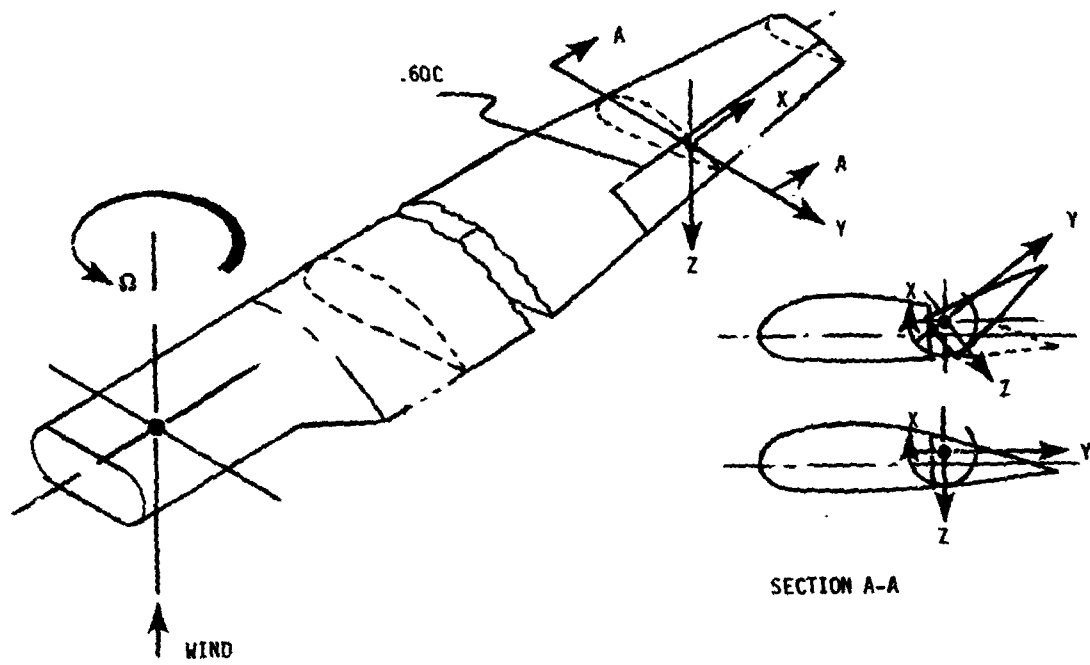


Figure 24. Aileron Coordinate System

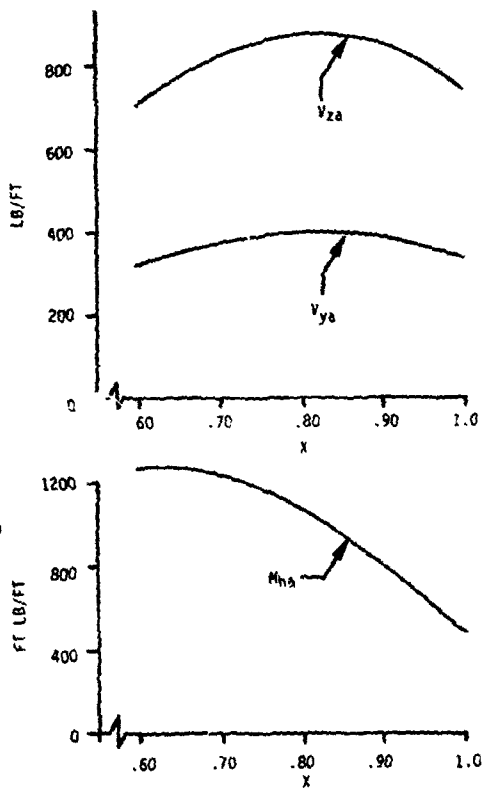


Figure 25. Aileron Aerodynamic Limit Loads for a 25% Overspeed Condition. Ailerons Deflected 45°.

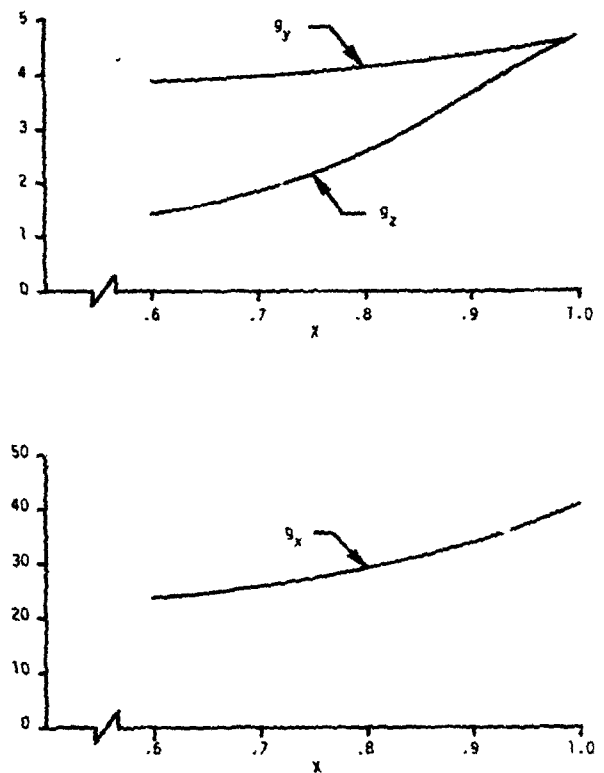


Figure 26. Aileron Inertial Limit Loads for a 25% Overspeed Condition. Ailerons Deflected 45°.

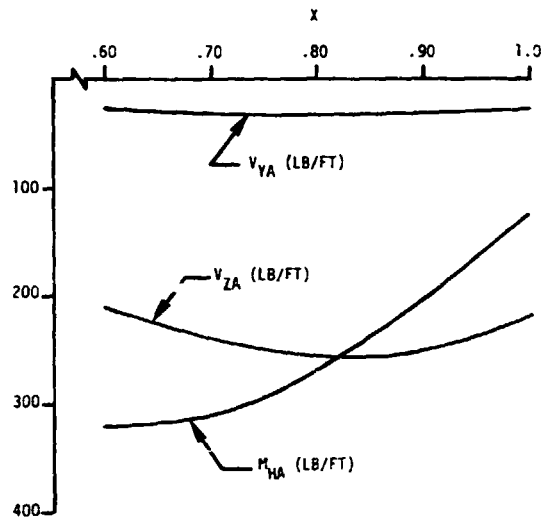


Figure 27. Mean Aerodynamic Aileron Loads at Rated Wind Speed. Fiftieth (50th) Percentile Cyclic Loads are 15% of Shown Mean Loads

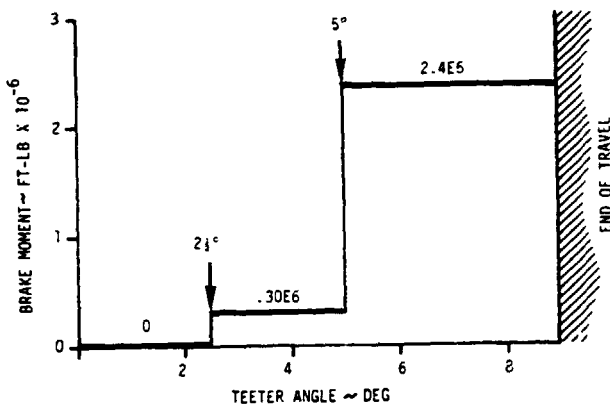


Figure 29. MOD-5A Tester Brake Schedule

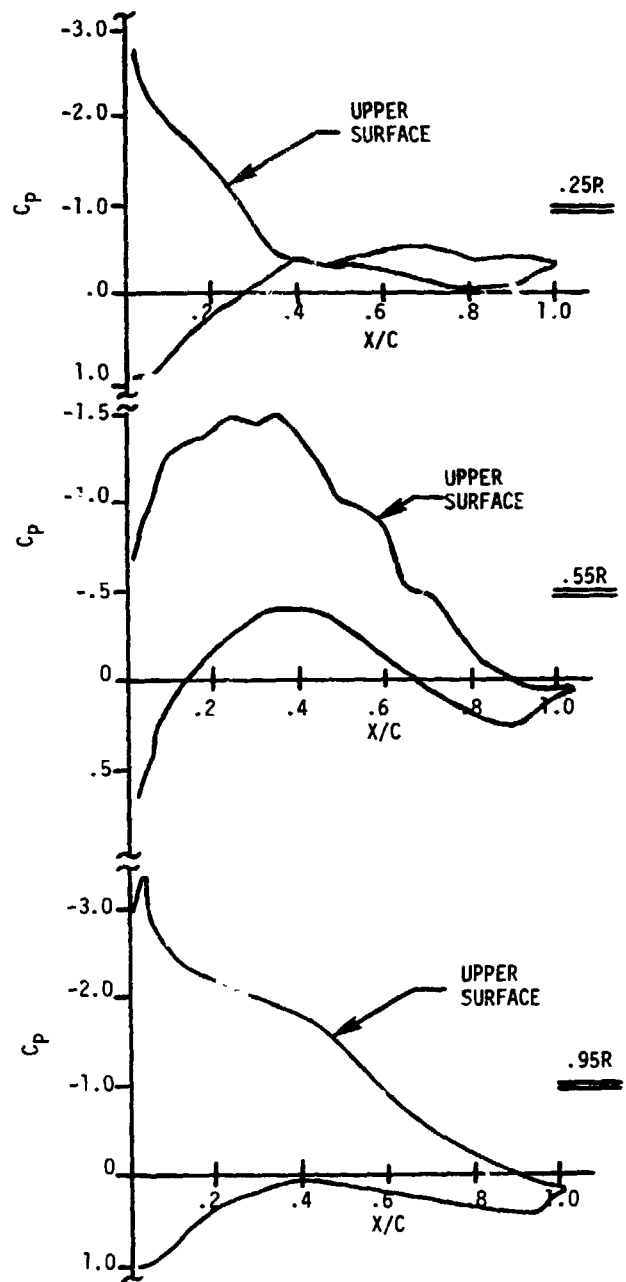


Figure 28. Airfoil Pressure Coefficients. Shown for Sections at $x=.25$, $.55$, and $.95$

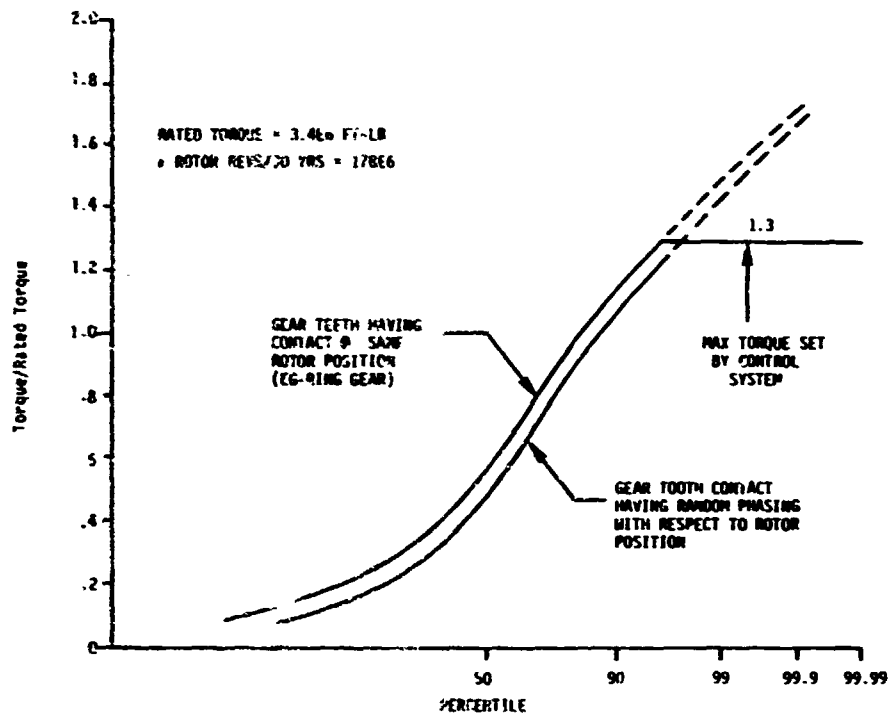


Figure 30. MOD-5A Gearbox Torque Duty Cycle

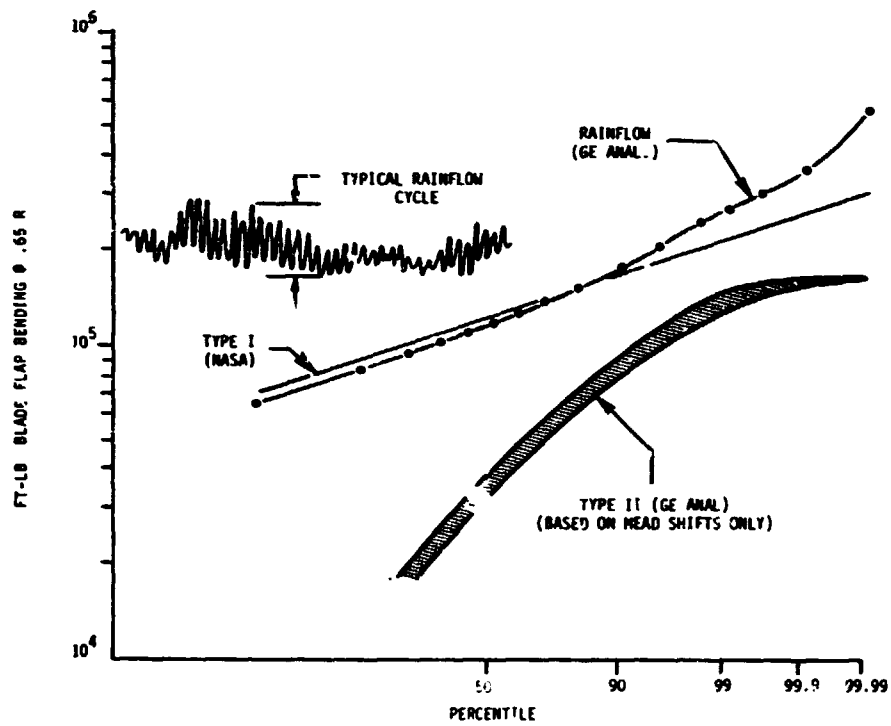


Figure 31. Rainflow Analysis of MOD-2 Test Data. Measurements Taken 3/11/82.

COMPARISON OF MEASURED AND CALCULATED DYNAMIC LOADS FOR THE MOD-2
2.5 MW WIND TURBINE SYSTEM

N95-27983

D. K. Zimmerman, S. A. Shipley and R. D. Miller

Boeing Aerospace Company
Seattle, WA 98124

ABSTRACT

The Boeing Company, under contract to the Electric Power Research Institute (EPRI), has completed a test program on the Mod-2 wind turbines at Goodnoe Hills, Washington. The objectives were to update fatigue load spectra, discern site and machine differences, measure vortex generator effects and to evaluate rotational sampling techniques. This paper shows the test setup and loads instrumentation, loads data comparisons and test/analysis correlations. Test data is correlated with DYLOSAT predictions using both the NASA interim turbulence model and rotationally sampled winds as inputs. The latter is demonstrated to have the potential to improve the test/analysis correlations. The paper concludes with an assessment of the importance of vortex generators, site dependence, and machine differences on fatigue loads. The adequacy of prediction techniques used are evaluated and recommendations are made for improvements to the methodology.

BACKGROUND

The Boeing Company, under contract to the Electric Power Research Institute (EPRI), conducted a loads development and rotational sampling test program on the Mod-2 wind turbines located at Goodnoe Hills, Washington. The test period was from June through August, 1983. These 300-foot diameter, 2500 kW, horizontal-axis wind turbines were developed for DOE/NASA, began operation in January, 1981 and were integrated into the Bonneville Power Administration (BPA) utility grid in June, 1982. Identical units are owned and operated by the Bureau of Reclamation (BuRec) in Medicine Bow, Wyoming and Pacific Gas and Electric Company (PGandE) in Solano County, California.

Since the completion of Mod-2 acceptance tests in June, 1982, wind turbine stability and performance had been improved with a new control algorithm and addition of vortex generators (VG) on the rotor blades. Little data on the effect of these changes on fatigue loads were available. Requirements for additional loads instrumentation were also recognized. The objectives of the loads development test were to collect loads data on the major structural subsystems in order to update the Mod-2 loads data base, to refine the fatigue load spectra and to update fatigue life projections. Site dependency was also investigated by comparing test data from the Goodnoe Hills and Solano units. The adequacy of loads and fatigue life methodology was evaluated, addressing such issues as fatigue cycle counting methods and load phasing.

Previous tests also revealed that some of the analytic fatigue load prediction techniques used during the Mod-2 design needed improvement. The cyclic loads due to deterministic sources such as wind shear, upwind tower shadow, yaw error and gravity loading were reasonably well understood and

predicted adequately. The most notable shortcoming was the inability to predict accurately the dynamic response to turbulence and its variations across the rotor disk. In conjunction with Pacific Northwest Laboratories (PNL), Boeing also completed a rotational sampling test program funded by EPRI aimed at improving test/analysis correlations. Unit #2 at Goodnoe Hills was used to measure wind velocities at several locations on the rotating rotor. These were used as input to a computer simulation of the wind turbine (DYLOSAT) to predict structural loads. A comparative analysis of the predicted loads with actual test data was made, to develop a better understanding of wind turbulence and to assess the ability of DYLOSAT to predict cyclic loads.

TEST DESCRIPTION

System Description

A photo of the Goodnoe Hills site is shown in Figure 1. Looking west, the Mod-2 wind turbines are designated (left to right), Unit #1, Unit #3 and Unit #2. The general arrangement and characteristics of the Mod-2 configuration are shown in Figure 2. It is designed for operation at sites where the annual average wind speed is 14 mph measured at 30 feet (20 mph @ hub height). The wind turbine generates electricity when the wind speed at hub height (200 feet) exceeds 14 mph. For winds exceeding 27.5 mph, the system produces rated power of 2500 kW.

Test Configuration

The loads development tests were performed on Units #2 and #3. Vortex generators were installed to improve aerodynamic stability and increase performance. Unit #2 had vortex generators installed on the blade midsections (70% VG) throughout the entire test program. Unit #3 started the test with no VG and subsequently had VG installed on the midsection (70% VG) and tip (100% VG). The vortex generators on the midsection and tip are illustrated in Figure 3.

The control system had been improved considerably since acceptance testing, during which the system occasionally exhibited dynamic instability due to aerodynamic nonlinearities at the peak of the power-blade angle curve. Control system improvements were incorporated into Units #2 and #3 before the start of loads development testing.

Test results from Units #2 and #3 were compared with data from a previous test on the PGandE machine (Unit #5) at Solano, California. This wind turbine had 70% VG and was identical to the Goodnoe Hills units except for a slight difference in nominal pitch schedule in below rated wind speed.

The rotational sampling tests were performed on Unit #2 concurrent with the loads development test.

Test Instrumentation

To meet the objectives of the loads test program, approximately 53 new loads and strain channels were added. The primary new instrumentation included additional flapwise bending loads in the rotor, pitch actuator force, nacelle pitch and yaw bending, upper tower bending and yaw drive torque. Figure 4 shows the location of the critical load measurements monitored in this test program.

Instrumentation for the rotational sampling test included the existing engineering instrumentation and special instrumentation (16 channels) installed on the rotor. The special rotor instrumentation included wind flow probes mounted at the leading edge of the blades at Stations 360 and 1205, and a differential pressure probe mounted on the trailing edge of one blade at Station 1120. In addition, accelerometers were located at Stations 360 and 1209 on one blade and a temperature transducer at Station 1205 on Blade 2.

Real time evaluation of the wind stability conditions was made by PNL, derived from an acoustic sounder located 3 diameters upwind of Unit #2. The acoustic sounder provided measurement of wind velocity over the elevation from 30m to 220m above the ground at 10m intervals.

A layout of the test data center is shown in Figure 5. Data from the wind turbines under test and meteorological data from the BPA and PNL towers were transmitted via the existing intra-site system to the data center adjacent to Unit #2. The data center recorded the data on analog tape and also transmitted the data to the NASA mobile data system (MDS). A digital data system (DDAS) supplied by Boeing provided on-site data processing capability for the calibrations and the loads development tests. Data was also digitized at the PNL trailer for the rotational sampling tests.

Wind Observations

Earlier wind turbine testing identified the need to develop a systematic scheme to sort loads data, accounting for the changing wind turbulence and gradient conditions observed during a test. A wind code defining the turbulence and wind gradient, similar to that employed by PGandE for performance evaluation, was used to sort cyclic loads data at both the Goodnoe Hills and Solano sites (Figure 6). Although this effort was not completely successful because of the distance of the met towers from the wind turbines, it was demonstrated that the Solano site experienced high shear/low turbulence and the Goodnoe Hills site high shear/high turbulence during their test periods. The higher turbulence levels appeared to be associated with higher cyclic loads observed at the Goodnoe Hills site. It was also demonstrated that the wind conditions observed at Goodnoe Hills were characteristic of both seasonal (summer) and annual conditions. The loads development tests and rotational sampling tests were run in parallel in winds of opportunity, ranging up to 38 mph at hub height.

LOADS DATA EVALUATION

Loads data recorded on magnetic tape at the data center were digitized and processed in real time at the DDAS. Raw data were monitored in real time on brush records. Data for each load channel was collected over 5-minute intervals and digitized at 10 samples per second. This sample rate was sufficient to cover responses through 4 per rev, which included the fundamental frequencies of the tower (1.26 per rev), drive train (0.45 per rev) and rotor flapwise mode (3.72 per rev). Typical digitized data traces are shown in Figure 7.

Data were reduced to the form of summary wind bins plots and tabular output. A total of 724 8-inch floppy discs (5 minutes, 9 channels each) were obtained. Each disc contained the digitized data for the run, atmospheric temperature and pressure, wind code and processed fatigue loads corrected to standard sea level conditions.

Although summary loads data in raw form were available as an output of the test phase, further data manipulation was required to differentiate site and machine differences, determine the effect of vortex generators and to assess the usefulness of sorting by the wind code. These tasks involved curve fitting scattered data, extrapolating to higher winds, cross plotting and sorting.

Site and Unit Differences

Pretest predictions of mean loads with the current control laws were updated using the DYLOSAT computer program. Both DYLOSAT predictions and test data confirmed that loads for Unit #5 tended to be lower than Units #2 and #3 due to small pitch schedule differences. Pretest predictions of cyclic loads using DYLOSAT were not made because of inability to prescribe proper turbulence inputs to the model.

DYLOSAT predictions generally correlated well with mean flapwise loads data, as shown in Figures 8 through 17. Both predictions and test data show the effects of pitch scheduling: slightly decreasing pitch angle up to 20 mph, constant pitch from 20 to about 27 mph (rated wind speed), and rapidly increasing pitch angle to hold rated power above 27 mph. The data scatter is typical of that observed in previous tests and at least partially due to plotting loads versus met tower wind speed, which is known to differ from that at the wind turbine by approximately ± 2 mph. Flapwise load data measured at the same station but on opposite blades were very consistent for Units #2 and #3. Data from Units #2 and #3 were in good agreement in below-rated winds, although small variations were noted in above-rated winds, probably due to small aerodynamic differences between the rotors. Mean flapwise loads for Unit #5, shown in Figure 10, tended to be lower than Units #2 and #3 because of the difference in pitch schedule.

The pitch control actuator force was measured on Units #2 and #3 but not on Unit #5. On both Units #2 and #3 actuator force was deduced by using the pressure differential from the rod to the head end, a technique employed during Mod-2 acceptance testing. In addition, on Unit #3 the actuator rod eye was instrumented and calibrated to read rod force directly (OIL301) to verify the previous measurement technique.

The mean actuator rod force for Unit #3 is shown in Figure 13. The pretest predictions shown were based on very limited test data obtained during Mod-2 acceptance testing. Very good correlation was obtained by the two measurement techniques on Unit #3, validating the previous method.

A comparison of test data and DYLOSAT predictions for mean quill shaft torque are shown in Figures 14 and 15. These plots are equivalent to performance plots (power versus wind speed). The latter are usually developed from smooth wind data, however, minimize data scatter. Nevertheless, the quill shaft data is in fair agreement with DYLOSAT predictions. The data suggest that Unit #2 performance is slightly better than Unit #3. Unit #2 appears to reach rated torque at 27 mph and Unit #3 at 28 mph.

The mean tower bending moment data is compared to DYLOSAT predictions in Figures 16 and 17. The data are the vector sum of bending about two horizontal axes at Sta. 600. DYLOSAT predictions appear to be somewhat higher than data, particularly at near-rated wind speed. Unit #2 data also is slightly higher than Unit #3, indicating that the mean thrust and performance of Unit #2 should be higher.

Cyclic flapwise load data for Unit #2 and #3 with 70% VG were very similar. Curve fits to the cyclic loads data at Sta. 370 on Unit #2 are shown in Figure 18. The curve fits are based on trends predicted by the DYLOSAT program, using the NASA interim turbulence model as input, amplitude adjusted to fit the measured data.

Cyclic load data for Unit #5 was curve fitted in a similar manner. The mean cyclic flapwise load data for Units #2, #3 and #5 are compared in Figures 19. There is good agreement between the recent data for Units #2 and #3 and acceptance test data. The differences are mainly due to the type of curve fit employed. During acceptance testing a power law fit with wind speed was assumed; for the loads development test the curve fits were based on DYLOSAT trends. There is a clear difference in cyclic loads between Goodnoe Hills and Solano. Solano cyclic loads were approximately 20 percent lower at all wind speeds.

Tower cyclic loads at Sta. 600 are compared in Figure 20. The recently measured tower cyclic loads on Units #2 and #3 are higher than acceptance test. Recent control system changes may have resulted in control system response more closely coupled to the tower mode, which would increase the tower response. Unit #5 cyclic tower loads are approximately 20 percent lower than Units #2 and #3, most likely due to the lower turbulence at the Solano site.

The cyclic teeter angles during operation for all units are compared in Figure 21. The teeter data was similar to acceptance test data indicating 70 percent VG have not adversely affected teeter response. The expected high teeter response for Unit #5 due to severe wind gradient characteristic of the Solano site did not materialize. Severe gradients occasionally did occur during the test period at Solano, but did not affect the teeter response statistics.

Vortex Generator Effects

The effect of VG was evaluated by comparing mean and cyclic load data on Unit #3 for three VG configurations. Data analysis concentrated on determining variations in rotor flapwise loads and drive train loads. Statistical analysis of the mean and cyclic data for 5-minute intervals was performed on site at the DDAS. To determine the effect of VG on performance more accurately, 10 minute averages in smooth wind conditions were later processed in Seattle.

Curve fits to the mean flapwise loads data at Sta. 370 are compared in Figure 22. Unit #3 with 0% VG was unable to achieve rated power below 34 mph. This resulted in a continued increase of flapwise moment with wind speed because the blade could not unload to spill power. With the addition of 70 percent VG, however, Unit #3 reached rated power at a lower wind speed. In above-rated winds, the mean flapwise loads decreased as the collective pitch increased significantly to spill power. For below-rated wind, a slight increase in mean flapwise loads was noted for 70% VG compared to 0% VG. A small increase was also noted in mean load between 70% and 100% VG.

Unlike the mean loads, the cyclic loads data for both 5 and 10 minute data samples failed to reveal any statistically significant difference in cyclic loads for different VG configurations.

Improved performance with vortex generators is discussed in Reference 1. A typical performance plot is illustrated in Figure 23.

Comparison of Fatigue Counting Methods

Existing fatigue cycle counting procedures include the method used on Mod-2, NASA wind bins based on 1P sampling, rainflow, and others. The Mod-2 method was selected for compatibility with the fatigue life methodology being followed. As part of loads methodology assessment, the Mod-2 fatigue counting method using the DDAS was compared with a rainflow procedure using the Datamyte 400. This device is a solid state, software controlled histogram processor/recorder used for field recording of analog data (one channel at a time). A major advantage of the Datamyte 400 is its ability to process and store large quantities of data spanning months of testing.

The Mod-2 fatigue cycle counting method determines the major cyclic load excursions about a mean load, ignoring minor reversals and a prescribed dead band (Figure 24). It is believed that addition of these loads to long period load cycles due to a varying mean wind and startup/shutdown load cycles fairly represents the fatigue load damage potential.

The Datamyte rainflow algorithm has the potential to produce superior fatigue life estimates and still is compatible with current fatigue life methodology. The rainflow algorithm is a range-pair method but counts only those cycles which complete a hysteresis loop, as shown in Figure 25. It produces a histogram format of cyclic data which can be correlated with cumulative probability and exceedance distributions produced by current methods.

The cumulative distribution of the flapwise cyclic load at Sta. 370 over a 5 minute interval is shown in Figure 26. The 50 percentile level by the Mod-2 method is consistent with the Datamyte rainfall algorithm, but the 0.999 percentile level is lower. The most notable difference in the two methods is the shape of the cumulative distributions. The Datamyte 400 results are clearly non-Gaussian. This trend persists for 20 minute data samples as well.

The comparison of the two methods of counting load cycles is presented in a form more useful for fatigue life analysis in Figure 27. This plot shows the number of exceedances of a certain load level and reflects not only the difference in the distribution but also the difference in the total number of fatigue cycles counted. Although there is generally good agreement, the tails of the distributions are different, suggesting the present method is somewhat unconservative for low probabilities of occurrence.

ROTATIONAL SAMPLING TEST/ANALYSIS CORRELATION

The rotational wind sampling test was conducted by Boeing and directed by PNL with the objective of developing an improved wind model. Following the test, PNL reduced and analyzed the wind data (Reference 2); PNL results were used in the Boeing analysis. The wind model is required as input into the improved theoretical aeroelastic computer program (DYLOSAT) that Boeing has developed for calculating dynamic loads on the wind turbine. This study assessed the suitability of the wind model and the DYLOSAT program to predict dynamic loads by comparing analysis with loads measured in the rotational wind sampling test.

Analytic Methods

The analytic model of the wind turbine system consists of a matrix of second order non-linear differential equations of the form

$$[M(t)] \ddot{q} + [c(t)] \dot{q} + [k] q = F(t) \quad (1)$$

where the forcing function $F(t)$ is derived from theoretical aerodynamics and a wind description. A computer code (DYLOSAT) was developed to calculate the aerodynamic forcing function from a description of the wind, to formulate load equations and to solve the equations of motion and load equations. A sketch of the DYLOSAT model is shown in Figure 28.

Equation (1) can be solved in either the time or the frequency domains. For both of these solutions, the aerodynamic model is based on a strip momentum rotor analysis developed on a finite number of spanwise segments. Finer segments are used near the tip to increase numerical accuracy because the aerodynamic forces (resulting in rotor loads and hub torque) are concentrated towards the tip.

Calculating the aerodynamic forces on each segment requires definition of the wind turbulence at each segment. Much of this study was devoted to assessing two wind turbulence models (the NASA interim turbulence model and the rotationally sampled wind turbulence model) and two solution methods (frequency response analysis and time history analysis).

a) The NASA Interim Turbulence Model

The NASA interim turbulence model is based on wind data collected by PNL at Clayton, New Mexico from a vertical plane array of anemometers on several meteorological towers. The NASA Lewis Research Center used the wind turbulence spectrum from this data to develop a non-dimensional curve as a function of rotor speed harmonics (Figure 29). Using this non-dimensional curve with the empirical equations shown below, the rms turbulence wind velocity amplitude can be calculated at specified steady state wind velocities and rotor speed harmonics.

$$V(.75r, \psi) = V_0 + \delta V_5 (V_0, .75r/h_0) \left[\frac{\cos(n\psi)}{n + 0.75} \right]$$

where

$$\begin{aligned} V(.75r, \psi) &= \text{wind speed at } 75\% \text{ rotor radius } r \\ &\quad \text{and rotor azimuth } \psi \\ V_0 &= V(0, \psi) = \text{wind speed at hub height} \\ \psi_j &= \psi \text{ for blade 1, } \psi + \pi \text{ for blade 2} \\ \delta V_5 &= V_0 [1 + .75 r/h_0]^\alpha - (1 - .75 r/h_0)^\alpha \\ \alpha &= .35 [1 - .55 \log(V_0)] / [1 - .19 \log(h_0/10)] \\ h_0 &= \text{hub elevation} \\ n &= \text{harmonic number} \end{aligned}$$

The cyclic wind velocity is assumed to vary linearly with rotor radius from zero at the hub to a maximum at the tip. From a large amount of Mod-2 wind turbine test data, using $\alpha = .24$ for all wind speeds produced the best data fit. Consequently, this value of α was used for this study. Utilizing random harmonic analysis techniques, the wind is assumed to act sinusoidally on the blade at each harmonic frequency as shown conceptually in Figure 30. The sinusoidal wind turbulence is assumed to be completely in-phase over the total blade. For the two blades, the sinusoidal wind turbulence is assumed in-phase on each for the even harmonics and 180° out-of-phase for the odd harmonics. These rms turbulence wind velocity amplitudes were used in calculating the turbulence induced aerodynamics of the forcing function.

b) Rotationally Sampled Wind Turbulence Model

The wind velocity was measured dynamically at four blade locations, Stations 360 and 1206, on both blade 1 and 2 as shown conceptually in Figure 31. Wind spectra as a function of rotor speed harmonics were calculated by PNL from time segments of the wind data collected at each of the measurement stations. This yielded the rms wind turbulence velocity amplitude spectra at four stations on the rotor. In addition, cross spectra between measurement stations of the wind data were calculated to yield the phase relationship between the spectra as a function of rotor speed harmonics.

The rotationally sampled wind turbulence model has in concept refined the NASA interim turbulence model from one wind turbulence spectrum used on both blades to four wind turbulence spectra on the rotor and the phase angle relationship between each spectra. The velocity amplitude and phase relationship at any other station on the rotor is assumed from linear interpolation or extrapolation of the spectra data on each blade.

c) Frequency Response Analysis

Frequency domain analysis of the equations of motion is similar to the power spectral density technique that utilizes random harmonic analysis. The equations are solved for steady state solutions from a series of sinusoidal forcing functions of ω , $\omega + \Delta\omega$, $\omega + 2\Delta\omega$, etc., with magnitude equal to the square root of the forcing function spectrum at the respective frequencies. Because the equations are nonlinear, classical methods of solving for the particular solution of the second order differential equations could not be used. The method used was to solve the equations as a time history solution with a sinusoidal forcing function of the correct magnitude and frequency. From the time history solution, the steady state cyclic amplitude for the corresponding forcing function frequency is obtained and produces one solution point for that frequency. Solutions over the frequency range of interest for the wind turbine comprise the frequency domain analysis. In the case of the load equations, the load output spectrum is also obtained by this method and the rms loads are obtained by integrating the load output spectra. Because, the loads on a wind turbine are primarily caused at harmonics of the rotor speed, the equations of motion and load equations were only solved at the harmonics (1P + 5P).

d) Time History Analysis

The time history analysis involves numerical integration of Equation (1) with the actual wind wind turbulence time histories used as input for the forcing function. Loads and responses as a function of time are obtained as part of the solution. A spectral analysis of the resulting time histories was used for determining the frequency and amplitude content of the load. The response time histories were also compared to test data.

Results and Discussion

The data collection and data reduction of the rotationally sampled wind data was performed by PNL and reported in Reference 2. From the large quantity of test data recorded, PNL reduced four cases of data segments of approximately eight minutes each from which three cases were chosen for use in this analysis. The three cases analyzed are shown in Table 1.

a) Rotationally Sampled Wind

The rotationally sampled wind turbulence spectra for case 1 (a typical case), for the four blade test locations, are shown in Figure 32. The rotationally sampling wind instrumentation measured wind fluctuations from two sources, the turbulence in the wind (including variations due to the blade rotating through the turbulent eddies), and the variations due to the blade rotating through wind shear. This latter source shows up in spectral plots primarily at the 1P harmonic of the rotor rotational speed. Examining the spectrum in Figure 32 shows that the magnitude at 1P is significantly larger than the higher harmonics. Since the instruments at stations 1205 rotate through a larger range of wind shear than those at stations 360, it would be expected that the trend of the turbulence spectrum being highest at the first harmonic compared to the higher harmonics would be more pronounced for

stations 1205 than 360, but this was not observed. The instruments on both blades follow the same track so there is good agreement between the two blades as shown in Figure 32.

The coherence of two signals is a good indication of the usefulness of the cross spectrum for use in a frequency domain analysis. A low coherence indicates that the two signals are uncorrelated and although a cross spectrum and a phase angle relationship can be calculated, the results have little significance. Figure 33 presents the coherence of the signals at the four test stations referenced to the signal from the instruments on blade 2 at station 1205. From Figure 33 it is apparent that the signals are uncorrelated for most harmonics. The coherence of the first harmonic is high probably because of the velocity fluctuations from rotating through the shear layers, which should produce highly correlated signals. If the velocity fluctuations from rotating through shear were removed from the signals, the coherence for just the turbulence signals would most likely be very low at all harmonics.

The low coherence indicates that the correlation between signals is poor and the calculated phase angles between stations and as a function of harmonics are not valid. Unfortunately, the phase angle relationship between wind spectra is important for frequency domain analyses and greatly affects the load calculations.

b) Frequency Domain Loads Analysis

Bending moment loads were calculated at rotor station 370 and 1164 by DYLOSAT with the NASA interim turbulence model and the rotationally sampled turbulence wind model; results were compared to experimentally measured loads for the three cases. Because the phase angles from the rotationally sampled wind were meaningless, only the wind spectra were used as input to DYLOSAT. The phase angle relationship of the wind on each blade at a given station was assumed to be the same as for the NASA interim turbulence wind. That is, the wind was in-phase at all points on a blade and was in-phase between blades for the even harmonics and 180° out-of-phase between blades for the odd harmonics. Figure 34 presents the bending moments for case 1.

The total bending moment is also shown in this figure. The total load is calculated as the root-sum-square of the first through fifth harmonics. It is apparent that the rotationally sampled wind model produces results considerably higher than the NASA interim turbulence model or test results. These loads can be attributed to the lack of a phase angle relationship between the wind measurement stations and that a worst case phase angle relationship was assumed for the even harmonics from which most of the load is associated.

The NASA interim turbulence model produces results that are closer to test in some cases and not as close in others, compared to the rotationally sampled wind. There appears to be no consistency in the results; using either wind turbulence model for calculating absolute loads for design purposes would be risky. The lack of phase angle relationships between the wind spectra precludes using these techniques for calculating absolute loads. Their use can only be justified when determining trends in the loads.

c) Time History Loads Analysis

The time history analysis of DYLOSAT to calculate structural loads is the most direct approach in the use of DYLOSAT. The rotationally sampled wind is directly input into the computer program to force the wind turbine model at the appropriate test locations on the rotor. The time history bending moment loads from DYLOSAT can be directly compared to the bending moment loads recorded during testing. Figures 35 through 37 shows a twenty second segment for Case 1 of the bending moment test results and the predictions for rotor stations 370 and 1164 and tower station 600. Comparing the test and analysis results shows a definite correlation between the time history signals. Although the signals do not match identically, the characteristics are similar.

Comparisons of the spectral content of the time history analyses and data are shown in Figures 38 and 39. From these figures, the frequency content of the analysis and test agrees very well for the rotor up to the first blade bending frequency of approximately 1.2 Hz. For frequencies above 1.2 Hz, the agreement deteriorates because the theoretical model of the rotor has only one asymmetric mode above 1.2 Hz. The amplitudes of the spectra from the analysis tend to be higher throughout the spectra. This can be attributed to the lack of sufficient rotationally sampled wind time series to define the wind turbulence adequately over the rotor. With only two test locations on each blade, the theoretical model required a linear interpolation and extrapolation of the wind time history signals to define the wind over the entire blade. This effectively defines the wind as being highly correlated between the test data and the interpolated data which would produce higher load predictions.

CONCLUSIONS AND RECOMMENDATIONS

The loads development test program was considered successful when measured against the primary program objective. A significant improvement in the Mod-2 fatigue loads data base was accomplished, providing more accurate Mod-2 fatigue life estimates than previously available. Although the full matrix of wind gust and gradient conditions could not be completed, the data obtained was shown to be typical of the Goodnoe Hills site. Data gathered during the test program was adequate for the purpose of evaluating site and machine differences and the effect of VG on loads and performance.

The most important output of the test program was refinement of the fatigue load spectra compared to acceptance test results. Mean loads data were shown to be in good agreement with predictions, validating use of the DYLOSAT computer program for this purpose. Cyclic load distributions were refined based on the additional load channels monitored in this program, improved calibration and data processing methods.

Test data provided insight into machine and site differences and the effect of VG on loads and performance. Little difference in loads was noted between similar machines at the same site. Variations in turbulence levels and wind gradient were found to be more relevant. Cyclic load levels between Solano and Goodnoe Hills were found to differ by approximately 20%, attributable to the

difference in turbulence levels. The addition of VG was demonstrated to improve performance, increase mean loads for below-rated wind speeds, decrease mean loads for above-rated wind speeds, but have little effect on cyclic loads.

The analysis explored several loads methodology concerns including fatigue cycle counting methods, load/strain correlation and load phasing. The Datamyte 400 (rainflow) algorithm was shown to be more severe than present methods, which may affect fatigue life estimates. On the other hand, load/strain correlations indicate that loads/stress methodology was otherwise very conservative.

Although the loads development tests met many program objectives, the data review and methodology assessment revealed several deficiencies. Some of these deficiencies may be overcome simply by extension of the testing program to longer periods of time. Others were more fundamental in nature, suggesting a need to modify present methods or to adopt new approaches yet to be defined. In particular, sorting of cyclic loads data by a simplified wind gradient/turbulence code needs to be developed. To reduce data scatter, improved methods of averaging data such as disc averaging need to be developed. Various fatigue cycle counting methods should be evaluated over the short and long term.

The rotational sampling test results showed that much work remains to develop an acceptable wind turbulence model. Based on the cross spectral analyses and low coherence between the wind time series, there is much less correlation in the wind between spatial locations than that used in the NASA interim turbulence model and the similar approach taken when using the rotationally sampled wind data. The turbulence of interest appears smaller in length than the distance between measurements, giving very little spatial correlation. Utilizing rotationally sampled wind turbulence spectra is difficult because of this low coherence.

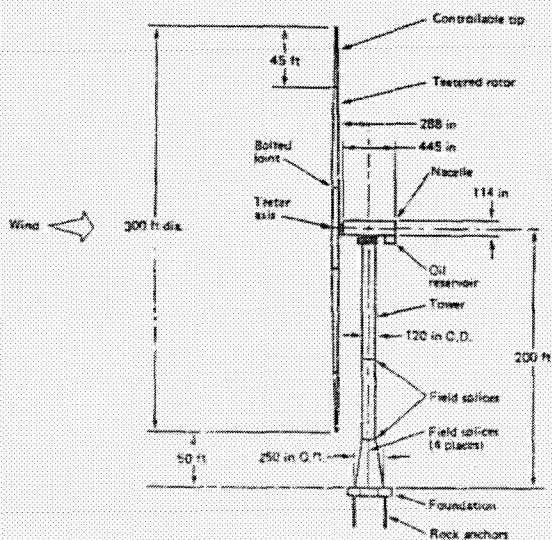
Using the time series of the rotationally sampled wind directly with DYLOSAT shows more promise. Correlation of the spectral analysis of the time series from test and DYLOSAT was fair and could be much improved with more closely spaced test stations or a better interpolation scheme. Only a better defined wind model is required until design cyclic loads can be predicted analytically with confidence. The wind model must be able to define turbulence on the rotor with the observed spectra characteristics and low coherence. If possible, this detailed definition should be derivable from meteorological tower data using only a few measurements locations.

REFERENCES

1. Miller, G. E.; "Comparative Performance Tests on the Mod-2, 2.5 MW Wind Turbine With and Without Vortex Generators," Horizontal-Axis Wind Turbine Technology Workshop sponsored by DOE/NASA, Cleveland, Ohio, May 8-10, 1984.
2. Connell, J. R.; George, R. L.; Sandborn, V. A.; "Rotationally Sampled Wind and Wind Turbine Response at Goodnoe Hills Mod-2, Unit No. 2, Measured in July-August, 1983: A Preliminary Analysis", Research Project RP 1996-12, PNL, December 1983.



Figure 1. Mod-2 Wind Turbine Site at Goodnoe Hills, WA



Rated power	2,500 KW
Rotor diameter	300 ft
Rotor type	Teetered - tip control
Rotor orientation	Upwind - 2.5° tilt
Rotor airfoil	NACA 230XX
Rated wind @ hub	27.5 mph
Cut-off wind speed @ hub	45 mph
Rotor tip speed	275 ft/sec
Rotor rpm	17.5
Generator rpm	1,800
Generator type	Synchronous
Gear box	Compact planetary gear
Hub height	300 ft
Tower	Soft shell type
Pitch control	Hydraulic
Yaw control	Hydraulic
Electronic control	Microprocessor
System power coefficient (max)	0.362

Figure 2. Mod-2 Features and Characteristics

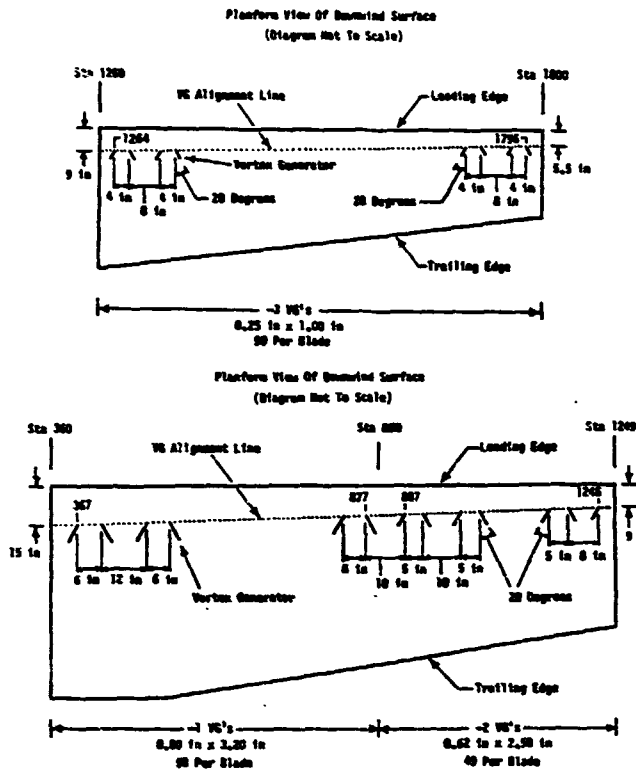


Figure 3. Vortex Generator Installation on Mod-2 Blade

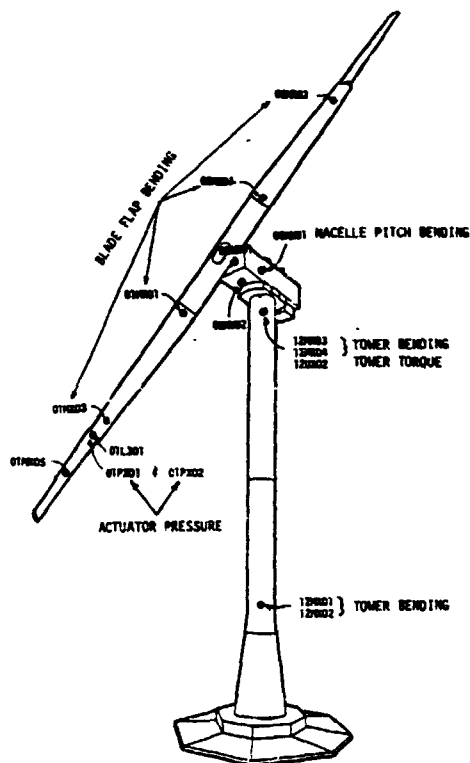


Figure 4. Critical Load Measurements

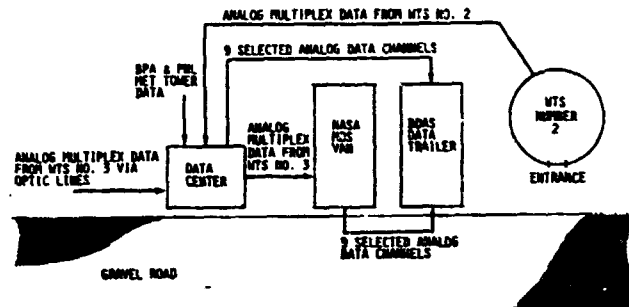


Figure 5. Layout of Test Data Center

GUST

INCR. SEVERITY ->

	0	1	2
WIND SHEAR SEVERITY	0-0 CALM	0-1	0-2
1	1-0	1-1	1-2
2	2-0	2-1	2-2 LARGE SHEAR LARGE TURB.

GUST

SHEAR

0	$\frac{V_{350} - V_{200}}{V_{200}} < .05$	$\left \frac{V_{350} - V_{200}}{V_{200}} \right < .1$ and $\left \frac{V_{450} - V_{200}}{V_{200}} \right < .1$
1		
2	$\frac{V_{350} - V_{200}}{V_{200}} \geq 0.1$	$\left \frac{V_{350} - V_{200}}{V_{200}} \right \geq .25$ or $\left \frac{V_{450} - V_{200}}{V_{200}} \right \geq .25$

Figure 6. Wind Code

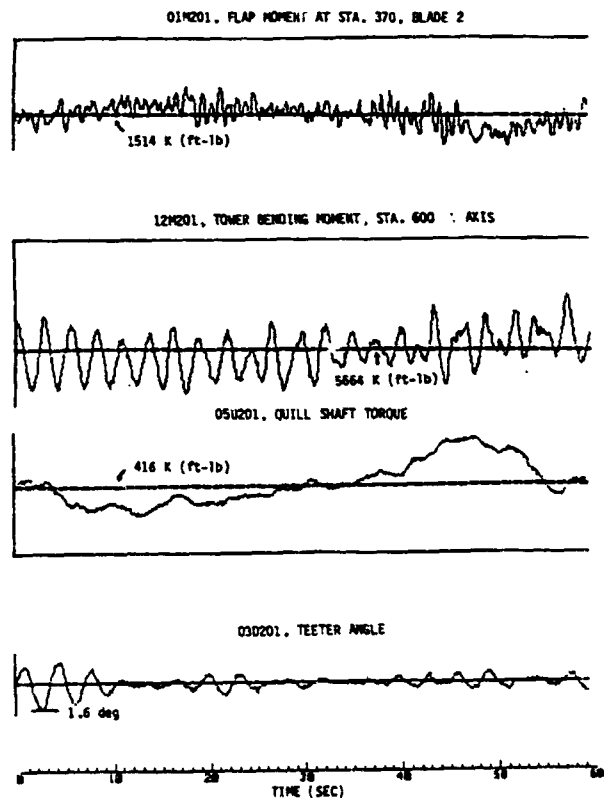


Figure 7. Typical Data Traces

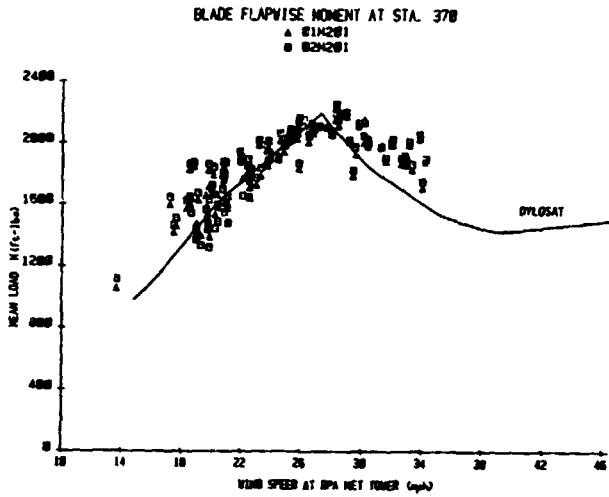


Figure 8. Mean Flapwise Moment at Sta. 370 (Unit #2, 70% VG)

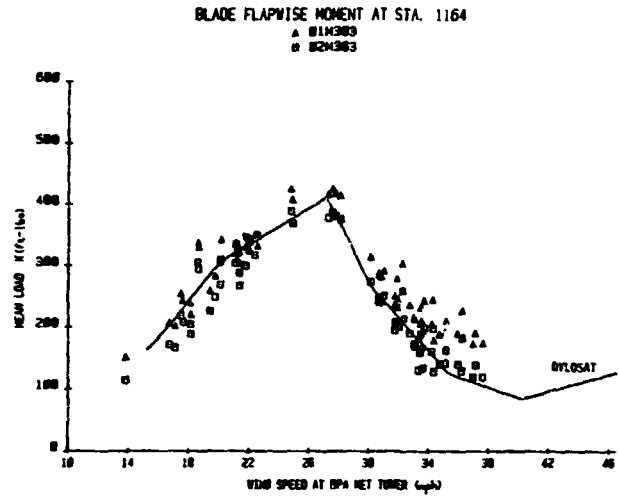


Figure 11. Mean Flapwise Moment at Sta. 1164 (Unit #3, 70% VG)

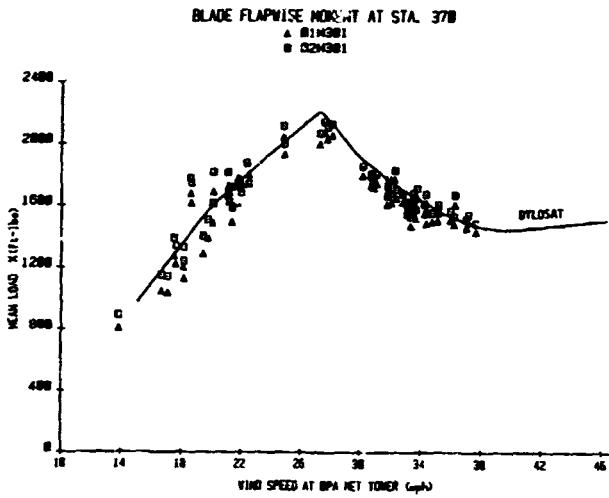


Figure 9. Mean Flapwise Moment at Sta. 370 (Unit #3, 70% VG)

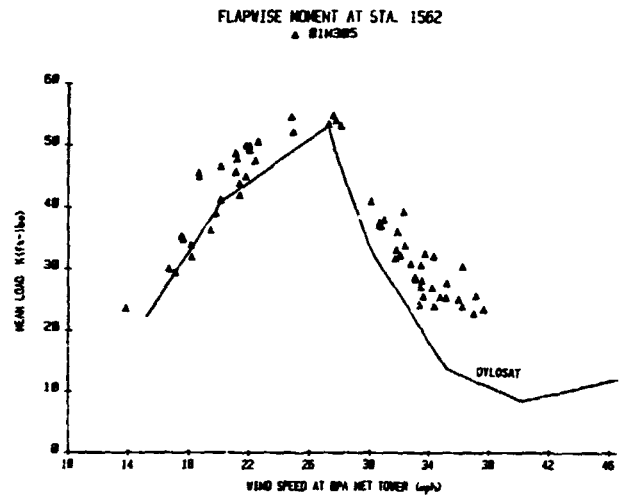


Figure 12. Mean Flapwise Moment at Sta. 1562 (Unit #3, 70% VG)

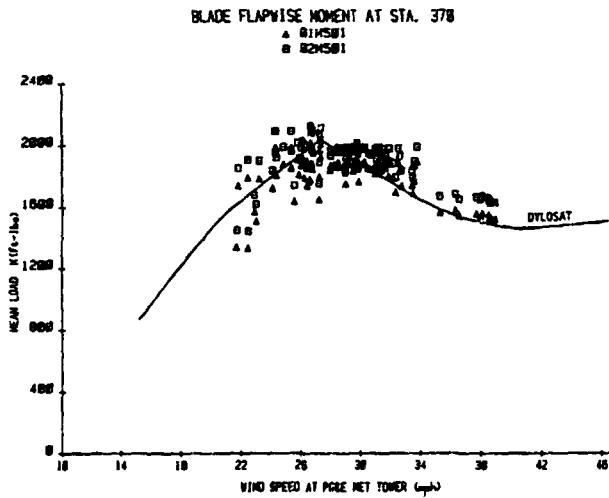


Figure 10. Mean Flapwise Moment at Sta. 370 (Unit #5, 70% VG)

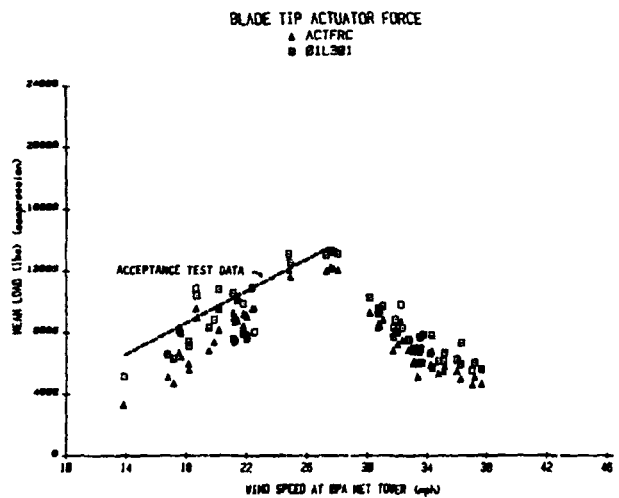


Figure 13. Mean Blade Tip Actuator Force (Unit #3, 70% VG)

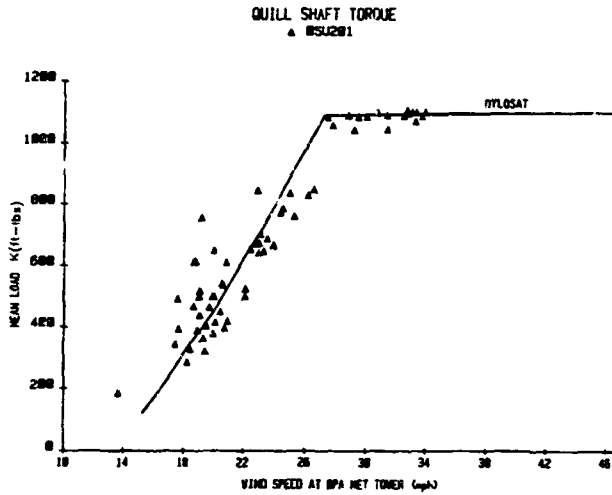


Figure 14. Mean Quill Shaft Torque (Unit #2, 70% VG)

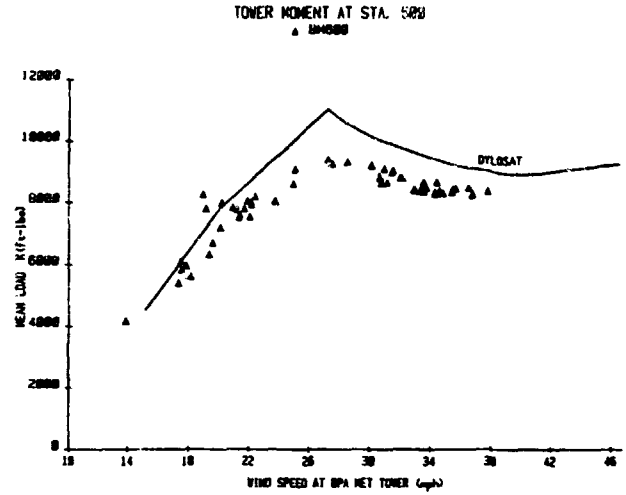


Figure 17. Mean Tower Moment at Sta. 600 (Unit #3, 70% VG)

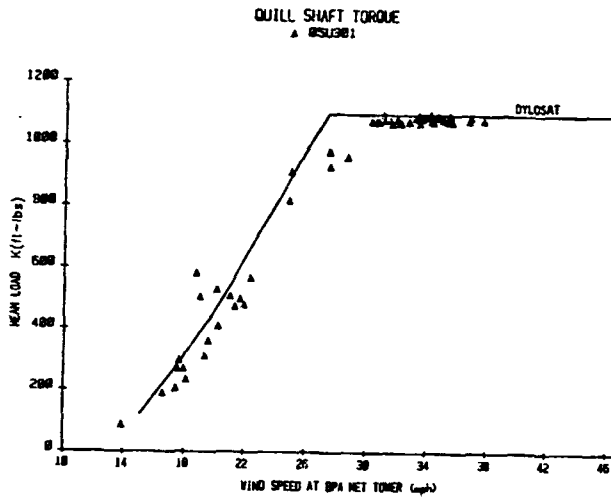


Figure 15. Mean Quill Shaft Torque (Unit #3, 70% VG)

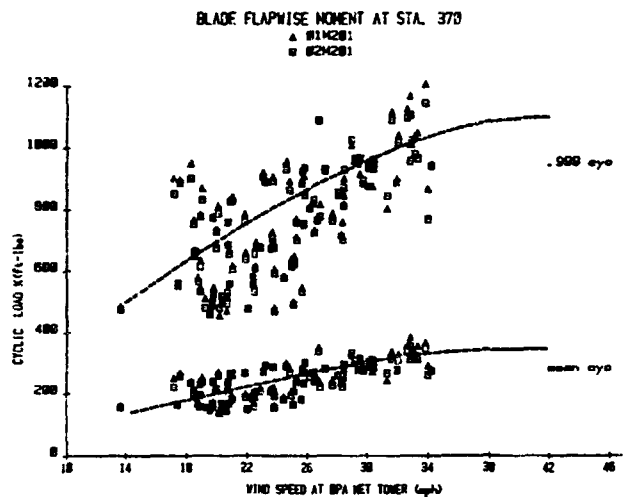


Figure 18. Cyclic Flapwise Moments at Sta. 370 (Unit #2, 70% VG)

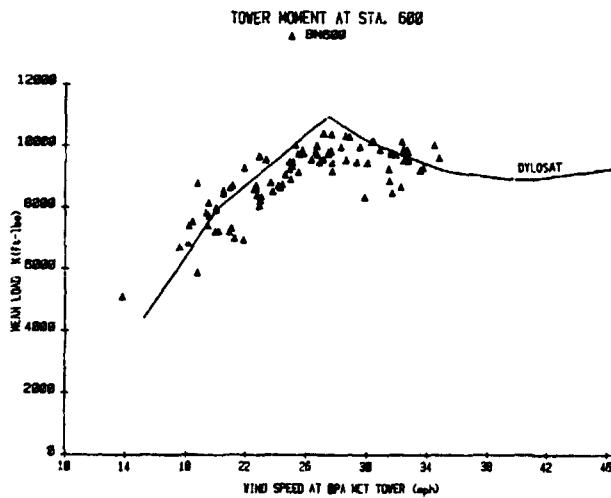


Figure 16. Mean Tower Moment at Sta. 600 (Unit #2, 70% VG)

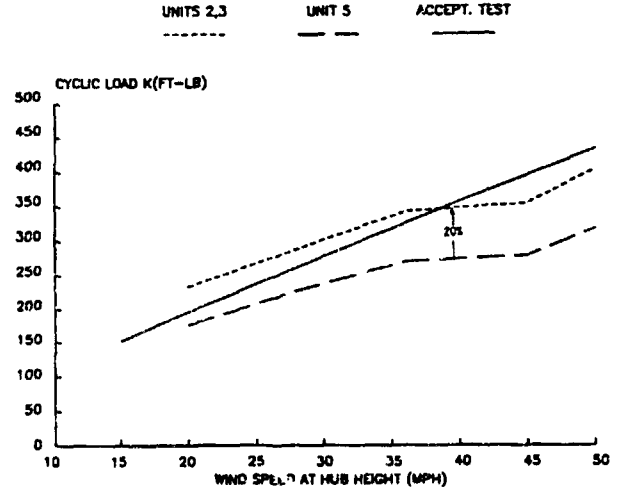


Figure 19. Comparison of Mean Cyclic Flapwise Moment at Sta. 370

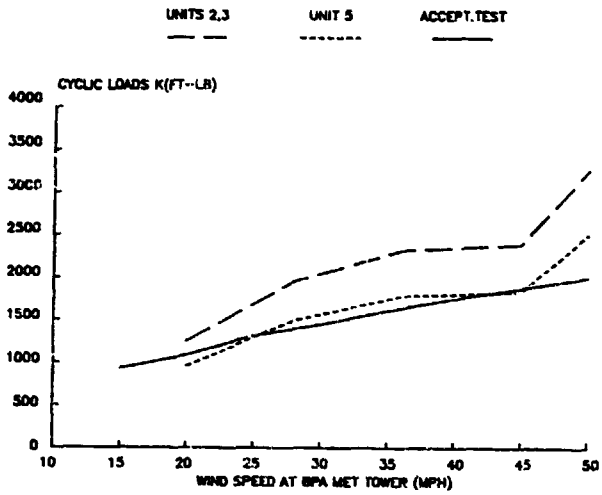


Figure 20. Comparison of Mean Cyclic Tower Moment at Sta. 600

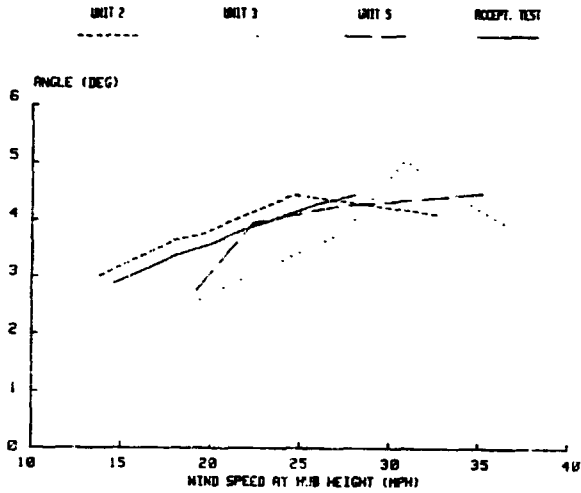


Figure 21. Comparison of Cyclic Teeter Angle

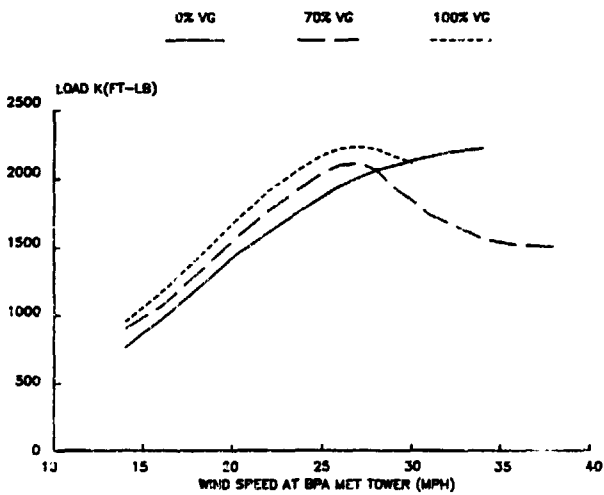


Figure 22. Effect of VG on Mean Flapwise Moment at Sta. 370 (Unit #3)

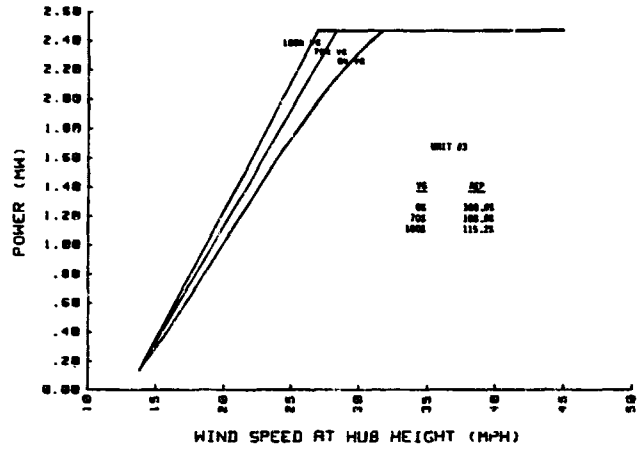


Figure 23. Effect of VG on Performance (Unit #3)

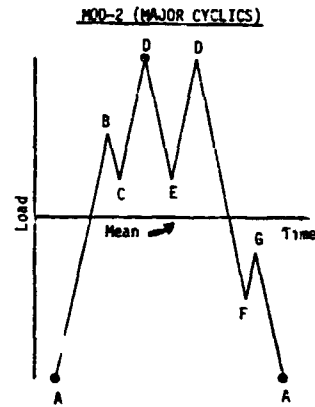


Figure 24. Mod-2 Fatigue Load Cycle Counting Procedure

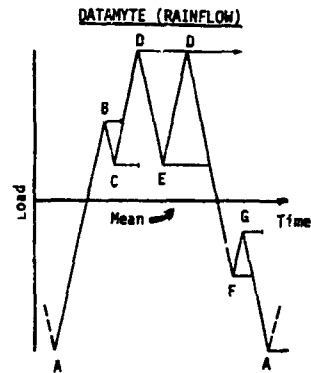


Figure 25. Rainflow Fatigue Load Cycle Counting Procedure

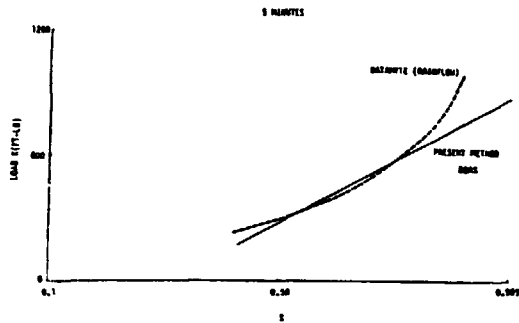


Figure 26. Cumulative Distribution of Cyclic Flapwise Moment at Sta. 370 for Datamyte and Present Method (5 min. sample)

DDAS DATAMYTE

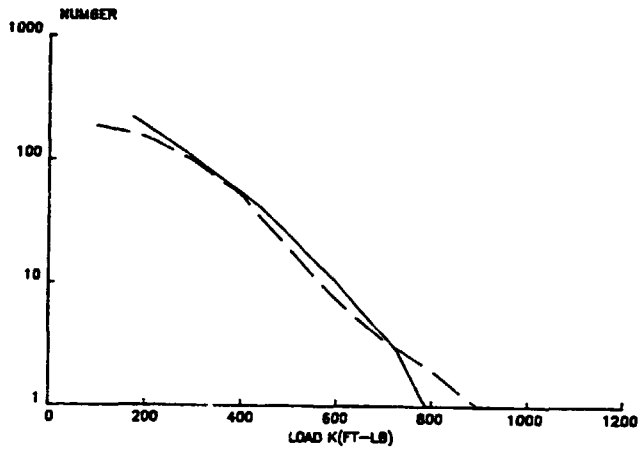
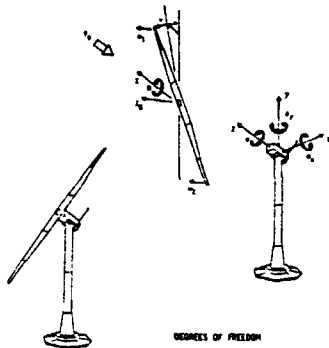


Figure 27. Exceedance Plot of Cyclic Flapwise Moment at Sta. 370



- DEGREES OF FREEDOM
- q₁ - 1ST DYN. FLAP BENDING
 - q₂ - 1ST ANTI-SYM. FLAP BENDING
 - q₃ - 2ND FLAP BENDING
 - q₄ - 1ST TOWER SIDE BENDING
 - q₅ - 1ST TOWER TORSION
 - q₆ - 1ST BLADE PITCH
 - q₇ - 1ST TOWER TORSION
 - q₈ - 1ST BLADE PITCH
 - q₉ - 1ST TOWER TORSION
 - q₁₀ - 1ST BLADE PITCH
 - q₁₁ - 1ST TOWER TORSION
 - q₁₂ - 1ST BLADE PITCH
- where:
- $$q_1 = \frac{1}{2} \frac{d^2 \theta}{dt^2}$$
- $$q_2 = \frac{1}{2} \frac{d^2 \theta}{dt^2}$$

Figure 28. DYLOSAT Model of a Two-Bladed Wind Turbine

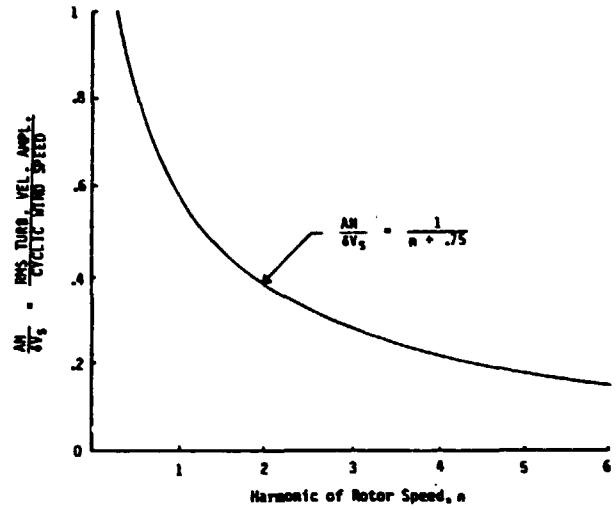


Figure 29. NASA Interim Turbulence Normalized Spectrum

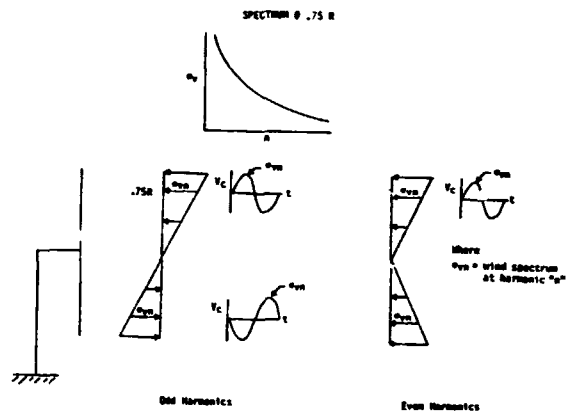


Figure 30. Conceptual Description of the NASA Interim Turbulence Model

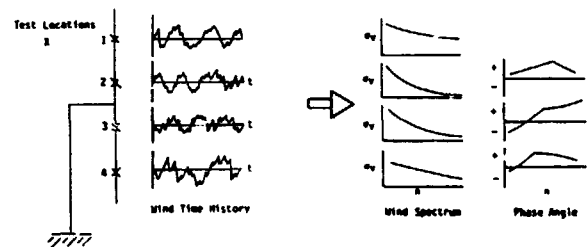


Figure 31. Conceptual Rotationally Sampled Wind Model

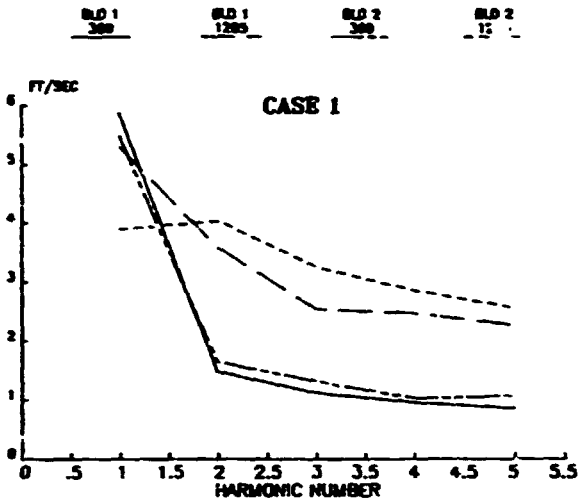


Figure 32. Rotationally Sampled Wind Spectra

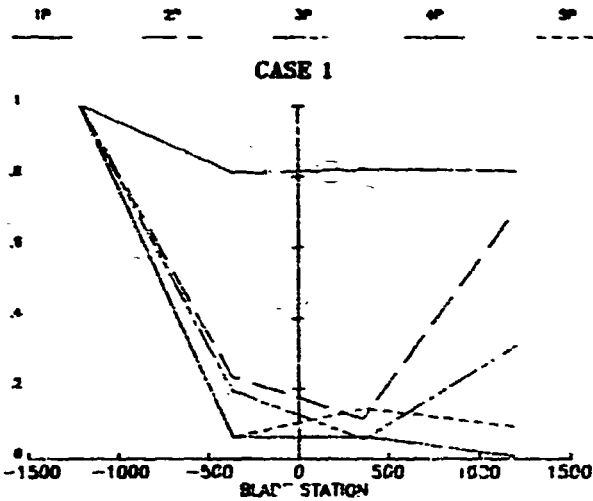


Figure 33. Rotationally Sampled Wind Coherence

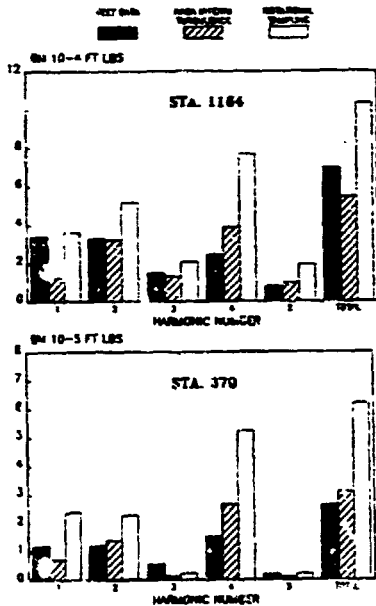


Figure 34. Rotor RMS Bending Moment - Case 1

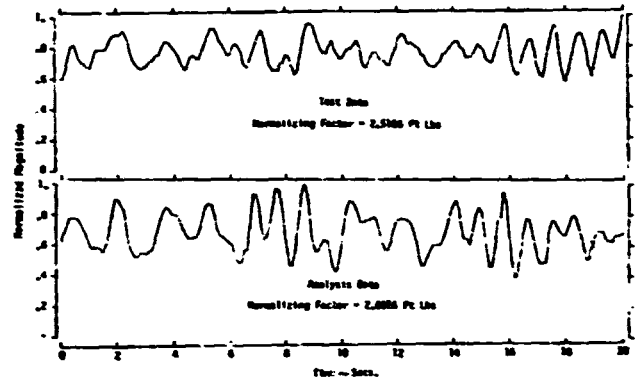


Figure 35. Bending Moment Time History at Rotor Station 370

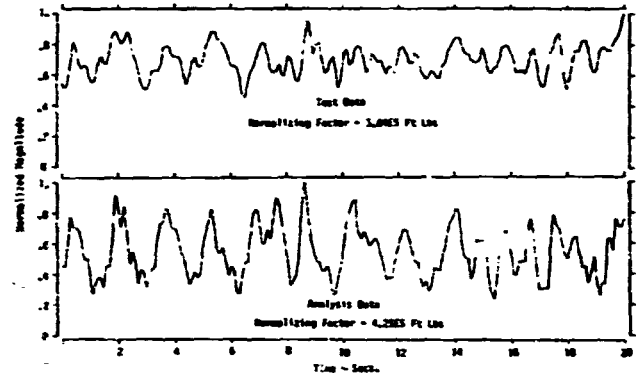


Figure 36. Bending Moment Time history at Rotor Station 1164

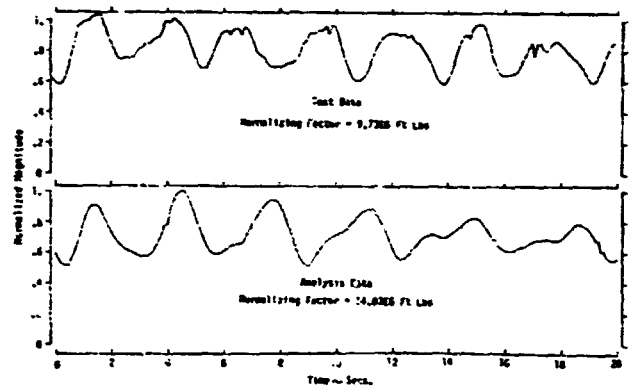


Figure 37. Bending Moment Time History at Lower Station 600

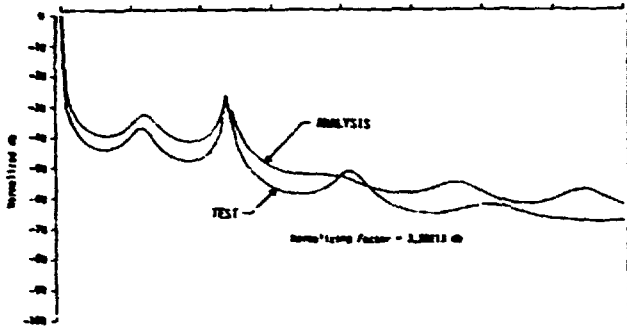


Figure 39. Spectral Analysis of Bending Moment Time History at Rotor Station 370

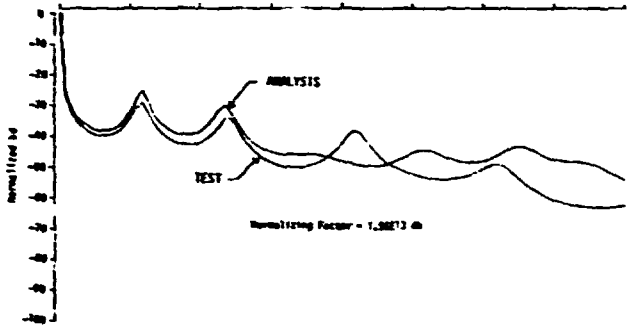


Figure 39. Spectral Analysis of Bending Moment Time History at Rotor Station 1164

Table 1
Rotationally Sampled Wind Test Conditions

Case 1

Date: 8/4/83 21:22 PST $V_{mean} = 32.7$ MPH

Case 2

Date: 8/5/83 17:03 PST $V_{mean} = 21.0$ MPH

Case 4

Date: 8/10/83 12:51 PST $V_{mean} = 27.1$ MPH

ANALYSIS METHODS FOR WIND TURBINE
CONTROL AND ELECTRICAL SYSTEM DYNAMICS

E. N. Hinrichsen

Power Technologies, Inc.
Schenectady, New York

ABSTRACT

The integration of new energy technologies into electric power systems requires methods which recognize the full range of dynamic events in both the new generating unit and the power system. Since new energy technologies are initially perceived as small contributors to large systems, little attention is generally paid to system integration, i.e. dynamic events in the power system are ignored. As a result, most new energy sources are only capable of base-load operation, i.e. they have no load following or cycling capability. Wind turbines are no exception. Greater awareness of this implicit (and often unnecessary) limitation is needed. Analysis methods are recommended which include very low penetration (infinite bus) as well as very high penetration (stand-alone) scenarios.

INTRODUCTION

Electric power systems are the largest readily available market for new energy sources. Interconnection with utility power systems is generally a prerequisite for economic use. The technical issues of interconnection can be viewed in different ways. For the purposes of this paper the two extreme views will be called 'connection' and 'integration'. Connecting a new power source to an electric power system is analogous to connecting an appliance to an outlet. If the appliance is compatible with the voltage and frequency present at the outlet and if the current drawn does not exceed the rating of the wires connecting the outlet, interconnection is successful. This view is the one most likely taken when small sources are connected to large systems. It is the classic low penetration perspective. Implicit in this perspective is the assumption that the power system is an immense, static reservoir of energy, devoid of any dynamics.

Integrating a new power source into an electric power system is a very different activity. A typical scenario which requires integration rather than connection is an isolated 5 MW diesel power plant to which 2 MW of wind turbines are added. Such a plant may supply power to an island, with loads varying between 3 MW during the day and 1.5 MW during the night. Integration is necessary whenever the power system is finite with respect to the new source, i.e. it is inherently associated with high penetration.

This paper examines analysis methods used for wind turbine interconnection studies to determine why the connection viewpoint has generally been taken, and what the consequences have been. It is shown that this viewpoint has not only prevailed in wind turbines but in many other new energy technologies as well.

The material is organized in six parts:

- o Part 1 is a review of the relevant features of power system controls and dynamics

- o Part 2 discusses the relevant characteristics of wind turbines
- o Part 3 defines requirements for integration of new energy sources
- o Part 4 identifies the reasons why new energy sources are often connected rather than integrated
- o Part 5 discusses the course taken in interconnecting wind power
- o Part 6 contains conclusions and recommendations.

1. CHARACTERISTICS OF ELECTRIC POWER SYSTEMS

Let us recall the characteristics of power systems that are relevant to integration of new power sources:

- o Equilibrium of Generation and Load

System frequency only remains at the nominal value as long as generation and load are equal. Load is not controlled by the utility but by its customers. If load exceeds generation, system frequency and generator speeds will decrease because kinetic energy is drawn from the rotating inertias to make up the generation deficiency.

- o Primary (Turbine) Control

Individual generator speed controllers (governors) respond to the decrease in speed and admit more steam or water to their respective turbines. This is the initial (primary) response of the system to a disturbance. It takes place at each machine, which has an active speed controller. The speed controllers have proportional characteristics, i.e. every new equilibrium between generation and load is associated with a new system frequency. The use of proportional speed controllers with the same regulation (droop) from zero to rated load permits sharing of load in proportion with generator capabilities.

o Secondary (System) Controls

Another control function is needed to return system frequency to the desired value. Load frequency control is a system function with slow integral characteristics. It operates by remotely raising the speed setpoints of participating generators. In addition to load frequency control, secondary control exercised at the system level is also responsible for economic dispatch and unit commitment. Economic dispatch gives the source with the lowest incremental cost preference to supply the next load increment. Unit commitment predetermines a reliable and economic generation mix for future, predicted loads.

o Load Cycle and Spinning Reserve

Within a 24 hour period the minimum load in an electric utility system is typically 40 to 70% of the maximum level. The secondary (system) control functions which establish and maintain economic and reliable use of system resources must therefore change generation mix and generation levels daily, both in a predictive and an adaptive manner. The dispatch of system resources exercised at the system control level must also provide a suitable reserve of spinning, on-line generation for contingencies, i.e. there must be generators which operate below rated power, ready to increase their generation when a sudden generation deficiency occurs. The spinning reserve must be distributed to a sufficient number of generating units so that the aggregate speed of response of generating units is fast enough to arrest a frequency decay. It should be noted that most large steam turbines have rates of response of only 1 to 2% of rating per minute due to large thermal time constants of turbines and steam generators.

2. PROCESS CHARACTERISTICS OF WIND TURBINES

There are five peculiarities which characterize wind turbines from the viewpoint of system integration:

o Non-Steady Energy Source

The bandwidth of input energy fluctuations ranges from nearly zero to about 1 Hz. This causes output fluctuations reflecting both the input spectrum and drive train torsional modes excited by the non-steady energy input.

o High Turbine Inertia and Low Torsional Stiffness Between Turbine and Generator

This causes low frequency torsional modes below 1 Hz and decouples turbine and generator during disturbances.

o Speed/Torque Characteristics

This can vary from constant speed variable torque for a synchronous generator to variable speed constant torque for a variable speed generator. Induction generators occupy an intermediate position between these two extremes.

o Voltage/Reactive Power Characteristics

Synchronous generators provide waveform, phase balance, and variable reactive power for voltage control. Induction generators provide waveform and phase balance, but absorb reactive power and cannot provide voltage control. Frequency converters used with variable speed wind turbines may neither provide good waveform and phase balance nor voltage control and may actually depend on the presence of a strong power system for commutation of their thyristors.

o Turbine Control

If the turbine has variable pitch blades, energy capture can be controlled. The choice of the controlled variable (torque, power or speed), the type of control (proportional or integral or both), and the gain of the control loops determine how the turbine operates in an interconnected system.

3. REQUIREMENTS FOR SYSTEM INTEGRATION

From the description of power system characteristics we can draw two conclusions:

o New power sources should be able to follow changes in load. Changes in generation due to load following must be associated with changes in frequency. Load following capability should be dispersed throughout the system to achieve an adequate rate of response. Dispersal is also desirable so that parts of a system can survive as electrical islands after a system breakup.

o New power sources should be able to operate at different levels of generation in response to commands

from a system dispatch center. Whether a particular generating unit will be used for base-load or cycling duty depends on the resource mix of the particular system. Since different systems have different resource mixes, a particular technology may be used for base-load in one system and for cycling in another system. Any inherent restrictions a particular generation process imposes on operating flexibility should be built into the utility dispatch strategy, not implemented in the control design of generating units.

4. TYPICAL DEVELOPMENT OF A NEW ENERGY TECHNOLOGY

The need for analyzing interconnection issues typically arises at a time when the new process itself is not fully understood and the associated equipment is under development, i.e. when analytical resources are preoccupied with process and equipment issues. Since the process is new, a low penetration scenario is always envisioned at the outset [1]. It is not surprising that the interconnection viewpoint taken at this time is that of connection, not integration. Unfortunately, this is also the time at which decisions must be made about control of the process. In this manner, the operating characteristics of new utility power sources are often established before any thought has been given to system integration. The result of this are sources only suitable for base-load operation. Examples other than wind are steam plants with once-through steam generators (supercritical) and steam plants with nuclear reactors [1]. It is interesting to note that in both of the latter cases process control was not changed when the original premise of low penetration was no longer valid.

Two other factors may aggravate this systematic flaw in our method for developing new energy technologies. The first is the ever necessary economic justification. Proponents of new technologies obviously assume base-load duty for their economic calculations because it minimizes the impact of fixed costs. It may very well be that after a long process of economic justification, organizations find it intolerable to contemplate control systems which would allow a new source to do anything but maximize energy output. They may feel that any other mode of operation would invalidate their economic justification. The second factor is the recently enacted PURPA Law. Independent power producers selling power to utilities want to maximize revenue and are only interested in contributing to the base-load component of the utility load. Manufacturers producing equipment for sale to independent power producers will find little demand for features necessary for system integration.

5. DEVELOPMENT OF WIND POWER

The phenomena just described have strongly influenced wind power development. Preoccupation with process requirements and low penetration scenarios has led to many wind turbine designs without load following or cycling capability. It may be argued that contrary to steam plants with supercritical and nuclear steam generators wind will always be a low penetration

technology. In the author's opinion, such reasoning is flawed because it overlooks that wind turbines may be very competitive in small isolated systems with high fuel costs.

The following three examples illustrate how these thoughts have influenced wind turbine analysis and the resulting wind turbine control and equipment design.

o Damping of Torsional Modes

A common method for representing the electric utility system in wind turbine analysis is the so-called infinite bus. An infinite bus is dynamically equivalent to a generator with infinitely large rotating inertia and infinitely small electrical resistance, i.e. frequency and voltage of the utility tie are always constant. This is low penetration in its purest form, the utility system is always at steady state.

If torsional oscillations of wind turbine drive trains are examined with a simulation system that represents the utility system with an infinite bus, it is found that the best place to introduce damping of the predominant torsional mode is at the turbine. The mode shape reveals that the torsional amplitude is much higher at the turbine than at the generator. This is caused by high system inertia and low torsional stiffness between turbine and generator. This type of analysis had led to damping by modulating blade angle. It has been shown [3] that the mode shape of the dominant mechanical mode changes with penetration. If wind turbines dominate system inertia, as may be the case in small isolated systems, the predominant torsional motion shifts from the turbines to the generators. The effectiveness of damping by blade angle movement decreases. This relationship between torsional damping and penetration is not recognized when electrical system representation is based on an infinite bus.

o Turbine control

When wind turbine controls are analyzed in a simulation environment which does not allow frequency variations, primary speed control of individual generators with proportional controllers and secondary reference adjustment with integral controllers makes very little sense. In such an environment the obvious method for controlling a variable pitch wind turbine is to adjust blade angle to maintain constant power. This method provides the necessary

torque control and maximizes energy capture. This is what most wind turbine designers have done. The result is a resource suitable only for base-load and low penetration.

o Variable Speed Wind Turbines

In the last two years there has been much interest in variable speed, constant frequency wind turbine generators. This type of wind turbine uses frequency converters to change variable frequency to constant frequency alternating current. Frequency converters are difficult to apply in high penetration scenarios because they may need frequency and voltage references and they may distort waveshapes. A designer of such a system has to recognize that the wind turbine must be able to follow load with changes in generator frequency in order to participate in primary control. There is a simple test which determines whether a variable speed wind turbine with frequency converters can be integrated into a power system. If it can function as a stand-alone source for a variable load, it can be integrated. The validity of this test is not limited to variable speed wind turbines. It can be applied to any new energy technology. It is easy to see why this test is valid. The historical basis of utility systems is interconnection of autonomous, stand-alone sources. Interconnection improves economy and reliability, but is not a prerequisite for operation. A source capable of stand-alone operation in a variable load system has all the attributes necessary for system integration.

6. CONCLUSIONS AND RECOMMENDATIONS

What conclusions can one draw after surveying power system integration of new technologies in general and of wind turbines in particular?

The first conclusion would have to be that any claims about successful integration of wind turbines should be very modest. Connection would be a more appropriate term. Our analysis methods and our control design have largely ignored dynamics inherent in the power system. In most actual installations the implicit assumption of low penetration has fortunately been justified. The second conclusion is that the same situation exists in almost all other new energy technologies. It exists in nuclear steam plants, supercritical steam plants and there are signs that it may happen in photo-voltaic power sources. The particular scientific and engineering community always considers its technology to be the star of the show and assumes without examination that other technologies can play supporting roles as needed [2]. This somewhat parochial view is one of the main causes of a structural flaw in our method of organizing energy development efforts.

Recommendations range from the necessary minimum goal of increased awareness in the wind turbine community to the desirable maximum goal of better analysis tools and improved control design.

Increased awareness is needed because there are several potential applications in the United States where the present analysis methods are unsuitable because the implicit assumption of low penetration is no longer valid. One example are the Hawaiian islands other than Oahu. These islands have excellent wind resources and small electrical systems (5-100 MW).

A recent study of controls for variable pitch wind turbines for NASA-Lewis includes analysis methods and control designs suitable for high penetration scenarios [3]. The basic difference between the traditional and the recommended analysis method is that with the latter the candidate system must function not only in an infinite bus but also in a stand-alone environment. Stand-alone simulation is a necessary complement to infinite bus simulation. Both are abstractions, and both have the advantage of computational simplicity. The actual applications lie between these two extremes.

REFERENCES

- [1] R. P. Schulz, "Impacts of New Energy Technology Generation and Storage Processes on Power System Stability and Operability", Proceedings of Conference on Research Needs for the Effective Integration of New Technologies into the Electric Utility, pages 193-217, St. Michaels, MD, 7/26-7/30/82.
- [2] L. H. Fink and W. E. Feero, "Effective Integration of New Technologies into Electric Energy Systems", IEEE Pas Volume 101, No. 7, pages 1833-1842, July 1982.
- [3] Z. N. Hinrichsen, "Control of Large Wind Turbine Generators Connected to Utility Networks", DOE/NASA/0252-1, NASA CR-168200, May 1983.

CONTROL SYSTEM DESIGN FOR THE MOD-5A 7.3 MW WIND TURBINE GENERATOR

Robert S. Barton, Theodore J. Hosp, George P. Schanzenbach

General Electric Company, AEPD
King of Prussia, Pa., 19406

DOE/NASA Horizontal-Axis Wind Turbine Technology
Workshop, May 8-10, 1984, Cleveland, Ohio.

ABSTRACT

This paper provides descriptions of the requirements, analysis, hardware development and software development phases of the Control System design for the MOD-5A 7.3 MW Wind Turbine Generator. The system, designed by General Electric Company, Advanced Energy Programs Department, under contract DEN 3-153 with NASA Lewis Research Center and DOE, provides real time regulation of rotor speed by control of both generator torque and rotor torque. A variable speed generator system is used to provide both airgap torque control and reactive power control. The wind rotor is designed with segmented ailerons which are positioned to control blade torque. The central component of the control system, selected early in the design process, is a programmable controller used for sequencing, alarm monitoring, communication, and real time control. Development of requirements for use of aileron controlled blades and a variable speed generator required an analytical simulation that combined drivetrain, tower and blade elastic modes with wind disturbances and control behavior. An orderly two phase plan was used for controller software development. A microcomputer based turbine simulator was used to facilitate hardware and software integration and test.

INTRODUCTION

The MOD-5A Wind Turbine Generator design program was started in July, 1980. After conceptual design and preliminary design phases were completed, the MOD-5A configuration was rated at 7300 KW and featured a synchronous generator and two-speed rotor operation through a shiftable gearbox.

When final design and procurement started, it was found desirable to minimize the gearbox complexity and to provide a drivetrain back-torque during controlled shutdowns. The latter reduced cyclic loads that were design drivers for the aerodynamic partial span control. A variable speed generator subsystem was selected to meet these needs. The partial span control was subsequently replaced with an aileron control, and the variable speed generator subsystem provides a startup assist by motoring the rotor.

The MOD-5A design was performed under Contract DEN 3-153 for NASA Lewis Research Center and DOE by General Electric Company, Advanced Energy Programs Department.

MOD-5A SYSTEM

The MOD-5A model 304.2 system, operating parameters and features are shown in Figure 1. Control logic is provided by a programmable controller located in the nacelle. Operator control terminals are located at ground level in a separate building and remotely at a utility dispatch site. Automatic control of the MOD-5A operation provides for high availability and good energy capture in the NASA design wind regime and other wind regimes.

REQUIREMENTS

The control system of the MOD-5A was required by the design statement of work to:

- o provide automatic unattended failsafe operation of the wind turbine
- o provide ground level manual control for checkout and maintenance
- o provide power quality acceptable to a utility
- o provide remote dispatcher monitoring and control

Internal requirements were also established. Experience with MOD-1 indicated critical control multiplexing through sliprings should be avoided. A purchased controller with sensor and control interface software and hardware was desirable for initial units to permit concentration on the application process control software.

DEVELOPMENT PLAN

The development and configuration control planning established a two phase software development. During the first phase, a target controller hardware, a software development unit, and a wind turbine simulator were used to design, develop, code, debug, integrate, and checkout a full controller software package. This initial package was based on preliminary issued control system requirements. In parallel with the first phase development, control system analysis and wind turbine hardware design activities were ongoing. Design change requirements were accumulated, but not implemented during the first phase of software development.

The second phase of control system development incorporated the final control system requirements into hardware and software. A large portion of the first phase software was included and streamlined as a result of development experience. As major changes occurred in the MOD-5A configuration prior to the final requirements, this two phase plan worked well.

CONTROL PLAN

The system control plan for the MOD-5A model 304.2 is shown in Figure 2. This emphasizes the rotor and drivetrain control functions. Active control functions and critical sensors are shown in Table 1. Speed is the primary controlled parameter, using both ailerons to control wind torque at the rotor and a cycloconverter in the variable speed generator subsystem to control generator airgap torque. The utility reactive power or voltage is also controlled by the cycloconverter.

AILERON CONTROL

Aileron control of rotor torque was introduced to MOD-5A in mid-1983 with model 304.2. A 40% chord, 40% span plain aileron arrangement is used. Control properties were developed from wind tunnel test data. Three mechanically independent aileron sections, each driven by a hydraulic actuator, are used on each blade. An emergency accumulator is mounted with each actuator. Position servo loop electronics and valving, position sensing, and a latch are built into each actuator. The main hydraulic supply is mounted on the rotor support yoke with blade isolation check valves. The controller sends position commands to aileron pairs, such as both tip sections, and compares feedback positions signals to detect servo errors. A rotor stopping brake at the yoke is used to reach a full stop as the ailerons are not predicted to completely halt the rotor.

The rotor operating map is shown in Figure 3. These characteristics are included in the simulation model which is described later. Aileron control is used above 3 rpm to control rotor speed until the generator is synchronized. Generator airgap torque control holds system speed for wind speeds less than rating, including an automatic speed change from low range to high range. For wind speeds above rating, the aileron control holds rotor torque at the rated level of 3.38 million foot-pounds.

GENERATOR CONTROL

The MOD-5A variable speed generator subsystem is a Scherbiustat type drive comprised of a wound rotor or doubly fed induction machine and a rotor circuit cycloconverter. The speed-power envelope for the subsystem is shown in Figure 4. The rotor circuit is rated at 1500 KVA, 20% of the total power rating. This permits generating operation of the wind rotor from below 12 rpm to about 17.5 rpm. The generator has 6 pole construction with a 60 Hz synchronous speed of 1200 rpm.

The cycloconverter controller responds to torque and reactive power reference signals. It provides quadrature control of thyristor firing to maintain both generator power angle and excitation level. Feedback signals are supplied from generator speed, bus voltage, bus current, and stator current. The wind turbine speed controller drives the torque reference in proportion to speed error, as shown in Figure 4. This provides a speed-torque characteristic similar to a 3.5% slip machine, which damps the drivetrain oscillatory modes.

The speed controller reference is slowly moved automatically between the high and low speed ranges, depending on average power output. This keeps the wind rotor in an efficient tip speed range, as illustrated in Figure 3. The steady aileron position and output power versus wind speed are shown in Figure 5.

PERFORMANCE SIMULATION

An analytical model of the MOD-5A drivetrain control and tower bending modes is shown in Figure 6. This is a much simpler model than the dynamics model used to predict system frequencies and loads. The controls model includes a two inertia drivetrain and models the first blade flap elastic mode and the tower bending mode.

The bending modes are excited by rotor thrust changes arising from wind disturbances and aileron control action. As the MOD-5A aileron control is not used to provide drivetrain damping, the possibility of interaction with the tower bending mode was minimized, but the degree of freedom was retained in the model. The drivetrain and tower bending mode damping coefficients are small and these modes will oscillate if excited.

ROTOR SPEED CONTROL LOOP

A linearized rotor speed control loop in Z transform notation is shown in Figure 7 for a 40 mph operating condition. The block diagram indicates the digital and analog parts of the loop. Elements to the left of the vertical dashed line are carried out in the wind turbine controller, which has a cycle time of 0.1 seconds. The control algorithm has an integral gain of 5°/sec/rpm and a proportional gain of 30°/rpm, implemented digitally. A deadband of +0.07 rpm is used with the proportional gain to avoid steady oscillation from wind turbulence. The overall gain is varied with aileron position to keep loop gain constant. Digital clamps are provided to prevent integrator wind-up and to limit the aileron position command, but are not shown in the diagram.

The aileron servo-actuator response is represented as a 5 rad/sec. first order characteristic. Rate limits are used in the time domain representation. Mechanical elements include the slope of the aerodynamic torque vs. aileron position curve, system inertia, and a complex pole-zero from the generator inertia outside the control loop. This is an off-line model and does not include the airgap torque control loop, which looks like a viscous damper.

Speed feedback design used a digital sensor that counts toothed wheel magnetic pickup pulses over 0.05 seconds and periodically updates the value sent to the controller. The controller's analog to digital conversion time and memory update time are also included in the loop model.

The Bode plot in Figure 7 shows both the ideal analog model characteristics and the additional phase shift introduced by the digital time delays. A bandwidth of 1 rad/sec. is used for the rotor control loop. The 58° phase margin and 16 dB gain margin indicate the gain could be raised 10dB if necessary. Minimum requirements are 30° phase margin and 6 dB gain margin.

GENERATOR SPEED CONTROL LOOP

The generator linearized speed control loop characteristics are shown in Figure 8. This loop has a bandwidth of 17 rad/sec., which is too fast for implementation within the controller 0.1 second cycle time without unacceptable phase shift. The error summing junction and torque reference are provided by an analog circuit which obtains its speed reference from the controller. Operation of the cycloconverter and the generator rotor electrical dynamics is modeled as an 80 rad/sec. first order characteristic.

Ample gain and phase margins are evident in the Bode plot. Interaction with the rotor speed control loop is negligible with the large bandwidth difference. The closed loop characteristics of the generator speed control loop are mechanically similar to a high slip induction generator. By changing the proportional gain term, the effective slip is changed, within limits imposed by the mechanical frequencies of the wind turbine structure.

The cycloconverter torque reference signal is scaled from 40% of rated torque in a motoring direction to 120% of rated torque in a generating direction. When the aileron control is operating to maintain steady state rated torque, the damping effect of the generator speed-torque slope is active. With the scaling, maximum transient torque is limited to 120% of rating on an infrequent basis.

A more complex generator and cycloconverter model was also prepared as generally described in Reference 2. This model includes the electrical dynamics of the generator and the quadrature controller and is used to determine voltage and reactive power, as well as real power conditions. It will not be further described in this paper.

TIME DOMAIN SIMULATION RESULTS

The controls analysis simulation model was used to examine transient response of the MOD-5A wind turbine. Response to a 5 mph wind step is illustrated in Figure 9. Wind steps are not real phenomenon, but a step input excites all response modes and provides insight into response characteristics. The lightly damped tower bending mode is seen in Figure 9, set c. Clamping of the generator airgap torque is seen in set b. When the torque is clamped, the damping provided by the generator control is no longer present and the torque discontinuity slightly excites a generator inertia oscillation. Note that the aileron response to the rotor speed controller, shown in Figure 9, in set d, is not noticeable until 1.5 seconds after the step. The proportional control deadband limit was reached at this point and the proportional gain path became active.

The response to a sinusoidal wind gust is shown in Figure 10. A fully immersed rotor model is used. The 9 mph, 12 second gust is a far more severe event than found in nature. Initial transient response is similar to that observed for the wind step, but there is an undershoot when the disturbance returns to the original steady wind value. The speed swing is more severe than occurred with the wind step.

Note in Figure 10, set b, that total output power follows the speed oscillation as generator rotor power varies with speed. Stator power represents airgap torque and is clamped for the initial portion of the response.

Aileron response is outside the proportional deadband from 4 to 11 seconds and from 12 to 13 seconds, as shown in set d of Figure 10. The slower acting integral aileron control returns the system to initial conditions in less than 60 seconds.

A more realistic steady wind is illustrated in Figure 11. The NASA interim turbulence definition produces significant excitation at even multiples of the rotor speed. The sinusoidal gust noted in Figure 10 is also applied in Figure 11. A twice per revolution forced response is observed in all but the final aileron position and rate traces. This illustrates the beneficial effect of the aileron proportional deadband. Without the deadband, the aileron control would respond to the speed oscillation and cause unacceptable wear and maintenance. The deadband value would be field adjustable to match site turbulence characteristics.

A steady drivetrain and output power oscillation of about 10% peak to peak results from the turbulence model. Fatigue design of the drivetrain includes this and larger wind induced stress ranges. If necessary, the generator controller torque-speed slope could be field adjusted to reduce this amplitude.

Finally, a loss of load transient from a rated wind condition of 32 mph is illustrated in Figure 12. The generator airgap torque drops to zero and the generator inertia oscillates in a lightly damped manner around the rotor inertia. Rotor speed increases enough to drive the aileron actuators at their 5°/second limit for almost 7 seconds, as shown in Figure 12, set d. Maximum rotor speed is about 18.25 rpm. Software and failsafe hardware overspeed trip points were defined above this transient overspeed to avoid nuisance shutdowns to lockout which would require a site maintenance visit.

The transient response analyses also included down gusts, as well as up gusts and examined all wind speed conditions. Time delay effects and controller gains were defined on the basis of these analyses.

CONTROL SYSTEM ARRANGEMENT

A simplified block diagram of the MOD-5A control system is shown in Figure 13. The number of command and sensor signals that each line represents is noted. An "S" indicates a digital serial data signal. Over 70% of the signals to the controller are from the nacelle and rotor which is why the main controller cabinet is located in the nacelle. The three serial data links are not time-critical to wind turbine control.

The emergency shutdown panel is a relay logic circuit that provides deadman type initiation of aileron controlled shutdown if the main controller or critical backup sensors indicate a failure. This panel also causes a shutdown if control power is lost.

A further backup emergency shutdown (BESD) circuit to detect overspeed is mounted on the rotor. Each blade has an acceleration or g-switch that is oriented radially to respond to speed. The switch circuit is independent of the emergency shutdown panel. All aerodynamic control functions are tested automatically before every MOD-5A startup. The aileron servo actuators are used to move the control surfaces and each emergency shutdown circuit is operated to assure return to full aileron deployment. A test circuit is included in the g-switches to check both minimum and maximum trip levels on each startup.

Ground control equipment is housed in the electrical equipment building shown in Figure 14. The variable speed generator subsystem cycloconverter and isolation transformer are shown at the right, with the 4160 volt switchgear. Auxiliary power distribution and control connection cabinets are to the left. Batteries are mounted in a separate, vented area. A small office area contains the system display panel, site operator terminal, and engineering data equipment.

The system display panel is shown in Figure 15. It provides a panic button and master key control panel at the upper left. Two closed circuit video monitors are included in the first unit design. One camera observes the interior of the nacelle and the other views the rotor. The right panel provides switch controlled digital meters for quick observation of operating conditions and electrical status.

The main controller equipment shown in Figure 16 is mounted in a double bay cabinet in the nacelle. An air to air heat exchanger cools the cabinet without a refrigerant cycle for higher availability. The cabinet air is internally circulated, but is not connected to outside air. In addition to the controller equipment and interface modules, sensor conditioning circuits are installed in the controls equipment cabinet.

CONTROLLER DEVELOPMENT

Controller hardware and software development followed the two phase plan noted in a prior paragraph. The plan permitted accommodation of the major changes that occurred when the variable speed generator and ailerons were introduced into the system design.

Equipment selection was made early and a target controller hardware assembly was procured for development use. Controller requirements are shown in Table 2. A single board computer system meets most of the requirements, but would have required more integration effort than planned. A high-end programmable controller, the Eagle Signal Eptak 700, was selected. It has multiple coding language capability and a proven industrial reliability record. With the tremendous growth in microcomputer based equipment, more equipment choices are now available than when the MOD-5A equipment selection was made. An updated selection was not made for the first few units because of the software development investment.

A wind turbine simulator was developed using another programmable controller, the Analog Devices MACSYM 2 and a custom analog board. The simulator provided sensor inputs and simulated operation of the MOD-5A

to the controller. It was valuable in debugging and testing the integrated controller software.

Controller development milestones are shown in Table 3. A fully integrated software package was completed and is ready for wind turbine hardware integration.

Software modes are shown in Figure 17. Vendor software provides real world signal interfacing with controller memory, real time clock values, and the master operating system. Application software is used to initialize outputs and variables on a cold start, execute on a 0.1 second real time basis and properly sequence through the main program modules.

The main program modules are as follows:

- o Input Signal Manager (ISM)
- o Data Processing
- o Mode Logic
- o Data Archive
- o Power Generation
- o Manual
- o Communication
 - Remote Terminal
 - Site Terminal
 - Control Data System (CDS)
- o Startup
- o Ramp
- o Yaw
- o Alarm
- o Normal/Emergency Shutdown
- o Rotor Hydraulic Pump Module
- o Output Signal Management (OSM)
- o Memory Test (background)

The data processing module computes averages, adds signal biases, and packs data. Mode logic establishes flags for the executive to mine which other modules to run. The manual module provides individual command outputs, with overall checking, in response to site terminal inputs.

Data archive uses over half of the random access memory (RAM) to store both a moving window of sensor data prior to a shutdown event, and also a window after the event. Lockout events require personnel at the site to command a restart and the restart software requires an archive dump. The archive data will assist in trouble shooting and maintenance. A memory test module operates in whatever time is not being used for control functions and sequentially checks RAM.

OPERATOR INTERFACE

Both the site and remote standard operator devices are 300 baud printing terminals. They provide a log of operation on event, demand, or time. A sample output is shown in Figure 18. Alarm outputs are noted when states change and command inputs are time tagged. The controller does not rely on a continuously active terminal, but may be modified to require this. If the terminal is shut off, the log data is sent out by the controller, but will be lost.

In place of the standard phone line remote terminal serial link, a parallel control and data interface may be used at the MOD-5A site. A parallel interface was planned for the Hawaiian Electric Company, (HECO), with an operator interface through the HECO dispatch computer using microwave transmission of data through a HECO multiplexor.

DEVELOPMENT RESULTS

Controller software was successfully integrated and checked out using the development controller and simulator. A timing check of the worst condition was made. It took 89 msec. to execute within the desired 100 msec. executive time cycle. The control subsystem specification requires less than 200 msec. so ample margin is evident. A normal cycle takes 83 msec., of which 10 msec. is from the controls data system, which is not permanently installed.

Application memory was planned at 20K bytes of programmable read only memory (PROM) and 20K bytes of RAM. Actual usage was 17.7K PROM and 17.3K RAM. 14K of the RAM usage is for archive data storage. Adequate margin exists for changes during hardware integration and field checkout.

Simulator outputs are shown in Figures 19, 20 and 21. A normal startup and power generation in an increasing wind is shown in Figure 19. There are three aileron movements of about 30° at symbol A during the startup check sequence followed by a motion to the startup angle. The rotor is motored to part speed, then the ailerons are active at B to control the rotor speed which follows an increasing reference. Synchronization and power generation occurs at C and the ailerons continue to their aligned position for maximum torque.

After the lower speed range is reached at D, wind speed steps were added at E, which first raise output power, then enter active aileron control at F. The power average causes automatic transition to the higher speed range at G. Continued wind steps above rating at H illustrate aileron control response. Random wind speed fluctuations are simulated and the power response is, therefore, oscillatory over a small range.

The yaw drive control sequences the push-pull hydraulic actuator and gripper drive system. A ratchet action occurs if there is a large yaw error as a full actuator stroke is only 10°. Response to large initial errors in both directions is shown in Figure 20. As the drive moves, the error is reduced. Motion occurs at 0.50°/second and the average continuous drive rate is just below 0.25°/second.

Finally, a yaw correction and a transition from electrical to aerodynamic torque control are illustrated in Figure 21. Random fluctuations in wind direction and speed are simulated.

CONCLUSIONS

The MOD-5A system and the control subsystem will provide well behaved performance in fluctuating winds. Analytical models are available for site specific performance analysis.

Software integration was completed successfully with the development controller and simulator. Timing and memory goals were met. The two phase development plan successfully accommodated major configuration changes.

The control subsystem was defined in detail with drawings and specifications and the software is ready for hardware integration.

ACKNOWLEDGEMENTS

The authors gratefully thank Art Birchenough (NASA) for support and review, Ray Wolfgang (GE) for analytical support, Roy Schaefer (GE) for simulator development, Jim Zimmerman (GE) and Linda Quam (GE) for software development and integration, and Don Dale (GE) and Keith McFarland (GE) for control equipment design.

REFERENCES

1. Barton, R.S., Lucas, W.C. "Conceptual Design of the 6 MW MOD-5A Wind Turbine Generator", Proceedings of the Fifth Biennial Wind Energy Conference and Workshop, SERI/CP-635-1340, Vol 1, pp. 157-168, October 1981.
2. Mayer, C.B., "High Response Control of Stator Watts and Vars for Large Wound Rotor Induction Motor Adjustable Speed Drives", IEEE Transactions IAS79:27F, pp. 817-823.

Table 1- Active Control Functions

ROTOR

AILERONS - 3/BLADE, POSITION CONTROL
 SPEED - REGULATED WITH AILERONS
 TEETER BRAKES - TWO LEVEL CONTROL, ALARMS
 STOPPING BRAKES - OFF/ON CONTROL
 ROTOR HYDRAULICS - OFF/ON, ALARMS
 G-SWITCH - BACKUP OVERSPEED SENSOR, TEST

NACELLE AND YAW

EMERGENCY SHUTDOWN PANEL - CONTROLLED BACKUP
 GEARBOX LUBE - OFF/ON, ALARMS
 GENERATOR LUBE - OFF/ON, ALARMS
 YAW HYDRAULICS - OFF/ON, ALARMS
 ROTOR POSITIONER - OFF/ON
 YAW DRIVE - SEQUENCED OFF/ON CONTROL, ALARMS
 GENERATOR SPEED - REGULATED WITH CONVERTER

GROUND AND ELECTRICAL

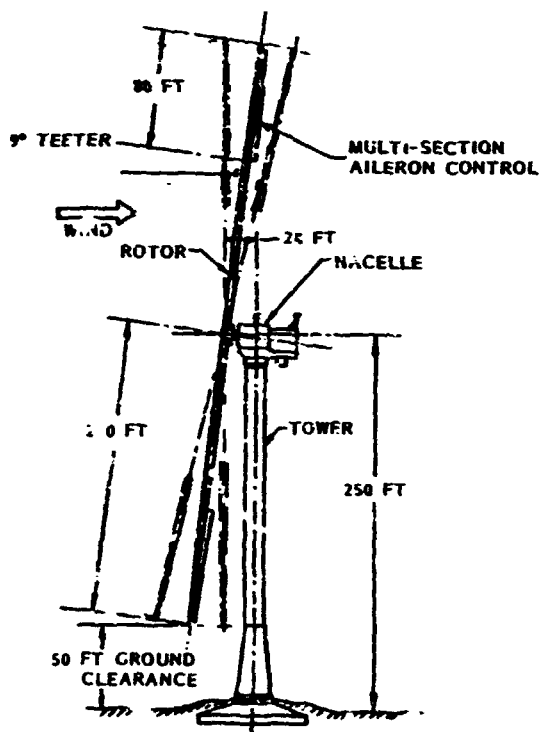
CYCLOCONVERTER - TORQUE CONTROL, VAR/VOLT CONTROL
 SWITCHGEAR - TRIP/CLOSE CONTROL, ALARMS
 INTRUSION ALARM
 LOCAL OPERATOR CONTROL - ENABLE, SETPOINTS, DATA
 REMOTE OPERATOR CONTROL - ENABLE, SETPOINTS, DATA

Table 2- Controller Hardware Requirements

- INPUT SIGNAL
 - 19 ANALOG
 - 69 DISCRETE (20 mA)
- OUTPUT SIGNAL
 - 6 ANALOG
 - 26 DISCRETE (3A/20A)
- SERIAL COMMUNICATIONS
 - (2) 20 mA 300 BAUD
 - (1) 20 mA 1200 BAUD
- CAPACITY
 - 64K
 - 20% USER PROGRAM
 - 20 K RAM
 - 8K ECL 3 & RAM
 - 16K I/O
- LANGUAGE
 - [] ASSEMBLY

Table 3- Control Subsystem Development Milestones

PHASE I	COMPLETED CONCEPTUAL DESIGN	4/81
	COMPLETED REQUIREMENTS FOR SYNCHRONOUS GENERATOR PARTIAL SPAN CONTROL	7/81
	COMPLETED EQUIPMENT SELECTION FOR CONTROLLER AND SIMULATOR	1/82
	COMPLETED CODING	7/82
	COMPLETED SOFTWARE MODULE CHECKOUT	12/82
PHASE II	COMPLETED SYSTEM INTEGRATION	4/83
	COMPLETED REVISION A REQUIREMENTS FOR VARIABLE SPEED GENERATOR	7/83
	COMPLETED SOFTWARE DESIGN WITH REVISION B REQUIREMENTS FOR AILERONS	10/83
	COMPLETED CODING AND MODULER CHECKOUT	2/84
	COMPLETED SYSTEM INTEGRATION	4/84



OPERATIONAL CHARACTERISTICS

RATED POWER	7300 KW AT 0.90PF
RATED WIND SPEED	32 MPH AT 250 FT
CUT-IN/CUT-OUT WIND SPEED	14/60 MPH AT 250 FT
MAXIMUM WIND SPEED (SURVIVAL)	130 MPH AT 250 FT
POWER CONTROL	MULTI-SECTION AILERONS
ROTOR RPM-SET SPEED	13.7/16.8 RPM ($\pm 10\%$)
ENERGY CAPTURE/YR	21.3×10^6 KWH (NASA SPECIFIED WIND SPEED DURATION CURVE, 14 MPH AT 32 FT, 100 % AVAIL)
TOTAL WT ON FOUNDATION	1804 K-LB

FEATURES

- WOOD LAMINATE BLADES WITH HIGH PERFORMANCE AIRFOIL - UPWIND, TEETERED
- NON-ROTATING ROTOR SUPPORT
- HYBRID EPICYCLIC/PARALLEL SHAFT GEARBOX
- VARIABLE SPEED/CONSTANT FREQUENCY OPERATION, WITH 2 SET POINTS
- SOFT SHELL TOWER, TUNEABLE BELL SECTION

Figure 1- MOD-5A System Model 304.2

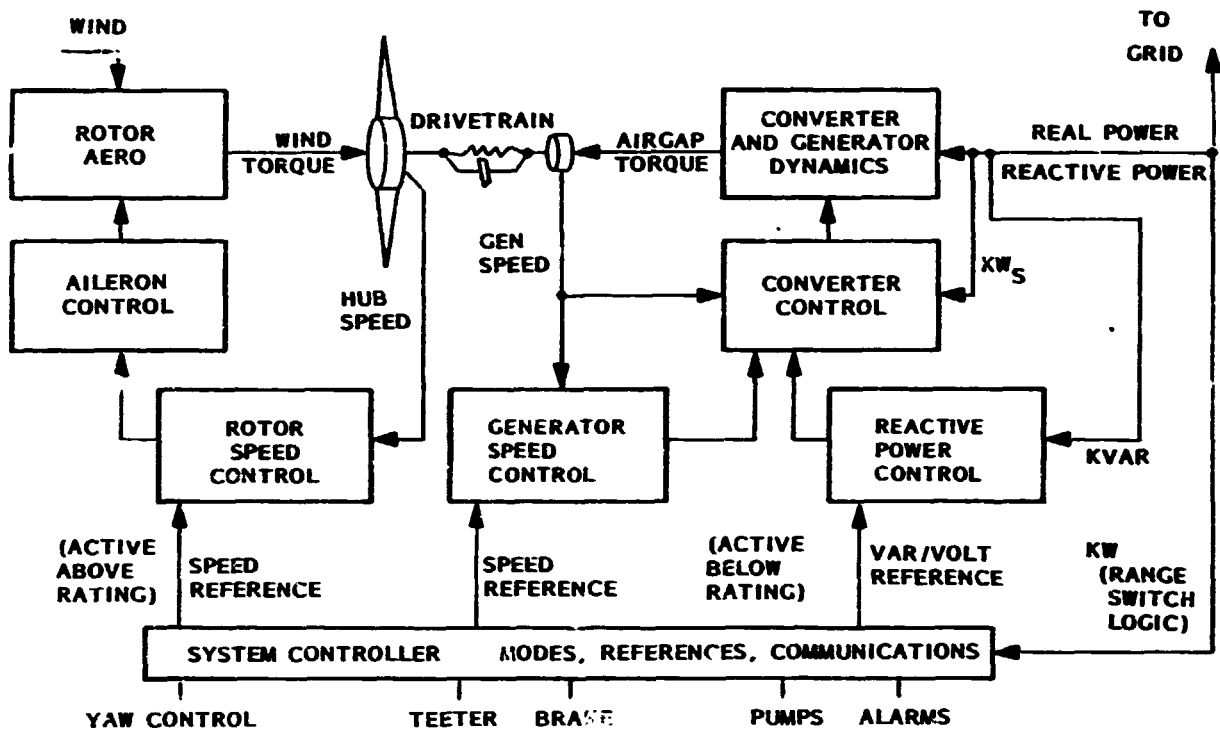


Figure 2- System Control Plan Block Diagram

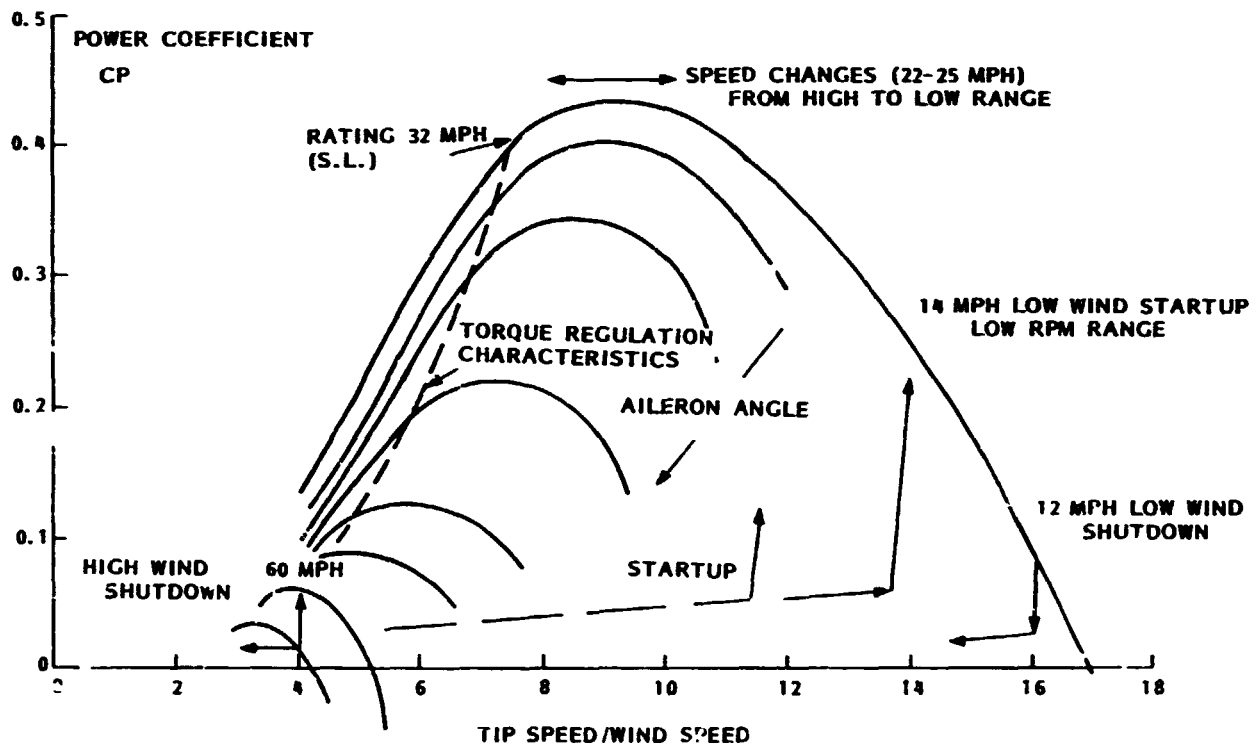


Figure 3- Rotor Operating Regime

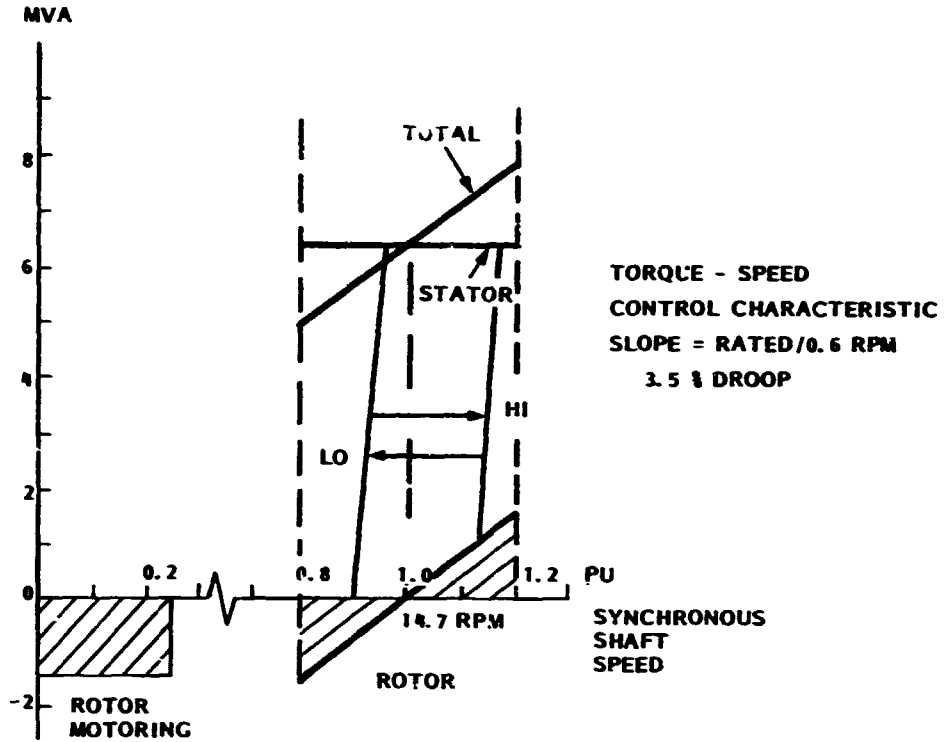


Figure 4- Generator Operating Regime

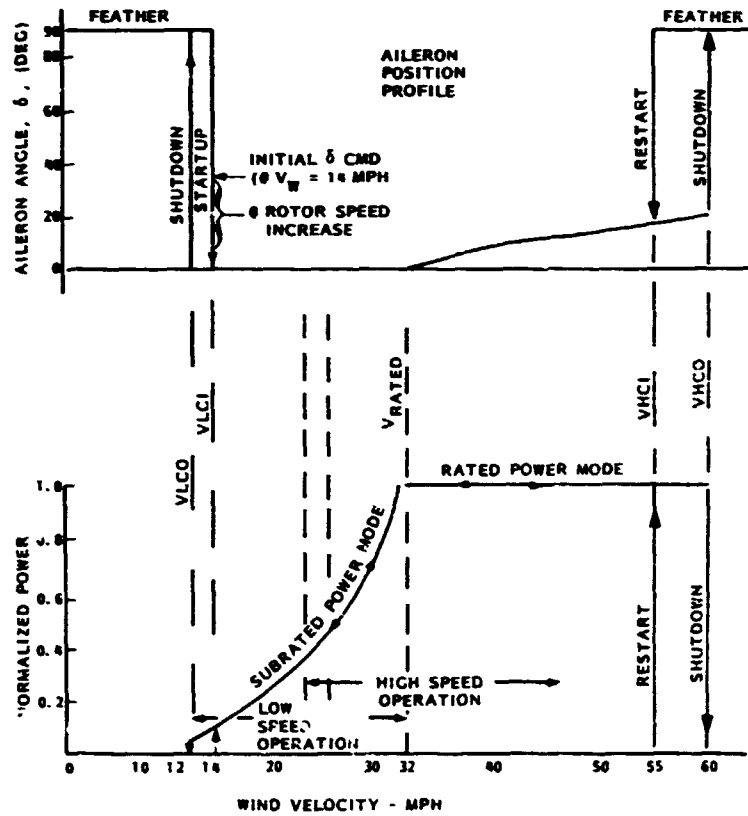
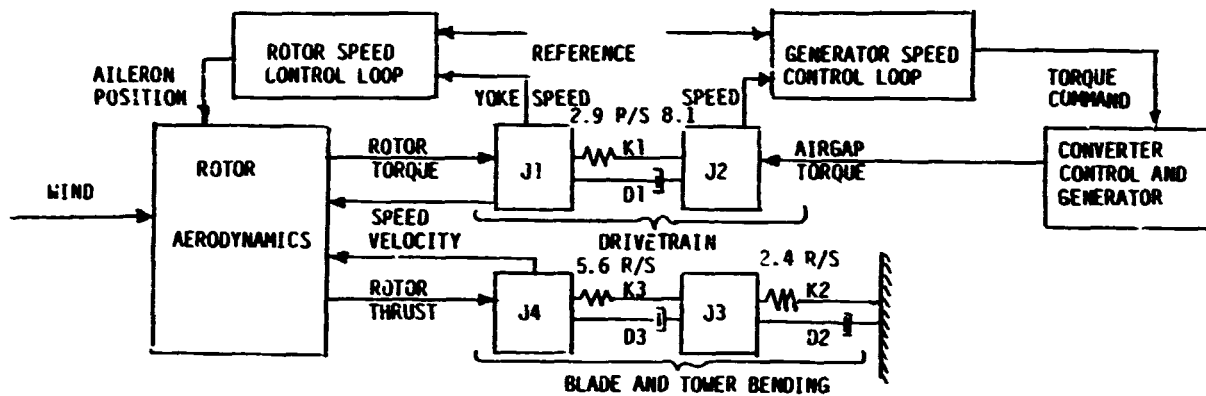


Figure 5- Aileron Position and Output Power Versus Wind Speed



- J1 - Rotor Inertia $40 \cdot 10^6 \text{ slug-ft}^2$
- J2 - Generator & High Speed Shaft Inertia reflected to Rotor $(745 \cdot 30)(82.16)^2 = 5.2 \cdot 10^6 \text{ slug-ft}^2$
- J3 - Tower Mass $2.9 \cdot 10^6 \text{ slug}$
- J4 - Blade Flap Mass $1.06 \cdot 10^7 \text{ slug}$
- K1 - Drivetrain Spring Constant $3.30 \cdot 10^9 \text{ ft-lb/rad}$
- K2 - Tower Spring Constant $1.67 \cdot 10^5 \text{ lbs/ft}$
- K3 - Blade Flap Spring Constant $3.370 \cdot 10^4 \text{ lbs/ft}$
- D1 - Drivetrain Damping Coefficient $3.8 \cdot 10^6 \text{ ft-lb/(rad/sec)}$
- D2 - Tower Damping Coefficient 6960 lb/(ft/sec)
- D3 - Blade Flap Damping Coefficient $379^5 \text{ lb/(ft/sec)}$

Figure 6- Simulation Model Diagram

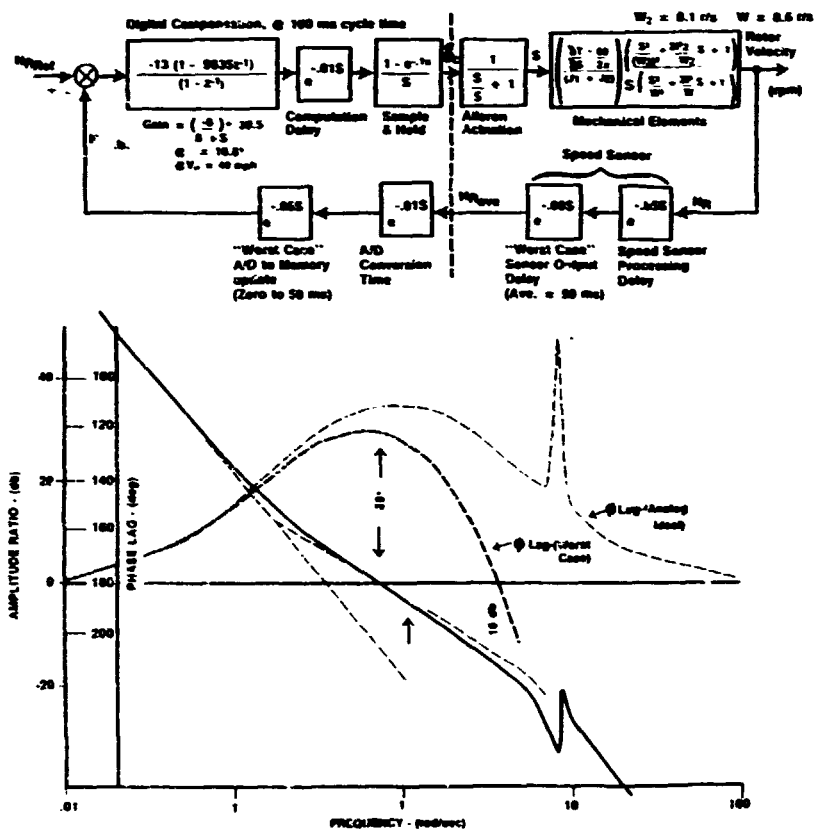


Figure 7- Rotor Speed Loop Characteristics

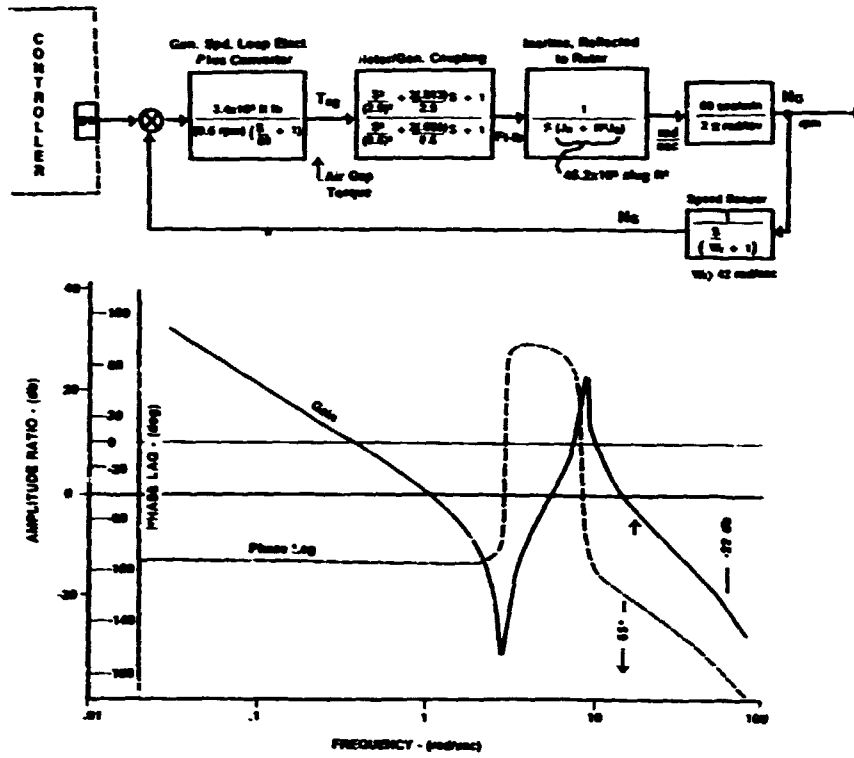


Figure 8- Generator Speed Loop Characteristics

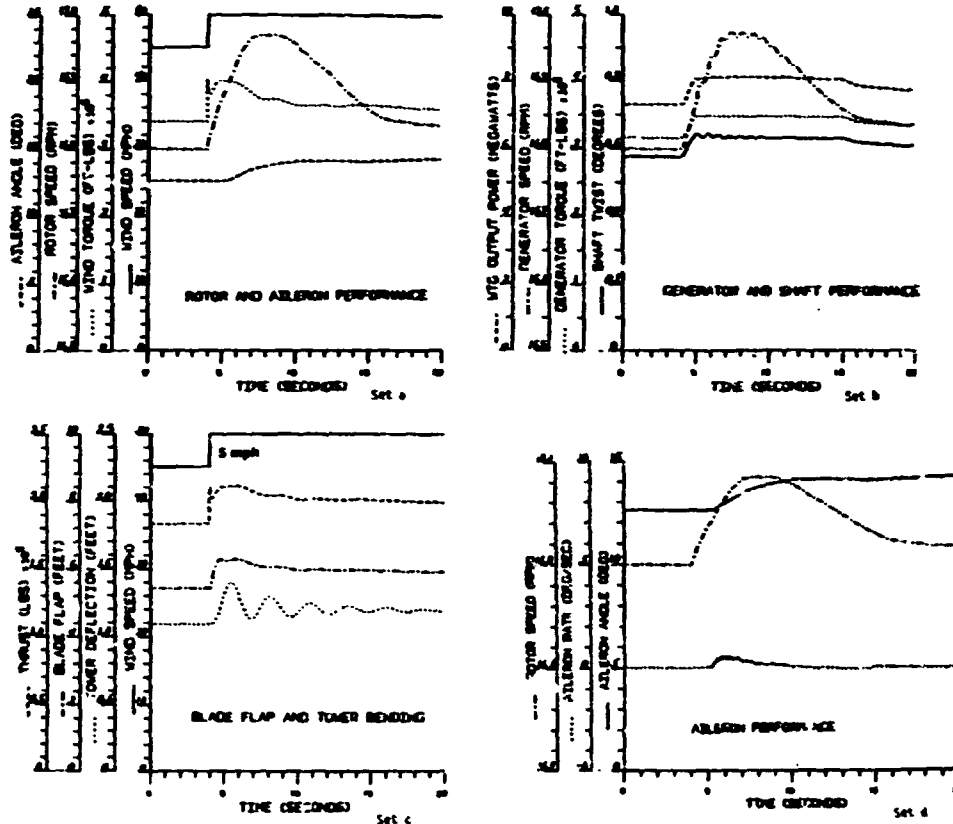


Figure 9- Response To Step Wind Change

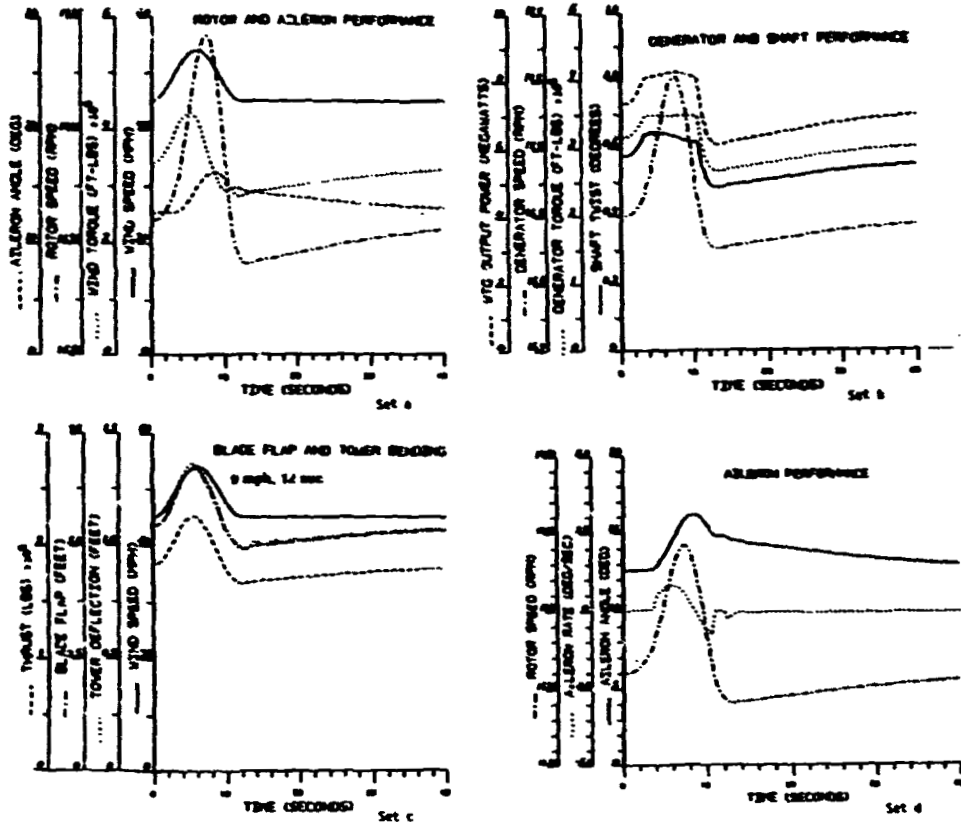


Figure 10- Response To 1-Cosine Wind Change

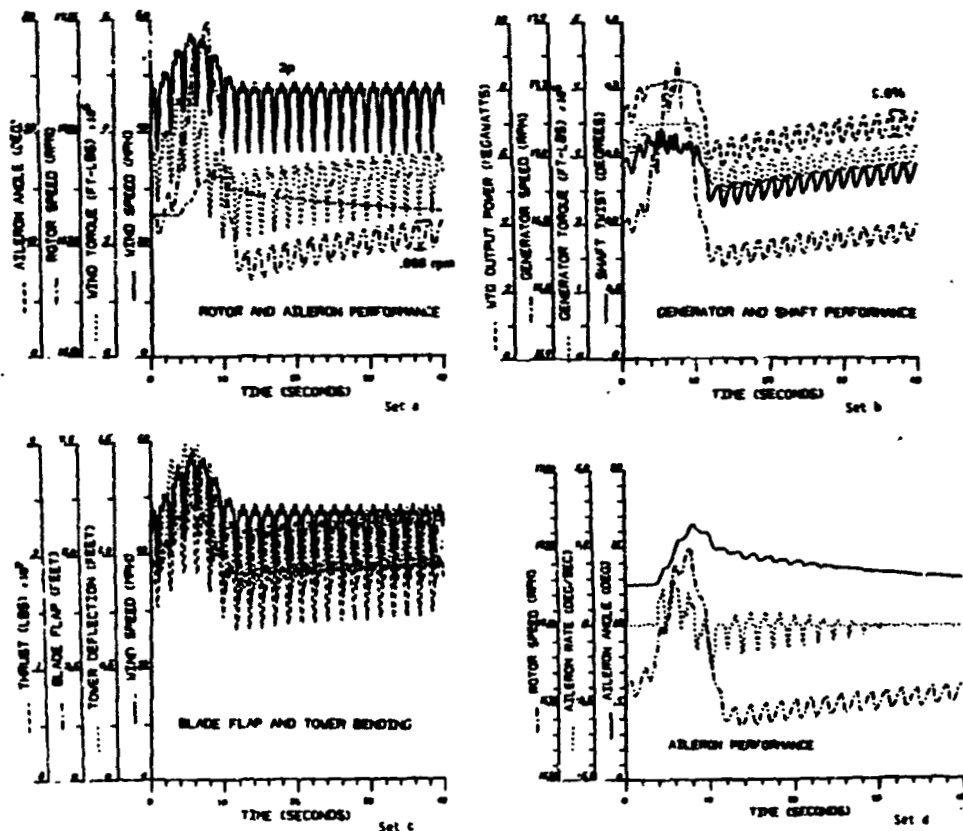


Figure 11- Response To 1-Cosine Wind Change Plus Turbulence

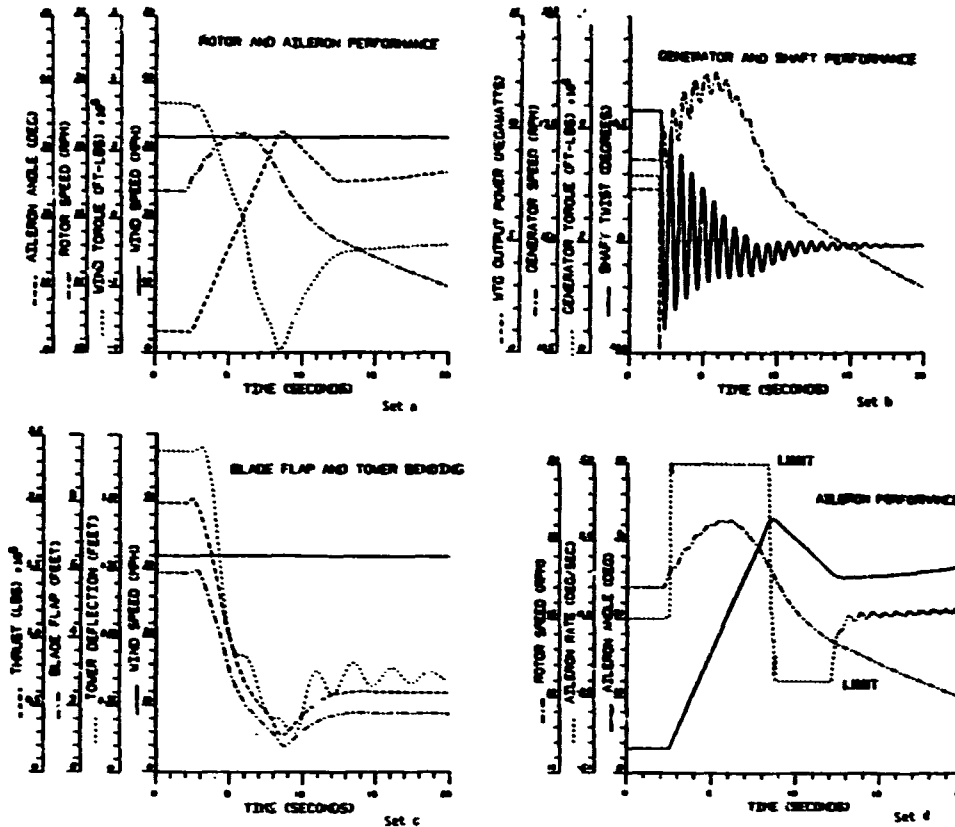


Figure 12- Response To Loss Of Load

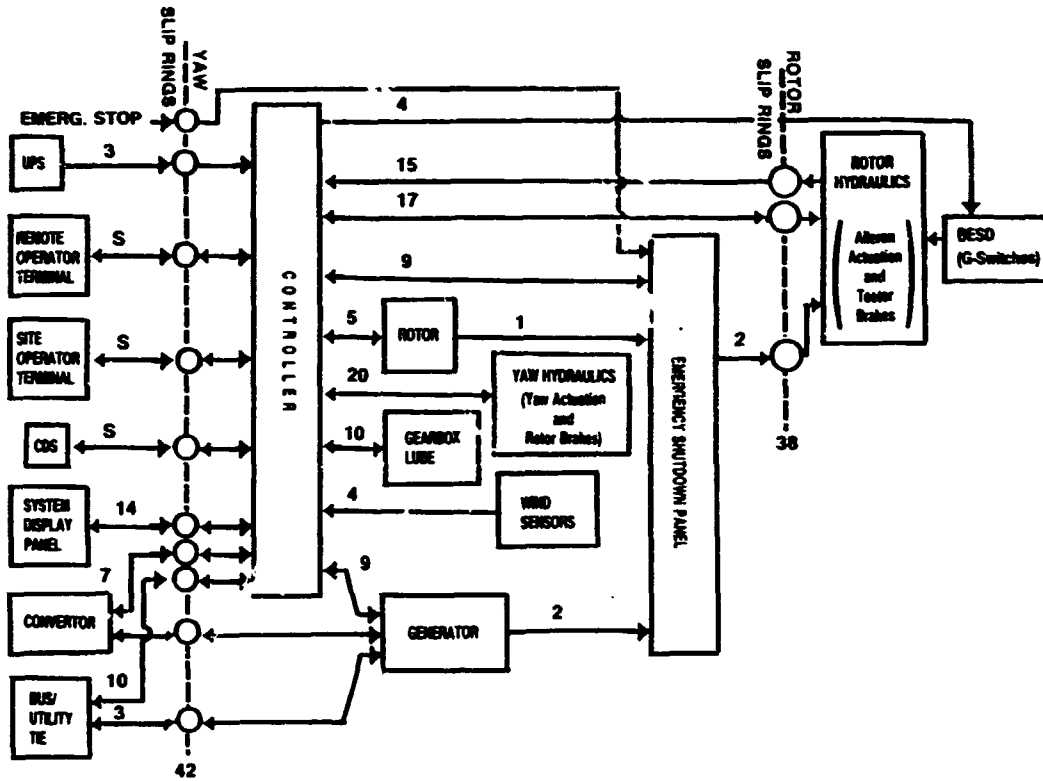


Figure 13- Control Subsystem Block Diagram

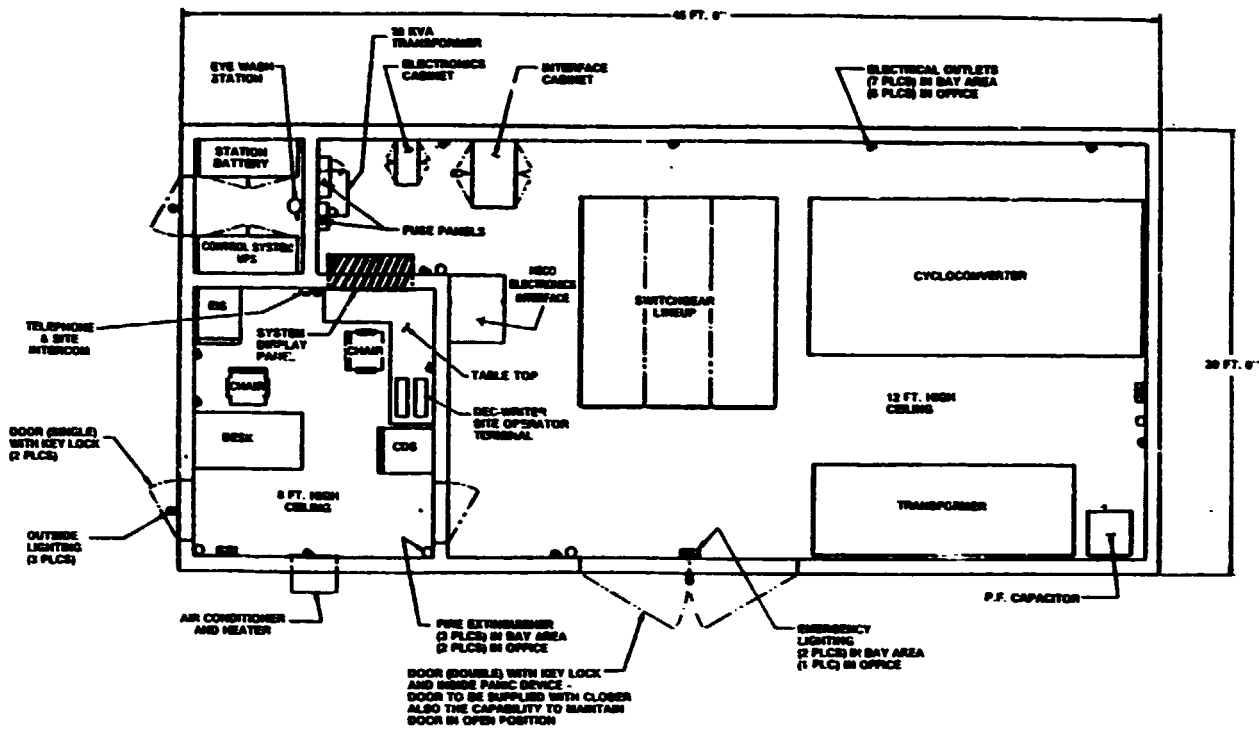


Figure 14- Electrical Equipment Building

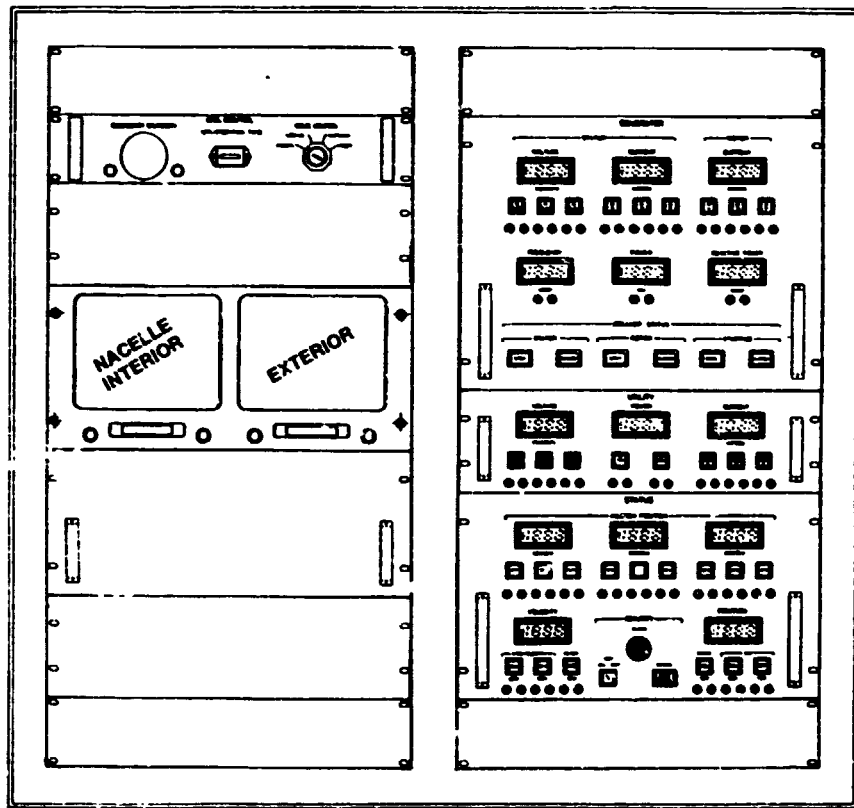


Figure 15- Operator Display Panel

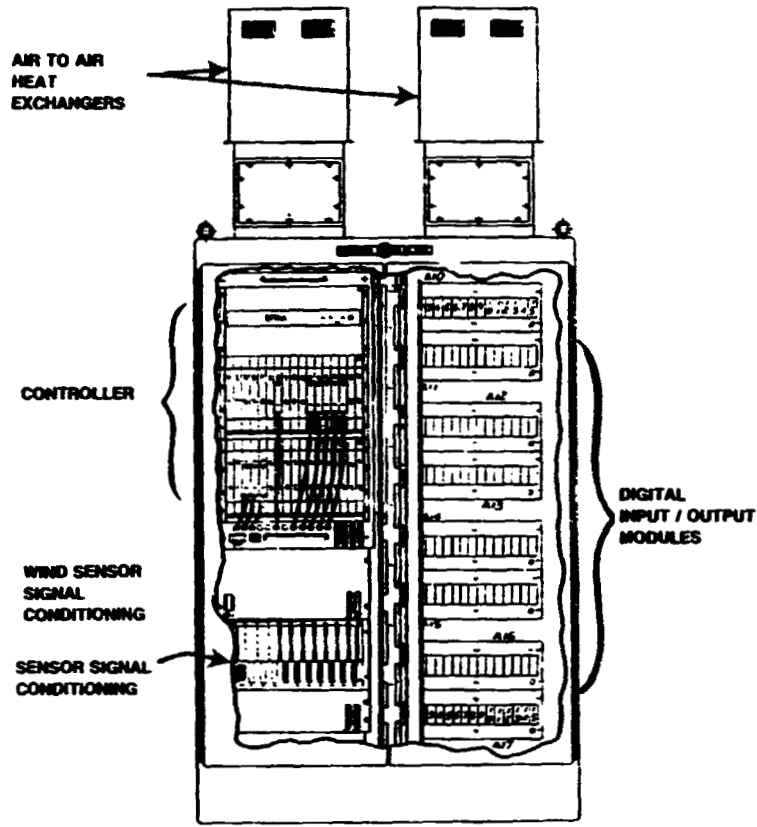


Figure 16- Nacelle Control Equipment Cabinet

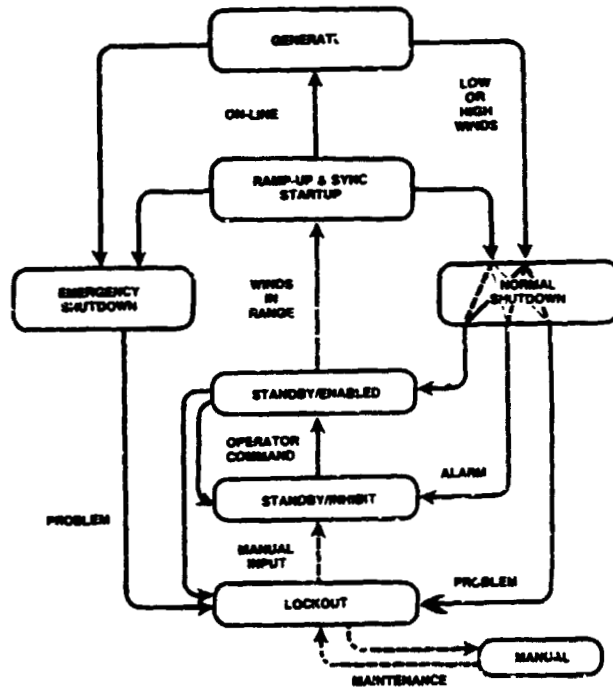


Figure 17- Software Control Mode Interaction

```

0.00 0.00.00 MOD 5A SUMMARY DATA UNIT 5H 001
CONTROL YESTER  MIN PRODUCED  TAX  SET POINTS
SITE  .0  CURR FROM  .0  7.3  17.9
-----
TIME  ALRN  MPH  MW  MWH  HDBE
-----
0.00.12  0  10
0.00.12  0  .1  -.19  .0  LD
0.00.18  + 11
0.00.18  + 00
0.00.24  + 00
0.00.24  - 10
0.00.30  - 11
0.00.30  - 00
0.00.30  - 00
0.00.40  0  .1  -.19  .0  SDI
000000000
01427  0.01.48
00424  14.27.04
01  14.27.18
14.27.24  0  .1  -.19  .0  SDE
14.33.24  0  15.0  -.19  .0  SU
14.35.30  0  15.0  -.14  .0  RHP
14.40.30  0  15.0  1.14  .0  PWR
11  14.41.30
14.41.36  0  15.0  1.30  .0  PWR
31  14.41.48
14.41.54  + 51
14.43.18  0  15.0  1.70  .0  HSD
14.43.24  - 51
01  14.43.42
14.43.48  0  25.0  -.19  .0  SDE
14.47.42  0  25.0  -.19  .0  SU
14.49.48  0  25.0  -.17  .0  RHP
14.54.18  0  25.0  1.41  .0  PWR
14.55.30  0  25.0  5.75  .0  HSD
14.55.34  + 55
14.55.34  - 55
14.57.00  0  25.0  -.17  .1  SDI
01  14.57.30
14.57.30  0  39.8  -.19  .1  SDE
15.01.30  0  39.8  -.19  .1  SU
15.03.30  0  39.8  -.18  .1  RHP
15.07.54  0  39.8  1.18  .1  PWR
15.12.36  0  39.8  7.26  .4  HSD
15.12.42  + 61
15.12.48  - 61
15.14.18  0  39.8  -.15  .4  LD
15.29.18  0  39.8  -.23  .4  LD
15.44.18  0  39.8  -.21  .5  LD
15.59.18  0  39.8  -.19  .5  LD
16.03.54  0  39.8  -.23  .4  SDI
01  16.04.04
16.04.04  0  15.0  -.23  .4  SDE
16.08.06  0  15.0  -.19  .4  SU

```

```

PAGE HEADINGS
POWER UP
ALM 10 TEETER ANGLE
ALM 11 TEETER ACCUM
PRESS LD
80 - LOCK OUT RELAY
85 - YAW BRAKE/GRIPP
KEYSWITCH RESET
PASSWORD - ENABLE TERMINAL CHD INPUT
SET TIME
SET DATE
CHD SBE
AUTO SEQUENCE
REQUEST PRINTOUT
CHD NORMAL SHUTDOWN
ALM 51 CHD HSD

```

L'NB TEMP

INTRUSION ALN

```

4.24 16.08.12 MOD 5A SUMMARY DATA UNIT 5H 001
CONTROL YESTER  MIN PRODUCED  TAX  SET POINTS
SITE  .0  CURR FROM  51.0  7.3  17.9
-----
TIME  ALRN  MPH  MW  MWH  HDBE
-----
16.09.48  0  15.0  -.19  .4  SU
16.10.04  0  15.0  -.17  .4  RHP
16.13.04  0  15.0  1.24  .4  PWR
16.25.54  0  54.9  7.20  1.5  HSD
16.26.00  + 79
16.26.00  - 79
16.27.30  0  54.8  -.15  1.5  LD
16.42.30  0  54.8  -.19  1.5  LO

```

GENERATOR VIBRATION

Figure 18- Sample Operator Terminal Output

ORIGINAL PAGE IS
OF POOR QUALITY

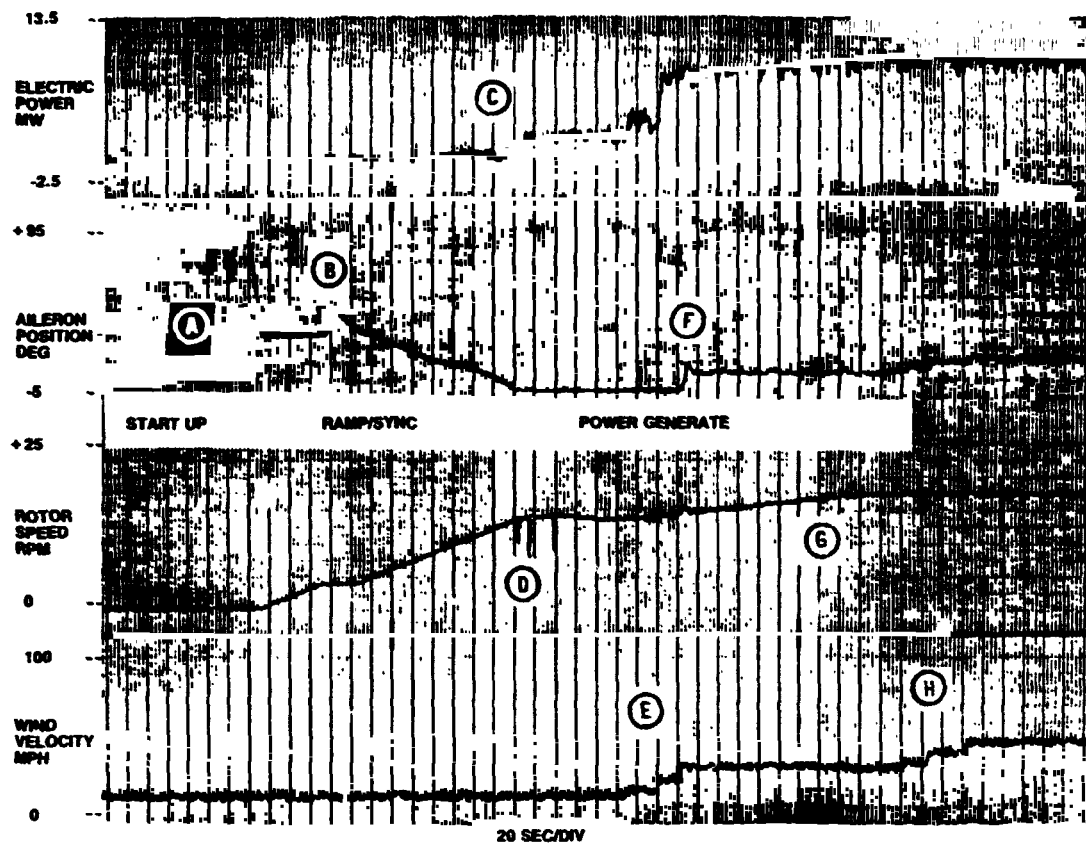


Figure 19- Startup Simulation On Development System

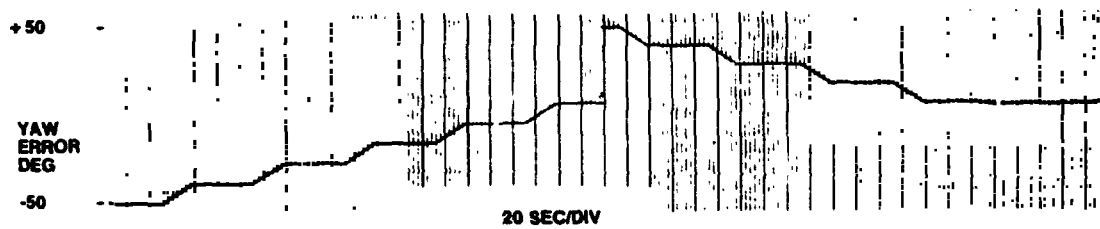


Figure 20- Yaw Drive Simulation On Development System

ORIGINAL PAGE IS
OF POOR QUALITY

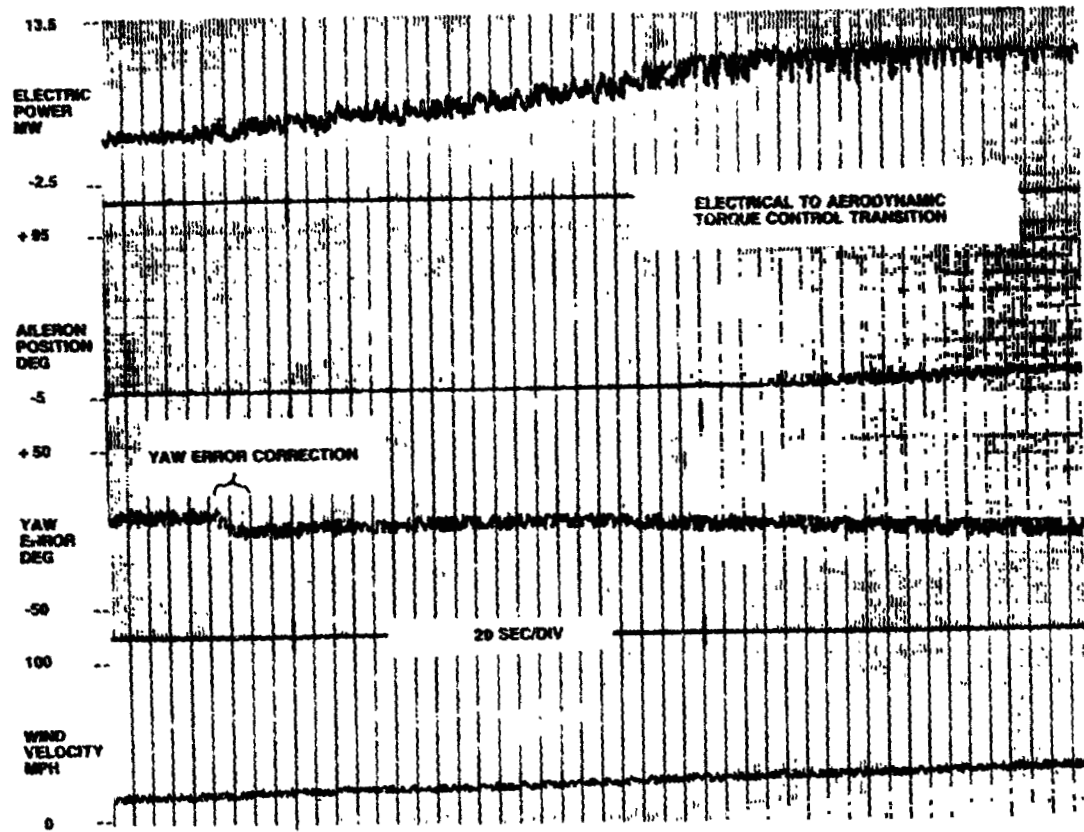


Figure 21- Operating Simulation On Development System

USE OF BLADE PITCH CONTROL TO PROVIDE POWER TRAIN
DAMPING FOR THE MOD-2, 2.5-MW WIND TURBINE*

W. A. Blissell, Jr.

Boeing Aerospace Company
Seattle, Washington

ABSTRACT

The Control System for the MOD-2 wind turbine system is required to provide not only for startup, RPM regulation, maximizing or regulating power, and stopping the rotor, but also for load limiting, especially in the power train. Early operations with above-rated winds revealed an instability which was caused primarily by coupling between the quill shaft and the rotor air loads. This instability caused the first of several major Mod-2 Control System changes which are reviewed in the paper.

INTRODUCTION

The need for power train damping on the Mod-2 Wind Turbine system (WTS) arose from a series of design choices, the principal ones being

- o Selection of steel for the 300 ft diameter rotor, resulting in a large polar moment of inertia,
- o Use of a two-element rotor shaft arrangement: a hollow, low-speed shaft for reacting rotor mass and normal loads and moments, and a central quill shaft for transmitting rotor torque to the remainder of the power train,
- o Selection of a relatively low torsional stiffness for the quill shaft to reduce response to two-per-revolution torques and favor longer fatigue life.

The quill shaft is coupled to a synchronous generator through a step up gear box and high speed shaft (Figure 1). In a power-generating mode, the synchronous generator rotor is locked to the interfacing power grid frequency tightly enough that the power train behaves (dynamically) very nearly as if the generator were fixed to ground. The resulting natural frequency is 0.14Hz and its motions are lightly damped.

INITIAL CONTROL SYSTEM

The initial system for controlling blade pitch was designed to accomplish a number of functions:

- o Startup, in which rotor aerodynamic torque is employed to accelerate the power train to synchronous speed,
- o RPM regulation prior to generator synchronization
- o Maximizing power in below-rated-power winds
- o Regulating power in above-rated-power winds
- o Limiting rotor loads in the presence of gusts, and
- o Shutdown (in non-emergency situations), in which the rotor is decelerated to a stop

Experience with Mod-2 operations, starting in early 1981, convincingly showed that power train damping was a mandatory addition to the array of control system functions.

At that point in the Mod-2 development, the control system had the configuration illustrated in Figure 2, power train damping having been provided through hub rate error feedback. Several other features of this control system are noteworthy:

- o Blade schedule switching at below-rated conditions to improve energy capture,
- o Control mode switching between below-and above-rated conditions,
- o Proportional control for short-term power regulation and integral control for long-term regulation,
- o Notch filter to reduce blade activity at the two-per-revolution (2P) frequency (0.58Hz)

Below-rated-power operations employed a blade pitch schedule designed for near-maximum energy capture but maintaining positive control authority; namely, an increase in blade pitch should produce a reduction in power. This schedule is shown on Figure 3 which also notes the blade pitch mechanical limit at -5 deg. As indicated on the figure, "hysteresis" was also provided to reduce schedule- and mode-switching activity. At above-rated conditions control was effected through the proportional, integral and hub rate error loops to regulate power at 2.5 MW.

In use, this control system generally produced tight power regulation in above-rated winds but had relatively high blade activity at the tower natural frequency (0.37Hz). Its least attractive quality, however, was that it occasionally allowed large amplitude, unstable oscillations near the power train natural frequency to develop at near-and above-rated power conditions. As Figure 4 shows, these events developed very rapidly and were only terminated by entering the shutdown mode, usually involuntarily. Test data indicated that blade pitch excursions to low angles - even to the mechanical stops - were occurring. It seemed evident that the resulting control authority reversals both initiated and sustained such oscillations. The specific cause for the initial blade pitch excursions was not pinpointed but noise in the hub rate error signal was suspected. Blade pitch limits which prevented loss or reversal of control authority were then implemented in the software and effectively eliminated unstable coupling between the power train and control system. A notch filter to reduce blade activity at the tower frequency was added

*Presented at the DOE/NASA Workshop on Horizontal Axis Wind Turbine Technology, May 8-10, 1984 in Cleveland, Ohio.

At this stage of its development, the initial control system had evolved into one which had materially improved availability of the Mod-2 but still had four significant problems to be solved:

- 1) Noise on the hub rate error signal,
- 2) Transients caused by mode switching,
- 3) Operation away from maximum power blade angles with below-rated winds, and,
- 4) Low stability margins, principally because of the lower and 2P notch filters.

The need to solve these problems set the stage for a new approach to the control system design.

NEW CONTROL SYSTEM

These requirements dictated that certain features of the proportional and integral control loops and the blade pitch subsystem loop - be retained. Solutions for the four problems noted were developed as outlined below:

Hub Rate Error

The hub rate signal is obtained from an encoder on a rim of the low speed shaft. The signal is noisy because of encoder sampling and because it responds to both shaft vibration and variation in rpm concentricity. Nominal hub rate is subtracted from the noisy hub rate to obtain hub rate error, a process which results in a low signal to noise ratio and causes spurious blade activity. It was observed that hub rate and power rate were highly correlated. Therefore, a differentiating circuit was incorporated in the new design and the derived power rate filtered and summed with the proportional and integral signals as shown in Figure 5. By removing the hub rate error measurement noise, the use of power rate allows higher rate gains and increases system damping.

Mode Switching

With the initial control system, even as modified, variations in wind speed about the rated power point caused switching transients between the below- and above-rated control modes. This problem was eliminated by employing the power control mode both above and below rated power. The below-rated blade pitch schedule was made to follow the blade limit so that blade pitch is commanded to the limit. This approach also reduces below-rated blade activity substantially. The limit has been shaped to more closely follow the maximum power curve below 1 MW as indicated on Figure 6.

Operation Away From Maximum Power Blade Angles

The new blade pitch control law commanding the blade to the limit when below rated power improves energy capture to the maximum extent consistent with maintaining positive control authority. Additional stability margin has been provided for WTS #5 so the blade pitch limit is set at slightly higher angles, indicated on Figure 7, than for WTS #1 to #4 (Figure 6).

Destabilization Due to Notch Filters

Analytical studies were performed to improve stability margins at the power train frequency. The changes permitted slightly greater blade activity at lower frequency but increased phase margin and provided better damping of the power train. The 2P notch filter was revised to allow higher rate gains without amplifying 2P response.

Proportional, integral and derivative gains and rate filter time constants were adjusted to increase system stability and still provide satisfactory attenuation of tower bending excitation.

TEST RESULTS

Initial testing of the new control system was done with WTS #2 at Goldendale, Washington, beginning in early September, 1982. The results gave every indication that the goals of the new design had been achieved, namely,

- o The system was well damped - Figures 8 and 9
- o Energy capture generally matched predictions - Figure 10
- o Above-rated power was regulated within ± 200 KW - Figure 9

In addition, below-rated blade activity was lowered by more than 50 per cent and 2P oscillation amplitudes reduced.

Installation of the new control system in WTS #5 was done in late October, 1982, and results were similar to those observed on WTS #2. After almost two uneventful months of operation, WTS #5 entered a divergent oscillation which resulted in a generator overcurrent shutdown in winds described by site personnel as extremely gusty and over 40 mph. Examination of the data, included in Figure 11, indicated that the instability occurred at a frequency of 0.26 Hz and was primarily a control system mode.

Additional detailing of the simulation mathematical model and analyses pinpointed the increase in blade control authority with increasing wind speed as the culprit. Accordingly, provisions were incorporated to reduce the above-rated proportional and derivative gains in a manner which gradually reduces the overall system gains as wind speed increases. An additional conservatism was included by halving the proportional loop gain (Figure 12). Initially tested in March, 1983, this version of the new control system is installed in all five Mod-2's and has demonstrated that the stability problems have been solved but gust response and power regulation have suffered. At this writing, the development activity is aimed at improving the balance between stability and power regulation.

CONCLUDING REMARKS

Development of the control system for the Mod-2 wind turbine system has been a learning experience. In the beginning, this system was conceived as being an uncomplicated means for controlling a relatively simple device. This conception dovetailed neatly with the universal need to keep new project development costs low and the initial control system design was accomplished at a modest cost. Once Mod-2 operations began, the need for additional development effort became evident and, over the succeeding two-plus years, the control system grew to be nearly as complex as a contemporary launch vehicle or missile. The development cost, much of it funded by Boeing, has been much greater than originally projected.

In retrospect, it seems evident that additional effort put into developing a more detailed, comprehensive simulation could have helped avoid some of the problems which were encountered. However, operational experience was also needed to identify the really significant details and, especially, to determine the ways in which the real wind turbine and its environment differed from the analytical models.

For the present and future, the lesson learned from the Mod-2 control system development is this: the system analysis and design work must be supported with sophisticated simulation capabilities and be performed by a staff of skilled, experienced control system engineers. This is the approach we have applied to the Mod-5B.

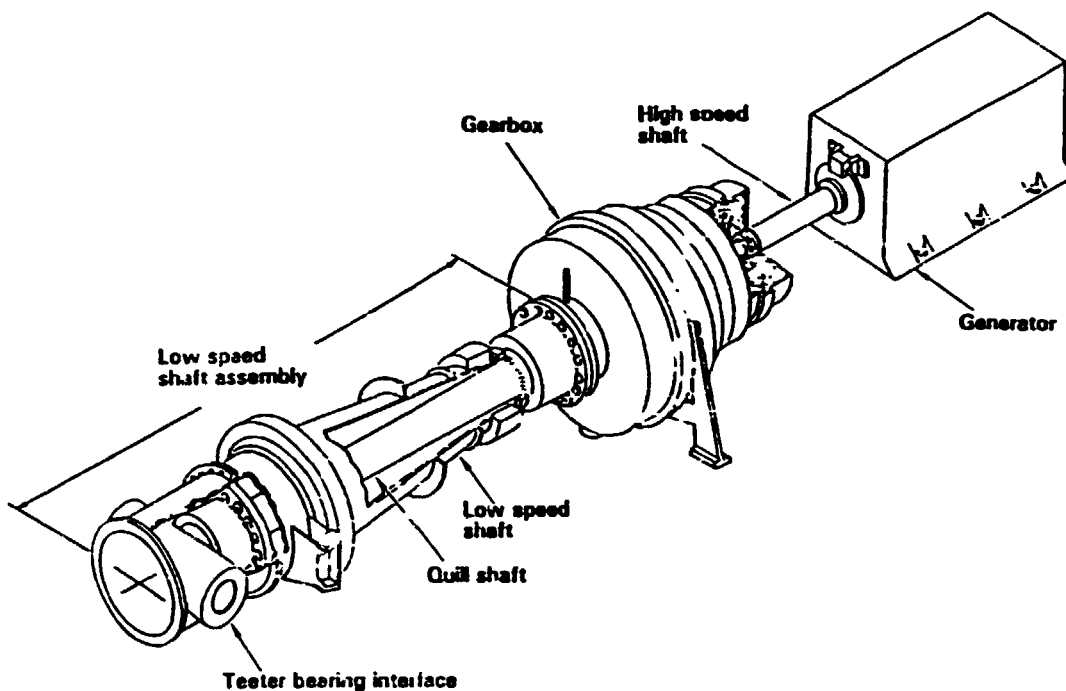


Figure 1 - Power Train

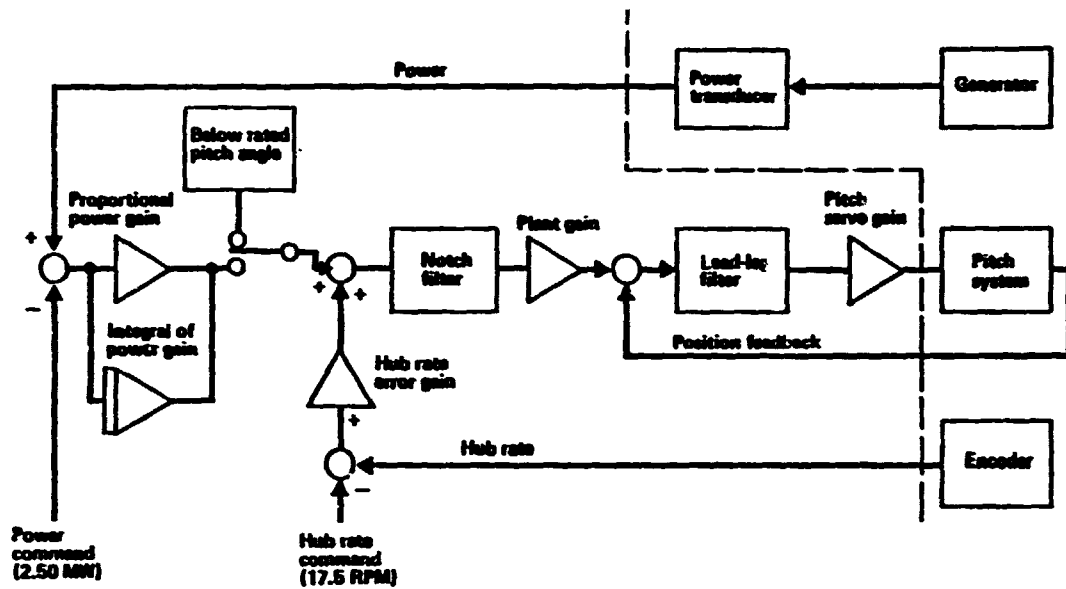


Figure 2 - Initial Control System Functional Diagram

Standard Sea Level Conditions
April 1982 Configuration

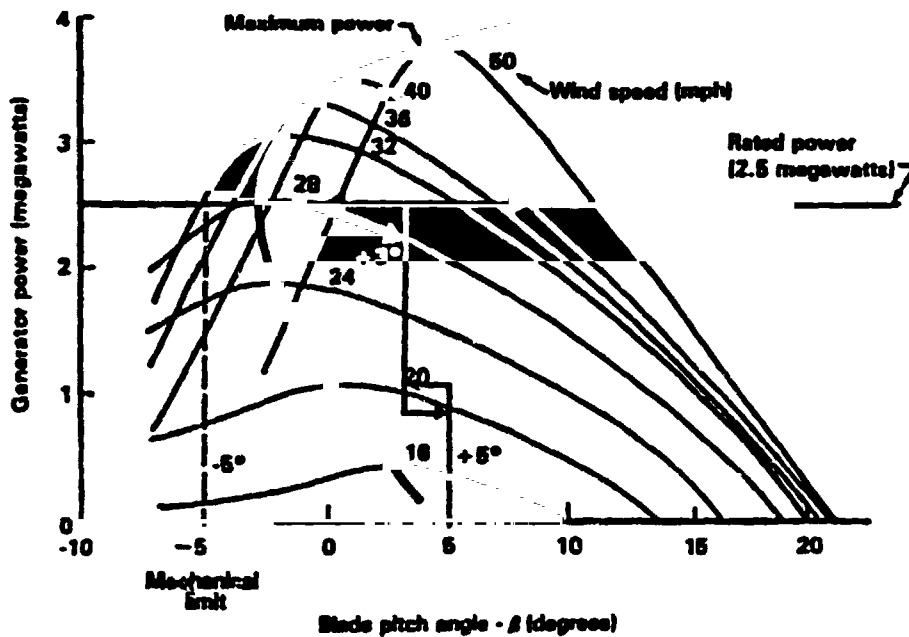


Figure 3 - Original Pitch Schedule

ORIGINAL PAGE IS
OF POOR QUALITY

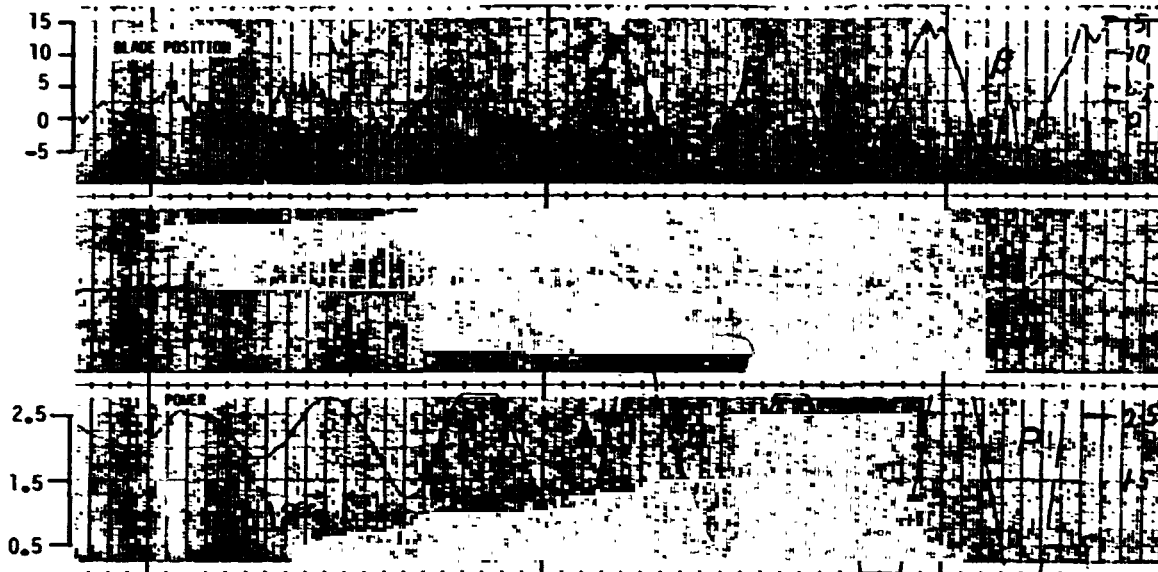


Figure 4 - WTS#2 Power Oscillation, May 12, 1982

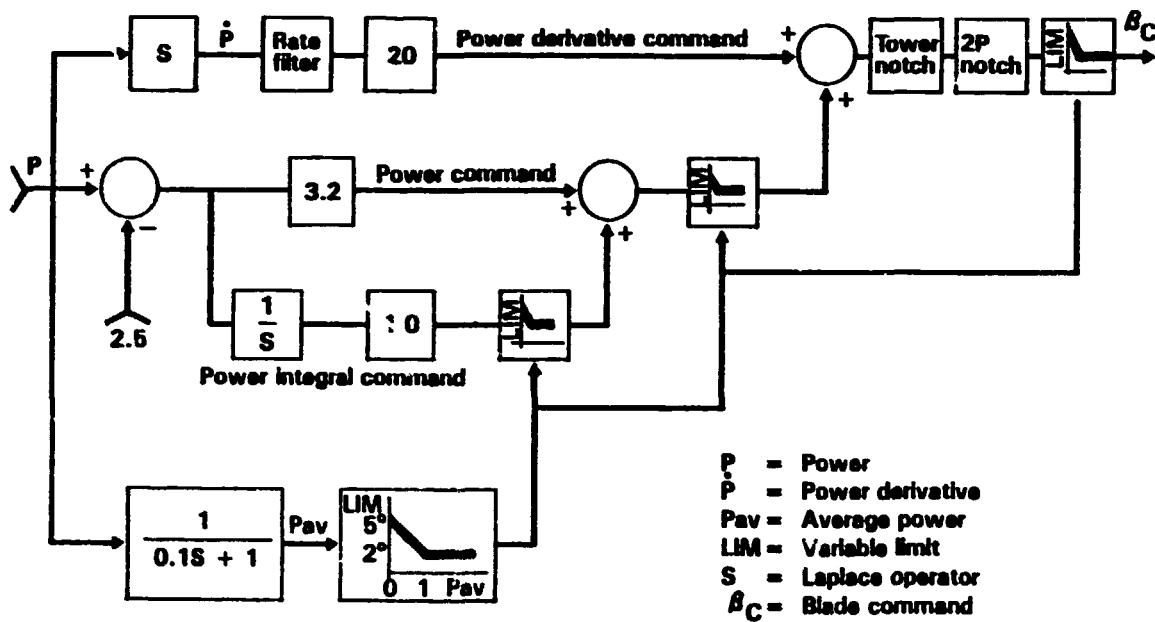
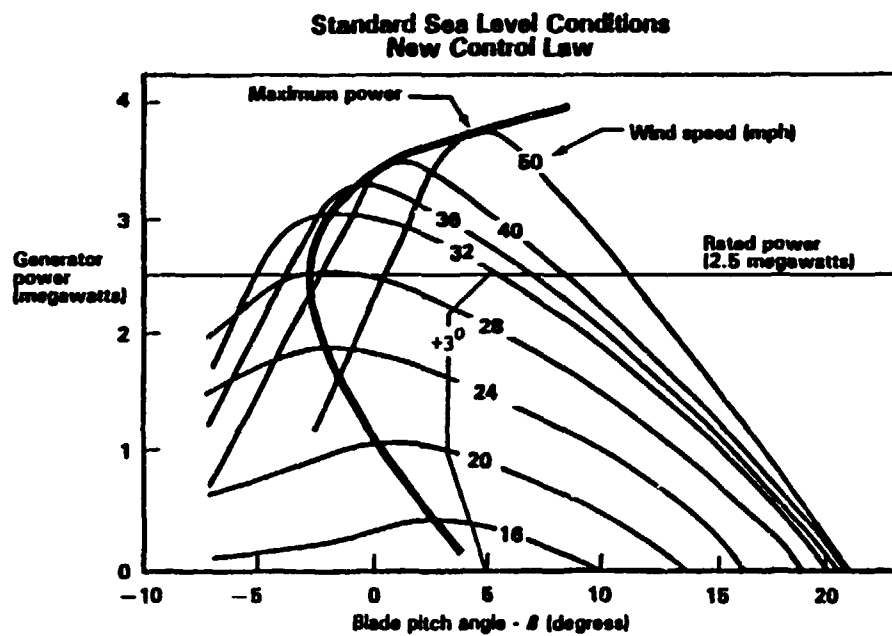
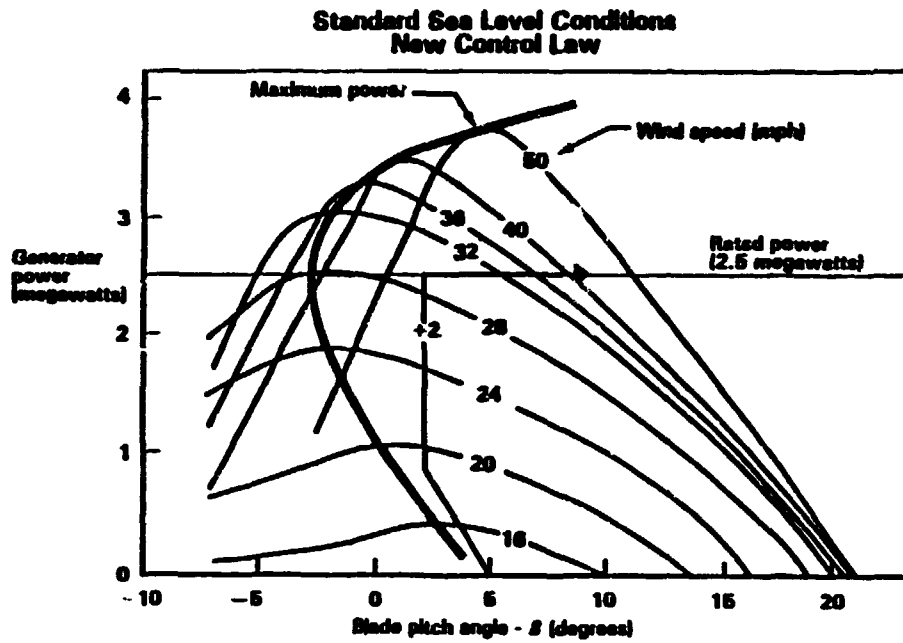


Figure 5 - New Control System Functional Diagram



DATE 10-26-82 TIME 10:54AM

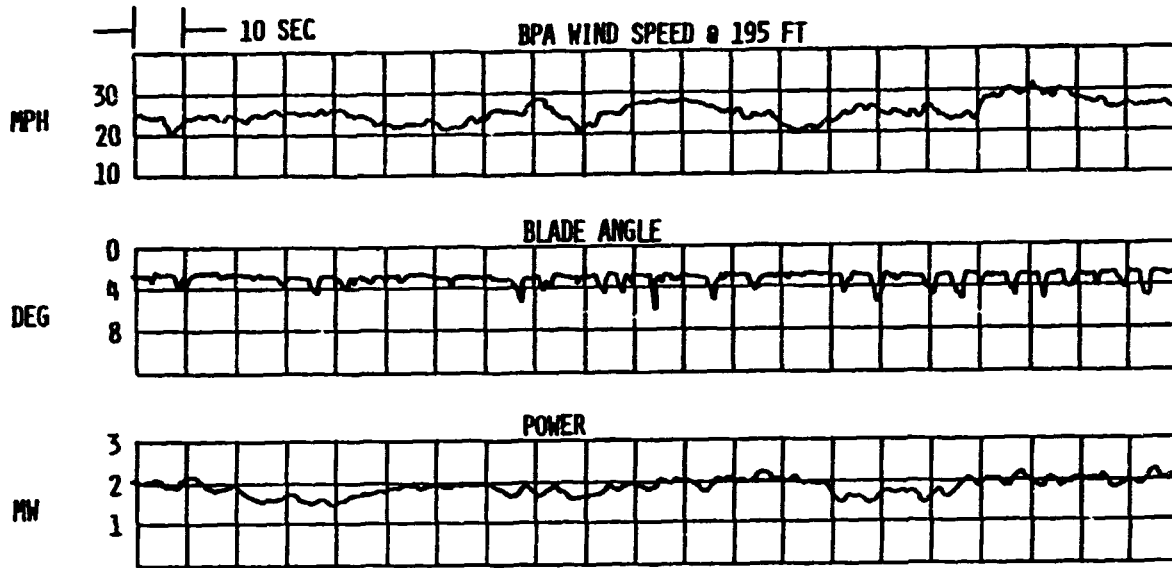


Figure 8 - WTS#2 Performance - Below Rated Power

DATE 10-26-82 TIME 3:30PM

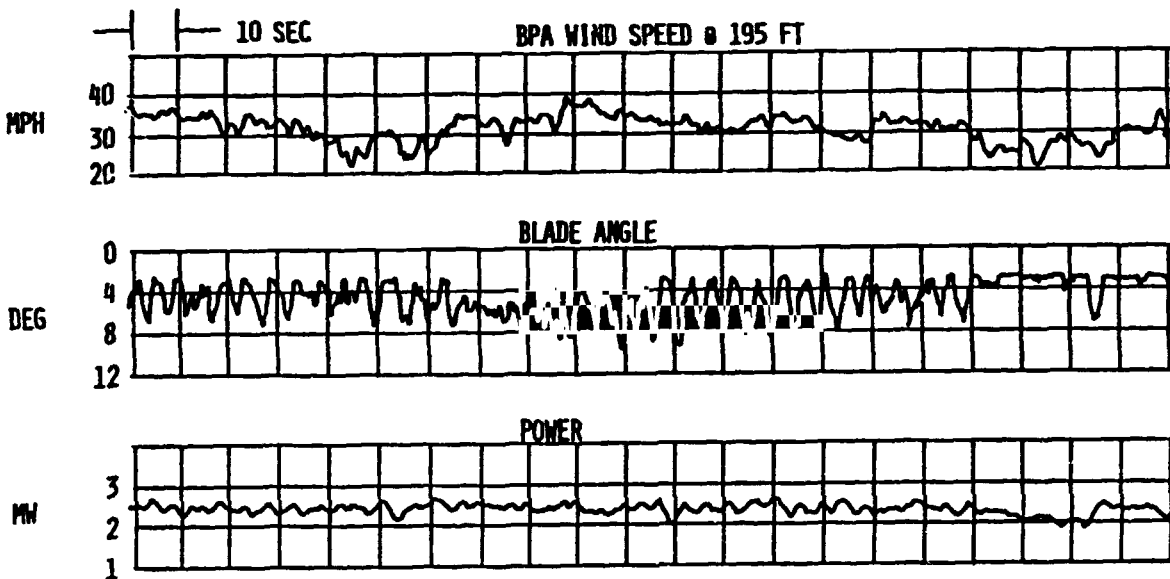


Figure 9 - WTS#2 Performance - Above Rated Power

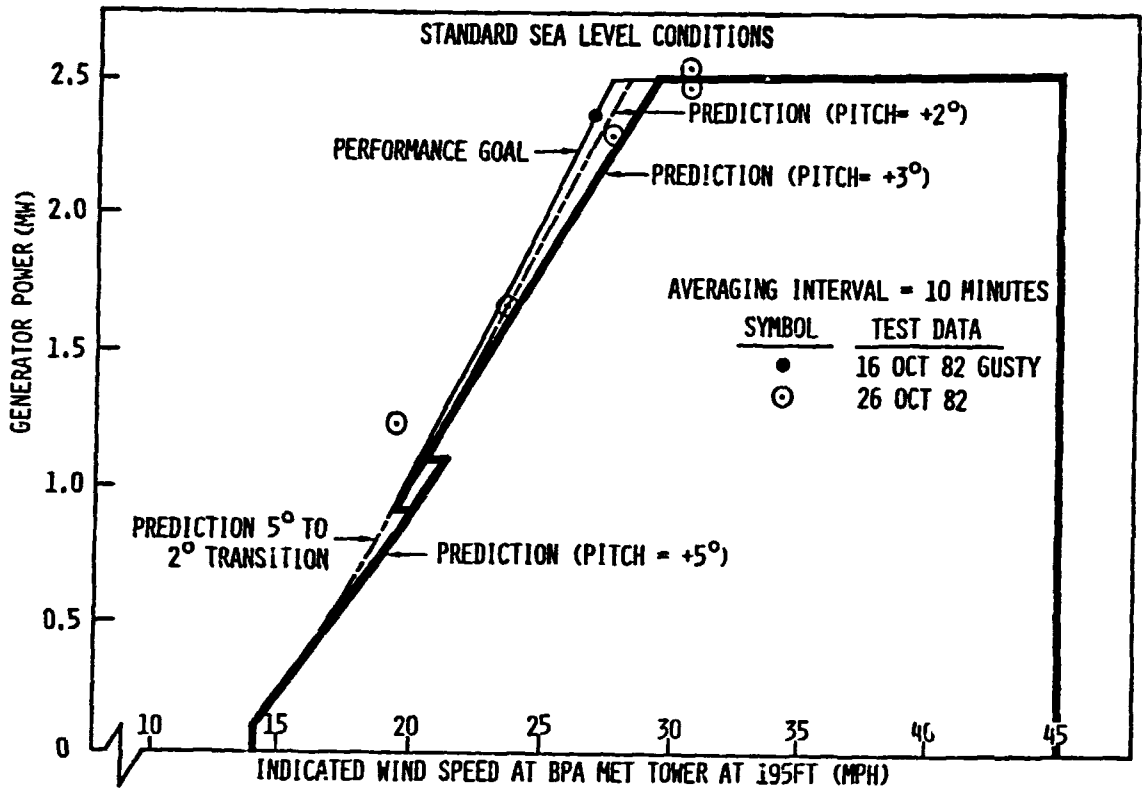


Figure 10 - WTS#2 Performance Data, October 1982

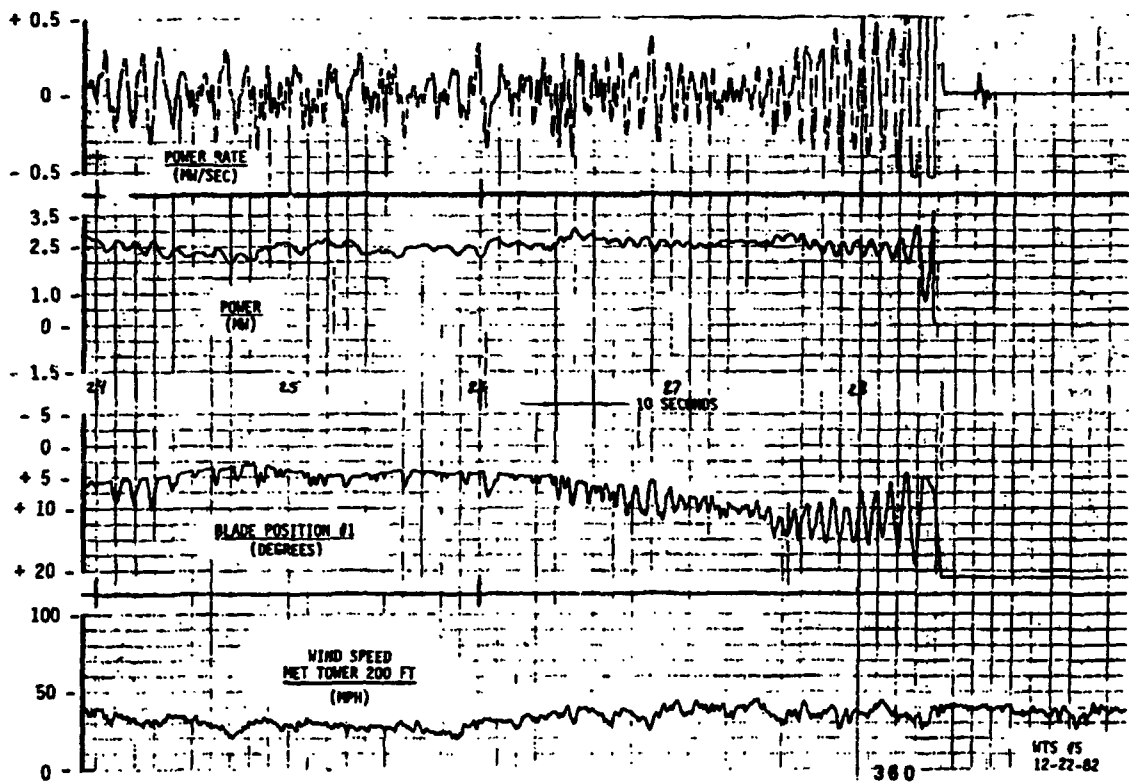


Figure 11 - WTS#5 Divergent Oscillation in High Winds, December 22, 1982

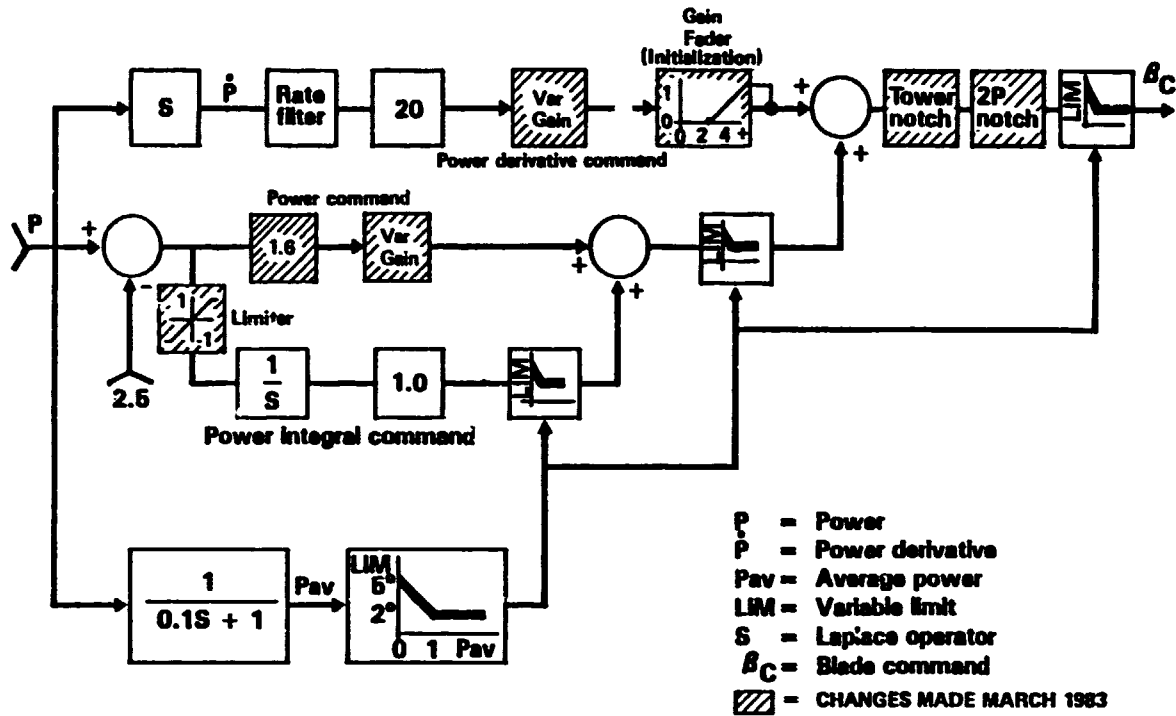


Figure 12 - Modified New Control System Functional Diagram

A CONCEPTUAL FRAMEWORK FOR EVALUATING VARIABLE SPEED GENERATOR OPTIONS FOR WIND ENERGY APPLICATIONS

T.W. Reddoch
Electrotek Concepts Inc.
Knoxville, Tennessee

T.L. Hudson
Oak Ridge National Laboratory
Oak Ridge, Tennessee

T.A. Lipo
University of Wisconsin
Madison, Wisconsin

E.N. Hinrichsen
Power Technologies Inc.
Schenectady, N.Y.

R.J. Thomas
Cornell University
Ithaca, N.Y.

ABSTRACT

Interest in variable speed generating technology has accelerated as greater emphasis on overall efficiency and superior dynamic and control properties in wind-electric generating systems are sought. This paper reviews variable speed technology options providing advantages and disadvantages of each. Furthermore, the dynamic properties of variable speed systems are contrasted with synchronous operation. Finally, control properties of variable speed systems are examined.

INTRODUCTION

The development of wind energy as a viable electric generating option for intertie to electric utility systems dictates total system requirements which include an effective and efficient wind turbine system as well as an acceptable interaction with the electric utility system. Fulfilling both of these needs places significant constraints on the turbine generator design since aerodynamic needs do not necessarily correspond with those of the electric utility system. As a result, a total system approach is required in order to capture essential characteristics to satisfy both needs.

Historically, large horizontal turbine designs have sought a constant speed configuration utilizing a synchronous generator. Such designs tend to minimize mechanical resonance problems. Some vertical axis turbines and many small horizontal axis machines have utilized variable speed arrangements, usually induction generators. Most of these efforts have concentrated on rather simple electrical configurations. In an effort to raise the overall productivity and efficiency of wind turbine systems, recently, attention has been directed to variable speed options for large horizontal axis machines with emphasis on a total wind turbine/generator/utility design. The additional degree of freedom that variable speed provides has to be integrated into a control concept that considers not only the process needs, i.e., the wind turbine and its energy source, but also the total system needs, i.e., the power system and its operation. In the past, most variable speed efforts have utilized available configurations out of convenience rather than developing a system from the "ground floor" for wind energy application. This paper will focus on a conceptual framework for assessing variable speed technology and its application to wind energy with a goal of developing an approach which is an alternative to a synchronous interconnection.

CONCEPTUAL FRAMEWORK

The issue of variable speed electric generating systems must be considered relative to their application to wind energy. Largely, the choice of system and the configuration to date has dwelled on "what's available." A key item for best overall system effectiveness and efficiency is the design of the turbine/generator/utility interface combination. Aeroturbine performance requirements must be coordinated with the design of the variable speed generator. As a result, the turbine generator system, its dynamic interaction with the electric utility system, and the overall control system must be designed as an integrated process. (See Figure 1.)

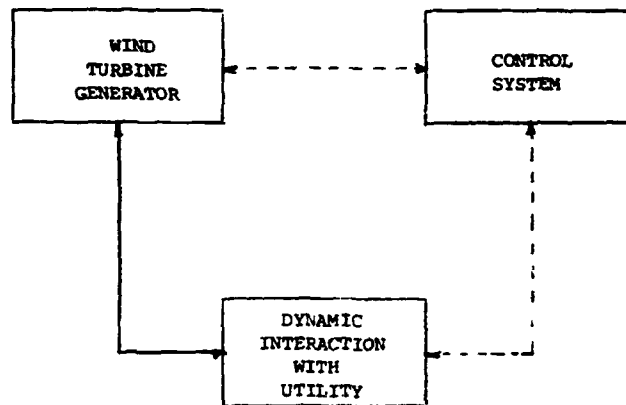


Figure 1. Wind Turbine/Generator/Utility Process

The three conceptual components shown in Figure 1 are key elements of the variable speed system. The solid line represents the natural interaction between wind system and the utility system. The dotted lines represent the control requirements which must shape the turbine-generator response as well as the turbine-generator interaction with the electric system. In an effort to develop future variable speed systems as well as evaluate present designs, the following activities are recommended:

- o Evaluate the variety of converter-variable speed options and assess them for their shortcomings and establish target requirements for new systems.

- o Characterize the dynamic interaction between variable speed systems and electric utility systems.
- o Develop strategy requirements and control systems for various converter-variable speed option for both the turbine-generator pair and its interaction with the electric system.
- o Develop computer models for various converter-variable speed options.
- o Design field tests for the various options to validate the computer models.

VARIABLE SPEED TECHNOLOGY OPTIONS

It is apparent that the number of possible candidate variable speed systems is very large and it is not feasible to cover in detail all such systems. In particular the number of feasible schemes appears to vary inversely as the power rating of the WTG. For additional details on the various options, the reader is directed to Lipo [1].

DC Generator with Line Commutated Inverter Bridge

Probably the most straightforward variable speed system utilizes a DC generator with inversion of the generated DC power to AC by use of a line commutated rectifier bridge. Current flow is in 120 degree blocks at the line frequency on the AC side of the inverter thus requiring filtering at the AC terminals of the bridge to suppress harmonic current flow into the power system and to correct the power factor to unity. Because of the heavy filtering required to eliminate unwanted harmonics of the simple six pulse bridge, other bridge configurations are also in common use. For example, the dual six pulse bridge arrangement results in the elimination of the lowest frequencies, the 5th and 7th harmonics components inherent in simple bridge configurations while halving the next lowest components, the 11th and 13th. An advantage of the dual bridge configuration is that each bridge need only be rated at one-half the KVA rating of the single bridge. It should be mentioned that such alternatives are generic to any of the systems to be discussed which utilize bridge configurations.

While not strictly necessary, some filtering of the DC voltage of the bridge is typically employed so as to minimize stray losses in the generator due to harmonic currents. The simplest type of filter is to simply use a DC link inductor to simply smooth the current. Such systems are said to utilize a DC current link and when the size of the inductor is large the converter-generator system operates much like a current source. An alternative to filtering is to place a capacitor across the terminals of the DC machine and employ a much smaller link inductor which is now selected primarily to limit charging current into the capacitor. In this case the current into the motor is smoothed by providing a low impedance path to harmonic currents. Such a

configuration is said to employ a DC voltage link. When the capacitance is large the converter-generator system appears much like a voltage source to the power system.

It is well known that the power factor of a line commutated bridge varies in direct proportion to the ratio of DC to AC voltage. Hence, in order to maintain good power factor at the terminals of the bridge, the inverter must be controlled such that the voltage on the DC side of the bridge must be maintained constant at its maximum permissible value. In converter terminology such a control is usually called constant extinction angle control in which the inverter is commutated such that the inverter thyristors have just sufficient time to recover blocking ability before forward voltage is reapplied.

Special advantages of this system include:

- o Minimal torque pulsations.
- o Straightforward control algorithm.

Disadvantages of this system are:

- o Maintenance and reliability concerns.
- o DC fault protection.
- o Control response limitations.

Synchronous Generator with Thyristor Rectifier and Inverter

Another class of systems suitable for wind power generation is a synchronous generator supplying power through a DC current link rectifier-inverter. Commutation of the line side inverter is accomplished by taking VARs from the power system. Commutation of the machine side converter is provided by leading VARs from the synchronous machine. In this case, excitation of the machine is by means of a brushless exciter. Electrical generated power must pass through the rectifier-inverter so that the converters must be rated at the full machine rating. One-hundred and twenty degree blocks of current now flow on the AC sides of both the rectifier and inverter. Again, the harmonic content on either the machine side or utility side converters can be reduced by more elaborate bridge configurations.

Important special advantages of this system include:

- o Wide speed range.
- o High frequency torque pulsations.
- o Strong electrical damping.
- o Rapid reclosure after a fault.

Potential disadvantages of this system are:

- o Low frequency torque pulsations near synchronous speed.
- o High harmonic distortion.

Doubly Fed Induction Generator with DC Current Link Rectifier and Inverter

Another type of system which bears a great similarity to the synchronous generator scheme is the doubly fed induction generator. The system again uses a rectifier-inverter with a DC current link wherein the machine side converter is connected to three phase rotor windings by means of slip rings. Current flow is in 120 degree blocks at slip frequency on the AC side of the rotor connected converter and 60 Hz on the AC side of the stator connected converter. In principle, operation either above or below synchronous speed is possible. Synchronous speed in this case is defined as the point at which the rotor rotates synchronously with respect to the stator rotating MMF when the slip rings are shorted. When the machine generates below synchronous speed, power is supplied to the utility from the stator windings. However, power must be supplied to the rotor windings of the machine through the slip rings. The power required is essentially proportional to the difference between rotor speed and rotor synchronous speed (slip frequency) times rated power. Hence, the rectifier-inverter need only be rated for a fraction of rated power (slip power). In this mode of operation the rotor side converter operates as a variable frequency inverter. Conversely, when the machine generates power above synchronous speed, power is also extracted from the rotor via the slip rings. Again the converters need have a rating equal only to slip power. The rotor side converter operates in this case as a rectifier.

Among the particular advantages of this system are:

- o Converter ratings based on slip power.
- o Control response.
- o Harmonics.
- o VAR control.

This system has several particular drawbacks including:

- o Restricted speed range.
- o Torque pulsations.
- o Slip rings.
- o Lagging power factor.

Doubly Fed Induction Generator with DC Voltage Link Rectifier and Inverter

Whereas DC current link converter configurations obtain commutation volt-amperes from the connected supply, DC voltage link systems typically (but not inevitably) rely on commutation energy from special purpose capacitor circuits or by means of self commutating switches (transistors or gate turn on devices (GTO)). Such converters are inherently more expensive than DC current link converters. However, costs of such converters are decreasing rapidly with the development of new high power transistors and switches. If the desired speed range is small the

rotor connected converters need only handle a small fraction of rated power and the possibility of using a DC voltage link may be practical. Such a voltage link configuration has a rotor connected converter which operates in forced commutation while the stator connected converter commutates naturally. Other arrangements are possible in which the stator side converter (or both) are force commutated.

In general, forced commutated converters can be operated in either of two modes. In the six step mode the converter switches are triggered at the lowest possible rate to ensure a desired output frequency. In this case, the converter AC side line voltage assumes a quasi-rectangular wave shape which forms the dual of the DC link converter. Harmonics voltages of 5, 7, 11, 13, etc., times the fundamental are produced which in turn, induce currents of these frequencies in the corresponding AC current. In the pulse-width-modulated (PWM) mode, the switching frequency is modulated to eliminate undesirable harmonics. The switching frequency is sufficiently high that harmonic torques of concern in a wind turbine generator application are effectively eliminated. The presence of harmonics plus the large DC filter requirements of the six step mode suggests that PWM operation would be the preferred triggering scheme in this application.

Special advantages of a voltage link system are:

- o Smooth transition through synchronous speed.
- o High frequency torque pulsations only.
- o Smaller per unit rating than equivalent DC current link system.
- o VAR control.

Important disadvantages of this system are:

- o Cost.
- o Complexity.

Doubly Fed Induction Generator and Cycloconverter

An alternative to DC current or voltage link systems is the cycloconverter which is a device which transforms line frequency power to adjustable frequency power without an intermediate DC link. Numerous cycloconverter configurations have been proposed but the 36 thyristor arrangement is most widely used. This type of converter operates essentially as a voltage source. The cycloconverter is effectively a sampling type of converter where the input frequency is fixed and the sampling frequency changes with output frequency. In order to construct an output waveform, samples are taken from the three phase input. With proper modulation of the cycloconverter the current is nearly sinusoidal with superimposed harmonics related line frequency and to the switching frequency of the cycloconverter bridges. Because of the limits imposed by the sampling theorem, the output becomes progressively distorted as the output frequency is increased with about 1/2 the input frequency being the maximum obtainable with a 36 thyristor configuration.

The most pertinent special advantages of the cycloconverter fed, doubly fed induction generator scheme appear to be:

- o Power factor control.
- o Smooth transition through synchronous speed.

Several important drawbacks exist for this scheme which restrict somewhat its usefulness. They are:

- o Torque pulsations.
- o Harmonic structure of the injected line currents.
- o Behavior during single phase fault.

Cycloconverters can also potentially replace the dual converter bridge of a synchronous generator system. However, because the ratio of input to output frequency is restricted such an application would imply that the frequency of the generator would have to be kept relatively low (below 15 Hz) or relatively high (above 360 Hz) to provide for low harmonic distortion. Operation at such low or high frequencies would probably seriously restrict the design of the synchronous generator. Also, since full rated power would now pass through the cycloconverter, severe filtering problems could occur. Finally, serious power factor correction problems would arise, particularly for the low frequency option in which commutating VARs are required from the utility side to provide commutation energy for the cycloconverter.

DYNAMIC INTERACTION WITH THE UTILITY SYSTEM

The dynamic interaction of wind turbines and electric utility systems has been the attention of a number of studies. These studies have largely concentrated on wind turbine-generator systems which utilize synchronous generators [2]. A result of those studies was the observation of significant dynamic interaction within the turbine-generator system and between the wind turbine-generator system and the electric utility system. The internal oscillation is the so called first torsional mode which is highly oscillatory and lightly damped. If a synchronous generator is used as the electrical converter, these variations are faithfully reproduced thus producing a highly variable output power. In general, damping is provided through blade pitch control.

As interest has accelerated in variable speed generating technology, the properties of these systems have been examined more closely [3, 4]. In order to distinguish between variable speed generators (asynchronous) and synchronous operation two significant points should be made. In synchronous operation the torsional compliance between the electric generator and the utility system is low. As a result wind turbine-generator drive train swings against the utility. For variable speed systems (except for low speed slip induction generators), the compliance between the generator and the utility is high relative to the turbine-generator and drive train causing the generator to swing against the turbine. Hence, synchronous systems use blade pitch

control most effectively while variable speed systems use electric torque control to regulate torsional oscillation. Clearly, the dynamic properties are quite different.

Variable speed wind turbines also permit programmed variations of turbine speed as a function of wind speed, power level, or other process variables. This additional degree of freedom can have important benefits, such as higher turbine efficiency or reduced structural loads.

Most of the benefits of variable speed can be achieved with a relatively small speed range (20-30% of nominal speed). A small speed variation is also desirable to limit rotor exposure to natural frequencies. If slow turbine blade angle control is superimposed on fast generator torque control, the speed range required for input energy variations can be reduced significantly.

Dynamic interactions between wind turbine and utility system can largely be eliminated by variable speed. Within the constraints of rotor inertia and speed range, the generator can deliver constant energy even though the turbine is operating in a variable energy medium.

CONTROL SYSTEM REQUIREMENTS

The fundamental difficulty with control of wind turbines is the variation of input energy caused by changes in wind speed. In present designs of wind turbines, the variation in input energy causes changes in shaft torque because speed is held constant for synchronous generator operation. The drive train must be designed for the resulting torque excursions, both the steady state levels and the variations which can excite torsional resonances. There is little torsional compliance between present wind turbines and power systems.

The successful control of any system depends upon several key items. These include:

- o Specification of the input to which the system must respond.
- o Specification of the desired transient and steady-state response.
- o Some degree of modeling of the plant to be controlled, including sensors for measurement of output responses and control actuators for modification of the system input.

The control problems associated with variable speed wind turbines are much the same as those associated with fixed speed machines. The major difference being in the physical conversion process and perhaps the choice of control variables. Of course there is flexibility in what can be achieved with a variable speed system which is not present in fixed speed systems. The input specifications are roughly the same; that is, the turbine is to extract some measure of power from a widely varying source, the wind. The output specification is the delivery of power to an electric utility system at constant voltage and frequency and at as constant a power level as is practical. The problem of control of both mechanical

and electrical systems to produce smooth power from a sometimes rapidly varying wind source is both difficult and formidable whether fixed or variable speed is chosen. Both the fixed and variable speed systems require speed and/or torque control systems. A fixed speed system requires fixing blade rotation at some reference speed in the face of sometimes strong disturbances. A variable speed controller will probably require maneuvering the speed of the wind turbine to a point of maximum power capture during normal wind capture conditions and to some specified power setting during a power limit mode.

Several problems exist with current horizontal axis wind turbine systems that can be overcome by asynchronous operations:

- 1) Fixed-speed turbine efficiencies can be optimized through gearing selections for only one wind velocity. Net power capture is therefore less than could be achieved at wind speeds other than the optimal design speed.
- 2) A complex rotor-blade pitch-angle control servomechanism is required to limit power flow at average wind velocities above rated. This mechanism acts to limit mechanical wind torque by reducing turbine efficiency.
- 3) The mechanical shaft system is prone to very lightly damped oscillations for average wind velocities below rated. This behavior is due to the large rotor blade inertia, quill shaft compliance, and large step up gearing to the high speed generator shaft. These oscillations produce undesired stresses on the shaft components and make resynchronization of the generator after fault clearance difficult.
- 4) With turbine speed fixed, fluctuations in wind velocity produce corresponding mechanical torque fluctuations which pass essentially unattenuated into electrical power flow producing an undesirably large variance in electrical power.

A variable speed control system capable of fast control of generator torque can be used to adjust turbine efficiency, absorb wind gusting energy, and provide damping for shaft oscillations thus alleviating some of the difficulties encountered with fixed speed systems. Variable speed systems are of course, not without potential problems of their own.

The key control features for variable speed wind turbines are fast, electrical torque control at the generator and slow, mechanical speed control at the turbine. The programmed variations of turbine speed in response to other process variables can be introduced as changes to the turbine speed setpoint or the generator torque setpoint.

Turbine-Generator Control

In order to discuss specific trade-offs in control system design between fixed and variable speed systems, consider Figure 2. This diagram depicts a somewhat simplistic but yet generic wind turbine together with its various inputs and outputs including wind velocity, the blade pitch angle, and the rotational speed. Functionally, the aeroturbine combines these quantities to produce mechanical torque. The electrical torque produced by the electrical conversion process along with the utility

tie and the mechanical shaft torque are driven to some particular value in steady state. If a mismatch occurs, the deviation is used through the mechanical dynamics (including shaft compliances, gear-box, and inertias) to accelerate or de-accelerate the machine speed. Note the implicit feedback control loop. In a fixed speed system, the blade pitch angle is adjusted so that the difference between mechanical and electrical torque is a constant and hence the speed is constant.

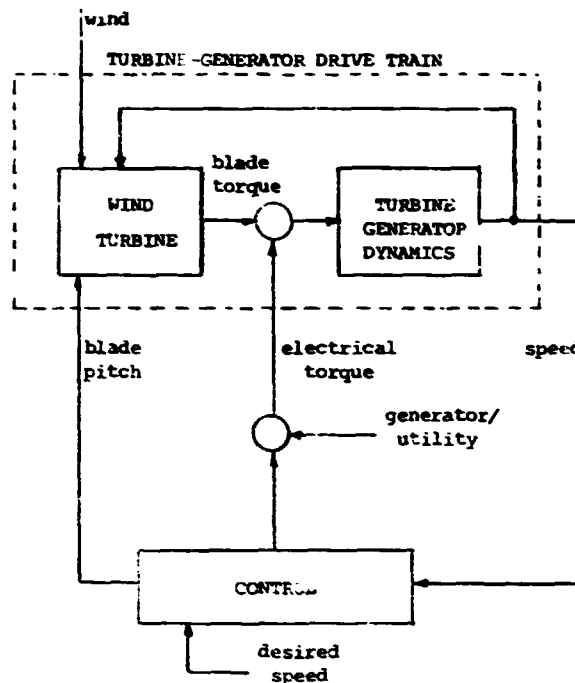


Figure 2. Wind Turbine-Generator System

Blade pitch and electrical torque are regarded as controllable inputs and wind speed as uncontrollable input. In a fixed speed synchronous system, the electrical torque is controllable through the exciter of a synchronous machine and not at all with an induction machine. Typically the exciter of a synchronous machine is used to control VAR flow, power factor, or for the regulation of terminal voltage.

In a real sense, blade pitch and electrical torque are equivalent speed regulating mechanisms excepting that one is electrical and one is mechanical. In all cases speed is shaped through the mechanical dynamics.

In a fixed speed system the desired speed is that speed which produces a 60 Hz electrical waveform. In a variable speed system, desired speed will probably depend on some filtered version of the wind speed. Figure 2 shows control through both the electrical torque and the blade pitch angle. Control through manipulation of electrical torque is more achievable in a variable speed system because in introducing the isolation between grid and machine, additional electrical control is available. One of the values of the variable speed generating options is this additional degree of freedom of effective control.

In variable speed systems, it is interesting to note that power can be spilled by either increasing the speed of the machine thus allowing the spilled energy to go into rotational energy, or by decreasing the machine speed to a more (but appropriate) inefficient operating point thus requiring more wind for the same output power. Either scheme will work for regulating power. Overspeed control would be preferable because the stored energy could be re-captured. However, the degree of overspeed will be determined through structural requirements. Clearly, there are trade-offs between turbine design, blade control, and electrical control that needs examination.

System Control Strategy

Wind turbine system control requirements should be based on the highest credible penetration of machines. It is well to remember that utility system needs are often neglected when new energy technologies are developed [5]. Essential system requirements of variable speed wind turbines are:

- o Proportional control of line frequency as a function of load. This is necessary so that generation can be adjusted in response to changes in load and that load can be shared with other sources in a controlled manner. Frequency control cannot be accomplished by turbine speed control because line frequency is no longer dependent on turbine speed. Converter equipment used in the variable speed system cannot depend on line frequency for commutation.
- o Control of line voltage. This is necessary to provide voltage support to the power system. Var generation as well as var absorption should be possible.

While the feasibility and philosophy of variable speed control system design have been examined, there are additional problems that may occur. Because of recent trends in wind turbine mechanical design to "flexible" systems (flexible blades, teetering hubs, soft shafts, etc.) many modes exist in the structural and torsional design. These are cause for concern and the flexible design policy needs to be re-examined in light of the possibility of exciting these modes with variable speed operation. Mode avoidance can be accomplished to some extent through control policy but would not be preferable to designing the troublesome mechanical modes out by rigid blade and tower construction if possible.

In addition, electrical speed control is favored over mechanical control because of its simplicity. There are no rotating couplings to leak or pneumatic actuators to fail. It remains to be seen what

generator torque requirements are necessary to accomplish the control. Finally, the specification of the input and output are an issue. The control system designs should be flexible enough to follow a reasonable variation in the wind while the output should have the capacity for arbitrary smoothing (at the expense of loss of wind capture).

CONCLUSIONS

An examination of variable speed electric generating systems for wind energy has been provided. The three key elements discussed include variable speed options, dynamics of variable speed systems, and control. The merits of the variable speed system include high wind turbine collection efficiency and superior dynamic properties with the addition of proper controls. Inefficiency in the variable generator can be minimized through careful design.

ACKNOWLEDGEMENT

This work has been supported by the U. S. Department of Energy, Wind Energy Technology Division through the Oak Ridge National Laboratory under the management of Martin Marietta Energy Systems. Helpful suggestions by J. S. Lawler of the University of Tennessee aided in the preparation of the text are appreciated.

REFERENCES

- [1]. T.A. Lipo, "Variable Speed Generator Technology Options for Wind Turbine Generators," DOE/NASA Wind Turbine Technology Workshop, Cleveland, Ohio, May 8-10, 1984.
- [2]. E. N. Hinrichsen and P. J. Nolan, Dynamics of Single- and Multi-Unit Wind Energy Conversion Plants Supplying Electric Utility Systems," DOE/ET/20466-78/1, August, 1981.
- [3]. E. N. Hinrichsen, "Differences in Dynamic Behavior of Synchronous and Induction Machines in Wind Turbine Generators," Proceedings of the Fifth Biennial Wind Energy Conference and Workshop (WWV), Volume II, pps. 407-412, October 1981.
- [4]. E. N. Hinrichsen, "Controls for Variable Pitch Wind Turbine Generators," IEEE Transaction on PAS, Volume PAS-103, No. 4, April 1984.
- [5]. L. H. Fink and W. E. Feerc, "Effective Integration of New Technologies into Electric Energy Systems," IEEE Transactions on PAS, Volume PAS-101, No. 7, July 1982.

VARIABLE SPEED GENERATOR TECHNOLOGY OPTIONS FOR WIND TURBINE GENERATORS

T.A. Lipo
 Department of Electrical and Computer Engineering
 University of Wisconsin
 Madison, Wisconsin

ABSTRACT

The electrical system options for variable speed operation of a wind turbine generator is treated in this paper. The key operating characteristics of each system are discussed and the major advantages and disadvantages of each are identified.

INTRODUCTION

Adjustable speed operation of AC motors by use of frequency converters is making rapid inroads in the DC drive market. On the other hand, the concept of variable speed as applied to power generation rather than power utilization has, except for several prototype systems, not been widely exploited. The rapid development of AC adjustable speed drives has, however, resulted in an array of alternatives which also have potential application for variable speed power generation. This paper will focus on the options available for variable speed wind turbine generators (WTGs) together with the advantages and disadvantages of each. In particular, potential configurations for large wind turbine generators rated above 1 MW are emphasized.

CANDIDATE VARIABLE SPEED SYSTEMS FOR LARGE WIND TURBINE GENERATORS

The field of adjustable speed machine systems is an active and growing discipline such that a completely comprehensive treatment of technology options is an extremely difficult task. In particular the number of feasible options appears to vary inversely with the power rating of the WTG. This paper will be concerned primarily with identifying major technology options primarily at WTGs rated above 1 MW. A less comprehensive assessment of technology options for lower power WTGs are summarized in the second portion of this paper.

DC Generator with Line Commutated Inverter Bridge

Probably the most straightforward variable speed system for a WTG utilizes a DC generator with inversion of the generated DC power to AC by use of a line commutated rectifier bridge as shown in Fig. 1. Current flow is in 120° blocks at line frequency on the AC side of the inverter and filtering at the AC terminals of the bridge is needed to suppress harmonic current flow into the power system and to correct the power factor to unity. Because of the heavy filtering required to eliminate unwanted harmonics of the simple six pulse bridge of Fig. 1, other bridge configurations are also in common use. For example, the dual six pulse bridge arrangement of Fig. 2 results in the elimination of the lowest frequencies, the 5th and 7th harmonic components inherent in the bridge configuration of Fig. 1 while halving the next lowest components, the 11th

and 13th. An advantage of the dual bridge configuration of Fig. 2 is that each bridge need only be rated at one-half the KVA rating of the single bridge of Fig. 1. It should be mentioned that such alternatives are generic to any of the systems to be discussed which utilize six pulse bridge configurations.

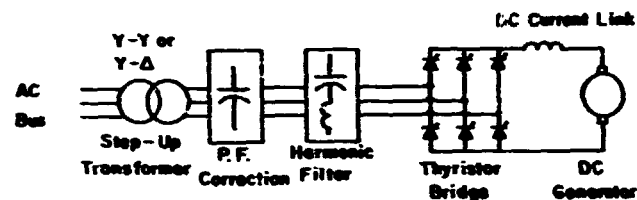


Fig. 1 DC Generator with DC Current Link and DC/AC Inverter.

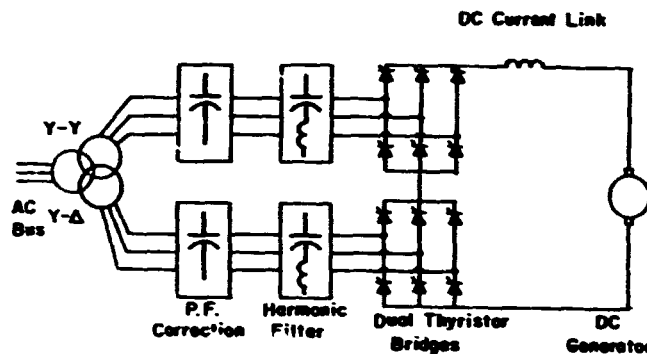


Fig. 2 DC Generator with DC Current Link and Dual DC/AC Inverters.

While not strictly necessary, some filtering of the DC voltage of the bridge is typically employed so as to minimize stray losses in the generator due to harmonic currents. The simplest type of filter is to simply use a DC link inductor as shown in Fig 1 to smooth the current. Such systems are said to utilize a DC current link and when the size of the inductor is large, the converter/generator system operates much like a current source. An alternative to the filtering problem is the placement of a capacitor across the terminals of the machine and employ a much smaller link inductor which is now selected primarily to limit charging current into the capacitor as shown in Fig. 3. In this case the current flow from the machine is smoothed by providing a low impedance path to harmonic currents. Such a configuration is said to employ a DC voltage link

arriving from the converter. When the capacitance is large the converter/generator system appears much like a voltage source to the power system.

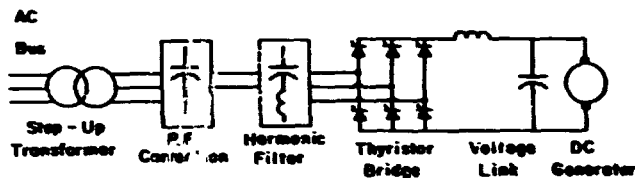


Fig. 3 DC Generator with DC Voltage Link and DC/AC Inverter

It is well known that the power factor of a line commutated bridge varies in direct proportion to the ratio of DC to AC voltage. Hence, in order to maintain good power factor at the terminals of the bridge, the inverter must be controlled such that the voltage on the DC side of the bridge must be maintained constant near its maximum permissible value. In converter terminology such a control is usually called constant extinction angle control in which the inverter is commutated such that the inverter thyristers have just sufficient time to recover blocking ability before forward voltage is reapplied.

Operation of the DC generator at a variable speed, however, implies a variable DC voltage since the internal generated EMF of the machine varies directly proportional to speed. If the speed range of the WTG is small (10 to 15%) the DC side voltage can be maintained at its rated value, however, by simply increasing the field excitation of the DC generator as speed decreases. Such a control strategy implies a slight overdesign of the generator in order to overflux the machine and accommodate the extra field heating. Alternatively, for larger speed ranges the DC voltage at the inverter terminals must be reduced to match the varying DC generator voltage by control of the inverter extinction angle. Since the system power factor would then vary, such a control would imply a larger capacitor bank for power factor correction.

Special advantages of this system include:

1) Minimal Torque Pulsation. Since the generator is DC rather than AC the torque pulsations associated with harmonic currents due to switching of the machine side converter is eliminated. Some residual torque pulsations will remain depending upon the degree of DC side filtering. However, the frequency of these pulsations are 360 Hz and multiples of 360 Hz which are unlikely to cause resonance problems.

2) Straightforward Control Algorithm. Whereas the control of AC machines in a variable speed application often becomes rather complex, the corresponding control of a DC machine is simplicity itself, and is a long established technology.

Several unique disadvantages which could influence application of this system to a WTG application are:

1) Maintenance and Reliability Concerns. The shortcomings of DC machines in these important categories have been long cited, perhaps overly so. Since most WTG installations do not require continuous operation, brush and commutator maintenance should not be particularly difficult. However, reliability questions concerning a large mechanically commutated machine in the environment of a WTG remain to be resolved.

2) DC Fault Protection. This system shares with most other configurations the advantages of quickly isolating the machine from the AC system. Rapid control of the

converter bridge can prevent fault current contributions from the DC machine when faults occur on the AC side of the converter. However, rapid interruption of faults on the machine side of the converter necessitates a DC breaker which is more expensive and requires more maintenance than an AC breaker.

3) Control Response Limitations. One of the potential advantages of variable speed systems over constant speed systems is the potential ability to damp torsional oscillations of the WTG. Such an application would however, require torque control over a wide bandwidth. In comparison to many AC systems which will be discussed, the speed of response of the system of Fig. 1 is relatively slow since torque control is accomplished by adjustment of the field current. The inherently large field time constant would be difficult to overcome if rapid changes in torque were necessary.

Problems involved with rapid control of torque could clearly be avoided with armature control. However, since power factor is an important consideration, modulation of the voltage of the converter bridge of Fig. 1 would probably be impractical. Use of a chopper intermediate stage would accomplish this task but such a force commutated device is considered as impractical for WTGs of large kilowatt rating. Such configurations are more suitable for lower power applications which will be addressed later.

Synchronous Generator with Thyristor Rectifier and Inverter

Another class of system suitable for wind power generation is a synchronous generator supplying power through a DC current link rectifier/inverter as illustrated in Fig. 4. Commutation of the line side inverter is again accomplished by taking VARs from the power system. Commutation of the machine side converter is provided by taking VARs from the synchronous machine. In this case, excitation of the machine is by means of a brushless exciter.

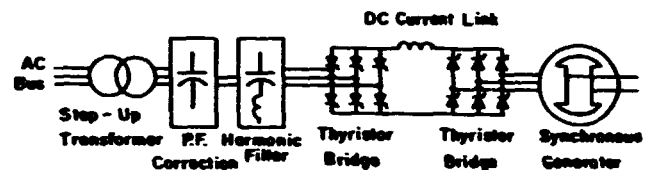


Fig. 4 Synchronous Generator with DC Current Link and DC/AC Inverter.

Electrical generated power must pass through the rectifier/inverter so that the converters must be rated at the full machine rating. In this case 120° blocks of current flow on the AC sides of both the rectifier and inverter. Again, the harmonic content on either the machine side or utility side converters can be reduced by more elaborate bridge configurations. In particular, the synchronous generator is frequently wound as dual three phase winding groups wherein each group feeds six pulse bridges in much the same manner as Fig. 2. If the speed range is again narrow (10-15%) the line side inverter can be maintained at its minimum extinction angle by adjusting the field current of the synchronous generator with speed in much the same manner as for the DC generator.

Important special advantages of this system include:

1) Wide Speed Range. In general, the switching frequency of the machine side converters is limited by the subtransient reactance of the machine. With typical per unit numbers, frequencies of 150-200 Hz are readily

obtainable.

2) High Frequency Torque Pulsations. The torque pulsations are again multiples of six times the frequency of the machine side converter. Since a typical frequency range of the machine side inverter in a wind power application is 30-90 Hz the torque pulsations will range from 180 to 540 Hz, which is comfortably above the measured resonances of the wind generator.

3) Strong Electrical Damping. Again strong damping of mechanical oscillations can be initiated from the machine side of the mechanical system. Since the frequency range of the rectifier is relatively high (30-90 Hz), effective control of oscillations can be maintained over the speed range.

4) Rapid Reclosure After a Fault. Upon a line interruption following a fault, the inverter is isolated from the line and hence the commutation energy to switch the inverter is lost. However, the current flow in the DC link can be maintained as circulating current by simultaneous firing of a thyristor in the top and bottom of the inverter bridge. Upon clearing of the fault, current can be rapidly established on the AC side of the converter by suitable control.

This system has a number of potential disadvantages among which are:

1) Low Frequency Torque Pulsations Near Synchronous Speed. The DC side ripple harmonics of the bus side converter is fixed at 360 Hz whereas the ripple DC link harmonics of the machine side converter are six times the inverter frequency. When the machine approaches synchronous speed the superposition of the two frequencies in the DC link can produce sum and difference "beating" frequencies. Since these beat frequencies pass into the machine, torque harmonics much lower than that produced by either converter operating independently can arise. These currents can produce torques which resonate with the mechanical system. This beating effect can be minimized with proper selection of the DC link reactor and control of the machine side converter.

2) High Harmonic Distortion. Again the current on the AC side of the converter set is comprised of 120° blocks. These quasi-rectangular currents are relatively large since the converter is rated at full rated power of the generator. The harmonic content injected into the power system can again be reduced with the more elaborate bridge configuration of Fig. 2.

If controlled starting as a motor is not required, it is possible to replace the machine side thyristor converter by a simple diode bridge. Torque control of the machine must now be accomplished by field control. Response of the system is similar to the DC system of Fig. 1 and rapid control of the armature current is sacrificed.

Doubly Fed Induction Generator with DC Current Link Rectifier and Inverter

Another type of system which bears a great similarity to the synchronous generator scheme of Fig. 4 is the doubly fed induction generator of Fig. 5. The system again uses a rectifier/inverter with a DC current link wherein the machine side converter is connected to three phase rotor windings by means of slip rings. Current flow is in 120° blocks at slip frequency on the AC side of the rotor connected converter and 60 Hz on the AC side of the stator connected converter.

In principle, operation either above or below synchronous speed is possible. Synchronous speed in this case is defined as the point at which the rotor rotates synchronously with respect to the stator rotating MMF when the slip rings are shorted. When the machine generates power below synchronous speed, power is supplied to the utility

from the stator windings. However, power must still be supplied to the rotor windings of the machine through the slip rings. The power required is essentially proportional to the difference between rotor speed and rotor synchronous speed (slip frequency) times rated power. Hence, if the speed range is limited the rectifier/inverter need only be rated for a fraction of rated power (slip power). It can be noted from Fig. 5 that in this mode of operation the rotor side converter operates as a variable frequency inverter. Conversely, when the machine generates power above synchronous speed, electrical power is also extracted from the rotor via the slip rings. Again the converters need have a rating equal only to slip power. The rotor side converter operates in this case as a rectifier.

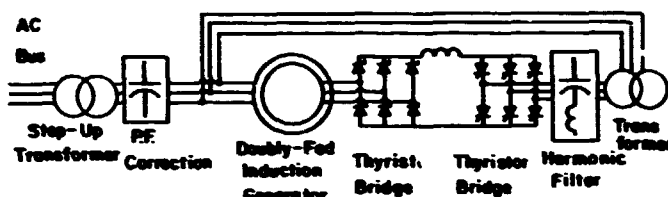


Fig. 5 Doubly Fed Induction Generator with DC Current Link and AC/DC/AC Rectifier-Inverter.

In addition to the usual step down transformer from the distribution voltage level, another transformer is typically provided to match the voltage level of the rotor windings to that of the stator. This transformer provides additional short circuit protection and helps reduce the ripple current content in the DC link. The turns ratio is usually selected so that the extinction angle of the inverter and retard angle of the rectifier are at their minimum values when the machine operates at maximum slip frequency.

Among the particular advantages of this system are:

1) Converter Ratings Based on Slip Power. As noted above the converters need be rated only at a fraction of rated power. For example, if the expected speed range is 10-15% then the converters need be rated only at 0.1-0.15 per unit power.

2) Control Response. Since the rotor connected bridge must control power at slip frequency the response of this system is not expected to be as good as the synchronous motor system of Fig. 4. Nonetheless, the response can be markedly improved compared with the DC generator configuration of Fig. 1.

3) Harmonics. Since the bridges handle only slip power, the corresponding current harmonics are also proportional to slip power and are more easily filtered than previous systems.

4) VAR Control. While the VAR requirements of this system are always positive (lagging VARs), a certain amount of VAR control is possible by coordinating the control angles of the rectifier and inverter. Hence, unity power factor operation could be achieved continuously with a fixed capacitor bank without the need for switching capacitors.

This system has several particular drawbacks including:

1) Restricted Speed Range. From the above discussion it is apparent that the power flow into the rotor reverses direction as the machine passes through synchronous speed. As a result, the rotor side bridge loses commutation energy and a "dead spot" exists in which control is lost. One possible solution to this problem is to provide forced commutation capability for the rotor side bridge. A number of such forced commutation circuits are possible

but a particularly simple arrangement is shown in Fig. 6. Since forced commutation is only required near synchronous speed, the size of the commutation capacitor would not be substantial. Note however that since the circuit utilizes the neutral connection of the rotor an extra slip ring must be provided.

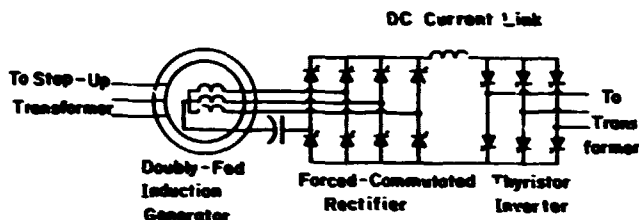


Fig. 6 Doubly Fed Induction Generator Arrangement with Force-Commutated Rectifier.

Another solution to the loss of control problem is to simply operate the system only above or below synchronous speed. Continuous operation above synchronous speed appears to be the preferred strategy due to the difficulty in operating with a bridge in the variable frequency inversion mode and the size penalties involved in operating an electrical machine below rather than above its nominal rated speed.

2) Torque Pulsations. The rectangular currents which flow in the rotor windings result in 5th, 7th, 11th, 13th, ... harmonics of slip frequency. These harmonic currents in turn interact with the fundamental component to produce electromagnetic torque pulsations at the 6th, 12th, 18th, ... harmonics of slip frequency. Since the slip frequency spans the range from near zero to, say 20 Hz, the sixth harmonic torque pulsation would vary from zero to 120 Hz. Although the amplitude of these pulsations is rather small, large amplification can occur at the mechanical resonant frequencies. It has been shown that by modulating the DC link current the amplitude of these pulsating torques can be reduced by a factor of ten [1]. Resilient couplings, for example a Holset coupling, can be used to reduce the amplitude of these injected torques to a manageable value. Nonetheless, the difficulty of torque pulsations appears to be a major disadvantage of this system.

3) Slip Rings. Presence of slip rings implies a potential maintenance issue which is not present with the synchronous generator scheme. Since the rotor current flows in 120° blocks the current in a given phase is zero over 60° intervals and these intervals can be substantial at low slip frequency. It is well known that rapid brush wear can occur under zero current conditions but the severity of the problem under discontinuous operation with a converter is apparently not well understood. Also, without careful design the quasi-rectangular currents can induce currents in the rotor body itself which could, potentially, cause deterioration of the rotor bearings. Both effects are potential concerns which needs to be addressed.

4) Lagging Power Factor. Since both the rectifier and inverter must absorb VARs to effect commutation, the overall power factor of this system cannot be raised to unity. A relatively substantial bank of power factor correcting capacitors would be required to supply the VAR need of both the induction generator as well as the converters.

As was the case for the synchronous generator configuration, the thyristor bridge (rotor connected bridge in the case of super synchronous operation) can be replaced by a simple diode bridge. Control of rotor power

is maintained by means of the firing angle of the inverter bridge. However, the possibility of starting the machine as a motor is again lost. The VAR input into the system cannot be adjusted since the inverter control must be dedicated to control of power.

Doubly Fed Induction Generator with DC Voltage Link Rectifier and Inverter

Whereas DC current link converter configurations derive commutation volt-ampere from the connected supply, DC voltage link systems typically (but not inevitably) rely on commutation energy from special purpose capacitor circuits or by means of self commutating switches (transistors or GTOs). Such converters are inherently more expensive than DC current link converters. However, costs of these converters are decreasing rapidly with the development of new high power transistor and gate turn-off (GTO) switches. If the desired speed range is small the rotor connected converters need only handle a small fraction of rated power and the possibility of using a DC voltage link may be practical. Such a voltage link configuration is shown in Fig. 7 in which the rotor connected converter is operated in forced commutation while the stator connected converter commutates naturally. Other arrangements are possible in which the stator side converter (or both) are force commutated.

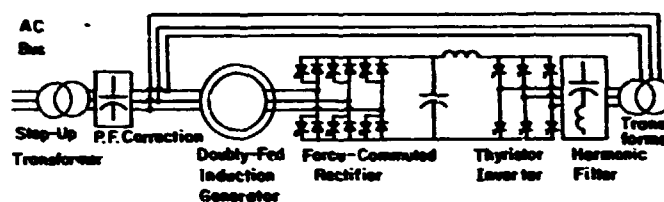


Fig. 7 Doubly Fed Induction Generator with DC Voltage Link and Force-Commutated Rectifier.

In general, forced commutated converters can be operated in either of two modes. In the six step mode the converter switches are triggered at the lowest possible rate to ensure a desired output frequency. In this case the converter AC side line voltage assumes a quasi-rectangular waveshape of 120° voltage blocks which, in effect, forms the dual of the DC link converter. Harmonic voltages of 5,7,11,13, ... times the fundamental are produced which, in turn, induce currents of these frequencies in the corresponding AC current. In the pulse-width-modulated or PWM mode the switching frequency is modulated so as to eliminate these undesirable harmonics. The switching frequency is sufficiently high that harmonic torques which would be of concern in a wind turbine generator application are effectively eliminated. The presence of harmonics plus the large DC filter requirements of the six step mode suggests that PWM operation would be the preferred triggering scheme for this application.

Special advantages of a voltage link system are:

1) Smooth Transition Through Synchronous Speed. Since commutation of the rotor side converter is now provided internally, the problem of "dead spots" near synchronous speed is eliminated. Control gains remain high throughout a wide speed range including synchronous speed so that strong damping of mechanical oscillations is always possible.

2) High Frequency Torque Pulsations Only. In general, the frequency of a PWM inverter is readily raised to the point where the resulting torque harmonics are well above the resonant frequencies of the mechanical system.

3) **Smaller Per Unit Rating than Equivalent DC Current Link System.** Since a PWM converter is equally capable of rectifying or inverting, operation of the generator above or below synchronous speed is possible. Hence, for a given variation in power from maximum to minimum speed, the rating of the PWM converter need be rated only at the difference between maximum and minimum power suggesting a slight saving in rating of the DC voltage link system compared to the DC current link.

4) **VAR Control.** Since the force commutated converter does not require VARs for successful operation it can actually supply VARs to the Generator thereby permitting the control of VARs as well as power. Operation of the system at unity or leading power factor appears possible with proper attention to the rating of the converters.

Important disadvantages of this system are:

1) **Cost.** There is a cost penalty for this system due to the requirements of high grade switches and/or extra components needed to accomplish forced commutation. However, the cost of such converters are rapidly dropping due to the emergence of new high power transistors and GTOs. Of all the configurations under consideration this system is perhaps the most dependent on emerging technology.

2) **Complexity.** Successful implementation of PWM schemes typically require a considerably more complicated voltage control algorithm which invites questions concerning reliability. Operation of the PWM converter both above and below synchronous speed implies an extra diode bridge to supply power during subsynchronous operation (shown in Fig. 8)

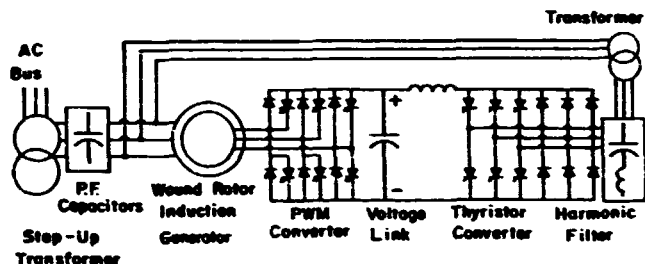


Fig. 8 Doubly Fed Induction Generator Scheme Capable of Operation Above and Below Synchronous Speed.

Doubly Fed Induction Generator and Cycloconverter

An alternative to DC current or voltage link systems is the cycloconverter configuration of Fig. 9. The cycloconverter is a device which transforms line frequency power to adjustable frequency power directly without use of an intermediate DC link. Numerous cycloconverter configurations have been proposed but the 36 thyristor arrangement shown in Fig. 9 is most widely used. This type of converter operates essentially as a voltage source. The cycloconverter is effectively a sampling type of converter where the input frequency is fixed and the sampling frequency changes with output frequency. In order to construct an output waveform, samples are taken from the three phase input. With proper modulation of the cycloconverter the current is nearly sinusoidal with superimposed harmonics related line frequency and to the switching frequency of the cycloconverter bridges. Because of the limits imposed by the sampling theorem, the output becomes progressively distorted as the output frequency is increased with about 1/2 the input frequency being the maximum obtainable with a 36 thyristor configuration.

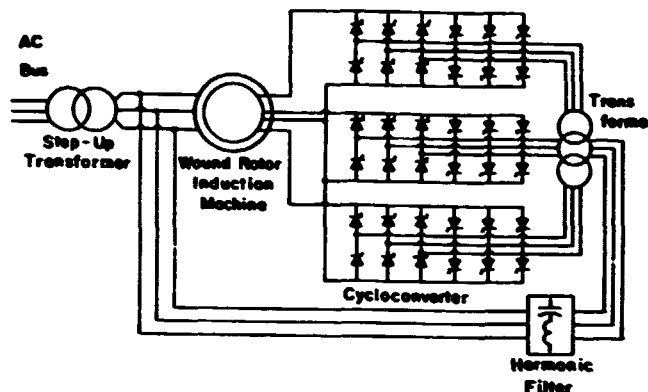


Fig. 9 Doubly Fed Induction Generator with Direct AC/AC Conversion.

As was the case for current and voltage DC link system, numerous types of cycloconverters are useful. For example, an 18 thyristor voltage source system can be employed. In this case the useful frequency range is limited to about 1/3 the input frequency. Current source cycloconverters are also in use. Such a cycloconverter is often called a "hidden link" cycloconverter since the current source mechanism is obtained by use of an AC inductor on the input side of the cycloconverter.

Since isolation is needed to prevent short circuits, cycloconverters are generally accompanied by an input transformer with three isolated secondaries. The turns ratio is selected to provide maximum output voltage under the highest slip power condition. In principle, the transformer could be omitted if the three rotor phases of the machine were isolated. However, this option is not considered practical for a WTG as it would require six slip rings rather than three.

The most pertinent special advantages of the cycloconverter fed, doubly fed induction generator scheme appear to be:

1) **Power Factor Control.** With proper control of the voltage applied to the rotor of the machine, the VARs consumed or supplied by the machine can be adjusted at will. In particular, by proper adjustment the VARs required to provide switching of the cycloconverter can be obtained from the stator of the machine itself so that the entire system is "self-supporting" and the machine is capable of supplying power at unity power factor.

2) **Smooth Transition Through Synchronous Speed.** This configuration shares with the PWM DC voltage link the capability of continuous operation at synchronous speed. The "dead zone" inherent in naturally commutated DC current link converter systems is not present in this arrangement. The WTG application appears to be a good match for the inherent performance capabilities of the cycloconverter since the speed range of the WTG is relatively narrow, requiring only a limited range of output frequencies from the cycloconverter. Since commutation takes place at a fixed rate (360 Hz), good control of the rotor current is maintained down to DC frequency so that damping of torsional oscillations can be provided even when the output frequency is near (or at) zero.

Several important drawbacks exist for this scheme which restrict somewhat its usefulness. They are:

1) **Torque Pulsations.** In general, harmonic torques produced by the switching of the cycloconverter are not of concern since the predominant frequencies are integer multiples of 360 Hz, which are well above the resonant fre-

quencies of the mechanical system. However, because the switching of the cycloconverter is not synchronously tied to the output frequency, harmonic components of the output are not rigorously tied to the fundamental frequency of the input. Low frequency torque pulsations could arise which may induce mechanical oscillations. In particular, a "beating" phenomenon occurs when the frequency approaches integer fractions of 60 Hz (2,3,6,10,12,15,... Hz). Amplitude of these pulsations are very small for high integer ratios of input to output frequencies (30:1, 20:1, etc.) but may become appreciable at lower ratios (4:1, 3:1 and 2:1). The most severe (2:1 and 3:1) can be avoided by restricting the frequency output (rotor slip frequency) to less than 20 Hz. The next most severe conditions for a WTG application are the 12 and 15 Hz cases which would have to be carefully examined.

2) Harmonic Structure of the injected Line Currents. One property which distinguishes the cycloconverter from the DC voltage or current link system is that the harmonic structure of the voltage output is not an easily predictable function. Harmonics are dependent not only upon the input frequency and switching instant but also upon the impedance presented to the cycloconverter during commutation (switching of the cycloconverter thyristors). Due to the asynchronous tie between input and output the harmonic structure of the output spans a frequency band rather than consisting of discrete harmonic components of the input. As a result the filtering problem is somewhat more complicated. Since tuned filters are inappropriate, a low pass filter must be used which implies heavy filtering requirements.

3) Behavior During Single Phase Line Fault. In general, buffering of the machine from the utility by means of a converter provides an inherent benefit in the event of system faults since the line side converter can be rapidly controlled to greatly reduce the fault contribution from the wind turbine generator. However, the characteristic of a single phase fault or single phase open circuit is particularly difficult for cycloconverter systems since large harmonic components including fundamental components of the line frequency are admitted into the output (i.e. appear on the rotor side of the cycloconverter) upon a single phase fault. Whereas six pulse converter bridge schemes can be equipped to handle such occurrences, a cycloconverter fed machine would probably require switching off the line resulting in a reliability concern relative to other alternatives.

Cycloconverters can also potentially replace the dual converter bridge of a synchronous generator system (Fig. 4). However, because the ratio of input to output frequency is restricted, such an application would imply that the frequency of the generator would have to be kept relatively low (below 15 Hz) or relatively high (above 360 Hz) to provide for low harmonic distortion. Operation at such low or high frequencies would probably seriously restrict the design of the synchronous generator. Also, since full rated power must now pass through the cycloconverter, severe filtering problems would occur. Finally, serious power factor correction problems would also arise, particularly for the low frequency option in which commutating VARs are required from the utility side to provide commutation energy for the cycloconverter.

VARIABLE SPEED OPTIONS FOR SMALLER WIND TURBINE GENERATORS

As the rating of the WTG is reduced the number of alternatives is enlarged. All of the previously mentioned schemes remain practical for lower power applications. However, in general, the per unit costs of wound field

machines such as the synchronous and wound rotor induction generator increase as ratings of such systems decrease, thereby permitting various DC and cage rotor induction generator configurations utilizing force commutation to become more competitive. If variable speed systems which require connection to passive loads rather than the utility grid are not considered, the following additional systems can be identified.

DC Generator with Chopper Based DC Voltage Link

Figure 10 shows a DC WTG scheme in which the generator is buffered from the output by a DC voltage link formed by a step down chopper. The voltage on the output side of the chopper (utility side) can be maintained constant by pulse width modulation of the chopper. Hence, the inverter bridge can be maintained at its minimum extinction angle over a wide variation in generator speed. Step up chopper arrangements are also possible in which the varying generator DC voltage is increased through the chopper to a higher constant level. Again current in the utility side inverter flows in 120° blocks. Filtering requirements can again be relaxed by resorting to more complex converter configurations (Fig. 2).

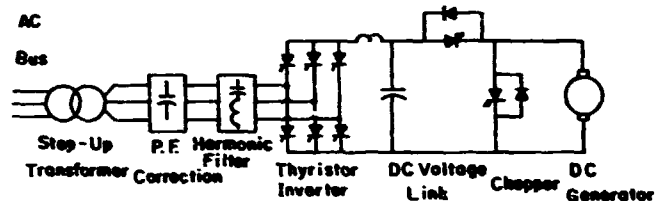


Fig. 10 DC Generator with 2 Quadrant DC/DC Step Up Chopper.

Induction Generator with DC Voltage Link

An AC alternative the chopper/DC generator is the DC voltage link system of Fig. 11 utilizing a PWM inverter together with a squirrel cage type induction generator. Again, the DC link voltage can be maintained constant by pulse width modulation of the machine side converter. Because such an induction generator requires lagging VARs, the converter must be force commutated. The utility side converter can again be controlled for best power factor operation (minimum extinction angle) necessitating only a minimal amount of power factor correction. The above comments concerning filtering again apply.

Operation of the machine side converter in the "six step" mode is again possible. However, since the level of excitation of a squirrel cage machine cannot be controlled by independent means as for the other machine types the DC link voltage will necessarily change in direct proportion to frequency. Since the DC link voltage cannot be maintained as constant, the utility side inverter control angle must be adjusted continuously so accommodate this variation. Hence, the power factor of the converter can not be kept constant but changes with control angle

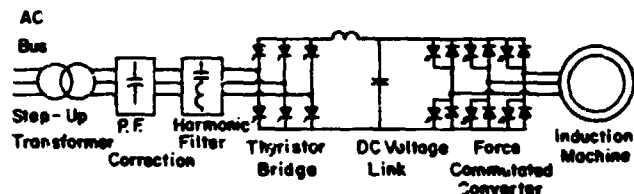


Fig. 11 Induction Generator with DC Voltage Link and AC/DC/AC Conversion

Induction Generator with DC Current Link

Another induction generator alternative incorporates the use of a DC current link rather than a voltage link. However, since excitation of the generator must again be provided by the machine side converter, forced commutation is needed. Figure 12 shows such a configuration utilizing an auto-sequential type of commutation scheme (ASC inverter). One problem which appears to be inherent in the operation of this system is that the DC side voltage varies widely with load and approaches zero when the machine is unloaded. As a result, the line side converter control angle varies widely resulting in a difficult power factor correction problem on the utility side of the converter.

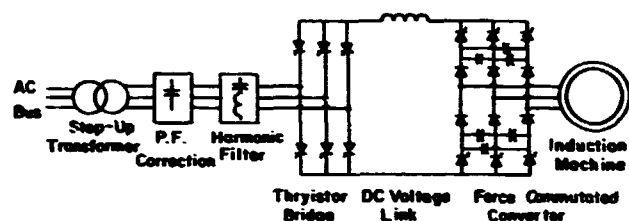


Fig. 12 Induction Generator with DC Current Link and AC/DC/AC Conversion.

Induction Generator with Cycloconverter

The cycloconverter forms the third class of converter which has been discussed and, indeed, as was the case for doubly fed induction generator and synchronous generators, this type of converter can also be utilized with a squirrel cage type of induction generator. However, in this case the generator frequency must be kept at a fraction of line frequency (60 Hz). VARs must be supplied both to commutate the cycloconverter and magnetize the induction generator and the numerous disadvantages appear to outweigh the benefits in this application.

Induction Generator with High Frequency Link Converter

One type of converter which has not been discussed heretofore is the high frequency link type of converter, as shown in idealized form in Fig. 13. In essence, this type of converter is a double ended cycloconverter which utilizes resonant type of commutation to step up the input frequency to a large value (10 KHz or more). Another cycloconverter is used to then reduce the link frequency power to a low value (for example 60 Hz). Numerous types of high frequency links have been proposed [2,3]. Such converters are in a less developed stage than other circuits and many important questions need to be resolved. For example, it is not known definitively whether excitation of a squirrel cage induction generator is possible with such a converter without power factor correcting capacitors. The questions concerning power factor and the degree of harmonic filtering needed to interface with a utility system have yet to be addressed. One major disadvantage of such schemes is the high device count which can number 72 thyristors or more, prompting questions concerning reliability. The inherent advantage of these circuits, namely low weight and compactness do not appear to be relevant in a WTG application.

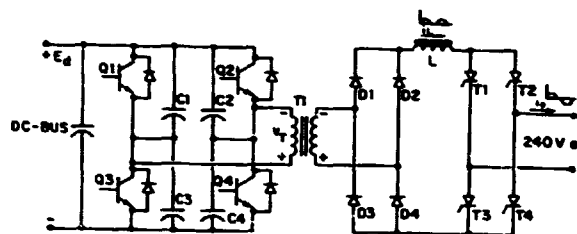


Fig. 13 High Frequency Link Self-Commutated Inverter (One Phase).

Permanent Magnet Generator Configurations

When ratings reach 10-20 Kw and less, the complexity of the choices for variable speed operation again becomes enlarged. In particular, such application ratings become amenable to the use of permanent magnet generators. Dual systems to those discussed for synchronous and induction generators (Figs. 4 and 11-13) become potential candidates to be examined. The key difference between permanent magnet generators and more conventional synchronous generators is the lack of an independently controllable excitation winding. Hence, the generator terminal voltage varies with speed necessitating control of the line side converter. As a result, power factor will change under varying load conditions.

CONCLUSION

The electrical systems options for variable speed operation of a wind turbine generator are extensive and may even be increasing as a result of emerging high power transistors and GTOs. This paper has presented a summary of the technology options and trade-offs between alternatives for variable speed electrical generating systems as applied to a wind turbine generator. The paper should help clarify some of the major issues involved in this application and assist in the selection of the proper technology.

REFERENCES

1. T.A. Lipo, "Analysis and Control of Torque Pulsations in Current Fed Induction Motor Drives", *Electric Machines and Electromechanics*, Vol. 3, April-June 1979, pp. 357-368.
2. P.M. Espelage and B.K. Bose, "High-Frequency Link Power Conversion", *IEEE Trans. on Industry Applications*, Vol. IA-13, No. 5, Sept./Oct. 1977, pp. 387-394.
3. F. Schwartz, "A Doublesided Cycloconverter", *IEEE Trans. on Industrial Electronics and Control Instrumentation*, Vol. IECI-28, No. 4, November 1981, pp. 282-291.

VARIABLE SPEED GENERATOR APPLICATION ON THE MOD-5A
7.3 MW WIND TURBINE GENERATOR

Robert S. B. ton

General Electric Company, AEPD
King of Prussia, Pa., 19406

DOE/NASA Horizontal-Axis Wind Turbine Technology
Workshop, May 8-10, 1984, Cleveland, Ohio.

ABSTRACT

This paper describes the application of a Scherbiustat type variable speed subsystem in the MOD-5A Wind Turbine Generator. As designed by General Electric Company, Advanced Energy Programs Department, under contract DEN 3-153 with NASA Lewis Research Center and DOE, the MOD-5A utilizes the subsystem for both starting assistance in a motoring mode and generation in a controlled airgap torque mode. Reactive power control is also provided. The Scherbiustat type arrangement of a wound rotor machine with a cycloconverter in the rotor circuit was selected after an evaluation of variable speed technologies that followed a system evaluation of drivetrain cost and risk. The paper describes the evaluation factors considered, the results of the evaluations and summarizes operating strategy and performance simulations.

INTRODUCTION

The MOD-5A Wind Turbine Generator design program was started in July, 1980. After conceptual design and preliminary design phases were completed, the MOD-5A configuration was rated at 7300 KW and featured a synchronous generator and two-speed rotor operation through a shiftable gearbox. The gearbox also provided drivetrain dynamics control through torsion bar springs and dampers as described in Reference 1.

When final design and procurement started, it was found desirable to minimize the gearbox complexity and to provide a drivetrain back-torque during controlled shutdowns. The latter reduced cyclic loads that were design drivers for the aerodynamic partial span control. A variable speed generator subsystem was selected to meet these needs. The partial span control was subsequently replaced with an aileron control, and the variable speed generator subsystem provides startup assistance by motoring the rotor.

The MOD-5A design was performed under Contract DEN 3-153 for NASA Lewis Research Center and DOE by General Electric Company, Advanced Energy Programs Department.

MOD-5A SYSTEM

The MOD-5A model 304.2 system is shown in Figure 1. A static Scherbiustat or Scherbiustat type variable speed generator subsystem is used. This arrangement can motor the blades up to above 3 rpm and is capable of generating with rotor speeds from 12 to 17.5 rpm.

System requirements for the subsystem were:

1. Reduce gearbox complexity by providing drivetrain stiffness and damping control.
2. Reduce aerodynamic shutdown loads by providing drivetrain back torque down to 12 rpm.
3. Motor high inertia rotor to above 3 rpm to assist aileron rotor starting.
4. Improve energy capture by changing speed ranges while delivering power.
5. Operate over a range from 67% to 100% of maximum speed while generating (system frequencies prevent using a larger range).
6. Regulate airgap torque in response to a system reference. This is used to control system speed, control drivetrain dynamics, and limit maximum torque.
7. Regulate reactive power or voltage

The major components of the variable speed subsystem are located as shown in Figure 2.

CONFIGURATION

The four methods shown in Figure 3 were initially considered to provide variable speed capability. The mechanical Scherbiustat system would drive the ring gear of a planetary gear stage using an induction motor variable speed drive. The static Kramer system is limited to speeds above the synchronous speed of the machinery and, therefore, requires a higher rated overspeed and higher converter power for the speed range. A study of A-C drive technology (Reference 2), was reviewed and applications of variable speed to wind generation (References 3 through 6) were considered. Either a Scherbiustat or a Load Commutated Inverter (LCI) type drive system, operated as a generator would meet the system requirements and were studied further.

EVALUATION

A variable speed subsystem specification was prepared and quotations were obtained to assist in the evaluation. Specification functional topics are shown in Table 1. Major generator requirements are shown in Table 2. Quotations were received from two GE components and from Siemens-Allis.

Both LCI and Scherbiustat arrangements met the system requirements. The GE LCI has an advanced digital control design and a market position in drive applications. A lower recurring cost is offered by the Scherbiustat due to a lower converter rating. Utility interface compatibility and preferences are still open issues. A Scherbiustat variable speed subsystem was selected for the MOD-5A model 304.2 design on subsystem cost.

LCI CONFIGURATION

The main LCI configuration used in the evaluation was based on a GE Drive Systems Department 10,000 hp drive. Arranged as shown in Figure 4, the major components of the LCI are a 4160 V salient pole machine and a dual channel rectifier-inverter. The arrangement, described in Reference 7, is capable of continuous speed variation from zero to maximum speed. A digital control is used and fault recovery logic is implemented in the converter firing control. Reactive power or voltage control is not used for drive applications and would require a small change to the control.

Each channel of the converter is a half-rated 6 pulse bidirectional rectifier-inverter. Dual machine windings and transformer connections provide the equivalent of 12 pulse performance with respect to harmonics. A wound stator type brushless exciter on the machine provides zero speed field control. The individual cells of each channel are shown in Figure 5 with some of the system features. Each bridge leg has 6 cells, but can operate with 5 cells, so a single shorted cell does not force an outage. A costly 4 KV fuse is avoided by providing sufficient leg impedance to limit fault currents to reasonable levels until the main circuit breaker operates to clear the fault.

Primary protection and switching are provided by a utility voltage level circuit breaker. Harmonic filters and power factor correction capacitance are also provided at the utility voltage. The capacitance compensates for the inverter stage reactive power demand. Control of the inverter firing angle permits operation over the full power range with a utility power factor near unity. In the generating mode, the converter operates as a line commutated device. When motoring for startup, the machine "load" provides commutation with field control.

SCHERBIUSTAT CONFIGURATION

The Scherbiustat circuit is shown in Figure 6. This also has a simplified one-line diagram of the Hawaiian Electric Company (HECO) distribution system at Kahuku on the island of Oahu where a MOD-5A installation was planned. The arrangement is similar to the GE supplied 15,000 hp drive used on the Princeton, N. J. pulse power generator described in Reference 8. A Canadian General Electric unit was used for evaluation. A wound rotor or doubly-fed machine is connected to the grid directly at the stator and through a cycloconverter at the rotor. Cycloconverters have been used for full power speed control of machines as described in Reference 9 and the Scherbiustat arrangement is an active research topic for wind turbine and other applications.

Three 4 KV circuit breakers are used to protect the cycloconverter (52-1), connect the stator to the grid (52-2), and short circuit the stator for starting (52-3). The cycloconverter rating of 1500 KVA provides for generator operation from 12 rpm to 17.5 rpm at the wind rotor and for motoring to 3+ rpm.

The cycloconverter is arranged as three standard 6-pulse reversing DC drives, as shown in Figure 7. With a machine turns ratio of near 1:1, the input voltage to the cycloconverter at maximum slip permits use of a single series cell with fuse protection. A completely redundant cell arrangement was used to provide ride-through capability in the event of a cell failure, similar to the LCI capability. A multiple winding, balanced impedance transformer is used to isolate the cycloconverter bridges and both sum and step-up their output to 4160 V. Power factor correction capacitance and harmonic filters are connected at the 4160 V bus. A hybrid control, the GE Directomatic II, was planned for the initial unit. The operating range of the Scherbiustat arrangement is shown in Figure 8. Machine stator power is available up to the 6500 KVA stator thermal rating. Through the cycloconverter power is supplied to the rotor below synchronous speed and extracted from the rotor above synchronous speed. The planned speed-torque control characteristic is also shown in high and low ranges. Control characteristic is determined by the wind turbine generator controller and would be the same for either a Scherbiustat or an LCI variable speed subsystem.

COMPARISON

Performance comparisons of the two subsystem arrangements were made and relative weighing factors were applied to the system criteria as shown in Table 3. Emphasis was placed on prototype unit performance, as well as volume production characteristics. The cost and performance comparisons were made at the full subsystem level, including utility voltage step-up level, housing of converter equipment, cable sizes, switchgear, and annual maintenance. For example, the time and cost to periodically clean the brush rigging compartment and replace brushes was included for the Scherbiustat arrangement. The evaluation details are not described in this paper.

An electrical-slanted comparison is shown in Table 4. This ranks the two configurations very close together.

Harmonic content is an issue for utility acceptance of static power converters, as used in both arrangements. IEEE Guide 519 (Reference 10) is generally used to establish harmonic control and reactive compensation levels, subject to utility requirements. These guidelines, along with the planned HECO/GE conditions are shown in Table 5.

As the LCI produces 12 pulse harmonic currents and is effectively DC fed, the filtering design necessary to provide a smooth output is not complex, but the filters have to contend with full power harmonic amplitudes. The Scherbiustat, with a 6 pulse cycloconverter, produces higher amplitude, more complex harmonics that vary with slip frequency, but only with 20% of the system output. An unfiltered, simplified analysis is shown in Figure 9, based on

Reference 11. The total output waveform distortion is about 5% prior to filtering. A complete site specific harmonic analysis was planned for MOD-5A.

Summarizing again, the overall evaluation determined that both subsystem arrangements met the requirements. While the LCI had more flexibility and was rated slightly higher than the Scherbiustat, it was also more costly for initial and volume production wind turbines. A Scherbiustat configuration was, therefore, selected for the MOD-5A. Utility preference was being evaluated and is still considered an open issue.

PERFORMANCE

A simulation model of the MOD-5A is shown in Figure 10. The important drivetrain and tower bending modes are included. Both simple and complex converter and generator models were developed. The simple model does not include the electrical dynamics, while the complex model does, and permits analysis of the quadrature real and reactive power regulator circuits that drive the cycloconverter firing control.

Gust performance of the simplified model is illustrated in Figures 11 and 12. The basic gust is a 12 second period, 9 mph, sinusoidal shape departing from an average 45 mph wind. A turbulent harmonic wind is added in Figure 12, in accordance with the NASA interim turbulence definition. Trade winds are not expected to be as turbulent as the NASA definition.

The generator torque level is clamped at just above rating by the control logic as shown in Figure 11, set b. Total output increases slightly above the clamp plateau as the generator speed continues to increase. The aileron aerodynamic control slowly operates to reduce the gust torque. The gust ends and the system speed and power slightly undershoots the initial conditions with a smooth well-behaved return in about a minute. The gust is modeled as fully immersing the rotor, which is a more severe than could occur in the field.

The effect of wind turbulence is shown in Figure 12. A steady oscillation of system speed and output power of about 10% peak to peak is predicted. This could be reduced by decreasing the slope of the speed-torque control characteristic.

CONCLUSIONS

A variable speed generator provides several benefits for the MOD-5A;

1. Back torque for shutdown assistance
2. Control of drivetrain dynamics
3. Starting assistance in low winds
4. Operating speed flexibility
5. Reactive power control

Either an LCI or a Scherbiustat variable speed subsystem will meet the MOD-5A technical requirements. A Scherbiustat was selected on cost. Utility preference and site specific analysis issues remain open.

ACKNOWLEDGEMENTS

The author gratefully appreciates the support and review provided by Len Gilbert, Frank Brady, and Francis Rooker of NASA and the technical support supplied by Mal Horton and Chuck Mayer of GE.

REFERENCES

1. Barton, R.S., Lucas, W.C. "Conceptual Design of the 6 MW MOD-5A Wind Turbine Generator", Proceedings of the Fifth Biennial Wind Energy Conference and Workshop, SERI/CP-635-1340, Vol 1, pp. 157-168, October 1981.
2. Bose, B.K., A Review of AC Drives Technology, TIS 81CRD127, GE, Schenectady, N.Y., June 1981 (good bibliography).
3. Lipo, T.A., Investigation of Variable Speed for Wind Turbine Power Generation, ECE-81-9, Department of Electrical and Computer Engineering, University of Wisconsin-Madison, August 1981.
4. Anderson, T.S., Hughes, P.S., Kirschbaum, H.S., Mutone, G.A., "Multiple and Variable Speed Electrical Generator Systems for Large Wind Turbines", Proceedings of Workshop held in Cleveland, Ohio, July 28-30, 1981, NASA Conference Publication 2230, DOE CONF-810752, SERI/CP-635-1273, pp. 125-138.
5. Douglas, R.R., "Conceptual Design of the 7 MW MOD-5B Wind Turbine Generator", Proceedings of the Fifth Biennial Wind Energy Conference and Workshop, SERI/CP-635-1340, Vol 1, pp. 169-182, October 1981.
6. Schwerchardt, H., Suchanek, V. "Converter-Fed Synchronous Generator Systems for Wind Power Plants", Crown-Boveri Review, Volume 69, pp. 57-64, Baden, Switzerland, March 1982.
7. Appiaris, J.C., Urano, A.S., System Benefits and Considerations when Using AC Adjustable Frequency Drives in Generating Stations, Presented at American Power Conference, Chicago, Illinois, April 27-29, 1981.
8. Mayer, C.B., "High Response Control of Stator Watts and Vars for Large Wound Rotor Induction Motor Adjustable Speed Drives", IEEE Transactions IAS79:27F, pp. 817-823.
9. Allen, J.A., Myeth, W.A., Herzog, G.W., Young, J.A.I., "Electrical Aspects of the 8750 hp Gearless Ball-Mill Drive at St. Lawrence Cement Company", IEEE Transactions on Industry Applications VOL IA-11 No. 6 pp. 681-687, Nov/Dec 1975.
10. Guide for Harmonic Control and Reactive Compensation of Static Power Converters, IEEE 519, July 1979.
11. Pelly, B.R., Thyristor Phase-Controlled Converters and Cycloconverters, Wiley-Interscience, 1971.

Table 1- Variable Speed Subsystem Requirements

- 3.1 Subsystem Definition**
 - 3.1.1 General Description**
 - 3.1.2 Subsystem Configuration**
 - 3.1.3 Interface Definition**
 - 3.1.3.1 Generator Mechanical Interfaces**
 - 3.1.3.2 Generator Electrical Interfaces**
 - 3.1.3.3 Converter Mechanical Interfaces**
 - 3.1.3.4 Converter Electrical Interfaces**
 - 3.1.4 Operational Description**
 - 3.1.4.1 Duty Cycle Description**
 - 3.1.4.2 Operational Power - Power Description**
- 3.2 Characteristics**
 - 3.2.1 Generator**
 - 3.2.1.1 Generator Characteristics**
 - 3.2.1.2 Generator Parameters**
 - 3.2.1.3 Generator Environmental Conditions**
 - 3.2.2 Converter**
 - 3.2.2.1 Characteristics**
 - 3.2.2.2 Converter Parameters**
 - 3.2.2.3 Converter Environmental Conditions**
 - 3.2.2.4 Converter Control**
 - 3.2.2.4.1 General**
 - 3.2.2.4.2 Control Modes**
 - 3.2.2.4.2.1 Initialization**
 - 3.2.2.4.2.2 Motoring**
 - 3.2.2.4.2.3 Synchronization**
 - 3.2.2.4.2.4 Torque Regulation**
 - 3.2.2.4.2.5 Reactive Power Regulation**
 - 3.2.2.4.2.6 Shutdown**
 - 3.2.2.4.2.7 Fault Monitoring**

Table 2- Generator Requirement Summary

- **5000/7500 KW @ 960/1440 RPM**
- **38,500 FT-LB AIR GAP TORQUE**
- **CLASS F INSULATION (105°C OVER 40°C)**
- **4160 V_{L-L} - EXTERNAL WYE**
- **7° INCLINATION**
- **SELF LUBE JOURNAL BEARINGS WITH PROVISION FOR EXTERNAL FLOOD LUB.**
- **MOTOR 0 TO 300 RPM/GENERATE 960 TO 1440 RPM - 1700 RPM; MECH OVERSPEED**
- **LOSSES 100 KW/300 KW @ NL/FL**
- **OPERATING TEMP - -20 TO + 40°C**
- **NON OPERATING TEMP - -40 TO + 50°C**
- **3300 FT ELEV / 7000 FT ELEV WITH DERATING**
- **SALT AIR**

Table 3- Evaluation Criteria And Weight

<u>CRITERION</u>	<u>WEIGHTING</u>
1. <u>Compatibility</u> - With Wind Turbine application and control system.	High (20%)
2. <u>Quality of Power Output</u> - Risk or degree of margin in meeting power quality requirements.	High (15%)
3. <u>Reliability</u> - Potential impact on WTG availability including effect of single failure modes.	High (15%)
4. <u>Product Maturity/Prototype Risk</u> - Confidence that system will work and perform as advertised on Prototype.	High (15%)
5. <u>Maintainability</u> - Ease of maintenance and trouble shooting.	Med. (10%)
6. <u>Customer Technology Acceptance</u> - Preferences/biases of utility customers.	Med. (10%)
7. <u>Life</u> - Probability of 30 year life.	Med. (10%)
8. <u>Schedule</u> - Prototype delivery schedule	Low (5%)
	100%

Table 4- Evaluation Comparison

COMPARISON OF LCI/SYNCHRONOUS MACHINE WITH CYCLOCONVERTER/ROUND ROTOR INDUCTION MACHINE (1 = POOR, 3 = AVERAGE, 5 = OUTSTANDING)

	(1) CYCLO/INDUC.	(2) LCI/SYNCH.	COMMENT
PERFORMANCE UNDER SINGLE PHASE FAULTS	3	5	1
PERFORMANCE UNDER THREE PHASE FAULTS	5	5	2
PERFORMANCE UNDER LINE SURGES	5	3	3
CONTROL RESPONSE	5	3	4
STARTING PERFORMANCE AS MOTOR	4	3	5
POWER FACTOR CONTROL	5	4	6
TORQUE HARMONICS DURING RUNNING	3	4	7
TORQUE HARMONICS DURING STARTING	4	3	7
HARMONIC FILTER REQUIREMENTS	3	4	8
MAINTENANCE	4	5	9
CIRCUIT COMPLEXITY	3	3	
	44	42	

COMMENTS.

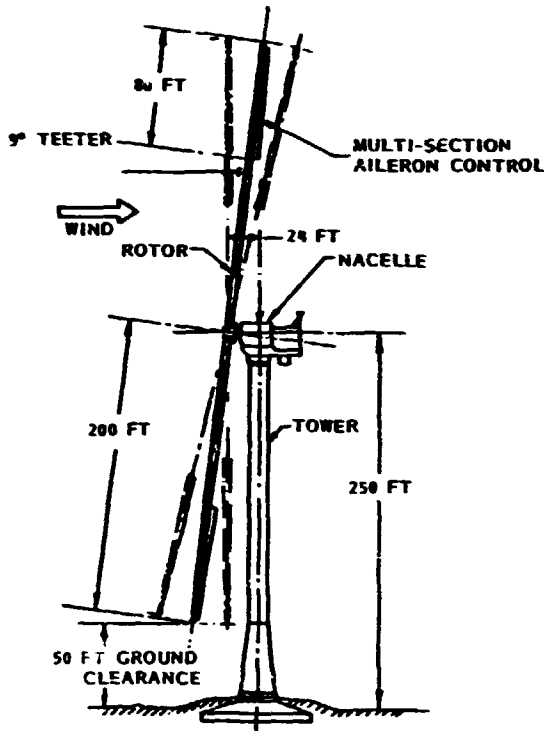
1. COULD RESULT IN DE-EXCITATION OF MACHINE IN (1)
2. BOTH CAN PROVIDE RAPID RECLOSE AFTER THREE PHASE FAULT
3. LINE SURGES COULD RESULT IN COMMUTATION FAILURES IN (2) CYCLO IS BUFFERED BY AN EXTRA TRANSFORMER
4. CURRENT IN DAMPER WINDINGS IN (2) OPPOSE RAPID CHANGES IN TORQUE WITHOUT MORE ELABORATE CONTROL SCHEMES (FIELD ORIENTED CONTROL)
5. HIGHER STARTING TORQUE AVAILABLE FROM CYCLO WHEN CONNECTED TO THE STATOR L.V. OF THE MACHINE FOR STARTING WHEN USING (1) AVAILABLE STARTING TORQUE IS PROPORTIONAL TO CYCLOCONVERTER RATING USING (2) IT DEPENDS UPON SIZE OF LINK INDUCTOR AND LIMITED TYPICALLY TO A SMALL FRACTION OF RATED TORQUE (ABOUT 0.1 PU)
6. POWER FACTOR CONTROL IS INHERENT IN THE CONTROL OF THE CYCLO POWER FACTOR CONTROL WITH (2) COMES WITH CAREFUL PHASE SHIFTING OF THE UTILITY SIDE BRIDGE IN CONJUNCTION WITH A BANK OF CAPACITORS (NOT NEEDED IN (1))
7. TORQUE HARMONICS OF (1) ARE MORE SEVERE DURING RUNNING IN THAT THEY TEND TO BE MORE RANDOM AND THEREFORE LESS PREDICTABLE TORQUE HARMONICS OF (2) ARE MORE SEVERE DURING STARTING DUE TO THE MODULATION OF THE DC LINK CURRENT TO ACHIEVE COMMUTATION OF THE MACHINE SIDE BRIDGE AT LOW ROTATIONAL SPEED
8. HARMONIC FILTERING IS MORE DIFFICULT WITH (1) DUE TO THE MORE RAND NATURE OF THE HARMONICS
9. MAINTENANCE IS A SMALL BUT NOTEWORTHY PROBLEM WITH (1)

Table 5- Power Quality

HECO/GE
(UNDER MEASUREMENT
CONDITIONS MUTUALLY
AGREED TO BY GE & HECO)

IEEE 519
(GUIDELINES)

VOLTAGE	- 46KV ±5% 3φ, 60 HZ
SUPERIMPOSED VOLTAGE	- NOT TO EXCEED 2V ON 115V SYSTEM
FREQUENCY	- ± 0.1 HZ NORMAL ± 0.4 HZ ABNORMAL 3 PER DAY
LINE NOTCHING	- 17500 VμS 5% D.F.
HARMONICS	- FILTER TO < 5% (46KV)
TELEPHONE (TIF)	- 1" T COORDINATION WITH TELEPHONE COMPANY
FLICKER	- FIX IF OCCURS
PF CORRECTION	- NEAR 1.0 PF, VAR REGULATE WITH FILTER, PF CAPS



OPERATIONAL CHARACTERISTICS

RATED POWER	7300 KW AT 0.98PF
RATED WIND SPEED	32 MPH AT 250 FT
CUT-IN/CUT-OUT WIND SPEED	14/60 MPH AT 250 FT
MAXIMUM WIND SPEED (SURVIVAL)	130 MPH AT 250 FT
POWER CONTROL	MULTI-SECTION AILERONS
ROTOR RPM-SET SPEED	13.7/16.8 RPM (± 10%)
ENERGY CAPTURE/YR	21.3 X 10 ⁶ KWH (NASA SPECIFIED WIND SPEED DURATION CURVE, 14 MPH AT 32 FT, 100 % AVAIL)
TOTAL WT ON FOUNDATION	1800 K-LB

FEATURES

- GOOD LAMINATE BLADES WITH HIGH PERFORMANCE AIRFOIL - UPWIND, TEETERED
- NON-ROTATING ROTOR SUPPORT
- HYBRID EPICYCLIC/PARALLEL SHAFT GEARBOX
- VARIABLE SPEED/CONSTANT FREQUENCY OPERATION, WITH 2 SET POINTS
- SOFT SHELL TOWER, TUNEABLE BELL SECTION

Figure 1- MOD-5A System Model 304.2

MAJOR SUBASSEMBLIES

- GENERATOR
- YAW SLIP RING ASSEMBLY
- POWER CABLING
- CONVERTER
- SWITCHGEAR
- STEP-UP TRANSFORMER
- STATION BATTERIES

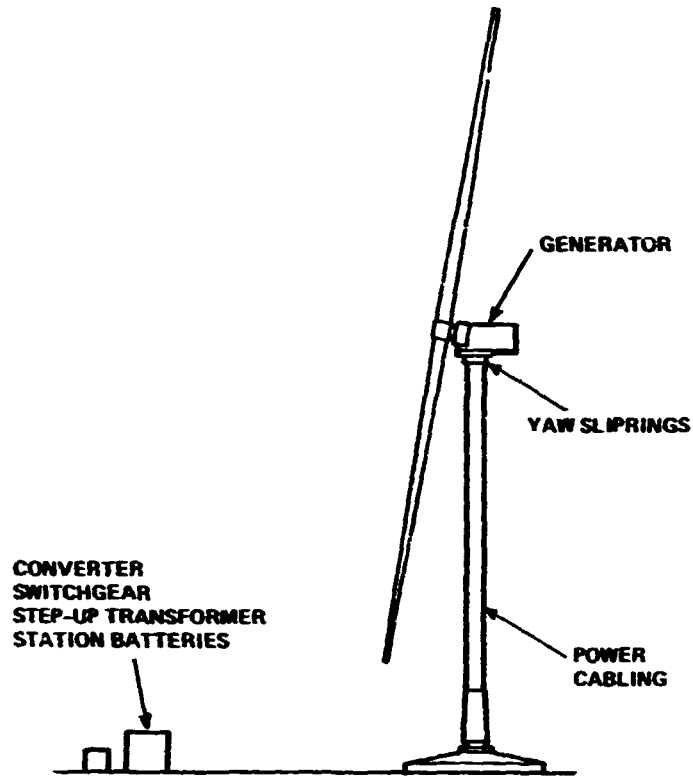


Figure 2- Generator Subsystem Equipment Locations

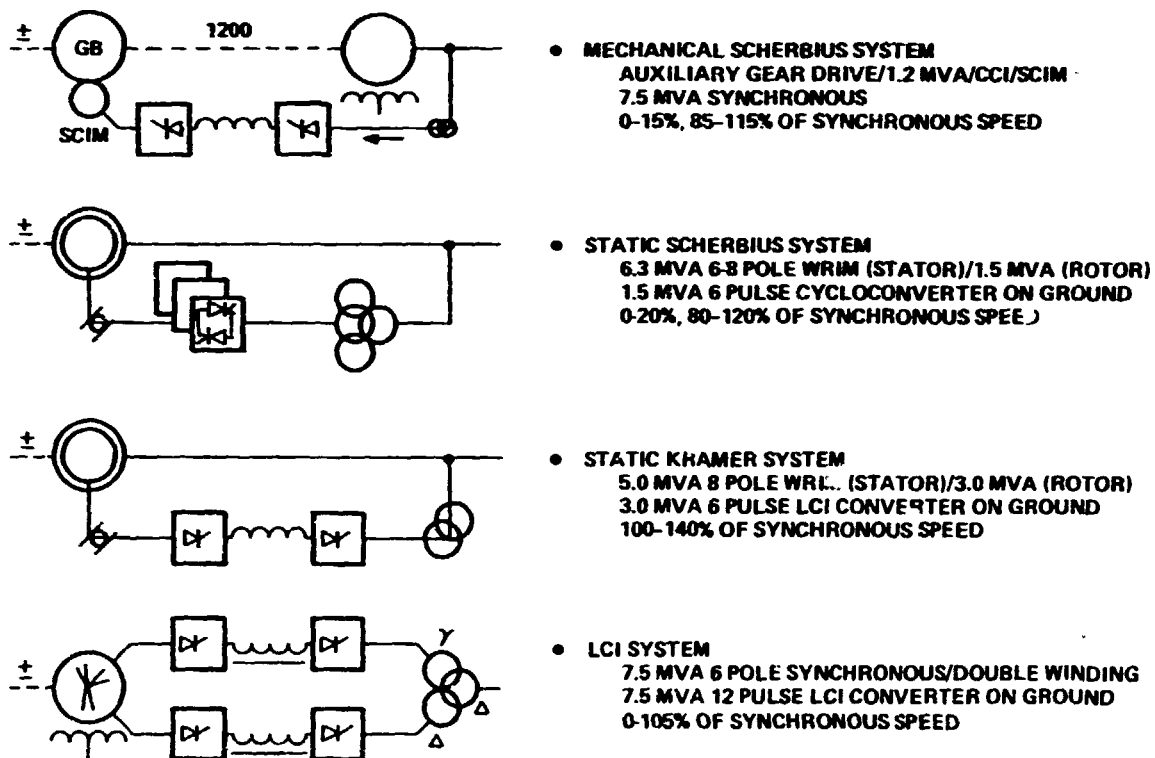


Figure 3- Variable Speed Configurations

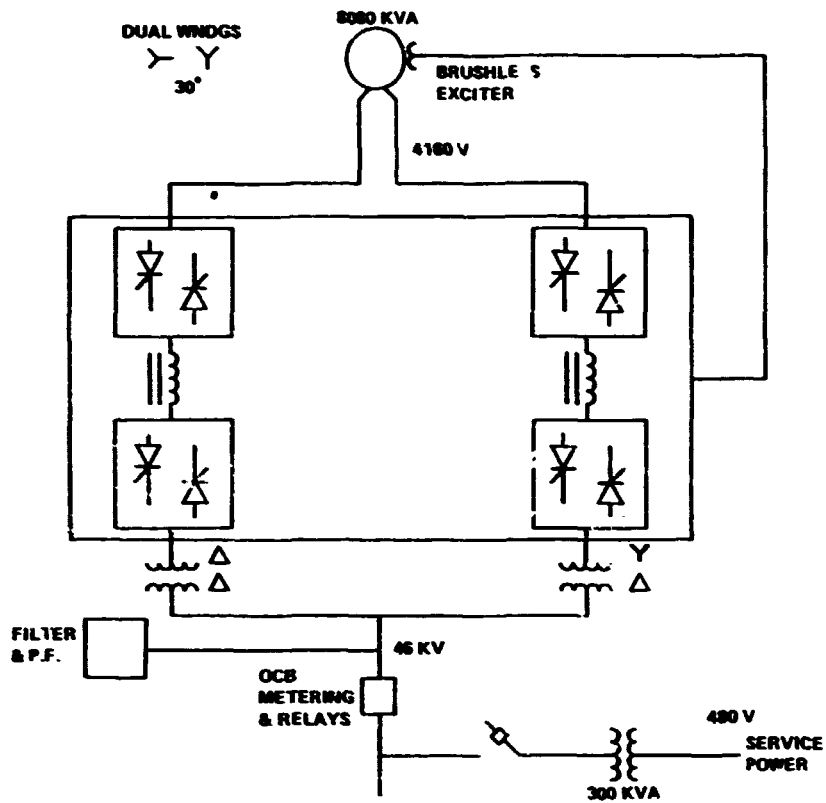
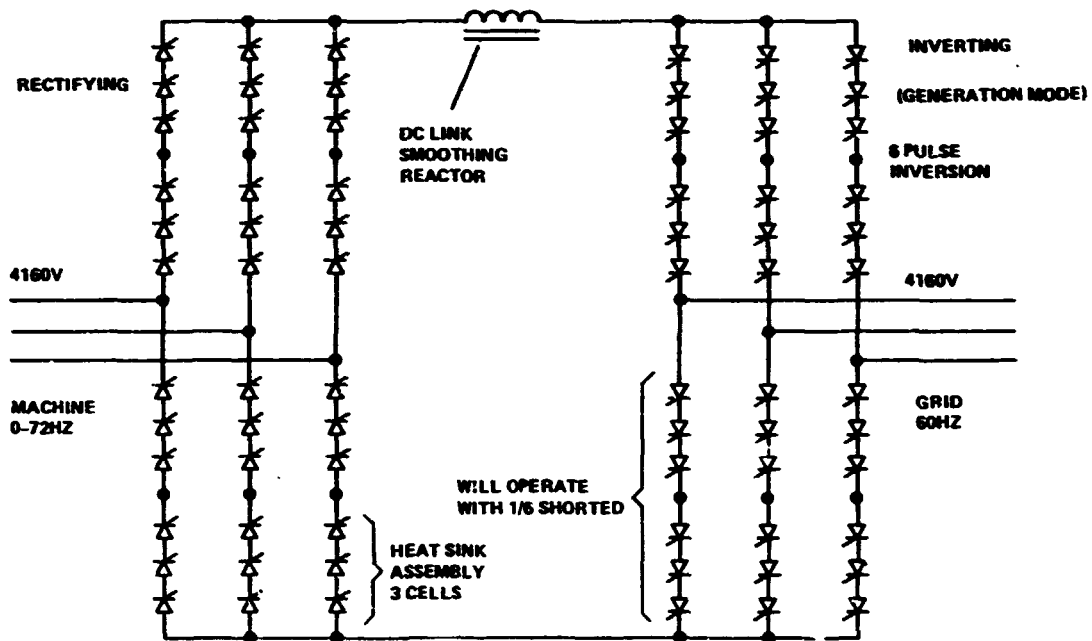


Figure 4- LCI Subsystem Arrangement



CONVERTER 4040 KVA (HALF OF LCI CONFIGURATION)

SHOWN: 24 HEAT SINK ASSEMBLIES, 72 CELLS
 TOTAL SYSTEM: 48 HEAT SINK ASMS., 144 CELLS
 FULL CONVERTER & REACTORS: 50' LONG x 5' DEEP x 7-1/2' HIGH; 20,000# APPROX
 REF: GEA 10816

Figure 5- LCI Converter Detail

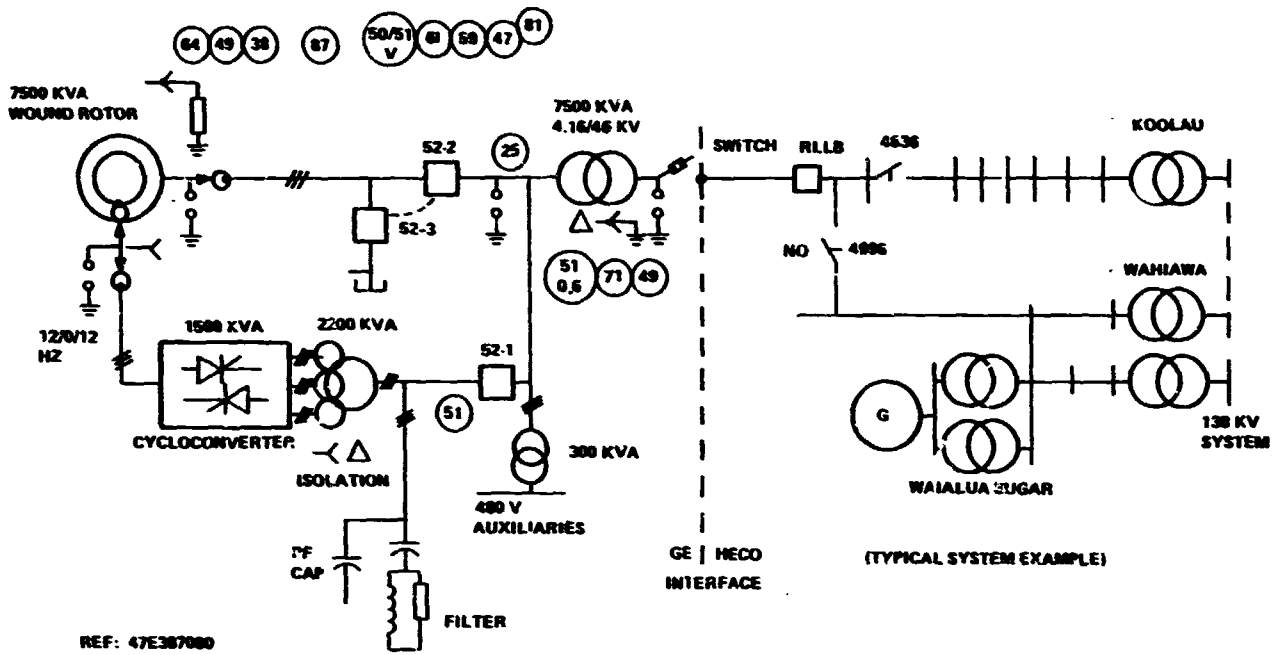


Figure 6- Scherbiustat Subsystem Arrangement

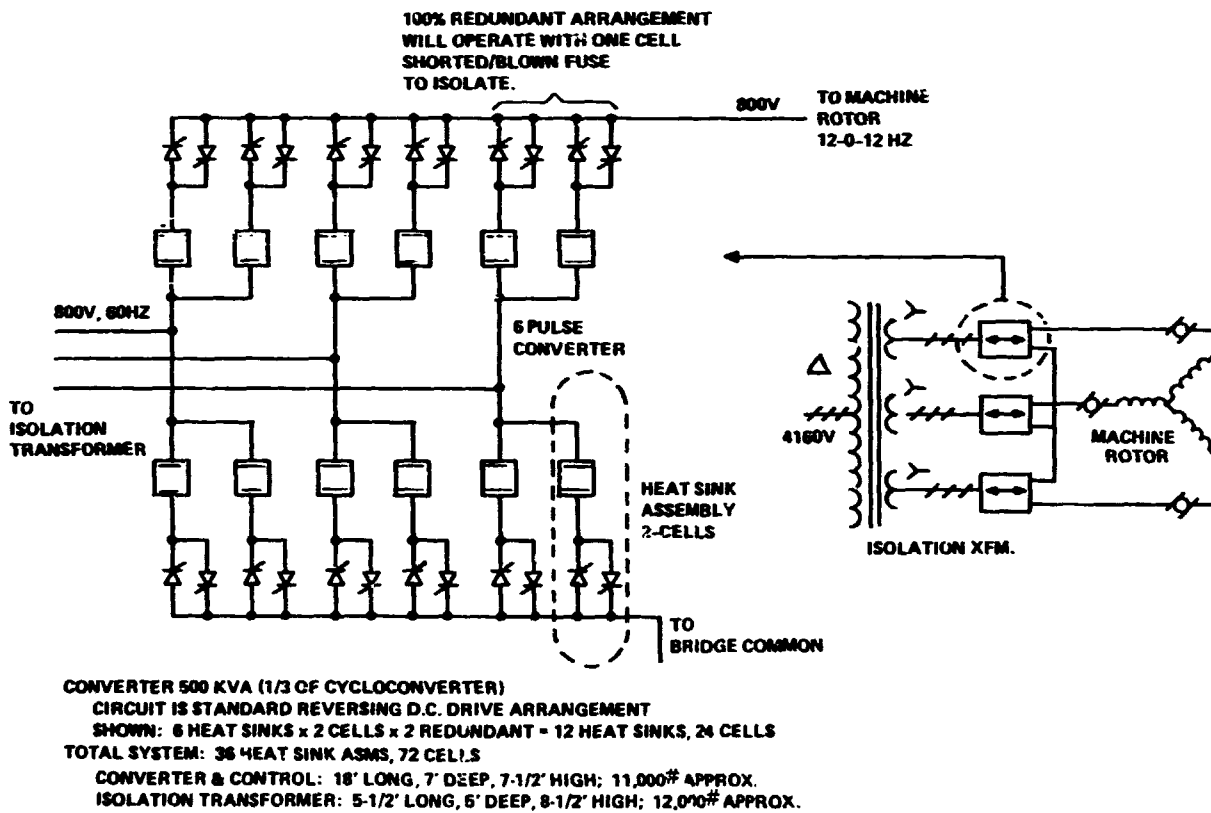


Figure 7- Scherbiustat Converter Detail

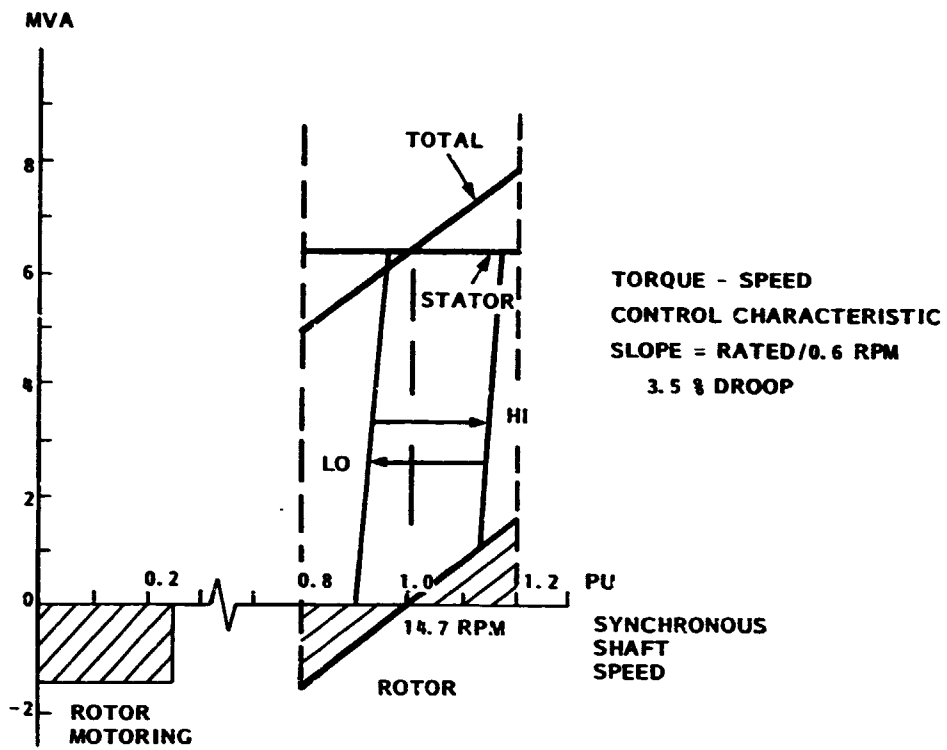


Figure 8- Generator Operating Regime

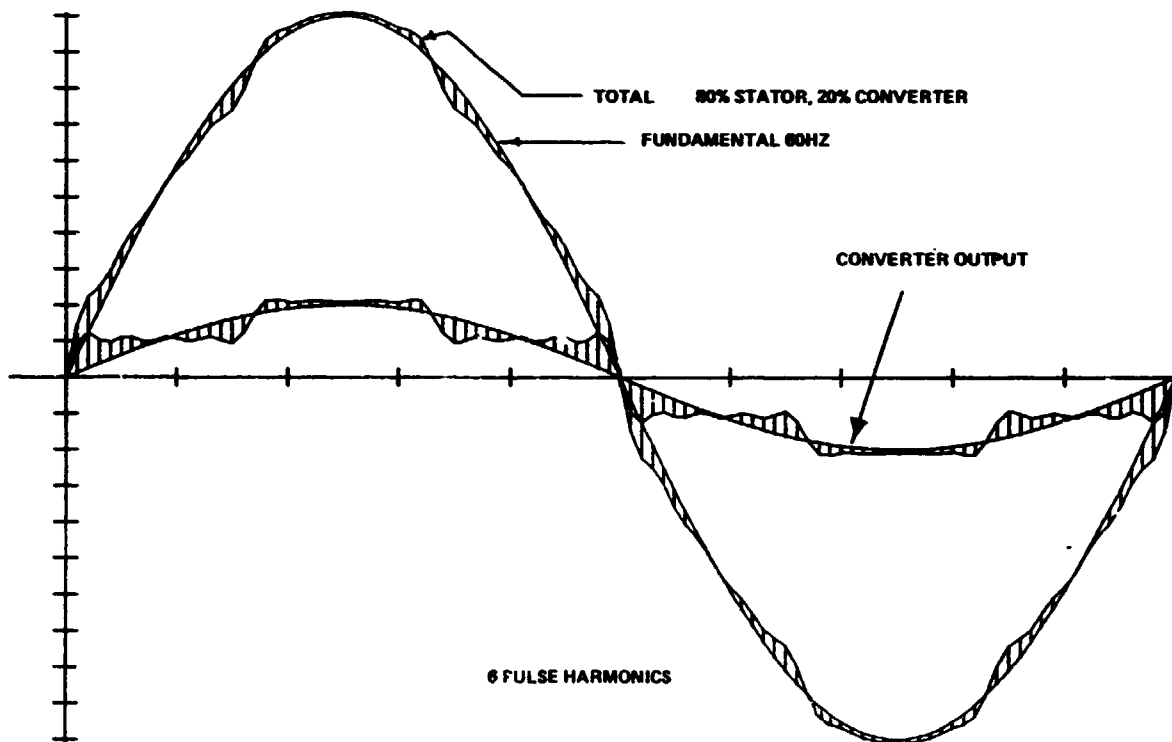
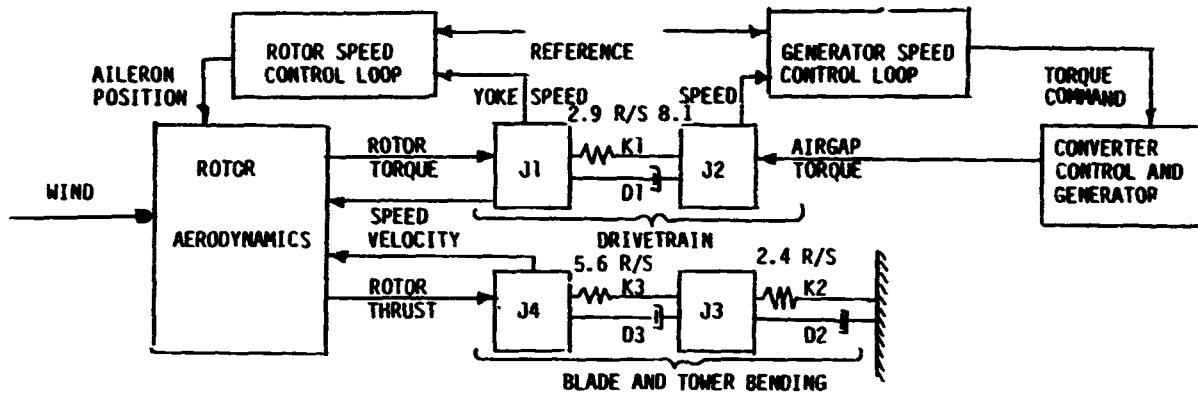


Figure 9- Harmonic Distortion



- | | |
|---|--|
| J1 - Rotor Inertia | $40 \cdot 10^6 \text{ slug-ft}^2$ |
| J2 - Generator & High Speed Shaft, Inertia reflected to Rotor | $(795:30)(82.14)^2 = 5.2 \cdot 10^6 \text{ slug-ft}^2$ |
| J3 - Tower Mass | $2.9 \cdot 10^6 \text{ slug}$ |
| J4 - Blade Flap Mass | $1.06 \cdot 10^5 \text{ slug}$ |
| K1 - Drivetrain Spring Constant | $3.30 \cdot 10^8 \text{ ft-lb/rad}$ |
| K2 - Tower Spring Constant | $1.674 \cdot 10^5 \text{ lbs/ft}$ |
| K3 - Blade Flap Spring Constant | $2.370 \cdot 10^6 \text{ lbs/ft}$ |
| D1 - Drivetrain Damping Coefficient | $3.0 \cdot 10^6 \text{ ft-lb/(rad/sec)}$ |
| D2 - Tower Damping Coefficient | $0.968 \text{ lb/(ft/sec)}$ |
| D3 - Blade Flap Damping Coefficient | 3785 lb/(ft/sec) |

Figure 10- Simulation Model Block Diagram

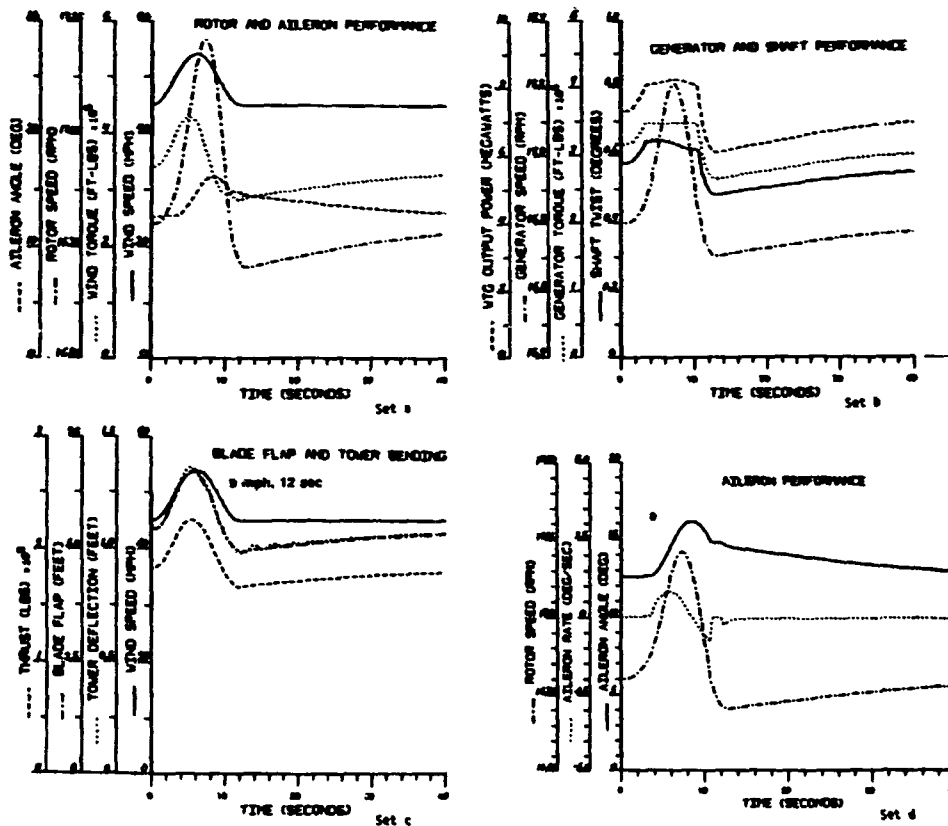


Figure 11- Response To 1-Cosine Wind Change

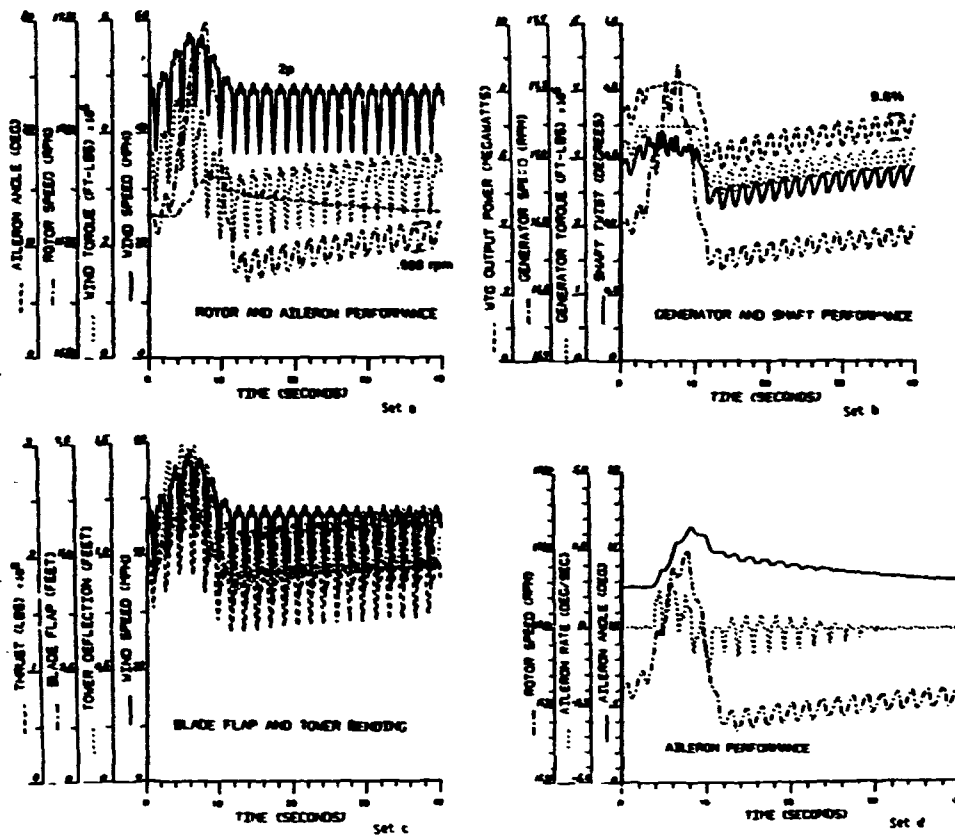


Figure 12- Response To 1-Cosine Wind Change With Turbulence

MEASUREMENT AND PREDICTION OF BROADBAND NOISE
FROM LARGE HORIZONTAL AXIS WIND
TURBINE GENERATORS

N95-27990

By

F. W. Grosveld & K. P. Shepherd, The Bionetics Corporation
 and
 H. H. Hubbard, VARC

ABSTRACT

A method is presented for predicting the broadband noise spectra of large wind turbine generators. It includes contributions from such noise sources as the inflow turbulence to the rotor, the interactions between the turbulent boundary layers on the blade surfaces with their trailing edges and the wake due to a blunt trailing edge. The method is partly empirical and is based on acoustic measurements of large wind turbines and airfoil models. Spectra are predicted for several large machines including the proposed MOD-5B. Measured data are presented for the MOD-2, the WTS-4, the MOD-OA, and the U.S. Windpower Inc. machines. Good agreement is shown between the predicted and measured far field noise spectra.

INTRODUCTION

Acoustic measurements are presented for four different horizontal axis machines and are compared with the results of an improved method of predicting broadband noise. This information is considered pertinent for the evaluation of environmental impact on communities located near wind turbine generators operated for large scale electric power generation.

The machines for which data are presented here and in References 1 through 6 are shown in the photographs of Figure 1. They consist of the MOD-2, the MOD-OA, the WTS-4 and the U.S. Windpower machine. The first three of these are government sponsored. All are self starting, have 2 or 3 blades, rotate in the range 17 to 72 rpm, and normally operate at wind speeds of 3 to 16 m/s.

Some dimensions and operational details are included in the table of Figure 2. MOD-2 is noted to be an upwind machine whereas the others are downwind machines. Rotor diameters range from 17.1 m to 91.4 m, rotor tip speeds from 66.5 to 122.4 m/s, blade areas from 15 to 236 m², and rated power outputs from 50 to 4200 kW. Calculated values are included for the proposed MOD-5B machine for which data are listed at the bottom of Figure 2.

DESIGNATION	TYPE	ROTOR DIAM, m	TIP SPEED, m/s	BLADE AREA, m ²	RATED POWER, kW
MOD-2	UPWIND	91.4	83.8	236	2500
WTS-4	DOWNWIND	78.4	122.4	195	4200
MOD-OA	DOWNWIND	38.1	80	28	200
USWP	DOWNWIND	17.1	66.5	15	50
MOD-5B	UPWIND	47.6	89.4	230	3200

Figure 2. - Dimensions and operating conditions for several large machines.

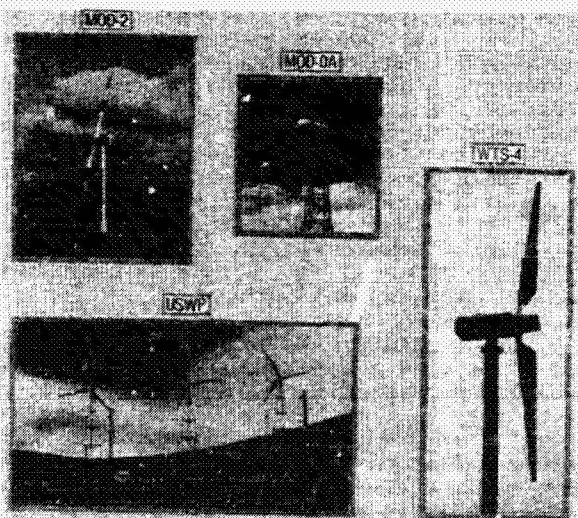


Figure 1. - Photographs of wind turbine generators for which acoustic measurements are presented.

NOISE MEASUREMENTS AND OBSERVATIONS

The machines described in Figures 1 and 2 represent wide ranges of size, output power rating and configuration. Resulting differences in their noise production are presented in Figures 3 through 8. Comparisons are made on the basis of one-third octave band spectra, narrow band spectra, dB(A) levels, and perception distances.

Effects of Size and Configuration

The one-third octave band spectra of Figure 3 were measured on axis and normalized to a distance of 100 m from each machine. Definite trends are observed. The spectra exhibit their highest levels at the low frequencies, with general reductions in level as frequency increases. Further, the machines having the highest power output also have the

highest noise levels. This latter trend is particularly evident at the low frequencies.

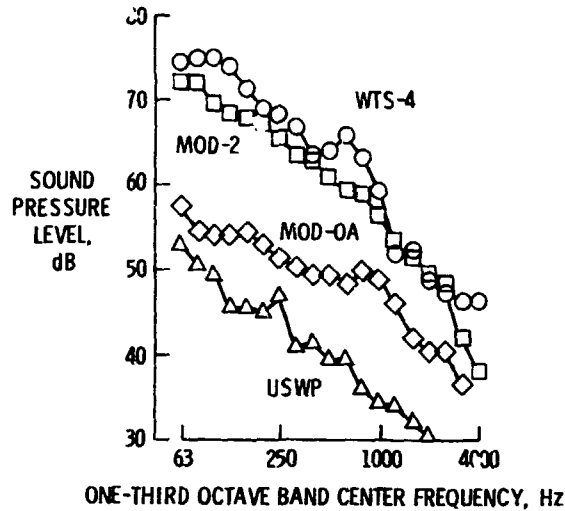


Figure 3. - Measured on-axis noise spectra at approximately rated power for four machines. (r = 100 m.)

A comparison of the narrow band noise spectra for large upwind and downwind machines is given in Figure 4. Data are narrow band ($\Delta f = 0.25$ Hz) and are limited to the frequency range below 100 Hz. The general reduction in level with frequency is seen to be about the same for both machines. The WTS-4 machine has a number of discrete peaks in its spectrum, particularly below 50 Hz. These are loading harmonics which occur at integral multiples of the blade passage frequency. Their amplitudes are enhanced because of the tower wake-blade interference encountered in this downwind configuration. In the MOD-2 spectrum only a few discrete peaks are evident and these are believed to be of electromechanical origin. No loading noise harmonics are apparent for this upwind configuration. The relatively lower levels of the MOD-2 spectrum are due in part to its lower tip speed.

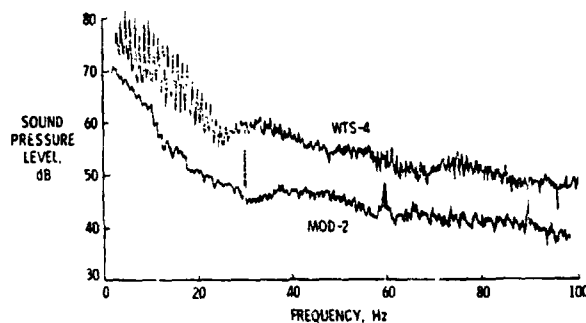


Figure 4. - Comparison of narrow band ($\Delta f = 0.25$ Hz) noise spectra at rated power, on axis, for the MOD-2 and WTS-4 machines. (r = 150 m.)

Effects of Output Power

The one-third octave band spectra of Figure 5 illustrate the differences in the noise output for the WTS-4 machine at two different power outputs. Data are for the on-axis measuring points for power outputs of 1,000 and 4,000 kW respectively. Higher levels are associated with the higher power output and are seen to occur at frequencies below about 1,000 Hz.

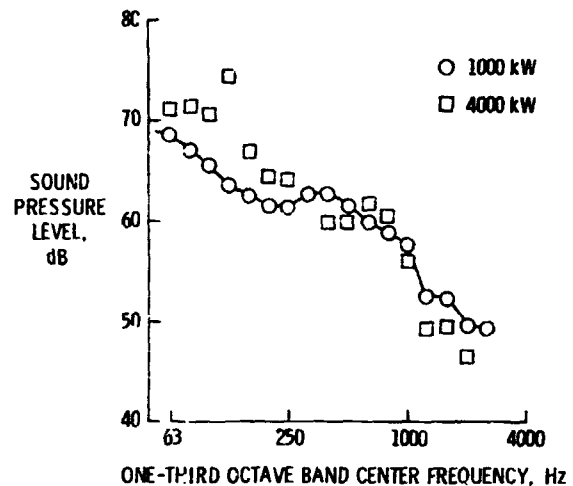


Figure 5. - Effects of power output on noise spectra measured on axis for the WTS-4 machine. (r = 150 m.)

Directivity Effects

Noise measurements for the machines of Figure 1 indicate that the noise radiation patterns are not sharply directional. At equal distances on-axis (upwind and downwind) essentially no differences are observed in either spectral shapes or sound levels. There are, however, consistent differences between measurements made on-axis and in the plane of rotation. Figure 6 shows one-third octave band spectra for the MOD-2 machine. Note that the in-plane data have relatively lower levels at low frequencies and higher levels at high frequencies than do the on-axis data. The result is a cross-over effect as seen in the figure.

Similar data are presented in Figure 7 to show a comparison between the MOD-2 and WTS-4 machines. The data points represent mean L_{eq} (dB(A)) levels for a large number of measurements for both machines. The noise radiation pattern curves in each case are estimated. The MOD-2 machine radiates essentially in a non-directional pattern. The WTS-4 radiation pattern on the other hand shows higher levels on-axis than in-plane. As suggested in Figure 6 the low frequency components are known to be relatively strong on-axis. Thus the skewness of the radiation pattern of the WTS-4 is due to the influence

of the low frequencies on the L_{eq} values.

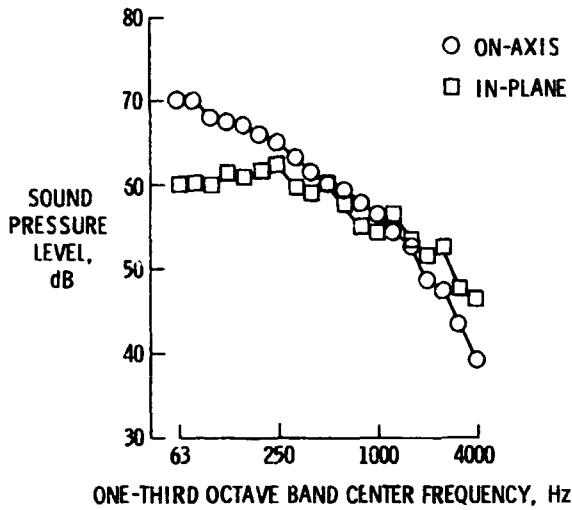


Figure 6. - Comparison of on axis and in plane noise spectra for MOD-2 machine. ($P = 2500$ kW, $r = 100$ m.)

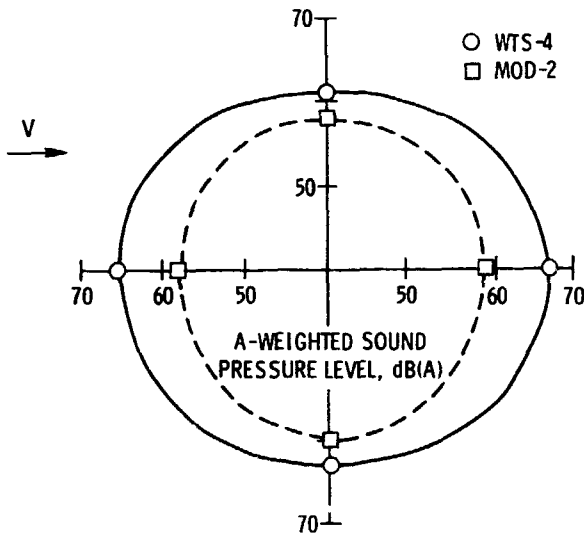


Figure 7. - Comparison of a-weighted noise radiation patterns for WTS-4 and MOD-2 machines. ($V_w = 7.6-13.4$ m/s, $r = 150$ m.)

Perception Distances

Observations of the radiated noise from a number of different machines and for a range of weather conditions have established a wind related directionality which is illustrated in Figure 8. The data points for the MOD-2 and the WTS-4 machines represent locations at which the noise during steady state operations is observable intermittently.

Note that the noise is observed at a much greater distance downwind than upwind, in spite of the fact that the noise radiation patterns of Figure 6 are nearly symmetrical. This skewness is due to refraction effects of the mean wind speed gradient, resulting in the formation of shadow zones upwind and propagation enhancement downwind. The distance from the machine to the shadow zone is dependent upon the height of the noise source above the ground surface and the wind speed gradient.

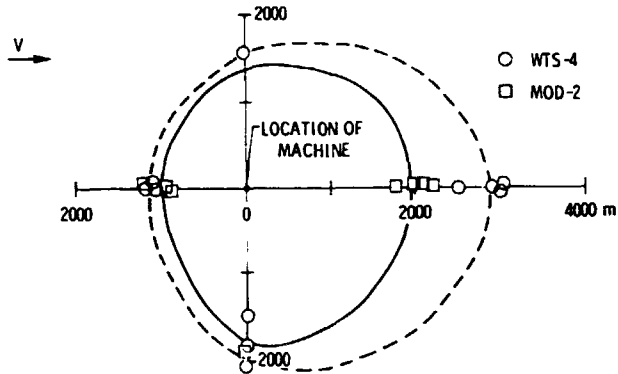


Figure 8. - Comparisons of perception distances for the WTS-4 and MOD-2 machines. ($V_w = 7.6-13.4$ m/s.)

BROADBAND NOISE PREDICTION

To adequately assess the impact of the wind turbine noise and to aid in the design and siting of machines that are acceptable to the community (Refs. 7 and 8), a thorough understanding of the underlying noise generation phenomena as well as prediction techniques are highly desirable. Current literature on wind turbine noise is limited. Most publications deal with the impulsive "thumping" noise caused by the blade cutting the wake behind its supporting tower, where the rotor is located downwind from the tower (Refs. 9-15). A prediction code for this type of noise is presented in Reference 16. Other possible sources of wind turbine noise are discussed in Reference 5 and some of these noise mechanisms are considered in References 1, 6, and 17-19. Reference 19 compares theory with experimental broadband noise data (Refs. 1 and 2) but results indicate that better prediction techniques are needed. In the next sections a broadband noise prediction scheme for horizontal axis wind turbine generators is presented.

Extensive noise measurements on current, large, horizontal axis wind turbine generators (Refs. 1-6) indicate the presence of three major aerodynamic source mechanisms of broadband noise (figure 9):

1. Loading fluctuations due to inflow turbulence interacting with the rotating blades.

2. The turbulent boundary layer flow over the airfoil surface interacting with the blade trailing edge.

3. Vortex shedding due to trailing edge bluntness.

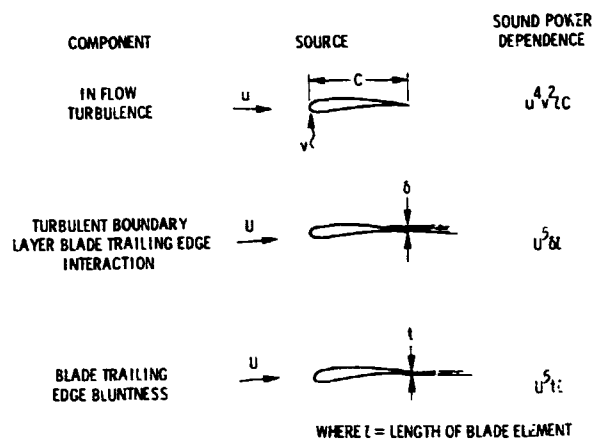


Figure 9. - Components of wind turbine broad band noise.

In contrast to the limited literature on wind turbine noise, the list of publications dealing with helicopter rotor noise is quite extensive. Although the concept of extracting energy from the flow by a wind turbine rotor is opposite of that of a helicopter rotor, which provides energy to the flow, the noise generating mechanisms show many similarities and an analogy between the two concepts is justified.

Inflow Turbulence

When the wind turbine rotor blades move through the turbulent air they encounter atmospheric inhomogeneities causing effective angle of attack changes which result in unsteady airfoil loading. This fluctuating force mechanism is a well known source for airfoil and helicopter rotor noise as described in References 19 and 20-42. To enable utilization of theoretical analyses from the literature for turbulent inflow source mechanisms applicable to helicopter rotors the contrast with wind turbine rotor mechanisms has to be discussed. When encountering inflow turbulence a helicopter rotor will ingest the turbulent eddy with a convection speed V_c , while for a wind turbine the eddy is blown into its rotor disc with a windspeed V_w . Downstream of the rotor plane of the wind turbine the flow is slowed down and the eddy is compressed. The lifting rotor of a helicopter accelerates the flow and the eddies are elongated. If the eddies are compressed rather than elongated and if the blade passage frequency is kept constant, the occurrence of blade loading correlation due to the chopping of a single eddy by more than one blade is reduced.

Turbulence Characteristics The length scale and the intensity of the inflow turbulence are dependent on meteorological conditions and height above the ground (Ref. 43). A helicopter flying at different altitudes will thus encounter different turbulence conditions, while for any given wind turbine the distance above the ground is fixed. For the wind turbines considered here the turbulence might be considered isentropic which means that fluctuations are approximately the same in all directions (Ref. 44). For horizontal axis wind turbine generators the longitudinal turbulence component is by far most important. This longitudinal component is assumed to be a horizontal sinusoidal gust of the form:

$$w = \bar{w} e^{i\omega(t-x/V_w)} \quad (1)$$

where \bar{w} is the square root of the root mean square turbulence intensity, ω is the rotational frequency, t is the time and x corresponds to a chordwise distance. The wind structure is strongly dependent on temperature gradient and turbulence ordinarily is stronger in the daytime than at night when the atmosphere is more stable. In this paper a standard day is assumed with a negative temperature gradient as a function of height above the ground. The root mean square turbulence intensity at elevation h is given by (Ref. 45):

$$\bar{w}^2 = \int \phi_x d\omega \quad (2)$$

where ϕ_x is the longitudinal turbulence spectrum at that elevation and is expressed in terms of a reference turbulence intensity w_r (Ref. 45):

$$\phi_x(\omega, V_w) = \frac{w_r^2}{\omega} \left[\frac{.104 \eta_0}{1 + .104 (\eta_0)^{5/3}} \right] \quad (3)$$

where η is the reduced frequency $\frac{\omega h}{V_w}$ and η_0 has the value of .0144 for a longitudinal gust. An expression for the reference turbulence intensity w_r as used in the structural analysis of the MOD-2 machine can be obtained from Reference 45:

$$w_r = .2 \left[2.18 V_w h^{-.353} \right] \frac{1}{1.185 - .193 \log h} \quad (4)$$

Substitution of Equation (3) in (2) yields, after integration, the root mean square turbulence intensity as a function of only wind-speed and height above the ground:

$$\bar{w}^2 = w_r^2 \left[h w_r / \{ V_w R(w_r - .014 w_r^2) \} \right]^{-2/3} \quad (5)$$

where w_r is given by Equation (4). The longitudinal turbulence spectrum ϕ_x has been integrated between a minimum frequency which was chosen very close to zero and a maximum frequency ω_{max} which was chosen such that high frequency (small extent) turbulence may be disregarded (Ref. 45).

Far-Field Noise Prediction - The induced fluctuating force $\frac{\partial F}{\partial t}$ per unit span is related to the horizontal gust by the aerodynamic transfer function $G(k)$:

$$\left(\frac{\partial F}{\partial t}\right)^2 = \omega_w^2 e^{2i\omega(t-x/v_w)} |G(k)|^2 \quad (6)$$

where $k = (\omega_w c_0 / 2v_w)$ and $G(k)$ is based on Osborne's asymptotic solution for the compressible extension of the Sears function (Refs. 28 and 35), which for low frequencies is approximated by:

$$G(k) = \frac{\sqrt{\rho} U c d r}{1 + 2\pi k} \quad (7)$$

Lighthill has shown that the sound pressure due to a fluctuating force F_i at a point with coordinate x_i ($i=1,2,3$) is given by the expression (Ref. 46):

$$p(t) - p_0 = \frac{x_i}{4\pi r_0^2} \left[\frac{1}{c_0} \frac{\partial F_i(t - r_0/c_0)}{\partial t} + \frac{1}{r_0} F_i(t - r_0/c_0) \right] \quad (8)$$

where c_0 is the speed of sound and r_0 is the distance between the source and receiver. If the source is considered to be a point dipole and the wavelength of the radiated sound is much smaller than the distance r_0 to the receiver the expression for the acoustic pressure in the far field formulated by Curle (Ref. 47) may be used:

$$p(\bar{r}, t) = \frac{\sin\phi}{4\pi c_0 r_0} \int \frac{\partial F(t - r_0/c_0)}{\partial t} \quad (9)$$

where \bar{r} is the vector from the origin to the receiver location (in the y-z plane) and ϕ is the angle between r_0 and the z-axis. Substituting Equations (6) and (7) into Equation (9) yields after integration and squaring the mean square sound pressure in the far field as being proportional to:

$$|p^2| = \frac{K_1(f) B \sin^2 \theta \rho^2 c_R \omega_w^2 U^4}{r_0^2 c_0^2} \quad (10)$$

where B is the number of blades, R is the radius of the rotor, and $K_1(f)$ is a frequency dependent scaling factor. To evaluate this scaling factor, the wind turbine rotor has been modeled as a dipole point source located at the hub and Equation (10) is compared with frequency spectra from the MOD-2 machine for which the noise was largely due to turbulent inflow (Refs. 15 and 16). The location of the peak intensity in the frequency domain is strongly dependent on blade velocity and longitudinal scale of turbulence (Ref. 24). The turbulence is dependent on height above the ground for non-varying meteorological condi-

tions. To account for different hub heights as well as different rotor diameters the location of the peak intensity in the frequency domain is given by:

$$f_{\text{peak}} = S U / (h - .7R) \quad (11)$$

where S is the applicable Strouhal number which is obtained from comparison with the measured MOD-2 noise spectra.

Power Output and Windspeed - If the power generated by the wind turbine is known rather than the wind speed, which is needed as input for Equations (4) and (5), it is necessary to know their relationship to enable noise predictions. Reference 48 suggests that for constant rotational speed machines the output power is linearly proportional to the wind-speed velocity and pitch angle. Between the cut-in speed and the rated wind speed the power output will vary approximately linearly with windspeed, which can be expressed by the equation:

$$v_w = \frac{P}{P_r} (v_{ra} - v_{ci}) + v_{ci} \quad (12)$$

where P_r is rated power output at the corresponding rated windspeed v_{ra} and v_{ci} is the cut-in windspeed at which no output power is produced. Equations (4), (5), (10), (11) and (12) are utilized to predict the noise spectra due to inflow turbulence for other machines and operating conditions.

Turbulent Boundary Layer-Trailing Edge Interaction

Noise is generated when the blade attached turbulent boundary layer convects into the wake at the trailing edge. Theoretical models of this trailing edge noise for helicopter blades are presented in References 20-22 and 48-60. The experimental and theoretical study in Reference 53 concludes that the trailing edge noise radiated from a local blade segment can be predicted by a first principles theory, which includes local Mach number, boundary layer thickness, length of the blade segment and observer position. A scaling law approach then was used for comparison with the noise radiation data from a stationary two-dimensional isolated airfoil segment. This theory will be utilized to predict the trailing edge noise generated by the blades of large horizontal axis wind turbine generators.

The scaling law prediction of Reference 53 gives for the trailing edge noise spectrum for an isolated airfoil:

$$SPL_{1/3} = 10 \log$$

$$\left\{ K_2 U^5 B \frac{\delta s}{r_0^2} \left(\frac{s}{s_{\max}}\right)^4 \left[\left(\frac{s}{s_{\max}}\right)^{1.5} + 0.5 \right]^{-4} \right\} \quad (13)$$

where $SPL_{1/3}$ is the one-third octave band sound pressure level, U is the local free stream velocity, B is the number of blades, δ is the local boundary layer thickness, s is

the airfoil span, r_0 the distance to the receiver, \bar{D} the directivity, S the Strouhal number and K_2 is a constant which equals 220 when SI units are used. Equation 13 is essentially the trailing edge noise prediction for a two-dimensional lifting surface in a uniform inflow. To predict the trailing edge noise from a rotating blade the blade is divided into small blade segments, with a length s , each experiencing a different local free stream velocity and each contributing to the noise at the receiver location. Because of the rotation this noise spectrum then is averaged around the azimuth. The local free-stream velocity U_x is given by:

$$U_x = 2\pi r_x n \quad (14)$$

where r_x is the distance from the local blade section to the center of the hub and n denotes revolutions per second. The thickness of the turbulent boundary layer at the trailing edge of the airfoil may be approximated by the turbulent boundary layer thickness of a flat plate which is given by (Ref. 62):

$$\delta = .37 c_x / (R_{N_x})^{-2} \quad (15)$$

where c_x is the chord at radius r_x from the hub and R_{N_x} is the local Reynolds number. Assuming a linearly tapered rotor blade and neglecting twist, c_x can be expressed in terms of the root chord (c_r), tipchord (c_t), radius (r_x) and blade diameter (D):

$$c_x = c_t + (1 - \frac{2r_x}{D}) (c_r - c_t) \quad (16)$$

The local Reynolds number is defined by:

$$R_{N_x} = \frac{U_x c_x}{\nu} \quad (17)$$

where ν is the kinematic viscosity. The directivity pattern of the radiated trailing edge noise, for an observer in the vertical ($\gamma=0$) plane perpendicular to the rotor plane is given by dipole like behavior from Reference 53:

$$\bar{D}(\theta, \frac{\pi}{2}) = \frac{\sin^2 \theta}{(1+M \cos \theta)^2 [1+(M-M_c) \cos \theta]^2} \quad (18)$$

where θ is the angle between the source-observer line and its projection in the ground plane. The convection Mach number of the turbulence, M_c , is set to an average value of .8 M as suggested in Reference 53. To correct for the directivity of the source outside the $y=0$ plane, the source is assumed to be a dipole radiator in those directions and the directivity function is the one proposed by Fink (Ref. 63):

$$\bar{D}(\theta, \psi) = \sin^2 \psi \bar{D}(\theta, \frac{\pi}{2}) \quad (19)$$

where ψ is the angle between the source-observer line and its projection in the $y=0$ plane. The Strouhal number in Equation 13 is

defined as the ratio of frequency (f) times the boundary layer thickness (δ) and the undisturbed free stream velocity (U_x):

$$S = \frac{f\delta}{U_x} \quad (20)$$

The peak Strouhal number, S_{max} , associated with trailing edge noise equals .1 (Refs. 63-65 and 53). Although a different value is reported in Reference 52, in the present study a value $S_{max}=.1$ is adopted.

Trailing Edge Bluntness Vortex Shedding Noise

Vortex shedding behind the trailing edges of thick struts has been studied in References 54-56. This phenomenon produces noise as the coherent vortex shedding causes a fluctuating surface pressure differential across the trailing edge. This was established in Reference 52 as being an important source of self-noise for airfoils with blunt trailing edges. The vortex shedding frequencies observed in References 54-56 had a peak Strouhal number of about .24 when based on the trailing edge thickness and a velocity dependence of approximately U_x^6 . This peak Strouhal number compares well with the ones found by other researchers who studied the vortex shedding behind wings, flat plates and circular and noncircular bodies (Refs. 23, 49, 52, and 57-60). In all cases, the turbulent boundary layer displacement thickness (δ^*) is much smaller than the characteristic dimension (t) from which the vortices are shed ($t/\delta^* > 40$). Experimental results from noise measurements on several trailing edge configurations in the NASA Langley Quiet-Flow Facility, however, indicated that for a trailing edge bluntness of equal thickness or smaller than the displacement thickness of the boundary layer a Strouhal number of .1 is applicable (Ref. 52). It was shown that the overall sound pressure level of the noise generated at the blunt trailing edge follows a $U_x^{2.3}$ dependence. Using the directivity pattern presented in Reference 53, the following scaling laws are derived for the one-third octave band sound pressure levels in the acoustic far field:

for $t/\delta^* > 1$:

$$SPL_{1/3} = \frac{K_3 B U_x^6 t s \sin^2 \theta \sin^2 \psi}{1 + M \cos \theta} \quad (21)$$

and

$$f_{max} = .25 \frac{U_x}{t + \frac{\delta_x}{4}} \quad (22)$$

for $t/\delta^* < 1$:

$$SPL_{1/3} = \frac{K_4 B U_x^{5.3} t s \sin^2 \theta / 2 \sin^2 \psi}{(1+M \cos \theta)^3 \left\{ 1+(M-M_c) \cos \theta \right\}^2} \quad (23)$$

and

$$f_{\max} = .1 \frac{U}{t} \quad (24)$$

where K_3 and K_4 are scaling constants. The constant K_4 has been obtained by comparing Equation (23) with the blunt trailing edge noise measurements from Figure 40 in Reference 52, which were first converted to one-third octave band data. The constant K_3 has been determined by equating Equation (21) and (23) for the case that the trailing edge bluntness is of the same thickness as the displacement thickness of the turbulent boundary layer. For most practical purposes the displacement thickness and the boundary layer thickness are related by:

$$\delta^* = \frac{\delta}{8} \quad (25)$$

Equations (21) through (25) are used to predict the noise from wind turbine blades with blunt trailing edges using the same calculation procedure as for turbulent boundary layer trailing edge interaction noise.

To assess the relative importance of all three major aerodynamic noise sources (figure 9) predictions have been made for a MOD-2 machine at a distance of 100 m on-axis. The noise contributions due to turbulent inflow, trailing edge bluntness and turbulent boundary layer trailing edge interaction relative to the total noise is depicted in Figure 10. The turbulent inflow related noise dominates the spectrum at the low frequencies and is broad in character while turbulent boundary layer trailing edge interaction noise becomes relatively more and more important when moving up the frequency scale. Noise due to trailing edge bluntness is confined to a more restricted frequency band with its center frequency related to the thickness of the trailing edge. All predictions are limited to the acoustic far field, on-axis and without distinction between upwind and downwind directions as no propagation effects are incorporated.

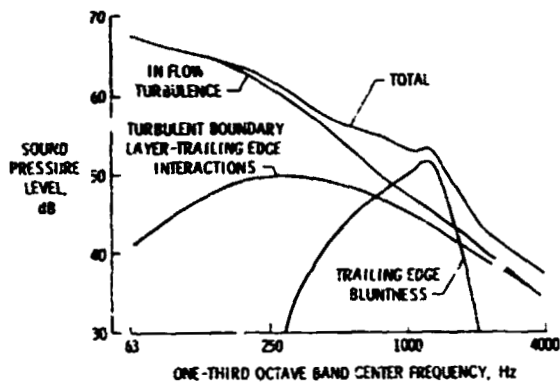


Figure 10. - On-axis broad band noise component predictions for the MOD-2 machine. ($V_w = 9.8$ m/s, $P = 1500$ kW, $r = 100$ m.)

COMPARISONS BETWEEN PREDICTIONS AND MEASUREMENTS

To show that reasonable agreement can be obtained between broadband noise predictions and far field noise measurements, comparisons have been made for four horizontal axis wind turbines with quite different physical characteristics (Figures 1 and 2). Also various distances, number of blades and power outputs are shown to give a good comparison with actual measured data. Figure 11 shows predictions and measurements for two downwind machines, MOD-OA and WTS-4, at different distances and different power outputs. Only the noise due to turbulent inflow is dependent on the actual power output (actually the turbulence intensity) as evidenced by the results depicted in Figure 11. Other noise source mechanisms are only dependent on rotational speed. The effect of the trailing edge bluntness of the three blades of the U.S. Windpower machine is shown in Figure 12 where the sharp peak around 2000 Hz in the noise spectrum disappears after the trailing edges have been sharpened.

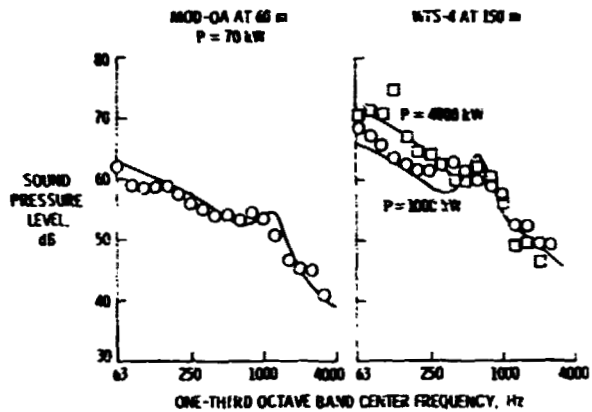


Figure 11. - Comparisons of measured and predicted on-axis broad band noise spectra for two downwind machines.

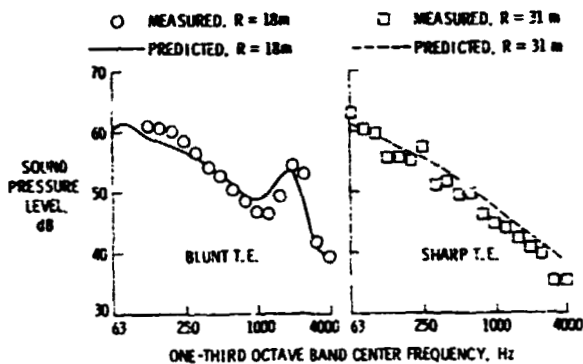


Figure 12. - Comparisons of measured and predicted broad band noise spectra for two different blade trailing edge configurations of the U.S. windpower inc. machine.

The predicted noise spectrum of a MOD-2 upwind machine at rated power is depicted in Figure 13 along with measured data points showing good agreement. In the same figure a broadband noise prediction is presented for a MOD-5B machine, at rated power, on axis, 200 m away from the hub. The difference is shown for a machine with sharp trailing edges and for the case that the blade trailing edges have the same bluntness as the MOD-2 machine. The noise signature of the MOD-5B is predicted to be 2-3 dB higher than the MOD-2 over the whole frequency range, both operating at rated power.

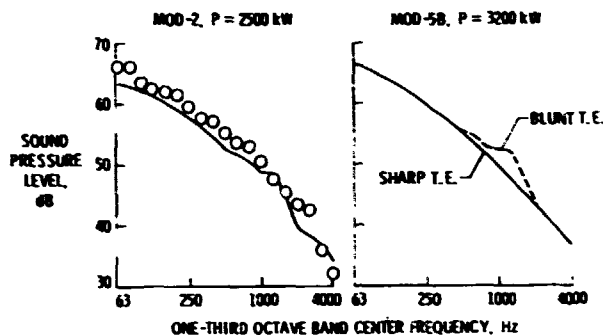


Figure 13. - Predicted on-axis broadband noise spectra for two upwind machines. ($r = 200$ m.)

CONCLUDING REMARKS

Noise measurements and observations have been presented for four large horizontal axis wind turbine generators with quite different characteristics in size and configuration. Effects of output power, directional radiation effects (up-, down-, and cross wind) and noise perception distances have been discussed based on field measurements. A method has been presented for predicting the broadband noise spectra of horizontal-axis, constant rotational speed machines, based on contributions from noise due to inflow turbulence, turbulent boundary layer-trailing edge interaction noise and noise due to a blunt trailing edge. Good agreement is shown between predictions and far field noise measurements of the four large wind turbine generators for various operating conditions. The prediction method includes the effects of distance from the machine, output power (windspeed), number of blades and tower and blade geometry. Broadband noise is predicted only on-axis and the method does not distinguish between upwind and downwind. Propagation effects other than distance are not included in the present prediction formulation.

REFERENCES

1. Hubbard, H.H., Shepherd, K.P., Grosveld, F.W.: Sound Measurements of the MOD-2 Wind Turbine Generator. NASA CR 165752,

July 1981

2. Shepherd, K.P. and Hubbard, H.H.: Sound Measurements and Observations of the MOD-OA Wind Turbine Generator. NASA CR 165856, February 1982
3. Shepherd, K.P. and Hubbard, H.H.: Measurements and Observations of Noise from a 4.2 Megawatt (WTS-4) Wind Turbine Generator. NASA CR 166124, VA, May 1983
4. Hubbard, H.H. and Shepherd, K.P.: Noise Measurements for Single and Multiple Operation of 50 kW Wind Turbine Generators. NASA CR 166052, December 1982
5. Grosveld, F.W., Shepherd, K.P. and Hubbard, H.H.: Radiation of Aerodynamic Sound from Large Wind Turbine Generators. Proceedings of Inter-Noise '82, pp. 323-326, San Francisco, May 17-19, 1982
6. Hubbard, H.H., Grosveld, F.W., and Shepherd, K.P.: Noise Characteristics of Large Wind Turbine Generators. Noise Control Engineering Journal, Vol. 21, No. 1, pgs. 21-29, 1983
7. Stephens, D.G., Shepherd, K.P., Hubbard, H.H. and Grosveld, F.W.: Guide to the Evaluation of Human Exposure to Noise from Large Wind Turbines. NASA TM 83288, March 1982
8. Shepherd, K.P., Grosveld, F.W. and Stephens, D.G.: Evaluation of Human Exposure to the Noise from Large Wind Turbine Generators. Noise Control Engineering Journal, Vol. 21, No. 1, pgs. 21-29, 1983
9. Balombin, J.R.: An Exploratory Survey of Noise Levels Associated with a 100 kW Wind Turbine. NASA TM 81486, 1980
10. Greene, G.C. and Hubbard, H.H.: Some Calculated Effects of Non-Uniform Inflow on the Radiated Noise of a Large Wind Turbine. NASA TM 81813, 1980
11. Kelley, N.D.: Acoustic Noise Generation by DOE/NASA MOD-1 Wind Turbine. Proceedings of the Second DOE/NASA Wind Turbine Conference, Cleveland, Ohio, February 24-26, 1981
12. Martinez, R., Widnall, S.E. and Harris, W.L.: Predictions of Low-Frequency Sound from the MOD-1 Wind Turbine. FDL Report No. 80-5, MIT, 1980
13. Savino, J.M., Wagner, L.H. and Sinclair, D.M.: Wake Characteristics of an Eight-Leg Tower for a MOD-0 Type Wind Turbine. DOE/NASA 1038-77/14, Department of Energy, December, 1977
14. Thompson, D.W.: Analytical Studies and Field Measurements of Infrasound Propagation at Howard's Knob, N.C. Dept. of Meteorology, Penn State University, Final Report 18, September, 1980

15. Wells, R.J.: MOD-1 Wind Turbine Generator Noise Studies. Corporate Research and Development Report, General Electric Company, Schenectady, N.Y., October, 1980
16. Viterna, L.A.: The NASA LeRC Wind Turbine Sound Prediction Code. Proceedings of the Second DOE/NASA Wind Turbine Conference, Cleveland, Ohio, February 24-26, 1981
17. Keast, D.N. and Potter, R.C.: A Preliminary Analysis of the Audible Noise of Constant Speed, Horizontal-Axis Wind Turbine Generators. DOE/EV-0089, UC-11, 60, July 1980
18. Kelley, N.D.: Noise Generated by Large Wind Turbines. Presented at Wind Energy Technology Conference, Kansas City, MO, March 16-17, 1981
19. George, A.R. and Chou, S.T.: Comparison of Broadband Noise Mechanisms, Analyses, and Experiments on Helicopters, Propellers, and Wind Turbines. AIAA Paper No. 83 0690 presented at the 8th Aeroacoustics Conference, Atlanta, Georgia, April 11-13, 1983
20. George, A.R.: Helicopter Noise: State of the Art. AIAA Journal of Aircraft, 15, (11), pp. 707-715, Nov. 1978
21. Schlinker, R.H. and Brooks, T.F.: Progress in Rotor Broadband Noise Research. Preprint #A-82-38-51-D, Presented at the 38th Annual Forum of the American Helicopter Society, Anaheim, CA, May 4-7, 1982
22. Ffowcs Williams, J.E. and Hall, L.H.: Aerodynamic Sound Generation by Turbulent Flow in the Vicinity of a Scattering Half-Plane. Journal of Fluid Mechanics 40, pp. 657-670, 1970
23. Berger, E. and Wille, R.: Periodic Flow Phenomena. American Rev. Fluid Mech. 4, 313, 1972
24. Aravamudan, K.S., Lee, A. and Harris, W.L.: A Simplified Mach Number Scaling Law for Helicopter Rotor Noise. Journal of Sound and Vibration, Vol. 57, No. 4, pp. 555-570, 1978
25. Amiet, R.K.: Noise Due to Rotor-Turbulence Interaction. NASA CP 2052, May 1978
26. Aravamudan, K.S., Lee, A. and Harris, W.L.: Wind Tunnel Investigations of Model Rotor Noise at Low Tip speeds. International Specialists Symposium on Helicopter Acoustics, NASA Langley Research Center, Hampton, VA, May 22-24, 1978
27. Brown, D. and Ollerhead, J.B.: Propeller Noise at Low Tip Speeds. AFAPL-TR-71-35, September 1971
28. Osborne, C.: Unsteady Thin Airfoil Theory for Subsonic Flow, AIAA Journal, Vol. 11, pp. 205-209, Feb. 1973
29. Ffowcs Williams, J.E. and Hawkings, D.L.: Theory Relating to the Noise of Rotating Machinery, Journal of Sound and Vibration, Vol. 10, pp. 10-21, 1969
30. SenGupta, G.: Analysis of Jet-Airframe Interaction Noise, AIAA Paper 83-0783, 8th Aeroacoustics Conference, Atlanta, GA, April 1983
31. Amiet, R.K.: Acoustic Radiation from an Airfoil in a Turbulent Stream. Journal of Sound and Vibration, Vol. 41, No. 4, August 1975
32. Whitfield, C.E.: An Investigation of Rotor Noise Generation by Aerodynamic Disturbance. NASA CR 157471, 1977
33. Leverton, J.W.: Helicopter Noise-Blade Slap. NASA CR 1221, October, 1968
34. Leverton, J.W.: The Noise Characteristics of a Large "Clean" Rotor. Journal of Sound and Vibration, Vol. 27, No. 3, April 1973
35. Homicz, G.F. and George, A.R.: Broadband and Discrete Frequency Radiation from Subsonic Rotors. Journal of Sound and Vibration, Vol. 36, No. 2, September 1974
36. Hayden, R.: Noise from Interaction of Flow with Rigid Surfaces: A Review of Current Status of Prediction Techniques. NASA CR 2126, October 1972
37. Sharland, I.J.: Sources of Noise in Axial Flow Fans. Journal of Sound and Vibration, Vol. 1, No. 3, pp. 302-322, 1964
38. Lowson, M.V. and Ollerhead, J.B.: A Theoretical Study of Helicopter Rotor Noise. Journal of Sound and Vibration, Vol. 9, pp. 197-222, March 1969
39. Lowson, M.V., Whatmore, A.R. and Whitfield, C.E.: Source Mechanisms for Rotor Noise Radiation. NASA CR 2077, August, 1973
40. Paterson, R.W. and Amiet, R.K.: Noise of a Model Helicopter Rotor Due to Ingestion of Turbulence. NASA CR 3213, November, 1979
41. Humbad, N.G. and Harris, W.L.: Model Rotor Low Frequency Broadband Noise at Moderate Tip Speeds. AIAA Paper 80-1013, June 1980
42. George, A.R. and Kim, Y.N.: High Frequency Broadband Rotor Noise. AIAA Journal, Vol. 15, No. 4, pp. 538-545, April 1977

43. Piercy, J.E., Embleton, T.F. and Sutherland, L.C.: Review of Noise Propagation in the Atmosphere. *Journal of the Acoustic Society of America*, Vol. 61, No. 6, June 1977
44. Ingard, U.: The Physics of Outdoor Sound. Proceedings of the 4th National Noise Abatement Symposium, 1953
45. Boeing Engineering and Construction: MOD-2 Wind Turbine System Concept and Preliminary Design Report. DOE/NASA 0002-80/2, July 1979
46. Lighthill, M.J.: On Sound Generated Aerodynamically; General Theory. Proceedings of the Royal Society, London, A 211, pp. 564-587, 1952
47. Curle, N.: The Influence of Solid Boundaries upon Aerodynamic Sound. Proceedings of the Royal Society, London, A 231, pp. 505-514, 1955
48. Anonymous: MOD-1 Windturbine Generator Analysis and Design Report. NASA CR 159495, General Electric Company, Space Division, March 1979
49. Chase, D.M.: Noise Radiated from an Edge in Turbulent Flow. *AIAA Journal*, Vol. 13, No. 8, August 1975
50. Amiet, R.K.: Effect of the Incident Surface Pressure Field on Noise Due to Turbulent Flow Past a Trailing Edge. *Journal of Sound and Vibration*, Vol. 57, pp. 305-306, 1978
51. Yu, J.D. and Tam, C.K.: An Experimental Investigation of the Trailing Edge Noise Mechanism. *AIAA Journal*, Vol. 16, No. 10, pp. 1045-1052, October 1978
52. Brooks, T.F. and Hodgson, T.H.: Prediction and Comparison of Trailing Edge Noise Using Measured Surface Pressures. AIAA Paper 80-0977, 6th Aeroacoustics Conference, Hartford, CT, June 4-6, 1980
53. Schlinker, R.H. and Amiet, R.K.: Helicopter Rotor Trailing Edge Noise. NASA CR 3470, Nov. 1981
54. Blake, W.K.: A Statistical Description of Pressure and Velocity Fields at the Trailing Edges of a Flat Strut. Report 4241, David W. Taylor Naval Ship Research and Development Center, Bethesda, MD, December, 1975
55. Blake, W.K., Maga, L.J. and Finkelstein, G.: Hydroelastic Variables Influencing Propeller and Hydrofoil Singing. Paper presented at the Winter Annual Meeting of ASME, Atlanta, GA, November, 1977
56. Blake, W.K. and Maga, L.J.: Near-Wake Structure and Unsteady Pressures at Trailing Edges of Airfoils. Reprint from *Mechanics of Sound Generation in Flows*, IUTAM/ ICA/AIAA Symposium, Gottingen, August 28-31, 1979
57. Krzywoblocki, M.Z.: Investigation of the Wing-Wake Frequency with Application of the Strouhal Number. *Journal of the Aeronautical Sciences*, Vol. 12, No. 1, January, 1945
58. Mendenhall, M.R., Spangler, S.B. and Perkins, Jr., S.C.: Vortex Shedding from Circular and Non-Circular Bodies at High Angles of Attack, AIAA Paper 79-0026, 17th Aerospace Sciences Meeting, New Orleans, January 15-17, 1979
59. Nishioka, M. and Sato, H.: Mechanism of Determination of the Shedding Frequency of Vortices Behind a Cylinder at Low Reynolds Numbers. *J. Fluid Mech.*, Vol. 89, Part 1, pp. 49-60, 1978
60. Katz, J. and Weiks, D.: Behavior of Vortex Wakes from Oscillating Airfoils. *AIAA Journal of Aircraft*, Vol. 15, No. 12, December 1978
61. Howe, M.S.: A Review of the Theory of Trailing Edge Noise. *Journal of Sound and Vibration*, Vol. 61, No. 3, December, 1978
62. Schlichting, H.: Boundary Layer Theory. McGraw-Hill, Inc., Sixth Ed., 1968
63. Fink, M.R. and Schlinker, R.H.: Airframe Noise Component Interaction Studies. *AIAA Journal of Aircraft*, Vol. 17, No. 2, February 1980
64. Fink, M.R.: Noise Component Method for Airframe Noise, *AIAA Journal of Aircraft*, Vol. 16, No. 10, October 1979
65. Fink, M.R.: Airframe Noise Prediction Method. Federal Aviation Administration Report No. FAA-RD-77-29, March 1977 (available from DTIC as A039-664)

**OBSERVED ACOUSTIC AND AEROELASTIC SPECTRAL RESPONSES
OF A MOD-2 TURBINE BLADE TO TURBULENCE EXCITATION**

N95-27991

N.D. Kelley
H.E. McKenna
E.W. Jacobs

Solar Energy Research Institute
Golden, Colorado 80401

ABSTRACT

Early results from a recent experiment designed to directly evaluate the aeroacoustic/elastic spectral responses of a MOD-2 turbine blade to turbulence-induced unsteady blade loads are discussed. The experimental procedure consisted of flying a hot-film anemometer from a tethered balloon in the turbine inflow and simultaneously measuring the fluctuating airload and aeroelastic response at two blade span stations (65% and 87% spans) using surface-mounted, subminiature pressure transducers and standard strain gage instrumentation. The radiated acoustic pressure field was measured with a triad of very-low-frequency microphones placed at ground level, 1.5 rotor diameters upwind of the disk. Initial transfer function estimates for acoustic radiation, blade normal forces, flapwise acceleration/displacement, and chord/flapwise moments are presented.

INTRODUCTION

Results from a 1982 experiment that examined the acoustic emission characteristics of a MOD-2 turbine concluded that knowing the acoustic and aeroelastic spectral responses of turbine rotor blades to inflow turbulence would be very important to our understanding of the physical processes surrounding the generation of acoustic noise by large horizontal-axis wind turbines. Because unsteady blade airloads are responsible for much of the turbine rotor aeroelastic response and are the source of the aerodynamic component of the radiated acoustic pressure field, as indicated in Figure 1, understanding the former may allow us to estimate in situ unsteady aerodynamic, aeroelastic responses of minimally instrumented turbines from properly executed and processed acoustic measurements. Hemphill [1], for example, showed that distinct acoustic source regions could be identified within the rotor disk of an operating MOD-2 turbine by phase-processing signals from a triad of microphones installed at ground level, upwind of the machine. Kelley et al. [2] found that substantial and sometimes violent dynamic aeroelastic responses (with accompanying high levels of acoustic radiation) can occur with symmetrically shaped airfoil sections operated at incidence angles just below static stall and immersed in a turbulent flow dominated by perturbation space-scales near the chord dimension.

The experiment was therefore designed to directly measure the aerodynamic, acoustic, and elastic responses of a MOD-2 rotor blade in order to (1) help develop a physical understanding of the acoustic generation process; (2) help identify unsteady airload magnitudes on minimally instrumented wind turbines; (3) help identify unknown sources of both low- and high-amplitude and low- and high-cycle fatigue loads; (4) help evaluate dynamic effects that may be associated with vortex generator spoilers installed along the blade's leading edge and the inboard 70% of the span; and (5) help establish the role of the spectral content of atmospheric turbulence in the earth's

boundary layer in acoustic noise production and turbine lifetime. This paper discusses a few of the early results of this experiment.

TEST CONFIGURATION

The Boeing MOD-2 Unit No. 2 was the turbine chosen for this experiment. This turbine is one of three MOD-2 machines at the Goodnoe Hills Wind Test Site near Goldendale, Washington, jointly operated by the NASA Lewis Research Center and the Bonneville Power Administration (BPA) for the U.S. Department of Energy. The Goodnoe Hills Site is well-equipped to perform such an experiment because a variety of detailed turbine operational and site meteorological information is available and because of the experimental nature of the site.

Turbine No. 2 was operated for this experiment under the standard operational sequence using Boeing's "five-degree control software" procedures. Vortex generators had been installed near the leading edge of the rotor covering the inboard 70% of each blade span. Groups of six subminiature pressure transducers were mounted to the upper and lower blade surfaces of Blade No. 1 at two span stations (65% and 87%, or Stations 1164 and 1526, respectively) and chordwise distances of 15%, 40%, and 85%. Station 1164 is located on the outer portion of the fixed section of blade while Station 1562 is located on the movable control tip slightly less than 8 m outboard of the gap between the fixed and movable sections. An accelerometer, with its sensitive axis parallel to the flapwise or out-of-plane direction, was mounted near the inboard surface pressure transducers at Blade Station 1209 (67% span). Standard measurements of strain-gage-derived chord and flapwise moments were made at the locations of the pressure transducers and transmitted via the turbine data system to SERI and NASA multi-channel recording facilities along with the remainder of available operational data. The turbine engineering data system limited the data bandwidth of the turbine-related parameters to 35.2 Hz.

Windfield/Turbulence Instrumentation

A commercially-available tethered balloon system, modified by SERI to carry a hot-film anemometer and its associated electronics and a radio-telemetry transmitter, was flown in the turbine inflow to acquire the mean and turbulence spectral characteristics. When the balloon was operated in a profiling mode, the details of the inflow vertical structure could also be examined. The tethered balloon system also carried a small package that sensed and radio-telemetered height (pressure), temperature, windspeed, and wind direction once every 10 s to a ground station located in the SERI Instrumentation Van. There, the data were recorded on two tape systems and presented in digital form in support of the experimental operations. The hot-film turbulence measuring system consisted of a

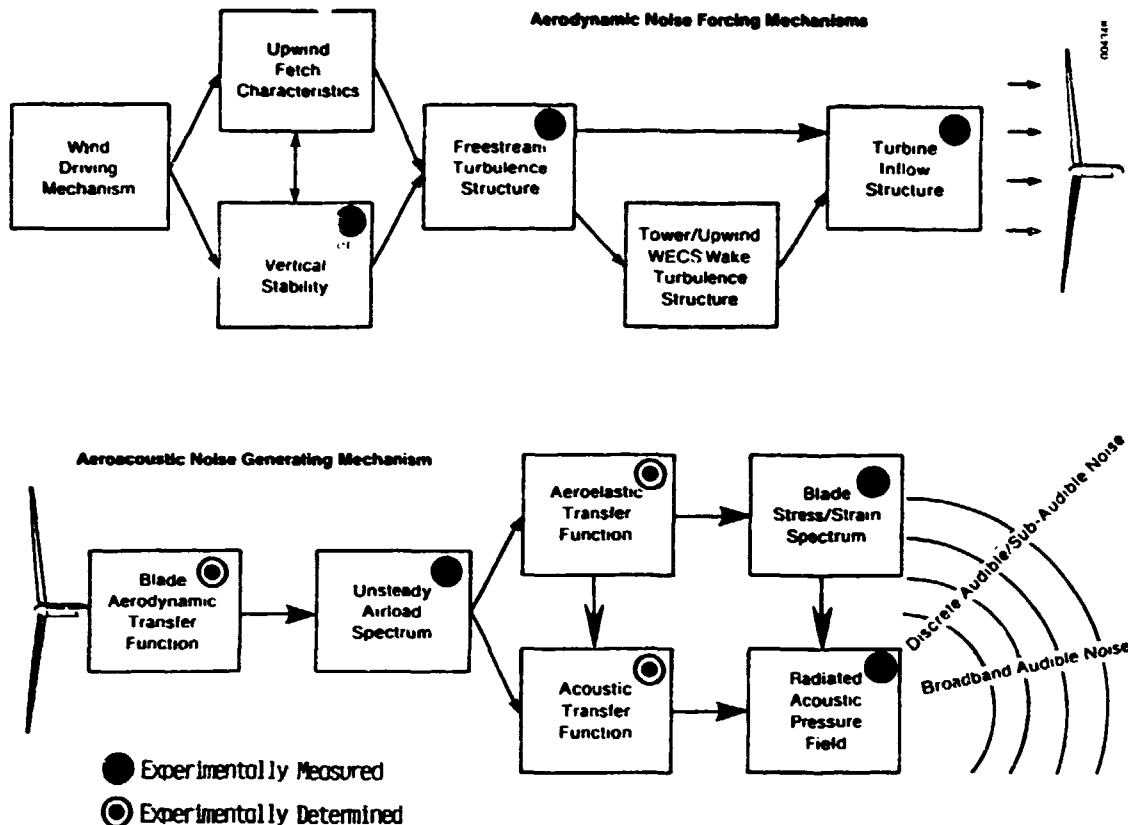


Figure 1. Physical processes responsible for aeroacoustic and aeroelastic blade responses.

0.15-mm-diameter sensor oriented to measure the vector sum of the local horizontal and vertical wind components, the associated bridge network, and a 50-mW digital radio-telemetry transmitter. The receiver, located in the SERI Van, converted the signal from digital to analog form for final processing by a 4th-order polynomial linearizer and time-parallel recording, with selected turbine and acoustic parameters on the same multichannel magnetic tape media. The dynamic range of the hot-film anemometer telemetry link is better than 70 dB and its data bandwidth is 125 Hz, but the final recording was limited to about 48 dB and 100 Hz.

Acoustic Instrumentation

Three very low-frequency (VLF) microphone systems were installed in a right-angle array pattern at ground level upwind of the turbine. The closest microphone to the rotor plane was placed 122 m upwind of the rotor axis. The two remaining microphones were located 15 m farther upstream (1.5 rotor diameters from the disk) and 15 m from each other along a line parallel to the turbine rotor plane. The low-frequency cutoff of the VLF systems was set at 0.1 Hz, and the upper response limit set by the final FM tape recording at 1250 Hz and available dynamic range.

TEST PROCEDURE

The general procedure followed during this experiment was to choose test conditions based on (1) a windspeed range (low range, turbine cut-in to 12 ms^{-1} and high, above 12 ms^{-1}); (2) a wind direction of $270 \pm 15^\circ$; and (3) rotor disk layer hydrodynamic stability as ex-

pressed by the gradient or bulk Richardson Number parameter. The tethered balloon system was flown in two modes. Vertical profiles of the rotor disk layer were made before and after each 30-min data run; i.e., heights ranging from about 15 to 108 m. During the actual data runs, the balloon was positioned near hub-height to provide a continuous record of the inflow turbulence for time-parallel recording with the blade surface pressures and acoustic data from which the blade responses could be calculated.

DATA REDUCTION PROCEDURES

The data reduction procedures included (1) data channel response evaluation and subsequent equalization; (2) sampling and Fourier transformation to rms spectral estimates; and (3) computation of turbulence response function estimates.

Data Channel Response/Equalization

The actual transfer function of the turbine engineering data system channels was experimentally measured. Figure 2 plots the modulus (magnitude) of the measured response. As shown, the half-power (-3 dB) point is 35.2 Hz. From our wind tunnel experimentation and previous MOD-2 acoustic measurements, we had good reason to believe there would be considerable response above this figure. We also knew the pressure transducers and strain gage instrumentation were capable of much wider response, because the available bandwidth was wholly limited by the low-pass filter in the telemetry system signal conditioning cards. From our actual measurements of the data channel response characteristics, and knowing the dynamic range of the

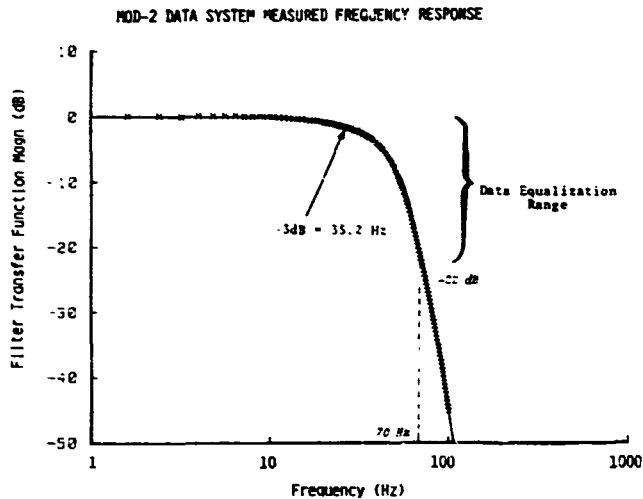


Figure 2. MOD-2 engineering data system channel amplitude response function.

FM recording processes used, we devised an equalization filter which was applied in the frequency domain after Fourier transformation. This equalization process is essentially the inverse of the response shown in Figure 2 with the maximum frequency at which it is applied at 70 Hz. This upper frequency limit was arrived at by conservatively estimating the dynamic range of the FM recording processes used by SERI and NASA at about 40 dB maximum. (We believe, for example, the actual SERI figure was between 43 and 48 dB.) At 70 Hz the data system analog filter response was -22 dB, which would allow for sufficient equalization and not exceed the assumed 40-dB dynamic range of the FM recordings. Thus, a maximum gain of 22 dB at 70 Hz is applied to the recorded data in the equalization process.

Sampling and Fourier Transformation

The results in this paper are derived from a data run recorded on the evening of 16 August 1983 between 2230 and 2300 hours local standard time. Because of the nonstationary characteristics of the atmospheric input, each 30-min data run has been divided into six 5-min segments. The final 5-min segment of this particular series was chosen for detailed response analysis reported on here because (1) a minimal vertical variation was found in the height of the hot-film anemometer with respect to the rotor disk (a standard deviation of 6 m, compared with other 5-min segments in which variations of more than ± 15 m were found); and (2) relatively substantial turbulent energy levels were found in the high-frequency range. Table 1 summarizes pertinent turbine operational and inflow turbulence values for this 5-min segment.

We chose a vertical window of ± 10 m from the mean hot-film anemometer height as the region from which we would extract blade dynamic data needed to calculate response estimates. This choice resulted in the definitions of the two segments of the rotor disk pictured in Figure 3. Previous experience indicated that subtle changes occur in the blade response as it ascends and descends (driven by gravity, most likely) and that therefore we should examine the response of the blade as it passed through the measured layer in both directions. By delaying data conversion and

Table 1. Summary of Important Turbulence Excitation and Turbine Operation Flow Angles for Analyzed Data Segment

Turbulent Layer Structure Parameters	
Mean measurement height (above tower base)	78 ± 6 m
Mean horizontal wind speed	7.39 ms^{-1}
Turbulence intensity	8.0%
Turbulence integral scale l	2.89 m ²
Turbine Blade Operating Angles	
Indicated mean blade angle (ref. at Sta. 1260)	$+0.62^\circ$
Calculated mean angle of attack (Sta. 1164)	11.6°
Calculated mean angle of attack (Sta. 1562)	9.6°

^a1.3 chords referenced at 80% span.

Fourier transformation a fixed amount from the time the blade was at the bottom of its travel (parallel to the tower base), we could start the 0.5-second conversion period to coincide with the windows shown in Figure 3. While some differences were noted, the data presented in this paper are based on the averages of responses found in the ascending and descending sampling windows. Inflow turbulence data were collected using the same sampling scheme and delayed to allow propagation at the 7.4 ms^{-1} mean windspeed to reach the disk (employing the frozen turbulence hypothesis). Similarly, acoustic data were calculated from the in-phase portion of the rms cross-spectral estimate from the two microphone systems parallel to the rotor disk and 1.5 diameters upstream. An additional delay of 0.5 seconds was added to account for the propagation time from the affected disk area to the microphones. The 5-min data segment resulted in a total record of 40 seconds containing 80 blade passages through the turbulent excitation layer from which the averaged rms spectral estimates were derived. A total of 81,920 data points were processed. The resulting resolution bandwidth of the transformation is 2 Hz.

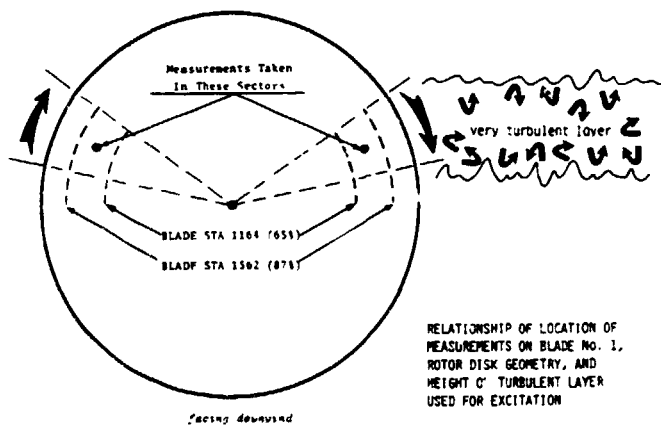


Figure 3. Relationship of measurement locations on Blade No. 1, rotor disk geometry, and height of turbulent layer used for excitation.

Response Estimate Calculations

The response estimates were calculated by taking the ratio of the equalized blade pressure or other turbine parameter rms spectral estimate to the reference turbulence spectrum. Thus, results are referenced in terms of the units of the particular parameter per ms^{-1} .

DESCRIPTION OF TURBULENCE EXCITATION

Figure 4 plots the detailed vertical windspeed profile measured immediately at the conclusion of the 5-min data segment. The minimum vertical resolution of this profile has been limited to 6 m. The turbulent excitation layer is characterized by the scatter in the data points. Figure 5 presents the averaged, normalized power spectral density of the turbulence in this layer which also served as the reference from which response estimates have been calculated. The relatively significant high-frequency (short wavelength) energy content is apparent even in this averaged spectrum. The location of the correlated turbulent eddy region, defined by frequencies higher than the integral scale l , is shown at right. Some differences in the spectral characteristics above this frequency may be noted.

TEST RESULTS

Representative examples of response estimates have been divided into three groups: acoustic, aerodynamic, and aeroelastic. While it would be interesting and perhaps significant in some cases, we have not attempted to combine these categories in this paper.

VERTICAL INFLOW STRUCTURE AT 1.5 ROTOR DIAM UPSTREAM

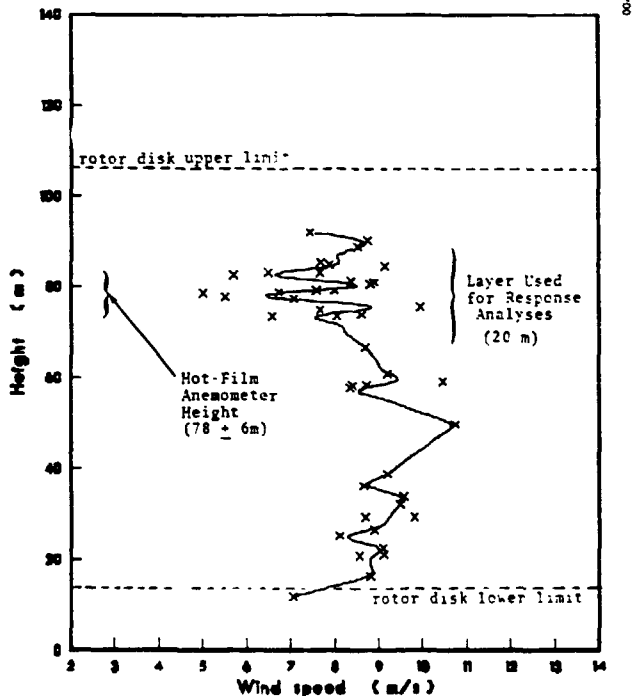


Figure 4. Details of vertical inflow structure measured 1.5 rotor diameters upstream of H00-2 disk.

INFLOW TURBULENCE EXCITATION: SPECTRUM AT 78 m

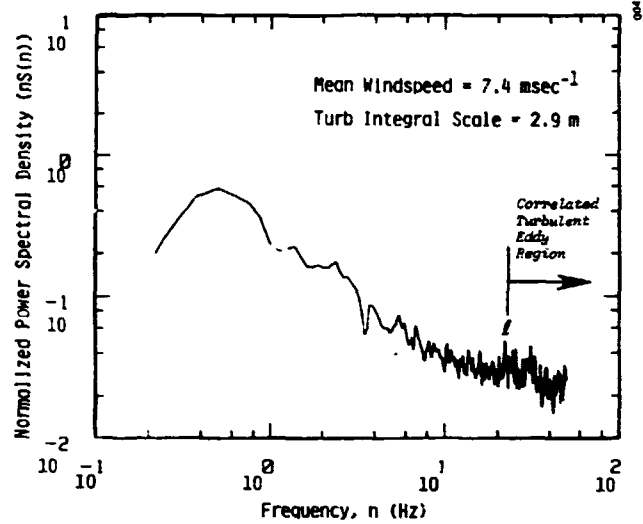


Figure 5. Averaged normalized power spectral density of turbulent excitation layer at 78 m.

Low-Frequency Acoustic Response Estimates

Figure 6 plots the low-frequency acoustic radiation response in Pa/ms^{-1} over a range of 2 to 100 Hz (the acoustic data were not limited by the turbine engineering data system low-pass filters and so can be presented to 100 Hz). The abscissa has also been calibrated in terms of the reduced frequency parameter k (shown in italics) as referenced to the chord dimensions and relative blade speed at 80% span. The k parameter is defined by $k = \omega c / U$, where c is the chord dimension; f , the cyclic frequency; and U , the relative blade speed.

Blade Aerodynamic Response Estimates

Two examples of the blade aerodynamic response are given in Figures 7 and 8. Figure 7 plots the normal force response in units of $\text{kPa}/\text{ms}^{-1}$ as measured at the 40% chord position at both the inboard (65% span or Blade Station 1164) and outboard (87% span or Blade Station 1562) span locations. Figure 8 indicates the differences in response seen at the 15% and 40% chord positions at the outer span station (1562).

Blade Aeroelastic Response Estimates

Figures 9, 10, 11, and 12 are a representative look at the aeroelastic response of the blade. Figures 9 and 10 plot the chord and flapwise moment responses in N/ms^{-1} at the inboard (Station 1164) and outboard (Station 1562) span locations. Figures 11 and 12 present the flapwise acceleration and displacement responses in $\text{ms}^{-2}/\text{ms}^{-1}$ and m/ms^{-1} , respectively, at Blade Station 1209 on the fixed-pitched portion of the blade.

RESPONSE IN TERMS OF TURBULENCE SPACE SCALE

Previous SERI wind tunnel experiments with symmetrically shaped airfoil sections [2] showed that strong and occasionally violent buffet-type responses could develop at incidence angles approaching but remaining below static stall. In terms of the reduced frequency parameter k , the buffet onset was generally found to be near $k = 0.5$ and extended to at least $k = \pi$. The

SPECTRAL AEROACOUSTIC RESPONSE

RUN: A05/06
 WSPD: 7.39 m/s
 PARM(s): Low Freq Acoustic Radiation
 UNITS: Pa/m/sec

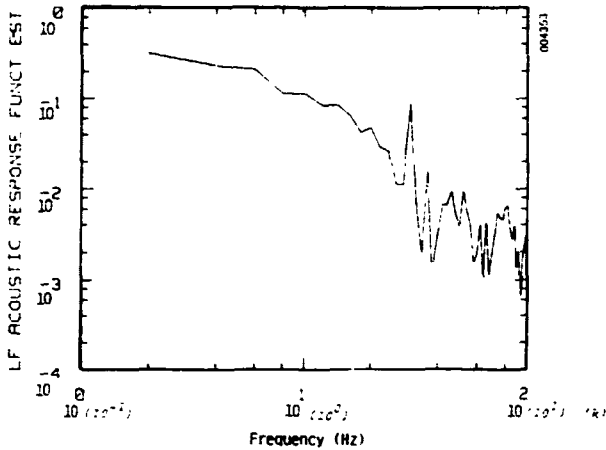


Figure 6. Measured low-frequency acoustic radiation response function.

SPECTRAL AERODYNAMIC RESPONSE

RUN: A05/06
 WSPD: 7.39 m/s
 SPAN STA(s): 1562
 CHORD STA(s): 15 & 40%
 PARM(s): Normal Force
 UNITS: (kPa)/(m/sec)

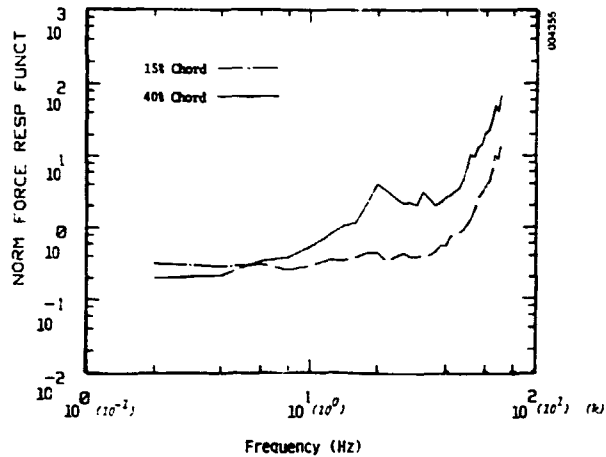


Figure 8. Measured normal pressure force response functions at Blade Station 1562 (87%) at 15% and 40% chord stations.

SPECTRAL AERODYNAMIC RESPONSE

RUN: A05/06
 WSPD: 7.39 m/s
 SPAN STA(s): 1164/1562
 CHORD STA(s): 40%
 PARM(s): Normal Force
 UNITS: (kPa)/(m/sec)

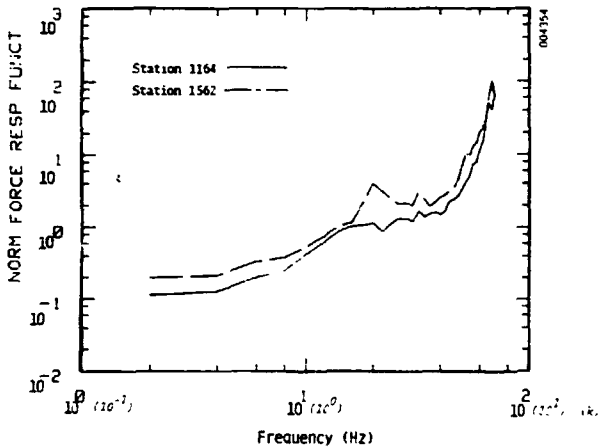


Figure 7. Measured normal pressure force response functions at 40% chord and Blade Stations 1164 (65%) and 1562 (87%) span.

SPECTRAL AEROELASTIC RESPONSE

RUN: A05/06
 WSPD: 7.39 m/s
 SPAN STA(s): 1164/1562
 PARM(s): Chord Moment
 UNITS: N-m/m/sec

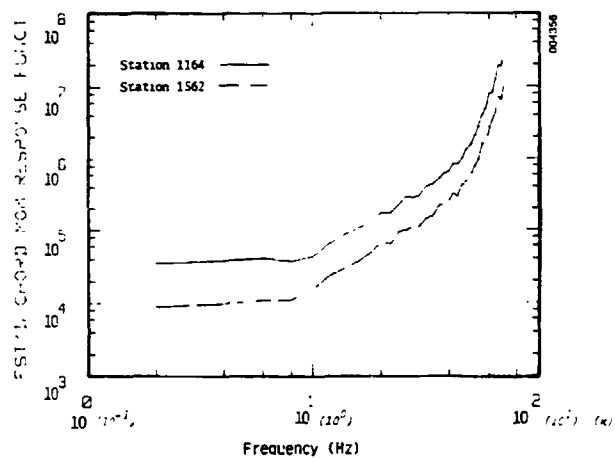


Figure 9. Measured blade chord moment response functions at Blade Stations 1164 and 1562.

response shown on most of the previous figures seems to extend higher than that figure. However, these tests agreed with the wind tunnel results in that the buffet response also increases as the flow perturbations or turbulent eddy size approaches the dimensions of the section chord. Figures 13, 14, and 15 have been replotted using the acoustic, 40%-chord normal force and chord moment response data of Figures 6, 7, and 9 of the turbulent eddy size or perturbation wavelength normalized by the chord dimension at 80% span. The wavelengths defined by the integral turbulent length scale l are also shown. As previously mentioned, the turbulent integral scale roughly refers

to the largest correlated eddy size or, in other words, the upper limit on correlated turbulence space scales.

CONCLUDING REMARKS

This preliminary assessment of the unsteady response of MOD-2 turbine blade, from one rather well-behaved case, indicates that unsteady blade loads are very sensitive to the spectral content of the turbulence encountered around the swept area of the rotor disk. The greatest sensitivity appears to be to turbulent eddy sizes on the order of the blade chord or less. A

SPECTRAL AEROELASTIC RESPONSE

RUN: A05/#6 SPAN STA(s): 1164/1562
 WSPD: 7.39 m/s
 PARM(s): Flap Moment
 UNITS: (N-m)(m/sec)

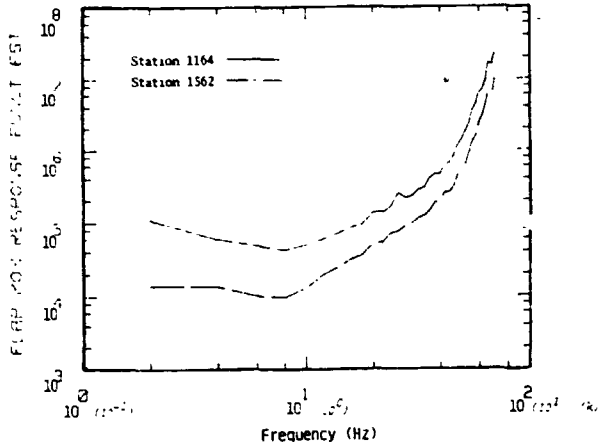


Figure 10. Measured flap moment response functions at Blade Stations 1164 and 1562.

SPECTRAL AEROELASTIC RESPONSE

RUN: A05/#6 SPAN STA(s): 1209
 WSPD: 7.39 m/s
 PARM(s): Flap Displacement
 UNITS: m/m/sec

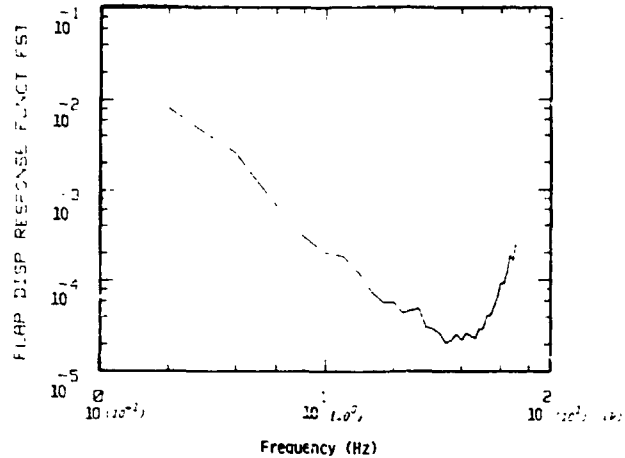


Figure 12. Measured flapwise displacement response function at Blade Station 1209.

SPECTRAL AEROELASTIC RESPONSE

RUN: A05/#6 SPAN STA(s): 1209
 WSPD: 7.39 m/s
 PARM(s): Flap Acceleration
 UNITS: (m/sec^2)/(m/sec)

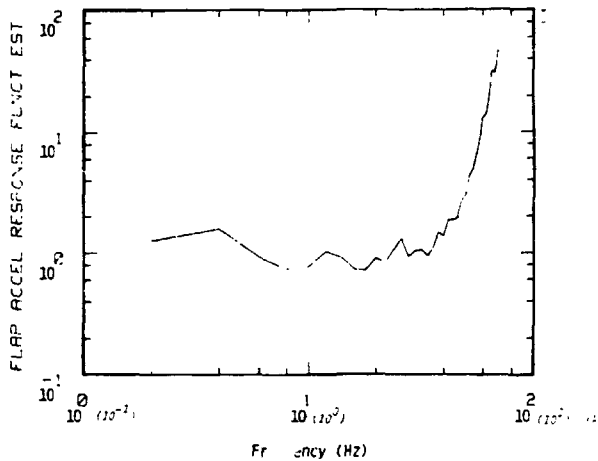


Figure 11. Measured flapwise acceleration response function at Blade Station 1209.

SPECTRAL AEROACOUSTIC RESPONSE

RUN: A05/#6 SPAN STA(s): 1209
 WSPD: 7.39 m/s
 PARM(s): LF Acoustic Radiation
 UNITS: (Pa)/(m/sec)

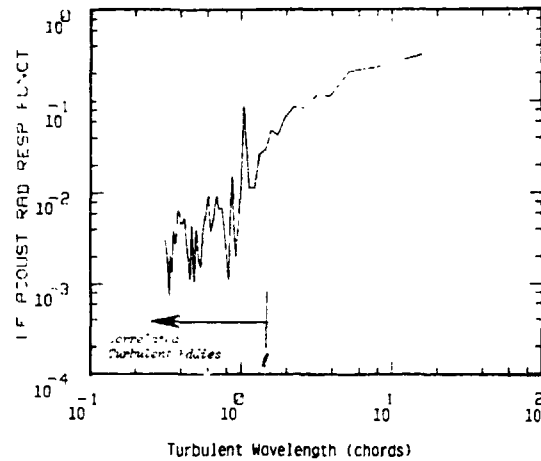


Figure 13. Measured low-frequency acoustic radiation response as a function of turbulence space scale.

correlation also seems to exist between the turbulence integral scale and the resulting unsteady blade response as indicated by the acoustic, aerodynamic, and aeroelastic response estimates.

The outboard blade station (1562) on the movable tip is noticeably less sensitive to the turbulence until the turbulence scales become less than the section chord length. One possible explanation for this is that the mean attack or incidence angle of the flow with respect to the outer span station is about 1° less than the inboard station and thus slightly farther away from the static stall condition, a situation that we know from our wind tunnel experience usually

indicates a reduced unsteady response. Also, the inboard section was fitted with vortex generators whose function is to delay separation and increase the maximum section lift.

The data-system-imposed maximum bandwidth limitation of an equalized 70 Hz prevents us from determining when the curves begin to fall. However, Figure 6, which contains the acoustic radiation response estimate, seems to indicate that a peak may exist at around 80 Hz, and it hints at one even higher. Additional measurements with wider data bandwidths are needed to confirm the effective upper limits of turbulence sensitivity, but some clues may be gathered

SPECTRAL AERODYNAMIC RESPONSE

RUN: A05/#6
 WSPD: 7.39 m/s
 SPAN STA(s): 1164/1562
 CHORD STA(s): 40%
 PARM(s): Normal Force
 UNITS: (kPa)/(m/sec)

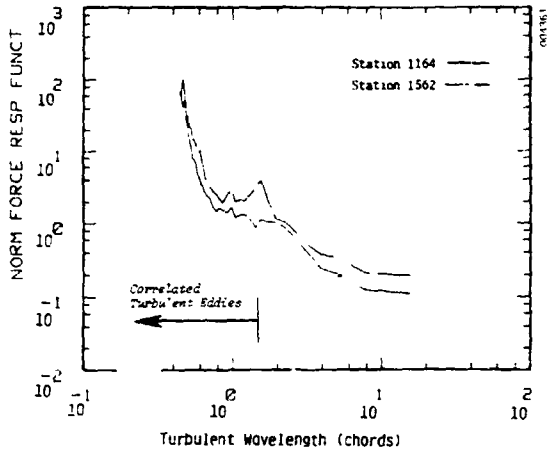


Figure 14. Measured 40% chord normal force response function at Blade Stations 1164 and 1562 as a function of turbulent space scale.

from the SERI acoustic data set which has been analyzed statistically up to 160 Hz in 1/3-octave bands.

ACKNOWLEDGMENTS

The authors wish to express their appreciation to members of the staff of the MOD-2 Program of the Boeing Aerospace Corporation and in particular to Ron Schwemmer, Don Fries, Jack Betty, and Howard Woody for their professional dedication and assistance. We wish to thank the Wind Energy Program Office of the NASA Lewis Research Center, and Larry Gordon, Harold Neustadter, and Virgil Kirkendahl in particular for their excellent coordination support. We appreciate the efforts of Dave Long of Fairchild-Weston in data support and Ben Willmarth of the B.C. Willmarth Co. in balloon operations. The experiment could not have proceeded as smoothly as it did without the splendid cooperation and support efforts of staff mem-

SPECTRAL ELASTIC RESPONSE

RUN: A05/#6
 WSPD: 7.39 m/s
 SPAN STA(s): 1164/1562
 PARM(s): Chord Moment
 UNITS: N-m/m/sec

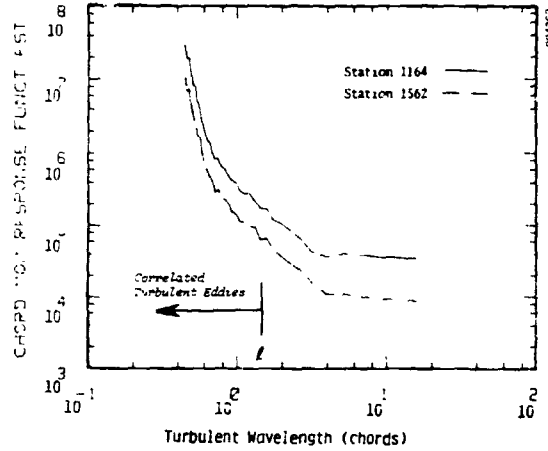


Figure 15. Measured blade chord moment response functions at Blade Stations 1164 and 1562 as a function of turbulent space scale.

bers of the Bonneville Power Administration, especially Ron Holeman and Roger Bennett. This work has been supported by the U.S. Department of Energy, Wind Energy Technology Division, under Contract Numbers EG-77-C-01-4042 and DE-AC02-83CH10093.

REFERENCES

1. Hemphill, R.R., An Acoustic Ranging Technique with Application to Assessment of Low-Frequency Acoustic Noise of Wind Turbines, SERI TP-215-1954, Golden, Colorado: Solar Energy Research Institute, May 1983.
2. Kelley, N.D., McKenna, H.E., Hemphill, R.R., Etter, C.L., Garrelts, R.L., and Linn, N.C., Acoustic Noise Associated with the MOD-1 Wind Turbine: Its Source, Impact, and Control, SERI TR-635-1166, Golden, Colorado: Solar Energy Research Institute, in preparation.

ANECHOIC WIND TUNNEL STUDY OF TURBULENCE
EFFECTS ON WIND TURBINE BROADBAND NOISE*

B. Loyd and W.L. Harris

Massachusetts Institute of Technology
 Cambridge, Massachusetts 02139

ABSTRACT

This paper describes recent results obtained at MIT on the experimental and theoretical modelling of aerodynamic broadband noise generated by a downwind rotor horizontal axis wind turbine. The aerodynamic broadband noise generated by the wind turbine rotor is attributed to the interaction of ingested turbulence with the rotor blades. The turbulence was generated in the MIT anechoic wind tunnel facility with the aid of biplanar grids of various sizes. The spectra and the intensity of the aerodynamic broadband noise have been studied as a function of parameters which characterize the turbulence and of wind turbine performance parameters. Specifically, the longitudinal integral scale of turbulence, the size scale of turbulence, the number of turbine blades, and free stream velocity were varied. Simultaneous measurements of acoustic and turbulence signals were made. The sound pressure level was found to vary directly with the integral scale of the ingested turbulence but not with its intensity level. A theoretical model based on unsteady aerodynamics is proposed.

NOMENCLATURE

B	Number of rotor blades
b	Rotor blade span
c	Rotor blade chord
c_0	Ambient speed of sound
$D_r(\phi, f)$	Power spectral density of the dipole radiation
f	Frequency
k_x	x component of turbulent wavenumber vector
m	Rotational harmonic
M_0	Rotational Mach number at radial position R_0
ρ_0	Ambient density
R_0	Radial location of the effective velocity
r	Radial position
$\langle S_{pp}(x, t) \rangle$	Radiation spectra
U_0	Velocity
x	Vector coordinate
Λ	Integral scale of turbulence
Λ_f	Longitudinal integral scale of turbulence
ϕ	Azimuthal angle
Ω	Rotational speed

I. INTRODUCTION

The potential advantages derived from wind power as a source of world energy needs are not independent of their environmental impact. The essential factor in such an environment impact is the negative aspects associated with the aerodynamic noise generated by

wind turbines^{1,2,3,4}. The aerodynamic noise generated by wind loading on the blades of wind turbine may be classified as: (1) Gustin noise resulting from Doppler modulation of the steady blade loads, (2) blade tower wake interaction noise generated by continued blade passage through the downwind wake of the wind turbine support tower, and (3) broadband noise due to blade interaction with incident turbulence. Previous research at MIT has addressed Gustin noise and blade tower wake interaction noise from a theoretical and experimental perspective^{3,4}. This paper presents results of our investigation of the effects of turbulence on wind turbine broadband noise.

II. EXPERIMENTAL APPARATUS

The MIT anechoic wind tunnel facility was used to investigate the effects of controlled free-stream turbulence on the broadband noise generated by a scaled model wind turbine. Turbulence of varying intensity and scale was generated in the wind tunnel test section by inserting biplanar grids of different sizes in the tunnel contraction section. The experimental apparatus used in obtaining and analyzing both turbulence and acoustic data is described.

II.A. THE M.I.T. ANECHOIC TUNNEL

The wind tunnel has a 1.52x2.29-m inlet open-jet test section which is enclosed in a 3.65x3.65x7.3-m anechoic chamber. The sides of the chamber were covered with Cremer blocks and the floor of the chamber was covered with 15-cm-thick polyurethane foam. The anechoic properties of the tunnel were measured and the acoustic cutoff frequency above which free-field conditions prevail was found to be 160 Hz. The effects of the shear layer of the open jet on refraction and scattering of acoustic waves were studied by using aeolian tones as sound source and were found to be insignificant under the present test conditions. The details of the aerodynamic and acoustic calibrations of the wind tunnel facility are described in Harris and *et al.*⁵

II.B. WIND TURBINE MODEL

Experiments were conducted on a 1/53 scale model of the NASA-DOE MOD-1 wind turbine. NASA 0012 model rotor blades were used. The blades have a 5.08 cm chord, -8° linear twist, and a radius of 59.6 cm.

II.C. TURBULENCE GENERATION

The grids employed in this study were designed based on the data of Baines and Peterson.⁶ The grids were biplanar consisting of bars of 1.91 cm with a mesh size of 15 cm and bars of 8.9 cm with a mesh size of 50.8 cm. The grid solidity were 0.23 and 0.32 respectively. The grid Reynolds number based on the lowest tunnel velocity were 9×10^4 and 3×10^5 , respectively.

*Presented at the DOE/NASA Wind Turbine Technology Workshop, May 8-10, 1984 in Cleveland, Ohio.

The longitudinal and vertical integral scales Λ_f and Λ_g of the grid generated turbulence were determined near the axis of rotor. For convenience, we estimated Λ_f from the Eulerian integral time scale τ_e . The values of τ_e were determined from the extrapolated zero intercept of the power spectra of longitudinal and vertical velocities. The length scales, then are given by

$$\Lambda_f = U_o \tau_{ef}; \quad \Lambda_g = U_o \tau_{eg} \quad (1)$$

The measured longitudinal and vertical integral scales of grid generated turbulence were observed to be independent of free-stream velocity. In absence of grids, the Eulerian time scales were very large and fluctuating. This resulted in large length scales that vary considerably with free-stream velocity, but do not follow any definite pattern.

The biplanar grids used to generate the controlled turbulence were located 2.08 m from the plane of the rotor. This corresponds to approximately 15 mesh lengths for the small grid and 4.6 mesh lengths for the larger grid. The controlled turbulence is assumed isotropic at the rotor plane. Characteristic turbulence data are given in Table 1.

II.D. INSTRUMENTATION

Data flow for all the experiments was from microphones and hot wire sensors to a magnetic tape and later from the magnetic tape to a spectrum analyzer.

The acoustic measurements were made on axis and in the plane of the rotor as shown in Fig. 1. Acoustic signals were measured using two 1/2 inch B&K microphones type 4133. Wind screens were used on both microphones. The on axis microphone was amplified with a B&K 2107 frequency analyzer, while the off axis microphone was amplified by a B&K 2604 microphone analyzer. The microphones were calibrated using a B&K piston phone type 4220.

The fluctuating velocity signals were measured with a DISA 55H24 S-type hot wire sensor. The probe was calibrated over the anticipated test velocities and the responses of both wires were found to be roughly linear. The probe was placed at 91.6% span 12 cm upstream of the blade of the rotor. DISA 55D05 constant temperature anemometers were used in conjunction with a DISA 55D15 linearizer. Both signals were monitored constantly with two (true) rms voltmeters type HP 3400 A. The gain control on one of the linearizers was used to achieve uniform sensitivity of both wires.

The X-wire signals were fed into a home-built sum and difference unit to yield the longitudinal and vertical components of the velocity. The signal from the summing unit was passed through a Krohn Hite model 3340 filter to eliminate the offset voltage inherent in the linearizer output signal. Acoustic, turbulence, rpm and flow speed measurements were made simultaneously. A schematic of instrumentation used in the acquisition of turbulence, acoustic, and rpm data is shown in Fig. 2.

The measured acoustic, turbulence, and rpm signals were recorded on magnetic tape with an Ampex FR1300 14 channel recorder. The recorded signals were

subsequently analyzed with a Nicolet 660B dual channel FFT analyzer and plotted on a Tektronix 4662 digital plotter. All of the data was analyzed by taking the averages of 50 time windows of the taped signal.

III. EXPERIMENTAL RESULTS

To investigate the effects of ingested turbulence on the emitted broadband noise, the turbine blade pitch, flow speed, and number of blades were fixed at 15°, 10.1 m/sec and 2 respectively while the controlled turbulence was varied. Typical results are shown in Figs. 3 and 4. Comparing Figs. 3 and 4 we observe that an increase in length scales along with a decrease in turbulence intensity, has a significant effect on the broadband noise spectrum. The smaller scale and higher intensity turbulence dominates the spectrum at the lower frequencies while the larger scale and lower intensity turbulence dominates at the higher frequencies. The longer length eddies tend to produce a more pronounced blade-to-blade correlation effect and leads to more positive and negative interference between acoustic waves generated by the wind turbine blades.

Figures 5 and 6 show the influence of free stream velocity on the radiated broadband noise. The observed increase in sound pressure level with increasing forward speed is attributed to the corresponding increase in the rms value of the turbulence in the tunnel with increased forward speed. Note the difference in rpm between Figs. 5 and 6. This difference is a result of both cases corresponding to a fixed blade pitch of 15°.

The relatively negligible effect of number of wind turbine rotor blades on the generated broadband noise is shown in Figs. 7 and 8. The main difference being an increase width of peak centered at approximately 3,000 Hz with increasing number of blades.

The off axis microphone verified the above results. The off axis microphone sound pressure level was always less than that of the on axis microphone confirming the dipole nature of the broadband noise. A typical comparison between on axis and off axis microphone readings is shown in Figs. 7 and 9.

IV. BROADBAND NOISE THEORY

When there is no significant blade-to-blade correlation Aravamudan and Harris' have shown that the spectrum of low-frequency broadband noise may be expressed as

$$\langle S_{op}(x, f) \rangle = \frac{f^2 \sin^2 \phi}{2U_o C^3 r^2 \rho_o (1+bf/U_o)} \quad (2)$$

$$\times \sum_{n=-\infty}^{\infty} D_r(f-n\Omega) J_n^2 \left\{ \frac{fR_o \sin \phi}{c_o} \right\}$$

where

$$D_r(f) = \frac{\tau_c^2 U_c^2 b^2 c^2 (0.4548)}{g^2} \omega_f^{2.4} \int_0^{\infty} dk_y \frac{\{[(f/U_o)^2 + k_y^2]^{1/2} + J_1^2 \{ (M_o^2 \pi c / B^2) [(f/U_o)^2 + k_y^2]^{1/2} \} + J_2^2 \{ (M_o^2 \pi c / B^2) [(f/U_o)^2 + k_y^2]^{1/2} \}\}}{\{1 + (2\pi^2 c / B^2) [(f/U_o)^2 + k_y^2]^{1/2}\} \{1 + 1.793 A_f^2 [(f/U_o)^2 + k_y^2]^{7/3}\}} \quad (3)$$

The two-dimensional model of rotor blade-turbulence interaction developed above is equivalent to exploiting the effective radius approach at 80% span, to assuming chordwise and spanwise compactness, and to a neglect of retarded time considerations associated with the sweep of the skewed gusts in the spanwise direction. Our objective in developing this model is to correlate the measured data. Additional experiments and calculations are in progress with a goal of correlating theory and experiment.

V. CONCLUSIONS

Measurements in the M.I.T. anechoic wind tunnel of broadband noise generated by a 1/53 scale model of the NASA-DOE MOD-1 wind turbine have been made. The experiments and related analytical development described in this paper are concerned with the effects of turbulence on broadband noise generated by a model wind turbine. Our measurements suggest the following:

1. The smaller scale and higher intensity turbulence dominates the broadband noise spectrum at the lower frequencies while the larger scale and lower intensity turbulence dominates at the higher frequencies.
2. The sound pressure level of the broadband noise spectrum increases with increasing forward speed due to the corresponding increase in the rms value of the turbulence in the tunnel.
3. Increasing the number of blades from two to three has a negligible effect on the sound pressure level of the broadband noise spectrum.
4. Off-axis microphone measurements confirm the dipole nature of the broadband noise generated by the model wind turbine.
5. A broadband noise model has been developed and is to be compared with experimental results.

REFERENCES

1. Stephens, D.G., Shepherd, K.P., Hubbard, A.H., and Grosveld, F.W., "Guide to the Evaluation of Human Exposure from Large Windturbines", NASA Technical Memorandum 83288.
2. Kelley, N.D., "Acoustic Noise Generation by the DOE/NASA MOD-1 Wind Turbine", Wind Turbine Dynamics, NASA Conference Publication 2185, pp. 375-388, 1981.
3. Marcus, E.N. and Harris, W.L., "An Experimental Study of Windturbine Noise from Blade-Tower Wake Interaction", AIAA 8th Aeroacoustics Conference, April 11-13, 1983, Atlanta, Georgia, AIAA-83-0691.

4. Martinez, R., Widnall, S.E., and Harris, W.L., "Predictions of Low-Frequency and Impulsive Sound Radiation from Horizontal-Axis Wind Turbines", Transactions of the ASME, Journal of Solar Energy Engineering, Vol. 104, pp. 124-130, May 1982.
5. Harris, W.L. and Lee, A., "Development of Experimental Techniques for the Study of Helicopter Rotor Noise", Aeroacoustics: Fan Noise and Control; Duct Acoustics; Rotor Noise, Edited by Schwartz, I.R. Volume 44, Progress in Astronautics and Aeronautics, AIAA: 1976, pp. 615-629.
6. Baines, W.D. and Peterson, E.G., "An Investigation of Flow Through Screens", Transactions of ASME, 73, pp. 467-480, 1951.
7. Aravamudan, K.S. and Harris, W.L., "Low Frequency Broadband Noise Generated by a Model Rotor", Journal of the Acoustical Society of America, 66, pp. 522-533, 1979.

ACKNOWLEDGEMENTS

This research was partially supported by the National Aeronautics and Space Administration under Grant NAG 3-378. Dr. W.A. Spera, NASA Lewis Research Center, performed as grant monitor.

Table 1:
 Characteristics of Turbulence $U_0 = 10.1$ m/sec

	Grid #0 (free stream)	Grid #1 1.92x15.38cm	Grid #2 8.97x51.28cm
Longitudinal Scale (cm)	34.4	9.6	14.6
Vertical Scale (cm)	20.4	5.8	9.3
Ratio of Λ_v/Λ_l	0.79	0.61	0.64
Intensity	1.7%	6.25%	11%
Solidity	0	0.23	0.32
Grid Reynolds Number	--	9×10^4	3×10^5

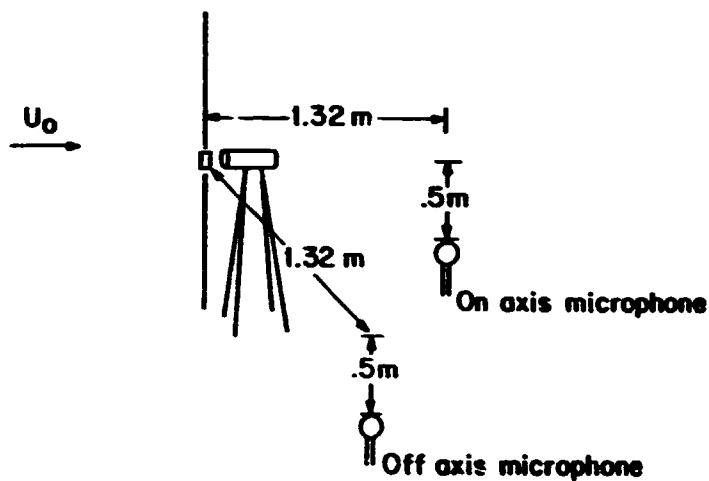


FIGURE 1 - POSITION OF MICROPHONES

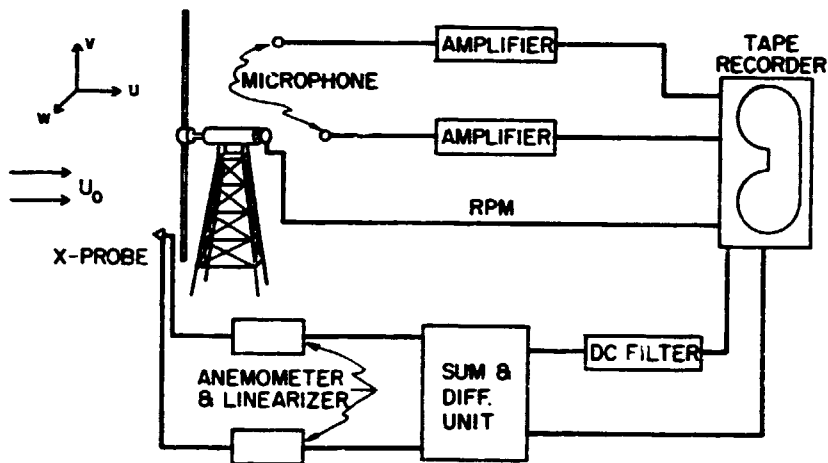


FIGURE 2 - SCHEMATIC OF INSTRUMENTATION

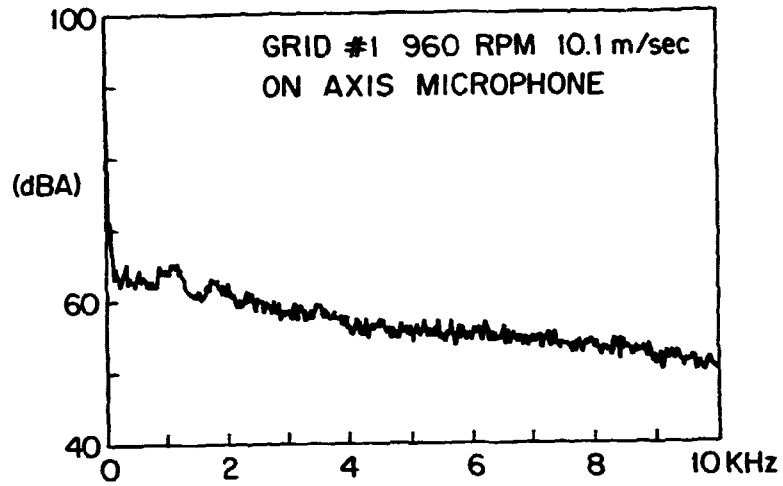


FIGURE 3 - SOUND PRESSURE LEVEL WITH GRID #1

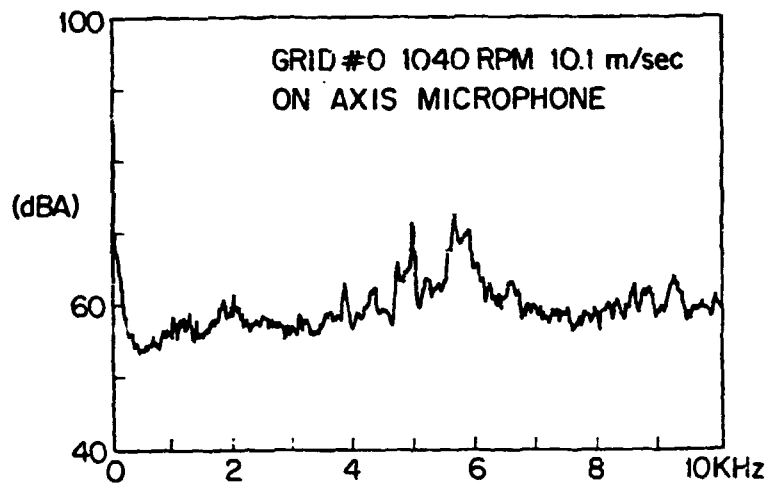


FIGURE 4 - SOUND PRESSURE LEVEL WITH NO GRID

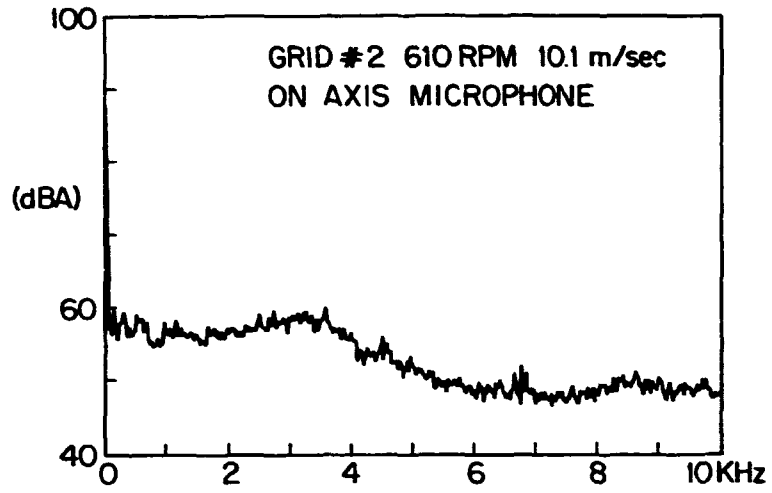


FIGURE 5 - EFFECT OF FREE STREAM VELOCITY ON SOUND PRESSURE LEVEL, $U_o = 10.1 \text{ m/s}$

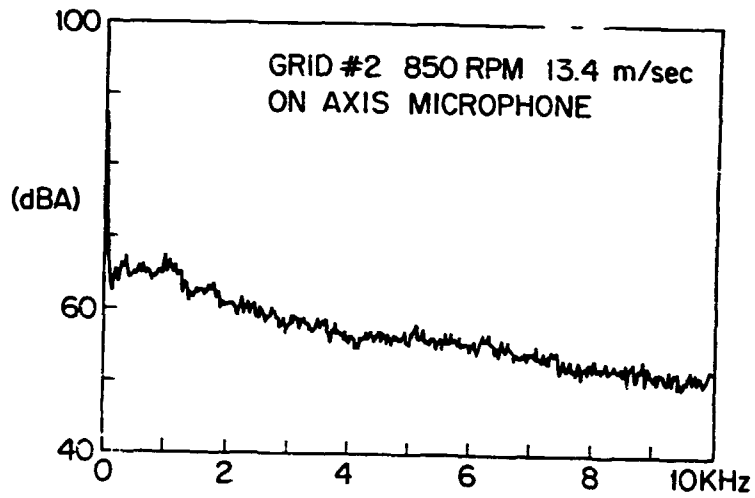


FIGURE - 6 EFFECT OF FREE STREAM VELOCITY ON SOUND PRESSURE LEVEL, $U_o = 13.4 \text{ m/s}$

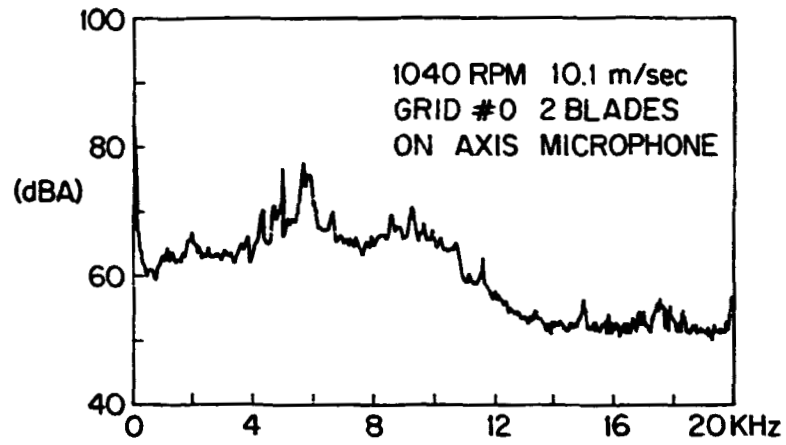


FIGURE 7 - EFFECT OF NUMBER OF BLADES ON SOUND PRESSURE LEVEL, B = 2

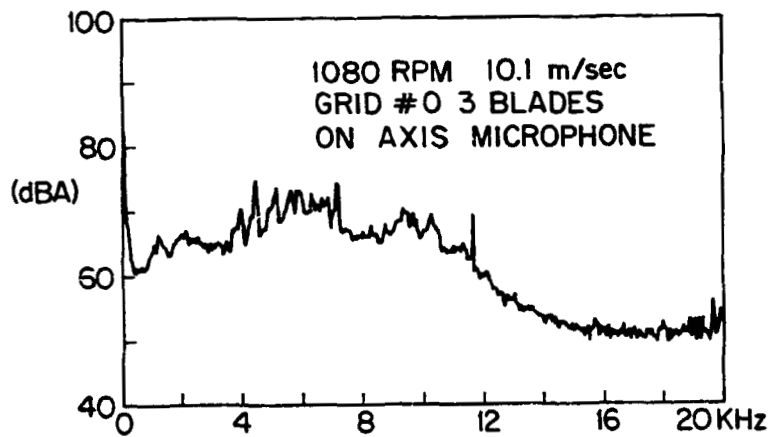


FIGURE 8 - EFFECT OF NUMBER OF BLADES ON SOUND PRESSURE LEVEL, B = 3

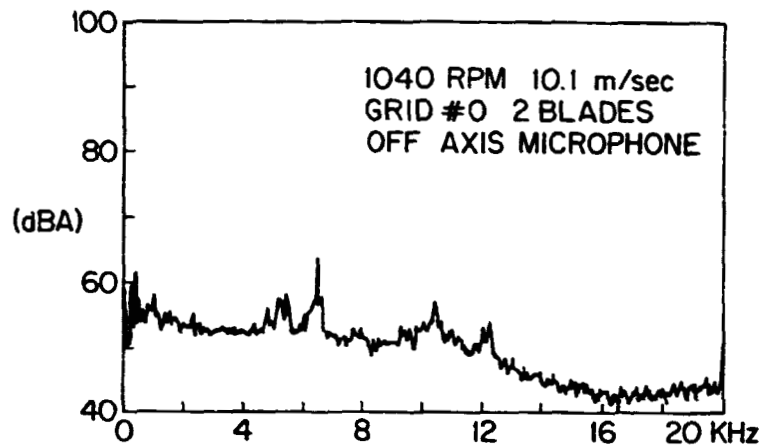


FIGURE 9 - SOUND PRESSURE LEVEL, NO GRID, B = 2, OFF AXIS MICROPHONES

REPORT DOCUMENTATION PAGE			Form Approved OMB No. 0704-0188	
Public reporting burden for this collection of information is estimated to average 1 hour per response, including the time for reviewing instructions, searching existing data sources, gathering and maintaining the data needed, and completing and reviewing the collection of information. Send comments regarding this burden estimate or any other aspect of this collection of information, including suggestions for reducing this burden, to Washington Headquarters Services, Directorate for Information Operations and Reports, 1215 Jefferson Davis Highway, Suite 1204, Arlington, VA 22202-4302, and to the Office of Management and Budget, Paperwork Reduction Project (0704-0188), Washington, DC 20503.				
1. AGENCY USE ONLY (Leave blank)	2. REPORT DATE May 1995	3. REPORT TYPE AND DATES COVERED Final Contractor Report		
4. TITLE AND SUBTITLE Collected Papers on Wind Turbine Technology			5. FUNDING NUMBERS WU-776-33-41 C-NAS3-25776	
6. AUTHOR(S) David A. Spera, editor				
7. PERFORMING ORGANIZATION NAME(S) AND ADDRESS(ES) DASCON Engineering 29301 Wolf Rd. Bay Village, Ohio 44140			8. PERFORMING ORGANIZATION REPORT NUMBER E-9439	
9. SPONSORING/MONITORING AGENCY NAME(S) AND ADDRESS(ES) National Aeronautics and Space Administration Lewis Research Center Cleveland, Ohio 44135-3191			10. SPONSORING/MONITORING AGENCY REPORT NUMBER NASA CR-195432 DOE/NASA/5776-2	
11. SUPPLEMENTARY NOTES Prepared under Interagency Agreement DE-AI01-76ET20320. Project Manager, Larry H. Gordon, Aerospace Technology Facilities Division, NASA Lewis Research Center, organization code 5700, (216) 977-7448.				
12a. DISTRIBUTION/AVAILABILITY STATEMENT Unclassified - Unlimited Subject Category 44 This publication is available from the NASA Center for Aerospace Information, (301) 621-0390.			12b. DISTRIBUTION CODE DOE Category UC-60	
13. ABSTRACT (Maximum 200 words) A major program of research and development projects on wind turbines for generating electricity was conducted at the NASA Lewis Research Center from 1973 to 1988. Most of these projects were sponsored by the U.S. Department of Energy (DOE), as a major element of its Federal Wind Energy Program. One other large-scale wind turbine project was sponsored by the Bureau of Reclamation of the U.S. Department of Interior (DOI). From 1988 to 1995, NASA wind energy activities have been directed toward the transfer of technology to commercial and academic organizations. As part of these technology transfer activities, a total of 22 previously unpublished manuscripts have been assembled and are presented here in order to share the results of valuable research on wind turbines with the wind energy community. A wide variety of wind turbine technology topics are discussed, including the following: Wind and wake models-3 papers; Airfoil properties-5 papers; Structural analysis and testing-5 papers; Control systems-3 papers; Variable-speed generators-3 papers; Acoustic noise-3 papers. Both experimental and theoretical investigations are described, with results which are relevant to the design, analysis, and testing of modern wind turbines. Wind energy activities sponsored under or related to the NASA/DOE wind turbine development program are documented in approximately 620 publications by over 520 authors and coauthors. A complete listing of citations to these publications, many with abstracts, can be obtained from the following reference: Spera, D.A., 1995, <i>Bibliography of NASA-Related Publications on Wind Turbine Technology, 1973-1995</i> , NASA CR-195462, DOE/NASA/5776-3, Cleveland, Ohio: NASA Lewis Research Center.				
14. SUBJECT TERMS Wind turbine; Wind energy; Wind power; Airfoils; Wind models; Control systems; Acoustic noise; Structural loads; Variable-speed generators			15. NUMBER OF PAGES 243	16. PRICE CODE A11
17. SECURITY CLASSIFICATION OF REPORT Unclassified	18. SECURITY CLASSIFICATION OF THIS PAGE Unclassified	19. SECURITY CLASSIFICATION OF ABSTRACT Unclassified	20. LIMITATION OF ABSTRACT	